Title

A study of the stellar population and dynamical environment of the Milky Way Galactic center with near-infrared adaptive optics photometry

Author

Gautam, Abhimat Krishna

Publication Date

2020

Peer reviewed|Thesis/dissertation

UNIVERSITY OF CALIFORNIA
Los Angeles

A study of the stellar population and dynamical environment of the Milky Way Galactic center with near-infrared adaptive optics photometry

A dissertation submitted in partial satisfaction
of the requirements for the degree
Doctor of Philosophy in Astronomy and Astrophysics

by

Abhimat Krishna Gautam

2020

ABSTRACT OF THE DISSERTATION

A study of the stellar population and dynamical environment
of the Milky Way Galactic center with
near-infrared adaptive optics photometry

by

Abhimat Krishna Gautam
Doctor of Philosophy in Astronomy and Astrophysics
University of California, Los Angeles, 2020
Professor Andrea M. Ghez, Chair

The proximity of the Milky Way Galactic center (GC) allows a unique perspective into how supermassive black holes (SMBHs) affect their surrounding stellar population. Several uncertainties still remain about the stellar population at the GC, notably the frequency of binary star systems at the GC and the distribution of dark stellar remnants surrounding the SMBH. In this thesis, we used over 13 years of Keck Observatory adaptive optics (AO) photometric flux measurements of the stellar population within approximately a half parsec of the GC SMBH in an effort to address the uncertainties about the GC stellar binary population and to probe the density of unseen stars or compact objects near the SMBH.

First, we present an ≈ 11.5 year adaptive optics (AO) study of stellar variability and search for eclipsing binaries in the central ~ 0.4 pc ($\sim 10''$) of the Milky Way nuclear star cluster. In the study, we measured the photometry of 563 stars using the Keck II NIRC2 imager (K'-band, $\lambda_0 = 2.124$ µm). We achieved a photometric uncertainty floor of $\Delta m_{K'} \sim 0.03$ ($\approx 3\%$), comparable to the highest precision achieved in other AO studies. Approximately

half of our sample ($50 \pm 2\%$) shows variability. $52 \pm 5\%$ of known early-type young stars and $43 \pm 4\%$ of known late-type giants are variable. These variability fractions are higher than those of other young, massive star populations or late-type giants in globular clusters, and can be largely explained by two factors. First, our experiment time baseline is sensitive to long-term intrinsic stellar variability. Second, the proper motion of stars behind spatial inhomogeneities in the foreground extinction screen can lead to variability. We recovered the two known Galactic center eclipsing binary systems: IRS 16SW and S4-258 (E60). We constrained the Galactic center eclipsing binary fraction of known early-type stars to be at least $2.4 \pm 1.7\%$. We found no evidence of an eclipsing binary among the young S-stars nor among the young stellar disk members. These results are consistent with the local OB eclipsing binary fraction. We additionally identified a new periodic variable at the GC, S2-36, with a 39.43 day photometric period.

Second, we present the discovery of the first known eclipsing, ellipsoidal binary star system (S2-36) at the GC, with a binary orbital period of $\approx$ 78.8 days at a projected distance of $\approx$ 2 arcsec from Sgr A*. As the first dynamically soft stellar binary discovered in the region, S2-36 offers powerful constraints on the dark cusp density within $\sim$ 0.1 pc of the SMBH. We used new and existing near-infrared adaptive optics Keck Observatory imaging data collected over 13 years to measure the photometric and astrometric properties of S2-36. S2-36's proper motion suggests a distance $\lesssim$ 0.2 pc from the SMBH. A trended multi-band periodicity search of the photometric measurements in the K'- ($\lambda_0 = 2.124$ µm) and H-band ($\lambda_0 = 1.633$ µm) reveals a periodic signal with false-alarm probability of less than 10^{-4}. These results, combined with our flux and color measurements, suggest S2-36 is an ellipsoidal binary at the GC. Best-fit astrophysical binary models to the observed light curve consist of two red giant stars where the photometric variability originates from ellipsoidal variation and eclipses. However, with photometry measurements alone, our model fits have degeneracies in age and metallicity of the component stars (age $\approx$ 3 to 13.5 Gyr, [Fe/H] ≈ -1.5 to $+0.5$). The presence of an old, dynamically soft binary at the GC over its entire lifetime

implies few encounters with sources that would disrupt the binary. Under the assumption that the binary has spent its lifetime in the GC environment, the binary's survival places an upper limit of $\sim 10^4$ stellar-mass black holes ($M \sim 10 M_\odot$) within ≈ 0.1 pc of the SMBH, and a local two-body relaxation time $\gtrsim 5 \times 10^8$ yr. Our observations are consistent with X-ray estimates of compact objects in the GC and provide a powerful new constraint on the presence of the dark cusp at the GC.

Finally, we present new methodology and initial results for a photometric study to constrain the stellar binary fraction of the GC. With 873 stars, a larger stellar sample than previously ever used for a photometric binary search of GC stars, we detected a total of five likely periodic signals with our updated methods; two of the likely stars (S4-308 and S3-438) have not been previously identified as periodic variables in any previous study. We then provide an overview of the calculation of our experiment's sensitivity to photometric binaries and detail a Bayesian framework to combine the sensitivity and our experiment's detections to constrain the intrinsic GC stellar binary fraction. The methods outlined can be employed on future photometric studies of the GC stellar population to constrain its binary fraction, particularly for short-period binaries.

The dissertation of Abhimat Krishna Gautam is approved.

Tuan Do

Bradley M. S. Hansen

Smadar Naoz

Mark R. Morris

Andrea M. Ghez, Committee Chair

University of California, Los Angeles

2020

TABLE OF CONTENTS

1 Introduction **1**

1.1 Background and motivation 2

1.1.1 Limitations of previous photometric studies of the GC 6

1.2 Stellar variability in the Nuclear Star Cluster 8

1.3 The binary fraction of young stars at the Galactic center 8

1.4 Probing dark cusp predictions with binary evaporation 10

2 An Adaptive Optics Survey of Stellar Variability at the Galactic Center **15**

2.1 Introduction 15

2.2 Observations, Photometric Calibration, and Stellar Sample 22

2.2.1 Observations and Data Reduction 22

2.2.2 Systematics from Stellar Confusion and Resolved Sources 25

2.2.3 Artifact Sources from Elongated PSFs 26

2.2.4 Photometric Calibration 27

2.2.5 Final Photometric Quality 31

2.2.6 Stellar Sample 33

2.3 Stellar Variability 34

2.3.1 Identifying Variable Stars 34

2.3.2 Deriving the Variability Fraction 35

2.4 Periodic Variability 37

2.4.1 Periodicity Search Implementation 38

2.4.2 Definition of Significance 39

2.4.3 Aliasing in Periodicity Searches 39

2.5 Results 41

2.5.1 Variability Fraction 48

2.5.2 Periodically Variable Stars . . . 48
2.6 Discussion . . . 59
2.6.1 High stellar variability fraction at the Galactic center . . . 59
2.6.2 Constraints on the eclipsing binary fraction of young stars . . . 70
2.6.3 Other periodic and variable stars . . . 73
2.6.4 The precision of single PSF AO photometry . . . 75
2.7 Conclusion . . . 76
2.8 Appendix 2A: Photometric Calibration Details . . . 78
2.8.1 Reference Flux Bandpass Correction . . . 78
2.8.2 Iterative Calibrator Selection . . . 79
2.8.3 Local Photometric Correction . . . 84
2.9 Appendix 2B: Variability Study Details . . . 87
2.10 Appendix 2C: Periodicity Methodology Details . . . 88
2.10.1 Period Search Range . . . 88
2.10.2 Removal of long-term linear trends . . . 89

3 Identification of an Old Ellipsoidal Stellar Binary at the Milky Way Galactic Center and Dynamical Constraints on a Dark Cusp . . . 92
3.1 Introduction . . . 92
3.2 New observations and existing *GCOI* data . . . 96
3.2.1 Photometric calibration . . . 96
3.2.2 Astrometric measurements . . . 98
3.3 Data analysis . . . 98
3.3.1 Photometric model . . . 99
3.3.2 Astrometry proper motion model . . . 105
3.3.3 Comparison with NIR stellar color of nearby stars . . . 111
3.4 Results . . . 111
3.4.1 Identification of source type . . . 111

3.4.2 Stellar binary modeling . . . 120
3.5 Discussion . . . 131
3.5.1 Dynamical constraints on massive compact remnants and a dark cusp in the GC . . . 132
3.5.2 Migrated Binary System . . . 144
3.5.3 Future observational constraints . . . 145
3.6 Conclusions . . . 146
3.7 Appendix 3A: Photometric Calibration Details . . . 150
3.8 Appendix 3B: Multi-band Long-Term Slope Exploration . . . 153
3.9 Appendix 3C: Searching for periodicity in astrometric measurements . . . 155

4 Constraining the intrinsic stellar binary fraction of the Milky Way Galactic center with photometric monitoring . . . 157
4.1 Introduction . . . 157
4.2 Periodicity search improvements . . . 158
4.3 Constraints on intrinsic binary fraction from photometric detections with Bayesian inference . . . 168
4.3.1 Mock light curve generation of a stellar binary population . . . 168
4.3.2 Finding the best-fit population binary fraction . . . 172
4.4 Conclusion . . . 173

5 Conclusions . . . 175
5.1 Prospects for GC binary fraction constraints . . . 177
5.2 Tighter limits on the dark cusp with binary evaporation . . . 179

A Stellar Photometric Catalog . . . 181
A.1 Light curves of variability study sample . . . 199
A.2 Periodic Variable Detections . . . 341

A.2.1 Likely Periodic Variables 341
A.2.2 Possible Periodic Signals 341

LIST OF FIGURES

1.1 An example near-infrared (K'-band) laser guide star adaptive optics image of the Milky Way Galactic center (GC) from the *Galactic Center Orbits Initiative* dataset. This image is constructed from observations taken on 2015 August 10 and spans a field of view $10'' \times 10''$ (≈ 0.4 pc $\times \approx 0.4$ pc in projected distance at the GC). Sgr A* is marked on the image, and corresponds to the location of the supermassive black hole. 5

2.1 Calibration stars used for our initial and final calibration iterations in the variability analysis are circled and labeled (initial calibration iteration on left and final calibration iteration on right). The white star symbol indicates the position of Sgr A*. The dashed lines indicate the boundaries of the four quadrants centered on Sgr A*. These quadrants were used to select calibration stars distributed across our field of view. The background image is from the 10 August 2015 observation. We chose the final calibration stars so that at least one and no more than 3 would lie in each of the four quadrants. Dashed circles around each calibration star indicate $0.25''$ around the position of each star. We selected the final calibration stars so that none were located within $\approx 0.25''$ of each other. . . 27

2.2 The variability of our stellar sample plotted on our field of view. The color of each point on the maps is determined by the mean of the $\chi^2_{\rm red}$ of the nearest 20 stars to the point having $\chi^2_{\rm red} < 10$ (so as to not affect the mean value with highly variable stars). The star shape indicates the position of Sgr A* while the green dots indicate the positions of our photometric calibrators. The map on the left is generated before our local correction is applied, and the map on the right is generated after our local corrections have been applied. Before the local correction is applied, the outer regions of the field demonstrate higher variability as expected from anisoplanatic effects on the PSF shape. After the local correction is applied, this spatial preference for variability is largely removed. Since this process removes systematic contributions to variability, overall $\chi^2_{\rm red}$ values are lowered throughout the field of view. 29

2.3 Median photometric uncertainty of the stellar sample in this work, identified in at least 16 nights of observation, plotted by mean magnitude. Known early-type and late-type stars are indicated as dots colored blue and red, respectively. The binned median magnitude error identifies this work's photometric precision as a function of stellar magnitude. Also shown for comparison is binned median magnitude error from previous work studying variability at the Galactic Center by Rafelski et al. (2007) using Keck speckle photometry data. The values plotted here are calculated after conducting the local photometry correction on our dataset, detailed in Section 2.8.3. The floor of the photometric uncertainty begins to rise for stars fainter than $m_{K'} \sim 16$. Based on this, we limited the sample for our variability and periodicity search to stars with $\bar{m}_{K'} \leq 16$, indicated by the vertical dashed line. 30

2.4 The stellar sample used in the photometric variability analysis, consisting of $\bar{m}_{K'} < 16$ stars detected in at least 16 nights without confusion. The background image is from the 2012-05-15 observation. Blue, red, and orange circles indicate spectrally typed early-type, late-type, and unknown type stars respectively. Green circles indicate the stellar sample studied in the previous stellar variability analysis by Rafelski et al. (2007) using Keck Observatory speckle data. The dashed circles indicate the region cut around resolved sources where flux measurements of sources could be biased by the presence of the resolved source. The white star symbol indicates the position of Sgr A*, the location of the supermassive black hole. The large dotted circle indicates the region of our sample used to study the projected positional dependence of variability, out to 3″ from Sgr A*. 1″ corresponds to a projected distance ≈ 0.04 pc at the Galactic center. 32

2.5 Binned $\chi^2_{\rm red}$ distribution for our stellar sample identified in at least 23 observations. For variability, we drew a cut in this distribution at 5σ, which for stars identified in 16 observations (with $\nu = 16 - 1 = 15$) corresponds to $\chi^2_{\rm red} > 3.87$. Stars identified in a greater number of observations have a corresponding higher ν resulting in a 5σ cut for variability at lower $\chi^2_{\rm red}$ values, going down to $\chi^2_{\rm red} > 2.40$ for stars identified in all 45 nights. These $\chi^2_{\rm red}$ cuts for variability depending on the number of nights are indicated by the vertical shaded region. In this sample with the 5σ variability cut, $50 \pm 2\%$ of stars are variable. 41

2.6 Same as Figure 2.5, but for our spectroscopically confirmed early-type stellar sample (left) and late-type stellar sample (right) identified in at least 16 observations. $52 \pm 5\%$ of spectroscopically confirmed early-type stars are variable and $43 \pm 4\%$ of spectroscopically confirmed late-type stars are variable. The $\chi^2_{\rm red}$ cuts for variability depending on the number of nights are indicated by the vertical shaded region. 42

2.7 The dashed line indicates our 5σ $\chi^2_{\rm red}$ cut for variability as a function of number of nights. The stars identified as variable with this cut are in the shaded gray region. Dots colored blue/red are spectroscopically confirmed early-/late-type stars, while black dots correspond to stars that have unknown type. 43

2.8 *Top:* The variability fraction as a function of projected distance from Sgr A*, R. The solid black lines indicate the median 2σ region of this relationship using stars with $R \leq 3''$ from Sgr A*. *Bottom:* The surface density distribution of our non-variable and variable star populations as a function of projected distance from Sgr A*, $\Sigma_n(R)$ and $\Sigma_v(R)$. Solid lines indicate median fit across all MCMC samples and the shaded regions indicate 2σ significance regions of this fit. 44

2.9 *Top:* Variability fraction as a function of observed magnitude, m. The solid black lines indicate the median 2σ region of this relationship using our entire stellar sample across all our MCMC samples. The blue and red lines indicate the same regions for the known young- and late-type stars in our stellar sample. The dotted lines indicate the 1σ constraints on the overall variability fraction in our sample. *Bottom:* Probability distribution of our non-variable and variable star populations as a function of observed magnitude, $p_n(m)$ and $p_v(m)$. Solid lines indicate median fit across all MCMC samples and the shaded regions indicate 2σ significance regions of this fit. The non-variable and variable star populations in our data are shown as binned histograms. 45

2.10 Stars identified as variable on our experiment's field of view. Blue, red, and orange circles indicate spectrally typed early-type, late-type, or unknown type variable stars respectively. The background image is from the 2012-05-15 observation. . 46

2.11 Periodicity detections that pass the variability, periodicity, and frequency cuts in our search, with bootstrap false alarm test significance plotted against the variability amplitude. For clarity, only the most significant periodicity search detection is plotted for stars that have multiple detections passing the variability, periodicity, and frequency cuts. The stars that we identify as *likely periodic variables* (IRS 16SW, S2-36, and S4-258) stand out distinctly in significance and amplitude from other possible periodic detections identified in our experiment. . 53

2.12 Light curves (*left*) and periodograms (*right*) for the likely periodic variable stars IRS 16SW, S2-36, and S4-258. The horizontal dashed lines in the light curves indicate the weighted mean magnitude. The horizontal dashed green lines in the periodograms indicate the bootstrap test significance levels, while the vertical dashed red lines indicate periodogram peaks above 80% bootstrap significance. . 55

2.13 *Top:* An image of the field near S2-36 from the 2017-08-11 observation. S2-36 is circled in red, while nearby stars brighter than $m_{K'} = 14.5$ are circled in blue. The white star symbol indicates the position of Sgr A*, the location of the supermassive black hole. This observation is highlighted in the phased light curve as the red point. *Bottom:* Phased light curve of S2-36 at the 39.43 day period found in the periodicity analysis. The best fit first order sinusoid model to the observations is overlaid. The horizontal line and surrounding shaded region indicate the fit mean magnitude and its uncertainty, respectively. The red point indicates the observation highlighted on top. 56

2.14 Variability fraction as a function of experiment time baseline for NIR studies of resolved young, massive star populations (*left*) and of late-type, globular cluster (*right*). Variability fractions for the Galactic center young (*left*) and old (*right*) stars derived in this work (entire sample and smaller time baseline subsamples) are shown as black points. 62

2.15 *Left:* The cumulative distribution of proper motion velocity in our sample of stars, outside of an arcsecond of Sgr A*. We divided these stars into three groups, with the same number of stars in each group. This grouping helps select stars in the high proper motion tail of the distribution as the *fast* stars. Notably, the *fast* stars have proper motions comparable to or higher than that of the Galactic center magnetar, PSR J1745-2900, indicated by the vertical line. *Right:* The cumulative distribution of our variability metric, $\chi^2_{\rm red}$, amongst the three proper motion groups of stars. We found that the $\chi^2_{\rm red}$ distribution of the *slow* stars is significantly different from those of both the *medium* and *fast* stars ($> 2\sigma$ and $> 3\sigma$, respectively), while there is no significant difference amongst the distribution of *medium* and *fast* stars ($< 1\sigma$). 63

2.16 The young stars in our sample, indicated on the 2012-05-15 observation. We identify here the young disk and S-Star stellar populations from our sample. The young eclipsing binary systems detected in this experiment are labelled: IRS 16SW (Ott et al., 1999; Peeples et al., 2007; Rafelski et al., 2007) and S4-258 (E60, discovered by Pfuhl et al., 2014). We do not detect any eclipsing binary systems among the disk stars nor the young S-Star stellar populations. The star symbol indicates the location of Sgr A*, and 1 arcsec corresponds to a projected distance of ≈ 0.04 pc at the Galactic center distance. 69

2.17 *Top:* An image of the field near S4-129 from the 2010-07-06 observation. During this observation, S4-129 increased in brightness by ≈ 1.2 magnitudes compared to other observations near in time. Visual inspection of the field in this and other observations near in time did not reveal any sources of potential stellar confusion. S4-129 is circled in red, while nearby stars brighter than $m_{K'} = 14.5$ are circled in blue. This observation is highlighted in the light curve as the red point. *Bottom:* Light curve of S4-129 over our experiment's entire time baseline. The red point indicates the observation highlighted on top, during which we observed the brightening. 72

2.18 Light curves of the final calibration stars used in the variability analysis. Flux measurements before application of the local photometric correction are indicated in orange and flux measurements after application of the local photometric correction are indicated in black. The horizontal dashed line indicates the weighted mean magnitude. 83

2.19 *Left:* K' magnitude zeropoint corrections from the photometric calibration used in this work. The zeropoint correction is calculated as the mean of the difference between the measured photometric flux of the calibration stars and their recorded value. *Right:* The errors in the K' magnitude zeropoint corrections used in this work, calculated as the variance of the zeropoint magnitude adjustment in each observation. This zeropoint correction error in each observation dominates the photometric uncertainty in our measurements, and the median zeropoint correction error (dashed line) across our observations is $\sigma_{m_{K'}} \sim 0.025$. 84

2.20 Four example target stars of similar brightness from different areas of our field selected to highlight our local photometry correction. Each curve displays the residual of a star's flux in an observation from its respective mean magnitude across all observations while shaded regions indicate uncertainty in flux. Blue curves indicate the residuals for the four example target stars, while the black curves in each plot indicate the residuals for all the local stars for the target star. Small trends in measured flux correlate across target stars and their respective local stars, suggesting a local photometric bias. The red curve indicates the median residual of the local stars, which is subtracted from the flux measurements of the target star to correct for the photometric bias. The green curves indicate the residuals for the four example target stars corrected for the photometric bias, and include the additional additive uncertainty during the local correction step. 85

2.21 The Lomb-Scargle window power spectrum computed for our experiment's observation times at our periodicity search's frequency spacing is shown in the plots on the left. Note that frequencies larger than 1 day^{-1} are prone to aliasing and at periods larger than 10^4 days most signals will appear periodic due to this range being much larger than our overall observing time baseline. Our periodicity search range of 1.11 – 10,000 days is highlighted in white on the left plots and is zoomed in for more detail in the plots on the right. 88

2.22 S4-258 (E60: Pfuhl et al., 2014) is an eclipsing binary system at the Galactic Center. The left plot shows the light curve from S4-258 across our observations, where the dashed black line indicates the weighted mean magnitude, $\bar{m}_{K'}$, and solid gray line indicates the best-fit linear model to the data. This linear model can indicate a long-term dimming of the binary system. The right plot shows the same data, with the long-term linear dimming trend removed. 89

2.23 Lomb-Scargle periodogram of S4-258's light curve. The left plot shows the periodogram computed from our observations, while the right plot shows the periodogram once the long-term linear dimming trend is removed. The 1.1380 day peak in the periodogram constructed from the detrended light curve corresponds to the 2.2760 day binary period of the system. The 8.0637 day peak corresponds to an alias of the binary period. Removing the long-term linear dimming trend allows the binary period of the system and its alias to be detected. 90

2.24 Phased light curve of S4-258 at its binary period of 2.2761 days. The left plot shows the phased light curve from our observations before detrending, while the right plot shows the same light curve with the long-term linear dimming trend removed (shown in Figure 2.22). 91

2.25 Light curve (left) and periodograms (right) for the star S4-172. The horizontal dashed line in the light curve indicates the weighted mean magnitude. The horizontal dashed green lines in the periodograms indicate the bootstrap test significance levels, while the vertical dashed red lines indicate periodogram peaks above 80% bootstrap significance. S4-172 is an example where the long-term variability (corresponding to a peak $\sim$ 3000 days) is aliased as powerful peaks in the periodogram at shorter periods. 91

3.1 Keck NIRC2 photometric measurements for S2-36, in the K'- (top panels) and H-band (bottom panels). The left panels show the S2-36 light curve over our observation time baseline. The solid colored lines show the long-term linear trend components of the best-fit trended sinusoid model in each band, with 3σ uncertainty in the linear fit indicated by the shaded regions. The right panels show the same photometric data phased to $2\times$ the best-fit period from our trended Lomb-Scargle analysis and with the best-fit long-term linear trend removed. The solid, colored lines in each panel indicate the best-fit sinusoid model to the observed data, with 3σ uncertainty in the sinusoid fit indicated by the shaded regions. The trended, periodic model plotted here is the 4 parameter model (detailed in Section 3.3.1), which includes only the *base model*. 99

3.2 Trended, multi-band Lomb-Scargle periodogram for the S2-36 photometric measurements. The left and right panels draw the periodogram with respect to frequency and period of variability, respectively. The horizontal dashed green lines indicate the bootstrap test significance level. The vertical dashed orange lines indicate the periodogram peaks above 80% bootstrap test significance. The most significant peak in the periodogram is at 39.45 days or 0.0253 day^{-1}. The second peak at 1.02 days or 0.9774 day^{-1} corresponds to a sidereal day alias of the 39.45 day signal. 100

3.3 An image of the field near S2-36 from the 2009 May 4 observation. S2-36 is circled in the center of the image, and the location of the supermassive black hole at Sgr A* is indicated by the concentric circles. S2-36 is located $\approx 2.05''$ ENE of Sgr A* in projected distance. The linear (i.e. velocity) term of S2-36's accelerating proper motion model fit is indicated by the white arrow. The velocity term of S2-36's proper motion is 7.21 ± 0.06 mas/yr, relative to Sgr A*. S2-36 is moving approximately towards the northwest relative to Sgr A*. 107

3.4 A NIR color overview of the star S2-36 and its nearest astrometric neighbors. The upper left panel shows the location of S2-36 (green) on the field of view. The circled stars are located within 2 arcseconds of S2-36 and have mean magnitudes within 4 K' magnitudes of S2-36. Using the Schödel et al. (2010) photometric catalog, we constructed color-magnitude diagrams of the circled stars: in K_S and H filters (upper right panel) and in K_S and L filters (lower left panel). We also show the $H - K_S$ and $K_S - L$ color-color diagram (lower right panel). S2-36's observed NIR color relative to that of the nearby stellar population indicates that the star is likely a member of the nuclear star cluster and not a foreground or background star. 110

3.5 The K'-band apparent magnitude of different classes of periodic variability if located at the Galactic center distance and with $H - K'$ color and variability period as observed for S2-36. S2-36's K'-band apparent magnitude, with 1σ uncertainties, is shown as a vertical black bar. Besides ellipsoidal binaries, all periodic variability classes if located at the Galactic center would be expected to have fluxes much brighter than what is observed for S2-36. Only the ellipsoidal binary periodic variability class results in expected flux consistent with S2-36's observed K'-band flux. 116

3.6 The K'-band extinction and distance estimates of known periodic variable classes at S2-36's period. All periodic variability classes are shown with their respective 3σ estimate contours. The K'-band extinction for each class is calculated using our observed $H - K'$ color for S2-36, and the distance estimate uses both the observed $H - K'$ color and K'-band flux for S2-36. For comparison, the GC distance (Do et al., 2019, 1σ) and line-of-sight K'-band extinction towards S2-36 in the Galactic center (Schödel et al., 2010, 3σ) are plotted with their respective uncertainties as thick black lines. Furthermore, we plot the expected K'-band extinction from Galactic dust maps towards the Galactic center as the Grey band (Green et al., 2019, 3σ). Only the ellipsoidal binary extinction and distance estimates are consistent with those measured for the GC. Other periodic variability class extinction and distance estimates lie in an unphysical regime where, in order to be consistent with S2-36's photometric observations, they require much larger distances than the GC but do not expect a correspondingly high extinction. . . 117

3.7 Same as Figure 3.6, but only showing the two variability classes with the lowest distance estimates (ellipsoidal binaries and Type II Cepheids). 118

3.8 The best-fit binary model at age = 12.8 Gyr, [Fe/H] = 0.5. The top panel shows a mesh visualization of the model binary system on the plane of the sky at phase of 0.25. The axes are plotted in units of solar radii. The bottom panels show the K'-band and H-band model light curves for the best-fit model (red and blue solid lines, respectively). Our observations in each of these wavebands are plotted as the black points. 125

3.9 Residuals from the median model value for our age = 12.8 Gyr, [Fe/H] = 0.5 binary models. The residuals of our observed flux values from the median S2-36 binary model are shown in black. The colored bands indicate the 3σ (99.7%) uncertainty of our model residual magnitudes (red: K'-band, blue: H-band). . . 126

3.10 Corner plot showing the posterior distributions of all parameters estimated during the MCMC fitting procedure for the age = 12.8 Gyr, [Fe/H] = 0.5 binary models. A total of seven parameters were fit at each age, metallicity trial. The best-fit parameters (i.e., the parameters which yielded the maximum likelihood during fitting) in this age, metallicity trial are indicated in red. The binary model with these best-fit parameters is shown in Figure 3.8. 127

3.11 The $\chi^2_{\rm red}$ of the best-fit in each of our binary model light curve fitting trials, organized by the age and metallicity of each test (each trial's assumed age and metallicity are indicated by the blue dots in the plots). The left panel includes our 1 Gyr trial. At ages $\lesssim$ 3 Gyr, our models yield poorer fits since at those young ages red giant stars do not reach the size required for the large primary to produce the observed ellipsoidal variations at the binary period. The right panel excludes the 1 Gyr trials, to have clearer contrast in the 3–13.5 Gyr age trials. Generally, the 3–13.5 Gyr models yielded comparable $\chi^2_{\rm red}$ values, with slightly lower $\chi^2_{\rm red}$ values (i.e. slightly better fits) at higher metallicities or older ages. We achieve the best fit in all our fitting trials at age = 12.8 Gyr, [Fe/H] = 0.5. . . . 128

3.12 The distribution of select parameters at the best-fit model in our binary model light curve fitting trials conducted at different ages and metallicities. From top left, going clockwise: The mass of the primary star (M_1), the mass of the secondary star (M_2), the K'-band extinction ($A_{K'}$), and the binary system semimajor axis. 129

3.13 The binary softness parameter calculated for the old binary S2-36 (orange bands: 3 Gyr models, red bands: 13.5 Gyr models) over the possible distances from Sgr A*. We show both the current observed softness parameter for S2-36, s_0, and the maximum possible softness parameter expected over its lifetime, $s_{\rm hard}$. For comparison, we also plot the softness parameter for the young, long-period binary IRS 16NE (blue band). Contrary to Alexander & Pfuhl (2014), we found that IRS 16NE is expected to be a hard binary in the expected GC dynamical environment. The width of each band in this plot originates from different exponential slopes of the cusp density distribution γ. Specifically, $\gamma = \frac{5}{2}$, $\frac{7}{4}$, $\frac{3}{2}$, and 0 are indicated in each band as lines from top to bottom, respectively. The difference in softness parameter due to S2-36's age is a result of the different best-fit stellar masses and separation in our binary modeling procedure and is not dependent on the time S2-36 has spent in the GC. The range of possible S2-36 distances from Sgr A*, r, plotted here are provided from the measurement of its projected acceleration in its proper motion (see Section 3.3.2). IRS 16NE's possible distances originate from a linear, velocity fit to its proper motion. The minimum distance for IRS 16NE corresponds to its projected distance from Sgr A* while the maximum distance corresponds to assuming the projected velocity represents the maximum velocity to still remain bound to the SMBH. 133

3.14 The constraints on the maximum density ($n_*(r)$) and the maximum number ($N_*(< r)$) of evaporating objects from the ellipsoidal binary S2-36 are shown in the left and right panels, respectively. In these plots, we calculated constraints at a fixed $\gamma = 7/4$ power-law slope of the density profile, at two different typical masses of evaporating objects: $\langle M_* \rangle = 1.2 M_\odot$ and $\langle M_* \rangle = 10 M_\odot$. While $\langle M_* \rangle = 10 M_\odot$ is not expected to be realistic for the GC, it demonstrates an upper limit on the number and density of stellar mass black holes at the GC with typical masses $\sim 10 M_\odot$. The range of possible S2-36 distances from Sgr A*, r, plotted here are provided from the measurement of its projected acceleration in its proper motion (see Section 3.3.2). 137

3.15 The constraint on the number of $\langle 1.2 M_\odot \rangle$ objects in the Galactic center region as a function of distance. The upper limits from the binary evaporation of S2-36 are shown as the orange and red bands (orange: 3 Gyr models, red: 13.5 Gyr models). The range of possible S2-36 distances from Sgr A*, r, plotted here are provided from the measurement of its projected acceleration in its proper motion (see Section 3.3.2). We show the estimates calculated from assuming that the binary was initially as hard as possible (i.e. maximum S_h), or if the binary was initially at its current observed softness s_0 (i.e. $S_h = 1$). The width of each band in this plot originates from different exponential slopes of the cusp density distribution γ. Specifically, $\gamma = \frac{5}{2}$, $\frac{7}{4}$, $\frac{3}{2}$, and 0 are indicated in each band as lines from top to bottom, respectively. For comparison, estimates of the extended mass profile in the GC provide an independent estimate of the upper limit of $\langle 1.2 M_\odot \rangle$ objects in the GC, shown as the teal band. This limit was computed from enclosed mass estimates from Schödel et al. (2009). 138

3.16 The constraint on the number of $\langle 10 M_\odot \rangle$ objects in the Galactic center region as a function of distance. The upper limits from the binary evaporation of S2-36 are shown as the orange and red bands (orange: 3 Gyr models, red: 13.5 Gyr models). The range of possible S2-36 distances from Sgr A*, r, plotted here are provided from the measurement of its projected acceleration in its proper motion (see Section 3.3.2). We show the estimates calculated from assuming that the binary was initially as hard as possible (i.e. maximum S_h), or if the binary was initially at its current observed softness s_0 (i.e. $S_h = 1$). The width of each band in this plot originates from different exponential slopes of the cusp density distribution γ. Specifically, $\gamma = \frac{5}{2}, \frac{7}{4}, \frac{3}{2}$, and 0 are indicated in each band as lines from top to bottom, respectively. For comparison, the dark gray band shows the lower limit on stellar-mass black holes from observations of X-ray binaries (Hailey et al., subm.). 139

3.17 The minimum relaxation time as a function of distance as constrained by the evaporation of the soft binary S2-36 are shown as the orange and red bands (orange: 3 Gyr models, red: 13.5 Gyr models). The width of each band in this plot originates from different exponential slopes of the cusp density distribution γ. Specifically, $\gamma = 0, \frac{3}{2}, \frac{7}{4}$, and $\frac{5}{2}$ are indicated in each band as lines from top to bottom, respectively. For comparison, the grey lines show relevant relaxation timescales estimates for the GC environment (Yu et al., 2007): the local two-body relaxation timescale $t_{\rm rlx}$, the scalar resonant relaxation timescale $t_{\rm rlx}^{\rm res,S}$, and the vector resonant relaxation timescale $t_{\rm rlx}^{\rm res,V}$. The S2-36 constraints for the GC local two-body relaxation time are consistent with expectations only for low ages of S2-36 and high values of the cusp slope γ. The range of possible S2-36 distances from Sgr A*, r, plotted here are provided from the measurement of its projected acceleration in its proper motion (see Section 3.3.2). 143

3.18 Errors in magnitude of the zero-point corrections used in this work (K'-band observations in left panel, H-band observations in right panel), calculated as the variance of the zero-point calibration magnitude adjustment in each observation. Median zero-point correction errors are shown as dashed lines. For comparison, the median zero-point correction error from G19 is shown in black in the left panel. 150

3.19 Same as Figure 3.1, but with a 5 parameter periodic model that allows for different long-term trend slopes in each passband. With fewer observations, the H-band long-term trend slope is less well constrained than the K'-band long-term trend slope. Overall, we found that the K'-band observations significantly demonstrate a long-term dimming trend. The H-band observations may be consistent with the same long-term dimming trend or no slope. However, our observations are not consistent with the long-term trend to be originating from dust extinction alone (see also Figure 3.20). 153

3.20 Posterior distributions of the long-term linear trend slopes in S2-36's photometric measurements in the K'-band (red histogram) and the H-band (blue histogram). The solid and dotted vertical lines indicate the best fit and 1σ uncertainties to the slope, respectively, in each band. The vertical cyan lines indicate the expectation of the slope in the H-band observations if the K'-band long-term dimming was solely caused by extinction (using the Nogueras-Lara et al. (2018) extinction law). The long-term trend in S2-36's photometry are inconsistent with dust extinction alone. 154

3.21 Trended, multi-band Lomb-Scargle periodogram for the S2-36 astrometric measurements. The left and right panels draw the periodogram with respect to frequency and period of variability, respectively. The horizontal dashed green lines indicate the bootstrap test significance level. The vertical dashed orange lines indicates the most significant peak in the astrometry periodogram: at 5483 days or 1.824×10^{-4} day^{-1}, with 75.9% false significance. The large values of the normalized L-S power in the periodogram are a result of a good fit for an overall linear trend, which originates from the star's approximately linear proper motion. 155

4.1 Periodicity detections that pass the variability, periodicity, and frequency cuts in our search, with bootstrap false alarm test significance plotted against the variability amplitude. This plot is similar to Figure 2.11, but updated with our new multiband, trended periodicity search sample and the criteria for possible and likely periodic signals (listed in Table 4.1). For clarity, only the most significant periodicity search detection is plotted for stars that have multiple detections passing the variability, periodicity, and frequency cuts. The stars that we identify as *likely periodic variables* (IRS 16SW, S4-258, S2-36, S4-308, and S3-438) stand out distinctly in significance from other possible periodic detections identified in our experiment. 160

4.2 Likely periodic variable IRS 16SW. Keck NIRC2 photometric measurements are shown in the K'- (top row panels) and H-band (middle row panels). Of the observation plots, the left panels show the light curve over our entire experiment time baseline. The solid colored lines show the long-term linear trend components of the best-fit trended sinusoid model in each band, with 3σ uncertainty in the linear fit indicated by the shaded regions. The right panels show the same photometric data phased to $2\times$ the best-fit period from our trended Lomb-Scargle analysis and with the best-fit long-term linear trend removed. The solid, colored lines in each panel indicate the best-fit sinusoid model to the observed data, with 3σ uncertainty in the sinusoid fit indicated by the shaded regions. The bottom row panels show the Lomb-Scargle periodogram (in frequency space on left and in period space on right). The horizontal dashed green lines indicate the bootstrap test significance level. The vertical dashed orange lines indicate the periodogram peaks above 80% bootstrap test significance. 163

4.3 Likely periodic variable S4-258. Keck NIRC2 photometric measurements are shown in the K'- (top row panels) and H-band (middle row panels). Of the observation plots, the left panels show the light curve over our entire experiment time baseline. The solid colored lines show the long-term linear trend components of the best-fit trended sinusoid model in each band, with 3σ uncertainty in the linear fit indicated by the shaded regions. The right panels show the same photometric data phased to $2\times$ the best-fit period from our trended Lomb-Scargle analysis and with the best-fit long-term linear trend removed. The solid, colored lines in each panel indicate the best-fit sinusoid model to the observed data, with 3σ uncertainty in the sinusoid fit indicated by the shaded regions. The bottom row panels show the Lomb-Scargle periodogram (in frequency space on left and in period space on right). The horizontal dashed green lines indicate the bootstrap test significance level. The vertical dashed orange lines indicate the periodogram peaks above 80% bootstrap test significance. The floor in L-S power is due to the large amplitude of the long-term trend slope. 164

4.4 Likely periodic variable S2-36. Keck NIRC2 photometric measurements are shown in the K'- (top row panels) and H-band (middle row panels). Of the observation plots, the left panels show the light curve over our entire experiment time baseline. The solid colored lines show the long-term linear trend components of the best-fit trended sinusoid model in each band, with 3σ uncertainty in the linear fit indicated by the shaded regions. The right panels show the same photometric data phased to $2\times$ the best-fit period from our trended Lomb-Scargle analysis and with the best-fit long-term linear trend removed. The solid, colored lines in each panel indicate the best-fit sinusoid model to the observed data, with 3σ uncertainty in the sinusoid fit indicated by the shaded regions. The bottom row panels show the Lomb-Scargle periodogram (in frequency space on left and in period space on right). The horizontal dashed green lines indicate the bootstrap test significance level. The vertical dashed orange lines indicate the periodogram peaks above 80% bootstrap test significance. 165

4.5 Likely periodic variable S4-308. Keck NIRC2 photometric measurements are shown in the K'- (top row panels) and H-band (middle row panels). Of the observation plots, the left panels show the light curve over our entire experiment time baseline. The solid colored lines show the long-term linear trend components of the best-fit trended sinusoid model in each band, with 3σ uncertainty in the linear fit indicated by the shaded regions. The right panels show the same photometric data phased to $2\times$ the best-fit period from our trended Lomb-Scargle analysis and with the best-fit long-term linear trend removed. The solid, colored lines in each panel indicate the best-fit sinusoid model to the observed data, with 3σ uncertainty in the sinusoid fit indicated by the shaded regions. The bottom row panels show the Lomb-Scargle periodogram (in frequency space on left and in period space on right). The horizontal dashed green lines indicate the bootstrap test significance level. The vertical dashed orange lines indicate the periodogram peaks above 80% bootstrap test significance. 166

4.6 Likely periodic variable S3-438. Keck NIRC2 photometric measurements are shown in the K'- (top row panels) and H-band (middle row panels). Of the observation plots, the left panels show the light curve over our entire experiment time baseline. The solid colored lines show the long-term linear trend components of the best-fit trended sinusoid model in each band, with 3σ uncertainty in the linear fit indicated by the shaded regions. The right panels show the same photometric data phased to $2\times$ the best-fit period from our trended Lomb-Scargle analysis and with the best-fit long-term linear trend removed. The solid, colored lines in each panel indicate the best-fit sinusoid model to the observed data, with 3σ uncertainty in the sinusoid fit indicated by the shaded regions. The bottom row panels show the Lomb-Scargle periodogram (in frequency space on left and in period space on right). The horizontal dashed green lines indicate the bootstrap test significance level. The vertical dashed orange lines indicate the periodogram peaks above 80% bootstrap test significance. 167

4.7 The model mesh (left) and model light curve in the K'- and the H-band (right) of a mock detached binary system. In this system, the eclipses are narrow in phase. 170

4.8 The model mesh (left) and model light curve in the K'- and the H-band (right) of a mock detached binary system. In this system, the eclipses are wide in phase. Furthermore, the larger primary is tidally distorted and exhibits ellipsoidal variation. 171

4.9 The model mesh (left) and model light curve in the K'- and the H-band (right) of a mock detached binary system. In this system, the larger component is tidally distorted and exhibits ellipsoidal variability. The size of the smaller component leads to eclipses that are narrow in phase. 171

4.10 The model mesh (left) and model light curve in the K'- and the H-band (right) of a mock contact binary system. The difference in temperatures of the two stellar components leads to the different eclipse depths. 172

A.1 Possible periodic variable candidate S4-133. 342
A.2 Possible periodic variable candidate S3-364. 342
A.3 Possible periodic variable candidate S6-89. 343
A.4 Possible periodic variable candidate S5-60. 343
A.5 Possible periodic variable candidate S2-301. 344
A.6 Possible periodic variable candidate S0-33. 344
A.7 Possible periodic variable candidate S6-14. 345
A.8 Possible periodic variable candidate S2-284. 345
A.9 Possible periodic variable candidate S3-235. 346
A.10 Possible periodic variable candidate S1-148. 346
A.11 Possible periodic variable candidate S3-280. 347
A.12 Possible periodic variable candidate S1-15. 347
A.13 Possible periodic variable candidate S2-133. 348

LIST OF TABLES

1.1 Comparison of Recent Milky Way Galactic Center Photometric Studies 7

2.1 Observations used in variability analysis and their photometric quality 19
2.1 Observations used in variability analysis and their photometric quality 20
2.2 Observations used in variability analysis and their image quality 21
2.2 Observations used in variability analysis and their image quality 23
2.3 Fits to parameters of variability models 47
2.4 Criteria for Possible Periodic Signal 49
2.5 Likely Periodic Variable Stars 50
2.6 Possible Periodic Signals 51
2.6 Possible Periodic Signals 52
2.7 NIR Variability Studies of Spectrally-Typed Resolved Stellar Populations 60
2.8 Variability in Smaller Time Baseline Subsamples 61
2.9 Proper Motion Variability Groups 65
2.10 Initial Calibration Stars Bandpass Correction 77
2.11 Criteria for selecting final set of photometric calibration stars 81
2.12 Final Calibration stars 82

3.1 Bayesian Information Criteria (BIC) for Trended Sinusoid Fits 103
3.2 4 Parameter Trended Sinusoid Fit 104
3.3 Acceleration Proper Motion Model Fit 106
3.4 Near-Infrared Period-Luminosity Relationships 114
3.5 Implied extinction, distance, and GC apparent magnitude estimates from PLRs 119
3.6 Prior bounds on fitted binary parameters 123
3.7 New observations used for S2-36 photometric analysis 148
3.7 New observations used for S2-36 photometric analysis 149
3.8 Photometric Calibrator Star Bandpass Corrected Reference Fluxes 152

4.1 Criteria for Possible Periodic Signal 161

A.1 Catalog of stars in variability study sample 182
A.1 Catalog of stars in variability study sample 183
A.1 Catalog of stars in variability study sample 184
A.1 Catalog of stars in variability study sample 185
A.1 Catalog of stars in variability study sample 186
A.1 Catalog of stars in variability study sample 187
A.1 Catalog of stars in variability study sample 188
A.1 Catalog of stars in variability study sample 189
A.1 Catalog of stars in variability study sample 190
A.1 Catalog of stars in variability study sample 191
A.1 Catalog of stars in variability study sample 192
A.1 Catalog of stars in variability study sample 193
A.1 Catalog of stars in variability study sample 194
A.1 Catalog of stars in variability study sample 195
A.1 Catalog of stars in variability study sample 196
A.1 Catalog of stars in variability study sample 197
A.1 Catalog of stars in variability study sample 198

ACKNOWLEDGMENTS

I thank Professor Tuan Do for guiding me through the exciting science projects presented in my thesis and training me to be a scientist; Professor Andrea Ghez for pushing the boundaries of what I thought was even possible with my science and for also helping break down my scientific presentations and writing in order to make me a better science communicator; Professor Mark Morris for helping me fully consider the implications of my science; Professor Smadar Naoz for insightful discussions about dynamics and binaries, and the entire UCLA Galactic Center Group collaboration for always having an expert on whatever statistical, science, or software issues I ran into along the way of my thesis.

I also want to thank my fellow graduate student friends, especially my classmates in our huge 2014 cohort of eleven. The UCLA astronomy graduate community was invaluably supportive, particularly for a confused new grad student dropped in a giant, sprawling city. Their support has made possible being able to not only successfully complete my different academic milestones, but also made the past few years incredibly fun. I thank my friend Ellen Van Wyk, who in addition to being very supportive through the writing of this thesis also provided valuable design insight, helped me improve my plots, and joined me in nerding out over typography and visual design minutiæ.

I deeply love and thank my family for all their support, especially in order for me to pursue my educational goals, first in India, and then in the United States. My parents, Neelima and Dr. Amitabh Gautam, who have been unconditionally supportive of whatever I wanted to study. My best friend, Abhinav, for continually pushing his little brother to do more and better, and for sharing the helpful insight that there actually are people who study the stars professionally beyond just a hobby. My Baba (grandfather), Dr. Ambika Singh, who was my first scientific role model and who still wants to see everything I have written; my Nana (grandfather), Dr. Rama Shankar Singh, whose writing speed and efficiency I can

never match no matter how hard I try; and my Nani (grandmother), Shakuntala Singh, whose perpetual curiosity about what I work on has encouraged me to learn how to distill my research about pulsars, stars and black holes, and the center of the Milky Way, and then translate it all into Hindi. I am incredibly lucky to have inherited their deep and endless curiosity.

I am very fortunate to have had the opportunity to learn more about our Galaxy's center and share it with the world using astronomical observations conducted from the summit of Maunakea. Over the course of my thesis, I have had the privilege to learn first hand about the cultural importance of this mountain, the richness and the diversity of indigenous Hawaiian traditions, and the unique and special history of the Hawaiian island. I wish to recognize and acknowledge the very significant cultural role and reverence that the summit of Maunakea has always had within the indigenous Hawaiian community.

I acknowledge that results presented in this thesis are based on published works with additional coauthors. In particular, Chapter 2 is a version of Gautam et al. (2019). Chapter 3 is a version of a paper in preparation for publication with additional coauthors. The results in Chapter 4 are in preparation for publication with additional coauthors. The observations presented in this work were obtained at the W. M. Keck Observatory, which is operated as a scientific partnership among the California Institute of Technology, the University of California, and the National Aeronautics and Space Administration. The Observatory was made possible by the generous financial support of the W. M. Keck Foundation. I thank the staff of the Keck Observatory for their help in obtaining the observations presented in this thesis.

VITA

2010–2014 B.A. — Astrophysics (with Honors), Physics
University of California, Berkeley

2014–2016 M.S. — Astronomy and Astrophysics
University of California, Los Angeles

PUBLICATIONS

Rose, S. C., Naoz, S., Gautam, A. K., Ghez, A. M., Do, T., Chu, D. S., Becklin, E. E. 2020, [submitted]: On Socially Distant Neighbors: Using Binaries to Constrain the Density of Objects in the Galactic Center

Hosek Jr., M. W, Lu, J. R., Lam, C. Y., Gautam, A. K., Lockhart, K. E., Kim, D., Jia, S. 2020, AJ, 160, 143: SPISEA: A Python-Based Simple Stellar Population Synthesis Code for Star Clusters

Chen, Z., Gallego-Cano, E., Do, T., Witzel, G., Ghez, A. M., Schödel, R., Sitarski, B. N., Becklin, E. E., Lu, J. R., Morris, M. R., Dehghanfar, A., Gautam, A. K., Hees, A., Hosek Jr., M. W., Jia, S., Mangian, A. C., Matthews, K. 2019, ApJL, 882, L28: Consistency of the Infrared Variability of Sgr A* over 22 years

Do, T., Witzel, G., Gautam, A. K., Chen, Z., Ghez, A. M., Morris, M. R., Becklin, E. E., Ciurlo, A., Hosek Jr., M. W., Martinez, G. D., Matthews, K., Sakai, S., Schödel, R. 2019, ApJL, 882, L27: Unprecedented variability of Sgr A* in NIR

Do, T., Hees, A., Ghez, A. M., Martinez, G. D., Chu, D. S., Jia, S., Sakai, S., Lu, J. R., Gautam, A. K., O'Neil, K. K., Becklin, E. E., Morris, M. R., Matthews, K., Nishiyama, S., Campbell, R., Chappell, S., Chen, Z., Ciurlo, A., Dehghanfar, A., Gallego-Cano, E., Kerzendorf, W. E., Lyke, J. E., Naoz, S., Saida, H., Schödel, R., Takahashi, M., Takamori, Y., Witzel, G., Wizinowich, P. 2019, Science, 16 Aug 2019: Relativistic redshift of the star S0-2 orbiting the Galactic center supermassive black hole

Sakai, S., Lu, J. R., Ghez, A. M., Jia, S., Do, T., Witzel, G., Gautam, A. K., Hees, A., Becklin, E. E., Matthews, K., Hosek Jr., M. W. 2019, ApJ, 873, 65: The Galactic Center: An Improved Astrometric Reference Frame for Stellar Orbits around the Supermassive Black Hole

Jia, S., Lu, J. R., Sakai, S., Gautam, A. K., Do, T., Hosek Jr., M. W., Service, M., Ghez, A. M., Gallego-Cano, E., Schödel, R., Hees, A., Morris, M. R., Becklin, E. E., Matthews, K. 2019, ApJ, 873, 9: The Galactic Center: Improved Relative Astrometry for Velocities, Accelerations, and Orbits near the Supermassive Black Hole

Gautam, A. K., Do, T., Ghez, A. M., Morris, M. R., Martinez, G. D., Hosek Jr., M. W., Lu, J. R., Sakai, S., Witzel, G., Jia, S., Becklin, E. E., Matthews, K. 2019, ApJ, 871, 103: An Adaptive Optics Survey of Stellar Variability at the Galactic Center

Chu, D. S., Do, T., Hees, A., Ghez, A. M., Naoz, S., Witzel, G., Sakai, S., Chappell, S., Gautam, A. K., Lu, J. R., Matthews, K. 2018, ApJ, 854, 12: Investigating the Binarity of S0-2: Implications for Its Origins and Robustness as a Probe of the Laws of Gravity around a Supermassive Black Hole

CHAPTER 1

Introduction

The proximity of the Milky Way Galactic center (GC), at a distance of ≈ 8 kpc, makes possible resolved studies of the nature of stars in nuclear star clusters (NSCs). Furthermore, the GC also hosts a supermassive black hole (SMBH) with a mass of $\approx 4 \times 10^6\ M_\odot$ at the location of the radio source Sgr A* (Ghez et al., 2008; Schödel et al., 2009; Gillessen et al., 2009; Boehle et al., 2016; Gillessen et al., 2017; Collaboration et al., 2018; Do et al., 2019), providing a unique perspective to how supermassive black holes affect their stellar neighbors that is not possible for other galactic nuclei. Adaptive optics (AO) on near-infrared (NIR) 8–10 m class telescopes has been crucial for these diffraction-limited, resolved studies of the GC stars, revealing distinct stellar populations and allowing for the precise monitoring of stellar motions around the SMBH. While AO observations have given a deeper look at the closest stars to the GC SMBH, there are still fundamental open questions about how stars interact with a SMBH, including: (1) What is the binary fraction of stars at the GC? (2) Is there an unseen, dark cusp at the GC?

In this dissertation, we used over 13 years of AO photometric observations to constrain the astrophysical properties of the stellar population within ≈ 0.5 pc of the GC SMBH in an effort to address these open questions. Particularly, we performed a survey of stellar variability at the GC in order to constrain the physical properties of stars, including searching for stellar binaries. With the largest sample used for such a study at the GC to date, we have provided the tightest constraints so far on the GC eclipsing binary fraction along with a framework

to photometrically constrain the intrinsic binary fraction. We also probed for the presence of unseen stars or compact objects that may make up a *dark cusp* at the GC using stellar binaries in combination with dynamical models. This experiment serves as a novel upper bound on the density of a possible GC dark cusp at ~ 0.1 pc from the SMBH.

1.1 Background and motivation

The proximity of the GC makes it a compelling target to study in detail the physical processes taking place in the dense and extreme environments of galactic nuclei. However, interstellar extinction makes it a difficult observational target. As observers on Earth, we are situated approximately in the plane of the Milky Way Galaxy, and our line of sight towards the GC passes through a large amount of interstellar material in the Galaxy's plane. The intervening material results in large extinction at optical wavelengths (≈ 30 magnitudes), making observations of the GC at such wavelengths impossible. One method to overcome the limitations from extinction is to observe at wavelengths $\gtrsim 1$ µm in the near-infrared (NIR) where extinction is not as strong (e.g., $\approx$ 2–3 magnitudes at 2.2 µm).

Another observational challenge for studying the GC is the effect of atmospheric turbulence on large, ground-based telescopes. Distinguishing individual stellar sources in the high stellar densities near the SMBH in the GC requires the high resolution provided by the largest telescopes (i.e., diameters of 8–10 m). These large telescopes are ground-based and turbulence in the atmosphere makes it especially challenging for them to obtain diffraction limited imaging beyond short exposures (e.g. *speckle imaging*, Matthews et al., 1996; Ghez et al., 1998). The short exposure techniques, however, particularly struggle with image depth, with limited sensitivity to faint stars. The deployment of AO systems on the largest ground-based telescopes (e.g. Wizinowich et al., 2000) has allowed deep imaging and spectroscopic studies of the GC that approaches these telescopes' diffraction limits (Ghez et al., 2005; Eisenhauer et al., 2005).

The NIR AO observations have discovered that the GC is composed of several distinct populations of stars. NIR spectroscopic observations have revealed a population of more than 100 young, massive stars at the GC (Maness et al., 2007; Bartko et al., 2010; Pfuhl et al., 2011; Do et al., 2013a) of age $\approx$ 4–6 Myr (Lu et al., 2013). The GC young, massive stars are largely concentrated within the central 0.5 pc (Do et al., 2013a; Støstad et al., 2015). The majority of the nuclear star cluster stellar population consists of old stars with ages $>$ 1 Gyr (e.g. Blum et al., 2003; Do et al., 2013a; Nogueras-Lara et al., 2020). NIR observations sample the bright end of the old population, primarily composed of late-type M and K giant stars. This population has been observed to be more diffusely and isotropically distributed around the SMBH than the young star population (Schödel et al., 2009).

The presence of the young star population at the GC is especially puzzling when considering their proximity to the SMBH at the GC. Molecular clouds collapsing in close proximity to the SMBH would experience large tidal forces, making *in situ* formation difficult (Morris, 1993). Additionally, standard dynamical friction models that could migrate these stars from their sites of formation at further distances take longer than the lifetimes of these stars (e.g. Kim & Morris, 2003; Kim et al., 2004; Mapelli & Gualandris, 2016). Further work is required to understand both the nature and presence of the young, early-type stars at the GC.

There are still uncertainties about the nature of the stellar cusp at the Galactic center as well. Theoretical models and simulations suggest that a supermassive black hole like the one associated with Sgr A* should host stellar populations that are dynamically relaxed (Binney & Tremaine, 2008), and consequently the relaxed stellar populations should form a *density cusp* with a steep increase in density towards the SMBH (see e.g., Bahcall & Wolf, 1976, 1977; Hopman & Alexander, 2006; Bar-Or et al., 2013). However, astrometric and spectroscopic observations measuring the distribution of old, late-type red giants, that would be expected to trace a density cusp, find evidence of a flat profile (e.g. Do et al., 2009; Buchholz et al., 2009). Others have proposed a dark cusp as well, consisting of stellar

remnants like stellar mass black holes and neutron stars (Miralda-Escudé & Gould, 2000; Morris, 1993), with some evidence of the existence of such a cusp being provided by X-ray observations at larger distances from the SMBH (Hailey et al., 2018). The presence of a cusp has dynamical implications for objects at the Galactic center, such as more frequent evaporation of binary systems (e.g., Alexander & Pfuhl, 2014) or even the possible detection of black hole mergers with recently operating gravitational wave observatories like LIGO (e.g. Abbott et al., 2017; Hoang et al., 2018). The dark cusp at the GC requires further study to constrain observationally.

Deep, resolved, and precise photometry of the GC stellar population can offer unique opportunities to contribute towards these outstanding questions about the GC. While deep astrometric and radial velocity studies of the GC stellar population have been conducted with NIR AO-assisted observations, previous AO photometric studies of the GC have been limited. This is largely due to two challenges. The extreme crowding of stellar sources in the central regions of the NSC makes aperture photometry difficult or impossible as the point spread functions (PSFs) of stellar sources overlap. PSF fitting is required to estimate flux of stellar sources instead. Furthermore, in AO observations, the PSF shape varies across the observation field of view and over time. Anisoplanatism results in PSF variation as a function of the position of the star on the sky with respect to the laser guide star and the tip-tilt star that are used in AO observations (see e.g., Schödel et al., 2010). Weather, atmospheric conditions, and the performance of the AO system during observations further introduce fluctuations in the PSF shape. Such effects cause biases when estimating the flux of stellar sources by PSF fitting. When studying the flux or variability of stellar sources using AO datasets, this PSF variation must be accounted for in order for it to not greatly contaminate photometric studies with systematic variability.

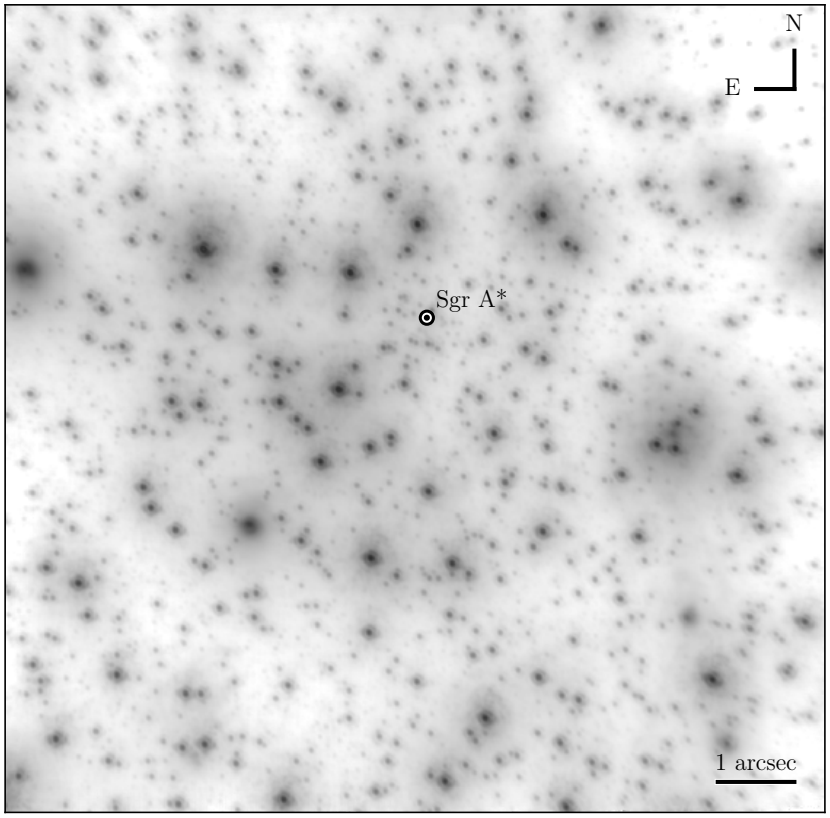

Figure 1.1: An example near-infrared (K'-band) laser guide star adaptive optics image of the Milky Way Galactic center (GC) from the *Galactic Center Orbits Initiative* dataset. This image is constructed from observations taken on 2015 August 10 and spans a field of view $10'' \times 10''$ (≈ 0.4 pc $\times \approx 0.4$ pc in projected distance at the GC). Sgr A* is marked on the image, and corresponds to the location of the supermassive black hole.

In Chapter 2, I discuss the imaging data set and the methodologies that I have developed as a part of this thesis to derive precise photometric measurements of stellar sources. The imaging dataset originates from the NIR observations of the GC obtained as a part of the *Galactic Center Orbits Initiative*, consisting of NIR AO imaging of the central $10''$ of the Galactic center conducted from 2006–2019. This field of view corresponds to a physical projected distance of ≈ 0.4 pc $\times \approx 0.4$ pc at the GC (see example image shown in Figure 1.1). In

particular, the long time baseline of the dataset and the consistent manner of observation has enabled the development of novel analysis. The methods presented in Chapter 2 have allowed us to achieve relative photometric uncertainty reaching down to $\sigma_{m_{K'}} \approx 0.03$ out to $m_{K'} \sim 16$. The level of precision in photometry that we reached with these techniques is comparable to the highest precision achieved by other AO photometric studies of resolved stellar populations (see e.g., Schödel et al., 2010).

1.1.1 Limitations of previous photometric studies of the GC

Previous photometric or stellar variability studies of the GC had been limited in a few aspects that our variability study in Gautam et al. (2019) (Chapter 2) addressed. A summary of these recent photometric studies is shown in Table 1.1. Pfuhl et al. (2014) used NIR AO photometry from the Very Large Telescope (VLT) to search for periodic variability, indicative of eclipsing binary systems. However the study only searched for binary variability and the sample was limited to the spectroscopically confirmed young star population at the Galactic center. Other AO photometric studies, such as that of Schödel et al. (2010), only reported single-epoch photometry. Previous studies without AO observations have largely focused on wider fields of view centered at the Galactic center (e.g. Peeples et al., 2007; Dong et al., 2017). These experiments suffered from confusion in the central regions of the nuclear star cluster, where rising stellar population density leads to crowding. Rafelski et al. (2007) studied photometric variability in the resolved stellar populations of the central $5'' \times 5''$ of the Galactic center. This study used Keck Observatory speckle data over a time baseline of 10 years. However, the speckle data and the "shift-and-add" image combination technique implemented in that study faced limitations with sensitivity and photometric precision, especially for stars fainter than $m_K \sim 14$, along with a smaller experiment field of view. Using LGSAO data, our variability study in Gautam et al. (2019) achieved greater depth with much higher precision at fainter magnitudes. Additionally, the NIRC2 imager used in our study allowed for a larger stellar sample with a wider, $10'' \times 10''$ field of view.

Table 1.1: Comparison of Recent Milky Way Galactic Center Photometric Studies

Study	FoV	Sample	Notes
Gautam et al. (2019)	$10'' \times 10''$	563 stars	$\approx 3\%$ phot. uncertainty to $m_{K'} \approx 16$
			Keck (10 m, ground-based) AO
			45 K'-band epochs over ≈ 11.5 years
Dong et al. (2017)	$2.3' \times 2.3''$	33070 stars	$\approx 0.4\%$ phot. uncertainty
			HST (2.4 m, space-based)
			8 F153M (1.53 µm) epochs, 2 F127M (1.27 µm) epochs over 4 years
Pfuhl et al. (2014)	$20'' \times 20''$	113 early-type stars	Phot. precision not provided.
			VLT (8.2 m, ground-based) AO
			102 K_S- and 34 H-band epochs over 9 years
			Eclipsing binary search only.
Schödel et al. (2010)	$40'' \times 40''$	7738 stars	$\approx 2\%$ phot. uncertainty to $m_{K_S} \approx 15$
			VLT (8.2 m, ground-based) AO
			single epoch H-, K_S-, and L'-band photometry
Rafelski et al. (2007)	$5'' \times 5''$	131 stars	$\approx 6\%$ phot. uncertainty to $m_K \approx 14$
			Keck (10 m, ground-based) Speckle
			50 K-band epochs over 10 years
Peeples et al. (2007)	$112'' \times 112''$	1785 stars	$\approx 3\%$ phot. uncertainty
			CTIO Telescope (1 m, ground-based) non-AO
			134 K-band epochs over 1.4 years
Tamura et al. (1996)	$\approx 25'' \times \approx 22''$	57 sources	NASA IRTF Telescope (3 m, ground-based) non-AO
			K-band observations over ≈ 2 years

1.2 Stellar variability in the Nuclear Star Cluster

While NIR AO astrometric and spectroscopic observations have improved knowledge of the Galactic center stellar population, no general stellar photometric variability study had been conducted of this population with NIR AO before our work presented in Gautam et al. (2019). Generally, a study of the photometric stellar variability of the stars at the GC offers a valuable new perspective to compare the stellar population to other similar populations in the Milky Way. Strong differences in the variability fraction compared to other stellar populations can suggest differences in the makeup of the GC population. Furthermore, differences in the variability fraction as a function of location in the GC or by brightness can reveal the presence of different stellar subpopulations.

Our variability study in Gautam et al. (2019), and detailed in Chapter 2, presents our work to investigate the following scientific aspects of the nuclear star cluster population within about half a parsec of the central SMBH:

- A characterization of the long-term ($\approx$ 11.5 year) variability of a young star cluster.
- A photometric search for stellar binaries.
- Search for stars on the instability strip undergoing pulsations.
- Search for microlensing events in the high stellar density of the GC.
- Constraints on dust column size and identification of stars whose variability can be ascribed to extinction.

1.3 The binary fraction of young stars at the Galactic center

Stellar binary systems are especially useful to learn about the Galactic center environment. Stellar multiplicity is typically a direct result of fragmentation during star formation (see

e.g., Duchêne & Kraus, 2013). Dynamical interactions with the dense Galactic center stellar environment and its central SMBH can further affect the observed binary fraction (e.g. Hills, 1988; Alexander & Pfuhl, 2014; Stephan et al., 2016, 2019, Rose et al., in prep.). Observational constraints on the GC binary fraction can therefore serve as a valuable method to test Galactic center star formation and dynamical evolution models.

In the Milky Way's local solar neighborhood, the binary fraction of solar-type stars is just under 50% (Raghavan et al., 2010). For higher primary star masses, the binary fraction rises dramatically, reaching $\approx 70\%$ for massive O-type stars (Sana et al., 2012). For B-type stars, the binary fraction is less well-constrained, with surveys suggesting a binary fraction $\gtrsim 60\%$ (Duchêne & Kraus, 2013). Furthermore, a significant fraction of massive stars reside in close binary systems. When considering binaries at periods < 20 days, Moe & Di Stefano (2013) found $\approx 21\%$ of B-type stars to be in close binaries while Sana et al. (2012) found $\approx 31\%$ of O-type stars to be in close binaries.

A comparison of the GC binary fraction with that of the local Milky Way environment can be a useful avenue to evaluate how star formation and dynamical processes differ in the vicinity of a supermassive black hole. However, the binary population of the GC young stars is not yet completely understood. So far, three young binary systems have been discovered at the GC: two contact, eclipsing and spectroscopic binaries, IRS 16SW (Ott et al., 1999; Peeples et al., 2007; Rafelski et al., 2007) and S4-258 (also known as E60; Pfuhl et al., 2014), and a long-period spectroscopic binary, IRS 16NE (Pfuhl et al., 2014). In addition to these direct detections of binaries, there is observational evidence to suggest additional binaries or binary products at the GC (e.g., Naoz et al., 2018; Ciurlo et al., 2020). While the observed binary fractions of GC young stars appear to be consistent with those of local massive stellar populations (Pfuhl et al., 2014; Gautam et al., 2019), the intrinsic binary fraction of the GC young stars has not yet been constrained. Photometric experiments with high photometric precision and large stellar samples offer a method for precise constraints on

the intrinsic binary fractions. Photometric experiments detect binary systems via eclipses or tidal distortions in stellar binary light curves. Eclipsing binary experiments can especially provide tight limits on the intrinsic stellar binary fraction at short binary periods (see e.g., Moe & Di Stefano, 2013, 2015).

In Chapter 2, as a part of our stellar variability survey presented in Gautam et al. (2019), we obtained the most precise constraint on the eclipsing binary fraction of GC young stars to date, $2.4\% \pm 1.7\%$, using the largest stellar sample so far for such work. We found that the eclipsing binary fraction is consistent with that of the local young, OB star population (Lefèvre et al., 2009). We additionally did not find any binaries amongst the young S-stars within ≈ 0.04 pc of the SMBH, consistent with binary capture models that explain the presence of the S-stars around the SMBH (e.g., Hills, 1988).

While the eclipsing binary fraction at the GC is consistent with the local young, OB star eclipsing binary fraction, there are limitations in drawing implications for the GC stellar population. The observed binary fraction can suffer from selection effects. Factors such as the intrinsic binary fraction of the population or the separation of binary systems can affect the observed binary fraction, but each have different implications about the formation and evolution of binaries at the GC. In Chapter 4, we lay out the methodology and initial results that we developed over the course of this thesis to address these limitations in the observed binary fraction. With this methodology employed in future work, we aim to provide constraints on the intrinsic binary fraction of young stars at the GC with our photometric binary detections.

1.4 Probing dark cusp predictions with binary evaporation

When compared to SMBHs in other galactic centers, the Milky Way SMBH has a relatively low mass (e.g. Gültekin et al., 2009). A lower central SMBH mass ($M_\bullet$) implies a shorter dynamical relaxation time ($T_{\rm relax}$) for the surrounding star cluster (see e.g., Hopman &

Alexander, 2006; Binney & Tremaine, 2008; Alexander & Hopman, 2009):

$$T_{\rm relax} \propto M_{\bullet}^{5/4} \tag{1.1}$$

A consequence of this scaling is that central SMBH masses $\lesssim 10^7 M_{\odot}$, such as the GC SMBH ($M_{\bullet} \sim 4 \times 10^6 M_{\odot}$), should have surrounding stellar clusters that have had sufficient time to relax within the age of the universe (Alexander & Hopman, 2009). In particular, the NSC around the GC SMBH is expected to have a relaxation time $T_{\rm relax} \sim 10^9$ yr, which is lower than the ages of the oldest stars in the NSC.

In such a relaxed population with a central SMBH that can regularly tidally disrupt and absorb stellar members of its surrounding cluster, a steep increase in density (a *density cusp*) is expected towards the central SMBH (Bahcall & Wolf, 1976, 1977; Hopman & Alexander, 2006). We assume that the stellar number density (n) follows a power law distribution with the distance from the central SMBH (r):

$$n \propto r^{-\gamma} \tag{1.2}$$

Bahcall & Wolf (1976) demonstrated in dynamical work that single mass populations with a central SMBH are expected to follow profiles with $\gamma = 7/4$. This scaling originates from a steady-state energy-flow assumption, where the negative energy flow from the absorption of a star by the black hole implies a flow of energy carried out by relaxation. In more complex populations composed of members with different masses, other values for γ can be expected (e.g., γ values as low as $3/2$, Bahcall & Wolf, 1977).

In a stellar population surrounding a SMBH where massive stars are common, a $\gamma = 7/4$ cusp profile is expected for the massive stars, while a shallower cusp profile ($3/2 < \gamma < 7/4$) is expected for the lighter stars. On the other hand, if the population is dominated by less massive members, the massive stars scatter more frequently with the less massive members. The massive stars in such a population settle into a steep cusp profile ($2 \lesssim \gamma \lesssim 11/4$), while the less massive members still remain in a shallow cusp profile ($3/2 < \gamma < 7/4$). In these

populations with few massive members, the strong disparity in cusp profile slopes results in strong mass segregation, with the most massive stars dominating the inner regions of the cluster (Alexander & Hopman, 2009).

Observationally, one way dynamical predictions of the density near the SMBH can be tested is by tracing the population of luminous stars in the NSC. In particular, the old giant stars in the GC with ages > 1 Gyr (Do et al., 2013a) are expected to belong to a relaxed population that can be used to test the dynamical predictions. However, observations suggest there are fewer giants in the GC close to the SMBH than are expected by cusp predictions (Buchholz et al., 2009; Do et al., 2009, 2013a; Gallego-Cano et al., 2018).

Several models have been proposed to explain why the GC may possess few old giant stars close to the SMBH. Giant stars are expected to have frequently collided with main sequence stars or stellar-mass black holes in the GC (Dale et al., 2009). These collisions may have resulted in the stripping of the giants' envelopes, or occasionally in more extreme mass-loss events such as giant core expulsion. Also, a fragmenting accretion disk may have previously existed around the SMBH. Interactions with dense clumps of gas in the disk may have stripped giant stellar envelopes (Amaro-Seoane & Chen, 2014; Kieffer & Bogdanovic, 2016). These giant-star mass-loss events can account for the paucity of old giants observed close to the central SMBH.

While the old stars may not follow dynamical predictions of a cusp, the GC may still possess a *dark cusp* made up of stellar remnants such as stellar-mass black holes and neutron stars (Morris, 1993; Miralda-Escudé & Gould, 2000). Of the remnants, the stellar-mass black holes are expected to make up the majority of the mass in the hypothesized dark cusp. Importantly, the stellar-mass black holes would not have been subjected to the same physical processes that may have led to the depletion of giants in the GC. Therefore the GC is still expected to retain its dark cusp.

The stellar-mass black holes making up the dark cusp are expected to originate from two different sources: as remnants of past episodes of star formation and from the infall of globular clusters. There is evidence of several episodes of star formation at the GC (Nogueras-Lara et al., 2020), with the most recent appearing to have taken place 4–6 Myr ago with a top-heavy initial mass function (Bartko et al., 2010; Lu et al., 2013). The numerous massive stars formed during these episodes are expected to leave behind massive stellar remnants. Through dynamical friction, $\approx 25,000$ stellar-mass black holes are expected to have sunk to within a parsec of the SMBH (Antonini, 2014; Generozov et al., 2018). Additionally, if globular cluster infall episodes have contributed to the buildup of the NSC, they are expected to inject stellar-mass black holes into the GC that should similarly sink towards the SMBH (Antonini, 2014). After dynamical relaxation, the overall population of stellar-mass black holes contributed from both scenarios is expected to form a cusp with a steep increase in density towards the central SMBH.

Observations of quiescent X-ray binaries in the central parsec of the GC do reveal evidence for a cusp of stellar-mass black holes (Hailey et al., 2018). However, X-ray observations suffer from source crowding, the X-ray brightness of Sgr A*, and hot gas emission in the innermost regions of the GC ($\lesssim 0.2$ pc). Therefore, these observations are limited in the constraints they can provide on the existence of a dark cusp close to the SMBH. Other tracers of the dark cusp are needed to properly constrain the population of stellar-mass black holes in the GC.

Dynamical effects serve as a powerful method to indirectly probe the presence of the dark cusp, specifically the proces of *binary evaporation*. The degree to which binary evaporation has occurred can place upper limits on the density of surrounding objects. Dynamically soft (i.e., loosely bound) stellar binary systems are susceptible to getting more loosely bound and eventually being evaporated (i.e. detached) due to encounters with the surrounding stars and stellar remnants. Therefore, the detection of a dynamically soft binary places upper

limits on the surrounding stellar density (Alexander & Pfuhl, 2014). Importantly, such a binary can constrain the density of objects that are not luminous but still have gravitational influence, like the components of the expected GC dark cusp. Alexander & Pfuhl (2014) calculated dynamical constraints on the GC dark cusp with the long-period, young stellar binary system IRS 16NE. However, due to the large component stellar masses of IRS 16NE, the binary is not dynamically soft and is unable to place significant constraints on the dark cusp via binary evaporation.

Chapter 3 details our work to identify the NIR periodic source S2-36 as a likely old stellar binary system. We model its light curve to estimate its binary and stellar components. We then use these modeled parameters in combination with dynamical models of binary interactions with the GC stellar population. Our calculations with the dynamical models allow us to then place upper limits on the density of the dark cusp at the GC.

CHAPTER 2

An Adaptive Optics Survey of Stellar Variability at the Galactic Center

2.1 Introduction

At a distance of ≈ 8 kpc, the Milky Way Galactic center contains the closest nuclear star cluster and a supermassive black hole (SMBH) with a mass of $\approx 4 \times 10^6\ M_\odot$ at the location of the radio source Sgr A* (Boehle et al., 2016; Ghez et al., 2008; Gillessen et al., 2009). Adaptive optics (AO) on near-infrared (NIR) 8–10 m class telescopes has allowed diffraction-limited, resolved imaging and spectroscopic studies of the stellar population in the crowded central regions of the Galactic center. The NIR spectroscopic observations have revealed a population of more than 100 young, massive stars (Maness et al., 2007; Bartko et al., 2010; Pfuhl et al., 2011; Do et al., 2013a) within the central 0.5 pc (Støstad et al., 2015; Do et al., 2013a) of age $\approx$ 4–8 Myr (Lu et al., 2013). This young star cluster is among the most massive in the Milky Way. Most members of the nuclear star cluster are old stars with ages > 1 Gyr (Do et al., 2013a). NIR observations sample the bright end of the old population, primarily composed of late-type M and K giant stars.

While AO observations have improved knowledge of the Galactic center stellar population, no general stellar photometric variability study has yet been conducted of this population with NIR AO. Pfuhl et al. (2014) used NIR AO photometry from the Very Large Telescope (VLT) to search for periodic variability, indicative of eclipsing binary systems. However the

study only searched for binary variability and the sample was limited to the spectroscopically confirmed young star population at the Galactic center. Other AO photometric studies, such as that of Schödel et al. (2010), only reported single-epoch photometry. Previous studies without AO observations have largely focused on wider fields of view centered at the Galactic center (e.g. Peeples et al., 2007; Dong et al., 2017). These experiments suffered from confusion in the central regions of the nuclear star cluster, where rising stellar population density leads to crowding.

Rafelski et al. (2007) studied photometric variability in the resolved stellar populations of the central $5'' \times 5''$ of the Galactic center. This study used Keck Observatory speckle data over a time baseline of 10 years. However, the speckle data and the "shift-and-add" image combination technique implemented in the study faced limitations with sensitivity and photometric precision, especially for stars fainter than $m_K \sim 14$, along with a smaller field of view. Using LGSAO data, our study is able to achieve greater depth with much higher precision at fainter magnitudes. Additionally, the NIRC2 imager used in our study affords a larger stellar sample with a wider, $10'' \times 10''$ field of view.

In this work, we performed a general variability study of the stellar populations in the Galactic center using 10 years of Keck AO imaging data. These long-term Galactic center monitoring data have previously been used primarily to derive astrometric measurements of the stars in the nuclear star cluster (e.g. Ghez et al., 2008; Yelda et al., 2014; Boehle et al., 2016). Using these data, we investigated the following scientific questions:

- *The long-term variability of a young star cluster:* While various sources contribute to the variability of young, massive stars, NIR observations are especially sensitive to phenomena such as dust extinction and accretion activity common in very young stars. While several recent studies have been conducted of NIR variability in other young star clusters (e.g. Glass et al., 1999; Rice et al., 2012, 2015; Lata et al., 2016), the time baselines of such studies only span a few months to a few years. Our experiment's

≈ 11.5 year time baseline offers a unique opportunity to study the long-term variability of stars in a young star cluster.

- *A search for binaries:* Binary systems are especially useful to learn about the Galactic center environment. Stellar multiplicity is typically a direct result of fragmentation during star formation (see e.g. Duchêne & Kraus, 2013). Dynamical interactions with the dense Galactic center stellar environment and its central SMBH can further affect the observed binary fraction (e.g. Hills, 1988; Alexander & Pfuhl, 2014; Stephan et al., 2016). The observed binary fraction can therefore constrain Galactic center star formation and dynamical evolution models. Photometry offers a method to search for binary systems, allowing for the detection of eclipsing binaries or tidally distorted systems. Our experiment offers the largest photometric sample of stars in the central half parsec of the Galactic center to search for binary systems.

- *Stars on the instability strip:* Precision photometry can reveal interesting classes of variable stars undergoing pulsations during periods of instabilities. Such stars (e.g. Classical Cepheids and Type II Cepheids, AGB stars, and Miras) often have characteristic periods, luminosities, and variability amplitudes that can reveal specific populations having associated ages or metallicities to which they belong (see e.g. Matsunaga et al., 2006; Riebel et al., 2010; Chen et al., 2017).

- *Search for microlensing events:* The high stellar density at the Galactic center makes microlensing events likely. Such events can be revealed through photometric monitoring, with brightening events associated with the passing of a foreground massive object in front of a background star.

- *Constraints on dust column size and identification of stars whose variability can be ascribed to extinction:* Wide-field studies of the Galactic center have found that the extinguishing material in the environment is clumpy and has structure on approximately

arcsecond spatial scales (e.g. Paumard et al., 2004; Schödel et al., 2010; Nogueras-Lara et al., 2018). Stars can display variability while passing behind such variations in the extinction screen due to the stellar proper motions. Examples of non-periodic variability on long time-scales therefore can probe fluctuations in the extinction screen towards the Galactic center and constrain the dust column size of possible extinguishing dust structures.

- *Investigate properties of AO photometry and anisoplanatism:* AO data faces challenges for obtaining precision photometry. In a crowded field, flux is estimated by point spread function (PSF) fitting to isolate flux contributions of individual stars (see e.g. Schödel et al., 2010). However due to anisoplanatic effects, atmospheric conditions, and performance of the AO system during observations, the PSF shape varies over time and across a field of view such as that used in this work. In this work, we investigated the properties of such effects and developed a method to perform corrections to single PSF AO photometry estimates.

Section 2.2 describes our observations, data reduction methods, and our photometric calibration process. Section 2.2 also details the selection of the stellar sample used in this work. In Section 2.3, we describe our methods to identify variable stars and to constrain the variability fraction. Section 2.4 details our methods to identify periodically variable stars. Our results are detailed in Section 2.5. In Section 2.6, we review what our results reveal about the Galactic center stellar population and environment. We summarize our findings in Section 2.7.

Table 2.1: Observations used in variability analysis and their photometric quality

Date (UTC)	MJD	Total Stars Detected	Stars in Sample	Absolute Phot. Zeropoint Error (K' mag)	Relative Phot. Med. Error (K' mag)
2006-05-03	53858.512	1768	500	0.179	0.035
2006-06-20[S]	53906.392	1456	493	0.197	0.049
2006-06-21[S]	53907.411	1759	508	0.181	0.041
2006-07-17	53933.344	2179	501	0.172	0.031
2007-05-17	54237.551	2514	511	0.202	0.066
2007-08-10[S]	54322.315	1246	479	0.189	0.045
2007-08-12[S]	54324.304	1539	503	0.185	0.054
2008-05-15	54601.492	2089	524	0.193	0.039
2008-07-24	54671.323	2189	515	0.165	0.022
2009-05-01[S]	54952.543	1650	506	0.181	0.019
2009-05-02[S]	54953.517	1302	507	0.179	0.021
2009-05-04[S]	54955.552	1788	519	0.182	0.020
2009-07-24	55036.333	1701	501	0.185	0.026
2009-09-09	55083.249	1921	517	0.174	0.031
2010-05-04[S]	55320.546	1235	490	0.178	0.043
2010-05-05[S]	55321.583	1631	522	0.177	0.038
2010-07-06	55383.351	1956	502	0.184	0.036
2010-08-15	55423.284	1826	515	0.176	0.037
2011-05-27	55708.505	1563	494	0.200	0.027
2011-07-18	55760.346	2031	506	0.210	0.033
2011-08-23[S]	55796.280	2052	516	0.214	0.025
2011-08-24[S]	55797.274	1640	492	0.212	0.028
2012-05-15[S]	56062.518	1778	522	0.209	0.030
2012-05-18[S]	56065.494	1252	494	0.208	0.020
2012-07-24	56132.310	2344	517	0.206	0.020
2013-04-26[S]	56408.564	1418	475	0.162	0.075
2013-04-27[S]	56409.566	1313	478	0.168	0.042
2013-07-20	56493.325	1805	509	0.161	0.035
2014-05-19	56796.524	1483	497	0.159	0.033
2014-08-06	56875.290	1778	508	0.156	0.034
2015-08-09[S]	57243.298	1435	490	0.163	0.041
2015-08-10[S]	57244.291	1884	497	0.161	0.026

Table 2.1 (cont'd): Observations used in variability analysis and their photometric quality

Date (UTC)	MJD	Total Stars Detected	Stars in Sample	Absolute Phot. Zeropoint Error (K' mag)	Relative Phot. Med. Error (K' mag)
2015-08-11[S]	57245.303	1662	499	0.162	0.032
2016-05-03	57511.515	1661	490	0.197	0.022
2016-07-13	57582.363	1389	476	0.170	0.034
2017-05-04[S]	57877.536	1307	471	0.168	0.036
2017-05-05[S]	57878.531	1705	489	0.160	0.023
2017-07-18	57952.402	1125	469	0.168	0.033
2017-07-27	57961.274	652	361	0.151	0.077
2017-08-09[S]	57974.321	1168	472	0.164	0.028
2017-08-10[S]	57975.285	1264	472	0.173	0.026
2017-08-11[S]	57976.283	1495	483	0.176	0.026
2017-08-23[S]	57988.268	1311	477	0.192	0.027
2017-08-24[S]	57989.268	1016	469	0.200	0.029
2017-08-26[S]	57991.255	1377	475	0.183	0.027

Note. — Median astrometric and photometric errors were computed for stars in our study's sample detected in the corresponding observation. Absolute photometric zeropoint errors were calculated after conducting initial calibration, using bandpass corrected reference fluxes for non-variable stars from Blum et al. (1996) in our experiment's field of view. Relative photometric errors were determined after our calibration and local correction method were applied.

[S]Denotes consecutive nights of observations that were combined into single epochs in previous publications from our group for astrometric study. In this work, we split multiple night combined epochs into single night epochs for greater time precision.

Table 2.2: Observations used in variability analysis and their image quality

Date (UTC)	MJD	Frames	Astrometric Med. Error (mas)	Med. FWHM (mas)	Med. Strehl Ratio
2006-05-03	53858.512	107	0.332	57.61	0.35
2006-06-20[S]	53906.392	50	0.347	60.10	0.31
2006-06-21[S]	53907.411	119	0.320	56.59	0.38
2006-07-17	53933.344	64	0.320	57.73	0.37
2007-05-17	54237.551	76	0.334	58.02	0.36
2007-08-10[S]	54322.315	35	0.385	63.57	0.24
2007-08-12[S]	54324.304	54	0.352	55.66	0.34
2008-05-15	54601.492	134	0.298	53.47	0.30
2008-07-24	54671.323	104	0.297	58.95	0.33
2009-05-01[S]	54952.543	127	0.341	63.82	0.32
2009-05-02[S]	54953.517	49	0.361	58.26	0.36
2009-05-04[S]	54955.552	56	0.339	53.49	0.43
2009-07-24	55036.333	75	0.332	61.82	0.27
2009-09-09	55083.249	43	0.357	58.20	0.36
2010-05-04[S]	55320.546	105	0.389	63.24	0.31
2010-05-05[S]	55321.583	60	0.325	60.37	0.34
2010-07-06	55383.351	117	0.326	61.11	0.32
2010-08-15	55423.284	127	0.314	58.16	0.30
2011-05-27	55708.505	114	0.402	64.00	0.29
2011-07-18	55760.346	167	0.331	58.14	0.28
2011-08-23[S]	55796.280	102	0.361	59.76	0.36
2011-08-24[S]	55797.274	102	0.371	62.13	0.31
2012-05-15[S]	56062.518	178	0.339	59.69	0.31
2012-05-18[S]	56065.494	68	0.389	68.25	0.26
2012-07-24	56132.310	162	0.319	58.41	0.35
2013-04-26[S]	56408.564	75	0.368	65.63	0.25
2013-04-27[S]	56409.566	79	0.376	70.80	0.25
2013-07-20	56493.325	193	0.347	58.63	0.36
2014-05-19	56796.524	147	0.384	64.20	0.30
2014-08-06	56875.290	127	0.347	56.89	0.36
2015-08-09[S]	57243.298	43	0.553	62.63	0.32
2015-08-10[S]	57244.291	98	0.499	57.02	0.38

2.2 Observations, Photometric Calibration, and Stellar Sample

2.2.1 Observations and Data Reduction

We used laser guide star adaptive optics (LGSAO) high-resolution imaging of the Galactic center obtained at the 10-m W. M. Keck II telescope with the NIRC2 near-infrared facility imager (PI: K. Matthews) through the K' bandpass ($\lambda_0 = 2.124$ μm, $\Delta\lambda = 0.351$ μm). Observations were centered near the location of Sgr A* in the nuclear star cluster, with a field of view of the NIRC2 images extending about $10'' \times 10''$ ($10'' \approx 0.4$ pc at Sgr A*'s distance of $R_0 \approx 8$ kpc (Boehle et al., 2016)) and a plate scale of 9.952 mas/pix (Yelda et al., 2010, up to 2014 data) or 9.971 mas/pix (Service et al., 2016, post 2014 data). Observations used in this work were obtained over 45 nights spanning May 2006 – August 2017. We list details about individual observations in Tables 2.1 and 2.2, and the observational setup is further detailed by Ghez et al. (2008) and Yelda et al. (2014). Observations taken until 2013 have been reported in previous studies by our group (Ghez et al., 2008; Yelda et al., 2014; Boehle et al., 2016). Observations used in this work taken during 2014–2017 have not been previously reported.

Final images for each night were created following the same methods as reported by Ghez et al. (2008) and Stolte et al. (2008). We combined frames to construct final images separately for each night to achieve higher time precision, whereas in previous studies by our group, frames separated by a few days were combined into single final images (Ghez et al., 2008; Yelda et al., 2014; Boehle et al., 2016). Each frame was sky-subtracted, flat-fielded, bad-pixel-corrected, and corrected for the effects of optical distortion (Yelda et al., 2010; Service et al., 2016). The bright, isolated star IRS 33N ($m_{K'} \sim 11.3$) was used to measure a Strehl ratio and full width at half maximum of the AO-corrected stellar image (FWHM) to evaluate the quality of each frame. We constructed the final image for each observation by averaging the individual frames (weighted by Strehl ratio) collected over that night. We selected frames to create the final nightly image by a cut in the FWHM: frames used for the final nightly

Table 2.2 (cont'd): Observations used in variability analysis and their image quality

Date (UTC)	MJD	Frames	Astrometric Med. Error (mas)	Med. FWHM (mas)	Med. Strehl Ratio
2015-08-11[S]	57245.303	74	0.573	56.72	0.38
2016-05-03	57511.515	166	0.552	61.10	0.34
2016-07-13	57582.363	144	0.658	60.00	0.30
2017-05-04[S]	57877.536	112	0.721	70.77	0.26
2017-05-05[S]	57878.531	177	0.588	58.06	0.35
2017-07-18	57952.402	9	0.693	65.10	0.27
2017-07-27	57961.274	23	1.348	88.22	0.15
2017-08-09[S]	57974.321	23	0.828	62.73	0.30
2017-08-10[S]	57975.285	29	0.799	59.12	0.32
2017-08-11[S]	57976.283	87	0.770	53.19	0.37
2017-08-23[S]	57988.268	59	0.802	65.07	0.29
2017-08-24[S]	57989.268	41	0.825	61.48	0.33
2017-08-26[S]	57991.255	33	0.757	59.67	0.33

Note. — The median FWHM and Strehl quantities were calculated for IRS 33N across all frames used to construct the final image for the corresponding observation.

[S]Denotes consecutive nights of observations that were combined into single epochs in previous publications from our group for astrometric study. In this work, we split multiple night combined epochs into single night epochs for greater time precision.

image passed the condition $\mathrm{FWHM}_{33\mathrm{N}} \leq 1.25 \times \min(\mathrm{FWHM}_{33\mathrm{N}})$. This cut was implemented to reduce the impact of lower-quality frames in making the nightly images. The Strehl ratio weights used to average the individual frames were additionally used to calculate a weighted Modified Julian Date (MJD) time for the final image from the observation times of the individual frames used. This weighted MJD was adopted as the observation time for each data point used in this work.

The frames used to construct final images for each observation night were further divided into three independent subsets. Each subset received frames of similar Strehl and FWHM statistics, and the frames in each of the three subsets were averaged (weighted by Strehl ratio) to create three submaps. The standard deviation of the measured astrometric and photometric values in the three submaps were used for initial estimates of the astrometric and photometric uncertainties before additional sources of error were included during the astrometric transformation and photometric calibration processes.

We used the PSF-fitting software StarFinder (Diolaiti et al., 2000) to identify point sources in the observation epoch and submap images (detailed further by Ghez et al., 2008). The identifications yield measurements of flux and position on the image for each source. Importantly for this work, this step also involved computing the photometric uncertainty originating from our stellar flux measurements, F, during the point source identification. We use the variance in the three submaps as our estimate of the instrumental flux uncertainty (σ_F^2). The instrumental flux uncertainty was converted to an instrumental magnitude uncertainty, σ_m, with the following equation:

$$\sigma_m = 1.0857 \frac{\sigma_F}{F}. \tag{2.1}$$

Observations from individual epochs were matched and placed in a common reference frame (Jia et al. in prep.). The process provides astrometric positions for detected sources in each

observation and an estimate of the proper motion of each source. The reference frame is constructed using the same method outlined in Yelda et al. (2010) and further improved by Sakai et al. (2019).

2.2.2 Systematics from Stellar Confusion and Resolved Sources

Stellar confusion and proximity to resolved sources introduces biases in our photometric flux measurements. Stellar confusion originates from the individual proper motions of stars causing multiple stars to be positioned so that they can be confused during the PSF-fitting and cross-matching stage. In photometry, confusion results in misestimation of the stellar flux by biasing it when the PSFs of confused stars are blended together. During the cross-matching step, the proper motion of each star was fitted to an acceleration model. With the acceleration model, if the expected positions of two or more stars intersected with each other during an observation within $0.1''$ and had brightnesses within 5 magnitudes, the stars were identified as confused (Jia et al., 2019). If all intersecting stars were not each identified as separate detections, the photometric and astrometric measurements obtained for each confused star in that epoch were then removed from our dataset.

A similar problem can arise for resolved sources, leading to biases in photometry. During PSF-fitting, the flux from resolved sources was not modeled accurately with a single PSF, and therefore led to residual flux in an extended halo not captured by the fitted PSF. The flux in the extended halo could subsequently bias flux measurements derived for any sources lying in that halo. In this experiment, we identified resolved sources by visual inspection of the residual image for an observation night. This residual image was constructed by subtracting the PSF fits to each source from the observation's final image. Resolved sources appeared as those with extended flux still remaining in the residual image. We found that the extended flux for all resolved sources could be captured within $\approx 5\times$median $\mathrm{FWHM}_{33\mathrm{N}}$ of observations or typically $0.3''$. In each observation night, we therefore removed photometric and astrometric measurements for a star from our dataset if it passed within $0.3''$ of a resolved source.

Sources identified as resolved are shown with their respective 0.3″ boundaries on our experiment's field of view in Figure 2.4.

2.2.3 Artifact Sources from Elongated PSFs

Due to anisoplanatic effects, the PSF shape near the edges of our experiment's field of view was often elongated. During some observations, the elongated PSFs could lead our PSF fitting routine to report artifactual sources alongside stars located near the edges of our field of view. As a consequence of assigning some flux to the artifact, the PSF-fitting routine would report fluxes for the actual associated star that are too low. We therefore dismissed observations of any stars where they were affected by such an artifact.

We identified possible artifact sources by performing fits to their proper motion during the cross-matching stage, building on the methods outlined by Jia et al. (in prep.). The presence of artifact sources in our images was greatly dependent on the performance of the AO correction during a given observation, and therefore these sources were not present in every observation. We found, however, that artifact sources, when present, typically had the same position offset from their respective associated stars across observations. Artifact sources and their associated stars therefore have similar fitted values for proper motion. Any two apparent stars having positional separation $\leq 0.07''$ and proper motion difference ≤ 3 mas/yr were identified as a possible primary and artifact source candidate pair. The fainter object in such pairs is then added to a list of candidate artifact sources. We then removed from the list of candidate artifact sources any stars judged to be real stars by visual inspection of the images. Once the artifact sources were thereby verified, we removed any flux measurements of their associated stars from our dataset in the observations where the artifact source was present.

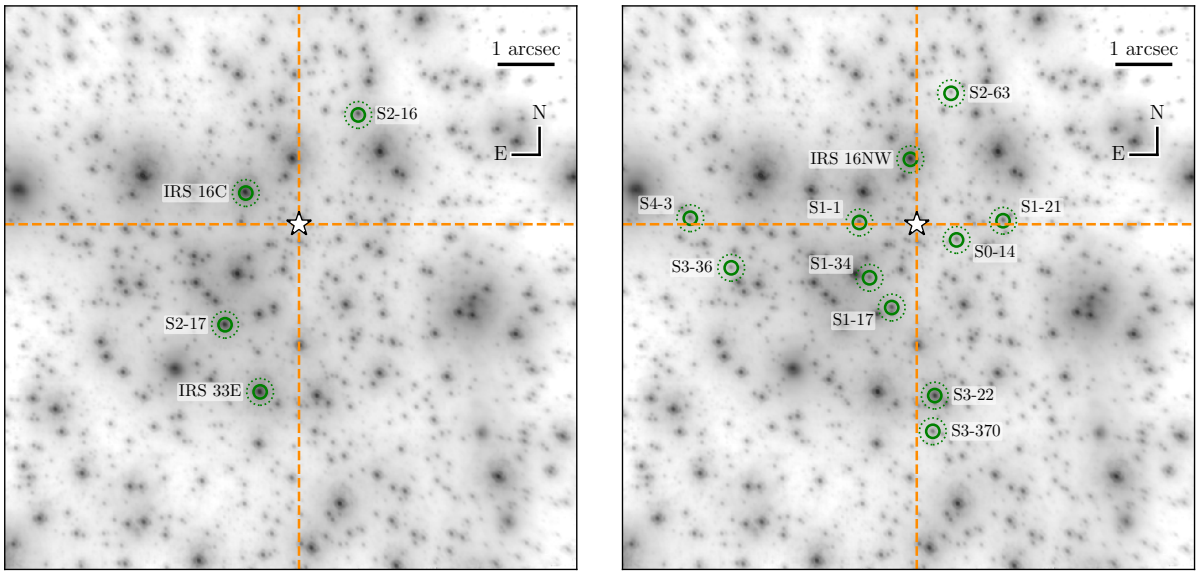

Figure 2.1: Calibration stars used for our initial and final calibration iterations in the variability analysis are circled and labeled (initial calibration iteration on left and final calibration iteration on right). The white star symbol indicates the position of Sgr A*. The dashed lines indicate the boundaries of the four quadrants centered on Sgr A*. These quadrants were used to select calibration stars distributed across our field of view. The background image is from the 10 August 2015 observation. We chose the final calibration stars so that at least one and no more than 3 would lie in each of the four quadrants. Dashed circles around each calibration star indicate 0.25″ around the position of each star. We selected the final calibration stars so that none were located within $\approx 0.25''$ of each other.

2.2.4 Photometric Calibration

We performed absolute photometric calibration of the stars in our dataset using photometry reported by Blum et al. (1996). In our experiment's field of view, several stars have K-band flux measurements from Blum et al. (1996). Four of these stars (IRS 16C, IRS 33E, S2-16, and S2-17) are not identified as variable by Rafelski et al. (2007) and do not appear as resolved sources in our images. We performed a bandpass-correction process, described

in Section 2.8.1, to convert the Blum et al. (1996) K-band fluxes for these four stars to NIRC2 K'-band flux. We then used these four stars as calibrator stars to perform an initial photometric calibration of all stars in our image across all observation epochs. The error in zeropoint correction from this initial calibration represents our experiment's error in absolute photometry, and is listed for each of our observations in Table 2.1.

We next performed an iterative procedure to select stable, non-variable stars in our experiment's field of view as photometric calibrators. In each calibration iteration, we selected the most photometrically stable stars distributed throughout our field of view and isolated enough to not be confused during the cross-matching process. Using these stable stars as photometric calibrators helped us obtain precise, *relative* photometric calibration, necessary for identifying variability. Our iterative process to select calibration stars is described in more detail in Section 2.8.2. Our final set of calibration stars selected by this process consists of IRS 16NW, S3-22, S1-17, S1-34, S4-3, S1-1, S1-21, S3-370, S0-14, S3-36, and S2-63. Table 2.12 summarizes the photometric properties of our final calibration stars and Figure 2.1 shows our initial and final set of calibration stars on our experiment's field of view.

After photometric calibration, we implemented and performed an additional correction to our photometry on local scales within the field beyond the zeropoint photometric calibration. The local photometric correction technique's implementation in our experiment is described in detail in Section 2.8.3. This correction accounted for a variable PSF across our field of view, which caused the flux measurements of stars derived by our PSF-fitting procedure to be under- or over-estimated. Since the PSF variation was spatially correlated, the bias in the flux measurement was expected to be similar for nearby stars of similar magnitudes. The photometric flux measurements and their corresponding uncertainties used in this work incorporate our local correction technique.

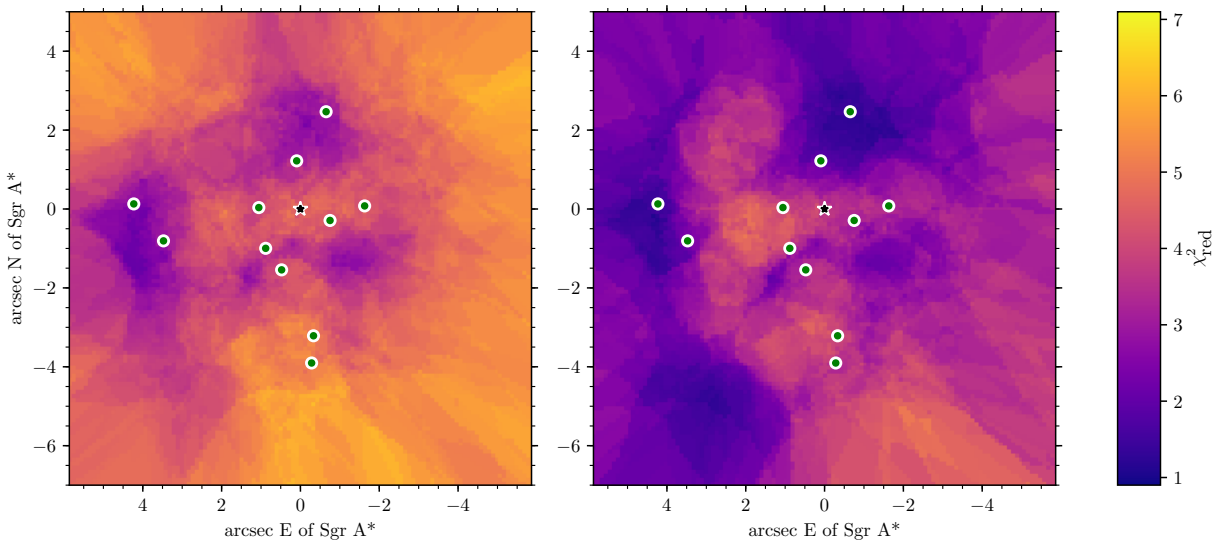

Figure 2.2: The variability of our stellar sample plotted on our field of view. The color of each point on the maps is determined by the mean of the $\chi^2_{\rm red}$ of the nearest 20 stars to the point having $\chi^2_{\rm red} < 10$ (so as to not affect the mean value with highly variable stars). The star shape indicates the position of Sgr A* while the green dots indicate the positions of our photometric calibrators. The map on the left is generated before our local correction is applied, and the map on the right is generated after our local corrections have been applied. Before the local correction is applied, the outer regions of the field demonstrate higher variability as expected from anisoplanatic effects on the PSF shape. After the local correction is applied, this spatial preference for variability is largely removed. Since this process removes systematic contributions to variability, overall $\chi^2_{\rm red}$ values are lowered throughout the field of view.

To evaluate the effectiveness of our local correction method in removing photometric biases from PSF variability, we examined the distribution of variability over the field. Figure 2.2 plots overall variability of our stellar sample as a function of position on the field. Before local correction was applied, the consequences of the anisoplanatic effects on our measured photometry are evident as higher variability towards the edges of our field of view. These

edge positions were located at a greater distance from the projected position of the laser guide star, towards the center of our field. After the local correction was applied, the overall variability in our sample originating from systematic effects was substantially reduced. Further, this correction reduced higher variability trends in the outer regions of the field where the influence of the anisoplanatic effects is most extreme. Section 2.6.4 further discusses the need for this correction and presents a comparison to other techniques developed for PSF variability.

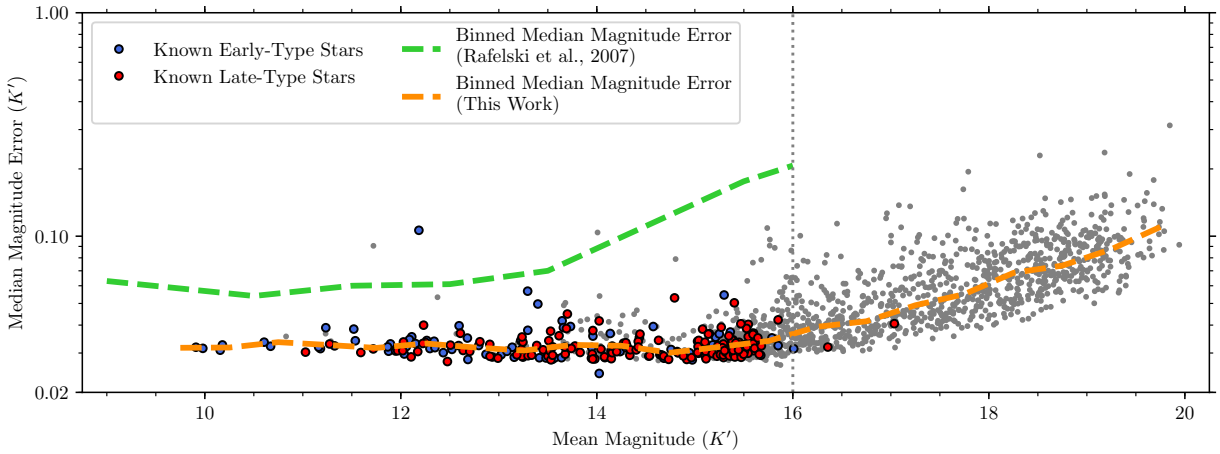

Figure 2.3: Median photometric uncertainty of the stellar sample in this work, identified in at least 16 nights of observation, plotted by mean magnitude. Known early-type and late-type stars are indicated as dots colored blue and red, respectively. The binned median magnitude error identifies this work's photometric precision as a function of stellar magnitude. Also shown for comparison is binned median magnitude error from previous work studying variability at the Galactic Center by Rafelski et al. (2007) using Keck speckle photometry data. The values plotted here are calculated after conducting the local photometry correction on our dataset, detailed in Section 2.8.3.

The floor of the photometric uncertainty begins to rise for stars fainter than $m_{K'} \sim 16$. Based on this, we limited the sample for our variability and periodicity search to stars with $\bar{m}_{K'} \leq 16$, indicated by the vertical dashed line.

2.2.5 Final Photometric Quality

The photometric quality of our data can be quantified by analyzing the median of the photometric uncertainty ($\sigma_{m_{K'}}$) for each star across all observations, as shown in Figure 2.3. Our observation's photometric uncertainty reaches a floor of $\sigma_{m_{K'}} \sim 0.03$ to a stellar magnitude of $m_{K'} \sim 16$. This floor primarily came from the zeropoint correction error's contribution to the photometric uncertainty (see Figure 2.19). For fainter stars at higher mean magnitudes, the photometric uncertainty of our observations rose up to $\sigma_{m_{K'}} \sim 0.1$ at $m_{K'} \sim 19$.

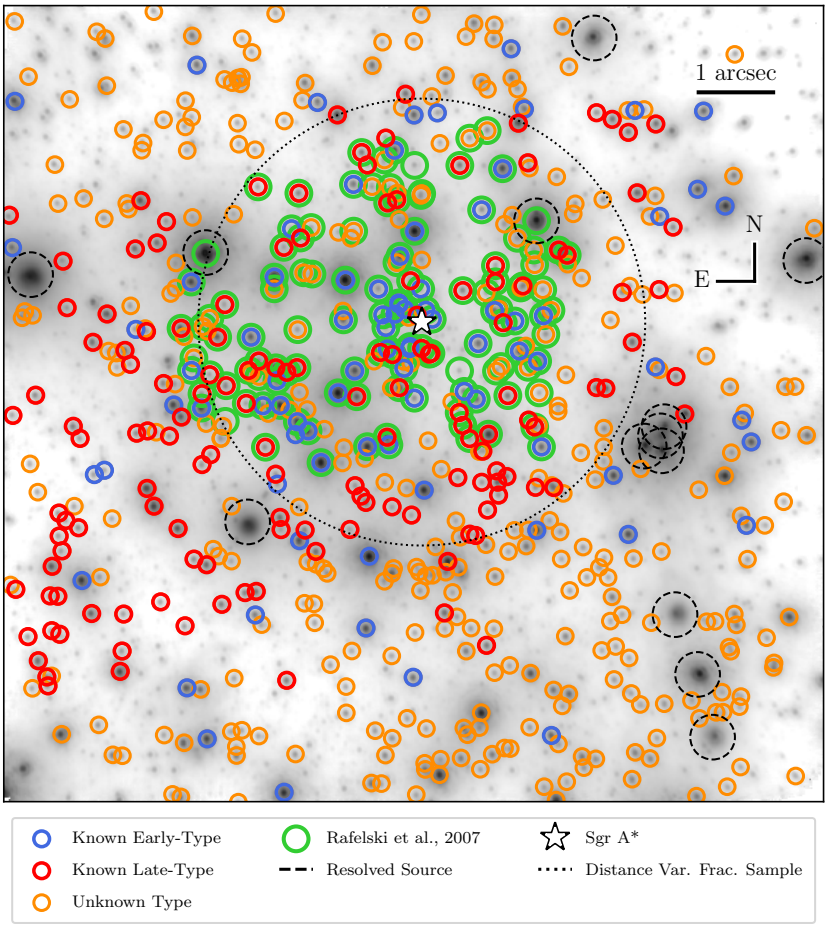

Figure 2.4: The stellar sample used in the photometric variability analysis, consisting of $\bar{m}_{K'} < 16$ stars detected in at least 16 nights without confusion. The background image is from the 2012-05-15 observation. Blue, red, and orange circles indicate spectrally typed early-type, late-type, and unknown type stars respectively. Green circles indicate the stellar sample studied in the previous stellar variability analysis by Rafelski et al. (2007) using Keck Observatory speckle data. The dashed circles indicate the region cut around resolved sources where flux measurements of sources could be biased by the presence of the resolved source. The white star symbol indicates the position of Sgr A*, the location of the supermassive black hole. The large dotted circle indicates the region of our sample used to study the projected positional dependence of variability, out to 3″ from Sgr A*. 1″ corresponds to a projected distance ≈ 0.04 pc at the Galactic center.

2.2.6 Stellar Sample

This experiment's stellar sample is shown in Figure 2.4. The stellar sample is composed of stars passing the following conditions:

- Detected in at least 16 nights out of 45 total nights, after accounting for confusion events and artifact sources, and without passing within $0.3''$ of a resolved source (see Sections 2.2.2 and 2.2.3).
- $\bar{m}_{K'} \leq 16$

The 16 night criterion is motivated by the contamination of our sample from artifact sources at the edges of our field of view. Our method to identify artifact sources (detailed in Section 2.2.3) was not able to recover all artifact sources that appear in fewer than 16 nights. The mean magnitude cut criterion, $\bar{m}_{K'} \leq 16$, originated from our dataset's photometric quality (see Section 2.2.5). At this magnitude, the floor in the photometric uncertainty, quantified by the mean magnitude error, begins to rise for stars $\bar{m}_{K'} \gtrsim 16$.

Under these criteria, 563 stars were identified and included in our photometric study. This sample of stars was further subdivided into known early- and late-type stars (identified by Paumard et al. (2006), Do et al. (2009), Gillessen et al. (2009), Bartko et al. (2009), Do et al. (2012), and manually assigned a spectral type by Do et al. (2013a)). Under our photometric sample selection criteria, 85 stars are known early-type stars and 143 are known late-type stars. These populations were studied separately for variability, detailed in Section 2.3, and are specifically indicated on our experiment's field of view in Figure 2.4.

2.3 Stellar Variability

2.3.1 Identifying Variable Stars

In order to identify variable light curves we computed the $\chi^2_{\rm red}$ statistic for our stellar sample. We calculated the weighted mean magnitude ($\bar{m}$) of each star in our stellar sample across all observation epochs, i, using weights at each observation from the magnitude uncertainty:

$$\bar{m} = \frac{\sum \frac{1}{\sigma_i^2} m_i}{\sum \frac{1}{\sigma_i^2}}. \tag{2.2}$$

The $\chi^2_{\rm red}$ quantity was then computed for each star to test against no variability:

$$\chi^2_{\rm red} = \frac{1}{\nu} \sum \frac{(\bar{m} - m_i)^2}{\sigma_i^2} \tag{2.3}$$

$$= \frac{1}{N-1} \sum \frac{(\bar{m} - m_i)^2}{\sigma_i^2}. \tag{2.4}$$

Here, the number of degrees of freedom, ν, was determined from the number of observations where a star is identified, N: $\nu = N - 1$. We expect a higher $\chi^2_{\rm red}$ value for stars with photometric measurements that deviate more often and more significantly from their mean magnitude.

We use a criterion in $\chi^2_{\rm red}$ to identify variable stars. We set the $\chi^2_{\rm red}$ variability threshold for each star such that the probability of obtaining its $\chi^2_{\rm red}$ value is less than 5σ given a Gaussian distribution of deviations from the mean. The specific $\chi^2_{\rm red}$ threshold for each star was based on its value of ν, between 15 – 44 in our sample. For $\nu = 44$ (star detected in all 45 nights), this variability threshold was at $\chi^2_{\rm red} > 2.40$, and went up to $\chi^2_{\rm red} > 3.87$ for $\nu = 15$ (star detected in 16 nights).

2.3.2 Deriving the Variability Fraction

We investigated the distribution of variability in our sample as a function of projected distance from Sgr A* and observed magnitude in K'. These models allow us to determine whether the location or the brightness of a star is correlated with its variability. Our fit to variability as a function of distance from Sgr A* was limited to those stars within $3''$ of Sgr A*. At greater distances, near the edges of our experiment's field of view, our sample started being affected by incompleteness due to the presence of artifact sources (see Section 2.2.3). We performed our fits to variability as a function of observed magnitude for all stars in our sample.

We used a mixture model analysis to model the stellar population, consisting of a variable and a non-variable population. Our models follow techniques similar to those outlined by Martinez et al. (2011). We assumed that the probability densities of stars in these populations at the Galactic center follow power law distributions, with R as the projected distance from Sgr A*: $\Sigma_v(R) \propto R^{\Gamma_{v,R}}$ and $\Sigma_n(R) \propto R^{\Gamma_{n,R}}$ for the variable and non-variable populations, respectively. The surface density of stars at projected distances close to the central black hole ($\lesssim 2$ pc) can be well described by power law distributions (see e.g. Do et al., 2013b; Gallego-Cano et al., 2018). To fit the mixture model, we obtained the likelihood of the variability fraction as a function of distance, Λ_R, following the form of the binomial distribution:

$$\Lambda_R \propto \prod_i \left[(F_R \Sigma_v)^{k_i} ((1 - F_R)\Sigma_n)^{k_i} \right]. \tag{2.5}$$

Here, the parameter F_R represents the variability fraction in the sub-sample used in our positional variability analysis and i represents the index of the individual stars of the sub-sample. We assigned $k = 1$ for variable stars and $k = 0$ for non-variable stars.

Similar to the projected distance probability density distributions, we assumed that the probability density distributions of the variable and non-variable populations with respect to observed magnitude, m, also follow power laws: $p_v(m) \propto m^{\Gamma_{v,m}}$ and $p_n(m) \propto m^{\Gamma_{n,m}}$ for the

variable and non-variable populations, respectively. The power law distribution in observed magnitude is expected to originate from the initial mass function, and has been observed previously for both early- and late-type stars at the Galactic center (see e.g. Bartko et al., 2010; Do et al., 2013a; Lu et al., 2013). To fit a mixture model from these distributions, we derived the likelihood of the variability fraction as a function of observed magnitude, Λ_m, again following the form of the binomial distribution:

$$\Lambda_m \propto \prod_i \left[(F_m p_v)^{k_i} ((1 - F_m) p_n)^{k_i} \right]. \tag{2.6}$$

Since only our fit to variability as a function of brightness used our entire stellar sample, we use its constraints on the variability fraction, F_m, as the overall variability fraction of our entire sample, F.

We used a Markov chain Monte Carlo algorithm, as implemented in the EMCEE software package (Foreman-Mackey et al., 2013), to fit our model parameters. In each trial sample, we normalized the individual power law distributions for the variable and non-variable populations over our experiment's bounds: $1 = \int_{\text{bounds}} 2\pi R \Sigma dR$ and $1 = \int_{\text{bounds}} p dm$ for our distance and brightness variability fits, respectively. We defined our variability model to have the following bounds in projected distance (R) and observed magnitude (m):

$$0.05'' \leq R \leq 3.00'', \tag{2.7}$$

$$9 \leq m \leq 16. \tag{2.8}$$

Our final variability models fitted the overall variability fraction of our sample, F_R and F_m, and two parameters each for the variable and non-variable population distributions with projected distance ($\Gamma_{v,R}$, $\Gamma_{n,R}$) and with magnitude ($\Gamma_{v,m}$, $\Gamma_{n,m}$). This gives each of our variability models a total of three parameters.

We can express our model as the fraction of variable stars as a function of distance from Sgr

A*:

$$f_{v,R} = \frac{F_R \Sigma_v}{F_R \Sigma_v + (1 - F_R)\Sigma_n} \tag{2.9}$$

$$= \frac{1}{1 + \frac{1-F_R}{F_R}\frac{\Sigma_n}{\Sigma_v}} \tag{2.10}$$

$$= \frac{1}{1 + c_R \frac{1-F_R}{F_R} R^{\alpha_R}}. \tag{2.11}$$

Here, $\alpha_R \equiv \Gamma_{n,R} - \Gamma_{v,R}$ and c_R is a constant factor originating from Σ_n/Σ_v used to obtain this relation.

Similarly, for observed magnitude we obtained:

$$f_{v,m} = \frac{1}{1 + c_m \frac{1-F_m}{F_m} m^{\alpha_m}}. \tag{2.12}$$

We additionally applied our brightness variability model to the known early- and late-type stars in our sample. Since the spectral typing originates from different spectroscopic surveys with incomplete spatial sampling across our experiment's field of view, we did not apply our distance variability model separately to the spectrally typed subsamples.

2.4 Periodic Variability

A major focus of the variability study in our stellar sample was to identify periodically variable stars. Periodic variability in observed flux has multiple origins. We were especially interested in identifying eclipsing or ellipsoidal binary systems and periodic variables such as Cepheids, RR Lyrae, and Mira variables.

The individual observations in our data set were unevenly spaced temporally, making it difficult to search for periodic signals through several commonly implemented periodicity search techniques, such as Fourier transforms, that rely on regular sampling. For our periodicity searches, we instead employed the Lomb-Scargle periodogram method, devised by Lomb (1976) and Scargle (1982). The Lomb-Scargle technique is specifically developed for

uneven temporal spacing and works by fitting Fourier components to the observed measurements. This makes it particularly optimized for detecting periodic signals that have an overall sinusoidal shape in their phased light curves.

2.4.1 Periodicity Search Implementation

We computed the Lomb-Scargle periodogram for all stars in our sample using the algorithm by Press & Rybicki (1989), implemented as part of the Astropy package (Astropy Collaboration et al., 2013).

Our uneven temporal spacing makes establishing detectability limits of periods in our periodicity search difficult. With regularly sampled data, the Nyquist limit establishes that the highest detectable frequency of a periodic signal is half of the sampling frequency. However, with sampling at a cadence with no underlying regularity in observation spacing, no similar limit can be determined (VanderPlas, 2018). In practice, due to the irregular spacing of observations, periods even shorter than the smallest observational spacing can still be detected. We used a period search range between 1.11 days and 10,000 days (between frequencies of 0.9 day^{-1} to 10^{-4} day^{-1}), as detailed in Appendix 2.10.1. Our trial periods for the Lomb-Scargle periodogram were derived from a uniform frequency grid. With our total observation span of $T = 4132.74$ days, our frequency spacing was dictated by the expected width of a peak in the periodogram: $\sim 1/T$ (VanderPlas, 2018). We chose an oversampling factor, $n_0 = 10$, to ensure that every peak in our periodogram is sufficiently sampled. This gave our final frequency grid spacing of $\Delta f = \frac{1}{n_0 T} = 2.420 \times 10^{-5}$ day^{-1}.

Our Lomb-Scargle periodicity searches were performed with standard normalization and a floating mean model. We additionally removed long-term linear trends from the light curve of each star before computing a periodogram. This removal of long-term linear trends is further detailed in Appendix 2.10.2.

2.4.2 Definition of Significance

We implemented a bootstrap false alarm test to assign significance to powers in our periodograms. We derive an estimates of false alarm probability (FAP) via the bootstrap methods outlined by Ivezić et al. (2014); VanderPlas (2018), using 10,000 mock light curves for each star. We define the significance of each power as $1 - \text{FAP}$. This technique estimated the likelihood of a power to appear in the periodogram given true observation cadence, typical brightnesses, and associated errors on the brightness for each star, but with no actual periodicity since measurements were shuffled when constructing each mock light curve. Importantly, this test does not give the probability that a given detection corresponds to a true periodic signal. Instead, the test estimates the likelihood that a periodogram peak does not originate from a non-periodic signal.

2.4.3 Aliasing in Periodicity Searches

The temporal spacing of our observations could introduce aliasing for real periodic signals in our data set, where secondary periodogram peaks could be introduced. Any true periodic signal is sampled by a window function at our observation times, and this window function's power spectrum (discussed in more detail in Section 2.10.1) is convolved with the true signal's power spectrum to create the observed power spectrum that can have secondary peaks or aliases. Based on our photometric data set alone, distinguishing between a periodic signal at the true periodic signal's period and its alias(es) on a periodogram is difficult.

Common aliases occur from typical observing cadences of an experiment. A true periodic signal is expected to have secondary aliased peaks appearing at $|f_{\text{true}} \pm \delta f|$, where δf is a strong feature in the observing window function (VanderPlas, 2018). In our experiment, the most common cadence was that originating from the length of a sidereal day: $\delta f = 1.0027\ \text{day}^{-1}$, leading to the strongest aliases of peaks in the periodogram. Other prominent features leading to aliases in our experiment came from our nightly observing cadence, $\delta f =$

1.0 day^{-1}, and yearly observing cadence, $\delta f \approx 2.7 \times 10^{-3}$ day^{-1}.

When considering detections in our periodogram, we excluded those that may originate from aliasing by long-term variations ($\gtrsim 1,000$ days). On such long time scales, we could not establish periodicity without observations of multiple periods. However, these long-term variations could be aliased to appear as strong detections in our periodicity search at periods shorter than 1,000 days. An example of this behavior is the star S4-172, shown in Figure 2.25, the long-term variability of which led to strong detections of periodicity at $\sim$ 100 and $\sim$ 365 days from aliasing. In our experiment, we found that stars with power $\gtrsim 50\%$ significance at periods longer than about a quarter of our observing baseline ($\frac{1}{4} \times T = \frac{1}{4} \times 4132.74$ days $= 1033.19$ days) could lead to strong detections at shorter periods.

2.5 Results

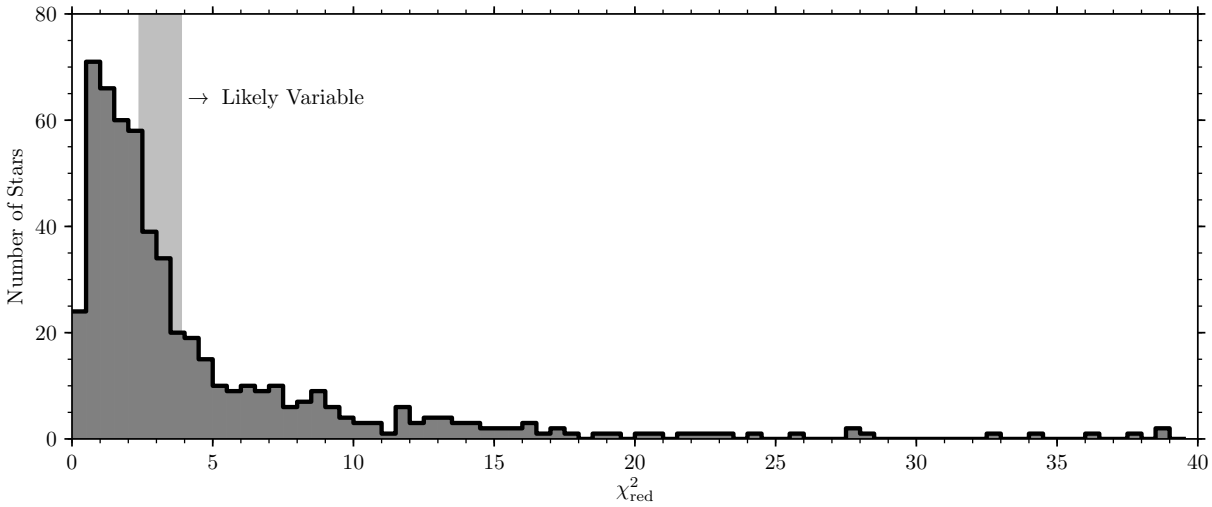

Figure 2.5: Binned $\chi^2_{\rm red}$ distribution for our stellar sample identified in at least 23 observations. For variability, we drew a cut in this distribution at 5σ, which for stars identified in 16 observations (with $\nu = 16 - 1 = 15$) corresponds to $\chi^2_{\rm red} > 3.87$. Stars identified in a greater number of observations have a corresponding higher ν resulting in a 5σ cut for variability at lower $\chi^2_{\rm red}$ values, going down to $\chi^2_{\rm red} > 2.40$ for stars identified in all 45 nights. These $\chi^2_{\rm red}$ cuts for variability depending on the number of nights are indicated by the vertical shaded region. In this sample with the 5σ variability cut, $50 \pm 2\%$ of stars are variable.

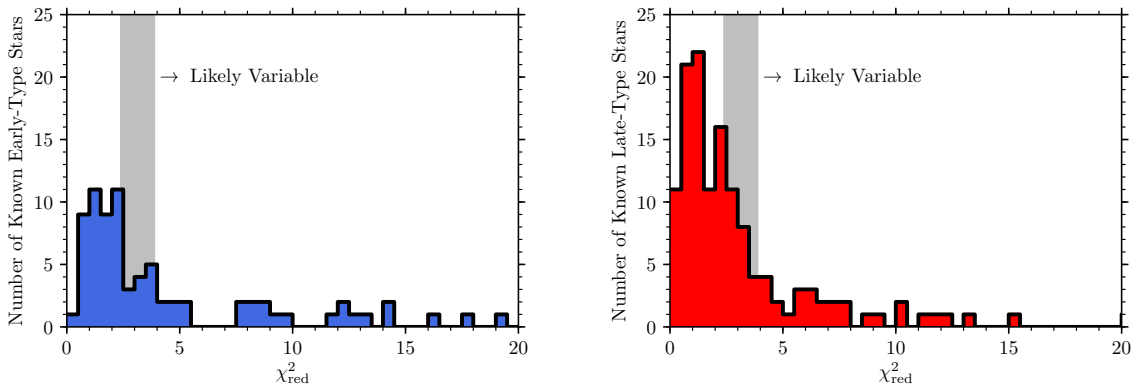

Figure 2.6: Same as Figure 2.5, but for our spectroscopically confirmed early-type stellar sample (left) and late-type stellar sample (right) identified in at least 16 observations. 52±5% of spectroscopically confirmed early-type stars are variable and $43 \pm 4\%$ of spectroscopically confirmed late-type stars are variable. The $\chi^2_{\rm red}$ cuts for variability depending on the number of nights are indicated by the vertical shaded region.

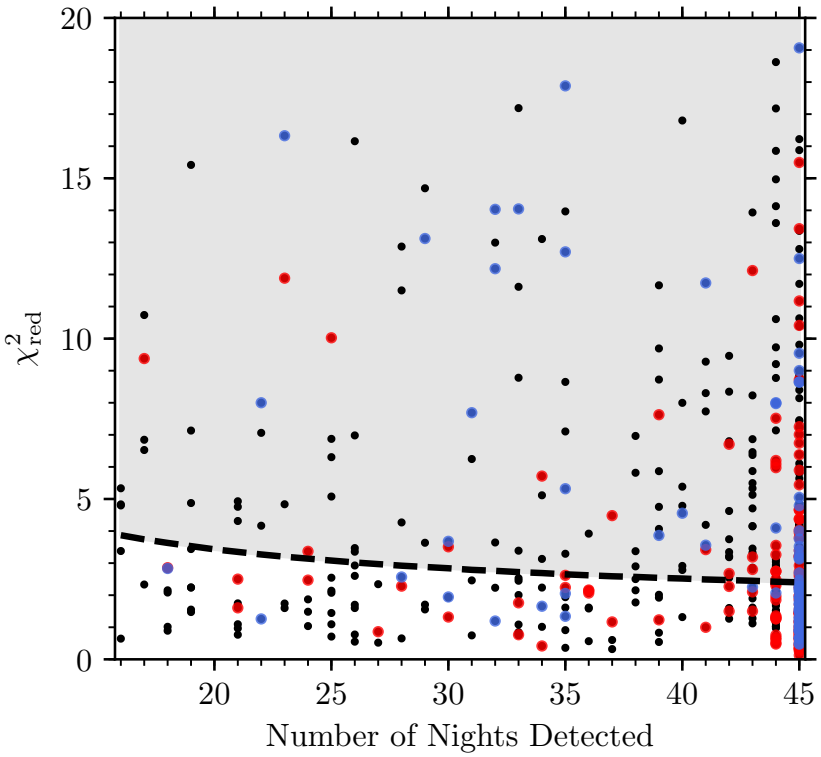

Figure 2.7: The dashed line indicates our 5σ $\chi^2_{\rm red}$ cut for variability as a function of number of nights. The stars identified as variable with this cut are in the shaded gray region. Dots colored blue/red are spectroscopically confirmed early-/late-type stars, while black dots correspond to stars that have unknown type.

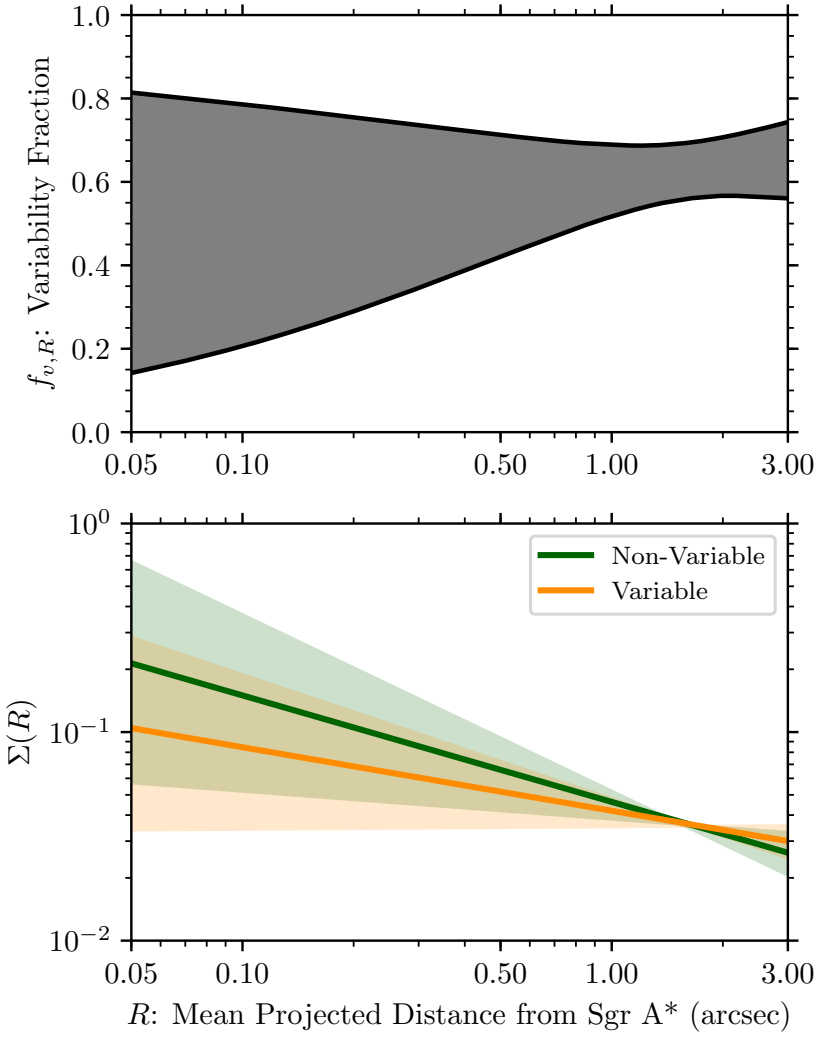

Figure 2.8: *Top:* The variability fraction as a function of projected distance from Sgr A*, R. The solid black lines indicate the median 2σ region of this relationship using stars with $R \leq 3''$ from Sgr A*. *Bottom:* The surface density distribution of our non-variable and variable star populations as a function of projected distance from Sgr A*, $\Sigma_n(R)$ and $\Sigma_v(R)$. Solid lines indicate median fit across all MCMC samples and the shaded regions indicate 2σ significance regions of this fit.

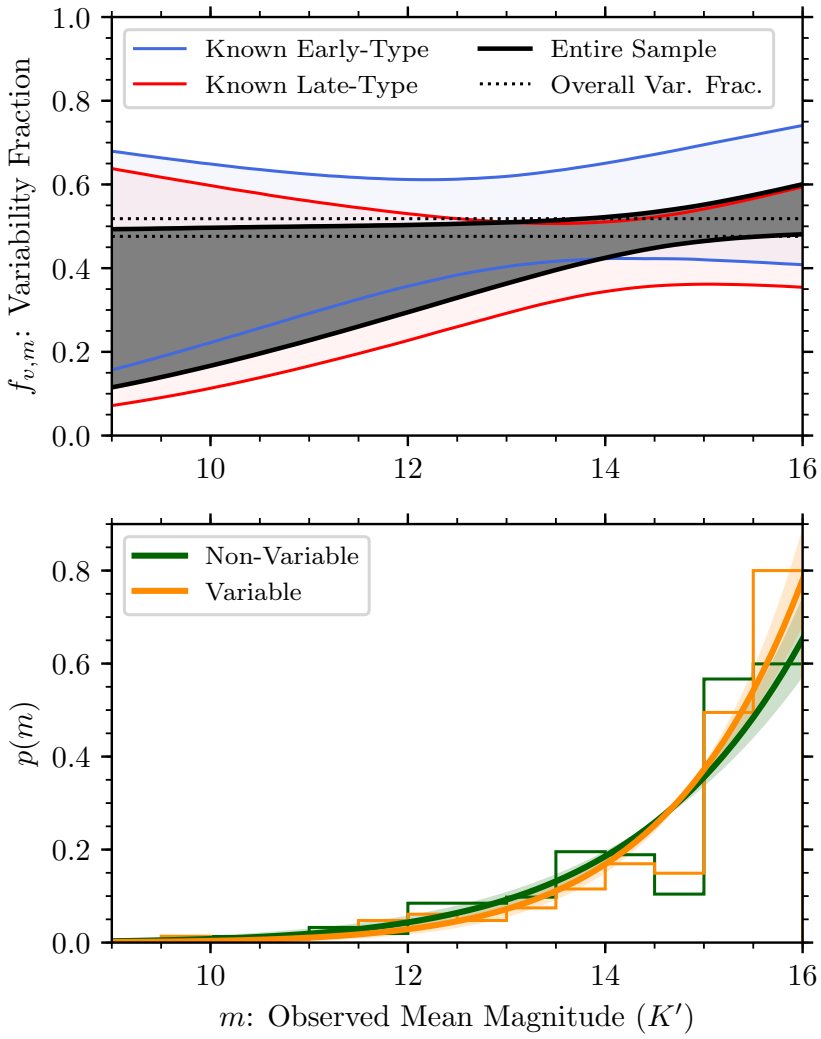

Figure 2.9: *Top:* Variability fraction as a function of observed magnitude, m. The solid black lines indicate the median 2σ region of this relationship using our entire stellar sample across all our MCMC samples. The blue and red lines indicate the same regions for the known young- and late-type stars in our stellar sample. The dotted lines indicate the 1σ constraints on the overall variability fraction in our sample. *Bottom:* Probability distribution of our non-variable and variable star populations as a function of observed magnitude, $p_n(m)$ and $p_v(m)$. Solid lines indicate median fit across all MCMC samples and the shaded regions indicate 2σ significance regions of this fit. The non-variable and variable star populations in our data are shown as binned histograms.

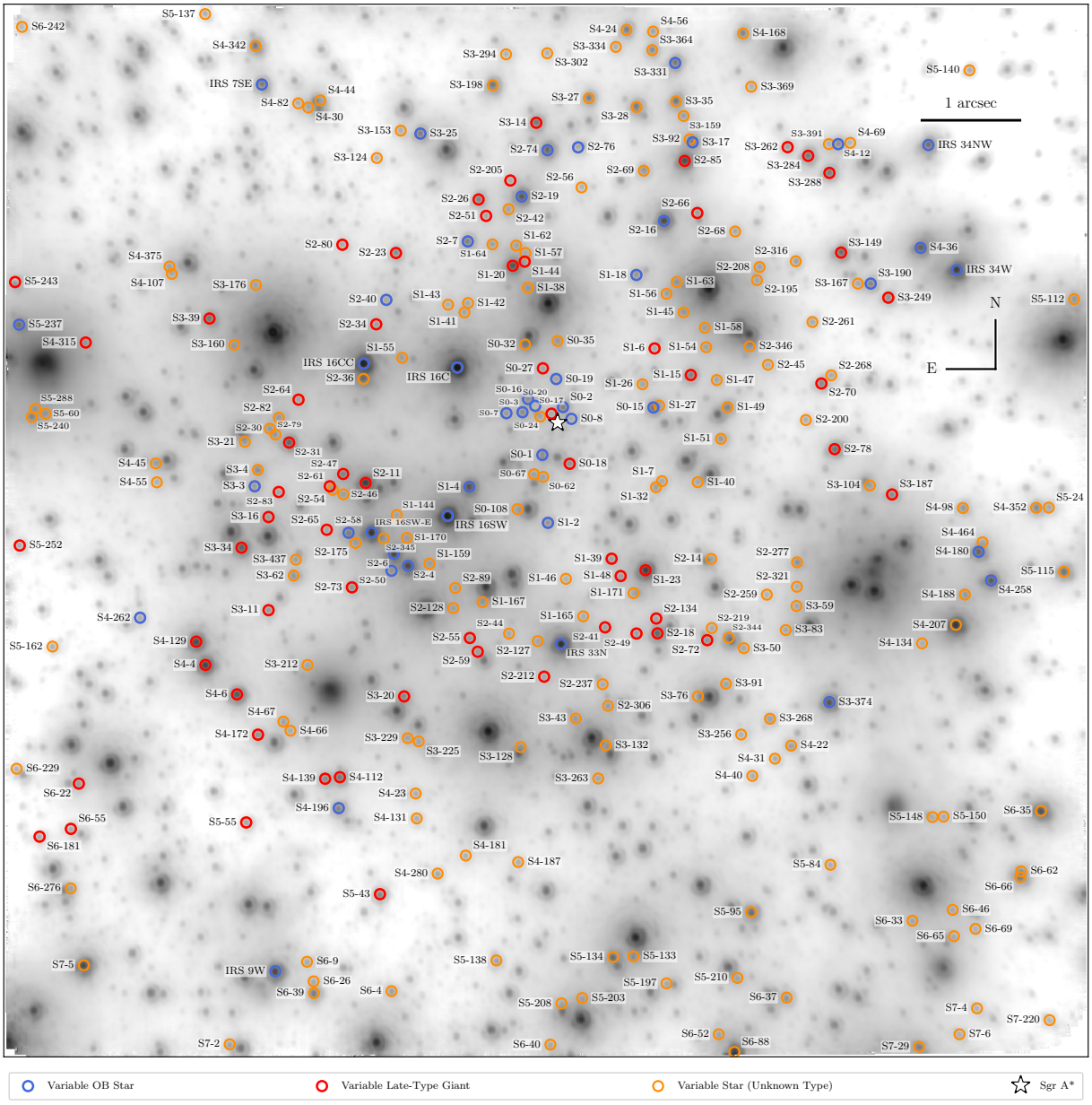

Figure 2.10: Stars identified as variable on our experiment's field of view. Blue, red, and orange circles indicate spectrally typed early-type, late-type, or unknown type variable stars respectively. The background image is from the 2012-05-15 observation.

Table 2.3: Fits to parameters of variability models

Parameter	Fit
Variability with distance	
F_R	0.63 ± 0.03
$\Gamma_{v,R}$	$-0.30^{+0.16}_{-0.15}$
$\Gamma_{n,R}$	$-0.51^{+0.18}_{-0.17}$
Variability with brightness	
$F = F_m$	0.50 ± 0.02
$\Gamma_{v,m}$	11.5 ± 0.8
$\Gamma_{n,m}$	9.4 ± 0.6
Variability with brightness, known early-type stars	
F_m	0.52 ± 0.05
$\Gamma_{v,m}$	$3.5^{+1.1}_{-1.0}$
$\Gamma_{n,m}$	2.1 ± 1.0
Variability with brightness, known late-type stars	
F_m	0.43 ± 0.04
$\Gamma_{v,m}$	8.5 ± 1.3
$\Gamma_{n,m}$	7.1 ± 1.0

2.5.1 Variability Fraction

With the $\chi^2_{\rm red}$ test for variability, we found that approximately half of the stars in our sample are variable. The $\chi^2_{\rm red}$ distribution for the stars in our variability sample is plotted in Figure 2.5, and the distributions for our sample's spectroscopically typed stars are shown in Figure 2.6. Figure 2.7 shows our sample's $\chi^2_{\rm red}$ distribution as a function of nights detected, overlaying our 5σ variability cut. Using the variable population models described in Section 2.3.2, we derived a variability fraction $F = 50 \pm 2\%$ among the stars in our sample. Light curves of "highly variable" stars (i.e.: $\chi^2_{\rm red} \geq 10.0$) are shown in Appendix A.1.

Our models also allow us to derive the variability fraction of stars as a function of projected distance from Sgr A* (Figure 2.8) and the observed magnitude (Figure 2.9). We do not find a significant change in the variability fraction as a function of projected distance (Table 2.3). We also find an increasing variability fraction for fainter stars in our samples, but this trend is not significant in our dataset.

When considering the spectrally-typed stars in our sample, we measured a variability fraction of $F = 52 \pm 5\%$ for the known early-type stars and $F = 43 \pm 4\%$ for the known late-type stars. We did not find a significant difference in the variability fractions as a function of magnitude for known early- nor known late-type star populations (Figure 2.9).

2.5.2 Periodically Variable Stars

Table 2.4: Criteria for Possible Periodic Signal

Criterion	Threshold
$\chi^2_{\rm red}$ Variability	$\geq 5\sigma$
Period Cut (from obs. baseline)	≤ 4132.74 d /4
	≤ 1033.19 d
Frequency Cut (from aliasing)	≤ 0.9 d^{-1}
Amplitude of Variability	$\geq 3 \times \bar{\sigma}_m$
(likely periodic threshold)	$\geq 5 \times \bar{\sigma}_m$
Bootstrap False Alarm Test	$\geq 90\%$
(likely periodic threshold)	$\geq 99\%$

Table 2.5: Likely Periodic Variable Stars

Star	Period (d)	Frequency (d^{-1})	K' Amplitude (Sinusoid Fit)	Amp. / $\bar{\sigma}_m$	$\bar{m}_{K'}$ (Sinusoid Fit)	Normalized Lomb-Scargle Power	Bootstrap False Alarm Test Significance
IRS 16SW	9.7238	0.1028	0.4833 ± 0.0132	14.21	9.9760 ± 0.0046	0.8579	100.00%
S2-36	39.4296	0.0254	40.3090 ± 0.0132	9.16	13.2899 ± 0.0049	0.7513	100.00%
S4-258	1.1380	0.8787	40.3414 ± 0.0171	9.21	12.5947 ± 0.0055	0.7650	99.91%

Table 2.6: Possible Periodic Signals

Star	Period (d)	Frequency (d^{-1})	K' Amplitude (Sinusoid Fit)	Amp. / $\bar{\sigma}_m$	$\bar{m}_{K'}$ (Sinusoid Fit)	Normalized Lomb-Scargle Power	Bootstrap False Alarm Test Significance
IRS 16SW^{S}	1.1112	0.8999	0.4696 ± 0.0130	13.81	9.9755 ± 0.0046	0.8527	100.00%
IRS 16SW^{D}	1.1146	0.8972	0.3949 ± 0.0137	11.62	9.9963 ± 0.0046	0.5450	97.58%
IRS 16SW^{Q}	10.8781	0.0919	0.3650 ± 0.0126	10.74	9.9729 ± 0.0046	0.5358	96.50%
S4-258^{S}	8.0637	0.1240	0.3318 ± 0.0165	8.96	12.6085 ± 0.0056	0.7511	99.78%
S2-72	12.5572	0.0796	0.0945 ± 0.0107	3.15	14.7411 ± 0.0039	0.5004	99.12%
S2-14	12.7509	0.0784	0.1169 ± 0.0122	3.76	15.6733 ± 0.0045	0.6553	98.76%
S2-58	84.6643	0.0118	0.1199 ± 0.0151	3.99	13.9289 ± 0.0050	0.5344	98.52%
S2-58	90.2084	0.0111	0.1144 ± 0.0147	3.81	13.9564 ± 0.0045	0.5240	97.81%
S4-139	24.6270	0.0406	0.1162 ± 0.0119	3.60	14.3908 ± 0.0042	0.5450	98.25%
S4-139	228.1610	0.0044	0.1141 ± 0.0121	3.54	14.3939 ± 0.0043	0.5155	95.14%
S4-139	12.5154	0.0799	0.1052 ± 0.0112	3.26	14.4095 ± 0.0042	0.5096	93.87%
S4-139	15.0768	0.0663	0.0988 ± 0.0106	3.06	14.4031 ± 0.0042	0.5011	91.86%
S3-27	26.5578	0.0377	0.1181 ± 0.0157	3.27	13.9328 ± 0.0047	0.5283	98.19%
S2-4	36.0896	0.0277	0.1831 ± 0.0128	5.72	11.9297 ± 0.0044	0.5276	97.16%
S2-4	23.2159	0.0431	0.1852 ± 0.0133	5.78	11.9258 ± 0.0045	0.5052	94.61%
S6-69	101.7584	0.0098	0.2042 ± 0.0292	3.18	15.9514 ± 0.0112	0.4964	96.27%

Table 2.6 (cont'd): Possible Periodic Signals

Star	Period (d)	Frequency (d^{-1})	K' Amplitude (Sinusoid Fit)	Amp. / $\bar{\sigma}_m$	$\bar{m}_{K'}$ (Sinusoid Fit)	Normalized Lomb-Scargle Power	Bootstrap False Alarm Test Significance
S3-4	315.1572	0.0032	0.0999 ± 0.0103	3.16	14.6326 ± 0.0041	0.5247	95.63%
S1-6	3.6810	0.2717	0.2182 ± 0.0161	6.11	15.3949 ± 0.0062	0.7864	93.17%
S1-6	1.3679	0.7310	0.2289 ± 0.0174	6.40	15.3951 ± 0.0061	0.7764	90.60%

[S]Indicates a sidereal day alias of known periodic signal.

[D]Indicates a solar day alias of known periodic signal.

[Q]Indicates a quarter year (≈ 91.3 days) alias of known periodic signal.

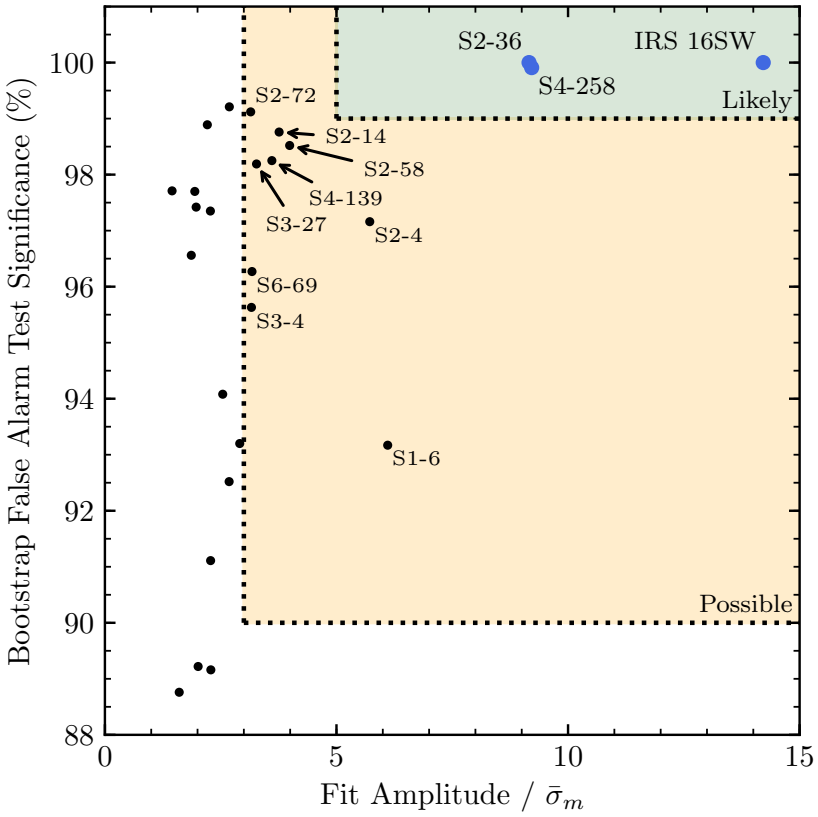

Figure 2.11: Periodicity detections that pass the variability, periodicity, and frequency cuts in our search, with bootstrap false alarm test significance plotted against the variability amplitude. For clarity, only the most significant periodicity search detection is plotted for stars that have multiple detections passing the variability, periodicity, and frequency cuts. The stars that we identify as *likely periodic variables* (IRS 16SW, S2-36, and S4-258) stand out distinctly in significance and amplitude from other possible periodic detections identified in our experiment.

We defined our possible periodic signals using a combination of criteria (summarized in Table 2.4) that were motivated by the characteristics of our periodicity search detailed in Section 2.4. In our periodicity search, we considered stars identified as variable by our $\chi^2_{\rm red}$ test for variability. We defined a maximum period for our periodicity search at $\frac{1}{4}\times$ our ob-

servation baseline: $\frac{1}{4} \times 4132.74$ d $= 1033.19$ d. We then removed as likely periodic any stars that had power exceeding 50% significance in our bootstrap false alarm test longer than the maximum period cutoff. At such long timescales, our observation baseline was not able to sample a possible periodic signal sufficiently often to claim periodicity. Further, any variability leading to high power in our Lomb-Scargle test at these long periods could easily get aliased to shorter periods to falsely resemble shorter-period variability. The minimum search period in our experiment was 1.11 d (from our maximum search frequency cut of 0.9 d^{-1}). Higher frequencies (i.e. shorter periods) than this threshold suffered from frequently aliased peaks.

We then imposed an amplitude threshold for the remaining detections in our periodicity search. To calculate the amplitude, we constructed a sinusoidal fit to the stellar light curve phased to each periodicity detection. To pass the threshold, the amplitude of the fit must exceed 3× the mean magnitude uncertainty for the star. This threshold is imposed to remove possible peaks originating from statistical fluctuations in our photometry. We finally used our bootstrap false alarm test significance to evaluate whether a star is likely to be periodically variable. If a periodicity detection exceeded 90% significance in the bootstrap false alarm test, the signal was then considered to be a *possible periodic signal*.

Three stars in our sample had periodic detections greatly exceeding the possible periodic signal detection amplitude and bootstrap false alarm criteria (IRS 16SW, S2-36, and S4-258; see Figures 2.11 and 2.12). Based on the three stars' detections, we developed stricter thresholds for these criteria with which we identified *likely periodic variables*: amplitude exceeding 5× the mean magnitude uncertainty, and detection exceeding 99% significance in the bootstrap false alarm test. Stars identified as likely periodic variables are listed in Table 2.5 and possible periodic signal detections are listed in Table 2.6. The significance and amplitude of these detections are plotted in Figure 2.11. Phased light curves of all possible signal detections are included in Appendix A.2.

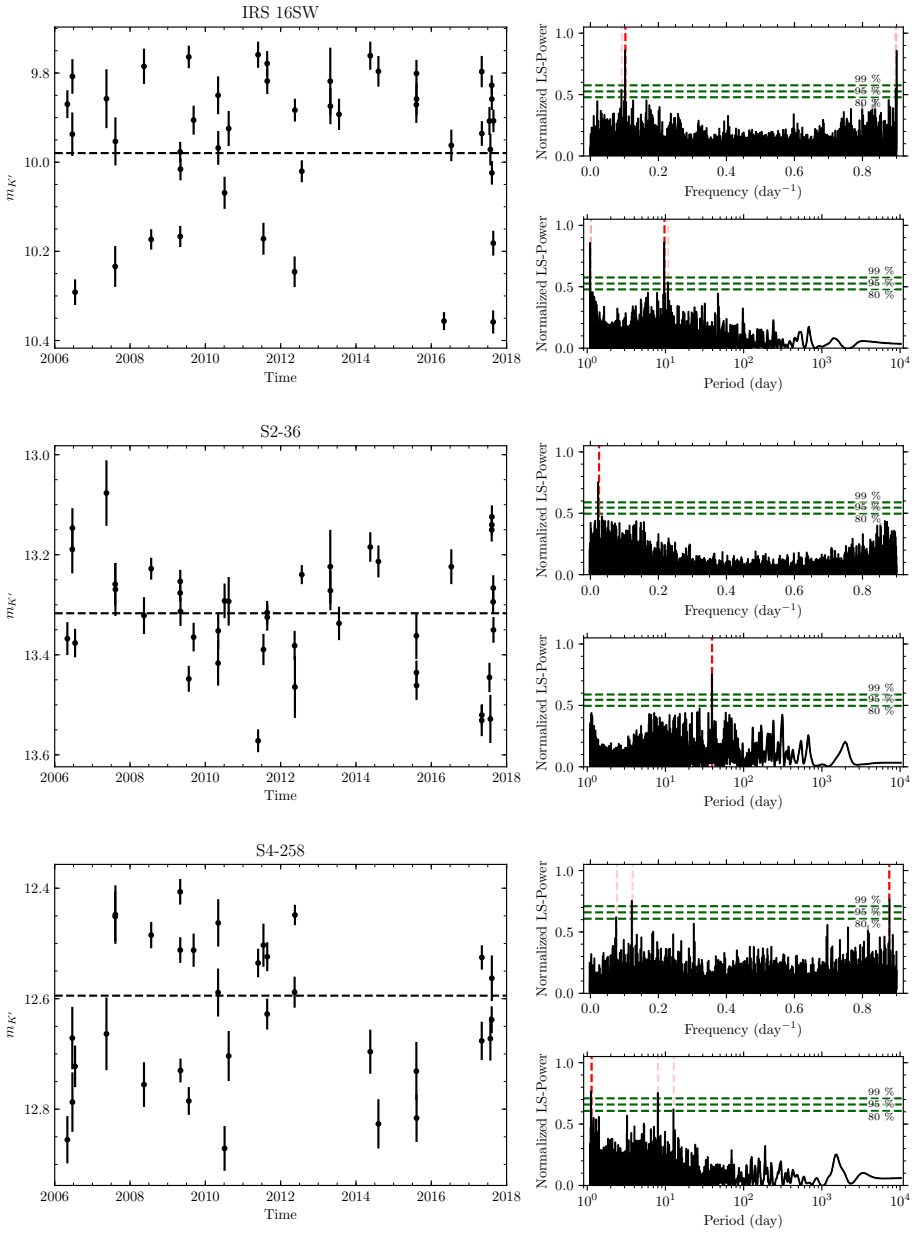

Figure 2.12: Light curves (*left*) and periodograms (*right*) for the likely periodic variable stars IRS 16SW, S2-36, and S4-258. The horizontal dashed lines in the light curves indicate the weighted mean magnitude. The horizontal dashed green lines in the periodograms indicate the bootstrap test significance levels, while the vertical dashed red lines indicate periodogram peaks above 80% bootstrap significance.

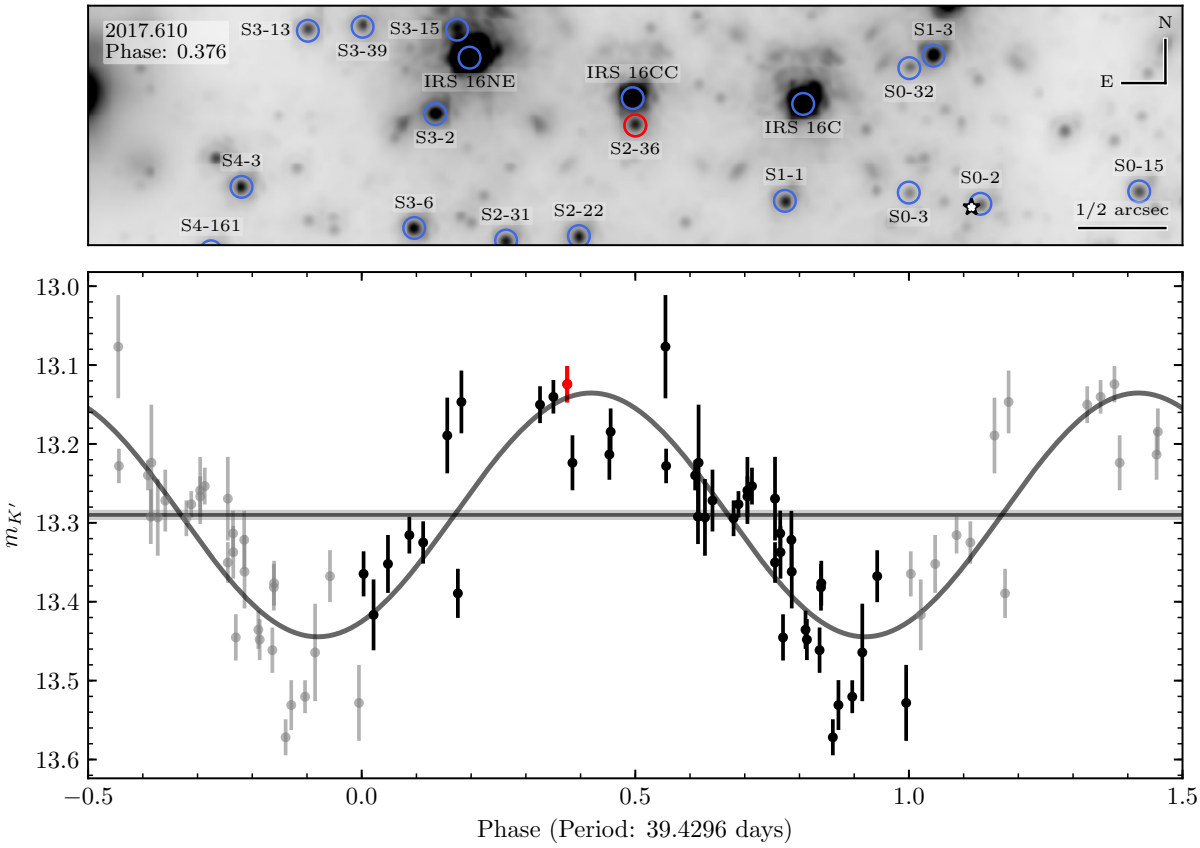

Figure 2.13: *Top:* An image of the field near S2-36 from the 2017-08-11 observation. S2-36 is circled in red, while nearby stars brighter than $m_{K'} = 14.5$ are circled in blue. The white star symbol indicates the position of Sgr A*, the location of the supermassive black hole. This observation is highlighted in the phased light curve as the red point. *Bottom:* Phased light curve of S2-36 at the 39.43 day period found in the periodicity analysis. The best fit first order sinusoid model to the observations is overlaid. The horizontal line and surrounding shaded region indicate the fit mean magnitude and its uncertainty, respectively. The red point indicates the observation highlighted on top.

2.5.2.1 Likely periodic variable stars

The stars with periodic signal detections passing our criteria for *likely periodic variable stars* are listed in Table 2.5. The likely periodic variables IRS 16SW and S4-258 are known eclipsing binary stars, which exhibit two eclipses with similar depths over their orbital period, and are therefore detected at half their binary period in the Lomb-Scargle periodicity search. Additionally, both of these stars have possible periodic signal detections at aliases originating from the length of a sidereal day (1.0027 day^{-1} frequency). IRS 16SW has additional signals passing for possible periodicity which are aliases originating from the length of a solar day (1.0 day^{-1} frequency) and the length of a quarter year (1.1×10^{-2} day^{-1} frequency). These aliases are specifically indicated in Table 2.6.

In addition to the known Galactic center eclipsing binary stars, we identified the star S2-36 as a likely periodic variable star. From our periodicity search, S2-36 has a period of 39.43 days (see Figures 2.12 and 2.13). The periodic variability in this star has not been reported previously.

2.5.2.2 Possible periodic signals

The stars with periodic signal detections passing our criteria for *possible periodic signals* are listed in Table 2.6, and phased light curves are provided in Section A.2.2. With the limitations from our experiment's photometric precision and observational cadence, it is difficult to conclude whether these represent true periodic variability. We highlight below characteristics of the possible periodic signals in our sample, in three different period regimes.

- *1 – 10 days:* Besides the aliased signals detected from the known periodic variables, IRS 16SW and S4-258, we find signals from S1-6 in this period regime. S1-6 has two signals passing for possible periodicity, at 1.37 and 3.68 days. The two periods detected correspond to sidereal day (1.0027 day^{-1} frequency) aliases of each other. It is difficult to favor photometrically one period over the other as the more likely astrophysical

signal if these cases are indeed detections of true periodic variability. This period regime is particularly interesting since detections could be indications of near-contact, short-period binary systems. The signals have roughly sinusoidal shaped phased light curves, but the limited significance and amplitude of these signals makes it difficult to confirm their validity as true astrophysical signals.

- *10 – 80 days:* In a longer period regime, we find more possible periodic signals. In this period regime, we do not expect to detect any sidereal day aliases from possible signals since aliased frequencies would be larger than our experiment's frequency search space.

  We found five stars with possible periodic signals in this period regime: S2-72, S2-14, S4-139, S3-27, and S2-4. As a known OB star, S2-4's possible periodic variability is difficult to explain as originating from eclipsing binary systems. The dip in its light curve is wide in phase, unexpected from eclipses at the observed period. Using NIR period-luminosity relations for these possible periodic signals at the observed periods (Riebel et al., 2010), the possible periodic variable signals in S2-72, S4-139, and S3-27 may be consistent with those of ellipsoidal binaries under typical Galactic center extinctions of $A_{K'} \approx 2$–3 magnitudes (Schödel et al., 2010). However, several of the possible periodic signals in this regime are detected in stars with light curves suggesting long-term variability trends over our observation baseline (i.e. S2-72, S2-14, S3-27, S2-4). The long-term variability trends may be causing the apparent periodicities by being aliased to shorter periods. Since the long-term variability trends of these stars do not appear as significant detections at long periods, the short period detections remain as possible signals under our periodicity search criteria. Future color observations can more precisely test if the variability is indeed consistent with known periodic variable classes.

- *>80 days:* In this period regime, S2-58, S4-139, S6-69, and S3-4 have possible periodic signals. While the periods and amplitudes of these stars are consistent with pulsations

in evolved stars or ellipsoidal binary systems, the observed mean magnitudes are too faint to be consistent with these classes of variables. Using NIR period-luminosity relations for these possible periodic signals at the observed periods (Riebel et al., 2010; Matsunaga et al., 2009), the periodic variability detections have mean magnitudes ~ 1 – ~ 3.5 too faint than what is expected under typical Galactic center extinctions of $A_{K'} \approx 2$–3 magnitudes (Schödel et al., 2010). Future observations in color of these stars can more precisely test these possibilities.

2.6 Discussion

2.6.1 High stellar variability fraction at the Galactic center

In this study, we find that $50 \pm 2\%$ of all stars show variability in the central 0.5 pc of Milky Way nuclear star cluster. This level of stellar variability is greater than what has been found in previous studies of both young clusters and globular clusters in the past. The long time baseline of this survey compared to previous surveys increases our sensitivity to long-term intrinsic brightness variations in stars. In addition, spatial variations in the foreground extinction and stellar confusion can cause brightness variations as the stars move.

Table 2.7: NIR Variability Studies of Spectrally-Typed Resolved Stellar Populations

Star Population	Paper	Variability Fraction	Time Baseline
Young, Massive Stellar Populations			
NGC 7380	Lata et al. (2016)	(57 variable stars identified)	4 months
Cygnus OB7	Rice et al. (2012)	$1.74 \pm 0.14\%$	1.5 years
Orion Nebula	Rice et al. (2015)	$8.17 \pm 0.24\%$	2.4 years
Quintuplet	Glass et al. (1999)	$8.5 \pm 1.5\%$	≈ 3 years
SMC OB Stars	Kourniotis et al. (2014)	$40.38 \pm 0.93\%$	≈ 8 years
Globular Cluster Late-Type Giant Populations			
M71	McCormac et al. (2014)	$0.11 \pm 0.02\%$	74 days
M4	Nascimbeni et al. (2014)	$0.40 \pm 0.07\%$	340 days
10 Galactic GCs	Figuera Jaimes et al. (2016a)	$0.49 \pm 0.06\%$	1.3 years
NGC 6715	Figuera Jaimes et al. (2016b)	$5.98 \pm 0.65\%$	2.3 years

Note. — We have recorded the number of variable stars identified for studies that do not report a variability fraction or total sample size.

Table 2.8: Variability in Smaller Time Baseline Subsamples

Data Used	Time Baseline (yr)	$F_{\rm young}$	$F_{\rm old}$
2006 – 2017	11.31	0.52 ± 0.05	0.43 ± 0.04
2006 – 2016	10.20	0.44 ± 0.05	0.36 ± 0.04
2007 – 2016	9.16	0.44 ± 0.05	0.32 ± 0.04
2008 – 2016	8.16	0.42 ± 0.05	0.32 ± 0.04
2009 – 2016	7.20	0.40 ± 0.05	0.32 ± 0.04
2010 – 2016	6.19	0.34 ± 0.05	0.22 ± 0.04
2011 – 2016	5.13	0.30 ± 0.05	0.19 ± 0.03
2012 – 2016	4.16	0.24 ± 0.05	0.17 ± 0.03
2013 – 2016	3.21	0.13 ± 0.04	0.07 ± 0.02
2014 – 2016	2.15	0.09 ± 0.03	0.06 ± 0.02
2015 – 2016	0.93	0.07 ± 0.03	0.03 ± 0.02

2.6.1.1 Variability from long time baseline

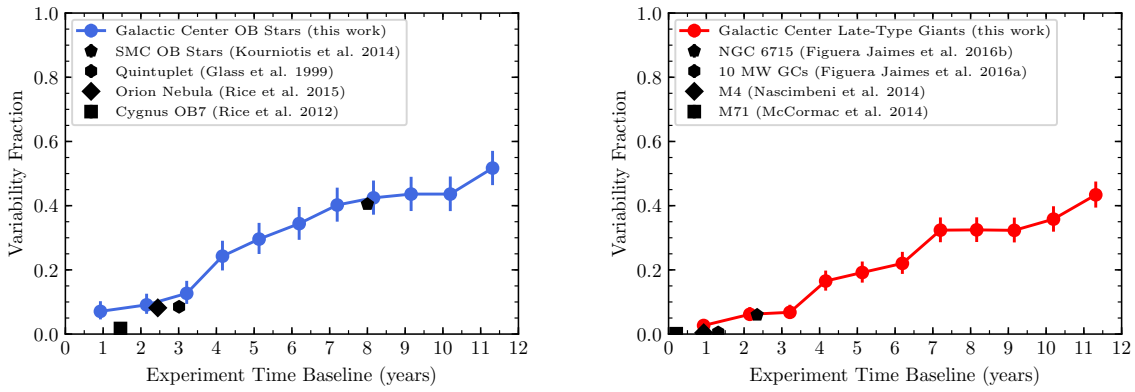

Figure 2.14: Variability fraction as a function of experiment time baseline for NIR studies of resolved young, massive star populations (*left*) and of late-type, globular cluster (*right*). Variability fractions for the Galactic center young (*left*) and old (*right*) stars derived in this work (entire sample and smaller time baseline subsamples) are shown as black points.

The higher level of variability we detect at the Galactic center can be largely accounted for by our experiment's long time baseline of $\sim$ 11.5 years. Most NIR stellar variability studies of other young, massive star populations or late-type giants in globular clusters have had overall time baselines on the order of several months to a few years (see Table 2.7 and Figure 2.14). To demonstrate the increase in sensitivity to variability with long time baselines in our experiment, we ran our variability models on smaller time baseline subsamples of our data, spanning from $\approx$ 1 year to $\approx$ 11.5 years (see Table 2.8).

Our models demonstrate much lower variability fractions at shorter time baselines. As Figure 2.14 and Table 2.8 demonstrate, only $\approx$ 7% of the known young, OB stars in our sample are variable and only $\approx$ 3% of the known old, late-type giants are variable with an experimental time baseline of $\approx$ 1 year. The variability fraction for both stellar type groups rises as the time baseline increases, reaching $\approx$ 52% and $\approx$ 43% in our complete time baseline for the young and old stars, respectively. When comparing to previous NIR

studies of stellar variability in other resolved young or old stellar populations, the variability fractions we find in our experiment are largely consistent if we account for the time baselines of the experiments (Figure 2.14). Overall, our smaller time baseline subsamples demonstrate that the high variability fractions in our experiment are largely due to the long time baseline.

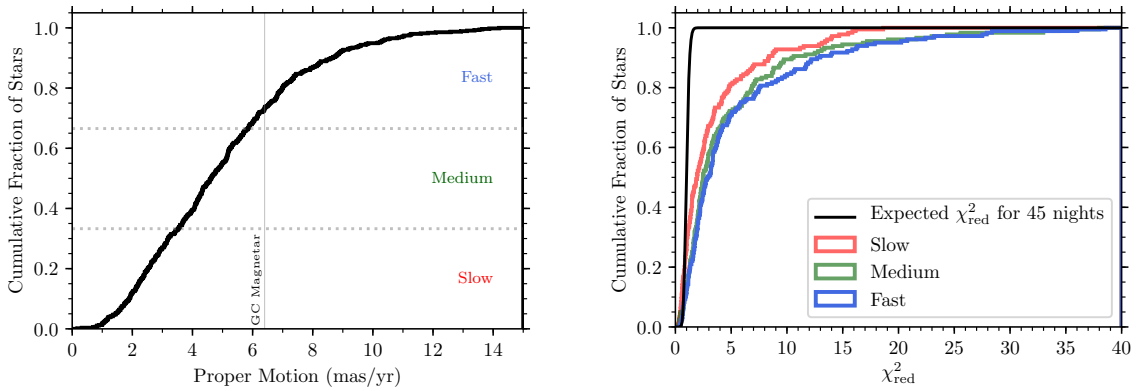

Figure 2.15: *Left:* The cumulative distribution of proper motion velocity in our sample of stars, outside of an arcsecond of Sgr A*. We divided these stars into three groups, with the same number of stars in each group. This grouping helps select stars in the high proper motion tail of the distribution as the *fast* stars. Notably, the *fast* stars have proper motions comparable to or higher than that of the Galactic center magnetar, PSR J1745-2900, indicated by the vertical line. *Right:* The cumulative distribution of our variability metric, $\chi^2_{\rm red}$, amongst the three proper motion groups of stars. We found that the $\chi^2_{\rm red}$ distribution of the *slow* stars is significantly different from those of both the *medium* and *fast* stars ($> 2\sigma$ and $> 3\sigma$, respectively), while there is no significant difference amongst the distribution of *medium* and *fast* stars ($< 1\sigma$).

2.6.1.2 Variability from Extinction Screen

The longer 11.5 year time baseline of our experiment allowed some of the additional variability to be contributed from stellar proper motions probing the foreground extinction screen. The Galactic center has large extinction and clumpiness in the foreground extinction screen

(e.g. Paumard et al., 2004; Schödel et al., 2010; Nogueras-Lara et al., 2018). Variability in the foreground extinction on large angular scales can result in correlated variability for several stars close together, and consequently would be lessened or removed during our local photometric correction step (Section 2.8.3). The typical separation of stars in our sample is ≈ 240 mas, with smaller separations in the central, more crowded regions of our field. Our experimental methodology would therefore not be very sensitive to features in the foreground extinction screen at much larger angular scales. However, there exist a large number of thin dust filaments identified with L-band observations of the Galactic center, with widths $\lesssim 100$ mas (Muzic et al., 2007; Clénet et al., 2004; Paumard et al., 2004; Ghez et al., 2005). These filaments may be traces of gas compressed by shocks at the Galactic center and could be confined by magnetic fields in the area (e.g. Morris et al., 2017). Similar streamer features are also identified at other infrared and radio wavelengths (e.g. Yusef-Zadeh et al., 1998; Zhao & Goss, 1998; Morris & Maillard, 2000; Paumard et al., 2001; Scoville et al., 2003; Morris et al., 2017) and may be related. These filaments are narrow enough to extinguish light from single stars in our sample at the Galactic center, and the resulting variability would consequently not be affected by our local photometric correction.

Radio observations of the Galactic center magnetar PSR J1745-2900 provide an empirical estimate of the extinction. Rapid changes in the observed Faraday rotation measure as the magnetar's rapid proper motion allowed probing different sightlines. The observations suggest fluctuations in the Galactic center magnetic field or free electron density on size scales $\sim$ 2 to $\sim$ 300 AU (Desvignes et al., 2018), lending evidence for the presence of a scattering screen of gas in the Galactic center environment. Previous observations have suggested that the central parsec of the Galactic center hosts well-mixed warm dust and ionized gas (Gezari & Yusef-Zadeh, 1991). If the magnetic field or free electron fluctuations implied by the Galactic center magnetar are associated with dust, they can result in NIR variability for similarly fast moving stellar sources due to varying extinction.

Table 2.9: Proper Motion Variability Groups

Group	Proper Motion (μ)	Var. Frac. (F)
Fast	$\mu > 5.89$ mas/yr	0.55 ± 0.04
Medium	$3.56 < \mu < 5.89$ mas/yr	0.51 ± 0.04
Slow	$\mu < 3.56$ mas/yr	0.41 ± 0.04

To explore the possibility that faster moving stars are more variable, we divided our stellar sample into three proper motion groups, each containing an equal number of stars: *slow*, *medium*, and *fast*; see Table 2.9 and Figure 2.15. The proper motion for each star was obtained from either a velocity or acceleration model fitted to the astrometric positions, depending on which model resulted in a fit with a lower $\chi^2_{\rm red}$ statistic. The velocity component of the chosen model's fit was then used for the proper motion analysis. To avoid stars poorly fit with the proper motion models, we excluded 8 stars from our proper motion groups that have measured orbits around Sgr A* (S0-1, S0-2, S0-3, S0-5, S0-16, S0-19, S0-20, and S0-38). The *fast* proper motion group in particular consists of stars with proper motions comparable to or exceeding the proper motion observed for the Galactic center magnetar (≈ 6.4 mas yr^{-1}; Desvignes et al., 2018), and we expect these stars to probe variations in the foreground extinction screen similar to those inferred for the Faraday screen of the magnetar.

We found that stars with larger proper motions in our sample are more likely to exhibit variability than stars with slower proper motions. The variability fractions of the three proper motion groups are listed in Table 2.9, and we find that the higher proper motion groups have significantly higher variability fractions. We further tested whether faster moving stars are more variable than slower stars by the two-sample Kolmogorov-Smirnov test (K-S test). Amongst the three proper motion groups, we derived the cumulative distribution of our photometric variability metric, $\chi^2_{\rm red}$. We computed the two-tailed K-S test p-value of all

pairs of distributions. The p-value gives the probability of the two sample distributions being drawn from the same underlying distribution. Between the *medium* and *fast* groups, we found $p = 60.22\%$, indicating a small difference ($< 1\sigma$) between the groups' respective $\chi^2_{\rm red}$ distributions. However, when comparing the *slow* group with both the *medium* ($p = 0.33\%$, $> 2\sigma$) and *fast* ($p = 0.04\%$, $> 3\sigma$) groups, we found more significant differences in the $\chi^2_{\rm red}$ distributions. Overall, our data demonstrate that slower stars have significantly lower variability in our experiment when compared to faster stars, and that variability is more likely for stars with faster proper motions. These results suggest that the foreground extinction is a contributor to our variability fraction since faster moving stars probe larger variations in the foreground extinction screen.

Furthermore, we consider in detail whether some of the most prominent long-term fluctuations in our variable star sample can be physically explained by the foreground extinction screen. Changes in the observed flux for a stellar source imply a change in optical depth, τ_λ:

$$\begin{aligned} A_\lambda &= -2.5 \log_{10}(I_\lambda / I_{\lambda,0}) && (2.13) \\ &= -2.5 \log_{10}(e^{-\tau_\lambda}) && (2.14) \\ &= \tau_\lambda(-2.5 \log_{10} e) \approx \tau_\lambda \times 1.086 && (2.15) \end{aligned}$$

Assuming a constant cross section, σ_λ, for extinguishing dust grains, changes in optical depth, $\Delta\tau_\lambda$, correspond to changes in column density, ΔN_d:

$$\Delta\tau_\lambda = \sigma_\lambda \Delta N_d \quad (2.16)$$

Amongst our highly variable stars (Section A.1), stars exhibiting long-period brightening or dimming have changes in observed flux approaching ≈ 0.5 magnitudes (e.g. S2-316, S4-12,

S4-262) to ≈ 1.0 magnitudes (e.g. S3-34). Following Paumard et al. (2004), we assume that extinction at K-band is about $0.1\times$ that in visual and that a magnitude of extinction at visual implies a column density of $\approx 2 \times 10^{21}$ cm^{-2} H atoms. These large dips in magnitude would imply changes in column density of $\approx 10^{22}$ cm^{-2}. Since these stars exhibited only either a dimming or brightening, it is difficult to establish a physical size to inhomogeneities in the foreground material if caused by extinction. However, such scales of extinction are consistent with those observed by Paumard et al. (2004) from large gas features like the *Minispiral* at the Galactic center.

Using stars that exhibit both brightening and dimming over our time baseline (e.g. S2-66, S3-249, IRS 7SE), we can estimate the density of dust in extinguishing filaments. These stars display momentary dips in flux of ~ 1 mag lasting ≈ 4 years. While there can be various physical geometries of the extinguishing material, such as dust blobs, sheets, or bow shocks, we assume here for simplicity that the dips originate from thin, filamentary structures located near the Galactic center. Under this physical assumption, the proper motion measurements of these stars in our dataset imply filament diameters of approximately 10^{-3} pc or 200 AU. Our diameter estimate assumes static filaments, but if the filaments themselves are also in motion near the stellar sources, the diameter estimate may increase by a factor of ≈ 2. The typical magnitude dips then indicate number densities in the extinguishing filaments of $\approx 3 \times 10^6$ cm^{-3}. These thin regions of high extinction could correspond to foreground high density filaments similar to those identified by Muzic et al. (2007). The densities are consistent with models of high density bow shocks at the Galactic center (Tanner et al., 2002). In fact, IRS 7SE's location is consistent with the X1 filament, proposed to be a bow shock source (Clénet et al., 2004; Muzic et al., 2007). Another highly variable star, S4-12, has a location consistent with the X4 filament (Muzic et al., 2007), a proposed bow shock source originating from IRS 3 (Viehmann et al., 2005; Yusef-Zadeh et al., 2017). The filaments could be responsible for the long-term flux dips observed in these two stars' light curves. S2-66 and S3-249, however, do not have corresponding filaments identified by Muzic et al.

(2007) that would be consistent with their locations. Rafelski et al. (2007) highlighted the long-term variability in the light curves of three stars (particularly S2-11) using independent data as also likely originating from their passage behind thin, high-density filaments. Our experiment's observations, taken at a later time, do not reveal similar features in these stars' light curves.

Our observations suggest that variations in the extinction screen can indeed account for some of the high variability fraction found in this experiment. With our K' dataset alone, however, it is difficult to assign this as the primary source of variability for any given star in our sample. Extensions of our variability study incorporating simultaneous observations at other wavebands over a long-period can add substantially to the study of extinction variations. Particularly, increased reddening during dips in flux would suggest dust extinction as the likely cause (see e.g. Rice et al., 2015).

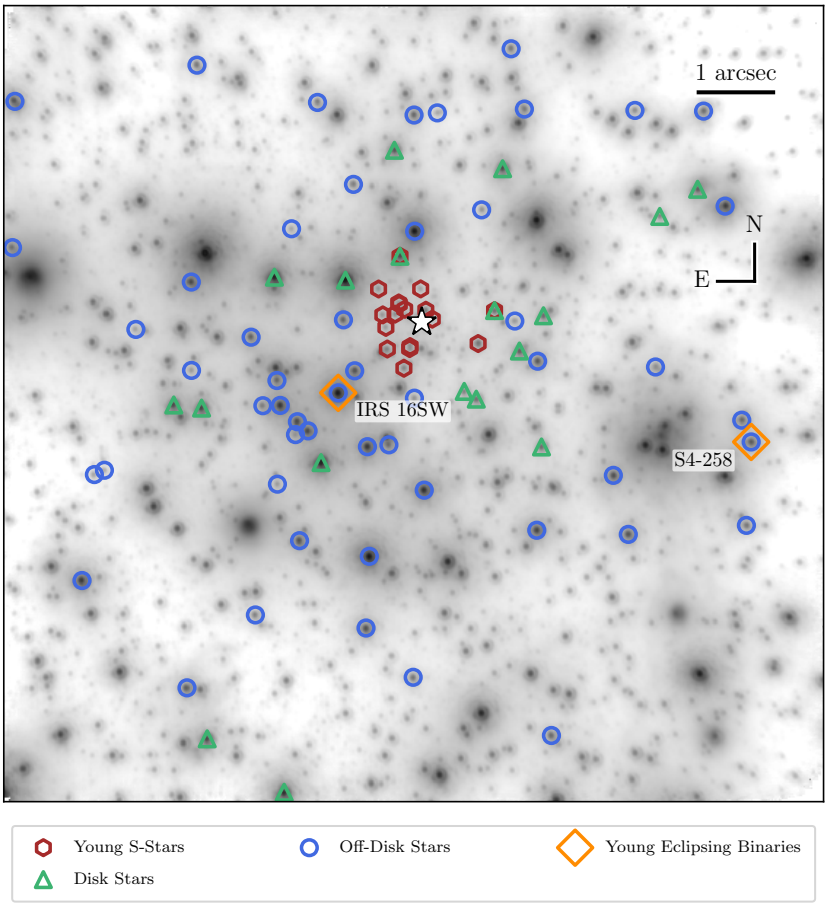

Figure 2.16: The young stars in our sample, indicated on the 2012-05-15 observation. We identify here the young disk and S-Star stellar populations from our sample. The young eclipsing binary systems detected in this experiment are labelled: IRS 16SW (Ott et al., 1999; Peeples et al., 2007; Rafelski et al., 2007) and S4-258 (E60, discovered by Pfuhl et al., 2014). We do not detect any eclipsing binary systems among the disk stars nor the young S-Star stellar populations. The star symbol indicates the location of Sgr A*, and 1 arcsec corresponds to a projected distance of ≈ 0.04 pc at the Galactic center distance.

2.6.2 Constraints on the eclipsing binary fraction of young stars

Our data provide the tightest constraints yet on the eclipsing binary fraction of the young stars in the nuclear star cluster by using a larger sample than previous works. In our sample of 85 stars, we recover the two previously discovered eclipsing binary systems: IRS 16SW (Ott et al., 1999; Peeples et al., 2007; Rafelski et al., 2007) and S4-258 (E60, discovered by Pfuhl et al., 2014) (see map in Figure 2.16). This places a lower limit on the eclipsing binary fraction of $2.4\% \pm 1.7\%$. Previous work using a sample of 70 young stars and detection of the same two binary systems, Pfuhl et al. (2014) determined a lower limit on the young star eclipsing binary fraction of $3\% \pm 2\%$.

We do not detect any eclipsing binaries amongst the young stellar disk members. In our sample, 18 stars were identified as likely members of the young stellar disk by Yelda et al. (2014). The two known eclipsing binaries are off-disk stars. While due to small number statistics this null detection is not unusual (66% probability of a null detection in this sample from our observed eclipsing binary fraction), the lack of binaries in the disk warrants future investigation. Binaries can serve as a way to characterize the differences of formation mechanisms of stars in the disk compared to off-disk stars (see e.g. Alexander et al., 2008; Levin & Beloborodov, 2003; Goodman & Tan, 2004; Nayakshin & Cuadra, 2005). Furthermore, there may be observational biases when assigning disk membership probabilities to binaries (Yelda et al., 2014; Naoz et al., 2018). Due to our sample size, we do not expect these biases to lead to a different conclusion about the relative eclipsing binary fraction of disk members versus non-disk members. However, these biases will be important when the sample of young stars increases.

We also do not detect any eclipsing binaries in the young S-star population (stars within a projected distance of 0.04 pc of the SMBH). Similar to the disk stars, the lack of eclipsing binaries in the young S-stars is not surprising given the small sample size (17 stars) in our experiment. However, if any S-stars are indeed binaries, we may expect to be more sensitive

to eclipsing systems since they tend to be in tighter orbits (Li et al., 2017). Better constraints on the binary fraction of S-stars is necessary since it can serve as an indicator of the stars' formation mechanisms. For example, if S-stars are captured components of tidally disrupted binary systems, they should no longer have a companion (Hills, 1988; Yu & Tremaine, 2003). Other recent observational constraints are consistent with this hypothesis (Chu et al., 2018).

The young nuclear star cluster eclipsing binary fraction is consistent with that of the local solar neighborhood. Lefèvre et al. (2009) find 40 OB binaries passing criteria similar to those of our experiment out of a sample of 2497 stars in a study of local OB variability with the HIPPARCOS satellite, giving a local OB eclipsing binary fraction of $1.60\% \pm 0.25\%$. Therefore, our estimate of the early-type eclipsing binary fraction at the Galactic center is consistent with the eclipsing binary fraction of local OB stars.

Improvements in the time sampling, sensitivity, sample size, or the addition of multiband photometry will allow tighter constraints in the eclipsing binary fraction. From our periodicity search parameters (Table 2.4), we are sensitive to binary periods longer than 2.22 days and amplitudes larger than $0.03 \times 5 = 0.15$ mags. These limits to our sensitivity to binary systems can be improved by the addition of photometry in another filter to eliminate false positives during periodicity searches. Furthermore, the Lomb-Scargle periodogram and the observation cadence used in this work are particularly optimized for detecting periodic signals that have an overall sinusoidal shape in the phased light curve. Therefore, our experiment is most sensitive to those systems that have eclipses wide in phase, expected from contact or near-contact binary systems. Future work is required to infer the overall binary fraction from these detections of eclipsing binary systems at the Galactic center.

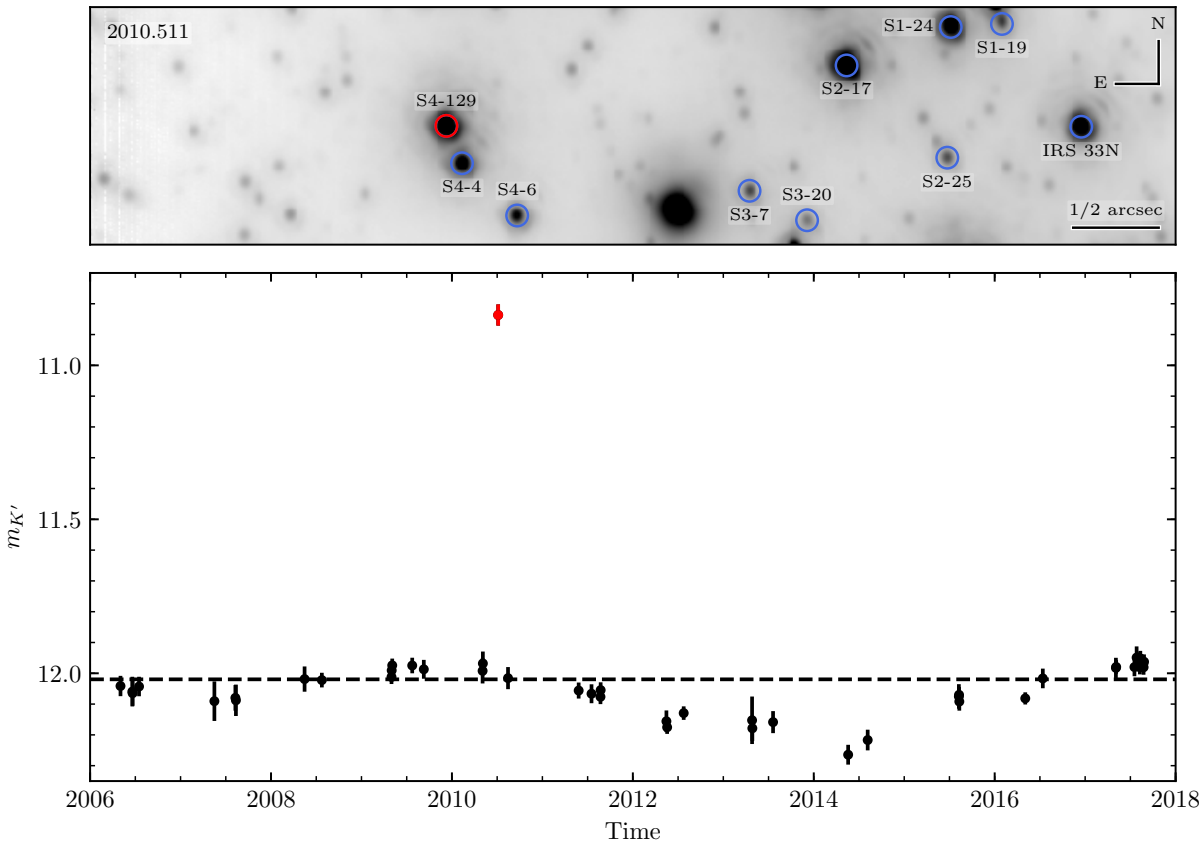

Figure 2.17: *Top:* An image of the field near S4-129 from the 2010-07-06 observation. During this observation, S4-129 increased in brightness by ≈ 1.2 magnitudes compared to other observations near in time. Visual inspection of the field in this and other observations near in time did not reveal any sources of potential stellar confusion. S4-129 is circled in red, while nearby stars brighter than $m_{K'} = 14.5$ are circled in blue. This observation is highlighted in the light curve as the red point. *Bottom:* Light curve of S4-129 over our experiment's entire time baseline. The red point indicates the observation highlighted on top, during which we observed the brightening.

2.6.3 Other periodic and variable stars

This study has revealed previously unidentified periodic variability in the star S2-36, with a period of 39.43 days (Section 2.5.2.1). The source's period and light curve could be consistent with an ellipsoidal binary system (potentially also eclipsing) or a Type II Cepheid star. Period-luminosity relations (Matsunaga et al., 2006; Riebel et al., 2010) suggest that the star's observed flux can be compatible with both classes of periodic variability under the typical range of extinctions towards the Galactic center (Schödel et al., 2010). Determining the likely source of this star's periodic variability requires additional observations beyond just the K'-band dataset in this work (Gautam et al. in prep.).

Besides S2-36 and the previously discovered eclipsing binary systems at the Galactic center, we did not find evidence for other periodic variable stars. Periodic fluctuations in flux may be expected from stars during periods of instabilities, and are particularly useful in revealing membership of the corresponding stars into populations with specific ages or metallicities. Notably, our periodicity search experiment is sensitive to the period and amplitude ranges of pulsating evolved stars. The first order pulsations of these stars, known as Mira variables (periods of 80 – 1000 days, NIR amplitudes $\sim$ 1 mag; see Catelan & Smith, 2015; Mattei, 1997), often host SiO masers and therefore can be particularly useful for Galactic center astrometric experiments (Yelda et al., 2010). However, we find no evidence of such stars in our experiment's field of view.

Stellar confusion is likely only a small contributor to variability in our sample. Only one star amongst our highly variable stars exhibits variability that can be clearly attributed to stellar confusion. S3-21 ($\bar{m}_{K'} = 15.28$) had a rapid brightness rise starting in 2012 due to it closely approaching the bright star S3-6 ($\bar{m}_{K'} = 12.69$). If stellar confusion were to be a larger contributor to variability in our sample, we would expect higher variability fractions in the highly crowded central arcsecond region, where stellar crowding leads to more confusion events. However, our data did not suggest any significant increases in variability in this

region (Figure 2.5). In general, with our implementation of checks for confused sources (see Section 2.2.2 and Jia et al., in prep.), we are able to largely reduce the effects of confusion.

In addition, the high density of objects at the Galactic center can lead to microlensing events, where a massive object passing in front of a star at the Galactic center can lead to a brief brightening event (Alexander & Loeb, 2001). Among our sample of highly variable stars, one star, S4-129, demonstrated brightening that could be the result of microlensing. S4-129 experienced a brightening of ≈ 1.2 magnitudes ($\approx 3\times$ increase in flux) during a single observation in our dataset (2010-07-06), and visual inspection of the star's local field in the images did not reveal any obvious sources of stellar confusion that could be the cause (see Figure 2.17). With just a single point in the brightening, it is difficult to put constraints on parameters of a possible lensing system. While this is the largest short brightening event in our sample, microlensing events have been predicted in the Galactic center environment from a variety of configurations (see e.g. Alexander & Loeb, 2001; Chanamé et al., 2001; Bozza & Mancini, 2005) and may be a small contribution towards the variability fraction in our sample.

Based on the K'-band observations alone in our experiment, it is difficult to determine a likely physical source of variability for all of our variable stars. A future study of variability of the Galactic center stars in color space can provide additional insight into sources of difficult-to-explain variability in our sample. Variability in the $H - K'$, H space can in particular reveal changes in dust extinction and accretion activity (Rice et al., 2015) or the presence of hot spots and cool spots on stars (Wolk et al., 2013). Without this extra color variability information, it is difficult to ascribe a specific source of variability to several stars in our sample.

2.6.4 The precision of single PSF AO photometry

While AO observations provide the angular resolution necessary to study the high stellar density of the Galactic center, there are two main challenges that must be overcome to achieve high-precision photometry. The extreme crowding of stellar sources in the central regions of the nuclear star cluster makes aperture photometry difficult or impossible as the point spread functions (PSFs) of the sources overlap. There is also variation in the PSF shape across the field of view and over time. Anisoplanatism results in PSF variation as a function of the position of the star with respect to the laser guide star and the tip-tilt star. Weather, atmospheric conditions, and performance of the adaptive optics system during observations further introduce fluctuations in the PSF shape. These effects cause biases when estimating the flux of stellar sources, and they therefore can be manifested in our data as a systematic variability in flux. Special efforts have to be made to account for these effects.

An approach to obtaining precise photometry from AO imaging data in a crowded field is PSF fitting and local calibration across the field. In our work, we used a single reference PSF across our entire field of view to derive initial photometric flux measurements. We expect that factors affecting PSF shape, such as anisoplanatic effects and atmospheric conditions, influence the PSF shapes and bias photometric measurements of nearby stars on the field of similar brightness in similar ways. Our local photometric correction removed these local trends in estimated flux (implementation detailed in Section 2.8.3). There are two metrics with which we evaluated the precision resulting from our methodology: photometric precision per observation epoch and median photometric precision across our entire time baseline. Across several individual observations our method achieved uncertainties of $\Delta m_{K'} \sim 0.02$ ($\approx 2\%$) to $m_{K'} = 16$ (see Table 2.1). Across all our observations, our method achieved a photometric uncertainty floor of $\Delta m_{K'} \sim 0.03$ ($\approx 3\%$) out to $m_{K'} \approx 16$ (see Figure 2.3).

Another approach to precise photometry with AO imaging data is to use separate reference PSFs across the field. In their AO photometric study of Galactic center stars, Schödel

et al. (2010) partitioned their images into smaller sub-frames, where the anisoplanatic effects over the sub-frame are small. A reference PSF was separately derived in each sub-frame, accounting for a variable PSF across the field of view. With this method, they were able to obtain photometric precisions as low as $\Delta m_{Ks} \sim 0.015$ ($\approx 1.5\%$) out to $m_{Ks} \approx 15$. The precisions we obtain with our techniques are comparable in several individual epochs.

The most comparable previous study to this work, a study of stellar variability in the Galactic center with Keck speckle data (Rafelski et al., 2007), achieved much lower precision than our method. With Keck speckle data, uncertainties of $\Delta m_K \sim 0.06$ out to $m_K \approx 13$ were obtained, with uncertainties reaching $\Delta m_K \sim 0.21$ at $m_K \approx 16$ (see Figure 2.3). Our method achieves much higher precision to fainter magnitudes. While much of this improvement comes from the greater depth AO imaging provides, our more robust calibration procedure and selection of stable calibrator stars also deliver more precision in relative photometry.

2.7 Conclusion

In this work, we presented an analysis of stellar variability and a search for eclipsing binary systems in the central $10''$ of the Galactic center with NIR laser-guide star AO data. Our photometric calibration and local correction techniques achieved photometric uncertainties reaching $\approx 3\%$ across our entire dataset and $\approx 2\%$ in several individual observations. This photometric precision is comparable to the highest precision achieved by other AO photometric studies using single-PSF fitting.

We have compiled the first catalog of photometric variables in the central half-parsec of the Galactic center with NIR AO imaging. We found that among our stellar sample of 563 stars identified across at least 16 observation nights, $50 \pm 2\%$ of stars displayed variability. Within this sample, $52 \pm 5\%$ of known early-type stars and $43 \pm 4\%$ of known late-type stars displayed variability. The variability fractions of the typed stars in our sample are much greater than that of other young, massive star populations or late-type giants in globular

Table 2.10: Initial Calibration Stars Bandpass Correction

Star Name	$K_{\mathrm{Blum+96}}$	$K_{\mathrm{Blum+96}} - K'_{\mathrm{NIRC2}}$	K'_{NIRC2}
IRS 16C	9.86 ± 0.05	-0.15 ± 0.01	10.01 ± 0.06
IRS 33E	10.02 ± 0.05	-0.16 ± 0.01	10.18 ± 0.06
S2-17	10.03 ± 0.07	-0.14 ± 0.01	10.17 ± 0.08
S2-16	11.90 ± 0.22	-0.26 ± 0.01	12.16 ± 0.23

References. — Blum et al. (1996)

clusters. The higher variability fraction relative to other studies can largely be accounted for by the longer time baseline of our experiment. Variations in the foreground extinction screen also contribute to the high variability fraction.

In a periodicity search of our photometric dataset, we recovered the two previously discovered eclipsing binary systems at the Galactic center: IRS 16SW and S4-258 (E60). We additionally identified a new periodically variable star at the Galactic center, S2-36, with a period of 39.43 days. Additional observations across other wavelengths or spectroscopic follow-up observations of this star can determine the physical source of the periodic variability.

We detected no evidence of an eclipsing binary system among the S-star population within $1''$ of the central black hole, nor among the young stellar disk. We measured a lower limit on the eclipsing binary fraction of $2.4 \pm 1.7\%$ among the young stars at the Galactic center. Our constraints on the Galactic center eclipsing binary fraction are consistent with the local OB star eclipsing binary fraction under observational limits similar to those of our experiment (Lefèvre et al., 2009).

2.8 Appendix 2A: Photometric Calibration Details

2.8.1 Reference Flux Bandpass Correction

Synthetic photometry was used to convert the Blum et al. (1996) photometry (hereafter Blum+96) of the initial calibration stars (listed in Table 2.10) into Keck NIRC2 K'-bandpass photometry. The calibration stars were modeled using Geneva stellar evolution models with rotation and at solar metallicity (Ekström et al., 2012) combined with ATLAS model atmospheres (Castelli & Kurucz, 2004). Since the stars belong to the young star population, an age of 3.9 Myr was adopted (Lu et al., 2013). By convolving the model atmospheres with the Blum+96 and Keck NIRC2 filter functions, the photometric offset between the filters could be calculated. However, it was first necessary to calculate the extinction for each star, since the bandpass correction depends on the extinction.

The extinction of each star was calculated from the $H - K$. IRS 16C, IRS 33E, and S2-17 each have Blum+96 $H - K$ measurements that we used. S2-16 did not have a Blum+96 $H - K$, so we instead used VLT NACO $H - Ks$ measurements (Schödel et al., 2010). The intrinsic colors of the calibrators were calculated from the model isochrones set at a distance of 10 pc and with no extinction. The intrinsic colors were constrained by the knowledge that IRS 16C, IRC 33E, and S2-16 are spectroscopically identified WR stars, and S2-17 is known to be an early-type ($M > 2M_{\odot}$), non-WR star (Do et al., 2013a). We then used the Nogueras-Lara et al. (2018) extinction law to convert the color excess into a total Ks-band extinction (NIRC2 system), obtaining values of 2.47 mag, 2.55 mag, 4.12 mag, and 2.29 mag for IRS 16C, IRS 33E, S2-16 and S2-17, respectively. The error on the extinction values are ± 0.08 mags or better, as a result of the uncertainties in the intrinsic and observed colors.

We then recalculated the synthetic photometry of the model isochrones, this time applying the extinction. From this synthetic photometry, the Blum+96 $K -$ NIRC2 K' bandpass corrections are found to be -0.15 mag, -0.16 mag, -0.26 mag, and -0.14 mag for IRS

16C, IRS 33E, S2-16 and S2-17, respectively. The extinction uncertainty only affects the final bandpass corrections at the 0.01 mag level or lower. The S2-16 bandpass correction appears to be an outlier relative to those of the other initial calibrators, but this is due to its significantly higher extinction. The bandpass corrections and the final reference photometry we use for our initial calibrator stars are listed in Table 2.10.

2.8.2 Iterative Calibrator Selection

During each photometric calibration iteration, we used reference flux measurements and corresponding uncertainties for each of our calibrator stars. We then used the weighted mean of the calibration stars' differences from their reference values to derive a correction to the zeropoint across our observations. This zeropoint correction was used to adjust the magnitudes of every star identified in each observation. We calculated an error in the zeropoint correction for each observation and added in quadrature to the instrumental flux uncertainty measurement for each star. This gave the total measurement uncertainty in flux for each star.

Following the initial calibration, we identified a new set of secondary calibration stars that increased the precision for the relative photometry across the observations. The selection of these secondary stars was based on a set of criteria detailed below to select bright, photometrically stable stars distributed across our field of view. We updated the chosen calibration stars' reference magnitudes to the weighted mean magnitude from the previous calibration step. To select stars that are photometrically stable, we chose stars with low $\chi^2_{\rm red}$ values (indicating low variability; further described in Section 2.3), and a low mean magnitude uncertainty across all epochs (to reduce the influence of high photometric uncertainty lowering the $\chi^2_{\rm red}$ value). These metrics used to select calibrator stars in each iteration were computed before applying local photometric correction (detailed in Section 2.8.3). We included a magnitude cutoff of $\bar{m}_{K'} \leq 15.5$ to limit our calibration stars to be brighter sources. We further imposed a requirement that our calibration stars be identified in all observation

epochs. Additionally, we checked a series of photometric and astrometric confusion criteria, selected to avoid choosing stars that could be confused with another nearby star during the calibration star identification process. For stars brighter than $m_{K'} = 12$, we checked if potential calibration stars that had no other neighboring stars within $0.2''$ and 1 magnitude in any observation epoch. The astrometric criterion was relaxed to $0.1''$ for stars dimmer than $m_{K'} = 12$, due to these stars having fainter PSF haloes. Finally, we imposed that at least two calibration stars and no more than three were used in each quadrant of our field of view, centered on the location of Sgr A*. We further required calibration stars to be at least $\sim 0.25''$ from each other. Imposing these final set of criteria limited the photometric calibration from biasing only small areas of the field for photometric stability with a higher density of calibration stars or resulting in other regions of the field with fewer calibrators to have more imprecise calibration. All these criteria selected bright and photometrically stable stars for each calibration iteration that were identified in all observation epochs, isolated in position and magnitude from nearby stars, and distributed across our field of view.

The above process to select new stable secondary calibration stars was repeated 3 times until it converged onto the same set of calibrators. Before each iteration, we refined our calibration star selection criteria ($\chi^2_{\rm red}$ and mean magnitude uncertainty) to better isolate stable stars. We used the mean magnitude and uncertainty on the mean magnitude for each of the calibrator stars from the previous iteration as their respective reference fluxes and uncertainties. Our iterative process converged to our final calibration star selection criteria detailed in Table 2.11, and our final set of calibration stars are listed in Table 2.12 and displayed on our field of view in Figure 2.1. Light curves of all final calibration stars, after the local photometric correction is applied (correction detailed in Section 2.8.3), are shown in Figure 2.18. By identifying stable secondary calibration stars, the iterative process effectively reduced the contribution to the photometric uncertainty originating from uncertainty in the zeropoint correction and achieve greater precision for relative photometry.

Table 2.11: Criteria for selecting final set of photometric calibration stars

Criterion	Calibrator Criterion Cutoff
$\chi^2_{\rm red}$	≤ 1.9
Mean Mag. ($m_{K'}$)	≤ 15.5
Mean Mag. Uncertainty	≤ 0.0295
Number of Epochs	$= 45$ (all)
Confusion criteria	
Nearest Star ($\bar{m}_{K'} \leq 12$)	$> 0.2''$
Nearest Star ($\bar{m}_{K'} > 12$)	$> 0.1''$
Nearest Star $\Delta m_{K'}$	> 1.0
Isolation criteria	
Nearest Calibrator	$\gtrsim 0.25''$
Calibrators per FoV quadrant	$2 \leq n \leq 3$

Note. — These criteria were used to select photometric calibration stars from the previous calibration iteration. Therefore, these criteria are not necessarily reflected in the statistics for the photometric calibration stars in the final calibration iteration listed in Table 2.12.

Confusion criteria were selected to avoid choosing calibration stars that could be confused with another star during our calibration star identification process. Calibration stars were chosen to pass both astrometric and photometric confusion criteria.

Isolation criteria were selected to avoid a high density of photometric calibrators in small regions of the field, in order to not bias only small areas of the field for photometric stability.

Table 2.12: Final Calibration stars

Star Name	Mean Mag. (K')	Error on Mean Mag. (K')	$\chi^2_{\rm red}$	Mean of Uncertainties (K')
IRS 16NW	10.155	0.019	1.411	0.029
S3-22	11.028	0.018	0.592	0.029
S1-17	12.171	0.018	0.517	0.029
S1-34	12.907	0.019	0.565	0.029
S4-3	12.907	0.019	1.108	0.029
S1-1	13.021	0.019	1.123	0.029
S1-21	13.214	0.019	1.644	0.029
S3-370	13.532	0.018	0.791	0.029
S0-14	13.572	0.018	1.023	0.029
S3-36	14.538	0.019	0.478	0.029
S2-63	15.341	0.019	1.880	0.029

Note. — Metrics here are computed before application of the local photometric correction.

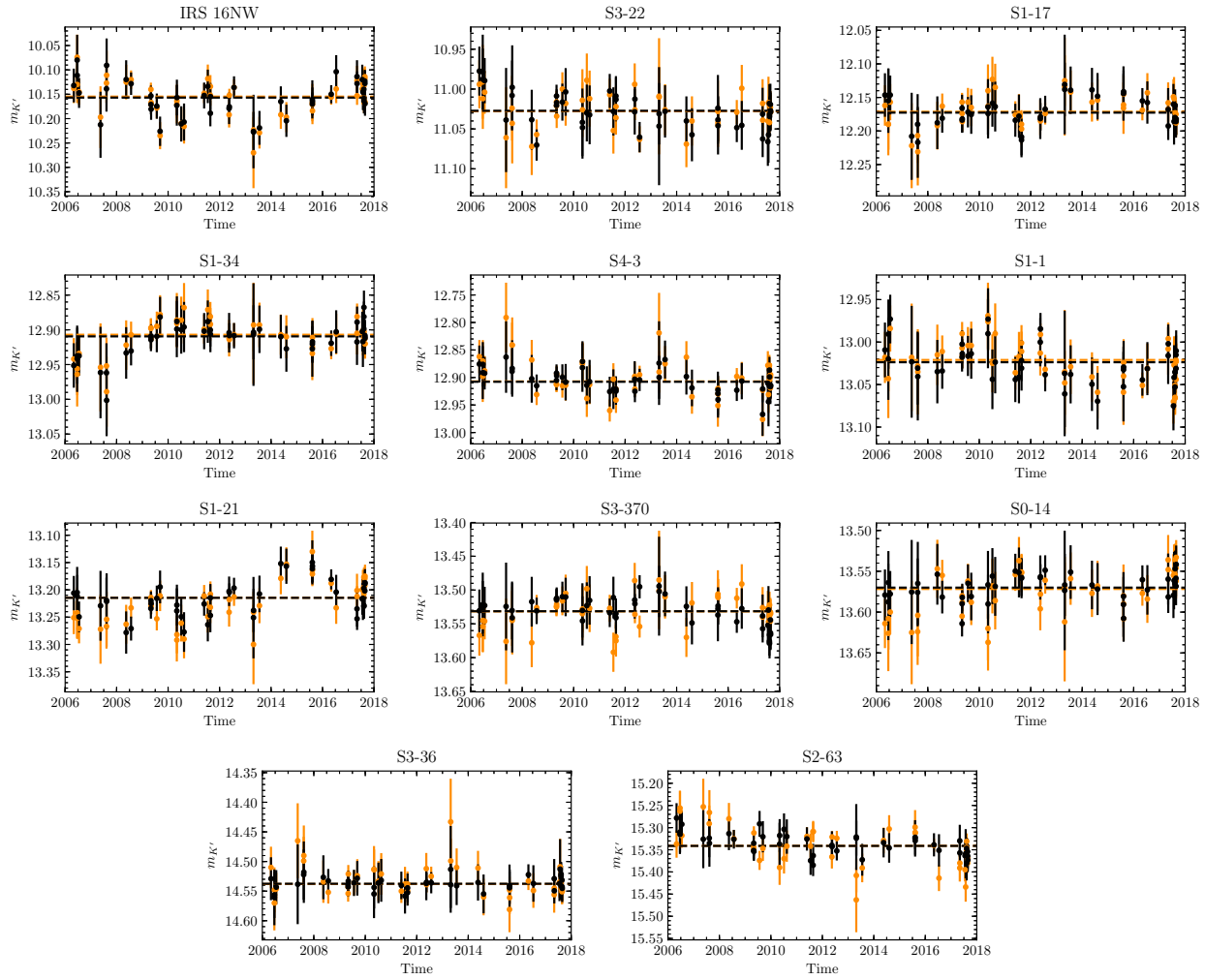

Figure 2.18: Light curves of the final calibration stars used in the variability analysis. Flux measurements before application of the local photometric correction are indicated in orange and flux measurements after application of the local photometric correction are indicated in black. The horizontal dashed line indicates the weighted mean magnitude.

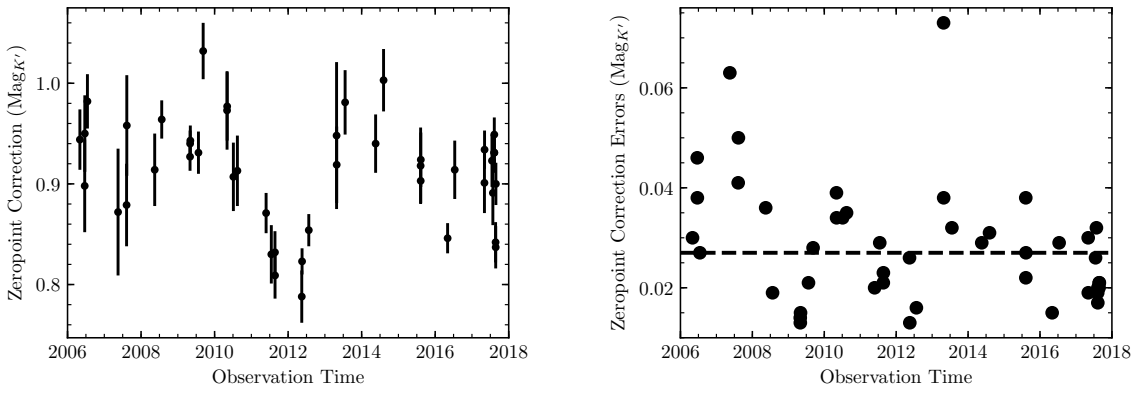

Figure 2.19: *Left:* K' magnitude zeropoint corrections from the photometric calibration used in this work. The zeropoint correction is calculated as the mean of the difference between the measured photometric flux of the calibration stars and their recorded value.
Right: The errors in the K' magnitude zeropoint corrections used in this work, calculated as the variance of the zeropoint magnitude adjustment in each observation. This zeropoint correction error in each observation dominates the photometric uncertainty in our measurements, and the median zeropoint correction error (dashed line) across our observations is $\sigma_{m_{K'}} \sim 0.025$.

2.8.3 Local Photometric Correction

We performed an additional correction to our photometry on local scales of the field beyond the zeropoint photometric calibration. The need for this correction became evident when we observed similar changes in flux measurements for stars of similar brightness and position on the field in an observation epoch. This effect and our correction, described below, is illustrated for four example stars from different locations on our field in Figure 2.20.

A variable PSF across the field can cause our flux measurement of stars from PSF-fitting to be under- or over-estimated. Since the PSF variation is spatially correlated, this bias in the flux measurement is expected to be similar for nearby stars. We attempted to correct for

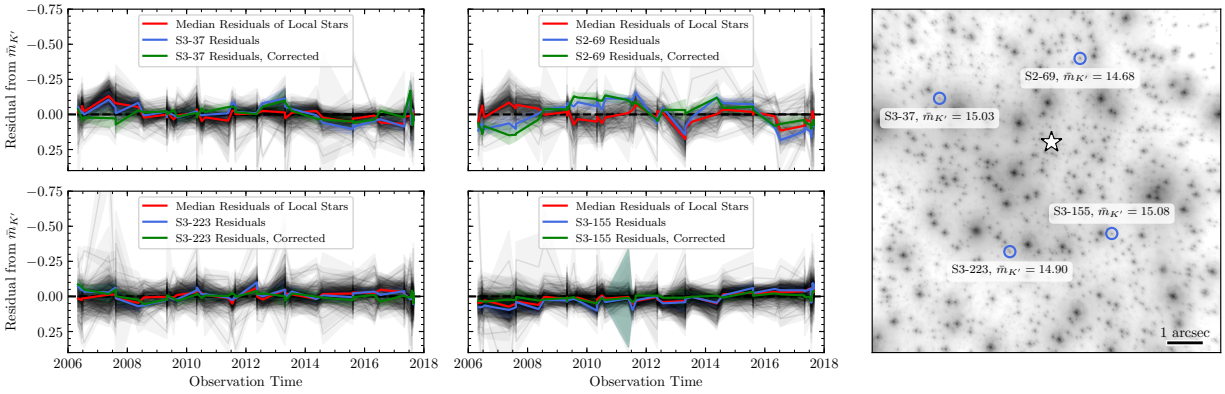

Figure 2.20: Four example target stars of similar brightness from different areas of our field selected to highlight our local photometry correction. Each curve displays the residual of a star's flux in an observation from its respective mean magnitude across all observations while shaded regions indicate uncertainty in flux. Blue curves indicate the residuals for the four example target stars, while the black curves in each plot indicate the residuals for all the local stars for the target star. Small trends in measured flux correlate across target stars and their respective local stars, suggesting a local photometric bias. The red curve indicates the median residual of the local stars, which is subtracted from the flux measurements of the target star to correct for the photometric bias. The green curves indicate the residuals for the four example target stars corrected for the photometric bias, and include the additional additive uncertainty during the local correction step.

this photometric variation in our dataset.

To determine the photometric bias, local stars were first determined for each star. These local stars were selected to be low variability stars in close proximity on the field and at a similar brightness to each target star. A star was identified as a local star if it was located within $2''$ and within 1.0 mag of the target star in any observation. From these, stars that were detected in fewer than 23 observations and had $\chi^2_{\rm red} > 20.0$ were removed as local stars to determine the photometric bias. This was to reduce the influence on the measurement of the photometric bias by variable stars and those whose mean magnitude was not very well constrained due to detections in too few observations. If the total number of local stars determined under these constraints was fewer than 8, the astrometric search radius was increased in steps of $0.25''$ and the photometric search radius was increased in steps of 0.25 mag until the number of local stars reached the minimum of 8. This ensured that the measurement of photometric bias was not dominated by the variations of too few stars.

With the local stars determined, the photometric bias was measured for each star. In each observation for the target star, the residual in magnitudes for local star i from its mean magnitude was measured,

$$R_i \equiv m_i - \bar{m}_i. \tag{2.17}$$

The median value over all local stars of the residual in each observation epoch, med(R_i), was subtracted from the target star's flux measurement in that observation. This corrected for the photometric bias measured from the local stars for every star in our sample.

With this correction, we also included an additive error to account for the uncertainty in flux introduced by this process. In each observation the error from the local correction was

calculated with

$$\mathrm{RMS}_R = \sqrt{\frac{\sum_i^N R_i - \mathrm{med}(R_i)}{N}} \tag{2.18}$$

$$\text{Local Correction Uncertainty} = \frac{\mathrm{RMS}_R}{\sqrt{N}}, \tag{2.19}$$

where N represents the total number of local stars in each observation used to correct for the photometric bias. The local correction uncertainty was then added in quadrature into the flux uncertainty determined during the zeropoint correction.

2.9 Appendix 2B: Variability Study Details

Table A.1 summarizes the sample of stars studied in this work. In addition to the variability metric used in this work, χ^2_{red}, we calculated additional variability metrics to aide in comparison of our stellar sample to other stellar samples.

The root mean square (RMS) calculated is that of the observed magnitude differences from the mean magnitude:

$$\mathrm{RMS} = \sqrt{\frac{1}{N} * \sum (m_i - \bar{m})^2} \tag{2.20}$$

The interquartile range (IQR) is the difference between the median of the half brightest and half dimmest observations (Sokolovsky et al., 2017). This method is more robust against outliers.

The von Neumann ratio, η, is the ratio of mean square of differences in successive observations to the variance of all observations (Sokolovsky et al., 2017). Higher values of $1/\eta$ indicate higher variability, defined as:

$$\frac{1}{\eta} = \frac{\sigma^2}{\delta^2} = \frac{\sum_{i=1}^{N} (m_i - \bar{m})^2/(N-1)}{\sum_{i=1}^{N-1} (m_{i+1} - m_i)^2/(N-1)} \tag{2.21}$$

The $1/\eta$ method picks out stars that are less smoothly variable, i.e. with greater differences in successive observations.

2.10 Appendix 2C: Periodicity Methodology Details

2.10.1 Period Search Range

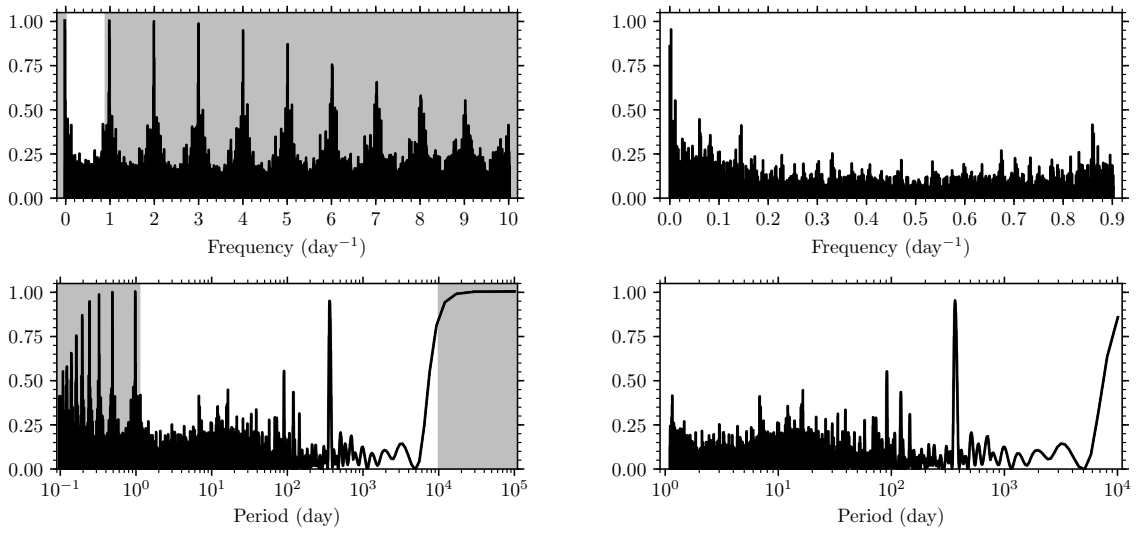

Figure 2.21: The Lomb-Scargle window power spectrum computed for our experiment's observation times at our periodicity search's frequency spacing is shown in the plots on the left. Note that frequencies larger than 1 day^{-1} are prone to aliasing and at periods larger than 10^4 days most signals will appear periodic due to this range being much larger than our overall observing time baseline. Our periodicity search range of 1.11 – 10,000 days is highlighted in white on the left plots and is zoomed in for more detail in the plots on the right.

We defined our periodicity search region by computing a window power spectrum for our observations (Figure 2.21). Notably, in this window power spectrum, periods shorter than about 1.11 days (frequencies $\gtrsim 0.9$ day^{-1} strongly suffer from aliasing due to the spacing of our observations being spaced apart by multiples of ≈ 1 day. Above 10,000 days, the normalized Lomb-Scargle power extends to 1.0, at periods extending much beyond our observation's time span. With these considerations in mind, we defined our periodicity search region between the frequencies of 0.9 day^{-1} to 10^{-4} day^{-1}, corresponding to periods between

1.11 days and 10,000 days. The remaining peaks in Figure 2.21 in our periodicity search range originate from our nightly observation cadence and the length of a sidereal day: at a period of ~ 1 day (frequency ~ 1 day^{-1}), and its harmonic rising up at a period of $\sim 10,000$ days (corresponding to a frequency ~ 0 day^{-1})). The ~ 350 days peak corresponds to our roughly yearly observation cadence, when the GC is visible in the night sky.

2.10.2 Removal of long-term linear trends

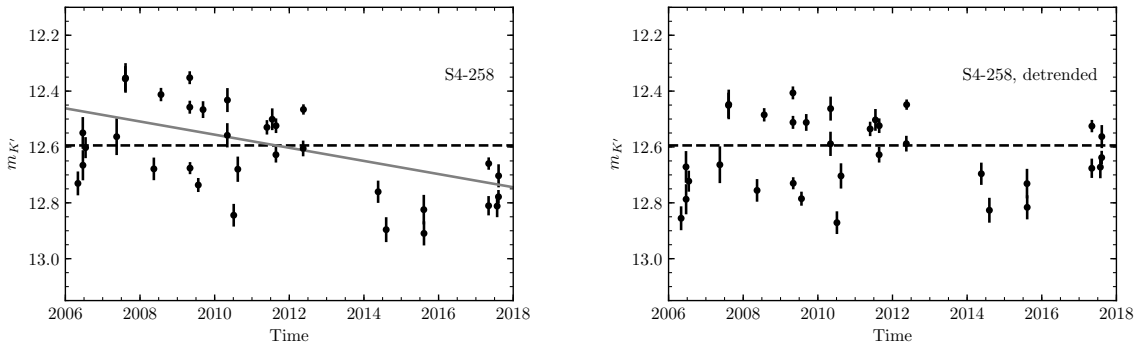

Figure 2.22: S4-258 (E60: Pfuhl et al., 2014) is an eclipsing binary system at the Galactic Center. The left plot shows the light curve from S4-258 across our observations, where the dashed black line indicates the weighted mean magnitude, $\bar{m}_{K'}$, and solid gray line indicates the best-fit linear model to the data. This linear model can indicate a long-term dimming of the binary system. The right plot shows the same data, with the long-term linear dimming trend removed.

In our periodicity search, we removed long-term linear trends from the light curves of stars before computing a periodogram. This removal resulted in stronger detections of periodic signals. This can be demonstrated particularly well for the known eclipsing binary system S4-258 (E60: Pfuhl et al., 2014). S4-258 exhibits a long-term linear dimming trend in our dataset, possibly caused by extinction, over our observation baseline (Figure 2.22). After removing the long-term linear trend, we find that the periodic signal is detected more strongly in the periodogram (Figure 2.23) and that the phased light curve demonstrates is much smoother

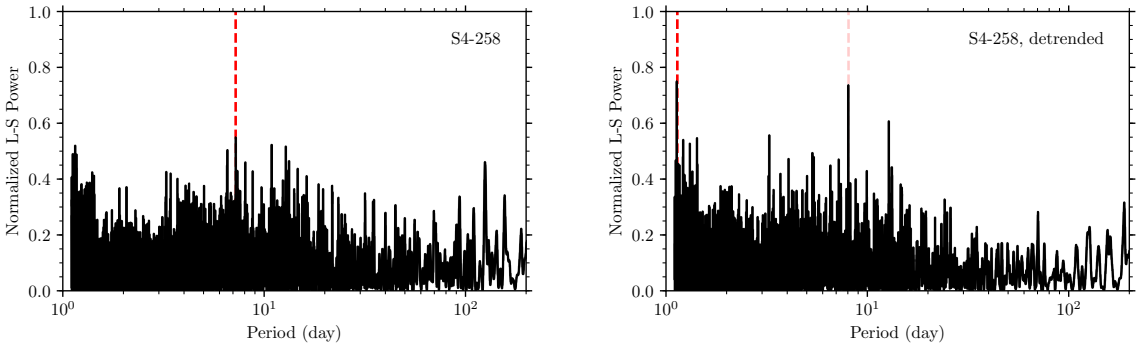

Figure 2.23: Lomb-Scargle periodogram of S4-258's light curve. The left plot shows the periodogram computed from our observations, while the right plot shows the periodogram once the long-term linear dimming trend is removed. The 1.1380 day peak in the periodogram constructed from the detrended light curve corresponds to the 2.2760 day binary period of the system. The 8.0637 day peak corresponds to an alias of the binary period. Removing the long-term linear dimming trend allows the binary period of the system and its alias to be detected.

(Figure 2.24).

Several stars in our sample display similar brightening or dimming trends to S4-258 (see Section A.1). Any periodic trends that may exist for our sample stars in addition to these low order variations can be detected more strongly once the linear variation is removed.

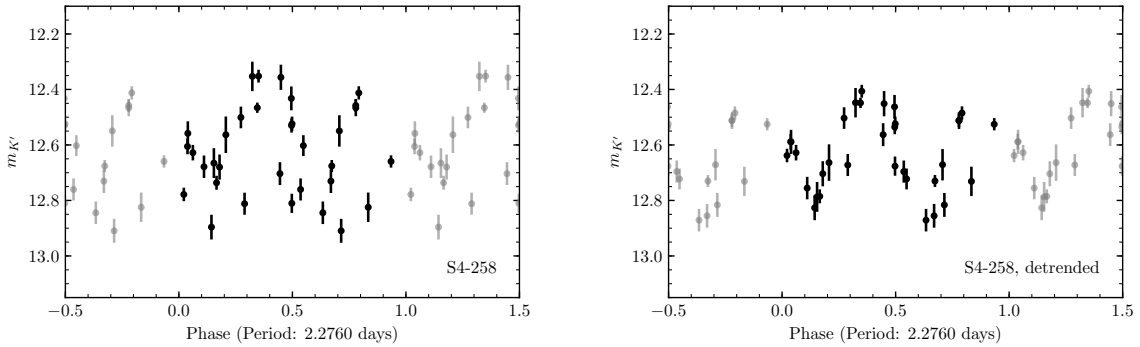

Figure 2.24: Phased light curve of S4-258 at its binary period of 2.2761 days. The left plot shows the phased light curve from our observations before detrending, while the right plot shows the same light curve with the long-term linear dimming trend removed (shown in Figure 2.22).

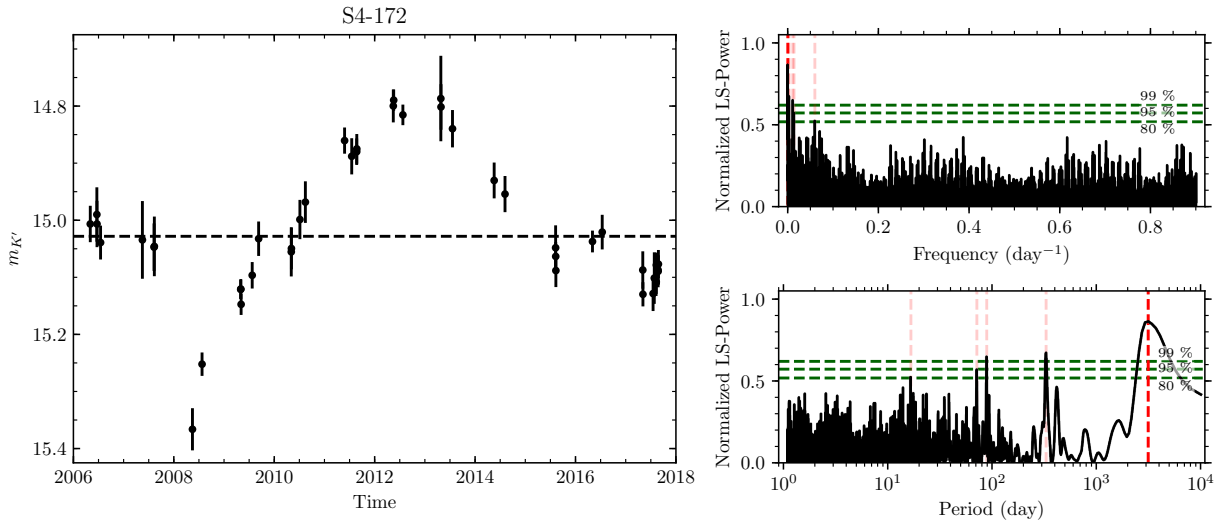

Figure 2.25: Light curve (left) and periodograms (right) for the star S4-172. The horizontal dashed line in the light curve indicates the weighted mean magnitude. The horizontal dashed green lines in the periodograms indicate the bootstrap test significance levels, while the vertical dashed red lines indicate periodogram peaks above 80% bootstrap significance. S4-172 is an example where the long-term variability (corresponding to a peak $\sim$ 3000 days) is aliased as powerful peaks in the periodogram at shorter periods.

CHAPTER 3

Identification of an Old Ellipsoidal Stellar Binary at the Milky Way Galactic Center and Dynamical Constraints on a Dark Cusp

3.1 Introduction

Near-infrared (NIR) astrometry and radial velocity observations of stars using 8–10 m class telescopes with adaptive optics (AO) have provided strong evidence for the presence of a supermassive black hole (SMBH) with a mass of $\approx 4 \times 10^6 M_\odot$ at the Milky Way Galactic center (GC) (e.g. Do et al., 2019; Collaboration et al., 2018; Gillessen et al., 2017; Boehle et al., 2016; Gillessen et al., 2009; Schödel et al., 2009; Ghez et al., 2008). The SMBH is surrounded by the Nuclear Star Cluster (NSC) with a total stellar mass of $\approx 10^7 M_\odot$, making it the most massive stellar cluster in the Galaxy (Chatzopoulos et al., 2015; Schödel et al., 2009). Observations provide evidence of high stellar densities in the central regions of the NSC, with $\approx 10^6 M_\odot$ enclosed within the central parsec of the GC, in addition to the mass of the SMBH.

When compared to SMBHs in other galactic centers, the Milky Way SMBH has a relatively low mass (e.g. Gültekin et al., 2009). A lower central SMBH mass implies a shorter dynamical relaxation time for the surrounding star cluster. The NSC around the GC SMBH is expected to have a relaxation time $\sim 10^9$ yr (Hopman & Alexander, 2006; Binney & Tremaine, 2008;

Alexander & Hopman, 2009), which is lower than the ages of the oldest stars in the NSC. In such a relaxed population with a central SMBH that can regularly tidally disrupt and absorb stellar members, a steep increase in density (a *density cusp*), is expected towards the central SMBH (Bahcall & Wolf, 1976, 1977; Hopman & Alexander, 2006; Alexander & Hopman, 2009). The MW NSC therefore offers a unique laboratory for experiments to study its dynamical nature, with a population that is expected to be dynamically relaxed and with stellar members that can be individually resolved by ground-based telescopes.

Observationally, one way to test dynamical predictions of the density near the SMBH is by tracing the population of luminous stars in the NSC. In particular, the old, giant stars in the GC with ages > 1 Gyr (Do et al., 2013a) are expected to belong to a relaxed population that can be used to test the dynamical predictions. However, observations suggest there are fewer giants in the GC close to the SMBH than are expected by cusp predictions (e.g. Buchholz et al., 2009; Do et al., 2009, 2013a; Gallego-Cano et al., 2018).

Several models have been proposed to explain why the GC may possess few old giant stars close to the SMBH. Giant stars are expected to have frequently collided with main sequence stars or stellar-mass black holes in the GC (Dale et al., 2009). These collisions may have resulted in the stripping of the giants' envelopes, or occasionally in more extreme mass-loss events such as giant core expulsion. Also, a fragmenting accretion disk may have previously existed around the SMBH. Interactions with dense clumps of gas in the disk may have stripped giant stellar envelopes (Amaro-Seoane & Chen, 2014; Kieffer & Bogdanovic, 2016). These giant-star mass-loss events can account for the paucity of old giants and the lack of a giant-star density cusp observed close to the central SMBH.

While the old stars may not follow dynamical predictions of a cusp, the GC may still possess a *dark cusp* made up of stellar remnants such as stellar-mass black holes and neutron stars (Miralda-Escudé & Gould, 2000; Morris, 1993). Of the remnants, the stellar-mass black holes are expected to make up the majority of the mass in the hypothesized dark cusp. Importantly,

the stellar-mass black holes would not have been subjected to the same physical processes that may have led to the depletion of giants in the GC. Therefore the GC is still expected to retain its dark cusp.

The stellar-mass black holes making up the dark cusp are expected to originate from two different sources: as remnants of past episodes of star formation and from the infall of globular clusters. There is evidence of several episodes of star formation at the GC (Nogueras-Lara et al., 2020), with the most recent appearing to have taken place 4–6 Myr ago with a top-heavy initial mass function (Lu et al., 2013; Bartko et al., 2010). The numerous massive stars formed during these episodes are expected to leave behind massive stellar remnants. Through dynamical friction, $\approx 25,000$ stellar-mass black holes are expected to have sunk to within a parsec of the SMBH (Generozov et al., 2018; Antonini, 2014). Additionally, if globular cluster infall episodes have contributed to the buildup of the NSC, they are expected to inject stellar-mass black holes into the GC that should similarly sink towards the SMBH (Antonini, 2014). After dynamical relaxation, the overall population of stellar-mass black holes contributed from both scenarios is expected to form a cusp with a steep increase in density towards the central SMBH.

Observations of quiescent X-ray binaries in the central parsec of the GC do reveal evidence for a cusp of stellar-mass black holes (Hailey et al., 2018). However, X-ray observations suffer from source crowding, the X-ray brightness of Sgr A*, and hot gas emission in the innermost regions of the GC ($\lesssim 0.2$ pc). Therefore, these observations are limited in the constraints they can provide on the existence of a dark cusp close to the SMBH. Other tracers of the dark cusp are needed to properly constrain the population of stellar-mass black in the GC.

Dynamical effects serve as another powerful method to probe the presence of the dark cusp, specifically with the process of *binary evaporation*. The degree to which binary evaporation has occurred can place upper limits on the density of surrounding objects. Dynamically soft (i.e., loosely bound) stellar binary systems are susceptible to getting more loosely bound and

eventually being evaporated (i.e. detached) due to encounters with the surrounding stars and stellar remnants. Therefore, the detection of a dynamically soft binary places upper limits on the surrounding stellar density (Alexander & Pfuhl, 2014). Importantly, such a binary can constrain the density of objects that are not luminous but still have gravitational influence, like the components of the expected GC dark cusp. Alexander & Pfuhl (2014) calculated dynamical constraints on the GC dark cusp with the long-period, young stellar binary system IRS 16NE. However, due to the large component stellar masses of IRS 16NE, the binary is not dynamically soft and is unable to place significant constraints on the dark cusp via binary evaporation. The discovery of a dynamically soft binary in the GC would allow such a framework to be employed.

In this work we study in detail the star S2-36 as a candidate old binary system at the GC and as a possible probe of the dynamical properties of GC stars. S2-36 was first identified as a 39.4 day periodic variable in an earlier NIR single-band photometric survey of stellar variability at the GC (Gautam et al., 2019, hereafter G19), but additional work and observations were necessary to confirm whether the variability indeed originates from a stellar binary. In this work, with the help of new observations, we first characterize the periodic variability of S2-36 more robustly than in G19. Using a combination of new multiband NIR photometric measurements and astrometric constraints on its NSC membership, we next demonstrate that S2-36's photometric variability is most consistent with originating from a red giant ellipsoidal binary located very close to the GC. We modeled the system's observed flux with astrophysical binary models, which provide estimates of S2-36's stellar and binary parameters. Finally, the age and loosely bound (i.e., dynamically soft) nature of the binary allow us to place tight constraints on the density of the dark cusp at S2-36's local environment, in close proximity to the SMBH.

This chapter is organized as follows: In Section 3.2, we describe our imaging observations and the derivation of the photometric and astrometric measurements we use for our subsequent

analysis. Section 3.3 describes our analysis of the observational data: the measurement of the NIR flux and color of S2-36, the photometric variability period from multiband observations, the proper motion relative to Sgr A*, and a comparison of its NIR flux and color relative to nearby stellar sources. Our analysis detects periodic variability in S2-36 much more robustly than G19, and the proper motion and NIR color of S2-36 demonstrate that it is likely a member of the NSC stellar population. Our results are described in Section 3.4: we demonstrate that S2-36 is likely a red giant ellipsoidal binary system (Section 3.4.1) and we estimate the stellar and binary orbital parameters of such a binary system assuming coeval component stars (Section 3.4.2). The presence of an old, dynamically soft binary in the GC environment places strong upper limits on the number of massive objects in the binary's vicinity, which are detailed in Section 3.5. Finally, we summarize our conclusions in Section 3.6.

3.2 New observations and existing *GCOI* data

In this work, we used laser guide star adaptive optics (LGSAO) high-resolution imaging observations of the Galactic center obtained at the 10-m W. M. Keck II telescope with the NIRC2 near-infrared (NIR) facility imager (PI: K. Matthews) as part of the *Galactic Center Orbits Initiative (GCOI)*. Our photometric analysis incorporated the same set of observations and data reduction techniques in the K'-bandpass ($\lambda_0 = 2.124$ µm, $\Delta\lambda = 0.351$ µm) as used in G19. In the present work, we report additional observations conducted in 2017–2019 using the K' and H ($\lambda_0 = 1.633$ µm, $\Delta\lambda = 0.296$ µm) bandpasses. The same photometric data reduction techniques as in G19 were carried out for the new observations reported in this work. Details of these observations are in Table 3.7.

3.2.1 Photometric calibration

We performed photometric calibrations using the methods presented by G19, with a few modifications. The modifications included updating the photometric calibrator stars used,

deriving initial calibration reference fluxes for the photometric calibrator stars, and extending the calibration methodology to the new H-band images in this work.

We selected stable, non-variable stars as photometric calibrators in a procedure similar to the one outlined by G19. Of the photometric calibrator stars used by G19, the star S0-14 started getting dimmer in new observations taken after 2017 and therefore could no longer serve as a stable photometric calibrator star in this work. We therefore repeated the iterative calibrator selection process detailed in G19, including the new 2018–2019 K'-band data. When repeating this process, we selected the following calibrator stars: IRS 16NW, S3-22, S1-17, S1-34, S4-3, S1-1, S1-21, S3-370, S3-88, S3-36, and S2-63. These calibrator stars are the same as those used by G19, with the exception of S0-14 being replaced by S3-88.

We re-derived new K'- and H-band reference flux measurements for our calibrator stars by using the photometry from the Schödel et al. (2010) photometric catalog. Instead of using absolute photometry measurements from seeing-limited observations conducted by Blum et al. (1996), as was done in G19, we use absolute photometry measurements from high-resolution, diffraction-limited observations conducted by Schödel et al. (2010) to derive reference flux measurements for the photometric calibrators. Since all 11 stable photometric calibrator stars are detected in the high-resolution survey by Schödel et al. (2010), we are able to use the same set of photometric calibrator stars in both our initial and final photometric calibration steps. Due to slight differences in the filter bandpasses for the ESO/VLT NAOS/CONICA observations used by Schödel et al. (2010) and the Keck NIRC2 observations used in this work, we performed a bandpass correction for reference flux measurements as described by G19. The bandpass corrections and the bandpass-corrected reference flux measurements for our reference calibrator stars are listed in Table 3.8.

The remainder of our photometric calibration in the H-band and K'-band datasets followed the same method as that outlined in G19. These procedures included using the same common

set of photometric calibrators in both bands, and performing a local photometric correction procedure to obtain the final flux measurements and corresponding uncertainties reported in this work. A comparison of the photometric calibration in this work and that of G19 is shown in Appendix 3.7.

Our entire photometric dataset consisted of 59 observations in the K'-band and 11 observations in the H-band. S2-36 is detected in 58 K'-band observations and all 11 H-band observations. The K' observations were taken between 2006.34 and 2019.63 (total baseline of 13.3 years) and the H observations were taken between 2017.35 and 2019.36 (total baseline 2.0 years). Individual observations each consist of combined images from individual frames taken over a single night. Therefore the shortest gaps between individual observations in our dataset are ≈ 1 day. Our complete calibrated photometric measurements for S2-36 are plotted in Figure 3.1.

3.2.2 Astrometric measurements

We obtained astrometric positions of S2-36 from prior astrometric analysis of GCOI data (Jia et al., 2019; Sakai et al., 2019). Imaging observations used for astrometry in this work were taken at the Keck Observatory between 1995 and 2017, with speckle holography used for earlier observations and AO used for later observations (detailed further by Jia et al., 2019). S2-36 was detected in 55 epochs in the observations used for astrometric analysis. The long time baseline of this astrometric data allowed for a more precise estimate of S2-36's proper motion relative to Sgr A* (Section 3.3.2).

3.3 Data analysis

We constructed a photometric variability model for S2-36 to estimate its variability period and NIR color, detailed in Section 3.3.1. Our model for the astrometric motion of S2-36 is detailed in Section 3.3.2, which we used to constrain the physical location of S2-36 in the

GC environment. We additionally examined the NIR color of S2-36 relative to other stellar sources in its proximity, detailed in Section 3.3.3.

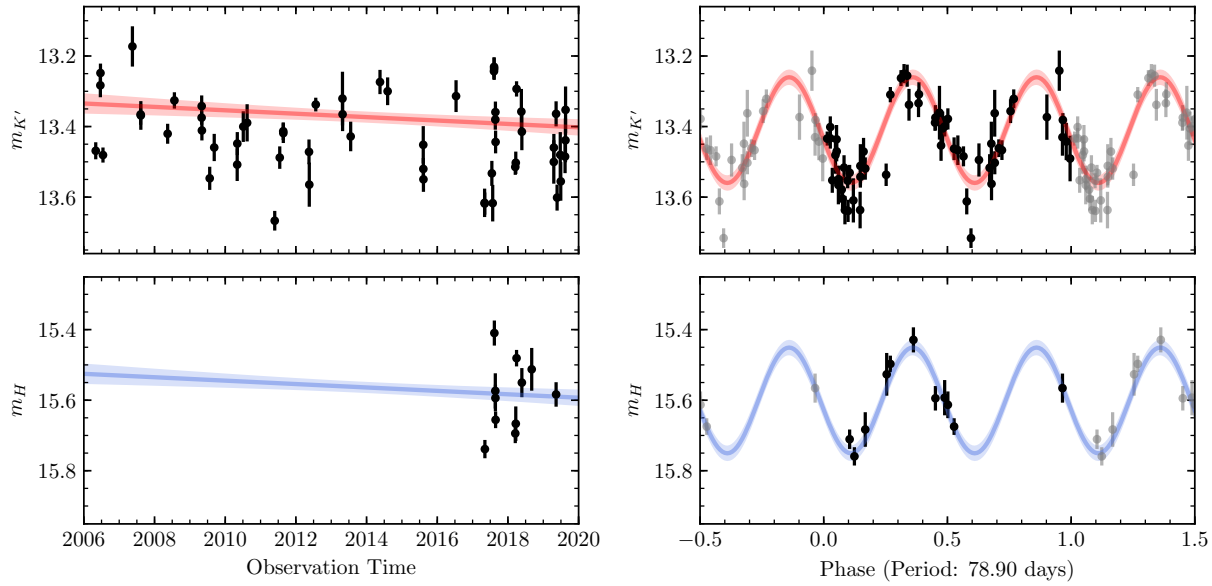

Figure 3.1: Keck NIRC2 photometric measurements for S2-36, in the K'- (top panels) and H-band (bottom panels). The left panels show the S2-36 light curve over our observation time baseline. The solid colored lines show the long-term linear trend components of the best-fit trended sinusoid model in each band, with 3σ uncertainty in the linear fit indicated by the shaded regions. The right panels show the same photometric data phased to $2\times$ the best-fit period from our trended Lomb-Scargle analysis and with the best-fit long-term linear trend removed. The solid, colored lines in each panel indicate the best-fit sinusoid model to the observed data, with 3σ uncertainty in the sinusoid fit indicated by the shaded regions. The trended, periodic model plotted here is the 4 parameter model (detailed in Section 3.3.1), which includes only the *base model*.

3.3.1 Photometric model

Our photometric model accounted for multiband periodicity in our K'- and H-band S2-36 flux measurement observations. Section 3.3.1.1 details our search for multiband periodic

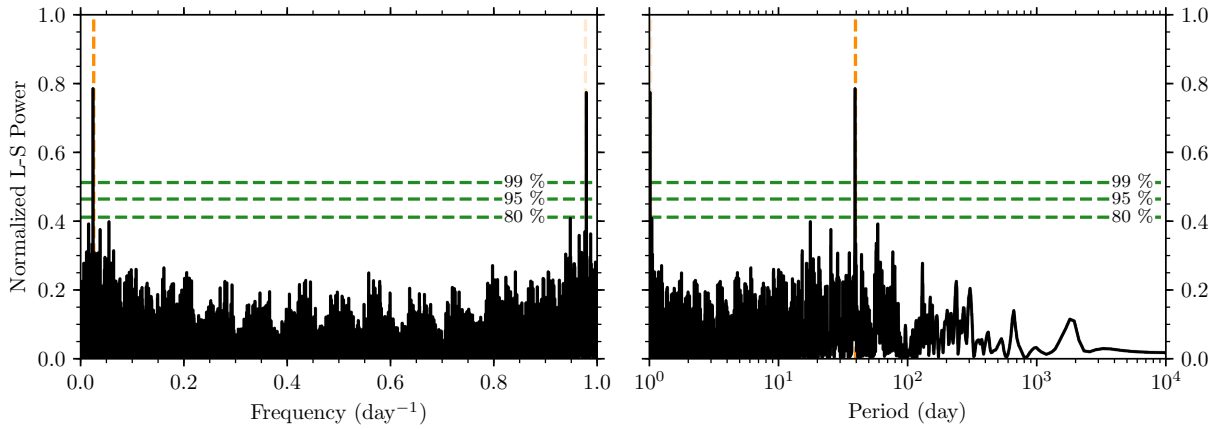

Figure 3.2: Trended, multi-band Lomb-Scargle periodogram for the S2-36 photometric measurements. The left and right panels draw the periodogram with respect to frequency and period of variability, respectively. The horizontal dashed green lines indicate the bootstrap test significance level. The vertical dashed orange lines indicate the periodogram peaks above 80% bootstrap test significance. The most significant peak in the periodogram is at 39.45 days or 0.0253 day^{-1}. The second peak at 1.02 days or 0.9774 day^{-1} corresponds to a sidereal day alias of the 39.45 day signal.

variability and the construction of our photometric model. We estimated the NIR $H - K'$ color of S2-36 using this photometric model in Section 3.3.1.2.

3.3.1.1 Multiband periodicity search

We searched for periodic variability in S2-36's photometric observations, since such variability can indicate an eclipsing or ellipsoidal binary system. G19 identified periodic variability in K'-band observations of S2-36 at a photometric period of 39.43 days. If the source of variability is an ellipsoidal or eclipsing binary with flux dips of similar depths, the detection would correspond to an ≈ 79 day binary orbital period for S2-36. We modified the methodology in G19 to simultaneously incorporate H-band data in our periodicity search (i.e., a multiband periodicity search), and to allow for long-term trends in the average stellar flux

(i.e., a trended periodicity search). Such long-term trends may be expected due to intrinsic stellar variability over long time baselines or due to the proper motion of stars behind spatial inhomogeneities in the foreground extinction screen (as suggested by G19). These methodology improvements, along with additional K'-band observations, allowed a more robust detection of periodicity in S2-36's light curve that is less prone to false detections.

Our periodicity search implementation extended the model outlined by VanderPlas & Ivezić (2015). The photometric periodicity search model consisted of sinusoidal variations with a long-term linear trend over the entire observation time baseline. Since the Lomb-Scargle periodogram searches for sinusoidal signals, eclipsing or ellipsoidal binary light curves with comparable eclipse depths are detected at photometric variability periods approximately half as long as the binary orbital periods (e.g., VanderPlas, 2018; Gautam et al., 2019). Our periodicity search model consisted of two different components for every period P searched:

1. A trended sinusoid *base model* to model the shared periodic signal across both K'- and H-bands:

$$\begin{aligned} m_{\rm base} = A_{\rm base} &+ B_{\rm base}(t-t_0) \\ &+ C_{\rm base}\sin\left[\frac{2\pi}{P}(t-t_0)\right] \\ &+ D_{\rm base}\cos\left[\frac{2\pi}{P}(t-t_0)\right]. \end{aligned} \tag{3.1}$$

2. Two *band-specific models* to model the residual periodic signal in each band not captured by the base model:

$$\begin{aligned} m_{K'\ \rm model} = A_{K'} &+ B_{K'}(t-t_0) \\ &+ C_{K'}\sin\left[\frac{2\pi}{P}(t-t_0)\right] \\ &+ D_{K'}\cos\left[\frac{2\pi}{P}(t-t_0)\right], \end{aligned} \tag{3.2}$$

$$
\begin{aligned}
m_{H\ \mathrm{model}} = A_H &+ B_H(t - t_0) \\
&+ C_H \sin\left[\frac{2\pi}{P}(t - t_0)\right] \\
&+ D_H \cos\left[\frac{2\pi}{P}(t - t_0)\right]. \qquad (3.3)
\end{aligned}
$$

The base and band-specific models were added to the weighted mean magnitude of observations in each band ($\overline{m}_{K'}$ and $\overline{m}_H$) to obtain the final model magnitudes for the respective band:

$$m_{K'} = \overline{m}_{K'} + m_{\mathrm{base}} + m_{K'\ \mathrm{model}}, \qquad (3.4)$$

$$m_H = \overline{m}_H + m_{\mathrm{base}} + m_{H\ \mathrm{model}}. \qquad (3.5)$$

For every test period in the periodogram, a total of 12 parameters were fit: A, B, C, and D for the base model and the two band-specific models. Our implementation of a multiband, trended Lomb-Scargle periodogram is available at an online software repository[1], forked from the software package GATSPY (VanderPlas et al., 2016; VanderPlas & Ivezić, 2015).

We implemented a bootstrap false-alarm test to assign significance to powers in the computed Lomb-Scargle periodogram, similar to the implementation in G19. We derived an estimate of false-alarm probability (FAP) extending the bootstrap methods outlined by Ivezić et al. (2014) and VanderPlas (2018), using 10,000 mock light curves in each observed waveband for the star. When generating a mock light curve in a given waveband, we first de-trended the observations by subtracting the best fit long-term linear trend for the respective band calculated during the Lomb-Scargle analysis. In each waveband, these de-trended observations were then randomly drawn, with replacement, at each observation time. After drawing the random observations, we added the long-term linear trend for each band back to the observations. This procedure allowed the mock light curves to include any observed long-term trends in order to properly account for the increase in the trended Lomb-Scargle periodogram power

[1] https://github.com/abhimat/gatspy

Table 3.1: Bayesian Information Criteria (BIC) for Trended Sinusoid Fits

Num. Parameters	BIC
4	-149.16
5	-146.86
6	-142.62
12	-117.45

when there is a significant long-term trend. We defined the significance of each periodogram power as $1 - \text{FAP}$. Higher significance for a given period detection in the periodogram indicated that the detection was less likely to be a false signal generated by flux measurement uncertainties or by our experiment's observation cadence.

Our multiband, trended Lomb-Scargle periodogram for the S2-36 photometric observations is shown in Figure 3.2, with bootstrap false-alarm significance levels indicated. We found that the most significant photometric period for S2-36 occurs at 39.45 days (normalized Lomb-Scargle power of 0.78). If a binary, the photometric period detection would correspond to a binary orbital period ≈ 78.90 days.

Using the bootstrap false-alarm test, the 39.45 day signal had FAP $< 10^{-4}$ or $> 99.99\%$ significance. We detected another peak in the Lomb-Scargle periodogram at a period of 1.02 days (normalized Lomb-Scargle power of 0.77; FAP $< 10^{-4}$ or $> 99.99\%$ significance). This period detection corresponds to a sidereal day ($\delta f = 1.0027$ day^{-1}) alias of the 39.45 day signal, and is expected by the nightly typical observing cadence in our experiment (G19).

At the most significant period identified in the periodicity search, we employed a Markov chain Monte Carlo (MCMC) algorithm to estimate uncertainties in the trended sinusoid's 12 fitting parameters. We first conducted a fit with all 12 parameters in our multiband,

Table 3.2: 4 Parameter Trended Sinusoid Fit

Parameter	Value
$A_{\rm base}$	-0.042 ± 0.004
$B_{\rm base}$	$(1.3 \pm 0.2) \times 10^{-5}$ mag day^{-1}
"	$(4.8 \pm 0.9) \times 10^{-3}$ mag year^{-1}
$C_{\rm base}$	0.147 ± 0.006
$D_{\rm base}$	0.028 ± 0.005
$\overline{m}_{K'}$	13.41
$\overline{m}_{H}$	15.60
t_0	2013.0 (JYear)
"	56292.75 (MJD)

trended sinusoid model. We performed additional trended sinusoid model fits with fewer fit parameters: with just the base model parameters (4 parameters), the base model with H-band slope parameter B_H (5 parameters), and the base model with both H- and K'-band slope parameters B_H and $B_{K'}$ (6 parameters). The 4-parameter and 5-parameter fits yielded tight constraints on all their respective fit parameters. With a 12-parameter fit, we found that our data do not constrain the individual band model parameters, except the band-specific slope parameters $B_{K'}$ and B_H. This fit resulted in correlations between the parameters in the base model and the band-specific models.

We calculated the Bayesian Information Criteria (BIC) to determine which trended sinusoid model to use in our subsequent analysis. The BIC is a quantity useful for model comparison, with lower BIC values resulting from better fits and fewer parameters. Generally, lower BIC values are preferred when selecting between models (see, e.g. Ivezić et al., 2019). Table 3.1 shows the BIC at the maximum likelihood location for each fit. Since the 4-parameter fit

yields the smallest BIC value, we prefer to use it in our subsequent analysis presented in this work. Our best-fit 4-parameter trended, periodic model is plotted with the data in Figure 3.1. The best-fit parameters from the 4-parameter model fit are presented in Table 3.2.

While the 5-parameter model does not yield the lowest BIC value, it allows the exploration of a possible difference in long-term trend slope between the two bandpasses. With the 5-parameter model, our observations suggest a stronger long-term fading in the K'-band observations than in the H-band. Furthermore, the slope of the long-term trend in H-band is inconsistent with that expected from the fading to have been caused by extinction alone. This analysis is presented in more detail in Appendix 3.8.

3.3.1.2 Estimate of $H - K'$ Color

To estimate the observed $H - K'$ color of S2-36, we used the long-term linear components of our trended sinusoid model. We derived the best-fit mean magnitude and corresponding uncertainties in each band at a specific time, $t_{\rm color}$. Since our observations started later in the H-band compared to the K'-band, we chose $t_{\rm color}$ to be temporally in the middle of the H-band observations. We calculated $t_{\rm color}$ as the mean of H-band observation times, weighted by the H-band magnitude uncertainties: $t_{\rm color} = 2018.01$.

At $t_{\rm color} = 2018.01$, we estimated $m_{K'} = 13.39 \pm 0.02$ and $m_H = 15.58 \pm 0.02$ from our long-term trended model fit. With these estimates, we derived a color of $m_H - m_{K'} = 2.19 \pm 0.04$.

3.3.2 Astrometry proper motion model

Table 3.3: Acceleration Proper Motion Model Fit

t_0	r_x (arcsec W of Sgr A*)	r_y (arcsec N of Sgr A*)	v_x (μas yr^{-1})	v_y (μas yr^{-1})	a_r (μas yr^{-2})	a_t (μas yr^{-2})
2008.87	-2.00 ± 0.00	0.44 ± 0.00	5118.5 ± 18.0	5072.4 ± 25.0	-31.3 ± 9.0	15.2 ± 11.0

Note. — 1σ uncertainties (68.27%) are indicated. In this table, acceleration is converted from rectangular coordinates (a_x, a_y) into polar coordinates $(a_{2\mathrm{D},r}, a_{2\mathrm{D},t})$. A negative $a_{2\mathrm{D},r}$ indicates acceleration towards the SMBH and a positive $a_{2\mathrm{D},t}$ indicates acceleration in the clockwise direction.

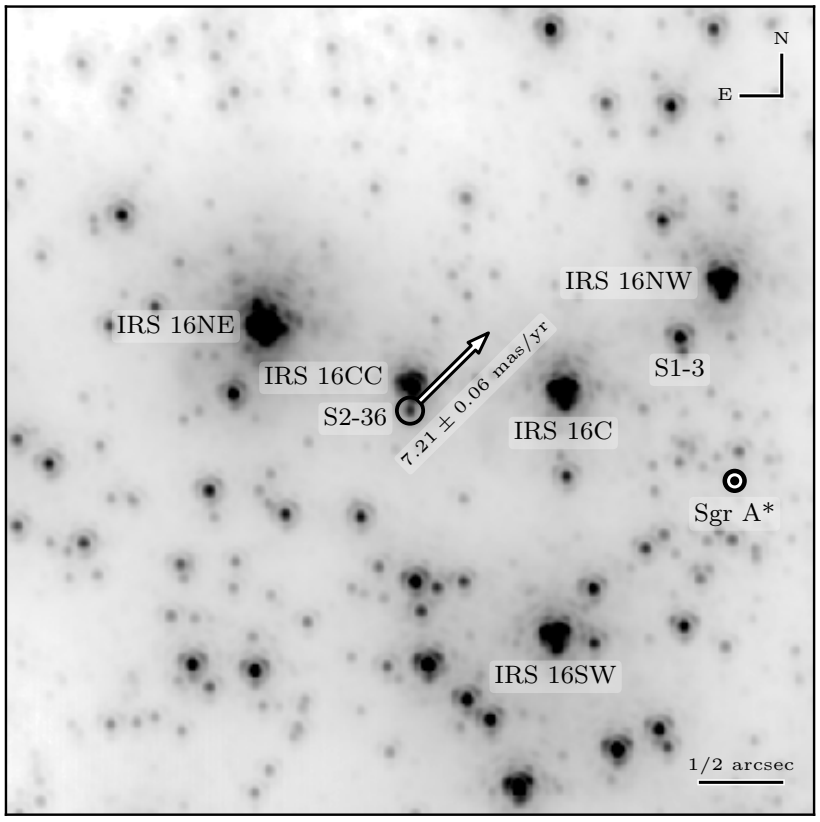

Figure 3.3: An image of the field near S2-36 from the 2009 May 4 observation. S2-36 is circled in the center of the image, and the location of the supermassive black hole at Sgr A* is indicated by the concentric circles. S2-36 is located $\approx 2.05''$ ENE of Sgr A* in projected distance. The linear (i.e. velocity) term of S2-36's accelerating proper motion model fit is indicated by the white arrow. The velocity term of S2-36's proper motion is 7.21 ± 0.06 mas/yr, relative to Sgr A*. S2-36 is moving approximately towards the northwest relative to Sgr A*.

We fit a second-order (i.e. accelerating) polynomial proper motion model to S2-36's astrometric measurement in order to estimate the physical distance of S2-36 to the SMBH. The acceleration proper motion model fit was conducted following the procedure from Sakai et al.

(2019). The acceleration proper motion model was defined as

$$x = r_{x,0} + v_x(t - t_0) + \frac{1}{2}a_x(t - t_0)^2 \tag{3.6}$$

$$y = r_{y,0} + v_y(t - t_0) + \frac{1}{2}a_y(t - t_0)^2, \tag{3.7}$$

where the (x, y) positions are defined as (arcseconds W of Sgr A*, arcseconds N of Sgr A*). The fit parameters and corresponding uncertainties are listed in Table 3.3. The velocity term extracted from the proper motion model is illustrated in the context of S2-36's surroundings in Figure 3.3.

The high value for the velocity projected on the sky ($v_{2D} = 7.21 \pm 0.06$ mas/yr) suggests that S2-36 is a member of the NSC population. Such a large velocity is expected for stellar members in the large velocity dispersion of the NSC but not for foreground or background stars in the Milky Way.

We used the sky projected component of S2-36's radial acceleration ($a_{2D,r}$) to estimate S2-36's physical distance (r) from the SMBH, assuming that the acceleration originates from the gravitational force of the SMBH's mass. The distance from the SMBH, r, is composed of the 2D distance between S2-36 and the SMBH measured on the plane of the sky, r_{2D}, and the distance between S2-36 and the SMBH along the line of sight, z:

$$r = \sqrt{z^2 + r_{2D}^2} \tag{3.8}$$

The acceleration from the SMBH (with mass $M_\bullet$) is

$$a = -\frac{GM_\bullet}{r^2} \tag{3.9}$$

The sky projected component of the SMBH's acceleration, $a_{2D,r}$, can then be expressed as

$$\frac{a_{2D,r}}{a} = \frac{r_{2D}}{r} \tag{3.10}$$

$$a_{2D,r} = a \times \frac{r_{2D}}{r} \tag{3.11}$$

$$a_{2D,r} = -\frac{GM_\bullet r_{2D}}{r^3} \tag{3.12}$$

$$a_{2D,r} = -\frac{GM_\bullet r_{2D}}{(z^2 + r_{2D})^{3/2}}. \tag{3.13}$$

From Equation (3.12), the r distance is

$$r = \left(\frac{GM_\bullet r_{2D}}{a_{2D,r}}\right)^{1/3}. \tag{3.14}$$

Similarly, from Equation (3.13), the z distance is

$$z = \pm\sqrt{\left(\frac{GM_\bullet r_{2D}}{a_{2D,r}}\right)^{2/3} - r_{2D}^2}. \tag{3.15}$$

Using the acceleration proper motion model fit and measurements of the SMBH mass and distance ($M_\bullet = 3.984 \pm 0.084 \times 10^6 M_\odot$ and $R_0 = 7.971 \pm 0.091$ kpc, Do et al., 2019), we estimate $z = 0.070^{+0.130}_{-0.037}$ pc and the distance of S2-36 from the SMBH to be $r = 0.105^{+0.109}_{-0.020}$ pc (with 3σ, 99.7% confidence intervals).

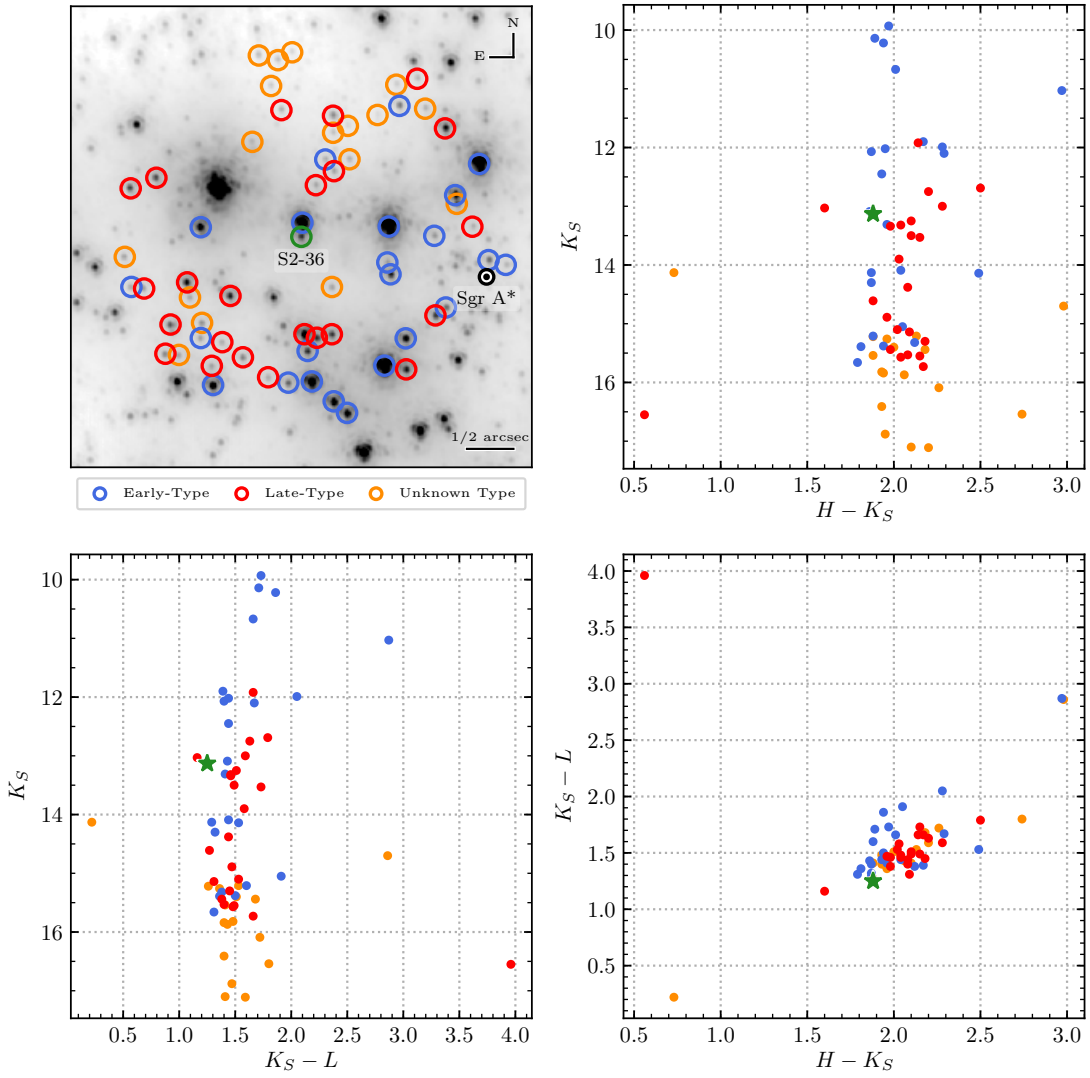

Figure 3.4: A NIR color overview of the star S2-36 and its nearest astrometric neighbors. The upper left panel shows the location of S2-36 (green) on the field of view. The circled stars are located within 2 arcseconds of S2-36 and have mean magnitudes within 4 K' magnitudes of S2-36. Using the Schödel et al. (2010) photometric catalog, we constructed color-magnitude diagrams of the circled stars: in K_S and H filters (upper right panel) and in K_S and L filters (lower left panel). We also show the $H - K_S$ and $K_S - L$ color-color diagram (lower right panel). S2-36's observed NIR color relative to that of the nearby stellar population indicates that the star is likely a member of the nuclear star cluster and not a foreground or background star.

3.3.3 Comparison with NIR stellar color of nearby stars

We examined the NIR color of S2-36 and compared it to that of nearby stellar sources in the NSC using the Schödel et al. (2010) photometric catalog. This comparison is shown in Figure 3.4. The NIR colors of S2-36 in both $H - K_S$ and $K_S - L$ and their similarity to the bulk of other stars in spatial proximity to S2-36 suggest that S2-36 is likely a member of the NSC environment. Due to extinction and dust reddening, stars foreground to the NSC would be expected to have bluer colors (i.e. lower $H - K_S$ and $K_S - L$ values than that of NSC stars), while stars background to the NSC would be expected to have redder colors (i.e. higher $H - K_S$ and $K_S - L$ values than that of NSC stars). Since S2-36's NIR colors do not exhibit either behavior, the NIR colors suggest that S2-36 is very likely a member of the NSC.

3.4 Results

We explore the origin of S2-36's observed photometric variability in Section 3.4.1. Our analysis indicates that with the observed NIR flux and color of S2-36 combined with S2-36's location at the NSC, S2-36's observed photometric variability most likely originates from a red giant ellipsoidal binary system. In order to observationally constrain the physical parameters of the binary system and its component stars, we constructed models of binary systems, detailed in Section 3.4.2. Our binary modeling assumes coeval component stars to constrain physical parameters such as stellar masses and separation.

3.4.1 Identification of source type

3.4.1.1 Methods to compare with known classes of periodic variability

Several classes of periodic stellar variability are known at the observed photometric period of S2-36, each with NIR period-luminosity relations (PLRs). These can include Cepheids: Type I / Classical Cepheids (Chen et al., 2017) and Type II Cepheids (Matsunaga et al.,

2006). In addition, classes of pulsations or periodic variability are known for evolved late-type giant stars (Riebel et al., 2010). First-order pulsations in late-type giant stars (also known as Sequence 1 or *Mira* Variables) typically occur at periods much longer ($\gtrsim$ 100 days) than that observed for S2-36. Higher order pulsation overtones occur at shorter periods with similarly well-constrained PLRs (Wood et al., 1999; Fraser et al., 2005). In particular at the 39.45 day photometric period of S2-36, periodic variability from second- (Sequence 2), third- (Sequence 3), and fourth-order (Sequence 4) pulsation overtones have been observed in evolved giant stars with well constrained NIR PLRs. Furthermore, an additional PLR exists for evolved giants (Sequence E) at the observed S2-36 photometric period, with observational evidence demonstrating that such variability originates from red giant ellipsoidal binaries (Nicholls et al., 2010).

The NIR PLRs for known classes of periodic variables allow testing for consistency with photometric observations of S2-36. The PLRs provide an intrinsic color and luminosity estimates for each variability class. The PLRs we use in this paper are described in the following format:

$$M_\lambda = a_\lambda \times [\log(P/1 \text{ day}) - c_\lambda] + b_\lambda. \tag{3.16}$$

Here, M_λ is an absolute magnitude at a given NIR band and P specifies the period of dominant photometric variability. For Sequence E binaries, the dominant photometric variability period, P, corresponds to approximately half the binary orbital period (Nicholls et al., 2010). a_λ and b_λ are observationally estimated parameters, and c_λ is a constant differing across PLR definitions in literature. There is also a residual scatter to each PLR, and is quantified by a residual standard deviation σ_λ. Since the PLRs measured by Riebel et al. (2010) are reported in extinction corrected apparent magnitudes, m_λ for the LMC, we subtracted a constant distance modulus, μ, from that work's published PLR intercept parameters, $b_{\lambda,\text{ published}}$, based on the LMC distance $d = 49.97 \pm 1.30$ kpc (Pietrzyński et al., 2013), in order to obtain PLRs

in absolute magnitudes, M_λ:

$$b_\lambda = b_{\lambda,\text{ published}} - \mu \tag{3.17}$$

$$\mu = m_\lambda - M_\lambda = 5\log(d/1\text{ pc}) - 5 \tag{3.18}$$

$$= 18.49 \pm 0.05 \tag{3.19}$$

The parameters of the NIR PLRs used in this work are collected in Table 3.4.

Table 3.4: Near-Infrared Period-Luminosity Relationships

Periodic Variability Class	a_{K_S}	b_{K_S}	c_{K_S}	σ_{K_S}	a_H	b_H	c_H	σ_H
Ellipsoidal Binaries (Sequence E)[R10]	-2.54 ± 0.02	-0.05 ± 0.10	0.0	0.246	-2.46 ± 0.02	-0.06 ± 0.09	0.0	0.237
Type II Cepheids[M06]	-2.41 ± 0.05	-4.00 ± 0.02	1.2	0.14	-2.34 ± 0.05	-3.94 ± 0.02	1.2	0.15
2^{nd}-order evolved giant pulsations (Sequence 2)[R10]	-3.93 ± 0.01	0.61 ± 0.08	0.0	0.149	-3.35 ± 0.02	-0.21 ± 0.08	0.0	0.181
3^{rd}-order evolved giant pulsations (Sequence 3)[R10]	-4.33 ± 0.02	0.78 ± 0.08	0.0	0.166	-4.06 ± 0.02	0.53 ± 0.08	0.0	0.169
4^{th}-order evolved giant pulsations (Sequence 4)[R10]	-4.46 ± 0.02	0.16 ± 0.08	0.0	0.135	-4.26 ± 0.02	0.07 ± 0.08	0.0	0.139
Type I / Classical Cepheids[C17]	-3.224 ± 0.073	-5.693 ± 0.022	1.0	0.120	-3.167 ± 0.075	-5.601 ± 0.023	1.0	0.124

Note. — 2MASS K_S and H photometry from the cited works are listed here. The calculated expected luminosity was converted from 2MASS K_S and H to NIRC2 K' and H photometry in order to compare with our observations of S2-36.

References. — R10: Riebel et al. (2010), M06: Matsunaga et al. (2006), C17: Chen et al. (2017)

Since the PLRs we use in our analysis (Riebel et al., 2010; Chen et al., 2017; Matsunaga et al., 2006) are derived from 2MASS K_S- and H-band photometry, we performed a passband correction to transform their NIR flux measurements into NIRC2 K'- and H-band photometry. We followed a similar bandpass correction technique as that outlined in Section 3.2.1 to derive our calibrator photometry. Since all PLRs had intrinsic NIR colors similar to that of evolved red giant branch stars in Riebel et al. (2010) ($H - K_S \sim 0.2$), we performed the bandpass correction using synthetic photometry of red giant model atmospheres. Using SPISEA (Hosek et al., 2020), we derived the 2MASS $H - K_S$ color for stars on the red giant branch. We then computed each of these stars' bandpass corrections from 2MASS K_S to NIRC2 K' and from 2MASS H to NIRC2 H. For a given 2MASS $H - K_S$ color from a PLR, we interpolated to the respective bandpass correction. Our calculated bandpass correction between K bands was NIRC2 K' − 2MASS $K_S \approx 0.003$ mag and between H bands was NIRC2 H − 2MASS $H \approx 0.03$ mag.

To test compatibility of S2-36's observed photometry with each of these periodic variable classes, we derived the extinction ($A_{K'}$), distance (d), and apparent magnitude at the GC ($m_{K',\,\mathrm{GC}}$) under the hypothesis that S2-36 is a member of each PLR's respective variability class. We first calculated intrinsic luminosities and NIR $H - K'$ colors at S2-36's photometric period of variability from each NIR PLR. We then used the Nogueras-Lara et al. (2018) NIR extinction law, and the difference between the observed S2-36 $H - K'$ color and the intrinsic $H - K'$ color from the PLR to derive an estimate of the line-of-sight extinction ($A_{K'}$) towards S2-36 assuming each class of variability:

$$A_{K'} = \frac{(m_H - m_{K'}) - (M_H - M_{K'})_{\text{var. class}}}{\left(\frac{\lambda_H}{\lambda_{K'}}\right)^{-\alpha} - 1}, \tag{3.20}$$

where $m_H - m_{K'}$ is the observed NIR color for S2-36 and $(M_H - M_{K'})_{\text{var. class}}$ refers to the intrinsic color for a variability class derived from the respective PLR at the period of variability. For each periodic variable class we also derived a distance estimate (d) using the

distance modulus:

$$\log_{10}\left(\frac{d}{10\text{ pc}}\right) = \frac{1}{5}(m_{K'} - M_{K',\text{ var. class}} - A_{K'}). \tag{3.21}$$

This distance estimate uses the absolute magnitude ($M_{K'}$) derived from the PLR at the variability period, the observed apparent magnitude ($m_{K'}$), and the extinction ($A_{K'}$) to derive a distance estimate. Assuming S2-36's location in the GC, we also estimated the expected apparent magnitude ($m_{K',\text{ GC}}$) for each variability class at the GC distance (d_{GC}):

$$\begin{aligned} m_{K',\text{ GC}} = \quad & M_{K',\text{ var. class}} + A_{K'} + \\ & 5\log_{10}\left(\frac{d_{\text{GC}}}{10\text{ pc}}\right). \end{aligned} \tag{3.22}$$

3.4.1.2 Results: Source of S2-36 Photometric Variability

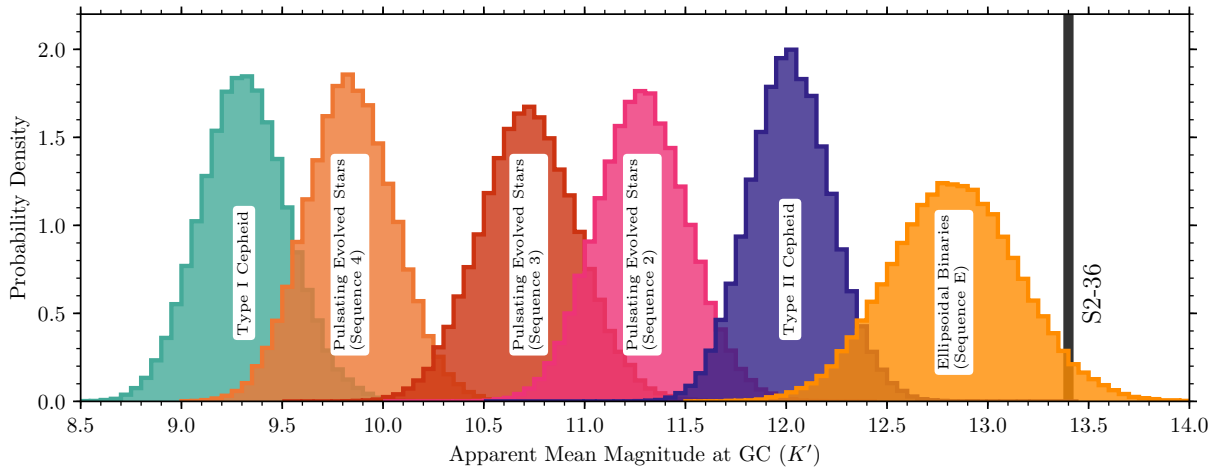

Figure 3.5: The K'-band apparent magnitude of different classes of periodic variability if located at the Galactic center distance and with $H - K'$ color and variability period as observed for S2-36. S2-36's K'-band apparent magnitude, with 1σ uncertainties, is shown as a vertical black bar. Besides ellipsoidal binaries, all periodic variability classes if located at the Galactic center would be expected to have fluxes much brighter than what is observed for S2-36. Only the ellipsoidal binary periodic variability class results in expected flux consistent with S2-36's observed K'-band flux.

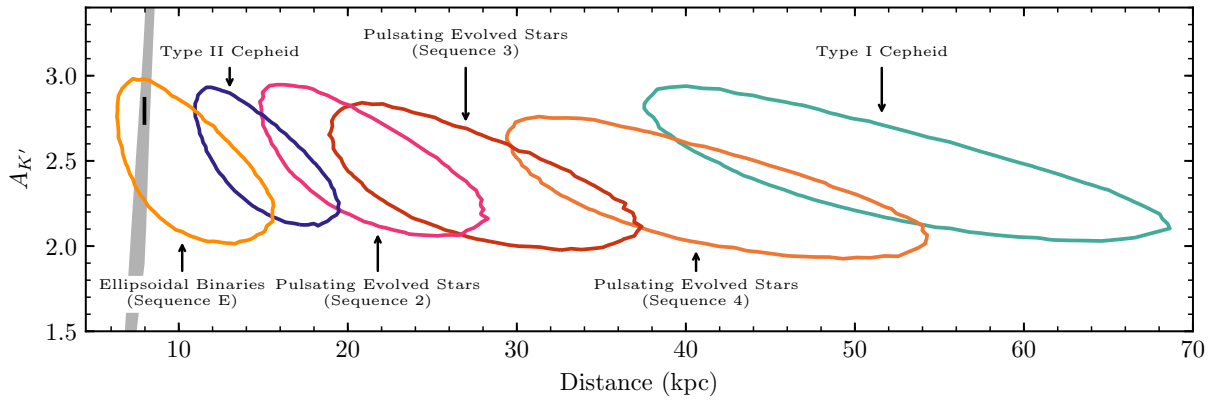

Figure 3.6: The K'-band extinction and distance estimates of known periodic variable classes at S2-36's period. All periodic variability classes are shown with their respective 3σ estimate contours. The K'-band extinction for each class is calculated using our observed $H - K'$ color for S2-36, and the distance estimate uses both the observed $H - K'$ color and K'-band flux for S2-36. For comparison, the GC distance (Do et al., 2019, 1σ) and line-of-sight K'-band extinction towards S2-36 in the Galactic center (Schödel et al., 2010, 3σ) are plotted with their respective uncertainties as thick black lines. Furthermore, we plot the expected K'-band extinction from Galactic dust maps towards the Galactic center as the Grey band (Green et al., 2019, 3σ). Only the ellipsoidal binary extinction and distance estimates are consistent with those measured for the GC. Other periodic variability class extinction and distance estimates lie in an unphysical regime where, in order to be consistent with S2-36's photometric observations, they require much larger distances than the GC but do not expect a correspondingly high extinction.

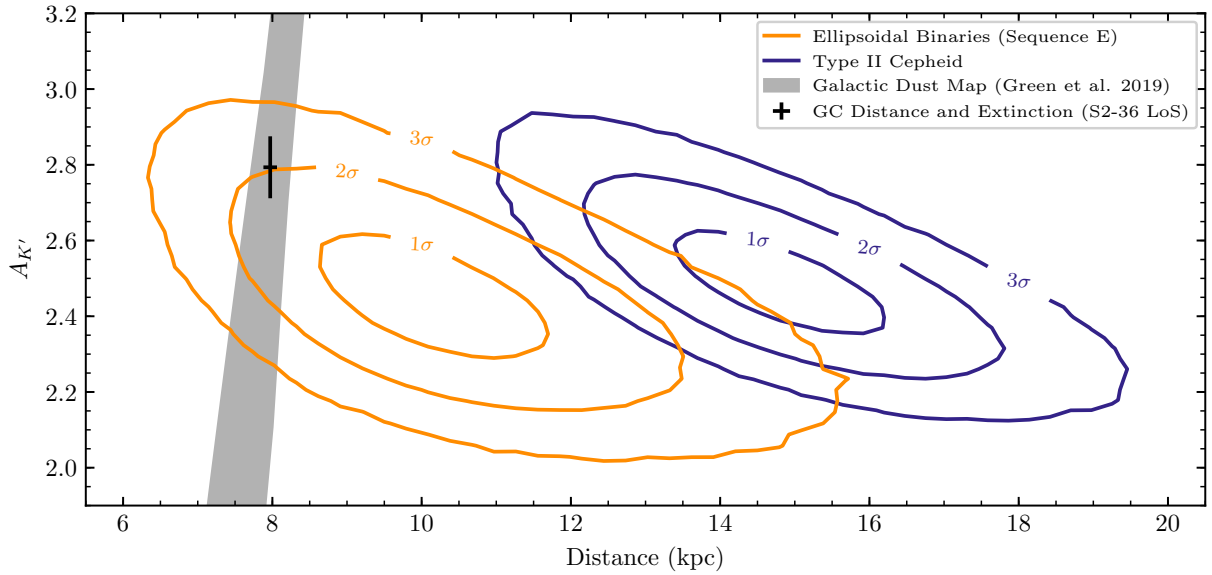

Figure 3.7: Same as Figure 3.6, but only showing the two variability classes with the lowest distance estimates (ellipsoidal binaries and Type II Cepheids).

Table 3.5: Implied extinction, distance, and GC apparent magnitude estimates from PLRs

Periodic Variable Class	Extinction ($A_{K'}$)	App. Magnitude at GC ($m_{K',\,\mathrm{GC}}$)	Distance (d, kpc)
S2-36, GC	$2.63^{+0.04\,\mathrm{a}}_{-0.08}$	13.40 ± 0.02	$7.971 \pm 0.091^{\mathrm{b}}$
Ellipsoidal Binaries (Sequence E)	2.42 ± 0.16	12.83 ± 0.32	$10.35^{+1.64}_{-1.43}$
Type II Cepheids	2.46 ± 0.14	12.02 ± 0.20	$15.05^{+1.46}_{-1.36}$
2^{nd}-order evolved giant pulsations (Sequence 2)	2.44 ± 0.15	11.29 ± 0.23	$21.11^{+2.32}_{-2.14}$
3^{rd}-order evolved giant pulsations (Sequence 3)	2.34 ± 0.14	10.72 ± 0.24	$27.35^{+3.20}_{-2.90}$
4^{th}-order evolved giant pulsations (Sequence 4)	2.28 ± 0.14	9.84 ± 0.22	$41.13^{+4.34}_{-4.00}$
Type I / Classical Cepheids	2.41 ± 0.15	9.31 ± 0.22	$52.41^{+5.41}_{-5.02}$

[a]Estimated from Schödel et al. (2010) K_S-band extinction map, converted to K'-band.

[b]Using R_0 measurement from Do et al. (2019).

Note. — 1σ uncertainties (68.27%) are indicated.

To evaluate the compatibility of S2-36's periodic variability with the different NIR PLRs, we compared the physical quantities derived for each PLR with their respective observational expectations. Specifically, we compared $A_{K'}$ with the extinction towards S2-36's line of sight from the extinction map by Schödel et al. (2010), d with the distance to the GC (R_0, Do et al., 2019), and $m_{K',\,\mathrm{GC}}$ with this work's measurement of the S2-36 mean magnitude in the K'-band.

Of the known classes of periodic variability at S2-36's photometric variability period of 39.45 days, our measured NIR flux and color are most compatible with the GC distance and extinction if S2-36 is an ellipsoidal binary (Sequence E) variable. The comparisons derived under each periodic variability class assumption are summarized in Table 3.5. Figure 3.5 displays the apparent magnitude of each variability class at the GC distance, using our NIR color measurements for S2-36. This figure shows that besides ellipsoidal binaries, the other periodic variability classes would expect a much brighter flux at the S2-36 period if it is located at the GC distance. Figures 3.6 and 3.7 show the estimates of $A_{K'}$ and d for each periodic variability class. While ellipsoidal binaries are compatible with both the GC distance and line of sight extinction to S2-36, other variability classes are incompatible at greater than 3σ confidence. Furthermore, Type II cepheids and other variability classes can further be ruled out to be compatible with our S2-36 photometric measurements by the physical argument that their implied extinctions and distances are incompatible with Galactic dust models (e.g. Green et al., 2019): while these other classes imply distances larger than R_0, their corresponding extinction estimates are much lower than what is expected at their distance due to Galactic dust distribution.

3.4.2 Stellar binary modeling

We constructed models of binary star systems and ran a fitting procedure to place constraints on the physical parameters of the binary system orbital configuration and the component stars based on the observed fluxes of S2-36. This procedure consisted of several steps de-

scribed in more detail in the following sections: stellar evolutionary models to derive the stellar parameters of the component stars in the binary (Section 3.4.2.1), deriving simulated light curves with an astrophysical binary modeling code (Section 3.4.2.2), and a Markov chain Monte Carlo (MCMC) fitting algorithm to estimate the best fit stellar parameters to our observed light curve (Section 3.4.2.3). The code we developed to assist in MCMC fitting of light curves with the PHOEBE binary light curve simulation software and to assist in interfacing with the SPISEA stellar population synthesis code is available at an online software repository, PHOEBE PHITTER[2]. The physical constraints on the binary and component stellar parameters from modeling our observations are detailed in Section 3.4.2.4.

3.4.2.1 Stellar parameters from evolutionary models

The stellar parameters of the component stars in our binary system models were derived using theoretical stellar isochrones calculated with the stellar population synthesis code SPISEA (Hosek et al., 2020). We used MIST isochrones (Choi et al., 2016; Dotter, 2016) computed at specific ages and metallicities to obtain stellar parameters. We assigned stellar atmospheres to the isochrone stars using the PHOENIX atmosphere grid (Husser et al., 2013), matching to the corresponding metallicity and stellar properties. At each age and metallicity, we calculated synthetic photometry for the isochrones at our experiment's observation bandpasses (K' and H) with the SPISEA code. To derive synthetic photometry for each isochrone, we used the NIR extinction law derived from wide-field GC observations by Nogueras-Lara et al. (2018).

From the isochrones, we linearly interpolated the stellar properties required during our MCMC fitting procedure (described in Section 3.4.2.3). Specifically, our MCMC fitter traversed radius as the parameter to select each component star, given a specific stellar evolutionary phase (e.g.: Red Giant Branch or Asymptotic Giant Branch). In our modeling,

[2] https://github.com/abhimat/phoebe_phitter

we chose radius as the primary parameter since the stars most closely matching S2-36's components rapidly evolve in radius and not as rapidly in other quantities, such as initial mass. This assisted our MCMC fitter's exploration of the parameter space. In addition to the stellar radius (R), the stellar properties we interpolated were stellar mass (M), effective surface temperature ($T_{\rm eff}$), and the passband luminosities ($L_{K'}$, L_H).

3.4.2.2 Binary light curve models

We generated binary models using the PHOEBE 2.1 binary light curve simulation software (Horvat et al., 2018; Prša et al., 2016). Our PHOEBE PHITTER software carried out the different steps necessary to fit our observed light curves to the binary models computed with PHOEBE: deriving stellar parameters and synthetic photometry of component stars from isochrones, generating mock binary system parameters, transitioning between detached, semidetached, and contact binary cases, and in allowing the exploration of the parameter space with MCMC sampling.

With PHOEBE, we constructed mock binary systems and simulated fluxes at our observation times. In addition to the interpolated stellar parameters, we passed additional parameters of the binary system to use for constructing the model binary system. These quantities included the binary orbital period (P), inclination of the binary orbital plane (i), and t_0. Since our model binary systems allowed semidetached and contact binaries, the binary orbital eccentricity (e) was fixed to 0, since such systems are not supported to have eccentric orbits in PHOEBE. We additionally fixed the binary system distance to the Galactic center distance R_0: $d = R_0 = 7971$ pc (Do et al., 2019). The line of sight extinction ($A_{K'}$) was left as a free model parameter. We included an additional model parameter, $A_{H,\rm mod}$, to allow small modification to the fluxes modeled in the H-band in addition to what is assumed from $A_{K'}$ and the extinction law:

$$A_{H,\rm mod} = A_{H,\rm observed} - A_{H,\text{ext. law prediction}}. \tag{3.23}$$

Table 3.6: Prior bounds on fitted binary parameters

Fitted Parameter	Prior Bound Low	Prior Bound High
$A_{K'}$	1.0	4.0
$A_{H,\,\mathrm{mod}}$	-2.0	2.0
R_1 ($R_\odot$)	$\min(R_{\mathrm{Stellar\ Phase}})$	$\max(R_{\mathrm{Stellar\ Phase}})$
R_2 ($R_\odot$)	$\min(R_{\mathrm{Stellar\ Phase}})$	R_1
i (°)	0.0	180.0
P (d)	73.0	85.0
t_0 (MJD)	53739.3	53818.2

The $A_{H,\mathrm{mod}}$ parameter could account for small deviations from the NIR extinction law.

Determining if a model binary system is a detached, semidetached, or contact binary system was determined before the simulated fluxes were calculated. PHOEBE currently requires setting up each of these configurations of model binary systems in a separate manner. When starting to set up a model binary system, we calculated the Roche overflow limit. If the maximum radius of the physically larger of the two stellar components in the model binary system was within 1.5% of the Roche overflow limit, the model was set up as a semidetached binary system. For smaller or larger cases, detached binary or contact binary models were used, respectively.

3.4.2.3 MCMC fitting

We used a Markov chain Monte Carlo algorithm, as implemented in the EMCEE software package (Foreman-Mackey et al., 2013), to fit our model parameters. In our modeling, we fit for seven parameters: $A_{K'}$, $A_{H,\mathrm{mod}}$, R_1, R_2, i, P, and t_0. Since the binary configuration

is expected to be close to the semidetached configuration, where only zero eccentricities are supported in our modeling, we assumed $e = 0$ in our models and did not include orbital eccentricity as a fit parameter.

We ran the MCMC fitting algorithm in a range of ages and metallicities. Our age ranges spanned from 100 Myr to 13.5 Gyr and with metallicities spanning [Fe/H] from +0.5 to -1.5. We assumed uniform priors for all seven parameters. The prior bounds for the fitted parameters are listed in Table 3.6.

3.4.2.4 Results: Physical Parameter Constraints from S2-36 Binary Modeling

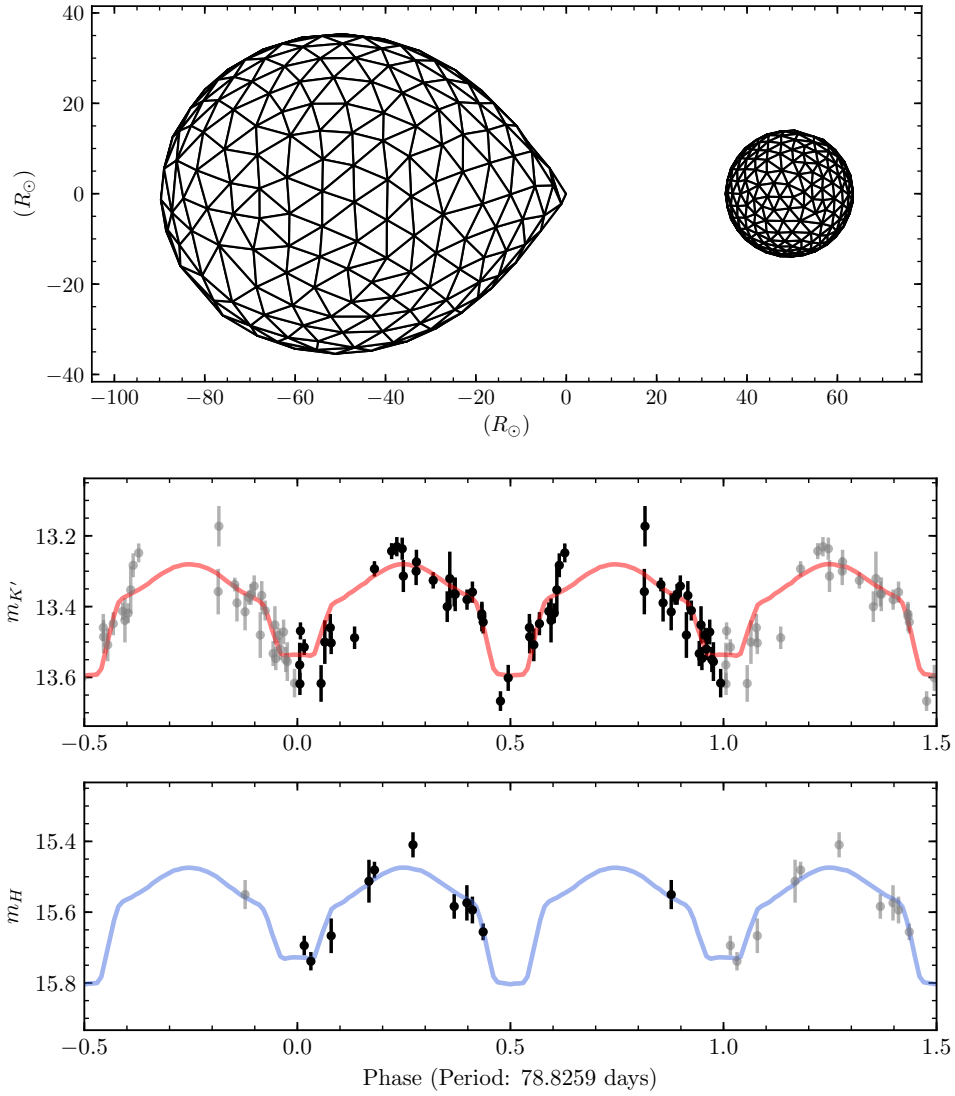

Figure 3.8: The best-fit binary model at age = 12.8 Gyr, [Fe/H] = 0.5. The top panel shows a mesh visualization of the model binary system on the plane of the sky at phase of 0.25. The axes are plotted in units of solar radii. The bottom panels show the K'-band and H-band model light curves for the best-fit model (red and blue solid lines, respectively). Our observations in each of these wavebands are plotted as the black points.

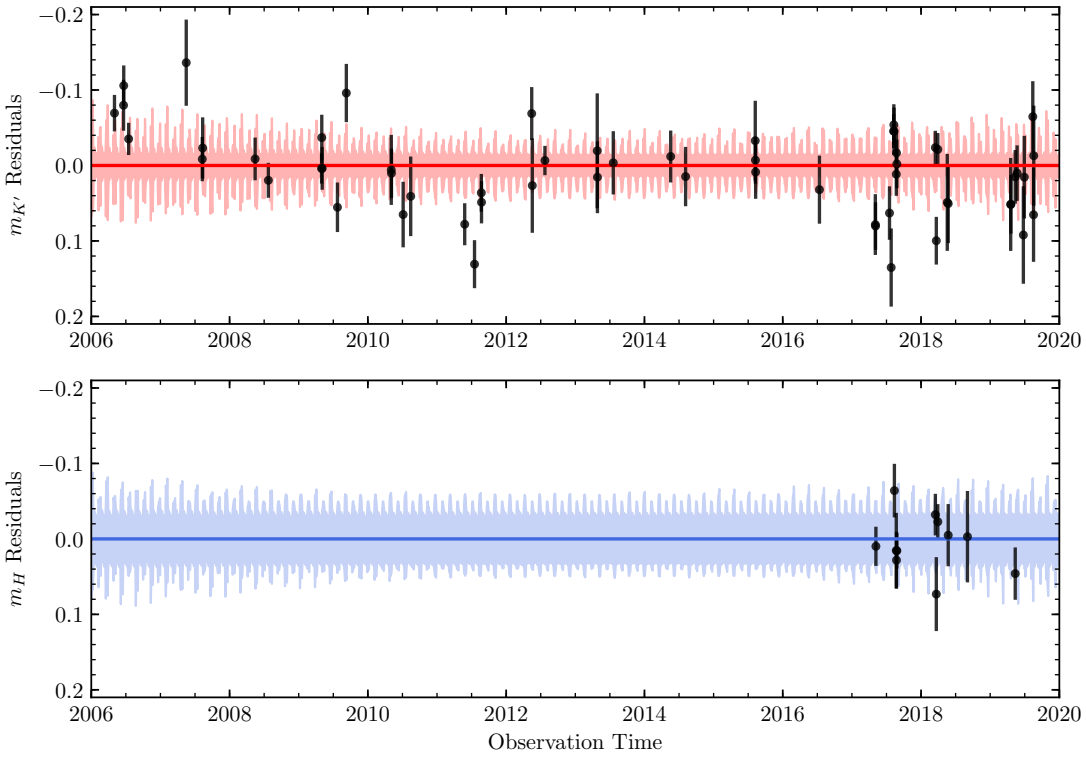

Figure 3.9: Residuals from the median model value for our age = 12.8 Gyr, [Fe/H] = 0.5 binary models. The residuals of our observed flux values from the median S2-36 binary model are shown in black. The colored bands indicate the 3σ (99.7%) uncertainty of our model residual magnitudes (red: K'-band, blue: H-band).

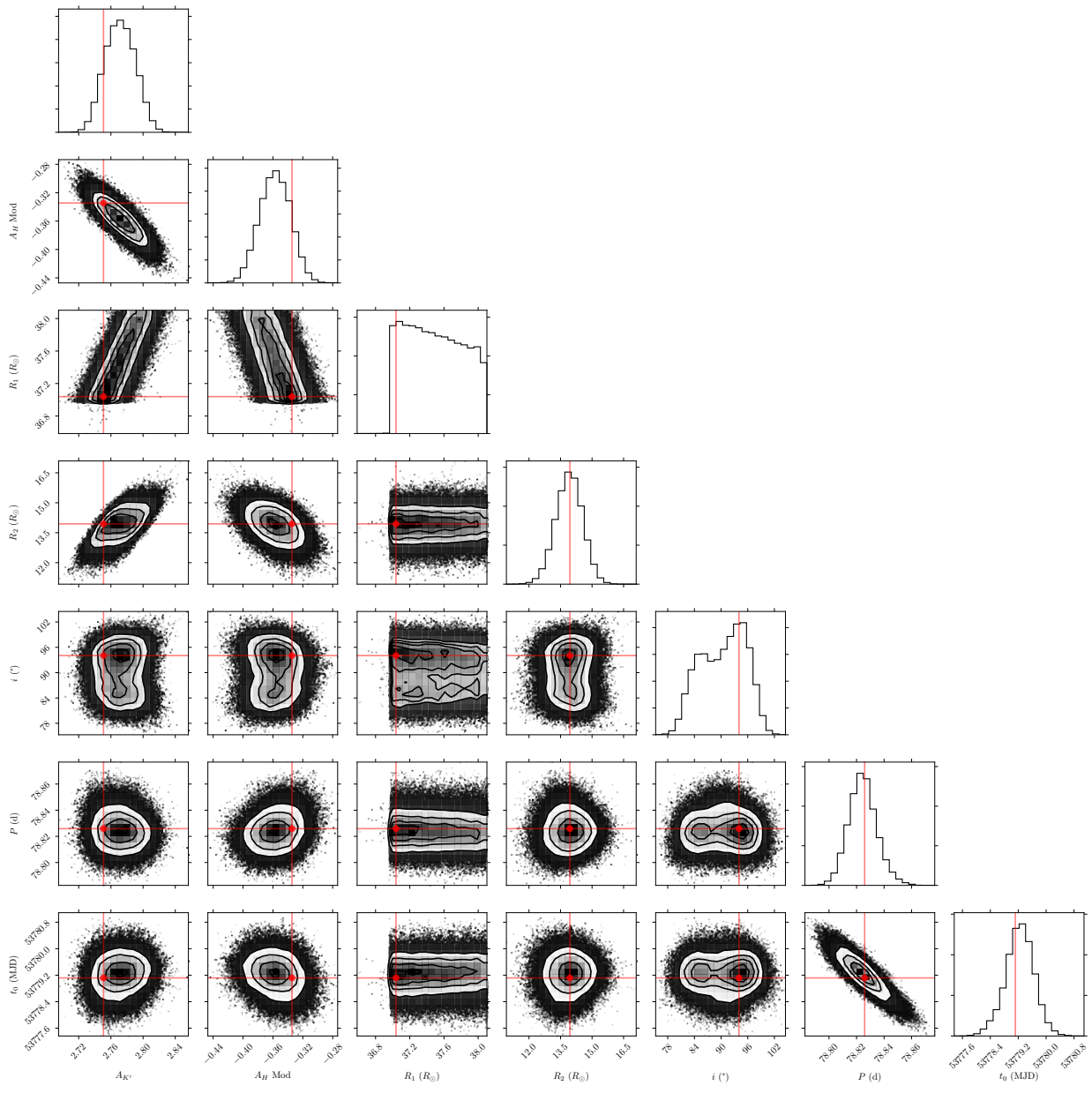

Figure 3.10: Corner plot showing the posterior distributions of all parameters estimated during the MCMC fitting procedure for the age = 12.8 Gyr, [Fe/H] = 0.5 binary models. A total of seven parameters were fit at each age, metallicity trial. The best-fit parameters (i.e., the parameters which yielded the maximum likelihood during fitting) in this age, metallicity trial are indicated in red. The binary model with these best-fit parameters is shown in Figure 3.8.

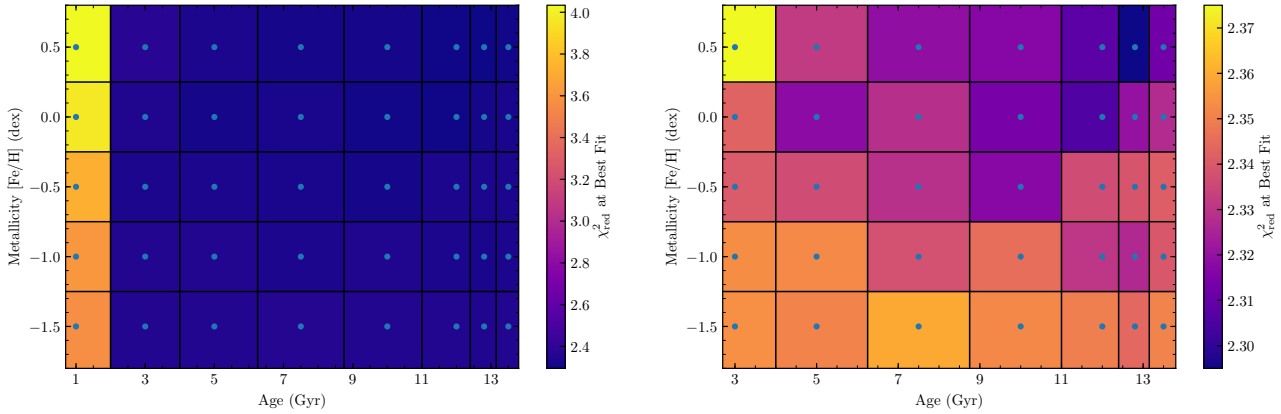

Figure 3.11: The $\chi^2_{\rm red}$ of the best-fit in each of our binary model light curve fitting trials, organized by the age and metallicity of each test (each trial's assumed age and metallicity are indicated by the blue dots in the plots). The left panel includes our 1 Gyr trial. At ages $\lesssim$ 3 Gyr, our models yield poorer fits since at those young ages red giant stars do not reach the size required for the large primary to produce the observed ellipsoidal variations at the binary period. The right panel excludes the 1 Gyr trials, to have clearer contrast in the 3–13.5 Gyr age trials. Generally, the 3–13.5 Gyr models yielded comparable $\chi^2_{\rm red}$ values, with slightly lower $\chi^2_{\rm red}$ values (i.e. slightly better fits) at higher metallicities or older ages. We achieve the best fit in all our fitting trials at age = 12.8 Gyr, [Fe/H] = 0.5.

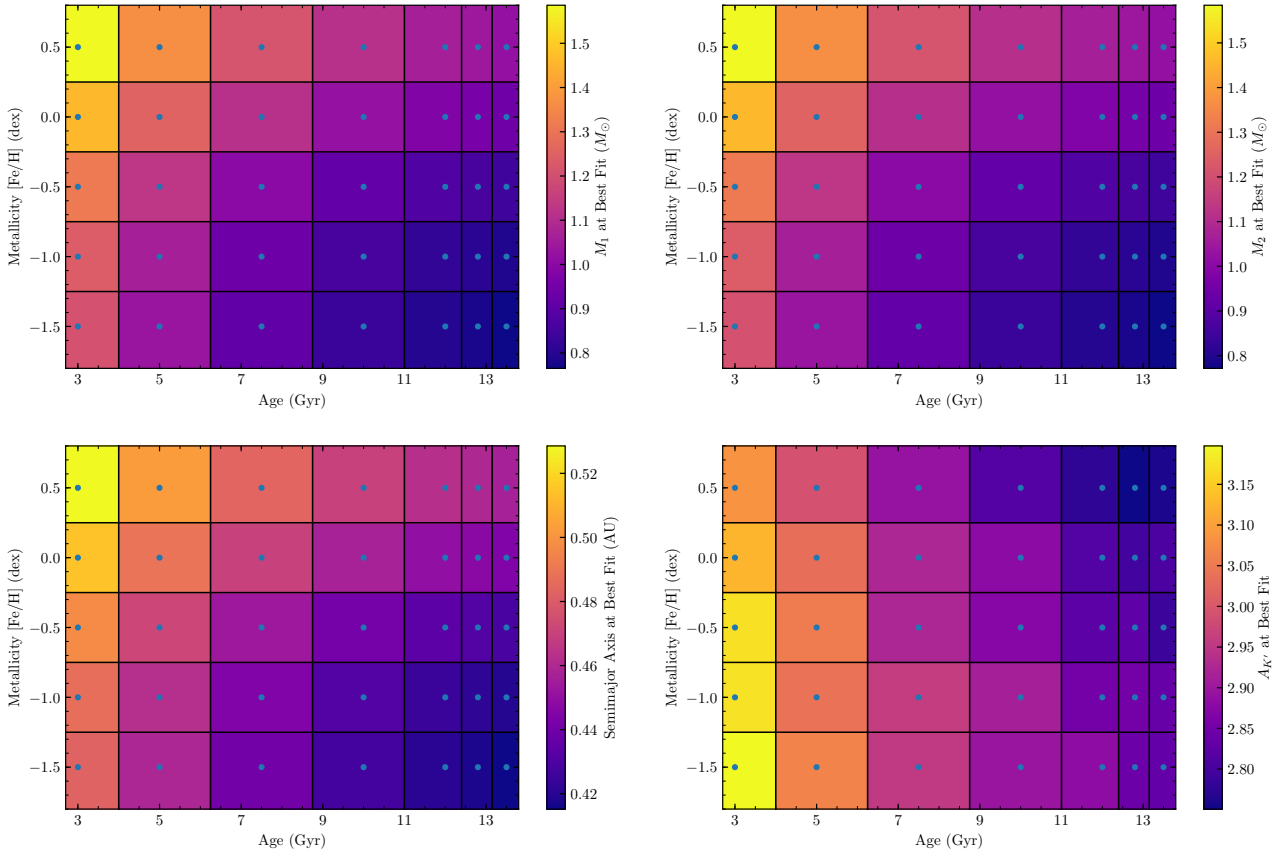

Figure 3.12: The distribution of select parameters at the best-fit model in our binary model light curve fitting trials conducted at different ages and metallicities. From top left, going clockwise: The mass of the primary star (M_1), the mass of the secondary star (M_2), the K'-band extinction ($A_{K'}$), and the binary system semimajor axis.

Following our single age and metallicity binary light curve fitting procedure, we obtained good fits to our observed light curves at stellar ages spanning between 3 Gyr to 13.5 Gyr. In this range of ages for our model fits, we obtain $\chi^2_{\rm red} \approx 2.5$, with slight variation based on stellar metallicity and ages of the component stars (see Figure 3.11). Figure 3.8 shows an example best-fit binary model at an age of 12.8 Gyr and metallicity [Fe/H] of +0.5 (this age and metallicity trial yielded the lowest best-fit $\chi^2_{\rm red}$ of all our age and metallicity trials). The binary model residuals from this age and metallicity trial are shown in Figure 3.9.

Figure 3.10 shows a corner plot from this age and metallicity trial, plotting the distribution of and correlation between the seven model parameters.

Despite the small differences in the best-fit binary and stellar parameters from our light curve fits across our entire age and metallicity range, some general properties can be drawn out about the binary system from. Generally, the best-fits in our models are at an extinction $A_{K'}$ between 2.8 and 3.0 magnitudes, with lower extinctions at older ages (see Figure 3.12). The best-fit deviation from the extinction law at H-band, $A_{H,\,\mathrm{mod}}$, is smallest at older ages (≈ -0.3 magnitudes in 13.5 Gyr models), and becomes larger at younger age models (≈ -0.5 magnitudes at 5 Gyr models). The negative sign in this deviation implies that the simulated binary flux needs to be made brighter in the H-band (i.e. less reddening or a shallower extinction law) in order to match the observed photometry. This deviation originates from the primary star in younger age binary fits being more luminous, and therefore requiring higher extinctions and a less steep extinction law to be consistent with our observations.

At ages $\gtrsim 3$ Gyr, our fits yielded consistent parameters for the component stars, with small deviations based on the age and metallicities of the our models. For the radius of the larger primary stellar component, R_1, we found best fits between $\approx 34R_\odot$ and $\approx 39R_\odot$, with physically smaller sizes being preferred at older or more metal-poor models. Stellar masses for the larger primary star, M_1, ranges between $\approx 0.8M_\odot$ and $\approx 1.2M_\odot$. Higher mass stars evolve at younger ages, so best-fit models at younger ages prefer larger masses for the larger primary star. The size and mass of the smaller secondary star in our best fits follow similar trends with respect to age and metallicity, with radius ranging between $\approx 13R_\odot$ and $\approx 14.5R_\odot$ and mass ranging between $\approx 0.8M_\odot$ and $\approx 1.2M_\odot$. This results in a stellar mass ratio $q \approx 1.0$ in the binary system. The semimajor axis was consistent in each of our binary fits, with $a \approx 0.45$ AU.

At ages $\lesssim 3$ Gyr, we obtained poorer binary light curve fits to our observations. At these younger ages, red giant branch stars do not reach the size required for the large primary

to produce the observed ellipsoidal variations at the binary period. The models therefore require an asymptotic giant branch star for the larger stellar component, with a much higher luminosity. In order to match the modeled fluxes to our observations a higher extinction $A_{K'}$ is implied, and a larger deviation from the extinction law, $A_{H,\,\mathrm{mod}}$, is required to compensate for the higher reddening implied by the higher extinction. At these young ages, the deviation from the extinction law exceeds beyond 5σ from the uncertainty derived by Nogueras-Lara et al. (2018). In our light curve fitting MCMC runs, deviations larger than 5σ to the NIR extinction law were not allowed, so consequently the fits at these younger ages are much poorer.

Our light curve models constructed with the assumption of two coeval evolved giant stars of the same metallicity imply that the S2-36 binary system is composed of near equal mass stellar components with ages between ≈ 3 to 13.5 Gyr. Select model binary system best-fit stellar and binary parameters in each of our age and metallicity trials between 3 and 13.5 Gyr are shown in Figure 3.12.

3.5 Discussion

We evaluate the implications of the star S2-36 being an old, red giant binary system in the GC environment. First, we determine the implications for the dynamical history of the GC environment if S2-36 has been present at its current location at the GC for its entire lifetime. This assumption can place tight upper limits on the number of massive stellar remnants in the vicinity of S2-36 and Sgr A*, and is detailed in Section 3.5.1. We then consider the alternative hypothesis that S2-36 was a member of an infalling cluster of old stars, and is therefore only a recent member of the inner region close to Sgr A*. Under this infall assumption, since the binary has not spent its lifetime in the high stellar densities expected close to Sgr A*, the binary's current configuration is not able to tightly constrain the stellar remnant population at the GC. We detail this consideration in Section 3.5.2.

3.5.1 Dynamical constraints on massive compact remnants and a dark cusp in the GC

Over its lifetime, a stellar binary system at the GC faces several dynamical encounters with the high density population of stars and stellar remnants in the region. In particular, these interactions can tighten or loosen the binary system. For loosely bound binary systems, strong interactions can cause the binary system to *evaporate*, where the stellar components dissociate (Binney & Tremaine, 2008). By observing the presence of a binary system, an upper limit can be placed on the number of interactions that would cause such a disruption. We follow the dynamical framework detailed by Alexander & Pfuhl (2014) and Rose et al. (2020) to calculate the constraints that a long-period, low-mass binary system at the GC can provide on the properties of its local environment.

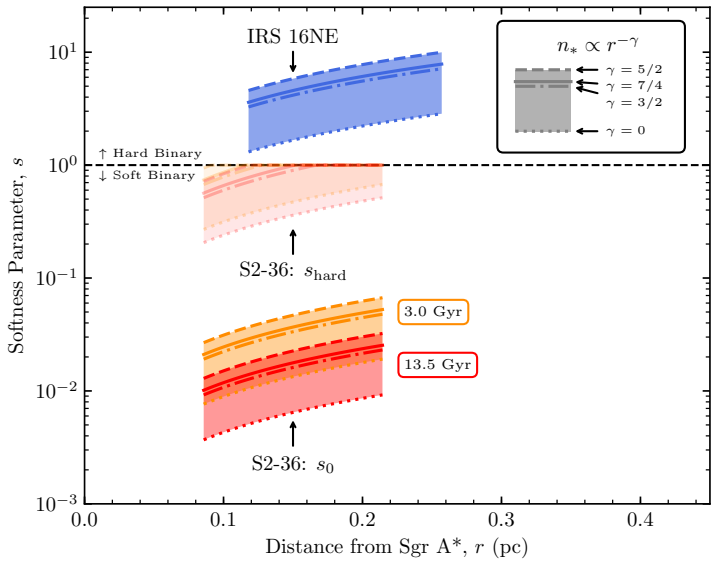

Figure 3.13: The binary softness parameter calculated for the old binary S2-36 (orange bands: 3 Gyr models, red bands: 13.5 Gyr models) over the possible distances from Sgr A*. We show both the current observed softness parameter for S2-36, s_0, and the maximum possible softness parameter expected over its lifetime, $s_{\rm hard}$. For comparison, we also plot the softness parameter for the young, long-period binary IRS 16NE (blue band). Contrary to Alexander & Pfuhl (2014), we found that IRS 16NE is expected to be a hard binary in the expected GC dynamical environment. The width of each band in this plot originates from different exponential slopes of the cusp density distribution γ. Specifically, $\gamma = \frac{5}{2}$, $\frac{7}{4}$, $\frac{3}{2}$, and 0 are indicated in each band as lines from top to bottom, respectively. The difference in softness parameter due to S2-36's age is a result of the different best-fit stellar masses and separation in our binary modeling procedure and is not dependent on the time S2-36 has spent in the GC. The range of possible S2-36 distances from Sgr A*, r, plotted here are provided from the measurement of its projected acceleration in its proper motion (see Section 3.3.2). IRS 16NE's possible distances originate from a linear, velocity fit to its proper motion. The minimum distance for IRS 16NE corresponds to its projected distance from Sgr A* while the maximum distance corresponds to assuming the projected velocity represents the maximum velocity to still remain bound to the SMBH.

3.5.1.1 Binary Softness

The fate of a binary in a stellar population is highly dependent on the binary system's *softness*, which compares the gravitational binding energy of the binary system to the typical kinetic energy of surrounding objects. The softness can be characterized by the softness parameter, s,

$$s \equiv \frac{|E_{12}|}{\langle M_* \rangle \sigma_*^2} = \frac{(GM_1M_2)/(2a_{12})}{\langle M_* \rangle \sigma_*^2}. \tag{3.24}$$

Here, '$*$' is used to denote the population of field objects that can disrupt the old binary system. E_{12} is the gravitational binding energy of a binary system with stellar masses M_1 and M_2 and a semi-major axis a_{12}: $E_{12} = -(GM_1M_2)/(2a_{12})$. $\langle M_* \rangle \sigma_*^2$ is the kinetic energy of the surrounding field objects. Following Alexander & Pfuhl (2014), in our calculations we similarly assume $\langle M_* \rangle = 1.2 M_\odot$.

For an $n_* \propto r^{-\gamma}$ cusp density distribution of the field objects surrounding a SMBH with mass $M_\bullet$, the velocity dispersion of the surrounding field objects (σ_*) can be calculated as (Alexander & Pfuhl, 2014):

$$\sigma_*^2(r) = v_\bullet^2(r)/(1+\gamma), \tag{3.25}$$

$$= (GM_\bullet/r)/(1+\gamma), \tag{3.26}$$

$$\sigma_*(r) = \sqrt{\frac{GM_\bullet/r}{1+\gamma}}. \tag{3.27}$$

Therefore, we obtain that the softness parameter in Equation (3.24) can be expressed as

$$s(r) = \frac{GM_1M_2}{2a_{12}} \frac{1}{\langle M_* \rangle} \frac{r(1+\gamma)}{GM_\bullet} \tag{3.28}$$

$$= \frac{1+\gamma}{2} \frac{M_1M_2}{M_\bullet \langle M_* \rangle} \frac{r}{a_{12}}. \tag{3.29}$$

A *soft binary* ($s < 1$) has lower gravitational binding energy than the typical kinetic energy of the background field objects, and is susceptible to dissociation by interactions with these

surrounding objects. On the other hand, *hard binaries* ($s > 1$) can have complex interactions with surrounding objects and are more resistant to dissociation. For very soft binaries ($s \ll 1$), where the binary binding energy is much smaller than the typical kinetic energy of surrounding objects, *evaporation* dominates. In this regime, the binary can easily get dissociated from multiple interactions (e.g. Binney & Tremaine, 2008; Alexander & Pfuhl, 2014). Generally, dynamical interactions in a stellar population result in harder binaries getting harder and softer binaries getting softer (Heggie, 1975; Hills, 1975).

Since soft binaries get softer with dynamical interactions, these binaries were typically even harder before the current observed configuration. We can designate the current observed softness parameter of a binary as s_0, and the maximum possible softness parameter over the lifetime of a soft binary as $s_{\rm hard}$. From these, we can define a maximal evolution ratio S_h:

$$S_h \equiv s_{\rm hard}/s_0. \tag{3.30}$$

Importantly, since soft binaries get softer with more interactions, $s_{\rm hard} \geq s_0$ and $S_H \geq 1$. Following Alexander & Pfuhl (2014), $s_{\rm hard}$ can be calculated as the minimum of $s = 1$ or s at the hardest softness parameter possible, a contact binary:

$$s_{\rm hard} = \min[1, s_{\rm contact}]. \tag{3.31}$$

We calculated $s_{\rm contact}$ by setting the semimajor axis of the S2-36 model binary system to the sum of the main sequence radii of the component stars: $a_{12} = R_{\rm MS,1} + R_{\rm MS,2}$. In our binary model systems, we obtained the main sequence radius of each of the stellar components ($R_{\rm MS}$) from the 1 Gyr age MIST isochrones at their respective metallicities (see Section 3.4.2.1 for details on our determination of stellar parameters from evolutionary models).

Figure 3.13 shows the estimates of the softness parameter for the old binary S2-36: in the observed configuration s_0 and the maximal possible softness parameter $s_{\rm hard}$. Importantly, the difference in the softness parameter as a function of S2-36's age does not originate from the time spent in the GC. The age of the binary system instead affects the best fit stellar

and binary parameters (as calculated from our binary modeling procedure, Section 3.4.2). At younger ages, higher masses are required for the component stars in the binary system. Consequently, the binary system is more tightly bound at these young ages yielding higher values for the softness parameter.

We found that at all possible ages for S2-36 and distances from the central SMBH, S2-36 is a dynamically soft binary system. As a soft binary, S2-36 is susceptible to binary evaporation in the GC environment. For comparison, we also plot the observed softness parameter for the long-period, young binary system IRS 16NE in Figure 3.13. Contrary to Alexander & Pfuhl (2014), we found that IRS 16NE is a dynamically hard binary: with $s \simeq 1$ for a flat density profile ($\gamma = 0$) or $s \gtrsim 3$ for steeper, cusp-like density profiles ($\gamma \geq 3/2$). Despite the long, ~ 224 day period of IRS 16NE, the high masses of the stellar components make it a dynamically hard binary system in the expected GC environment. Therefore, we found that IRS 16NE has not been susceptible to binary evaporation over its lifetime.

3.5.1.2 Stellar Remnant Number Constraint

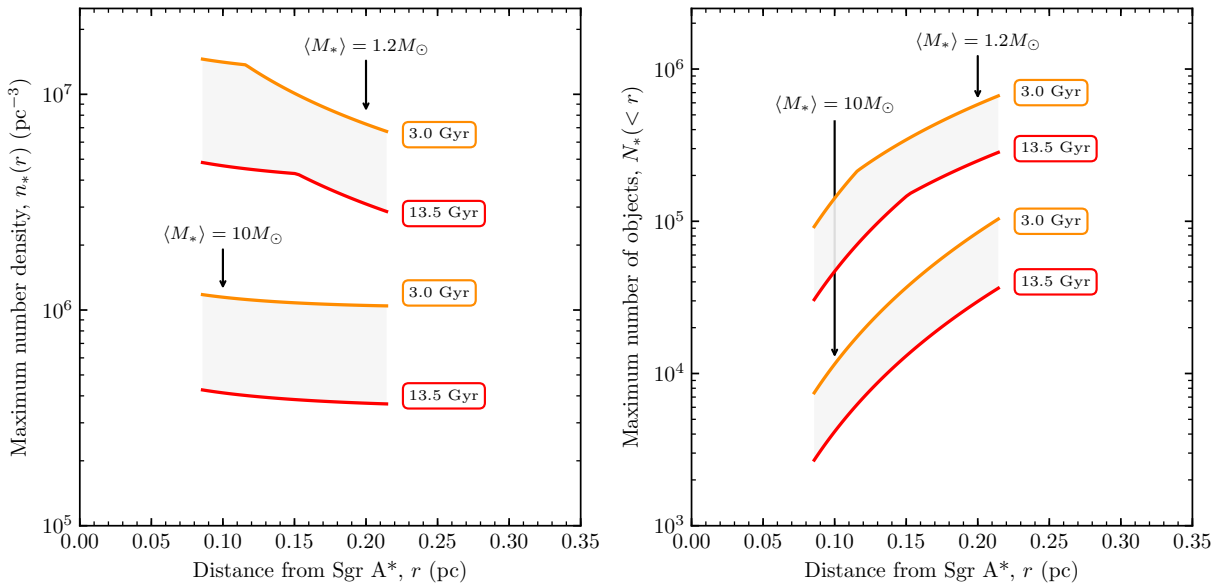

Figure 3.14: The constraints on the maximum density ($n_*(r)$) and the maximum number ($N_*(< r)$) of evaporating objects from the ellipsoidal binary S2-36 are shown in the left and right panels, respectively. In these plots, we calculated constraints at a fixed $\gamma = 7/4$ power-law slope of the density profile, at two different typical masses of evaporating objects: $\langle M_* \rangle = 1.2M_\odot$ and $\langle M_* \rangle = 10M_\odot$. While $\langle M_* \rangle = 10M_\odot$ is not expected to be realistic for the GC, it demonstrates an upper limit on the number and density of stellar mass black holes at the GC with typical masses $\sim 10M_\odot$. The range of possible S2-36 distances from Sgr A*, r, plotted here are provided from the measurement of its projected acceleration in its proper motion (see Section 3.3.2).

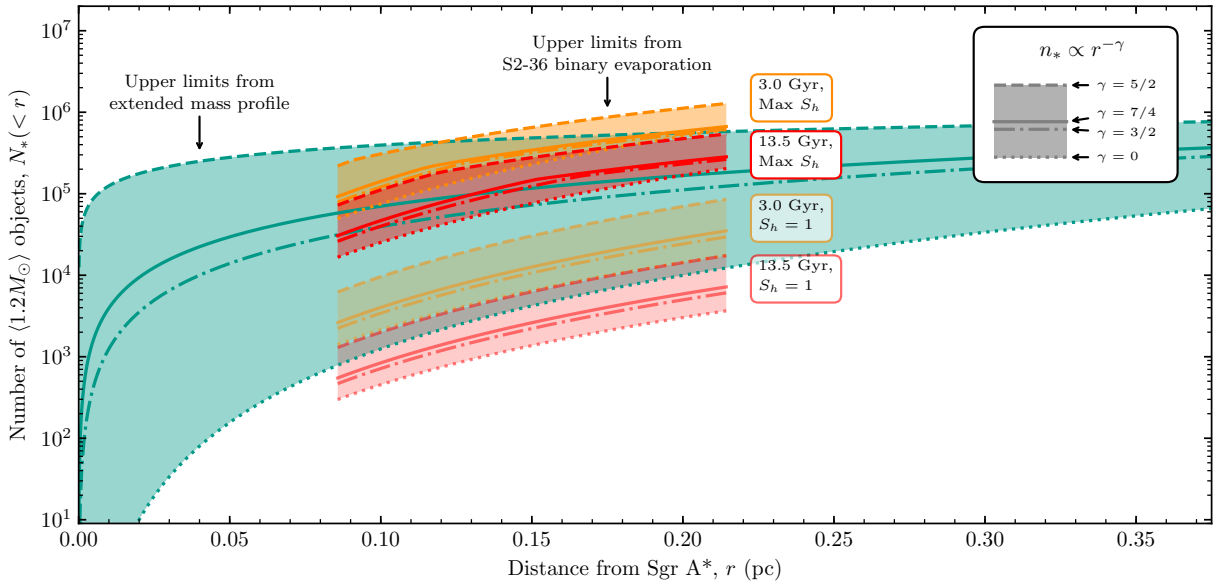

Figure 3.15: The constraint on the number of $\langle 1.2M_\odot \rangle$ objects in the Galactic center region as a function of distance. The upper limits from the binary evaporation of S2-36 are shown as the orange and red bands (orange: 3 Gyr models, red: 13.5 Gyr models). The range of possible S2-36 distances from Sgr A*, r, plotted here are provided from the measurement of its projected acceleration in its proper motion (see Section 3.3.2). We show the estimates calculated from assuming that the binary was initially as hard as possible (i.e. maximum S_h), or if the binary was initially at its current observed softness s_0 (i.e. $S_h = 1$). The width of each band in this plot originates from different exponential slopes of the cusp density distribution γ. Specifically, $\gamma = \frac{5}{2}$, $\frac{7}{4}$, $\frac{3}{2}$, and 0 are indicated in each band as lines from top to bottom, respectively. For comparison, estimates of the extended mass profile in the GC provide an independent estimate of the upper limit of $\langle 1.2M_\odot \rangle$ objects in the GC, shown as the teal band. This limit was computed from enclosed mass estimates from Schödel et al. (2009).

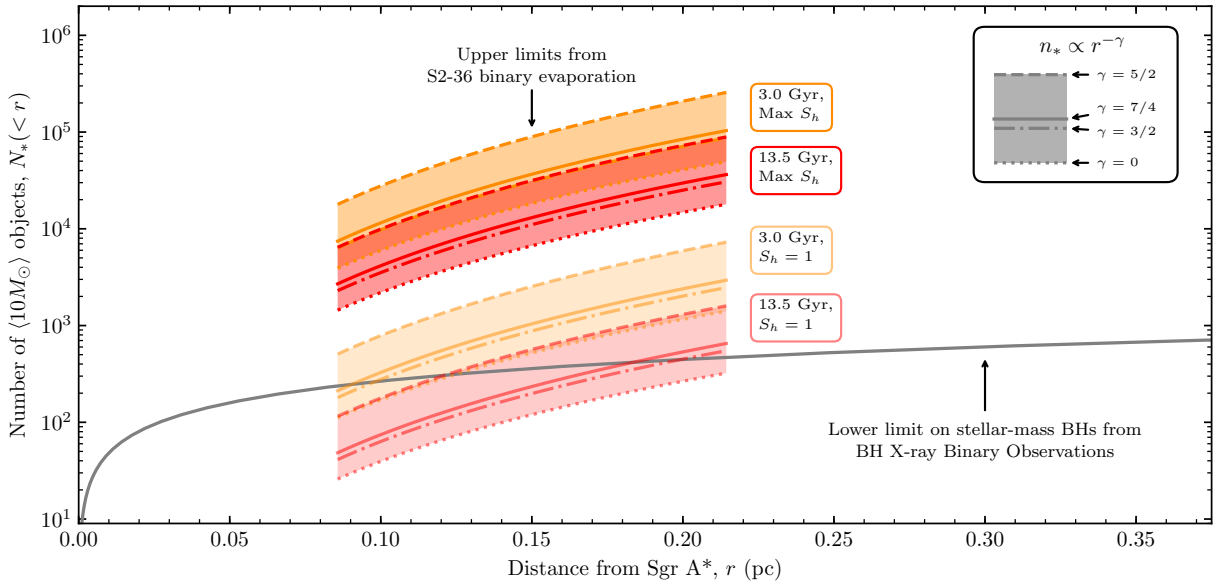

Figure 3.16: The constraint on the number of $\langle 10 M_\odot \rangle$ objects in the Galactic center region as a function of distance. The upper limits from the binary evaporation of S2-36 are shown as the orange and red bands (orange: 3 Gyr models, red: 13.5 Gyr models). The range of possible S2-36 distances from Sgr A*, r, plotted here are provided from the measurement of its projected acceleration in its proper motion (see Section 3.3.2). We show the estimates calculated from assuming that the binary was initially as hard as possible (i.e. maximum S_h), or if the binary was initially at its current observed softness s_0 (i.e. $S_h = 1$). The width of each band in this plot originates from different exponential slopes of the cusp density distribution γ. Specifically, $\gamma = \frac{5}{2}$, $\frac{7}{4}$, $\frac{3}{2}$, and 0 are indicated in each band as lines from top to bottom, respectively. For comparison, the dark gray band shows the lower limit on stellar-mass black holes from observations of X-ray binaries (Hailey et al., subm.).

The survival of S2-36 into its current age in the GC environment can constrain the density and number of surrounding massive objects that can gravitationally disrupt the binary system. From the currently observed configuration, we placed upper limits on the density and number of objects in S2-36's vicinity at the GC near the SMBH.

Following Binney & Tremaine (2008) and Alexander & Pfuhl (2014), we derived an estimate of the present-time evaporation timescale, $\tau_{\rm evap}$, of a soft binary system due to encounters from field stars:

$$\tau_{\rm evap} = \frac{1}{8}\sqrt{\frac{1+q_\sigma}{2\pi q_\sigma}}\frac{M_{12}\sigma_*(r)}{Gn_*\langle M_*^2\rangle a_{12}\log\Lambda_{12}(r)}. \tag{3.32}$$

Here, q_σ denotes the mass ratio between the binary components and the surrounding field objects of mass M_*: $q_\sigma = M_{12}/M_*$. $M_{12} = M_1 + M_2$ is the sum of the masses of the individual stellar components in the binary system. $\sigma_*(r)$ is the velocity dispersion of the surrounding field objects (see Equation 3.27). Finally, Λ_{12} is the Coulomb factor for evaporation over the possible impact parameters b: $\Lambda_{12} = b_{\rm max}/b_{\rm min}$ (see e.g. Binney & Tremaine, 2008). Λ_{12} for a soft binary can be estimated as (Alexander & Pfuhl, 2014):

$$\Lambda_{12} \sim 3\left(\frac{1+1/q_\sigma}{1+2/q_\sigma}\right)\frac{\sigma_*^2(r)}{v_{12}^2}. \tag{3.33}$$

Here, $v_{12} = \sqrt{GM_{12}/a_{12}}$.

As the present-time evaporation timescale, $\tau_{\rm evap}$ characterizes the timescale that a binary with its current observed orbital configuration (and current softness parameter s_0) would take to evaporate. However, since soft binaries get softer with more dynamical evaporations, the actual evaporation timescale, $t_{\rm evap}$, is longer than the present-time evaporation timescale, $\tau_{\rm evap}$. Using the maximal evolution ratio $S_h = s_{\rm hard}/s_0$ (Equation 3.30), we obtain a maximal bound on the actual evaporation timescale by making the assumption that the binary was initially hard as possible, with $s_{\rm init} = s_{\rm hard}$ (Alexander & Pfuhl, 2014). Furthermore, the age of the binary system, T_{12}, sets a minimal bound on the evaporation time. Therefore, the evaporation time of the binary can be limited to the following range:

$$T_{12} \leq t_{\rm evap} \leq \tau_{\rm evap} \times S_h. \tag{3.34}$$

Using Equation (3.32) for $\tau_{\rm evap}$, we calculated the number density of surrounding field objects,

n_*:

$$n_*(r) = \frac{1}{8\tau_{\rm evap}}\sqrt{\frac{1+q_\sigma}{2\pi q_\sigma}}\frac{M_{12}\sigma_*(r)}{G\langle M_*^2\rangle a_{12}\log\Lambda_{12}(r)} \tag{3.35}$$

We assumed a mass of the surrounding field objects, M_*, and γ for the slope of the cusp density distribution. We then constrained the number density of these surrounding field objects using our model parameters of S2-36 at a distance $r = R$: $n_*(R)$.

In order to obtain a conservative upper limit on the number density, we used Equation (3.34) to obtain that $\tau \geq T_{12}/S_h$:

$$n_*(r) \leq \frac{S_h}{8T_{12}}\sqrt{\frac{1+q_\sigma}{2\pi q_\sigma}}\frac{M_{12}\sigma_*(r)}{G\langle M_*^2\rangle a_{12}\log\Lambda_{12}(r)} \tag{3.36}$$

From our maximum density constraint (Equation 3.36), we further calculated a constraint on the number of field objects inside a radius r of the SMBH: $N_*(< r)$. Given a constraint of $n_*(R)$ at a radius R and assuming a power-law density distribution of field objects $n_*(r) = kr^{-\gamma} \propto r^{-\gamma}$, we obtain:

$$n_*(R) = kR^{-\gamma}, \tag{3.37}$$

$$k = R^\gamma \times n_*(R). \tag{3.38}$$

The number of field objects inside a radius r can therefore be constrained as:

$$N_*(< r) = \int_0^r 4\pi r^2 dr \times n(r), \tag{3.39}$$

$$= 4\pi k \int_0^r r^{2-\gamma} dr, \tag{3.40}$$

$$= \frac{4\pi k}{3-\gamma} r^{3-\gamma}, \tag{3.41}$$

$$N_*(< r) = \frac{4\pi R^\gamma \times n_*(R)}{3-\gamma} r^{3-\gamma}. \tag{3.42}$$

Our upper limits on the number of possible evaporating objects in S2-36's vicinity are shown in Figures 3.14 and 3.15. Assuming $\langle M_*\rangle = 1.2 M_\odot$, we found that the maximum number

density of evaporating objects is $\lesssim 10^7$ pc^{-3}, with lower numbers expected if S2-36 is older or has spent more time at the GC. This implies fewer than $\sim 10^6$ of these objects with S2-36's orbit around the SMBH. When comparing with upper limits provided by extended mass studies (e.g., $\leq 1.5 \times 10^6 M_\odot$ in the central parsec as measured by Schödel et al., 2009), we find that S2-36 evaporation can provide similar upper bounds on the density of surrounding objects (Figure 3.15), especially when considering the full range of possible softening that S2-36 may have experienced in the GC environment.

We additionally calculated an upper limit on the number of stellar-mass black holes implied by S2-36's survival in the GC. For this calculation, we assumed that the mass of surrounding field objects is $\langle M_* \rangle = 10 M_\odot$. While $\langle M_* \rangle = 10 M_\odot$ is expected to be too high for the GC environment, the assumption provides an upper limit on the total number of stellar mass black holes at the GC with typical masses $\sim 10 M_\odot$. Our upper limit constraints on the number of $10 M_\odot$ objects close to Sgr A* are shown in Figures 3.14 and 3.16. Assuming that S2-36 was initially as dynamically hard as possible ($s_{\rm init} = s_{\rm hard}$), we constrained the number of $10 M_\odot$ objects to $\lesssim 10^5$ within 0.2 pc of the SMBH. If instead S2-36 has not undergone many softening interactions over its lifetime (i.e. $s_{\rm init} \approx s_0$), the constraint of $10 M_\odot$ objects lowers to $\lesssim 10^3$ within 0.2 pc of the SMBH. For comparison, we also plot the estimates of the number of stellar-mass black holes derived from X-ray binary observations (Hailey et al. subm.). The x-ray observations represent an estimate of lower limit on the number of stellar-mass black holes at the GC.

In reality, we expect a complex spectrum of masses near the SMBH (e.g. Alexander & Hopman, 2009), with a lower average mass $\langle M_* \rangle \approx 1.2 M_\odot$. This mass spectrum will lower the expected number of $10 M_\odot$ objects since other objects also contribute to the binary evaporation process. However, since $\langle M_* \rangle$ is likely lower than $10 M_\odot$ in the GC, we therefore expect that our calculations can serve as an appropriate upper limit for the number of $10 M_\odot$ objects in the vicinity of the SMBH.

3.5.1.3 Long limits on the minimum relaxation time

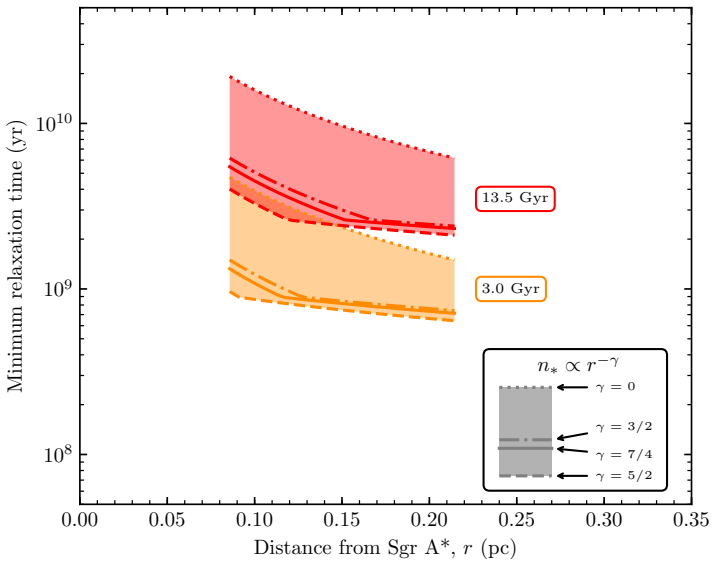

Figure 3.17: The minimum relaxation time as a function of distance as constrained by the evaporation of the soft binary S2-36 are shown as the orange and red bands (orange: 3 Gyr models, red: 13.5 Gyr models). The width of each band in this plot originates from different exponential slopes of the cusp density distribution γ. Specifically, $\gamma = 0$, $\frac{3}{2}$, $\frac{7}{4}$, and $\frac{5}{2}$ are indicated in each band as lines from top to bottom, respectively. For comparison, the grey lines show relevant relaxation timescales estimates for the GC environment (Yu et al., 2007): the local two-body relaxation timescale $t_{\rm rlx}$, the scalar resonant relaxation timescale $t_{\rm rlx}^{\rm res,S}$, and the vector resonant relaxation timescale $t_{\rm rlx}^{\rm res,V}$. The S2-36 constraints for the GC local two-body relaxation time are consistent with expectations only for low ages of S2-36 and high values of the cusp slope γ. The range of possible S2-36 distances from Sgr A*, r, plotted here are provided from the measurement of its projected acceleration in its proper motion (see Section 3.3.2).

The local two-body relaxation time quantifies the time for a star to lose memory of its initial velocity from the cumulative effect of two-body dynamical encounters (see e.g. Binney &

Tremaine, 2008). Constraints on the local relaxation time can inform models of dynamical evolution for the GC, such as recent episodes of star formation and the presence of massive stellar remnants or perturbations from massive gas structures (Alexander & Pfuhl, 2014). The relaxation time can be additionally used to constrain the environmental density, a procedure considered by Rose et al. (2020). The evaporation of soft binary systems, such as S2-36, place lower limits on the relaxation time at the GC.

Following Alexander & Pfuhl (2014), we obtain an estimate of the relaxation time, $t_{\rm rlx}$, using the present-time evaporation timescale, $\tau_{\rm evap}$:

$$t_{\rm rlx} \simeq 4.8 \frac{\log \Lambda_{12}}{\log(M_\bullet/M_*)} \frac{\sigma_*^2(r)}{v_{12}^2} \tau_{\rm evap} \tag{3.43}$$

Using Equation (3.34) to obtain that $\tau \geq T_{12}/S_h$, we can obtain a conservative lower limit on the relaxation time:

$$t_{\rm rlx} \gtrsim 4.8 \frac{\log \Lambda_{12}}{\log(M_\bullet/M_*)} \frac{\sigma_*^2(r)}{v_{12}^2} \frac{T_{12}}{S_h} \tag{3.44}$$

Our lower limit on the relaxation time constraints are shown in Figure 3.17. With the old and soft binary system S2-36, we obtain that $t_{\rm rlx} \gtrsim 1$ Gyr within ≈ 0.1–0.4 pc of the SMBH. Our constraint for the relaxation time approach the ≈ 1 Gyr value estimated for the GC at S2-36's distance from the SMBH (Yu et al., 2007). It is important to keep in mind that these limits assume that the binary S2-36 has spent its entire lifetime in the GC. If instead the binary has spent significant time at larger distances from the SMBH, older ages for S2-36 are allowed. We detail these considerations in the following section.

3.5.2 Migrated Binary System

While we observe S2-36 close to the location of Sgr A* and are able to astrometrically constrain its maximum distance from Sgr A* to ≈ 0.2 pc, the binary may have migrated to its present location from larger distances. Consequently, if S2-36 has not spent its lifetime in its present location, the dynamical implications outlined in Section 3.5.1 are limited.

The dynamical relaxation time grows larger at further distances from the SMBH. If the expected local evaporation time at a given distance from the central SMBH exceeds the relaxation time there, the binary is not expected to evaporate before dynamical migration takes place (Rose et al., 2020). As a result, the binary sinks towards the SMBH, until it reaches distances where evaporation time can exceed the relaxation time. In the GC environment around Sgr A*, this distance is expected to be ~ 0.1 pc from the SMBH (Rose et al., 2020). If S2-36 originated at a larger distance, we expect the binary would have sunk to its current location and has spent less time in the high densities close to the SMBH than its old age would imply.

Alternatively to having formed in the GC, S2-36 could have arrived at the GC via an infall of a globular cluster. Infalls of globular clusters have been demonstrated as possible sources of the stellar population at the GC (e.g. Tremaine et al., 1975; Capuzzo-Dolcetta & Miocchi, 2008; Antonini et al., 2012; Antonini, 2014; Perets & Mastrobuono-Battisti, 2014). As an old stellar binary system, S2-36 may have originated from one of these infall episodes. Consequently, since not having spent its lifetime in the high density environment of the GC, the GC dynamical constraints derived in Section 3.5.1 would no longer be implied by the presence of S2-36. Future spectroscopic measurements to determine the metallicity of the component stars in S2-36 can serve as a test for this hypothesis, since the detection of high metallicity would disfavor arrival via globular clusters which typically have low metallicity (e.g., Do et al., 2015).

3.5.3 Future observational constraints

Future observations and analysis can provide valuable constraints for S2-36 and answer some of the open questions about its nature. Spectroscopic observations would be particularly powerful, since they can determine if S2-36 is indeed composed of late-type stars, or if S2-36 is a stellar binary with measurements of changing radial velocity measurements. Furthermore, spectroscopic measurements could constrain the metallicity of S2-36 and can

test the hypothesis of S2-36's arrival to the nuclear star via globular cluster infall. However, spectroscopic observations of S2-36 have been limited due to its spatial proximity to the bright Wolf-Rayet star IRS 16CC (see e.g., Figure 3.3). The brightness of IRS 16CC in the low resolution plate scales of integral field spectrographs make extracting the spectrum of S2-36 difficult. Future, deeper spectroscopic observations may be able to circumvent this limitation.

Astrometric detections of binary systems provide an additional method to constrain the configurations of wide binary systems. Considering the luminosity difference and separation between the stellar components in our S2-36 binary models, we expect a photocentric semimajor axis for S2-36 of ≈ 40 μas (for observational models of astrometric binaries, see e.g. Koren et al., 2016). An astrometric binary with such a small photocentric semimajor axis is not detectable with current precision in astrometric surveys of the GC (Jia et al., 2019). Future experiments with higher precision astrometry measurements or higher resolution telescopes may be able to detect binarity in S2-36 astrometrically, and provide a method to more precisely constrain the binary configuration. Furthermore, astrometry also provides a method to detect long period binaries with wide separations to which photometric surveys such as G19 are not very sensitive. Therefore, such future astrometric binary surveys can serve as a valuable complement to photometric or spectroscopic surveys for the detection of other binary systems that can be used for the dynamical evaporation constraints detailed in this work.

3.6 Conclusions

With multiband near-infrared observations of the star S2-36, we have precisely measured periodic variability in the star's light curve, and determined its likely membership in the Milky Way Nuclear Start Cluster within ≈ 0.4 pc of the central supermassive black hole. Our analysis has demonstrated that of known classes of periodic variable stars, S2-36's

variability is most likely originating from a red giant ellipsoidal binary.

By fitting S2-36's observed light curve with model binary star systems composed of coeval stellar components, we determined that S2-36 is likely composed of two red giant branch stars (each of masses $\approx 0.8 M_\odot$ to $\approx 1.5 M_\odot$) orbiting at an ≈ 78.9 day period. The observed variability in flux originates from eclipses and tidal distortions in the larger stellar component of the binary, induced by the gravitational influence of the other star. Our models further indicate a binary age of 3 to 13.5 Gyr.

Such a low mass, long-period binary is dynamically soft in the GC environment, and can be disrupted by gravitational encounters by surrounding objects in its vicinity. If the binary has indeed spent its lifetime in the GC environment, the binary's survival places an upper limit of $\lesssim 10^5$ stellar-mass black holes ($M \sim 10 M_\odot$) within ≈ 0.2 pc of Sgr A*, and a local two-body relaxation time $\gtrsim 5 \times 10^8$ yr. Our observations are consistent with lower limits suggested by X-ray binary observations at further distances outside of the central 0.2 pc and provide a powerful new constraint on the presence of the dark cusp at the Galactic center.

Future spectroscopic observations can confirm the binarity of S2-36 and constrain the component stellar masses. With more precise astrometry, astrometric signatures of the binary orbit may also be detected and can constrain the orbital configuration of the binary. Additional old binaries may be detected in future binary surveys of the Milky Way Galactic center, and such systems may serve as powerful constraints on the dynamical makeup of the Galactic center.

Table 3.7: New observations used for S2-36 photometric analysis

Bandpass	Date (UTC)	MJD	Frames	Total Stars Detected	Absolute Phot. Zero-point Error (mag)	Relative Phot. Med. Error (mag)	Astrometric Med. Error (mas)	Med. FWHM (mas)	Med. Strehl Ratio
H	2017 May 7	57880.558	99	1591	0.222	0.025	0.827	55.23	0.21
H	2017 Aug 13	57978.276	41	1413	0.229	0.037	0.870	56.95	0.19
H	2017 Aug 23	57988.244	4	1164	0.237	0.059	1.537	83.15	0.10
H	2017 Aug 24	57989.264	25	1164	0.233	0.039	0.969	66.72	0.16
H	2017 Aug 26	57991.255	23	1164	0.228	0.025	0.849	64.13	0.16
K'	2018 Mar 17	58194.634	33	1861	0.051	0.025	0.382	56.39	0.41
H	2018 Mar 17	58194.635	27	1466	0.216	0.027	0.820	58.06	0.24
H	2018 Mar 22	58199.620	40	936	0.187	0.051	0.947	81.09	0.12
K'	2018 Mar 22	58199.621	45	1258	0.055	0.035	0.475	75.34	0.23
K'	2018 Mar 30	58207.623	25	1503	0.046	0.026	0.405	61.56	0.33
H	2018 Mar 30	58207.629	21	1118	0.202	0.025	0.866	65.14	0.18
H	2018 May 19	58257.545	7	408	0.221	0.066	1.698	89.38	0.10
K'	2018 May 19	58257.548	12	875	0.094	0.070	0.647	79.31	0.22
K'	2018 May 24	58262.517	43	1145	0.083	0.056	0.488	78.60	0.21
H	2018 May 24	58262.529	30	845	0.206	0.043	0.985	81.84	0.11

Table 3.7 (cont'd): New observations used for S2-36 photometric analysis

Bandpass	Date (UTC)	MJD	Frames	Total Stars Detected	Absolute Phot. Zero-point Error (mag)	Relative Phot. Med. Error (mag)	Astrometric Med. Error (mas)	Med. FWHM (mas)	Med. Strehl Ratio
H	2018 Sep 03	58364.259	66	1055	0.225	0.059	0.884	72.80	0.13
K'	2019 Apr 19	58592.571	64	1027	0.094	0.066	0.570	78.00	0.20
K'	2019 Apr 20	58593.581	113	1760	0.072	0.040	0.391	63.81	0.32
H	2019 May 13	58616.505	48	1572	0.209	0.032	0.827	61.10	0.21
K'	2019 May 13	58616.506	67	1851	0.069	0.036	0.389	60.63	0.34
K'	2019 May 23	58626.497	137	1957	0.067	0.038	0.389	60.80	0.34
K'	2019 Jun 25	58659.459	12	932	0.093	0.068	0.592	76.23	0.23
K'	2019 Jun 30	58664.457	10	1514	0.070	0.044	0.386	56.42	0.39
K'	2019 Aug 14	58709.292	34	1311	0.077	0.050	0.438	67.91	0.28
K'	2019 Aug 18	58713.244	13	1407	0.096	0.065	0.442	62.93	0.30
K'	2019 Aug 19	58714.316	23	1407	0.100	0.068	0.505	70.97	0.27

Note. — Median photometric and astrometric errors were computed for stars with $\overline{m}_{K'} \leq 16$ and detected in at least 16 K'-band observations. Absolute photometric zero-point errors were calculated after conducting initial calibration, using bandpass corrected reference fluxes for calibrator stars from Schödel et al. (2010). Relative photometric errors were determined after our calibration and local correction method were applied. The median quantities listed are computed for the individual frames in each epoch. The FWHM and Strehl quantities are calculated for IRS 33N.

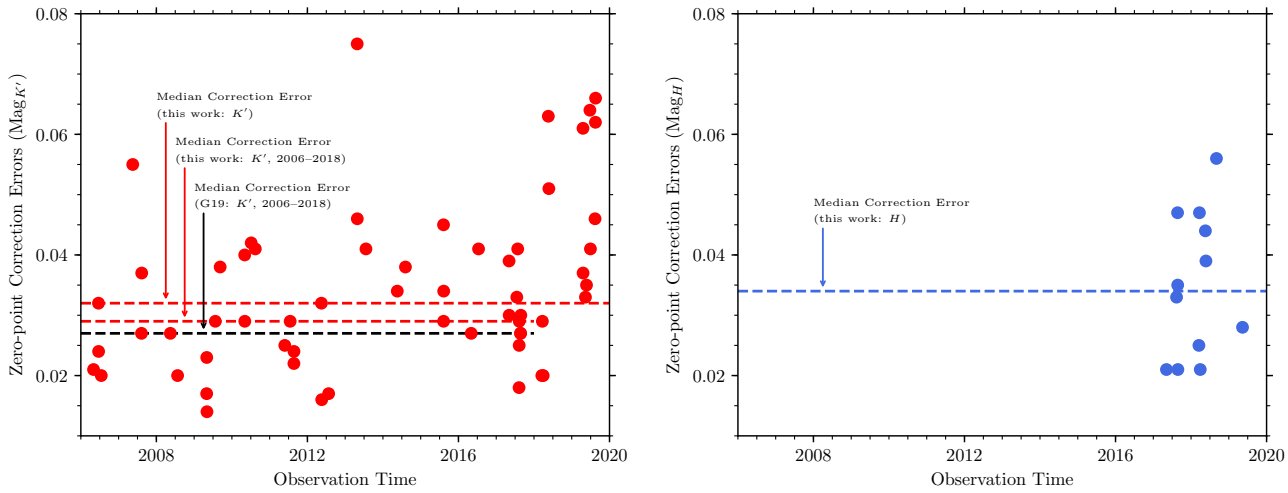

Figure 3.18: Errors in magnitude of the zero-point corrections used in this work (K'-band observations in left panel, H-band observations in right panel), calculated as the variance of the zero-point calibration magnitude adjustment in each observation. Median zero-point correction errors are shown as dashed lines. For comparison, the median zero-point correction error from G19 is shown in black in the left panel.

3.7 Appendix 3A: Photometric Calibration Details

Table 3.7 lists the new observations used in this work that were not included in the G19 variability survey. The table also collects several metrics that serve as indicators of the observation data quality.

Table 3.8 collects the bandpass corrections for the calibrator stars from the Schödel et al. (2010) catalog measurements to the respective NIRC2 bandpasses. The bandpass corrected $K'_{\rm NIRC2}$ and $H_{\rm NIRC2}$ are the reference calibrator magnitudes used for the absolute photometric calibration step used in this work.

The absolute photometric uncertainty is contributed by the uncertainty in zero-point correction during the initial, absolute photometric calibration. In G19, the median zero-point uncertainty across all their observations during absolute photometric calibration was 0.179

magnitudes. The median zero-point uncertainty across all K'-band observations during absolute photometric calibration in this work is 0.060 magnitudes, or 0.056 magnitudes when only considering the same observations as used in G19. The lower absolute photometry zero-point correction uncertainty in this work compared to G19 is a result of our revised calculation of calibrator star reference fluxes (detailed in Section 3.2.1), derived from the high resolution Schödel et al. (2010) catalog. The median zero-point uncertainty across all H-band observations during absolute photometric calibration in this work is 0.2215 magnitudes.

The final photometric uncertainty is largely contributed by the uncertainty in zero-point correction during the final (relative) photometric calibration step. This quantity is shown for all our observations in Figure 3.18. Across all observations in this work, the median zero-point correction error is 0.032 mag in K'-band and 0.034 mag in H-band. In G19, the median zero-point correction error was 0.027 mag. The difference largely originates from this work including observations in 2018 and 2019, several of which were derived from fewer frames leading to poorer image quality and higher uncertainty in the zero-point correction. When comparing the same observations as were used in G19, the calibration procedure used in this work leads to a median zero-point correction error of 0.029 mag. The remaining difference is small and is a consequence of the differences in photometric calibration that are detailed in Section 3.2.1.

Table 3.8: Photometric Calibrator Star Bandpass Corrected Reference Fluxes

Star Name	Spectral Type	$Ks_{\rm S10}$	$Ks_{\rm S10} - K'_{\rm NIRC2}$	$K'_{\rm NIRC2}$	$H_{\rm S10}$	$H_{\rm S10} - H_{\rm NIRC2}$	$H_{\rm NIRC2}$
IRS 16NW	Wolf-Rayet	10.14 ± 0.06	-0.05	10.19 ± 0.06	12.03 ± 0.06	-0.15 ± 0.01	12.18 ± 0.07
S3-22	Late-Type	11.03 ± 0.06	-0.05	11.08 ± 0.06	13.16 ± 0.07	-0.18	13.34 ± 0.07
S1-17	Late-Type	12.24 ± 0.07	-0.16	12.30 ± 0.07	14.49 ± 0.07	-0.19 ± 0.01	14.68 ± 0.08
S1-34	Late-Type	13.03 ± 0.07	-0.04	13.07 ± 0.07	14.63 ± 0.08	-0.13 ± 0.01	14.76 ± 0.09
S4-3	Late-Type	12.91 ± 0.07	-0.05	12.96 ± 0.07	14.86 ± 0.07	-0.16 ± 0.01	15.02 ± 0.08
S1-1	Early-Type	13.09 ± 0.07	-0.05	13.04 ± 0.07	14.95 ± 0.07	-0.15 ± 0.01	15.10 ± 0.08
S1-21	Early-Type	13.26 ± 0.06	-0.07 ± 0.01	13.33 ± 0.07	15.60 ± 0.07	-0.20 ± 0.01	15.80 ± 0.08
S3-370	Late-Type	13.59 ± 0.06	-0.05	13.64 ± 0.06	15.62 ± 0.07	-0.17 ± 0.01	15.79 ± 0.08
S3-88	Late-Type	14.23 ± 0.06	-0.05	14.28 ± 0.06	16.24 ± 0.07	-0.17 ± 0.01	16.41 ± 0.08
S3-36	Late-Type	14.61 ± 0.09	-0.05	14.66 ± 0.09	16.49 ± 0.09	-0.16 ± 0.01	16.65 ± 0.10
S2-63	Late-Type	15.29 ± 0.06	-0.05	15.34 ± 0.06	17.30 ± 0.07	-0.17 ± 0.01	17.47 ± 0.08

References. — S10: Schödel et al. (2010)

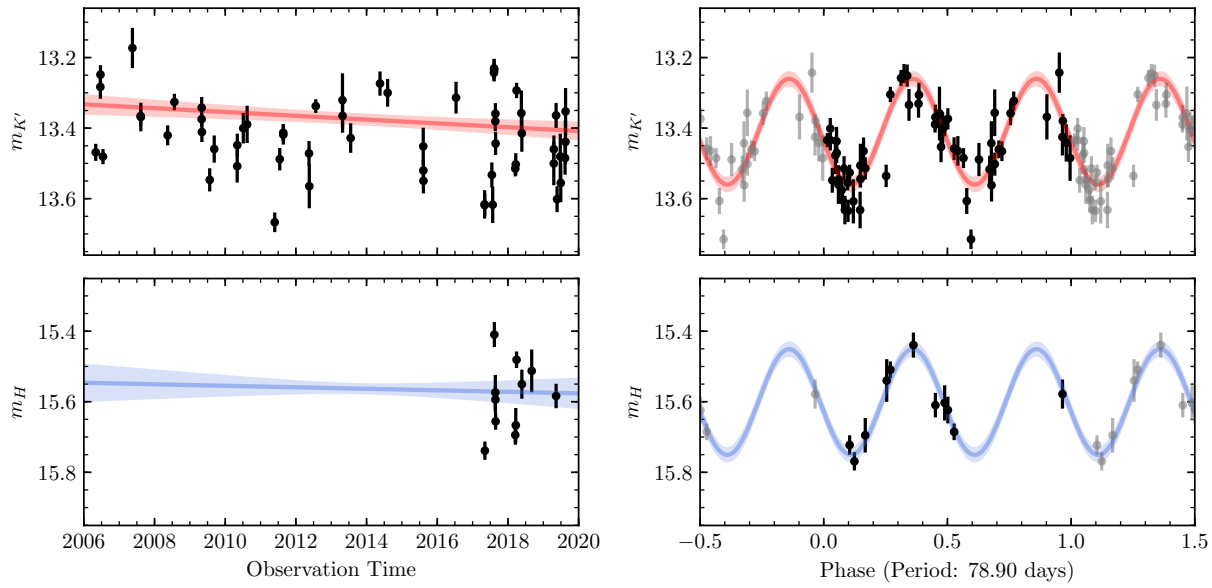

Figure 3.19: Same as Figure 3.1, but with a 5 parameter periodic model that allows for different long-term trend slopes in each passband. With fewer observations, the H-band long-term trend slope is less well constrained than the K'-band long-term trend slope. Overall, we found that the K'-band observations significantly demonstrate a long-term dimming trend. The H-band observations may be consistent with the same long-term dimming trend or no slope. However, our observations are not consistent with the long-term trend to be originating from dust extinction alone (see also Figure 3.20).

3.8 Appendix 3B: Multi-band Long-Term Slope Exploration

We calculated a fit of the S2-36 photometric measurements to a 5 parameter sinusoid model, as detailed in Section 3.3.1.1. This model allows for a possible difference in long-term trend slope between the K'- and H-band observations. Figure 3.19 shows our photometric data, and the best fit 5 parameter trended sinusoid model overlaid with corresponding uncertainties.

Figure 3.20 shows the constraints on the slope of the long-term linear trend in each obser-

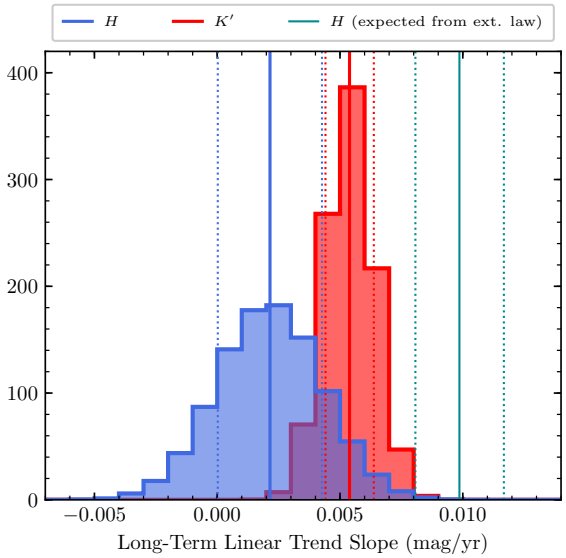

Figure 3.20: Posterior distributions of the long-term linear trend slopes in S2-36's photometric measurements in the K'-band (red histogram) and the H-band (blue histogram). The solid and dotted vertical lines indicate the best fit and 1σ uncertainties to the slope, respectively, in each band. The vertical cyan lines indicate the expectation of the slope in the H-band observations if the K'-band long-term dimming was solely caused by extinction (using the Nogueras-Lara et al. (2018) extinction law). The long-term trend in S2-36's photometry are inconsistent with dust extinction alone.

vation band. We found a slope in the K'-band of 0.005 ± 0.001 mag/yr and a slope in the H-band of 0.002 ± 0.002 mag/yr. The trended sinusoid fit suggests a small but significant long-term fading in the K'-band. The H-band long-term slope may be consistent with the K'-band slope or with no variation. With fewer data points in H-band, the H-band slope is less well constrained. However, our data does suggest that the H-band slope is not consistent with the observed long-term fading in the K'-band to be resulting from extinction. The H-band slope would be expected to be much steeper in order to be consistent with the Nogueras-Lara et al. (2018) extinction law.

3.9 Appendix 3C: Searching for periodicity in astrometric measurements

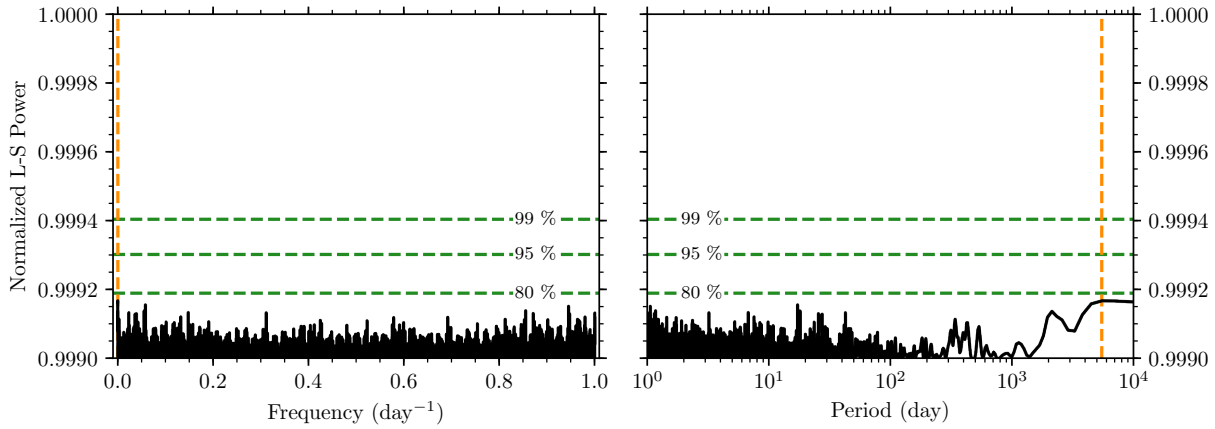

Figure 3.21: Trended, multi-band Lomb-Scargle periodogram for the S2-36 astrometric measurements. The left and right panels draw the periodogram with respect to frequency and period of variability, respectively. The horizontal dashed green lines indicate the bootstrap test significance level. The vertical dashed orange lines indicates the most significant peak in the astrometry periodogram: at 5483 days or 1.824×10^{-4} day^{-1}, with 75.9% false significance. The large values of the normalized L-S power in the periodogram are a result of a good fit for an overall linear trend, which originates from the star's approximately linear proper motion.

In Section 3.3.2, we found that the residuals of S2-36's astrometric measurements from the linear proper motion model appear to display long-term correlation, particularly in the x direction. To investigate if there is periodicity in the astrometric measurements (as would be expected in an astrometric binary; e.g.: Jia et al., 2019), we conducted a periodicity search on S2-36's astrometric measurements.

Our periodicity search on the astrometric measurements followed a similar framework to our multiband trended photometry periodicity search, detailed in Section 3.3.1.1. Instead of

the K' and H band-specific models, we used band specific models for x and y astrometry measurements. The multiband trended search for periodicity simultaneously in both x and y while the long-term trend allowed fitting for an overall linear proper motion, effectively fitting the proper motion with a linear and sinusoid model.

The periodogram from our astrometric measurement periodicity search is shown in Figure 3.21. We did not detect any significant signals in the astrometric measurements at any periods, including neither the photometric (39.45 days) or binary period (78.8 days) of S2-36. If S2-36 does indeed exhibit periodic astrometric modulation from its binary orbital motion, future work with more precise astrometric measurements may be able to detect it.

CHAPTER 4

Constraining the intrinsic stellar binary fraction of the Milky Way Galactic center with photometric monitoring

4.1 Introduction

Stellar binary systems are especially useful to learn about the Galactic center environment. Stellar multiplicity is typically a direct result of fragmentation during star formation (see e.g. Duchêne & Kraus, 2013). As such, the resulting binary fraction of a stellar population can encode imprints of the environment of formation (e.g., the cooling timescale of a collapsing molecular cloud). Dynamical interactions with the dense Galactic center stellar environment and its central SMBH can further affect the observed binary fraction (e.g. Hills, 1988; Alexander & Pfuhl, 2014; Stephan et al., 2016, 2019, Rose et al., in prep.; the dynamical implications of S2-36 in Chapter 3). The observationally measured binary fraction can therefore constrain Galactic center star formation and dynamical evolution models.

Photometric searches for stellar binaries are a valuable method to search for binary systems, allowing for the detection of eclipsing binaries or tidally distorted systems. The photometry dataset presented in Gautam et al. (2019), with the subsequent methodology improvements and new multiband observations were used for the study of S2-36 in Chapter 3, are a valuable dataset to provide a constraint on the GC binary fraction. In particular, the dataset offers the largest photometric sample of stars in the central half parsec of the GC to search for binary systems, while also achieving photometric precision comparable to the highest achieved with

LGSAO imaging.

With the variability analysis of the GC stellar population in the central half parsec, Gautam et al. (2019) provided the tightest constraint so far on the eclipsing binary fraction of young stars: $2.4\% \pm 1.7\%$. While this eclipsing binary fraction at the GC is consistent with the local young, OB star eclipsing binary fraction, there are limitations in the constraint's implications for the GC stellar population. The observed binary fraction can suffer from selection effects. Factors such as the observation cadence of the experiment, the intrinsic binary fraction of the population, or the separation of binary systems, for example, affect the observed binary fraction, but can have different implications about the formation and evolution of binaries at the GC.

In this chapter, we lay out the methodology that we have developed over the course of this thesis to address these limitations in the observed eclipsing binary fraction. We also present initial results with new detections of periodic sources. With this methodology employed in future work, we aim to constrain the intrinsic binary fraction of young stars at the GC with our photometric binary detections.

4.2 Periodicity search improvements

Binary systems can be revealed in photometric data by searches for periodic variability. We have implemented several changes in our periodicity search methodology since the work presented in Gautam et al. (2019) to both expand the search and more robustly detect periodic variability.

In this new work, we used the same K'- and H-band observations as used in Chapter 3. These consisted of 59 K'-band observations and 12 H-band observations, for a total of 71 observations, spanning a ≈ 13.5 year time baseline. The stellar photometric measurements were derived using the same calibration methodology as outlined in Section 3.2.1. The updated

methods incorporate a re-derivation of new K'- and H-band reference flux measurements for our calibrator stars by using photometry from the Schödel et al. (2010) photometric catalog.

When defining the periodicity search sample, we eliminated the $m_{K'} \leq 16$ magnitude cut that was implemented in Gautam et al. (2019). The cut was initially put in place for our variability search since the photometric precision floor of our dataset rises for stars fainter than $m_{K'}$ of 16. In its place, the amplitude of variability criterion for periodicity served as a sufficient check on stars with poor photometric precision without substantially reducing the sample size. The final sample size used in this work was defined as stars detected in at least 16 K'-band observations and with at least one H-band observation. This sample contained a total of 873 stars, with K'-band mean magnitudes ($\overline{m}_{K'}$) spanning between 9.99 and 19.06.

The periodicity search used in this work employs the same multiband, trended Lomb-Scargle periodogram implementation as was developed for the analysis of S2-36 in Chapter 3 (Section 3.3.1.1). The implementation simultaneously searched for periodic trends in both the K'- and the H-bands (i.e., a *multiband* periodicity search). The periodicity search also allowed for long-term linear trends in brightness (i.e., a *trended* search). Such trends can originate from long-term phenomena like the proper motion of stars behind a variable extinction screen, and can reduce the detectability of the periodic variability in periodicity searches (see Sections 2.10.2 and 3.3.1.1). The significance of a periodicity detection was calculated via a bootstrap false alarm test, the implementation of which for a mutiband, trended periodicity search is detailed in Section 3.3.1.1.

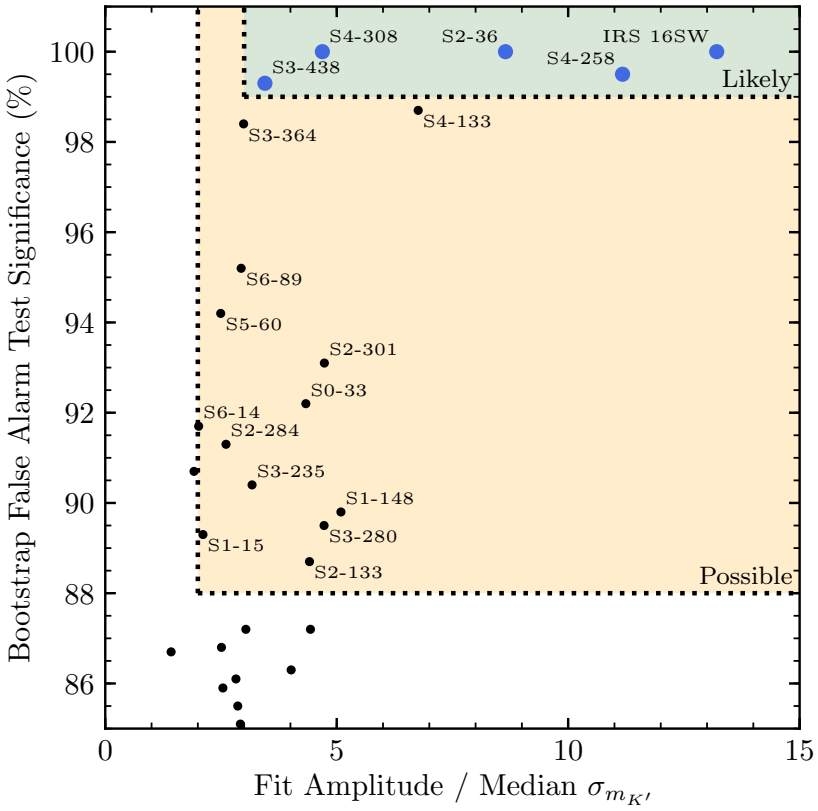

Figure 4.1: Periodicity detections that pass the variability, periodicity, and frequency cuts in our search, with bootstrap false alarm test significance plotted against the variability amplitude. This plot is similar to Figure 2.11, but updated with our new multiband, trended periodicity search sample and the criteria for possible and likely periodic signals (listed in Table 4.1). For clarity, only the most significant periodicity search detection is plotted for stars that have multiple detections passing the variability, periodicity, and frequency cuts. The stars that we identify as *likely periodic variables* (IRS 16SW, S4-258, S2-36, S4-308, and S3-438) stand out distinctly in significance from other possible periodic detections identified in our experiment.

We identified possible and likely periodic variable stars in a similar manner to Gautam et al. (2019) (see Section 2.5.2), with updated criteria for possible periodic signals based

Table 4.1: Criteria for Possible Periodic Signal

Criterion	Threshold
$\chi^2_{\rm red}$ Variability	$\geq 3\sigma$
Period Cut (from obs. baseline)	$\leq$ 4855.80 d /4
	$\leq$ 1213.95 d
Frequency Cut (from aliasing)	≤ 1.0 d^{-1}
Amplitude of Variability	$\geq 2 \times$ median($\sigma_{m_{K'}}$)
(likely periodic threshold)	$\geq 3 \times$ median($\sigma_{m_{K'}}$)
Bootstrap False Alarm Test	$\geq 88\%$
(likely periodic threshold)	$\geq 99\%$

on improved sensitivity in this new work. The periodicity detection criteria used to identify possible periodic signals in this work are summarized in Table 4.1, while Figure 2.11 compares the significance of these detections.

In addition to the likely periodic detections in the photometric flux measurements of IRS 16SW (Figure 4.2), S4-258 (Figure 4.3), and S2-36 (Figure 4.4), which were also previously identified in Gautam et al. (2019), we identify likely periodic variability in the stars S4-308 (Figure 4.5) and S3-438 (Figure 4.6). IRS 16SW and S4-258 are known young, eclipsing binary systems at the GC (Ott et al., 1999; Peeples et al., 2007; Rafelski et al., 2007; Pfuhl et al., 2014; Gautam et al., 2019). S2-36 was previously identified as a periodic variable by Gautam et al. (2019) and is a candidate old, red giant ellipsoidal binary system at the GC (see detailed analysis in Chapter 3). The periodic variability in the remaining two likely periodic variable stars, S4-308 and S3-438, has not been previously reported. As a star with $\overline{m}_{K'} \approx 16.9$, the detection of periodic variability in S4-308 is largely enabled by the extension of the periodicity search sample to fainter magnitudes. On the other hand, while S3-438 is a brighter source at $\overline{m}_{K'} \approx 15.0$, due to non-confused detections only after 2015, the detection of periodic variability in S3-438 is largely enabled by additional observations taken since those presented in Gautam et al. (2019). The significance of S3-438's detection is also greatly improved by its H-band observations. Due to their faint fluxes, S4-308 and S3-438 have yet been spectroscopically typed (e.g. Do et al., 2013a). The short periods of S4-308 and S3-438 may indicate young stellar eclipsing binary systems at the GC. Future spectroscopic follow-up of these stars is necessary to confirm if these stars are indeed young binary systems.

Besides the five likely periodic variables in our sample, we identified 13 possibly periodic variable stars as well. Their lower periodogram significance and smaller signal amplitude makes it difficult to determine with our experiment if the stars' variability is indeed periodic. We include their light curves with their respective best-fit periodic models in Appendix A.2.2.

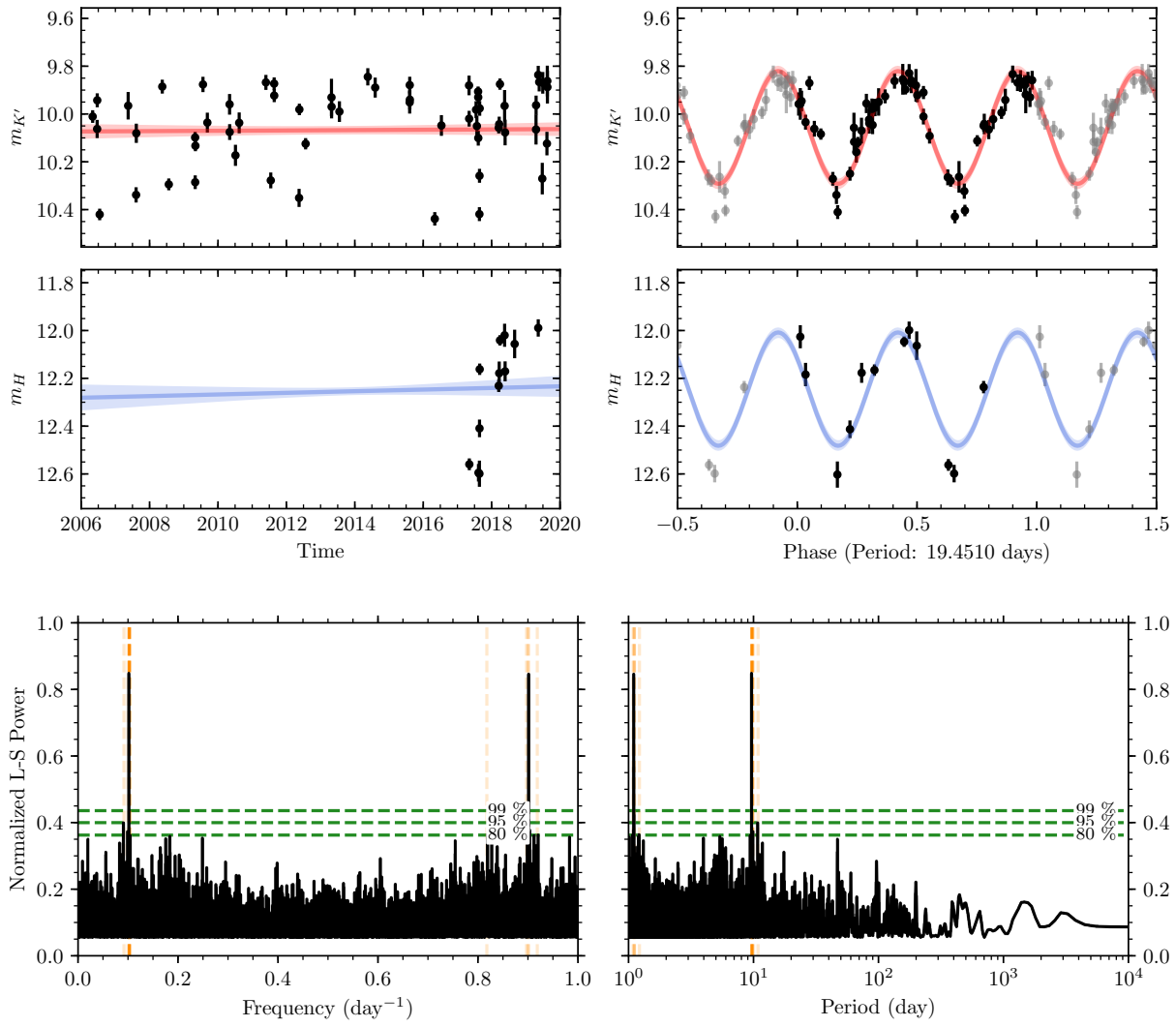

Figure 4.2: Likely periodic variable IRS 16SW. Keck NIRC2 photometric measurements are shown in the K'- (top row panels) and H-band (middle row panels). Of the observation plots, the left panels show the light curve over our entire experiment time baseline. The solid colored lines show the long-term linear trend components of the best-fit trended sinusoid model in each band, with 3σ uncertainty in the linear fit indicated by the shaded regions. The right panels show the same photometric data phased to $2\times$ the best-fit period from our trended Lomb-Scargle analysis and with the best-fit long-term linear trend removed. The solid, colored lines in each panel indicate the best-fit sinusoid model to the observed data, with 3σ uncertainty in the sinusoid fit indicated by the shaded regions. The bottom row panels show the Lomb-Scargle periodogram (in frequency space on left and in period space on right). The horizontal dashed green lines indicate the bootstrap test significance level. The vertical dashed orange lines indicate the periodogram peaks above 80% bootstrap test significance.

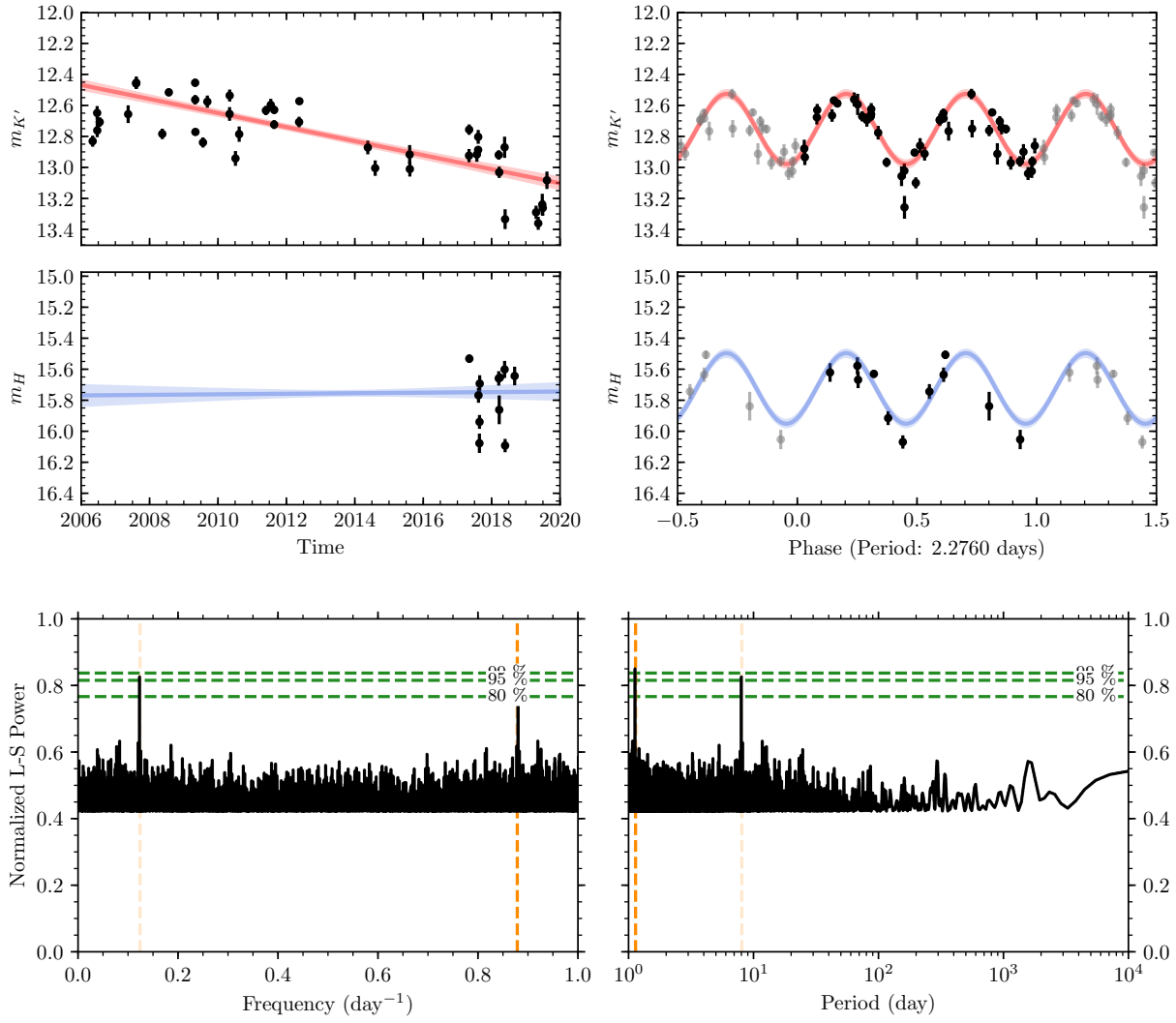

Figure 4.3: Likely periodic variable S4-258. Keck NIRC2 photometric measurements are shown in the K'- (top row panels) and H-band (middle row panels). Of the observation plots, the left panels show the light curve over our entire experiment time baseline. The solid colored lines show the long-term linear trend components of the best-fit trended sinusoid model in each band, with 3σ uncertainty in the linear fit indicated by the shaded regions. The right panels show the same photometric data phased to $2\times$ the best-fit period from our trended Lomb-Scargle analysis and with the best-fit long-term linear trend removed. The solid, colored lines in each panel indicate the best-fit sinusoid model to the observed data, with 3σ uncertainty in the sinusoid fit indicated by the shaded regions. The bottom row panels show the Lomb-Scargle periodogram (in frequency space on left and in period space on right). The horizontal dashed green lines indicate the bootstrap test significance level. The vertical dashed orange lines indicate the periodogram peaks above 80% bootstrap test significance. The floor in L-S power is due to the large amplitude of the long-term trend slope.

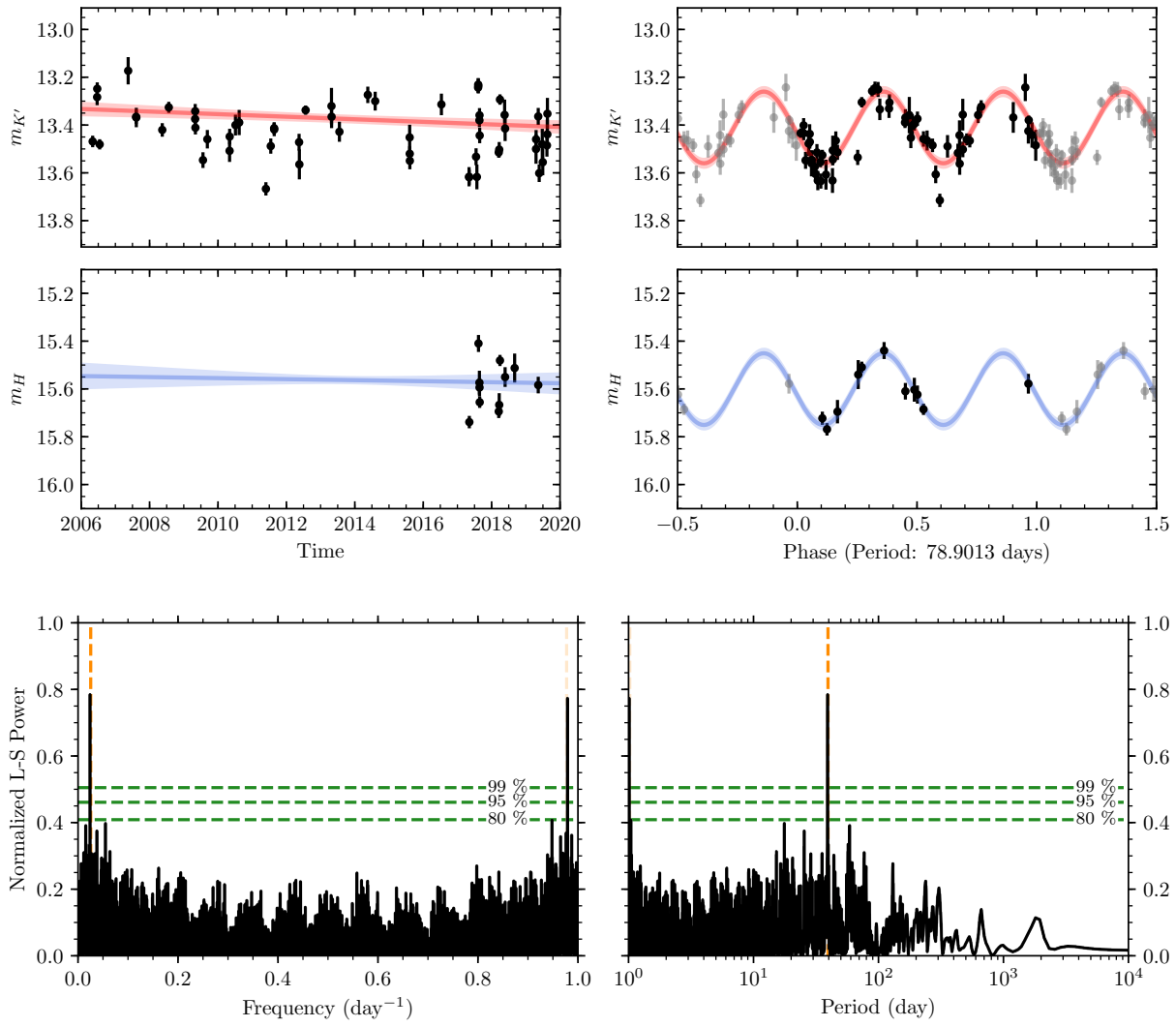

Figure 4.4: Likely periodic variable S2-36. Keck NIRC2 photometric measurements are shown in the K'- (top row panels) and H-band (middle row panels). Of the observation plots, the left panels show the light curve over our entire experiment time baseline. The solid colored lines show the long-term linear trend components of the best-fit trended sinusoid model in each band, with 3σ uncertainty in the linear fit indicated by the shaded regions. The right panels show the same photometric data phased to $2\times$ the best-fit period from our trended Lomb-Scargle analysis and with the best-fit long-term linear trend removed. The solid, colored lines in each panel indicate the best-fit sinusoid model to the observed data, with 3σ uncertainty in the sinusoid fit indicated by the shaded regions. The bottom row panels show the Lomb-Scargle periodogram (in frequency space on left and in period space on right). The horizontal dashed green lines indicate the bootstrap test significance level. The vertical dashed orange lines indicate the periodogram peaks above 80% bootstrap test significance.

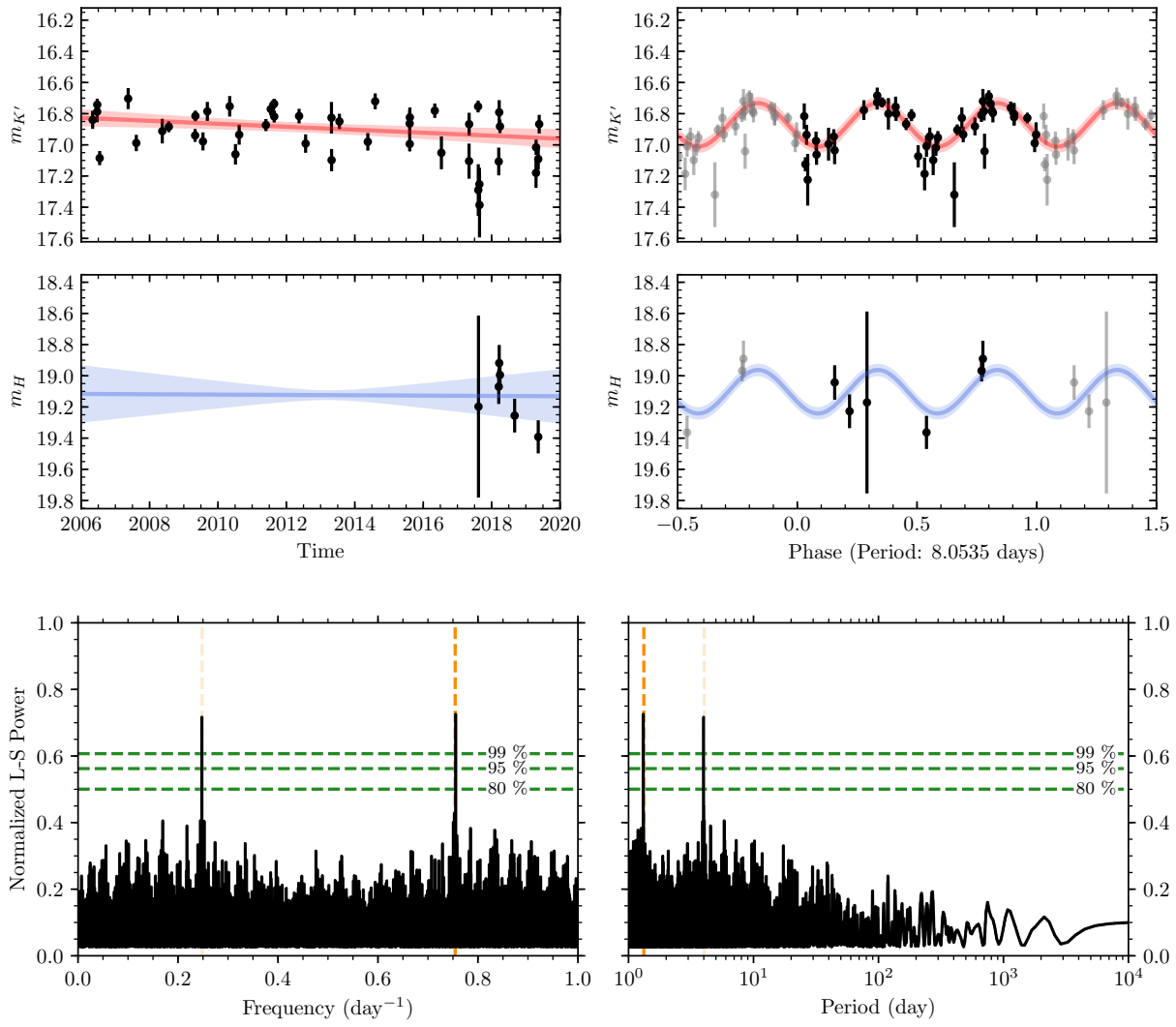

Figure 4.5: Likely periodic variable S4-308. Keck NIRC2 photometric measurements are shown in the K'- (top row panels) and H-band (middle row panels). Of the observation plots, the left panels show the light curve over our entire experiment time baseline. The solid colored lines show the long-term linear trend components of the best-fit trended sinusoid model in each band, with 3σ uncertainty in the linear fit indicated by the shaded regions. The right panels show the same photometric data phased to $2\times$ the best-fit period from our trended Lomb-Scargle analysis and with the best-fit long-term linear trend removed. The solid, colored lines in each panel indicate the best-fit sinusoid model to the observed data, with 3σ uncertainty in the sinusoid fit indicated by the shaded regions. The bottom row panels show the Lomb-Scargle periodogram (in frequency space on left and in period space on right). The horizontal dashed green lines indicate the bootstrap test significance level. The vertical dashed orange lines indicate the periodogram peaks above 80% bootstrap test significance.

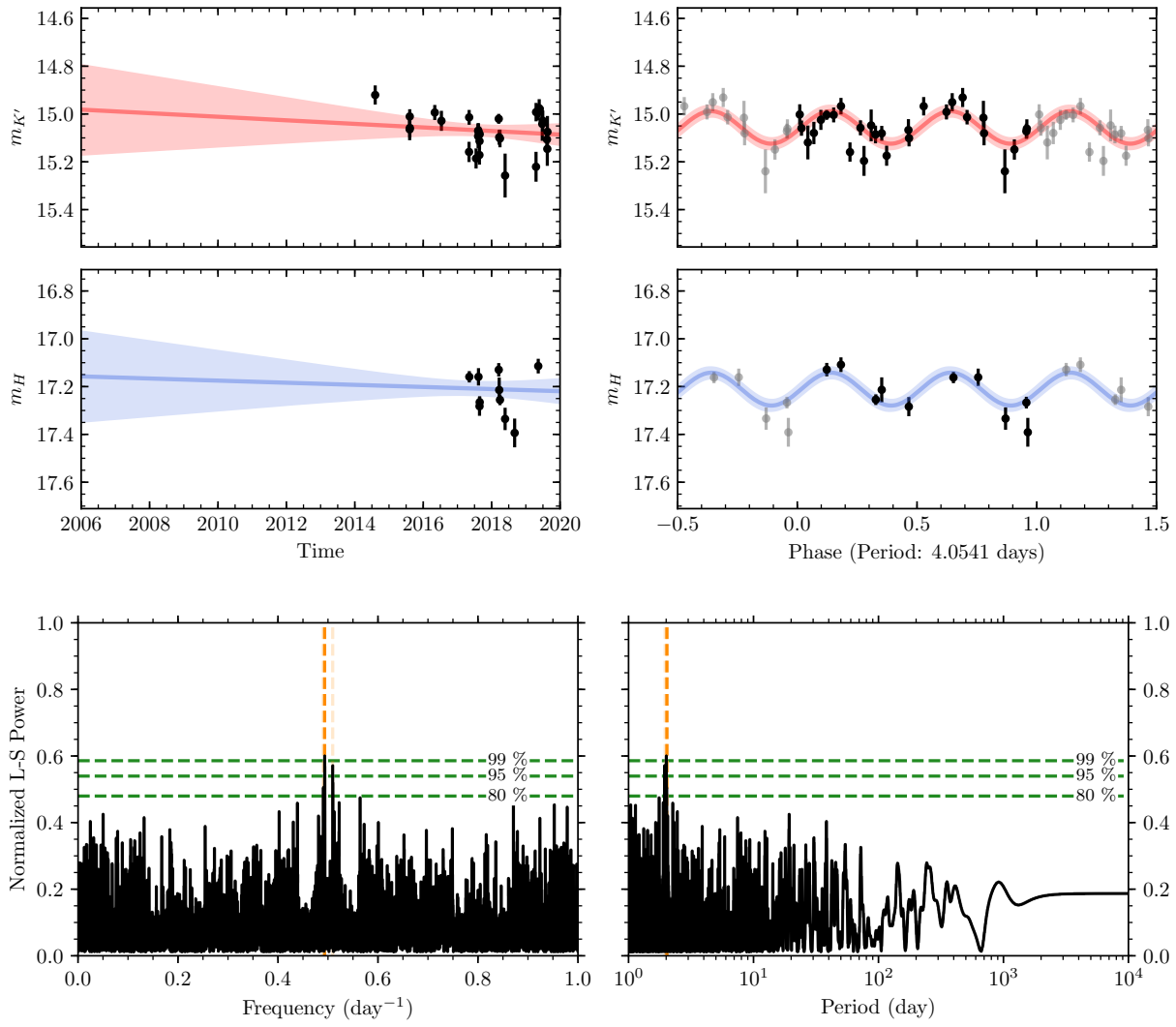

Figure 4.6: Likely periodic variable S3-438. Keck NIRC2 photometric measurements are shown in the K'- (top row panels) and H-band (middle row panels). Of the observation plots, the left panels show the light curve over our entire experiment time baseline. The solid colored lines show the long-term linear trend components of the best-fit trended sinusoid model in each band, with 3σ uncertainty in the linear fit indicated by the shaded regions. The right panels show the same photometric data phased to $2\times$ the best-fit period from our trended Lomb-Scargle analysis and with the best-fit long-term linear trend removed. The solid, colored lines in each panel indicate the best-fit sinusoid model to the observed data, with 3σ uncertainty in the sinusoid fit indicated by the shaded regions. The bottom row panels show the Lomb-Scargle periodogram (in frequency space on left and in period space on right). The horizontal dashed green lines indicate the bootstrap test significance level. The vertical dashed orange lines indicate the periodogram peaks above 80% bootstrap test significance.

4.3 Constraints on intrinsic binary fraction from photometric detections with Bayesian inference

To estimate an intrinsic binary fraction of the GC stellar population from our periodic source detections in Section 4.2, we developed a Bayesian framework. In this framework, we consider the bootstrap false alarm significance in the periodicity search, and the amplitude of variability (as is plotted in Figure 4.1) as our experiment's observations. From that we wish to constrain the binary fraction, F. In the Bayesian framework, we can write:

$$p(F|\text{obs}) = \frac{p(\text{obs}|F) \times p(F)}{p(\text{obs})}$$

Here, $p(F|\text{obs})$ is the *posterior* and $p(\text{obs}|F)$ is the *likelihood*, while $p(F)$ is the *prior* and $p(\text{obs})$ is the *evidence* term. In order to estimate which binary fraction F our observational results in Section 4.2 favor, the biggest challenge is estimating the likelihood, $p(\text{obs}|F)$.

We plan to estimate this likelihood in two parts: first by determining the periodicity search significance and amplitude we expect to arise from different types of mock binary systems expected at the GC (i.e., our experiment's sensitivity to stellar binaries, detailed in Section 4.3.1) and then by simulating trial populations at different binary fractions and computing the likelihood.

4.3.1 Mock light curve generation of a stellar binary population

In order to determine our experiment's sensitivity to binary system light curves, we generated a library of mock binary light curves. We first constructed a mock stellar binary population using stellar and binary parameters expected for young stars at the GC. In each mock binary system, we first drew a primary star's mass from the GC young stellar population initial mass function, as measured by Lu et al. (2013). We then determined the mass of the secondary star in the binary system with binary mass ratio estimated from local massive binaries (Sana et al., 2012). We also chose mock binary system orbital periods and eccentricities, each drawn

from their respective distributions estimated from local massive binary systems (Sana et al., 2012). Finally, we drew an inclination for the binary from a $\cos(i)$ distribution, the observed inclination distribution expected for randomly oriented binary systems.

In addition to the parameters drawn from observationally estimated distributions, we interpolated the remaining stellar parameters needed for binary light curve simulation from stellar evolutionary models, in a similar manner to the methods outlined in Section 3.4.2.1. In this work, since we are no longer limited to evolved, giant stars that rapidly evolve in stellar radius, we instead used the stellar mass to interpolate the remaining stellar parameters necessary for binary light curve generation.

We developed the software PHOEBE PHITTER[1] for the generation of model stellar binary light curves. This software interfaces with the PHOEBE binary light curve simulation software (Horvat et al., 2018; Prša et al., 2016) and with the SPISEA stellar population synthesis code (Hosek et al., 2020) in order to generate light curves for each mock binary system. The light curve generation procedure with PHOEBE PHITTER is described in more detail in Section 3.4.2.

We generated artificial binary light curves in the NIRC2 K'- and H-bands for a total of 10,000 mock stellar binary systems. Representative examples of different classes from this library of mock young eclipsing binaries are shown in Figures 4.7, 4.8, 4.9, and 4.10.

Our experiment's long time baseline makes it ideally sensitive for examining long-term trends on the orders of years. However, the experiment's sparse and non-uniform sampling makes it less sensitive to eclipsing binary systems with eclipses that are narrow in phase (e.g., 4.7). Our sensitivity to such systems in this experiment can be determined by drawing observations from our mock binaries that match the experiment's observation times, after randomizing

[1]PHOEBE PHITTER is available at an online software repository: https://github.com/abhimat/phoebe_phitter

the orbital phase of the binary. After drawing sample mock observations at observation times, we will also inject artificial noise into each data point to match the photometric precision characteristics of the respective observation night. These two steps will allow our synthetic light curves to reflect our observed light curves, in both the observing cadence and the photometric quality characteristics, in order to account for the effects of our experiment's observation characteristics on binary sensitivity.

Finally, we will conduct the same periodicity search analysis as described in Section 4.2 on the mock light curves. For each mock binary system, we will calculate a periodicity search significance and measure the fit amplitude.

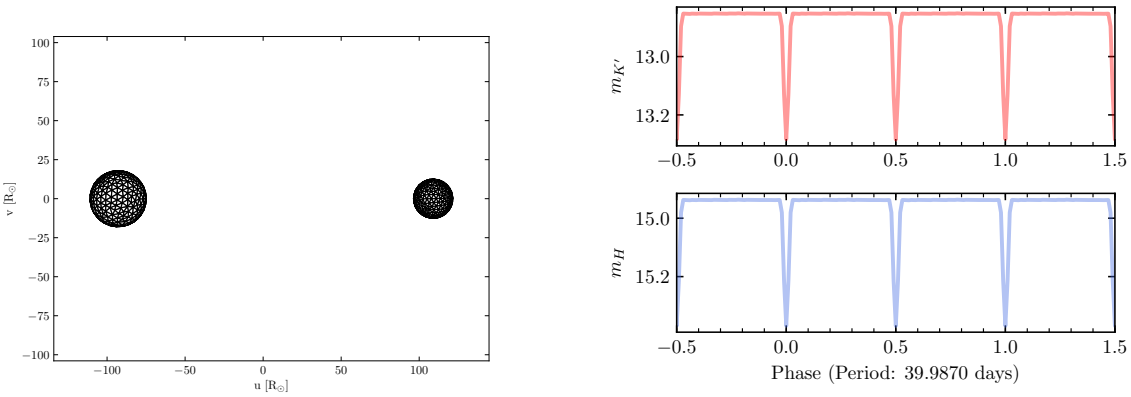

Figure 4.7: The model mesh (left) and model light curve in the K'- and the H-band (right) of a mock detached binary system. In this system, the eclipses are narrow in phase.

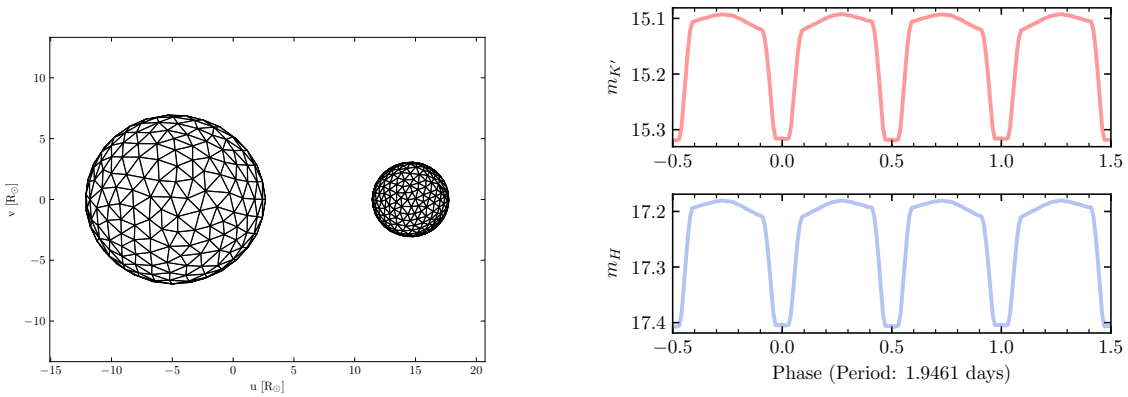

Figure 4.8: The model mesh (left) and model light curve in the K'- and the H-band (right) of a mock detached binary system. In this system, the eclipses are wide in phase. Furthermore, the larger primary is tidally distorted and exhibits ellipsoidal variation.

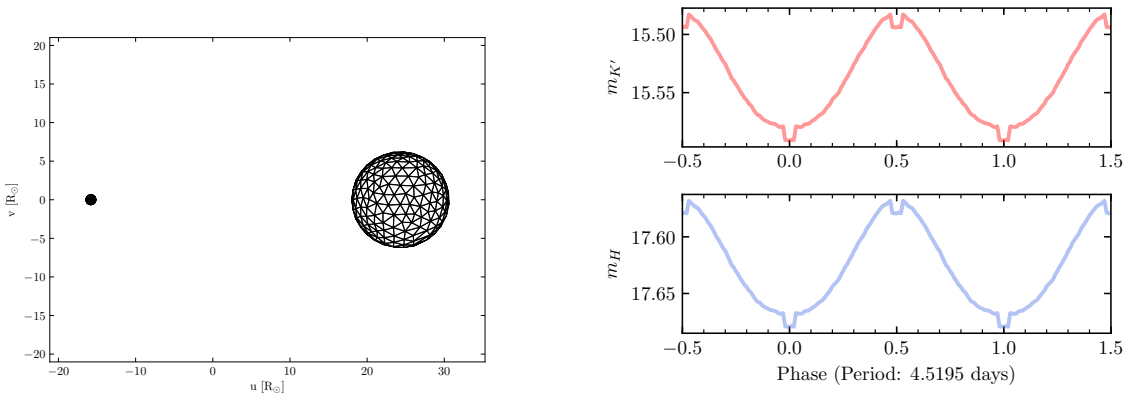

Figure 4.9: The model mesh (left) and model light curve in the K'- and the H-band (right) of a mock detached binary system. In this system, the larger component is tidally distorted and exhibits ellipsoidal variability. The size of the smaller component leads to eclipses that are narrow in phase.

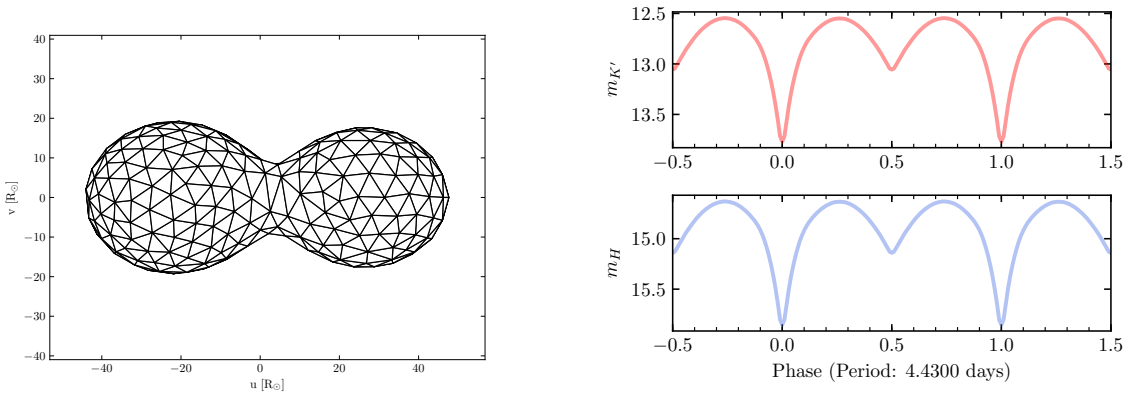

Figure 4.10: The model mesh (left) and model light curve in the K'- and the H-band (right) of a mock contact binary system. The difference in temperatures of the two stellar components leads to the different eclipse depths.

4.3.2 Finding the best-fit population binary fraction

After we calculate our experiment's sensitivity to binary systems, as described in Section 4.3.1, we will estimate the likelihood, $p(\text{obs}|F)$. Our method is to simulate trial populations at different binary fractions, with each trial population matching the flux distribution of our observed stellar sample. We will then compute the distribution of periodogram significance and periodicity amplitude for the mock populations, similar to what is observed for our experiment's sample. By performing a Markov chain Monte Carlo (MCMC) analysis to maximize the likelihood, we will compute at which binary fractions our observed distribution most closely matches the simulated distributions.

At each trial binary fraction, we will compute the expected periodogram significance and amplitude distribution in the following way: For each star in our sample, we will choose a mock binary light curve or a mock non-binary light curve, with the probability of that star's binarity determined by the trial binary fraction. If selecting a mock binary light curve, we will choose a random binary system from our mock binary library with a similar

mean magnitude to the respective star in our stellar sample. If selecting a non-binary, we will select a flat light curve with the same mean magnitude as the respective star in our stellar sample, with added random photometric noise as expected from our observations. After selecting a corresponding mock light curve for every star in our sample, we will then compute the mock population's significance and amplitude distribution (similar to that of our observed distribution in Figure 4.1). We will repeat this mock population trial in many permutations at the same trial binary fraction to obtain a model distribution of amplitudes and significances.

With the trial amplitude and significance distributions calculated at different trial binary fractions, we will next run an MCMC analysis to maximize our likelihood, $p(\text{obs}|F)$. Our analysis will determine which simulated binary fraction populations most closely match our observed sample in the distribution of periodicity search amplitudes and significances. Just as important as the *number* of detections of likely periodic signals, this framework also uses the information provided by the *flux amplitude* of detected periodic signals and the distribution of *non-detections* in our sample to constrain the binary fraction. With this methodology we aim to place lower bounds on the intrinsic binary fraction of the GC stellar population, and to constrain the binary fraction of close binary systems.

4.4 Conclusion

In this chapter, we have provided a methodology framework for constraining the intrinsic binary fraction of the Galactic center stellar population with photometric observations. We have achieved greater sensitivity to periodic signals since the variability study work presented in Gautam et al. (2019). This has been accomplished with the addition of new multi-band photometric observations and the implementation of a more robust search for periodicity, accounting for long-term trends and multi-band variability. In initial results, we have identified 5 likely periodic variables in a sample of 873. Of these likely periodic variable stars,

IRS 16SW and S4-258 have been previously confirmed as young, eclipsing binary systems at the GC (Ott et al., 1999; Peeples et al., 2007; Rafelski et al., 2007; Pfuhl et al., 2014; Gautam et al., 2019). The third, S2-36, was previously identified Gautam et al. (2019) as a periodic variable, and is a possible old, red giant ellipsoidal binary system (Chapter 3). The remaining two of the five periodic variables, S4-308 and S3-438, have not been previously identified as periodically variable stars. These stars may be young stellar eclipsing binary systems at the GC. Future spectroscopic follow-up of these stars can confirm if these stars are indeed young binary systems.

We have developed methodology to calculate our experiment's sensitivity to binary systems. This sensitivity is an important aspect of being able to determine the underlying binary fraction from our observations. We have simulated the light curves of a population of mock binary systems at the GC with parameters motivated by the GC initial mass function and that of massive, young binaries in the local solar neighborhood. With these mock light curves we can next determine which systems our experimental methods can detect.

With an estimate of our experiment's sensitivity to binary systems, we have developed a Bayesian framework to next constrain the intrinsic binary fraction. Importantly, our large sample, our significant detections and non-detections, and the amplitude of detected variability are all important components of being able to constrain the intrinsic binary fraction. With our framework, and our large photometric sample, we aim to place lower limits on the intrinsic binary fraction of the GC stellar population. We expect that the methods here can particularly tightly constrain the binary fraction of close binaries at the GC.

CHAPTER 5

Conclusions

While adaptive optics imaging has enabled studying the resolved stellar population around the Milky Way Galactic center supermassive black hole, long-term photometric studies of these stars have previously been limited. In this thesis, with over 13 years of Keck NIR photometry observations of the stellar population within approximately half a parsec of the GC SMBH, we have conducted a long-term stellar variability study of the GC stars, tightly constrained the eclipsing binary fraction of the GC young stars, and constrained the density of the non-luminous dark cusp within ~ 0.1 pc of the SMBH.

In Chapter 2, we presented a single-band photometric variability survey of stars within ≈ 0.5 pc of the SMBH. Over an ≈ 11.5 year time baseline with a sample of 563 stars, we found that half of all stars in the region are variable, with higher photometric variability observed for young, early-type stars than for old, late-type giants. While the variability fraction for the GC is higher than that found in other variability studies of young stellar populations or old stellar populations, we determined that the long time baseline of our survey can largely account for the higher variability. Unique to the Galactic center, we determined that the high variability is also contributed by the population's typically high stellar motions behind a variable foreground extinction screen. Many long-term variability events observed in our analysis have flux dips consistent with originating from high-density filaments identified in longer wavelength studies of the GC.

In our search for eclipsing binary systems as a part of our variability survey presented in

Chapter 2, we detected two eclipsing binary systems in the largest sample of GC young stars for such a study (85 known early-type stars). With our large sample, we have placed the tightest constraint so far on the young, eclipsing binary fraction of the GC: $2.4\% \pm 1.7\%$. This eclipsing binary fraction is consistent with that of local OB stars, $1.60\% \pm 0.25\%$, when considering binaries detectable at similar criteria to our experiment in Chapter 2 (Lefèvre et al., 2009). Our constraint suggests that the GC young star population is similar to the local Milky Way young stars. Theoretical models predict the dynamical depletion of young binary systems at the GC through merger or evaporation events (e.g., Stephan et al., 2016, 2019). A deviation of the GC eclipsing binary fraction from the local binary fraction on the expected scale of such depletions (from $\sim 10\%$ to $\sim 25\%$) within the lifetime of the GC young stars, though, would not be detected with our current eclipsing binary fraction constraint precision. Furthermore, the eclipsing binary fraction can be biased due to experimental time sampling and photometric sensitivity, and in order to conclusively determine how different the GC young star binary fraction is from young stellar populations in other environments, constraints on the intrinsic binary fraction are needed.

Additional work is necessary to constrain the intrinsic binary fraction of stars, as detailed in Chapter 4. We outlined an updated periodicity search methodology that takes advantage of recent Keck multiband photometric observations and accounts for long-term trends that are common in our experiment due to its long time baseline. With this methodology, we presented our initial results of likely periodic variables incorporating a larger sample of 837 stars with five likely periodic variable detections. Two of the five periodic variables, S4-308 and S3-438, have not been identified as periodically variable stars in any previous study. These two new detections may be young stellar eclipsing binary systems at the GC, but spectroscopic follow-up is necessary to confirm if the stars are indeed young binary systems. We modeled a population of mock young binary systems with stellar and binary parameters drawn from distributions expected for the GC. We will use mock light curves generated from our models, sampled at our observation times and with added photometric noise characteris-

tic of our observations and calibration, in order to determine our experiment's sensitivity to stellar binaries. After determining the sensitivity, we outlined a Bayesian framework that we will use to finally obtain a constrain on the intrinsic binary fraction from our observations. An eclipsing binary survey such as ours, can particularly help place tight constraints on the binary fraction of close binary systems at the GC with short orbital periods.

In Chapter 3, we performed a follow-up analysis of a 39.4 day periodic variable (identified earlier in our single-band photometric variability survey in Chapter 2). Using new multiband photometry and long-term astrometry, we determined that S2-36 is a member of the NSC and its photometric variability originates from an ellipsoidal and eclipsing red giant binary system. We fit S2-36's observed light curve to an astrophysical binary model to constrain its stellar and binary parameters. Our models suggest that it is composed of two red giant branch stars (each of masses spanning between 0.8 and 1.5 $M_{\odot}$) orbiting at an $\approx$ 79 day period. Our models also indicate that the component stars of the binary must be at least 3 Gyr in age. Such a low mass, long-period binary is loosely bound (i.e., dynamically soft) in the GC environment, and can therefore be disrupted by the frequent gravitational encounters expected from surrounding massive objects. If the binary has indeed spent its lifetime in the GC environment, it places tight upper limits on the surrounding density. Importantly, it serves as a novel probe on the dark cusp density, suggesting $\lesssim 10^4$ stellar-mass black holes ($M \sim 10 M_{\odot}$) within $\approx$ 0.1 pc of the central SMBH. Our observations are consistent with lower limits suggested by X-ray binary observations conducted at further distances outside of the central 0.2 pc and provide a powerful new constraint on the presence of the dark cusp at the Galactic center.

5.1 Prospects for GC binary fraction constraints

Our work presented in this thesis provides tight constraints on the observable binary fraction and a framework to constrain the intrinsic binary fraction. Additional avenues for binary

star detection and binary fraction constraints are necessary to get a full observational picture of the nature of the binary star population at the GC. Our work presented in this thesis on photometric searches for binaries can be complemented by two other methods for binary searches that have been applied to the GC stellar population: spectroscopic and astrometric searches for binaries.

While photometric searches are limited in sensitivity to stellar binaries at near edge-on inclinations, spectroscopic / radial velocity (RV) searches for binaries are sensitive to a greater range of inclinations. Furthermore, while there is a large variety of mechanisms that can cause photometric variability which contaminate photometric searches for binaries, such as stellar pulsations or extinction events, RV searches for binaries face fewer contaminations as fewer mechanisms can cause observed RV accelerations. RV searches near the central SMBH are still challenging, as the orbital motion around the SMBH must be well constrained before any RV binary searches (e.g. Chu et al., 2018). RV experiments can also have smaller sample sizes than photometric experiments with the typically smaller field of views of spectrographs, but due to their sensitivity to longer-period binaries that may be missed in photometric surveys due to small eclipses, they serve as a valuable complement to photometric surveys.

Another avenue for detecting binaries at the GC is by searches for astrometric binary systems, where the photometric center of a binary system wobbles over the course of the binary orbit and the motion can be detected astrometrically. An advantage of astrometric searches for binaries is sensitivity to face-on binary systems, to which systems both photometric and RV searches suffer in sensitivity. Furthermore, astrometric searches are particularly sensitive to longer period, further separated binary systems, which can have shallow eclipses or small RV amplitudes resulting in lower sensitivity in other searches. Like photometric searches, astrometric searches are derived from imaging data and similarly benefit to typically larger sample sizes. Astrometric binary searches however require well-constrained models of stellar

proper motions and astrometric reference frames (e.g. Jia et al., 2019).

The diversity of binaries detectable from all three methods will allow a more complete understanding of the GC binary population. While the photometric binary search methods presented here offer large sample sizes, our study suffers from low sensitivity to non-edge-on binary systems and longer-period binaries. Spectroscopic and astrometric searches for binaries complement these deficiencies in photometric monitoring experiments. With future observational work conducted on all three fronts, the GC binary fraction can be well constrained.

5.2 Tighter limits on the dark cusp with binary evaporation

The discovery of S2-36 as a likely red giant binary, presented in Chapter 3, has allowed the applications of binary evaporation models to characterize the dark cusp density close to the SMBH. A few questions still remain about the nature and characteristics of S2-36 that future observations and studies can address. Spectroscopic observations are the most promising avenue for confirming S2-36's binarity and better characterizing its makeup. First, spectroscopic observations can confirm if the stellar components of S2-36 are indeed late-type giant stars, as predicted by our work in Chapter 3. Such stars can be revealed by significant Na I features (see e.g., Do et al., 2013a). With multiple epochs of spectroscopic observations, changes in RV from the binary orbit can be revealed. Measurements of RV are particularly powerful since they provide estimates of the component stellar masses, which can therefore collapse the degeneracy on age and stellar parameters in our binary model fits from photometric data alone.

Another uncertainty about S2-36 is the length of time the system has spent in the GC environment. S2-36 may have formed in the GC environment as a part of the early formation events in the NSC that likely happened $\gtrsim 8$ Gyr ago (Nogueras-Lara et al., 2020). Alternatively, S2-36 may be a newer resident of the NSC, having been deposited by globular cluster

infall scenarios. These different scenarios may be disentangled and tested by spectroscopic metallicity studies, where chemical abundances can allow identifying the possible origin of the star (see e.g., Do et al., 2015). The different scenarios have important implications for the binary's dynamical constraints for the GC. If a recent arrival to the dense GC neighborhood, S2-36 may not have encountered many interactions to loosen it apart and the constraints it provides on the density may not be as tight.

Future detections of other long-period, loosely bound binaries at the GC can provide additional dynamical constraints. Such systems could allow more probes of the GC dark cusp density, especially if located at varying distances from the SMBH. Future photometric, spectroscopic, or astrometric searches for such binaries can yield more candidates. Our study of S2-36 in this thesis provides foundations for confirming future dynamically soft binaries, modeling their astrophysical properties, and deriving dynamical constraints on the dark cusp.

APPENDIX A

Stellar Photometric Catalog

Table A.1: Catalog of stars in variability study sample

Star	Mean Mag (K')	Mean Mag (H)	Spectral Type	Nights Det. (K')	Nights Det. (H)	$\chi^2_{\rm red}$	Var.? (G19)	Var.?	Var. Type	x_0 ($''$ E of Sgr A*)	y_0 ($''$ N of Sgr A*)	t_0	RMS	IQR	$1/\eta$
IRS 16C	9.99	12.14	Early	59	12	3.19	Yes	Yes		1.05	0.55	2009.989	0.10	0.10	3.98
IRS 16SW	10.06	12.25	Early	59	12	26.97	Yes	Yes		1.11	-0.95	2009.820	0.17	0.19	0.54
IRS 16NW	10.25	12.38	Early	59	12	0.83	No	No		0.08	1.22	2010.047	0.11	0.04	6.85
IRS 33E	10.27	12.55	Early	59	12	1.47	No	No		0.71	-3.14	2010.182	0.10	0.06	6.89
S2-17	10.71	12.76	Early	59	12	0.81	No	No		1.34	-1.88	2010.154	0.11	0.05	10.43
IRS 16CC	10.81	13.31	Early	59	12	21.46	Yes	Yes		1.98	0.60	2010.135	0.28	0.16	33.48
S5-89	10.92	13.35	Unknown	59	12	0.94	No	No		-0.79	-5.25	2010.162	0.09	0.04	10.22
S3-22	11.12	13.49	Late	59	12	0.54	No	No		-0.34	-3.21	2010.201	0.10	0.03	20.66
IRS 33N	11.26	13.46	Early	59	12	1.85	Yes	No		-0.03	-2.24	2010.161	0.12	0.06	5.57
IRS 16SW-E	11.28	14.47	Early	50	12	7.32	Yes	Yes		1.90	-1.12	2010.045	0.13	0.08	11.60
S6-12	11.31	13.79	Unknown	59	12	3.24	No	Yes		-0.21	-6.08	2010.161	0.10	0.11	3.04
S6-63	11.32	13.52	Early	56	10	2.11	No	No		1.87	-6.31	2011.057	0.18	0.07	1.41
IRS 29S	11.37	13.80	Late	59	12	0.54	No	No		-1.84	0.96	2010.201	0.10	0.04	11.23
S4-207	11.39	14.43	Unknown	59	12	8.26	Yes	Yes		-4.05	-2.08	2009.835	0.13	0.13	4.01
S1-24	11.43	13.61	Early	59	12	1.73	No	No		0.74	-1.65	2010.125	0.13	0.07	11.06
IRS 34W	11.61	14.60	Early	28	11	17.82	Yes	Yes		-4.07	1.55	2010.189	0.17	0.25	2.00
S5-183	11.62	13.54	Early	59	12	1.49	No	No		4.59	-3.44	2010.024	0.09	0.07	10.10
S1-23	11.68	14.04	Late	59	12	2.66	Yes	Yes		-0.90	-1.50	2010.144	0.10	0.09	13.61
S2-11	11.81	13.93	Late	59	12	3.57	Yes	Yes		1.97	-0.61	2009.813	0.11	0.06	12.75
S3-5	11.96	14.28	Early	59	12	1.78	No	No		2.96	-1.15	2009.910	0.10	0.07	14.32
S2-6	11.97	14.18	Early	59	12	7.41	Yes	Yes		1.66	-1.33	2010.067	0.11	0.13	4.76
S3-19	12.00	13.94	Early	22	12	1.16	No	No		-1.55	-2.79	2009.136	0.12	0.05	14.22
S6-88	12.03	—	Unknown	9	0	2.30	Yes	No		-1.80	-6.41	2009.451	0.48	0.43	2.35
S2-4	12.05	14.40	Early	59	12	7.05	Yes	Yes		1.52	-1.46	2010.007	0.14	0.14	3.83
S4-4	12.07	14.91	Late	59	12	18.84	Yes	Yes		3.61	-2.44	2009.973	0.18	0.28	21.98
S4-129	12.11	14.46	Late	59	12	18.86	Yes	Yes		3.69	-2.22	2009.999	0.19	0.15	0.77
S3-291	12.12	—	Late	28	0	1.98	No	No		-3.53	-1.25	2010.064	0.11	0.07	7.98
S3-2	12.14	14.38	Early	59	12	3.78	No	Yes		3.09	0.55	2010.014	0.15	0.12	15.50
S3-10	12.15	14.14	Early	59	12	0.40	No	No		3.34	-1.11	2009.944	0.09	0.03	13.78
S1-3	12.19	14.36	Early	59	12	1.76	No	No		0.32	0.88	2010.207	0.11	0.07	7.39
S2-8	12.21	14.13	Late	50	12	0.50	No	No		-1.96	0.89	2010.183	0.11	0.04	19.11
IRS 9W	12.23	14.70	Early	59	12	2.42	Yes	Yes		2.90	-5.59	2010.247	0.09	0.07	3.15
S2-16	12.23	15.77	Early	59	12	11.41	Yes	Yes		-1.07	2.06	2010.201	0.21	0.21	26.72
S1-17	12.27	14.74	Late	59	12	0.54	No	No		0.48	-1.53	2010.070	0.10	0.04	16.00

Table A.1 (cont'd): Catalog of stars in variability study sample

Star	Mean Mag (K')	Mean Mag (H)	Spectral Type	Nights Det. (K')	Nights Det. (H)	$\chi^2_{\rm red}$	Var.? (G19)	Var.?	Var. Type	x_0 ($''$ E of Sgr A*)	y_0 ($''$ N of Sgr A*)	t_0	RMS	IQR	$1/\eta$
S2-32	12.31	14.55	Late	59	12	0.76	No	No		1.13	2.78	2009.937	0.09	0.04	9.94
S2-85	12.32	15.21	Late	59	12	18.29	Yes	Yes	L	-1.29	2.67	2010.210	0.16	0.14	5.08
S7-5	12.33	14.72	Unknown	49	12	3.82	Yes	Yes		4.86	-5.52	2010.523	0.10	0.10	3.36
S6-89	12.33	14.86	Early	26	8	4.62	No	Yes		5.45	3.00	2009.877	0.23	0.31	1.61
S6-27	12.34	14.64	Late	59	12	0.34	No	No		4.08	-4.68	2010.175	0.09	0.03	15.35
S3-26	12.37	14.47	Early	59	12	1.04	No	No		-2.57	-2.07	2010.133	0.12	0.05	12.71
S4-71	12.39	14.61	Early	59	12	0.90	No	No		0.77	-4.09	2010.194	0.09	0.04	6.95
S3-30	12.43	14.77	Early	59	12	1.55	No	No		1.66	-2.94	2010.064	0.11	0.06	10.16
S3-374	12.45	15.07	Early	59	12	4.51	Yes	Yes		-2.76	-2.85	2010.080	0.14	0.12	9.02
S6-35	12.48	15.10	Unknown	44	9	2.39	Yes	No		-4.91	-3.96	2009.226	0.14	0.10	2.27
S1-4	12.53	14.78	Early	59	12	2.27	Yes	Yes		0.88	-0.66	2010.057	0.11	0.07	13.53
S1-5	12.57	14.95	Late	38	12	1.02	No	No		0.32	-0.89	2010.094	0.10	0.04	11.30
S1-20	12.58	14.79	Late	59	12	54.29	Yes	Yes	L	0.45	1.60	2010.147	0.24	0.45	16.28
S1-22	12.62	14.79	Early	35	12	1.28	No	No		-1.57	-0.52	2010.135	0.11	0.04	12.04
S4-344	12.67	15.18	Unknown	59	12	0.79	No	No		-1.43	-4.72	2010.131	0.11	0.04	23.50
S4-2	12.67	15.10	Late	10	12	1.46	No	No		3.76	1.65	2009.789	0.08	0.06	5.82
S2-19	12.71	14.92	Early	38	12	0.60	Yes	No		0.38	2.31	2010.075	0.13	0.03	12.98
S4-6	12.74	15.20	Late	59	12	3.98	Yes	Yes		3.28	-2.75	2010.123	0.12	0.12	8.69
S4-258	12.75	15.72	Early	43	12	38.31	Yes	Yes		-4.40	-1.63	2009.761	0.36	0.31	4.06
S4-36	12.76	15.54	Early	39	12	10.57	Yes	Yes		-3.69	1.78	2009.810	0.19	0.26	5.51
S1-14	12.79	14.77	Early	48	12	0.95	No	No		-1.32	-0.37	2009.666	0.10	0.04	23.80
S3-6	12.80	15.24	Late	38	12	0.89	No	No		3.23	-0.05	2010.040	0.10	0.05	12.99
S5-191	12.89	14.94	Early	59	12	0.65	No	No		3.18	-4.89	2010.357	0.10	0.04	12.94
S5-213	12.89	15.13	Late	59	12	0.47	No	No		4.98	-3.26	2010.066	0.08	0.04	16.38
S2-22	12.96	15.02	Early	59	12	0.92	No	No		2.30	-0.21	2010.168	0.10	0.04	13.03
S4-3	13.00	15.20	Late	59	12	0.29	No	No		4.22	0.12	2009.959	0.09	0.02	20.53
S1-34	13.01	14.76	Late	59	12	0.52	No	No		0.87	-0.99	2010.145	0.10	0.02	37.26
S2-31	13.02	15.49	Late	59	12	3.84	Yes	Yes		2.76	-0.19	2010.061	0.10	0.09	8.76
S3-156	13.05	15.33	Unknown	59	12	1.37	No	No		0.42	-3.37	2009.648	0.10	0.06	10.50
S2-18	13.10	15.52	Late	59	12	2.06	Yes	No		-1.00	-2.15	2010.123	0.12	0.08	21.47
S1-1	13.12	15.15	Early	59	12	0.68	No	No		1.04	0.03	2009.895	0.09	0.05	13.12
S4-180	13.18	15.90	Early	37	12	7.02	Yes	Yes		-4.29	-1.33	2011.094	0.11	0.08	2.72
S2-74	13.25	15.62	Early	59	12	2.76	Yes	Yes		0.11	2.78	2010.109	0.15	0.07	10.09
S2-5	13.26	15.42	Early	59	12	1.50	No	No		1.94	-0.79	2010.021	0.11	0.06	19.05

Table A.1 (cont'd): Catalog of stars in variability study sample

Star	Mean Mag (K')	Mean Mag (H)	Spectral Type	Nights Det. (K')	Nights Det. (H)	$\chi^2_{\rm red}$	Var.? (G19)	Var.?	Var. Type	x_0 ($''$ E of Sgr A*)	y_0 ($''$ N of Sgr A*)	t_0	RMS	IQR	$1/\eta$
S6-58	13.28	15.70	Unknown	59	12	1.47	No	No		3.22	-5.65	2010.151	0.10	0.05	10.21
S3-34	13.29	15.09	Late	59	12	330.16	Yes	Yes	L	3.24	-1.26	2010.374	0.55	1.13	32.44
S3-149	13.31	15.79	Late	59	12	5.97	Yes	Yes		-2.90	1.71	2010.286	0.11	0.17	4.42
S1-21	13.31	15.34	Early	59	12	0.87	No	No		-1.64	0.09	2010.177	0.10	0.05	15.98
S5-211	13.31	15.04	Late	59	12	0.21	No	No		4.46	-3.90	2010.061	0.09	0.02	25.21
S5-187	13.32	15.31	Early	59	12	1.27	No	No		-1.71	-5.55	2009.655	0.10	0.05	6.35
S0-13	13.32	15.51	Late	23	11	0.27	No	No		0.56	-0.41	2010.122	0.08	0.03	21.35
S1-68	13.32	15.59	Late	59	12	1.20	No	No		1.83	-0.65	2010.023	0.09	0.05	9.81
S4-1	13.33	15.64	Late	59	12	0.76	No	No		4.00	-0.36	2009.980	0.08	0.04	16.23
S2-21	13.35	15.45	Early	59	12	1.40	No	No		-1.62	-1.67	2010.222	0.10	0.07	14.84
S5-95	13.35	15.65	Unknown	59	12	2.69	Yes	Yes		-1.94	-4.99	2010.143	0.10	0.10	13.27
IRS 7SE	13.36	15.99	Early	49	12	61.67	Yes	Yes	L	2.99	3.46	2009.595	0.25	0.19	3.68
S5-134	13.37	15.83	Unknown	59	12	4.76	Yes	Yes		-0.53	-5.46	2009.951	0.13	0.14	12.97
S1-25	13.39	15.72	Late	59	12	0.85	No	No		1.68	-0.61	2010.098	0.10	0.05	67.61
S5-237	13.39	15.44	Early	32	9	9.03	Yes	Yes		5.49	1.02	2012.046	0.16	0.21	1.52
S2-36	13.41	15.60	Unknown	58	11	11.30	Yes	Yes		1.99	0.44	2009.947	0.15	0.15	1.33
S2-67	13.43	15.84	Late	59	12	1.27	No	No		-2.47	-0.88	2010.171	0.10	0.05	14.09
S4-143	13.48	16.06	Late	59	12	0.43	No	No		2.90	-3.25	2010.331	0.10	0.03	18.32
IRS 34NW	13.51	—	Early	41	0	53.28	Yes	Yes		-3.78	2.83	2010.283	0.57	0.79	12.17
S1-12	13.52	15.59	Early	59	12	0.56	No	No		-0.75	-1.03	2010.234	0.11	0.03	22.54
S2-78	13.55	16.05	Late	58	10	1.86	Yes	No		-2.82	-0.28	2010.204	0.13	0.08	13.03
S1-19	13.57	15.69	Early	59	12	0.79	No	No		0.43	-1.64	2010.024	0.10	0.04	14.54
S3-39	13.59	15.94	Late	59	12	1.72	Yes	No		3.56	1.08	2009.733	0.10	0.05	8.54
S2-77	13.60	15.99	Late	54	10	1.51	No	No		-1.76	-2.21	2008.709	0.11	0.05	9.28
S3-13	13.61	15.92	Late	59	12	0.96	No	No		3.84	0.98	2009.952	0.09	0.05	4.37
S3-7	13.61	16.03	Late	59	12	1.13	No	No		1.92	-2.61	2010.088	0.09	0.06	15.94
S3-370	13.63	15.86	Late	59	12	0.46	No	No		-0.29	-3.91	2010.136	0.10	0.02	33.18
S3-29	13.63	15.73	Late	59	12	1.04	No	No		1.44	-3.08	2010.219	0.09	0.04	14.91
S2-24	13.65	16.10	Late	58	12	1.16	No	No		-2.34	-0.89	2009.893	0.12	0.06	18.08
S0-14	13.68	15.73	Early	52	12	0.74	No	No		-0.76	-0.29	2010.316	0.12	0.03	34.35
S0-15	13.68	16.01	Early	48	12	11.92	Yes	Yes	L	-0.97	0.18	2009.722	0.18	0.16	14.32
S6-76	13.70	16.09	Late	59	12	0.78	No	No		5.18	-4.52	2010.291	0.09	0.04	6.76
S6-3	13.70	16.09	Unknown	32	12	1.78	No	No		-0.01	-6.01	2010.469	0.10	0.07	3.02
S3-198	13.73	16.49	Unknown	59	12	3.18	Yes	Yes		0.65	3.45	2009.959	0.10	0.12	4.98

Table A.1 (cont'd): Catalog of stars in variability study sample

Star	Mean Mag (K')	Mean Mag (H)	Spectral Type	Nights Det. (K')	Nights Det. (H)	$\chi^2_{\rm red}$	Var.? (G19)	Var.?	Var. Type	x_0 ($''$ E of Sgr A*)	y_0 ($''$ N of Sgr A*)	t_0	RMS	IQR	$1/\eta$
S4-287	13.74	15.89	Early	59	12	0.36	No	No		0.13	-4.77	2010.188	0.09	0.03	28.46
S3-331	13.74	15.93	Early	32	12	3.38	Yes	Yes		-1.22	3.65	2010.150	0.12	0.10	4.45
S7-27	13.75	16.12	Unknown	49	11	2.53	No	Yes		3.26	-6.36	2011.875	0.16	0.11	0.54
S5-34	13.75	16.23	Early	47	12	0.84	No	No		-4.33	-2.74	2010.071	0.09	0.05	4.84
S4-161	13.76	16.24	Late	59	12	1.04	No	No		4.42	-0.26	2009.943	0.09	0.05	16.90
S3-284	13.77	17.15	Late	22	12	3.68	Yes	Yes		-2.57	2.71	2010.347	0.11	0.12	3.80
S2-25	13.77	16.20	Late	59	12	1.39	No	No		0.76	-2.42	2010.330	0.11	0.06	22.76
S6-25	13.78	16.11	Unknown	57	12	1.42	No	No		0.71	-6.17	2010.070	0.11	0.06	2.94
S3-17	13.78	16.78	Early	24	12	23.61	Yes	Yes		-1.41	2.85	2009.185	0.19	0.26	1.51
S5-185	13.78	16.11	Unknown	59	12	0.95	No	No		3.00	-4.92	2010.475	0.10	0.04	15.72
S5-115	13.79	16.68	Unknown	49	5	3.41	Yes	Yes		-5.17	-1.55	2010.148	0.15	0.16	2.16
S4-59	13.80	16.13	Late	30	12	1.69	No	No		-3.15	2.65	2010.023	0.14	0.07	5.04
S3-134	13.80	16.12	Unknown	59	12	0.20	No	No		-1.39	-3.01	2010.208	0.10	0.03	43.87
S2-26	13.82	16.14	Late	59	12	42.99	Yes	Yes	L	0.79	2.31	2010.167	0.25	0.42	3.75
S3-35	13.82	16.63	Unknown	59	12	4.28	Yes	Yes		-1.21	3.28	2010.167	0.16	0.14	8.10
S4-112	13.87	16.24	Late	56	12	7.36	Yes	Yes		2.24	-3.61	2010.251	0.11	0.10	8.65
S5-71	13.88	16.15	Unknown	59	12	0.42	No	No		-1.75	-4.94	2009.691	0.10	0.03	32.58
S3-14	13.89	16.57	Late	41	12	6.27	Yes	Yes		0.18	3.07	2009.981	0.12	0.14	5.37
S6-31	13.91	16.25	Unknown	40	12	1.63	No	No		-2.12	-5.85	2010.015	0.10	0.09	4.32
S3-28	13.93	16.46	Unknown	59	12	4.05	Yes	Yes		-0.83	3.23	2010.134	0.11	0.08	4.57
S4-24	14.00	—	Unknown	45	0	5.94	Yes	Yes		-0.72	4.00	2010.423	0.15	0.16	1.83
S5-145	14.01	16.00	Unknown	59	12	0.76	No	No		-0.57	-5.54	2010.081	0.09	0.04	3.78
S3-27	14.01	16.38	Unknown	59	12	11.77	Yes	Yes		-0.33	3.32	2010.092	0.14	0.24	14.28
S2-7	14.03	16.15	Early	59	12	74.29	Yes	Yes	L	0.93	1.85	2010.257	0.30	0.52	5.84
S2-2	14.05	15.82	Late	34	12	0.45	No	No		-0.52	2.09	2010.141	0.09	0.03	15.01
S3-25	14.05	16.21	Early	59	12	1.83	Yes	No		1.41	2.95	2009.923	0.10	0.08	7.63
S3-207	14.05	16.37	Unknown	59	12	0.46	No	No		1.55	3.21	2009.989	0.10	0.04	10.31
S0-6	14.05	16.41	Late	45	12	1.15	No	No		0.02	-0.36	2010.779	0.10	0.04	6.45
S2-58	14.05	16.33	Early	53	11	3.77	Yes	Yes		2.14	-1.13	2010.157	0.13	0.11	8.19
S4-342	14.06	16.49	Unknown	36	8	20.24	Yes	Yes		3.07	3.86	2010.650	0.24	0.42	2.51
S1-13	14.06	16.38	Late	59	12	1.26	No	No		-1.14	-0.97	2010.185	0.11	0.05	28.45
S5-205	14.07	16.34	Unknown	59	12	1.07	No	No		-0.91	-5.81	2010.004	0.09	0.04	9.90
S6-66	14.07	16.72	Unknown	54	12	4.59	Yes	Yes		-4.71	-4.66	2009.332	0.14	0.15	5.31
S4-158	14.08	16.21	Late	59	12	0.42	No	No		-0.86	-4.33	2010.174	0.10	0.03	24.26

Table A.1 (cont'd): Catalog of stars in variability study sample

Star	Mean Mag (K')	Mean Mag (H)	Spectral Type	Nights Det. (K')	Nights Det. (H)	$\chi^2_{\rm red}$	Var.? (G19)	Var.?	Var. Type	x_0 ($''$ E of Sgr A*)	y_0 ($''$ N of Sgr A*)	t_0	RMS	IQR	$1/\eta$
S7-29	14.11	16.59	Unknown	31	9	2.95	Yes	Yes		-3.66	-6.38	2010.986	0.17	0.22	0.56
S4-25	14.12	16.48	Unknown	37	10	0.87	No	No		2.45	3.28	2009.729	0.09	0.06	10.55
S4-197	14.12	16.66	Unknown	59	12	1.26	No	No		-2.55	-3.71	2010.272	0.10	0.06	25.19
S3-288	14.12	17.64	Late	29	12	21.68	Yes	Yes		-2.77	2.54	2010.339	0.26	0.39	9.97
S0-2	14.12	16.13	Early	49	11	3.21	Yes	Yes		-0.01	0.17	2007.893	0.11	0.07	6.25
S5-202	14.13	16.12	Unknown	59	12	0.59	No	No		-0.51	-5.85	2010.094	0.09	0.04	10.21
S3-146	14.14	16.37	Unknown	58	10	2.81	No	Yes		-0.29	-3.35	2010.110	0.15	0.05	4.05
S1-15	14.14	16.37	Late	59	12	2.46	Yes	Yes		-1.36	0.49	2009.477	0.10	0.08	2.70
S5-199	14.16	16.78	Unknown	44	11	0.80	No	No		-4.20	-4.08	2009.569	0.11	0.05	4.81
S4-319	14.17	16.45	Late	59	12	0.72	No	No		4.68	-1.38	2010.042	0.10	0.05	17.16
S6-39	14.17	16.54	Unknown	59	12	3.53	Yes	Yes		2.51	-5.79	2009.801	0.10	0.08	6.66
S0-32	14.18	—	Unknown	58	0	1.54	Yes	No		0.32	0.79	2010.090	0.11	0.06	10.51
S2-344	14.18	16.55	Unknown	54	10	5.56	Yes	Yes		-1.73	-2.20	2012.518	0.13	0.08	4.88
S1-8	14.19	16.47	Early	59	12	2.24	No	Yes		-0.58	-0.92	2010.185	0.13	0.07	33.22
S3-190	14.20	17.08	Early	59	12	15.08	Yes	Yes		-3.19	1.41	2010.223	0.21	0.25	6.03
S4-170	14.21	16.41	Unknown	59	12	1.84	No	No		-0.57	-4.41	2010.181	0.12	0.08	37.56
S4-229	14.22	17.47	Unknown	23	10	1.85	No	No		-4.19	1.94	2010.123	0.13	0.07	2.40
S2-3	14.24	16.62	Late	55	12	0.60	No	No		-1.51	-1.41	2010.300	0.11	0.03	29.68
S3-88	14.24	16.42	Unknown	59	12	0.21	No	No		-0.85	-3.00	2010.102	0.10	0.01	53.41
S3-380	14.24	—	Unknown	37	0	0.62	No	No		2.41	3.19	2009.769	0.09	0.05	10.74
S2-57	14.24	16.49	Late	58	11	1.89	No	No		-1.15	-2.09	2010.273	0.10	0.06	12.66
S2-47	14.24	16.64	Late	59	12	2.08	Yes	No		2.19	-0.52	2010.214	0.11	0.07	13.32
S0-4	14.25	16.23	Early	36	11	1.74	No	No		0.45	-0.33	2010.008	0.11	0.06	11.32
S4-221	14.25	16.69	Late	59	12	0.77	No	No		2.69	-3.77	2010.222	0.11	0.04	25.18
S5-43	14.29	16.80	Late	59	12	6.74	Yes	Yes		1.84	-4.80	2010.260	0.11	0.12	8.28
S6-49	14.32	16.71	Unknown	39	12	0.91	No	No		-2.85	-5.77	2010.422	0.10	0.05	3.23
S5-240	14.32	16.51	Unknown	51	11	2.18	Yes	No		5.36	0.08	2011.220	0.10	0.10	1.23
S0-9	14.32	16.35	Early	59	12	1.84	No	No		0.22	-0.60	2009.769	0.10	0.08	5.78
S7-3	14.33	16.71	Unknown	59	12	0.65	No	No		4.17	-5.80	2010.379	0.09	0.04	8.77
S1-49	14.38	16.42	Unknown	59	12	7.10	Yes	Yes	L	-1.72	0.15	2010.287	0.13	0.12	7.43
S4-196	14.38	16.67	Early	59	12	5.19	Yes	Yes		2.24	-3.93	2010.135	0.10	0.09	3.86
S0-12	14.38	16.66	Late	6	12	2.64	No	No		-0.55	0.41	2009.012	0.13	0.09	11.04
S6-77	14.39	16.69	Late	56	12	1.23	No	No		5.06	-4.75	2010.476	0.11	0.06	8.54
S5-174	14.39	16.92	Unknown	49	12	1.31	No	No		-4.16	-3.94	2010.073	0.10	0.07	4.93

Table A.1 (cont'd): Catalog of stars in variability study sample

Star	Mean Mag (K')	Mean Mag (H)	Spectral Type	Nights Det. (K')	Nights Det. (H)	$\chi^2_{\rm red}$	Var.? (G19)	Var.?	Var. Type	x_0 ($''$ E of Sgr A*)	y_0 ($''$ N of Sgr A*)	t_0	RMS	IQR	$1/\eta$
S2-75	14.43	16.75	Late	59	12	0.52	No	No		2.63	-0.85	2010.082	0.10	0.03	28.72
S2-70	14.45	17.42	Late	59	12	15.94	Yes	Yes		-2.68	0.39	2010.154	0.23	0.13	13.75
S3-187	14.45	17.04	Late	59	12	8.87	Yes	Yes		-3.40	-0.75	2010.032	0.17	0.19	19.63
S5-170	14.47	16.68	Unknown	18	10	1.67	No	No		4.23	3.84	2009.509	0.08	0.05	2.73
S4-139	14.47	16.72	Late	59	12	5.37	Yes	Yes		2.40	-3.62	2010.074	0.09	0.12	4.47
S6-70	14.49	16.93	Unknown	35	11	0.99	No	No		-2.80	-6.15	2011.881	0.13	0.08	5.23
S3-208	14.49	16.38	Unknown	59	12	1.49	No	No		-0.98	-3.41	2010.198	0.09	0.05	17.24
S3-20	14.51	17.12	Late	58	11	3.47	Yes	Yes		1.58	-2.79	2009.965	0.11	0.09	6.93
S2-23	14.52	17.26	Late	59	12	5.39	Yes	Yes		1.65	1.74	2010.053	0.11	0.07	6.81
S3-96	14.54	17.18	Early	57	11	1.65	No	No		-3.13	-0.63	2010.217	0.12	0.06	7.89
S6-64	14.55	16.40	Unknown	32	12	1.00	No	No		-3.05	-5.86	2010.405	0.12	0.08	1.70
S3-249	14.56	17.76	Late	58	12	24.41	Yes	Yes	L	-3.38	1.28	2010.016	0.27	0.33	8.65
S3-364	14.58	16.84	Unknown	56	8	2.60	Yes	Yes		-0.96	3.80	2010.143	0.12	0.12	1.33
S4-352	14.58	17.60	Unknown	17	10	2.99	Yes	No		-4.88	-0.88	2009.519	0.20	0.10	9.57
S4-236	14.58	16.84	Unknown	52	12	0.31	No	No		-1.91	-4.22	2009.747	0.11	0.03	30.23
S0-3	14.62	16.79	Early	59	12	2.10	Yes	No		0.34	0.12	2008.393	0.11	0.06	7.67
S3-36	14.63	16.74	Late	59	12	0.11	No	No		3.47	-0.81	2010.145	0.09	0.02	42.82
S5-198	14.64	16.92	Unknown	59	12	0.95	No	No		0.51	-5.82	2010.297	0.09	0.03	22.06
S6-62	14.70	17.20	Unknown	54	12	5.87	Yes	Yes		-4.70	-4.60	2009.407	0.15	0.14	4.70
S4-12	14.70	17.63	Early	33	11	24.64	Yes	Yes	L	-2.86	2.84	2010.034	0.22	0.35	4.25
S3-4	14.70	17.80	Unknown	59	12	11.97	Yes	Yes		3.07	-0.48	2010.182	0.13	0.19	9.48
S5-83	14.71	16.91	Late	59	12	0.66	No	No		5.20	-0.94	2010.125	0.08	0.03	7.10
S3-162	14.71	16.90	Unknown	35	12	1.09	No	No		-0.05	-3.41	2010.743	0.09	0.06	9.02
S2-277	14.73	16.90	Unknown	59	12	2.20	Yes	Yes		-2.44	-1.44	2010.286	0.13	0.07	10.31
S1-2	14.74	16.84	Early	59	12	2.54	Yes	Yes		0.08	-1.02	2009.985	0.12	0.07	8.39
S0-1	14.77	16.97	Early	42	12	4.78	Yes	Yes		0.04	-0.26	2006.300	0.11	0.09	13.73
S1-10	14.77	16.59	Late	59	12	0.30	No	No		-1.10	-0.02	2010.139	0.11	0.02	43.83
S4-46	14.77	16.65	Late	59	12	0.22	No	No		3.84	-1.48	2010.066	0.09	0.02	25.00
S3-403	14.79	17.10	Unknown	40	11	2.27	No	No		-0.12	-3.38	2009.561	0.14	0.09	6.64
S5-12	14.82	17.51	Unknown	46	12	0.79	No	No		-4.28	-2.63	2010.189	0.11	0.06	9.46
S2-69	14.82	17.98	Unknown	59	12	16.72	Yes	Yes		-0.88	2.56	2010.273	0.23	0.19	14.68
S2-72	14.83	17.20	Late	57	10	4.07	Yes	Yes		-1.50	-2.24	2010.007	0.11	0.09	9.62
S4-98	14.87	17.30	Unknown	43	12	3.62	Yes	Yes		-4.12	-0.90	2009.807	0.10	0.12	8.52
S1-18	14.87	17.14	Early	58	12	2.87	Yes	Yes		-0.79	1.50	2009.682	0.12	0.05	4.65

Table A.1 (cont'd): Catalog of stars in variability study sample

Star	Mean Mag (K')	Mean Mag (H)	Spectral Type	Nights Det. (K')	Nights Det. (H)	$\chi^2_{\rm red}$	Var.? (G19)	Var.?	Var. Type	x_0 ($''$ E of Sgr A*)	y_0 ($''$ N of Sgr A*)	t_0	RMS	IQR	$1/\eta$
S5-243	14.89	17.39	Late	26	6	6.68	Yes	Yes		5.52	1.45	2007.596	0.20	0.19	0.58
S5-112	14.90	—	Unknown	35	0	4.96	Yes	Yes		-5.27	1.23	2009.265	0.19	0.20	1.41
S5-99	14.91	17.18	Late	59	12	0.36	No	No		4.61	-2.74	2010.082	0.10	0.03	30.64
S2-73	14.93	17.13	Late	31	12	3.14	Yes	Yes		2.13	-1.66	2009.926	0.11	0.08	9.85
S5-133	14.93	16.90	Unknown	57	11	13.31	Yes	Yes		-0.75	-5.45	2009.873	0.17	0.17	0.97
S3-223	14.98	17.51	Unknown	58	10	1.27	No	No		1.28	-3.37	2009.821	0.09	0.06	9.01
S3-11	14.98	17.44	Late	55	12	2.11	Yes	No		2.96	-1.90	2011.181	0.11	0.05	14.18
S6-37	14.99	17.60	Unknown	43	12	2.29	Yes	No		-2.31	-5.87	2010.256	0.13	0.09	2.22
S1-51	15.02	17.30	Unknown	59	12	3.43	Yes	Yes		-1.66	-0.17	2010.270	0.12	0.05	10.22
S1-33	15.04	17.13	Early	32	12	1.19	No	No		-1.25	-0.00	2009.977	0.10	0.04	14.82
S0-18	15.04	17.35	Late	50	12	37.97	Yes	Yes	L	-0.12	-0.42	2009.454	0.23	0.06	3.12
S0-5	15.07	17.11	Early	44	12	1.32	No	No		0.17	-0.36	2009.636	0.10	0.05	8.14
S2-62	15.07	17.41	Late	59	11	0.69	No	No		-1.03	-2.32	2010.009	0.11	0.03	22.63
S3-216	15.07	17.22	Unknown	59	12	0.75	No	No		-3.14	1.67	2009.725	0.11	0.05	8.39
S3-37	15.11	17.00	Late	59	11	1.77	No	No		3.42	1.36	2010.050	0.09	0.08	1.66
S4-172	15.12	17.37	Late	59	12	38.80	Yes	Yes	L	3.09	-3.17	2010.358	0.18	0.23	7.93
S3-16	15.13	17.34	Late	58	10	5.64	Yes	Yes		2.97	-0.95	2009.811	0.11	0.11	3.63
S3-3	15.13	17.22	Early	59	12	2.02	Yes	No		3.09	-0.64	2010.081	0.11	0.07	7.27
S5-193	15.13	16.89	Unknown	57	11	1.20	No	No		-1.16	-5.73	2009.874	0.10	0.04	5.58
S0-31	15.14	17.14	Early	57	8	2.43	No	Yes		0.57	0.45	2009.906	0.13	0.08	5.41
S5-159	15.16	17.36	Unknown	59	12	0.51	No	No		0.43	-5.60	2010.221	0.10	0.03	14.39
S4-315	15.17	17.44	Late	57	11	3.20	Yes	Yes		4.81	0.85	2009.738	0.16	0.11	2.68
S2-79	15.18	17.42	Unknown	55	9	5.07	Yes	Yes		2.87	-0.12	2009.530	0.12	0.14	4.38
S3-155	15.19	17.03	Unknown	59	12	0.56	No	No		-1.84	-2.83	2010.185	0.10	0.03	31.43
S4-168	15.19	17.13	Unknown	7	5	358.80	Yes	Yes		-1.91	3.97	2010.678	1.80	2.12	4.93
S6-44	15.19	17.36	Unknown	59	12	1.14	No	No		-2.15	-6.00	2010.113	0.11	0.07	4.47
S2-55	15.19	17.49	Late	58	12	1.73	Yes	No		0.90	-2.19	2009.600	0.11	0.07	5.61
S2-12	15.20	17.46	Late	52	12	1.36	No	No		1.64	1.14	2010.272	0.10	0.06	6.29
S2-71	15.21	17.34	Late	59	12	0.66	No	No		-0.88	-2.52	2010.060	0.10	0.03	26.39
S3-51	15.21	17.37	Unknown	59	12	0.55	No	No		-0.15	3.02	2010.104	0.10	0.04	8.19
S1-39	15.22	17.52	Late	55	12	3.02	Yes	Yes		-0.54	-1.38	2009.934	0.13	0.08	11.20
S3-32	15.22	17.47	Late	58	12	1.16	No	No		2.87	-1.77	2010.163	0.10	0.04	16.51
S2-30	15.22	17.61	Unknown	55	9	6.64	Yes	Yes		2.92	-0.05	2009.108	0.16	0.15	5.37
S0-7	15.23	17.28	Early	59	11	10.19	Yes	Yes	L	0.51	0.10	2010.379	0.12	0.09	11.50

Table A.1 (cont'd): Catalog of stars in variability study sample

Star	Mean Mag (K')	Mean Mag (H)	Spectral Type	Nights Det. (K')	Nights Det. (H)	$\chi^2_{\rm red}$	Var.? (G19)	Var.?	Var. Type	x_0 ($''$ E of Sgr A*)	y_0 ($''$ N of Sgr A*)	t_0	RMS	IQR	$1/\eta$
S0-11	15.23	17.31	Early	26	12	1.18	No	No		0.49	-0.06	2010.011	0.11	0.06	6.01
S1-52	15.23	—	Unknown	9	0	0.11	No	No		0.01	1.68	2007.924	0.07	0.02	18.21
S5-156	15.23	17.59	Unknown	59	12	1.22	No	No		-1.42	-5.45	2010.209	0.10	0.04	14.74
S3-192	15.24	17.49	Unknown	58	10	1.45	No	No		0.50	-3.47	2009.890	0.10	0.05	8.64
S4-277	15.24	17.48	Late	55	11	0.90	No	No		4.75	0.21	2009.665	0.11	0.05	3.88
S5-98	15.24	17.35	Unknown	59	12	1.14	No	No		1.04	-5.24	2010.354	0.09	0.03	20.54
S1-53	15.25	17.44	Unknown	59	12	1.44	No	No		1.67	-0.10	2009.524	0.09	0.08	5.26
S2-49	15.25	17.43	Late	59	12	3.24	Yes	Yes		-0.80	-2.14	2010.126	0.11	0.09	9.35
S1-32	15.25	17.57	Unknown	59	11	1.82	Yes	No		-0.99	-0.66	2010.144	0.12	0.07	16.08
S3-227	15.25	17.52	Unknown	59	12	1.74	No	No		0.03	-3.60	2010.028	0.10	0.08	8.58
S3-262	15.26	—	Late	50	0	19.18	Yes	Yes	L	-2.35	2.81	2010.084	0.22	0.15	4.60
S4-22	15.26	17.66	Unknown	59	12	2.88	Yes	Yes		-2.36	-3.30	2010.408	0.13	0.09	34.85
S3-385	15.27	17.38	Late	58	12	0.59	No	No		3.69	-1.46	2009.997	0.09	0.04	11.24
S2-82	15.27	17.52	Unknown	23	11	2.15	Yes	No		2.86	0.06	2009.160	0.15	0.05	6.31
S6-14	15.27	17.66	Unknown	46	12	1.74	No	No		-3.24	-5.16	2009.107	0.11	0.08	3.24
S2-84	15.28	17.59	Unknown	58	12	0.94	No	No		1.66	-2.47	2010.187	0.09	0.05	12.44
S2-29	15.28	17.42	Early	59	11	1.56	No	No		1.95	-2.16	2010.009	0.10	0.07	5.29
S4-86	15.28	17.35	Unknown	59	11	0.55	No	No		-0.66	-4.12	2009.691	0.09	0.04	16.66
S2-306	15.28	17.82	Unknown	54	10	14.49	Yes	Yes	L	-0.49	-2.89	2010.382	0.15	0.11	4.82
S1-45	15.29	—	Unknown	32	0	3.34	Yes	Yes		-1.28	1.10	2009.660	0.13	0.10	4.74
S3-268	15.29	17.55	Unknown	58	12	2.65	Yes	Yes		-2.15	-3.03	2010.422	0.11	0.07	17.69
S0-26	15.30	17.35	Early	42	12	2.54	No	Yes		0.33	0.21	2007.655	0.10	0.10	1.56
S3-348	15.30	17.47	Unknown	59	12	0.52	No	No		3.91	0.23	2009.944	0.10	0.03	15.92
S5-60	15.30	17.51	Unknown	56	10	3.02	Yes	Yes		5.22	0.12	2009.817	0.14	0.10	1.25
S1-63	15.31	17.96	Unknown	27	9	43.44	Yes	Yes	L	-1.22	1.41	2008.658	0.20	0.26	2.73
S4-45	15.31	17.60	Unknown	59	11	1.65	Yes	No		4.11	-0.41	2009.981	0.11	0.06	6.28
S0-35	15.31	17.58	Unknown	21	11	12.20	Yes	Yes	L	0.02	0.88	2009.499	0.17	0.17	7.07
S6-22	15.31	17.72	Late	59	11	3.86	Yes	Yes		4.91	-3.67	2010.284	0.11	0.08	4.18
S3-286	15.32	17.47	Late	59	12	1.13	No	No		3.41	-1.52	2010.090	0.09	0.05	13.87
S3-159	15.32	17.87	Unknown	57	10	3.29	Yes	Yes		-1.29	3.13	2010.052	0.14	0.12	9.15
S2-316	15.32	17.83	Unknown	44	12	14.53	Yes	Yes	L	-2.43	1.64	2009.665	0.16	0.10	7.86
S3-76	15.34	—	Unknown	17	0	39.99	Yes	Yes		-1.43	-2.77	2007.496	0.18	0.36	3.32
S2-50	15.35	17.48	Early	55	8	6.31	Yes	Yes		1.70	-1.51	2009.533	0.14	0.14	1.63
S2-61	15.35	17.49	Late	58	11	6.24	Yes	Yes		2.36	-0.65	2009.705	0.11	0.12	7.81

Table A.1 (cont'd): Catalog of stars in variability study sample

Star	Mean Mag (K')	Mean Mag (H)	Spectral Type	Nights Det. (K')	Nights Det. (H)	$\chi^2_{\rm red}$	Var.? (G19)	Var.?	Var. Type	x_0 ($''$ E of Sgr A*)	y_0 ($''$ N of Sgr A*)	t_0	RMS	IQR	$1/\eta$
S1-29	15.35	17.65	Unknown	57	8	1.79	No	No		1.07	0.16	2010.071	0.10	0.06	3.67
S3-43	15.35	17.46	Unknown	56	8	4.33	Yes	Yes		-0.16	-3.02	2009.661	0.10	0.10	2.80
S6-4	15.35	17.62	Unknown	59	12	2.40	Yes	Yes		1.72	-5.79	2010.138	0.10	0.04	7.48
S5-212	15.36	17.58	Late	58	11	1.62	No	No		4.03	-4.39	2010.182	0.11	0.06	4.67
S6-78	15.36	17.67	Unknown	59	12	1.00	No	No		4.38	-5.38	2009.990	0.09	0.05	11.18
S3-33	15.36	17.61	Unknown	49	11	1.25	No	No		3.32	-0.83	2010.120	0.10	0.06	17.97
S5-113	15.36	17.65	Unknown	58	12	1.64	No	No		-2.55	-4.80	2009.454	0.11	0.06	5.92
S3-38	15.37	17.76	Late	18	12	2.26	No	No		3.70	-0.10	2008.049	0.10	0.07	8.56
S4-312	15.37	17.62	Late	58	12	0.71	No	No		4.60	-1.54	2010.231	0.08	0.05	12.08
S4-8	15.38	17.58	Unknown	59	12	0.30	No	No		-0.45	-3.97	2010.186	0.10	0.02	22.73
S3-319	15.38	17.52	Unknown	59	12	0.43	No	No		3.57	-1.44	2010.045	0.09	0.03	15.60
S2-34	15.38	17.77	Late	58	11	4.63	Yes	Yes		1.84	1.00	2009.058	0.15	0.11	2.24
S4-176	15.38	17.62	Unknown	52	12	0.47	No	No		4.26	1.40	2010.293	0.09	0.03	11.44
S5-141	15.38	17.58	Unknown	58	11	1.38	No	No		4.34	-3.41	2010.171	0.10	0.06	4.54
S3-21	15.38	—	Unknown	38	0	26.38	Yes	Yes	C	3.20	-0.21	2009.590	0.19	0.21	7.98
S5-178	15.38	17.56	Late	59	12	1.27	No	No		4.85	-3.04	2010.330	0.09	0.05	5.42
S4-279	15.39	17.73	Unknown	39	12	0.43	No	No		4.00	2.59	2010.027	0.08	0.03	9.88
S2-59	15.39	17.87	Late	59	11	6.65	Yes	Yes	L	0.82	-2.33	2009.842	0.13	0.15	7.63
S3-23	15.39	17.82	Unknown	57	10	2.20	No	No		2.91	-1.37	2009.964	0.12	0.09	5.43
S5-138	15.39	17.77	Unknown	41	12	2.35	Yes	No		0.66	-5.48	2010.190	0.10	0.09	5.55
S2-81	15.39	17.80	Late	59	11	2.18	No	No		1.98	-2.04	2010.068	0.13	0.08	6.76
S4-188	15.39	17.96	Unknown	59	11	51.63	Yes	Yes	L	-4.14	-1.77	2010.496	0.25	0.26	6.12
S2-41	15.39	17.61	Late	59	12	4.77	Yes	Yes		-0.47	-2.09	2010.303	0.12	0.12	8.57
S1-48	15.40	17.56	Late	58	11	2.72	Yes	Yes		-0.63	-1.55	2009.947	0.10	0.09	2.72
S4-375	15.40	17.65	Unknown	59	10	4.57	Yes	Yes		3.94	1.62	2010.282	0.10	0.14	3.01
S2-345	15.40	—	Unknown	24	0	10.58	Yes	Yes		1.78	-1.18	2015.482	0.26	0.28	3.03
S1-50	15.41	17.73	Unknown	58	8	1.93	No	No		1.48	0.66	2009.664	0.12	0.07	5.31
S5-131	15.41	17.83	Late	58	12	1.20	No	No		4.87	-2.55	2010.240	0.10	0.06	13.43
S3-62	15.41	17.61	Unknown	29	10	2.96	Yes	Yes		2.70	-1.53	2011.039	0.11	0.06	5.70
S3-31	15.41	17.37	Unknown	55	11	1.66	No	No		3.39	0.39	2009.878	0.13	0.09	1.92
S6-80	15.42	17.73	Late	59	12	1.50	No	No		5.03	-4.86	2010.739	0.07	0.06	3.52
S3-128	15.42	17.83	Unknown	34	5	6.21	Yes	Yes		0.40	-3.30	2009.397	0.12	0.09	1.61
S1-175	15.42	17.67	Unknown	48	11	4.70	No	Yes		-1.41	-0.34	2014.063	0.17	0.10	11.34
S4-314	15.43	17.63	Early	59	12	0.64	No	No		4.41	-2.03	2010.075	0.08	0.04	22.86

Table A.1 (cont'd): Catalog of stars in variability study sample

Star	Mean Mag (K')	Mean Mag (H)	Spectral Type	Nights Det. (K')	Nights Det. (H)	$\chi^2_{\rm red}$	Var.? (G19)	Var.?	Var. Type	x_0 ($''$ E of Sgr A*)	y_0 ($''$ N of Sgr A*)	t_0	RMS	IQR	$1/\eta$
S2-60	15.44	17.61	Unknown	28	12	1.14	No	No		-1.45	2.06	2009.864	0.10	0.05	7.49
S2-63	15.44	17.73	Unknown	59	12	1.08	No	No		-0.65	2.47	2010.227	0.11	0.05	21.58
S3-314	15.45	17.60	Early	59	12	1.09	No	No		3.84	-0.09	2010.262	0.10	0.04	7.29
S1-62	15.45	17.88	Unknown	59	11	5.05	Yes	Yes		0.44	1.80	2010.021	0.11	0.10	2.08
S3-209	15.46	17.23	Unknown	58	11	0.89	No	No		-2.93	-1.98	2010.310	0.11	0.04	7.03
S0-19	15.46	17.63	Early	58	12	5.29	Yes	Yes		-0.01	0.40	2009.642	0.12	0.12	1.88
S5-165	15.47	17.72	Late	58	12	0.43	No	No		4.88	-2.86	2010.181	0.08	0.02	19.04
S1-66	15.47	17.70	Late	48	9	1.93	No	No		-0.81	-1.74	2009.970	0.13	0.07	12.84
S2-68	15.47	18.17	Unknown	59	12	11.07	Yes	Yes		-1.81	1.95	2010.217	0.14	0.23	2.19
S6-48	15.47	17.77	Late	49	11	1.48	No	No		4.88	-4.16	2009.975	0.08	0.06	6.06
S1-6	15.47	17.77	Late	33	10	7.31	Yes	Yes	L	-0.96	0.74	2008.886	0.12	0.13	2.55
S0-62	15.47	17.73	Unknown	59	12	4.32	Yes	Yes		0.16	-0.54	2010.228	0.12	0.11	5.22
S2-308	15.47	17.64	Late	54	10	0.89	No	No		-0.64	-2.85	2010.059	0.11	0.04	12.38
S2-40	15.47	17.66	Early	52	12	3.23	Yes	Yes		1.74	1.27	2009.828	0.11	0.09	2.96
S2-66	15.47	18.67	Late	28	6	146.99	Yes	Yes	L	-1.44	2.14	2009.690	0.41	0.33	2.37
S4-56	15.47	17.92	Unknown	44	5	3.41	Yes	Yes		-0.99	3.99	2010.465	0.13	0.09	1.50
S3-437	15.48	17.83	Unknown	38	12	4.65	Yes	Yes		2.69	-1.38	2013.944	0.13	0.08	12.65
S3-383	15.48	17.78	Late	59	11	1.23	No	No		3.92	-0.56	2010.082	0.09	0.05	13.10
S4-103	15.49	17.94	Unknown	59	11	2.33	No	Yes		4.21	-0.36	2010.052	0.11	0.08	12.37
S0-28	15.49	—	Late	40	0	8.52	No	Yes		-0.14	-0.49	2007.822	0.11	0.20	5.14
S6-142	15.49	17.85	Late	46	9	1.80	No	No		5.47	-3.56	2011.172	0.12	0.09	1.27
S5-24	15.49	18.38	Unknown	39	7	2.22	Yes	No		-5.00	-0.89	2010.110	0.11	0.09	0.77
S2-46	15.50	17.73	Unknown	59	11	1.62	Yes	No		2.17	-0.71	2010.099	0.10	0.06	5.66
S1-64	15.50	18.04	Unknown	59	11	9.42	Yes	Yes	L	0.66	1.82	2010.079	0.13	0.15	6.81
S2-134	15.50	17.67	Late	59	11	2.64	Yes	Yes		-0.99	-2.00	2010.568	0.12	0.08	7.29
S3-92	15.50	—	Unknown	17	0	3.53	Yes	No		-1.35	2.88	2009.116	0.13	0.10	1.52
S6-340	15.50	—	Unknown	35	0	7.79	No	Yes		-4.11	-4.39	2011.385	0.16	0.04	0.93
S4-105	15.50	18.26	Unknown	59	12	0.84	No	No		-2.82	-3.18	2010.228	0.12	0.04	34.86
S1-38	15.50	—	Unknown	23	0	5.10	Yes	Yes		0.31	1.38	2009.622	0.14	0.13	1.60
S7-2	15.51	17.85	Unknown	50	9	2.68	Yes	Yes		3.37	-6.31	2010.793	0.11	0.12	1.54
S0-16	15.51	17.70	Early	42	11	35.14	Yes	Yes	L	0.23	0.17	2007.593	0.33	0.31	2.63
S2-43	15.51	17.88	Unknown	58	11	0.90	No	No		-1.83	-1.14	2010.082	0.11	0.04	34.10
S1-26	15.51	17.71	Unknown	59	12	5.41	Yes	Yes		-0.88	0.39	2010.306	0.12	0.11	6.32
S1-67	15.51	17.83	Late	58	12	0.46	No	No		-1.43	-1.32	2010.456	0.11	0.04	19.68

Table A.1 (cont'd): Catalog of stars in variability study sample

Star	Mean Mag (K')	Mean Mag (H)	Spectral Type	Nights Det. (K')	Nights Det. (H)	$\chi^2_{\rm red}$	Var.? (G19)	Var.?	Var. Type	x_0 ($''$ E of Sgr A*)	y_0 ($''$ N of Sgr A*)	t_0	RMS	IQR	$1/\eta$
S6-341	15.52	—	Unknown	39	0	5.80	No	Yes		-4.12	-4.44	2010.942	0.18	0.07	0.79
S3-24	15.52	17.85	Unknown	46	5	4.00	No	Yes		3.29	0.45	2009.493	0.11	0.07	1.15
S3-109	15.53	17.96	Late	30	10	1.63	No	No		-3.19	0.42	2010.197	0.12	0.07	19.95
S1-59	15.53	17.32	Unknown	21	10	3.80	No	Yes		0.02	1.78	2007.241	0.12	0.10	1.82
S1-47	15.53	17.71	Unknown	57	12	5.02	Yes	Yes		-1.61	0.43	2010.417	0.13	0.12	3.65
S5-106	15.53	18.01	Unknown	41	12	2.19	No	No		-4.35	-3.20	2010.067	0.10	0.08	2.38
S3-139	15.53	17.75	Unknown	54	9	1.26	No	No		0.06	-3.35	2010.399	0.10	0.06	2.57
S1-55	15.54	18.00	Unknown	57	10	4.04	Yes	Yes		1.59	0.64	2008.856	0.12	0.12	8.35
S3-50	15.54	17.75	Unknown	59	12	2.37	Yes	Yes		-1.88	-2.33	2010.312	0.12	0.07	4.11
S2-198	15.54	17.93	Late	58	11	2.32	No	Yes		0.41	-2.48	2009.978	0.12	0.09	12.58
S3-169	15.54	17.91	Unknown	53	12	0.27	No	No		-3.39	0.37	2010.038	0.10	0.03	25.19
S0-29	15.54	17.58	Late	27	7	2.78	No	No		0.37	-0.44	2009.722	0.11	0.06	4.37
S5-6	15.55	18.42	Unknown	59	12	1.80	No	No		-4.81	-1.46	2009.544	0.14	0.08	6.78
S5-252	15.55	17.80	Late	45	9	4.85	Yes	Yes		5.50	-1.23	2012.288	0.17	0.12	0.95
S3-160	15.57	—	Unknown	19	0	5.63	Yes	Yes		3.30	0.79	2009.133	0.11	0.14	1.27
S2-317	15.57	17.82	Late	56	10	1.46	No	No		-0.71	-2.87	2010.148	0.10	0.05	5.80
S5-124	15.57	17.77	Unknown	44	11	1.82	No	No		-1.85	-5.16	2009.615	0.11	0.05	5.20
S1-54	15.57	18.05	Unknown	57	11	4.86	Yes	Yes		-1.51	0.75	2009.661	0.15	0.12	3.90
S2-83	15.58	17.95	Late	57	12	1.46	Yes	No		2.86	-0.69	2009.982	0.11	0.07	10.32
S4-97	15.58	17.68	Unknown	59	12	0.49	No	No		-0.95	-4.12	2010.207	0.11	0.03	21.19
S3-108	15.58	17.83	Unknown	59	12	1.37	No	No		-0.89	3.12	2010.133	0.13	0.09	7.82
S5-288	15.58	17.81	Unknown	49	10	3.83	Yes	Yes		5.33	0.16	2011.188	0.12	0.13	1.08
S6-53	15.58	—	Unknown	29	0	2.18	No	No		-3.69	-5.33	2009.250	0.11	0.07	2.64
S2-80	15.58	17.85	Late	59	12	2.21	Yes	Yes		2.20	1.81	2010.224	0.10	0.05	12.92
S6-8	15.59	17.83	Unknown	59	12	0.72	No	No		-0.76	-6.01	2009.881	0.10	0.04	3.97
S0-67	15.59	17.85	Unknown	52	12	3.36	Yes	Yes		0.25	-0.54	2009.197	0.11	0.10	2.53
S5-143	15.59	17.71	Late	36	12	1.88	No	No		4.01	-3.89	2010.237	0.11	0.05	10.11
S1-56	15.59	18.08	Unknown	57	10	56.47	Yes	Yes	L	-1.11	1.32	2009.763	0.23	0.32	3.11
S5-210	15.60	17.80	Unknown	58	10	4.36	Yes	Yes		-1.82	-5.66	2009.694	0.11	0.10	1.30
S2-212	15.60	17.79	Late	58	11	2.87	Yes	Yes		0.17	-2.59	2009.949	0.10	0.08	6.47
S1-36	15.60	17.79	Late	16	12	1.16	No	No		-0.53	-1.21	2010.227	0.14	0.08	6.79
S2-268	15.60	18.15	Unknown	59	12	4.50	Yes	Yes		-2.78	0.48	2010.071	0.14	0.11	10.64
S4-67	15.61	18.26	Unknown	58	10	7.62	Yes	Yes		2.82	-3.04	2010.016	0.16	0.16	2.25
S6-28	15.61	17.88	Late	56	11	1.43	No	No		5.01	-3.66	2010.052	0.10	0.06	10.90

Table A.1 (cont'd): Catalog of stars in variability study sample

Star	Mean Mag (K')	Mean Mag (H)	Spectral Type	Nights Det. (K')	Nights Det. (H)	$\chi^2_{\rm red}$	Var.? (G19)	Var.?	Var. Type	x_0 ($''$ E of Sgr A*)	y_0 ($''$ N of Sgr A*)	t_0	RMS	IQR	$1/\eta$
S2-42	15.61	17.98	Unknown	46	10	9.04	Yes	Yes	L	0.49	2.15	2009.692	0.12	0.14	3.25
S5-55	15.61	17.90	Late	39	12	13.87	Yes	Yes		3.20	-4.07	2010.520	0.14	0.17	12.49
S5-94	15.61	18.07	Unknown	35	12	0.94	No	No		4.92	2.12	2008.726	0.07	0.05	9.62
S4-310	15.62	17.41	Unknown	18	12	1.50	No	No		4.55	1.67	2008.981	0.09	0.07	5.67
S5-80	15.62	17.84	Unknown	36	12	0.63	No	No		0.24	-5.30	2009.782	0.10	0.05	5.76
S1-58	15.62	17.99	Unknown	55	11	6.70	Yes	Yes	L	-1.49	0.97	2010.095	0.13	0.15	4.93
S6-55	15.62	17.85	Late	52	11	1.96	Yes	No		5.00	-4.11	2010.196	0.09	0.04	6.92
S4-280	15.62	18.09	Unknown	49	12	3.18	Yes	Yes		1.23	-4.60	2010.339	0.12	0.09	18.89
S1-44	15.62	17.89	Late	48	7	8.09	Yes	Yes		0.33	1.64	2010.839	0.12	0.15	1.60
S2-64	15.62	17.78	Late	59	11	2.68	Yes	Yes		2.63	0.25	2010.053	0.13	0.09	2.37
S5-116	15.63	18.05	Unknown	18	12	2.39	No	No		2.55	-4.78	2007.445	0.10	0.09	8.88
S4-167	15.63	17.92	Unknown	50	12	0.41	No	No		3.73	2.42	2010.133	0.10	0.03	20.89
S5-180	15.63	17.78	Unknown	17	11	0.64	No	No		-2.79	-5.01	2008.004	0.10	0.04	5.06
S3-104	15.63	18.27	Unknown	57	11	6.50	Yes	Yes		-3.17	-0.66	2010.439	0.16	0.15	5.37
S4-273	15.63	17.89	Unknown	59	12	1.54	No	No		-1.15	-4.61	2009.965	0.09	0.05	6.97
S3-229	15.64	18.34	Unknown	59	11	6.46	Yes	Yes		1.56	-3.22	2010.224	0.15	0.17	7.66
S5-44	15.64	17.87	Late	59	12	1.89	No	No		3.52	-3.74	2010.094	0.10	0.05	12.30
S0-27	15.64	17.82	Late	55	11	2.95	Yes	Yes		0.15	0.55	2009.841	0.12	0.09	2.57
S3-176	15.64	—	Unknown	32	0	7.68	Yes	Yes		3.09	1.43	2009.859	0.17	0.14	2.83
S4-40	15.64	17.95	Unknown	59	12	1.98	Yes	No		-1.97	-3.61	2010.232	0.11	0.05	14.26
S1-37	15.64	—	Unknown	24	0	2.03	No	No		-1.33	0.46	2009.307	0.11	0.06	4.21
S5-25	15.64	18.01	Unknown	35	12	0.30	No	No		-2.58	-4.37	2010.133	0.10	0.02	15.94
S4-51	15.64	17.76	Unknown	30	12	0.37	No	No		3.17	2.63	2011.116	0.09	0.04	26.26
S6-40	15.65	17.82	Unknown	38	9	2.54	Yes	No		0.09	-6.34	2009.538	0.18	0.18	0.70
S3-132	15.65	—	Unknown	24	0	12.83	Yes	Yes	L	-0.51	-3.29	2009.618	0.15	0.25	2.08
S5-126	15.66	16.86	Unknown	59	12	0.60	No	No		-0.04	-5.47	2009.751	0.10	0.03	8.11
S1-65	15.66	17.80	Unknown	59	11	1.63	No	No		1.48	1.28	2009.943	0.11	0.07	3.62
S1-167	15.67	—	Unknown	25	0	6.67	Yes	Yes		0.77	-1.83	2009.394	0.14	0.13	2.82
S2-76	15.67	18.34	Early	47	11	7.65	Yes	Yes		-0.22	2.81	2011.550	0.15	0.15	3.41
S5-209	15.67	17.92	Unknown	56	12	1.03	No	No		-2.93	-5.15	2008.589	0.10	0.04	4.89
S4-140	15.67	18.03	Unknown	55	12	0.73	No	No		3.17	2.98	2010.071	0.08	0.03	18.27
S6-33	15.68	18.06	Unknown	58	11	2.45	Yes	Yes		-3.61	-5.09	2009.762	0.11	0.05	4.57
S6-181	15.68	18.00	Late	56	10	2.19	Yes	No		5.31	-4.21	2010.492	0.11	0.07	2.09
S2-261	15.68	18.26	Unknown	59	12	4.24	Yes	Yes		-2.60	1.01	2009.671	0.14	0.09	10.96

Table A.1 (cont'd): Catalog of stars in variability study sample

Star	Mean Mag (K')	Mean Mag (H)	Spectral Type	Nights Det. (K')	Nights Det. (H)	$\chi^2_{\rm red}$	Var.? (G19)	Var.?	Var. Type	x_0 ($''$ E of Sgr A*)	y_0 ($''$ N of Sgr A*)	t_0	RMS	IQR	$1/\eta$
S0-24	15.68	17.78	Unknown	53	11	3.83	Yes	Yes		0.20	0.09	2008.557	0.15	0.16	4.76
S5-203	15.68	17.96	Unknown	36	6	11.64	Yes	Yes		-0.23	-5.87	2009.735	0.17	0.18	1.13
S6-61	15.69	18.03	Unknown	40	9	1.41	No	No		-3.93	-5.26	2009.531	0.12	0.10	6.83
S3-263	15.69	17.84	Unknown	58	11	3.35	Yes	Yes		-0.40	-3.64	2010.140	0.11	0.11	6.46
S3-167	15.69	—	Unknown	55	0	38.25	Yes	Yes	L	-3.07	1.41	2009.976	0.29	0.47	15.28
S6-52	15.69	17.97	Unknown	55	10	2.87	Yes	Yes		-1.61	-6.24	2012.171	0.24	0.19	1.26
S1-31	15.69	18.01	Late	50	12	1.56	No	No		-0.99	0.54	2010.569	0.11	0.06	6.55
S3-225	15.69	18.08	Unknown	59	10	2.91	Yes	Yes		1.45	-3.26	2009.856	0.14	0.13	2.62
S6-30	15.69	17.89	Unknown	58	10	1.51	No	No		0.58	-6.20	2009.828	0.11	0.08	2.85
S4-31	15.69	17.92	Unknown	59	12	15.77	Yes	Yes	L	-2.21	-3.43	2010.415	0.13	0.09	8.74
S3-91	15.70	17.88	Unknown	59	10	5.04	Yes	Yes		-1.71	-2.67	2010.365	0.12	0.10	4.63
S4-107	15.70	17.77	Unknown	59	10	2.57	Yes	Yes		3.93	1.54	2011.962	0.09	0.10	4.07
S6-36	15.70	18.31	Unknown	55	9	1.77	No	No		-4.60	-4.28	2009.482	0.13	0.09	2.89
S1-170	15.70	—	Unknown	51	0	3.79	Yes	Yes		1.57	-1.19	2009.609	0.13	0.14	2.47
S3-65	15.70	18.02	Unknown	58	10	2.21	No	Yes		-1.24	-2.80	2009.687	0.10	0.06	8.73
S2-319	15.70	18.03	Late	57	7	1.31	No	No		0.99	-2.78	2009.644	0.10	0.05	7.95
S3-151	15.70	18.08	Late	56	11	2.17	No	No		1.91	-2.78	2009.954	0.15	0.08	3.67
S2-65	15.71	18.24	Late	59	11	9.18	Yes	Yes		2.36	-1.07	2009.829	0.19	0.16	13.89
S2-200	15.71	18.08	Unknown	39	12	2.86	Yes	Yes		-2.53	0.01	2009.425	0.13	0.11	19.87
S4-44	15.72	—	Unknown	37	0	8.65	Yes	Yes		2.40	3.32	2009.727	0.13	0.13	2.60
S3-215	15.74	18.18	Unknown	58	10	1.39	No	No		1.33	-3.30	2010.030	0.12	0.08	2.99
S1-40	15.74	—	Unknown	33	0	6.25	Yes	Yes		-1.41	-0.61	2010.207	0.13	0.13	6.50
S3-256	15.74	18.23	Unknown	43	12	14.47	Yes	Yes		-1.85	-3.18	2009.353	0.12	0.20	6.43
S5-127	15.74	17.88	Late	59	12	0.63	No	No		4.79	-2.64	2010.228	0.09	0.04	18.36
S0-108	15.74	17.77	Unknown	33	11	4.87	Yes	Yes		0.45	-0.90	2015.921	0.11	0.15	2.17
S2-208	15.74	18.56	Unknown	55	12	18.95	Yes	Yes	L	-2.05	1.58	2010.131	0.20	0.21	3.94
S2-51	15.74	18.15	Late	59	12	1.82	Yes	No		0.74	2.14	2009.837	0.11	0.07	5.61
S2-44	15.74	18.32	Unknown	59	11	3.81	Yes	Yes		0.52	-2.14	2009.503	0.15	0.10	2.56
S4-123	15.75	18.17	Unknown	59	12	1.02	No	No		2.27	3.63	2010.065	0.09	0.05	6.11
S1-41	15.75	17.99	Unknown	56	6	6.42	Yes	Yes		0.96	1.14	2010.300	0.14	0.16	2.79
S5-137	15.75	—	Unknown	23	0	7.65	Yes	Yes		3.59	4.19	2009.603	0.19	0.18	0.80
S2-346	15.75	—	Unknown	20	0	10.46	Yes	Yes		-1.96	0.78	2013.182	0.21	0.12	2.38
S4-217	15.76	18.08	Unknown	41	11	1.26	No	No		2.18	-4.04	2010.231	0.09	0.03	8.04
S3-90	15.76	18.06	Unknown	29	10	3.28	No	Yes		2.73	-1.56	2008.232	0.15	0.12	6.11

Table A.1 (cont'd): Catalog of stars in variability study sample

Star	Mean Mag (K')	Mean Mag (H)	Spectral Type	Nights Det. (K')	Nights Det. (H)	$\chi^2_{\rm red}$	Var.? (G19)	Var.?	Var. Type	x_0 ($''$ E of Sgr A*)	y_0 ($''$ N of Sgr A*)	t_0	RMS	IQR	$1/\eta$
S3-83	15.77	18.24	Unknown	53	11	3.78	Yes	Yes		-2.32	-2.12	2009.548	0.17	0.11	7.48
S2-205	15.77	18.07	Late	41	11	2.76	Yes	Yes		0.48	2.49	2010.052	0.10	0.04	4.60
S2-175	15.78	18.05	Unknown	33	7	14.61	Yes	Yes	L	2.07	-1.21	2009.495	0.17	0.22	1.43
S5-162	15.78	18.06	Unknown	59	12	1.69	Yes	No		5.17	-2.25	2010.076	0.09	0.08	4.54
S3-59	15.79	17.99	Unknown	57	11	5.54	Yes	Yes		-2.42	-1.88	2010.347	0.13	0.13	3.63
S4-131	15.79	18.33	Unknown	59	11	1.54	Yes	No		1.47	-4.04	2010.142	0.11	0.06	9.58
S4-262	15.79	17.77	Early	59	12	45.69	Yes	Yes	L	4.28	-1.96	2010.562	0.23	0.09	25.80
S3-120	15.79	18.05	Unknown	54	11	1.35	No	No		0.10	-3.29	2010.051	0.12	0.05	3.16
S3-294	15.79	18.34	Unknown	53	9	4.10	Yes	Yes		0.52	3.75	2010.542	0.20	0.13	0.90
S5-217	15.79	18.17	Unknown	59	11	0.82	No	No		2.45	-5.46	2010.004	0.10	0.04	12.97
S2-89	15.79	18.18	Unknown	57	5	4.91	Yes	Yes		1.06	-1.69	2010.077	0.13	0.10	5.49
S4-30	15.79	18.45	Unknown	54	5	13.73	Yes	Yes		2.52	3.23	2009.975	0.17	0.22	4.99
S2-14	15.79	18.22	Unknown	53	12	2.97	Yes	Yes		-1.56	-1.41	2010.393	0.12	0.09	7.24
S4-288	15.80	18.13	Unknown	38	12	0.82	No	No		-2.69	-3.95	2007.873	0.12	0.03	11.31
S2-128	15.80	—	Unknown	52	0	6.86	Yes	Yes		1.09	-1.89	2010.052	0.14	0.11	3.17
S5-79	15.80	18.07	Unknown	59	12	0.75	No	No		4.68	-2.46	2010.007	0.10	0.03	9.56
S3-123	15.80	17.96	Unknown	50	11	1.40	No	No		-1.14	-3.10	2009.922	0.10	0.06	9.39
S4-82	15.81	18.28	Unknown	58	11	2.10	Yes	No		2.62	3.27	2010.005	0.12	0.07	2.95
S1-159	15.82	18.34	Unknown	56	6	7.21	Yes	Yes		1.32	-1.43	2010.637	0.16	0.17	3.70
S3-241	15.82	18.11	Unknown	59	12	1.02	No	No		2.47	2.68	2010.342	0.08	0.05	10.71
S4-284	15.82	18.05	Unknown	58	11	1.15	No	No		-0.95	-4.70	2010.239	0.10	0.05	12.61
S2-219	15.82	18.11	Unknown	56	10	9.94	Yes	Yes	L	-1.57	-2.09	2009.939	0.13	0.14	3.74
S1-42	15.82	18.22	Unknown	56	8	6.85	Yes	Yes		0.92	1.23	2010.216	0.16	0.12	1.86
S1-7	15.82	18.16	Unknown	59	11	2.98	Yes	Yes		-1.05	-0.58	2010.057	0.11	0.10	10.69
S6-50	15.83	18.17	Unknown	33	12	1.18	No	No		-3.13	-5.61	2008.044	0.09	0.06	3.57
S4-42	15.83	—	Unknown	25	0	2.53	No	No		-0.01	4.12	2008.802	0.23	0.38	0.74
S2-39	15.83	18.19	Unknown	53	12	0.68	No	No		-1.94	-0.72	2010.771	0.12	0.04	16.87
S7-6	15.83	18.33	Unknown	30	10	3.00	Yes	Yes		-4.07	-6.25	2007.225	0.12	0.09	1.38
S3-338	15.83	18.30	Unknown	48	12	1.62	No	No		-3.82	-0.46	2010.136	0.11	0.08	8.08
S3-357	15.83	18.20	Unknown	59	12	0.38	No	No		3.14	2.32	2010.033	0.09	0.02	13.58
S5-216	15.84	18.31	Unknown	58	10	0.83	No	No		2.22	-5.55	2009.968	0.09	0.03	7.17
S2-127	15.84	—	Unknown	57	0	5.87	Yes	Yes		0.20	-2.21	2010.148	0.13	0.13	2.26
S4-220	15.84	—	Unknown	28	0	2.74	No	No		1.95	4.16	2009.918	0.16	0.17	0.65
S4-23	15.84	18.24	Unknown	59	12	8.83	Yes	Yes		1.47	-3.78	2009.563	0.13	0.15	3.02

Table A.1 (cont'd): Catalog of stars in variability study sample

Star	Mean Mag (K')	Mean Mag (H)	Spectral Type	Nights Det. (K')	Nights Det. (H)	$\chi^2_{\rm red}$	Var.? (G19)	Var.?	Var. Type	x_0 ($''$ E of Sgr A*)	y_0 ($''$ N of Sgr A*)	t_0	RMS	IQR	$1/\eta$
S2-195	15.84	18.07	Unknown	21	12	5.64	Yes	Yes		-2.03	1.45	2008.883	0.12	0.13	2.01
S6-26	15.85	18.35	Unknown	59	10	2.99	Yes	Yes		2.52	-5.68	2010.345	0.11	0.09	1.66
S5-150	15.85	18.29	Unknown	58	12	9.51	Yes	Yes		-3.91	-4.02	2009.922	0.13	0.11	2.99
S1-61	15.85	17.98	Unknown	28	12	0.60	No	No		-1.54	-0.97	2009.863	0.10	0.03	15.26
S6-9	15.86	18.33	Unknown	59	11	3.33	Yes	Yes		2.59	-5.48	2010.176	0.13	0.10	5.48
S5-84	15.86	18.35	Unknown	59	12	5.30	Yes	Yes		-2.74	-4.53	2009.918	0.15	0.14	5.96
S3-48	15.86	18.24	Unknown	50	12	1.71	No	No		-2.97	0.36	2010.409	0.13	0.05	17.18
S0-8	15.87	17.83	Early	53	11	6.02	Yes	Yes		-0.23	0.16	2008.370	0.13	0.10	0.88
S3-153	15.87	18.28	Unknown	59	11	1.96	Yes	No		1.60	2.98	2010.038	0.10	0.05	4.11
S4-278	15.87	18.27	Unknown	59	12	0.70	No	No		-2.52	-4.02	2010.112	0.10	0.03	10.60
S5-81	15.87	—	Unknown	27	0	2.94	No	No		4.21	3.21	2009.244	0.14	0.11	1.59
S6-262	15.88	18.13	Unknown	32	6	1.43	No	No		2.49	-6.46	2007.330	0.13	0.17	1.02
S4-50	15.88	18.39	Unknown	58	12	0.66	No	No		3.08	2.76	2010.565	0.09	0.03	8.74
S4-187	15.88	18.60	Unknown	58	11	11.41	Yes	Yes		0.43	-4.48	2010.301	0.16	0.18	19.94
S4-47	15.88	18.37	Unknown	58	11	2.80	No	Yes		2.57	-3.21	2009.974	0.14	0.10	10.46
S3-302	15.89	18.44	Unknown	57	9	2.42	Yes	Yes		0.09	3.77	2010.134	0.11	0.07	0.78
S1-27	15.89	18.55	Unknown	48	10	136.61	Yes	Yes	L	-1.03	0.19	2008.871	0.40	0.67	25.34
S4-66	15.90	18.36	Unknown	58	11	11.84	Yes	Yes		2.73	-3.13	2010.371	0.14	0.18	1.38
S4-74	15.90	18.28	Unknown	59	12	0.81	No	No		0.12	-4.16	2009.978	0.11	0.04	14.52
S6-59	15.90	18.30	Unknown	48	11	1.15	No	No		3.50	-5.53	2009.593	0.09	0.06	3.29
S2-56	15.91	18.24	Unknown	56	12	3.12	Yes	Yes		-0.26	2.39	2010.441	0.11	0.09	7.89
S2-45	15.91	—	Unknown	58	0	13.33	Yes	Yes	L	-2.15	0.57	2009.461	0.20	0.20	8.18
S3-369	15.91	18.63	Unknown	51	11	7.33	Yes	Yes		-1.97	3.42	2010.217	0.19	0.19	6.11
S0-20	15.91	17.96	Early	39	12	6.11	Yes	Yes		0.05	0.14	2008.089	0.14	0.16	0.88
S7-0	15.92	18.21	Unknown	59	12	1.50	No	No		4.05	-5.79	2010.193	0.10	0.06	4.98
S6-34	15.92	18.48	Unknown	24	10	1.82	No	No		5.28	3.32	2010.999	0.13	0.06	1.27
S4-63	15.92	17.97	Unknown	35	12	0.39	No	No		-0.29	-4.12	2010.019	0.10	0.02	14.98
S4-164	15.92	18.30	Unknown	45	12	1.21	No	No		3.75	2.33	2010.396	0.09	0.05	8.56
S5-155	15.94	18.40	Unknown	46	12	1.63	No	No		4.72	3.02	2009.628	0.08	0.05	6.06
S3-124	15.94	18.71	Unknown	59	12	21.16	Yes	Yes	L	1.85	2.72	2009.849	0.19	0.28	4.71
S5-4	15.94	18.32	Unknown	39	12	0.68	No	No		-2.39	-4.42	2009.825	0.11	0.03	11.50
S4-341	15.94	18.15	Unknown	45	12	0.74	No	No		4.18	-2.62	2009.378	0.09	0.06	7.65
S3-116	15.94	18.19	Unknown	55	12	0.36	No	No		2.24	2.34	2010.033	0.10	0.03	14.27
S5-208	15.95	18.01	Unknown	32	5	13.57	Yes	Yes		-0.01	-5.92	2009.446	0.20	0.26	0.61

Table A.1 (cont'd): Catalog of stars in variability study sample

Star	Mean Mag (K')	Mean Mag (H)	Spectral Type	Nights Det. (K')	Nights Det. (H)	$\chi^2_{\rm red}$	Var.? (G19)	Var.?	Var. Type	x_0 ($''$ E of Sgr A*)	y_0 ($''$ N of Sgr A*)	t_0	RMS	IQR	$1/\eta$
S2-304	15.95	18.24	Unknown	46	8	3.57	No	Yes		2.52	1.46	2009.803	0.11	0.09	2.01
S2-54	15.95	18.35	Unknown	58	11	6.97	Yes	Yes		2.29	-0.68	2009.512	0.15	0.16	11.67
S0-17	15.96	18.28	Late	57	11	11.99	Yes	Yes	L	0.05	0.01	2008.821	0.20	0.22	5.56
S5-49	15.96	18.47	Unknown	59	12	2.76	No	Yes		4.90	1.61	2009.661	0.14	0.14	8.11
S6-276	15.96	18.17	Unknown	56	8	5.93	Yes	Yes		5.00	-4.73	2010.832	0.17	0.12	1.11
S4-195	15.96	18.42	Unknown	18	8	1.99	No	No		2.42	3.81	2008.847	0.10	0.08	3.76
S3-171	15.96	18.20	Unknown	21	12	0.69	No	No		2.44	2.40	2008.434	0.09	0.03	27.94
S5-197	15.96	18.10	Unknown	57	11	1.86	Yes	No		-1.09	-5.73	2009.992	0.10	0.07	3.96
S5-118	15.96	18.72	Unknown	57	10	0.69	No	No		-4.85	-2.44	2010.044	0.10	0.06	4.18
S6-275	15.97	18.40	Unknown	18	9	1.23	No	No		-4.27	-5.06	2008.461	0.09	0.07	3.32
S4-152	15.97	18.27	Unknown	28	12	0.57	No	No		3.45	2.73	2007.250	0.08	0.04	8.04
S5-7	15.97	18.23	Unknown	59	11	1.18	No	No		1.04	-4.89	2010.172	0.11	0.07	10.12
S1-43	15.98	18.18	Unknown	59	11	3.87	Yes	Yes		1.11	1.21	2009.649	0.14	0.18	1.13
S5-22	15.98	18.48	Unknown	59	12	4.50	No	Yes		-3.06	-4.05	2009.907	0.12	0.11	1.10
S2-129	15.98	18.35	Unknown	58	11	0.87	No	No		-1.82	-1.21	2010.015	0.11	0.04	18.39
S6-69	15.98	18.46	Unknown	52	11	3.14	Yes	Yes		-4.25	-5.20	2009.190	0.19	0.15	2.86
S6-54	15.99	18.15	Unknown	55	6	2.63	No	Yes		-1.92	-6.18	2010.215	0.20	0.11	0.90
S5-259	15.99	18.38	Unknown	56	10	1.32	No	No		5.26	-1.88	2010.305	0.11	0.07	4.23
S3-388	15.99	18.29	Unknown	57	12	1.52	No	No		-2.43	-3.16	2010.340	0.11	0.04	10.33
S2-237	15.99	18.77	Unknown	57	10	3.08	Yes	Yes		-0.44	-2.67	2010.546	0.12	0.10	13.06
S3-334	15.99	18.66	Unknown	48	6	8.23	Yes	Yes		-0.60	3.82	2010.028	0.16	0.19	2.09
S4-109	16.00	18.41	Unknown	59	12	0.53	No	No		-2.49	-3.44	2010.118	0.11	0.02	25.43
S6-46	16.00	18.60	Unknown	53	5	3.29	Yes	Yes		-4.00	-4.99	2009.819	0.13	0.10	2.53
S4-181	16.00	18.56	Unknown	57	10	3.01	Yes	Yes		0.96	-4.40	2010.232	0.10	0.09	7.37
S4-464	16.01	18.94	Unknown	46	9	4.97	Yes	Yes		-4.33	-1.23	2013.647	0.16	0.13	1.79
S6-229	16.01	18.23	Unknown	36	7	6.20	Yes	Yes		5.56	-3.51	2007.370	0.13	0.15	0.65
S6-65	16.01	18.36	Unknown	53	8	2.33	Yes	Yes		-4.03	-5.25	2009.457	0.11	0.11	2.64
S7-4	16.01	18.50	Unknown	40	11	2.42	Yes	No		-4.27	-6.00	2008.418	0.15	0.16	1.14
S7-106	16.02	18.27	Unknown	19	10	1.59	No	No		5.26	-4.88	2010.564	0.10	0.07	1.02
S4-173	16.02	18.65	Unknown	59	12	2.49	No	Yes		-3.20	-3.10	2010.375	0.14	0.10	17.93
S5-200	16.02	18.62	Unknown	40	5	2.22	No	No		4.36	3.92	2010.156	0.13	0.08	1.09
S4-69	16.03	18.57	Unknown	26	10	5.45	Yes	Yes		-3.00	2.83	2010.265	0.12	0.10	1.45
S1-28	16.03	18.48	Unknown	55	11	2.05	No	No		-0.37	-1.05	2010.273	0.12	0.07	6.55
S1-57	16.04	18.44	Unknown	48	6	9.01	Yes	Yes	L	0.32	1.73	2010.422	0.17	0.21	2.16

Table A.1 (cont'd): Catalog of stars in variability study sample

Star	Mean Mag (K')	Mean Mag (H)	Spectral Type	Nights Det. (K')	Nights Det. (H)	$\chi^2_{\rm red}$	Var.? (G19)	Var.?	Var. Type	x_0 ($''$ E of Sgr A*)	y_0 ($''$ N of Sgr A*)	t_0	RMS	IQR	$1/\eta$
S5-107	16.04	18.64	Unknown	59	11	1.51	No	No		-4.60	-2.76	2009.994	0.11	0.07	3.29
S1-46	16.04	18.71	Unknown	59	12	20.40	Yes	Yes	L	-0.10	-1.60	2010.018	0.21	0.27	22.95
S4-55	16.04	18.32	Unknown	59	12	2.94	Yes	Yes		4.10	-0.58	2010.204	0.10	0.08	17.71
S5-148	16.04	18.82	Unknown	24	7	6.58	Yes	Yes		-3.82	-4.05	2009.194	0.14	0.13	3.41
S1-144	16.05	18.39	Unknown	47	6	4.42	Yes	Yes		1.63	-0.94	2008.913	0.13	0.07	1.48
S4-34	16.05	18.52	Unknown	58	12	1.94	No	No		1.60	-3.77	2009.979	0.12	0.06	11.26
S0-33	16.05	18.16	Unknown	33	11	3.16	No	Yes		0.65	-0.53	2010.172	0.15	0.13	3.44
S1-171	16.05	18.12	Unknown	48	7	12.26	Yes	Yes		-0.76	-1.73	2010.726	0.19	0.15	1.49
S3-435	16.06	18.09	Unknown	18	9	2.13	No	No		3.72	-0.06	2014.117	0.10	0.04	2.18
S2-259	16.07	18.31	Unknown	59	12	2.50	Yes	Yes		-2.13	-1.77	2010.002	0.14	0.08	3.91
S2-321	16.07	18.12	Unknown	52	11	2.09	Yes	No		-2.43	-1.69	2009.332	0.13	0.07	3.33
S3-391	16.08	18.87	Unknown	51	10	15.37	Yes	Yes	L	-2.79	2.82	2009.882	0.23	0.27	5.73
S6-242	16.08	—	Unknown	19	0	6.08	Yes	Yes		5.42	4.06	2008.630	0.21	0.28	0.59
S2-300	16.08	18.64	Unknown	59	11	1.18	No	No		0.26	2.88	2010.170	0.10	0.06	4.43
S7-220	16.09	18.42	Unknown	9	5	1.52	Yes	No		-4.98	-6.12	2010.839	0.18	0.09	2.82
S4-134	16.09	18.84	Unknown	58	10	2.55	Yes	Yes		-3.70	-2.26	2009.842	0.14	0.09	4.91
S3-212	16.09	18.11	Unknown	50	11	6.96	Yes	Yes		2.57	-2.46	2011.416	0.21	0.22	1.12
S1-165	16.11	18.47	Unknown	57	9	8.37	Yes	Yes		-0.25	-1.97	2010.061	0.19	0.20	7.48
S5-140	16.26	—	Unknown	20	0	619.16	Yes	Yes	L	-4.21	3.58	2010.701	1.82	3.07	10.37

Note. — The stars cataloged in this table were included in the Gautam et al. (2019) variability study. K'-band mean magnitudes, number of nights detected, $\chi^2_{\rm red}$, 'Var. ?', RMS, IQR, and $1/\eta$ columns have been calculated with new K'-band observations collected since the publication of that work (presented in Chapter 3). The 'Var. ? (G19)' column indicates if the star was identified as variable by Gautam et al. (2019). For some stars, the number of observations listed here are lower than that presented in Gautam et al. (2019) due to updated confusion criteria or improved identification of artifact sources. The stars predominantly affected by this change are those located near the edges of our experiment's $10'' \times 10''$ typical field of view.

We additionally include H-band mean magnitudes and number of nights detected for those stars that have been identified in the H-band observations presented in Chapter 3. Some stars in this table do not have H-band flux measurements (indicated by '—' in the 'Mean Mag (H)' column). Some of these stars have much bluer or redder H-band flux than is typically observed for GC stars, and were therefore not properly identified by our stellar alignment procedure. Alternatively, some stars may have H-band fluxes that are too faint to be detected in our observations.

Both the K'- and H-band flux measurements presented in this table were calculated with the updated flux calibration presented in Section 3.2.1. Variability type was determined for highly variable stars ($\chi^2_{\rm red} \geq 10.0$, Gautam et al., 2019) by visual inspection of the star's light curve and local field of the star in the images. 'C' indicates variability likely caused by confusion and 'L' indicates variability on timescales $\gtrsim 1$ year.

A.1 Light curves of variability study sample

Light curves of all stars included in the photometric variability study in Chapter 2 are collected in this section. K'-band observations are shown in blue while H-band observations are shown in red. In each light curve, the horizontal dashed-line indicates the weighted mean magnitude across all observations in the respective bandpass.

This section has been updated from Appendix C in Gautam et al. (2019) with the following changes: The light curves of all stars in the Gautam et al. (2019) sample are plotted here (i.e., the stars listed in Table A.1), and not just those with $\chi^2_{\rm red} \geq 10$ variability. New K'-band observations conducted in 2018 and 2019 are included in the light curves, with re-calculated $\chi^2_{\rm red}$ values from all K'-band observations. If a star in the sample has detections in our H-band observations, conducted 2017 – 2019, we have plotted the H-band light curve as well. Both the K'-band and H-band photometric measurements plotted in this section have been calibrated with the updated photometric calibration methods detailed in Chapter 3. Details of the new photometric observations are presented in Section 3.7 while details of the updated photometric calibration techniques are presented in Section 3.2.1.

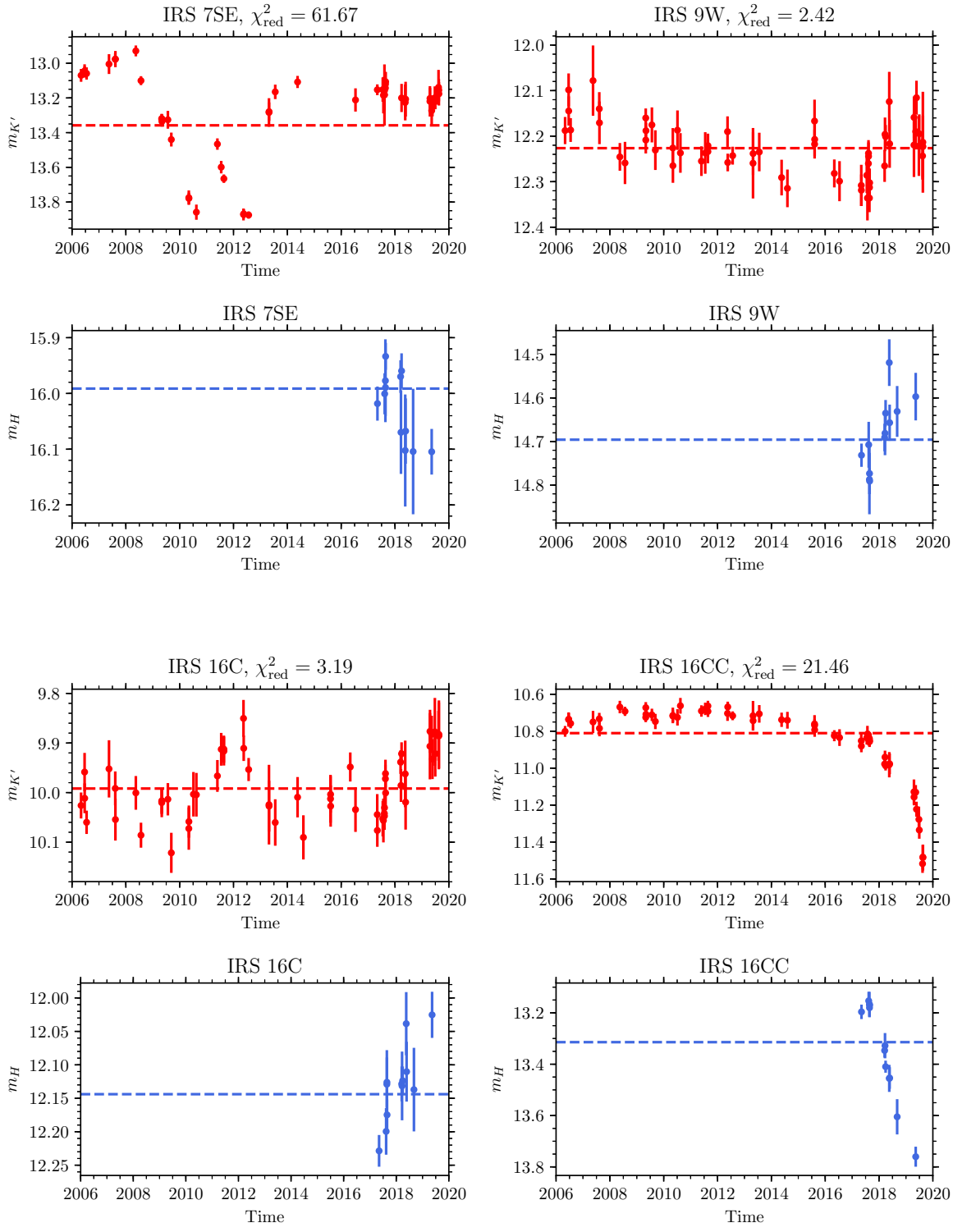
IRS 7SE, $\chi^2_{\rm red} = 61.67$
IRS 9W, $\chi^2_{\rm red} = 2.42$
IRS 7SE
IRS 9W
IRS 16C, $\chi^2_{\rm red} = 3.19$
IRS 16CC, $\chi^2_{\rm red} = 21.46$
IRS 16C
IRS 16CC
$m_{K'}$
m_H
Time

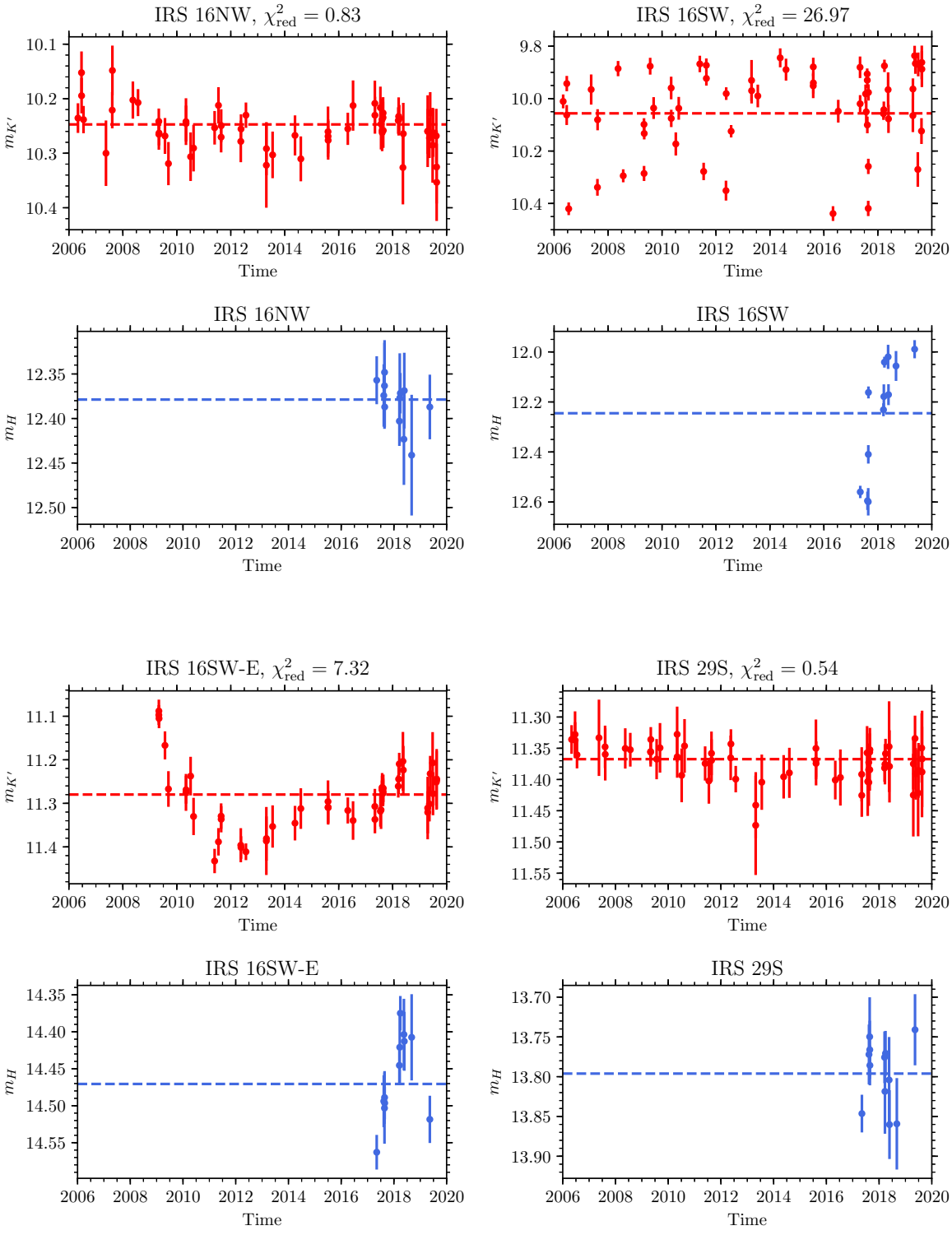
IRS 16NW, $\chi^2_{\rm red} = 0.83$
IRS 16SW, $\chi^2_{\rm red} = 26.97$
IRS 16NW
IRS 16SW
IRS 16SW-E, $\chi^2_{\rm red} = 7.32$
IRS 29S, $\chi^2_{\rm red} = 0.54$
IRS 16SW-E
IRS 29S
$m_{K'}$
m_H
Time

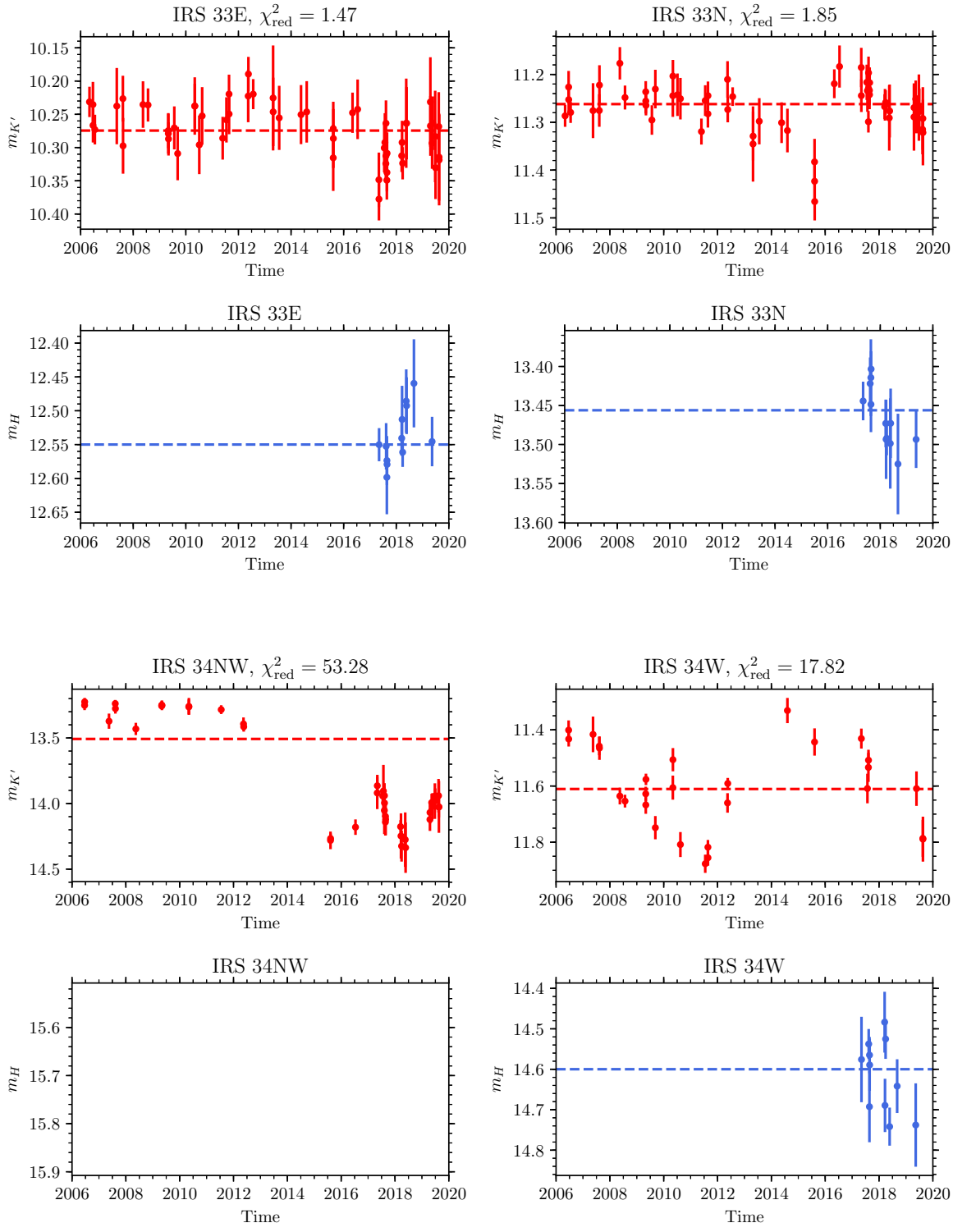
IRS 33E, $\chi^2_{\rm red} = 1.47$
IRS 33N, $\chi^2_{\rm red} = 1.85$
IRS 33E
IRS 33N
IRS 34NW, $\chi^2_{\rm red} = 53.28$
IRS 34W, $\chi^2_{\rm red} = 17.82$
IRS 34NW
IRS 34W
$m_{K'}$
m_H
Time

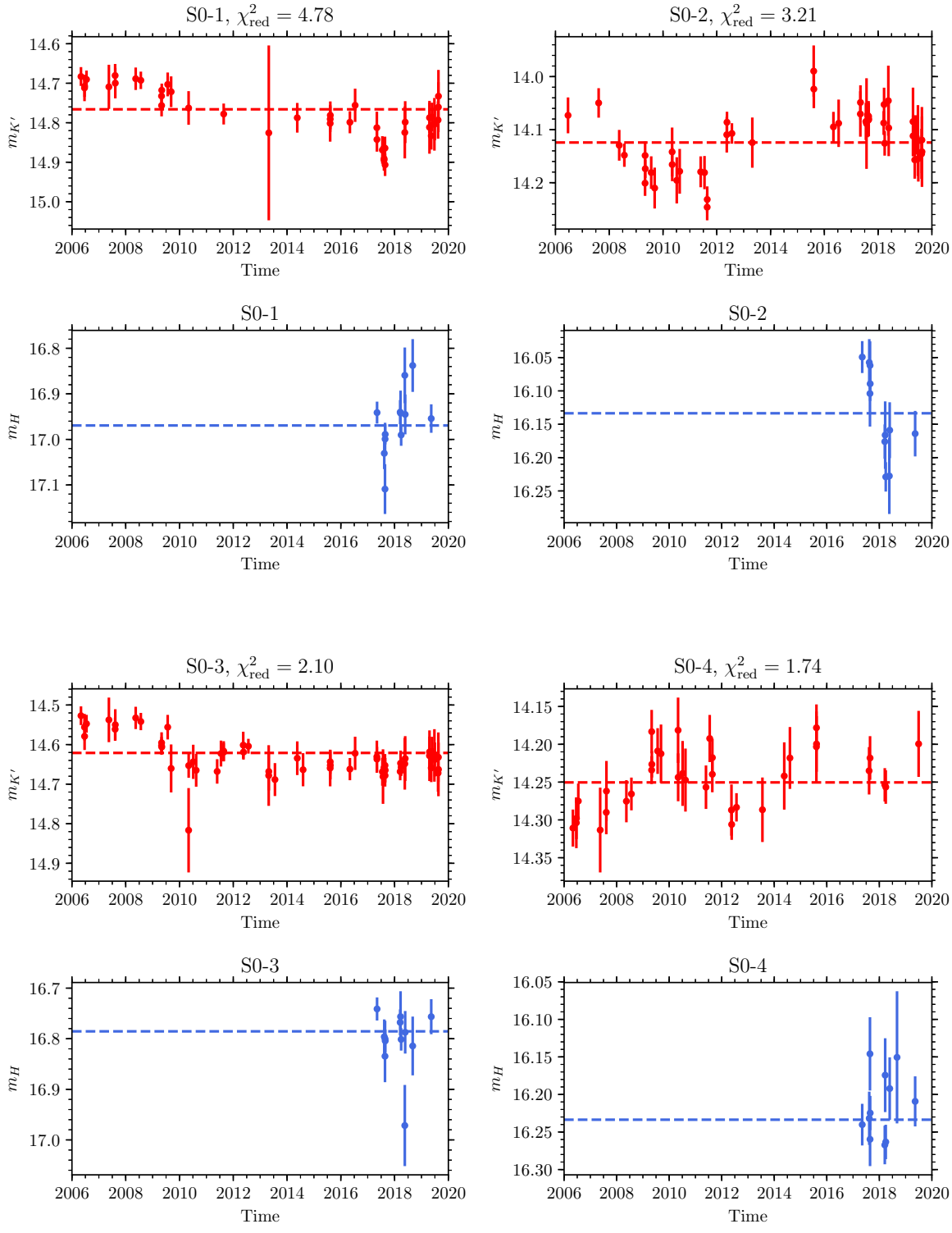
S0-1, $\chi^2_{\rm red} = 4.78$
S0-2, $\chi^2_{\rm red} = 3.21$
S0-1
S0-2
S0-3, $\chi^2_{\rm red} = 2.10$
S0-4, $\chi^2_{\rm red} = 1.74$
S0-3
S0-4
$m_{K'}$
m_H
Time

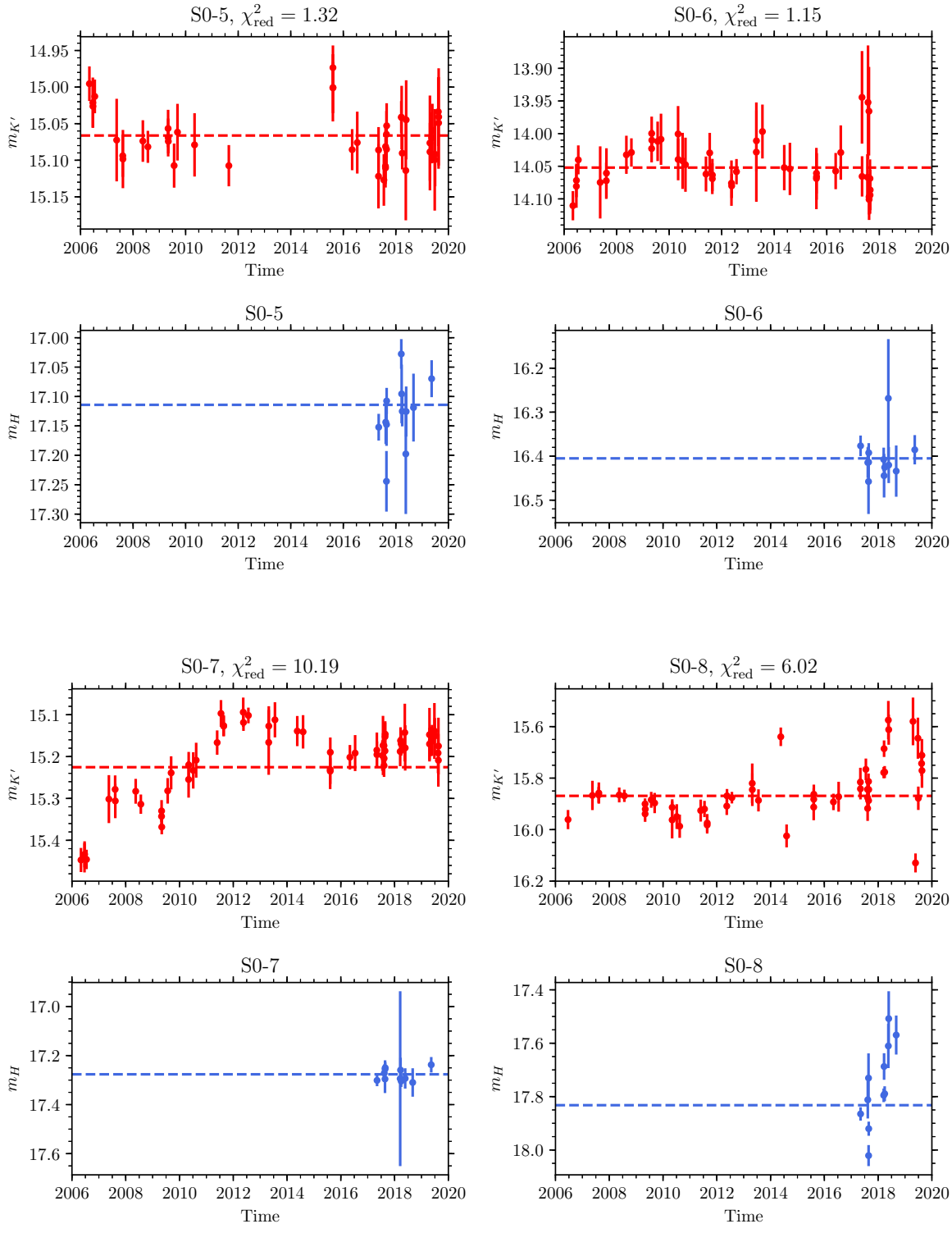
S0-5, $\chi^2_{\rm red} = 1.32$
S0-6, $\chi^2_{\rm red} = 1.15$
S0-5
S0-6
S0-7, $\chi^2_{\rm red} = 10.19$
S0-8, $\chi^2_{\rm red} = 6.02$
S0-7
S0-8
$m_{K'}$
m_H
Time

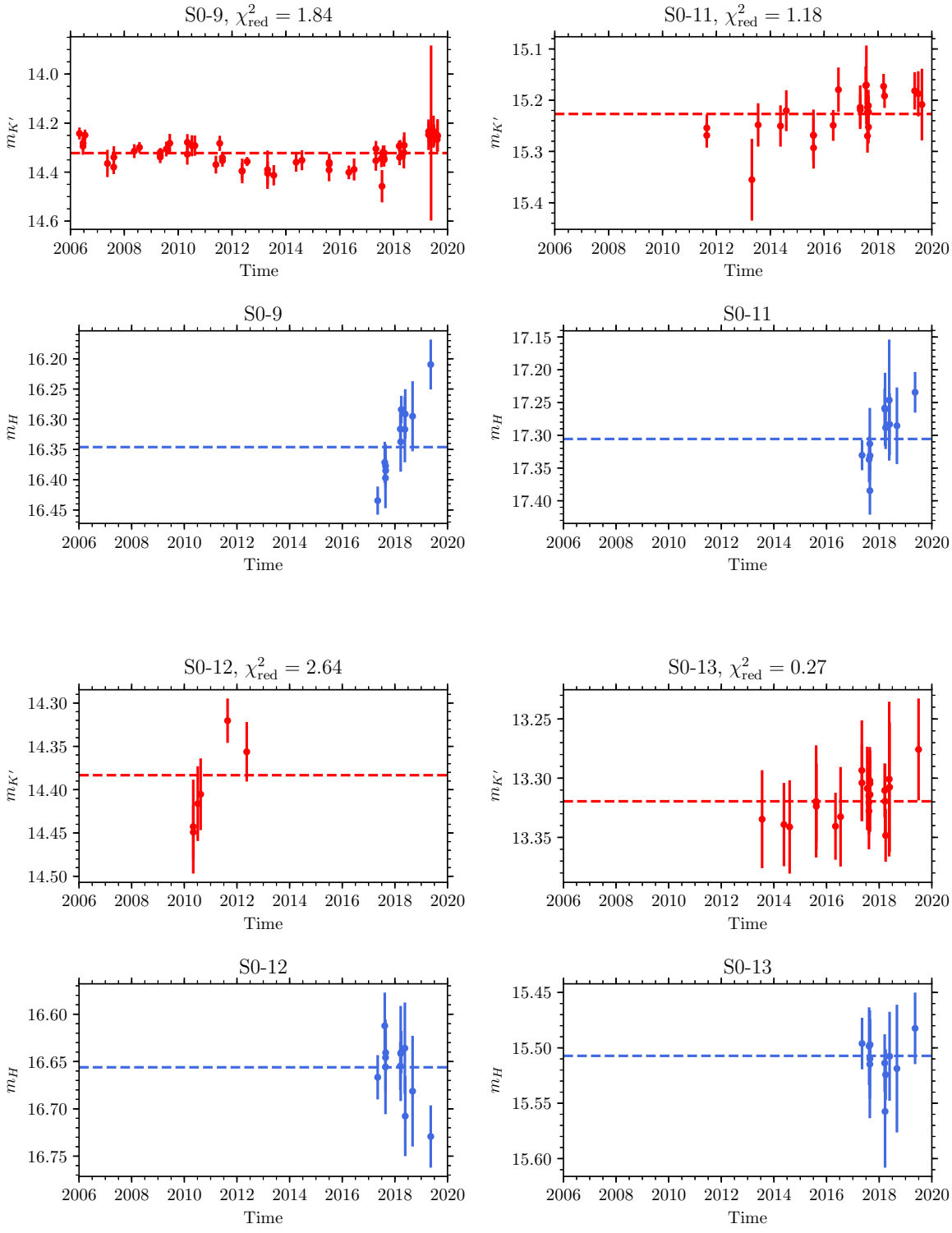
S0-9, $\chi^2_{\rm red} = 1.84$
S0-11, $\chi^2_{\rm red} = 1.18$
S0-9
S0-11
S0-12, $\chi^2_{\rm red} = 2.64$
S0-13, $\chi^2_{\rm red} = 0.27$
S0-12
S0-13
$m_{K'}$
m_H
Time

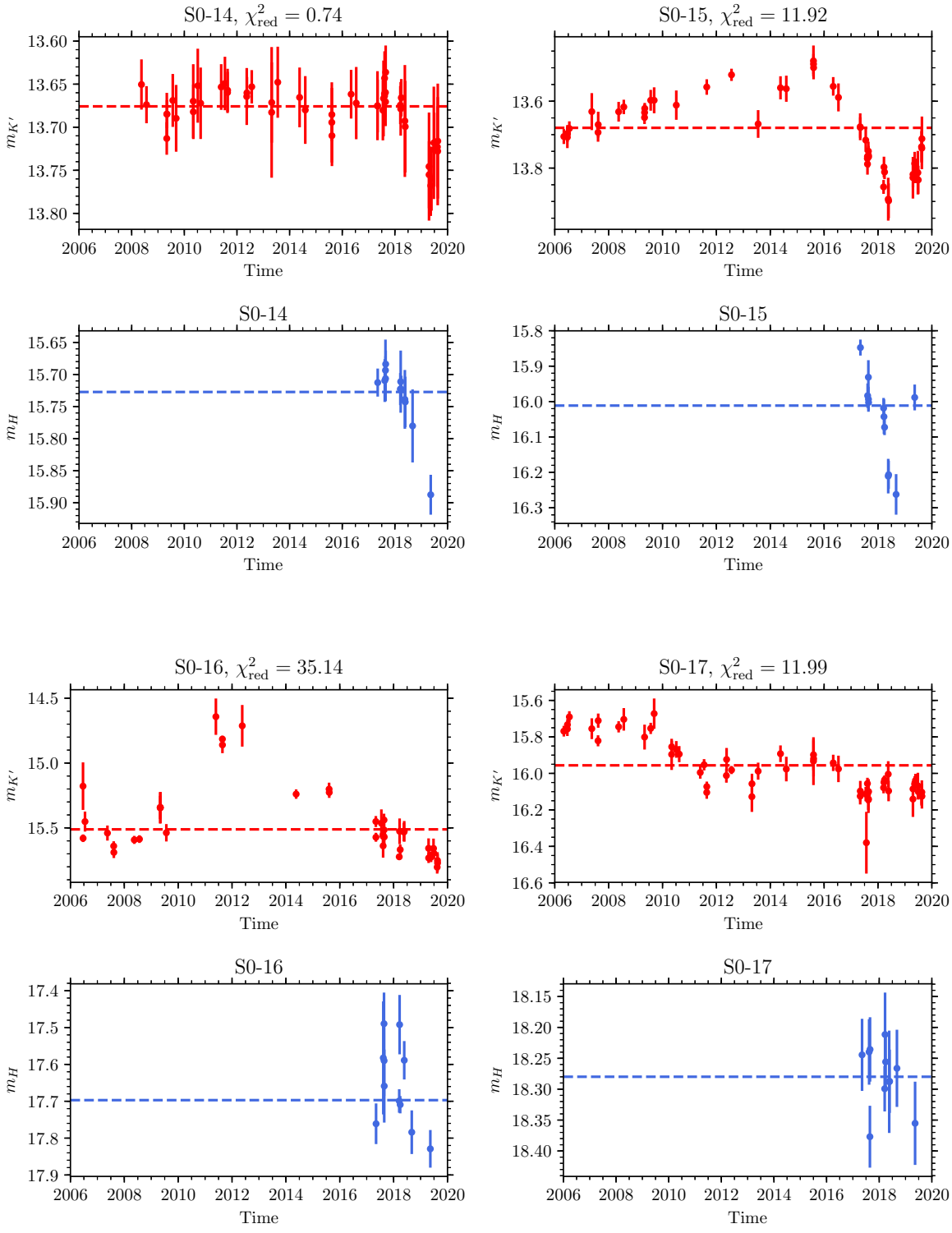
S0-14, $\chi^2_{\rm red} = 0.74$
S0-15, $\chi^2_{\rm red} = 11.92$
S0-14
S0-15
S0-16, $\chi^2_{\rm red} = 35.14$
S0-17, $\chi^2_{\rm red} = 11.99$
S0-16
S0-17
$m_{K'}$
m_H
Time

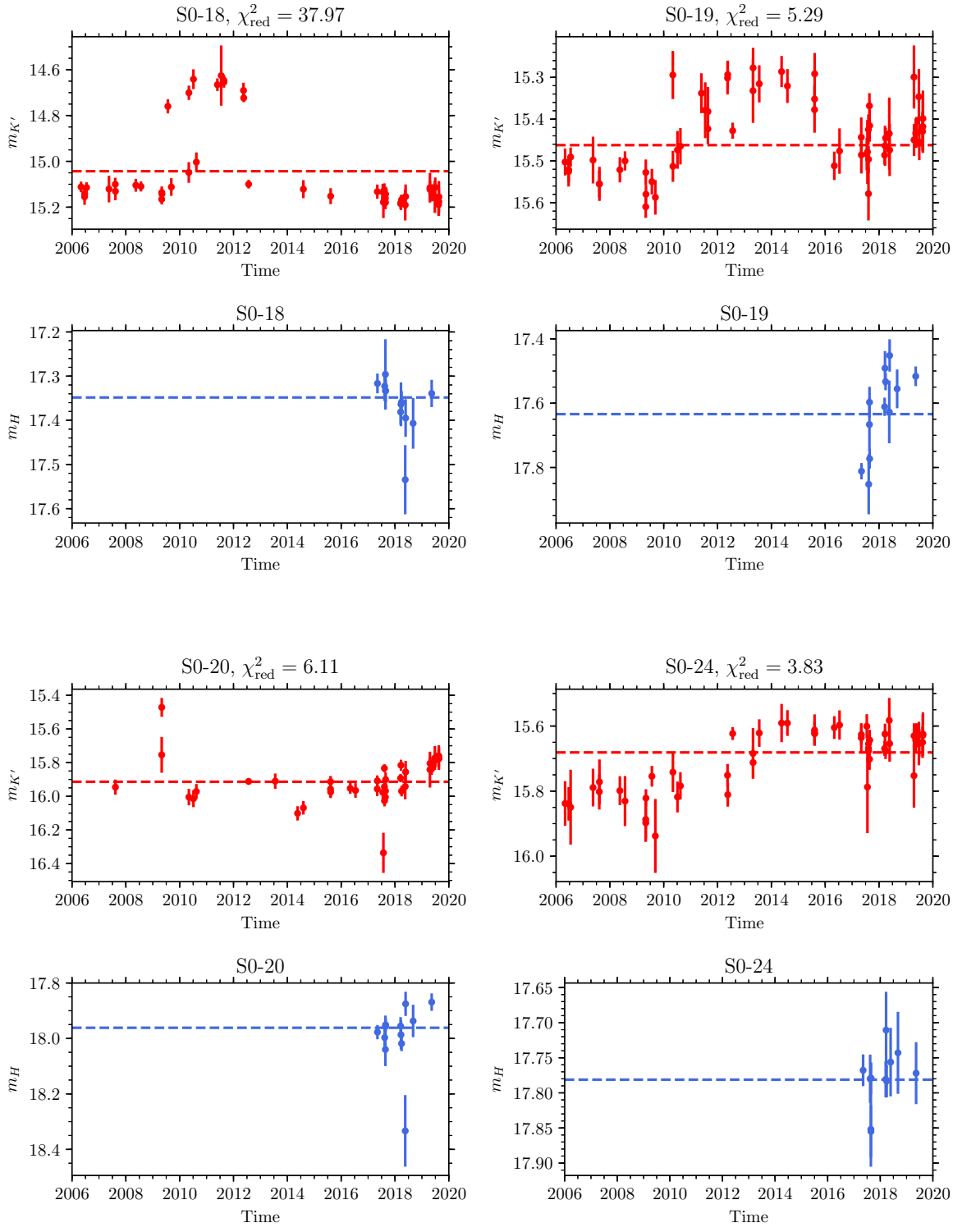
S0-18, $\chi^2_{\rm red} = 37.97$
S0-19, $\chi^2_{\rm red} = 5.29$
S0-18
S0-19
S0-20, $\chi^2_{\rm red} = 6.11$
S0-24, $\chi^2_{\rm red} = 3.83$
S0-20
S0-24
$m_{K'}$
m_H
Time

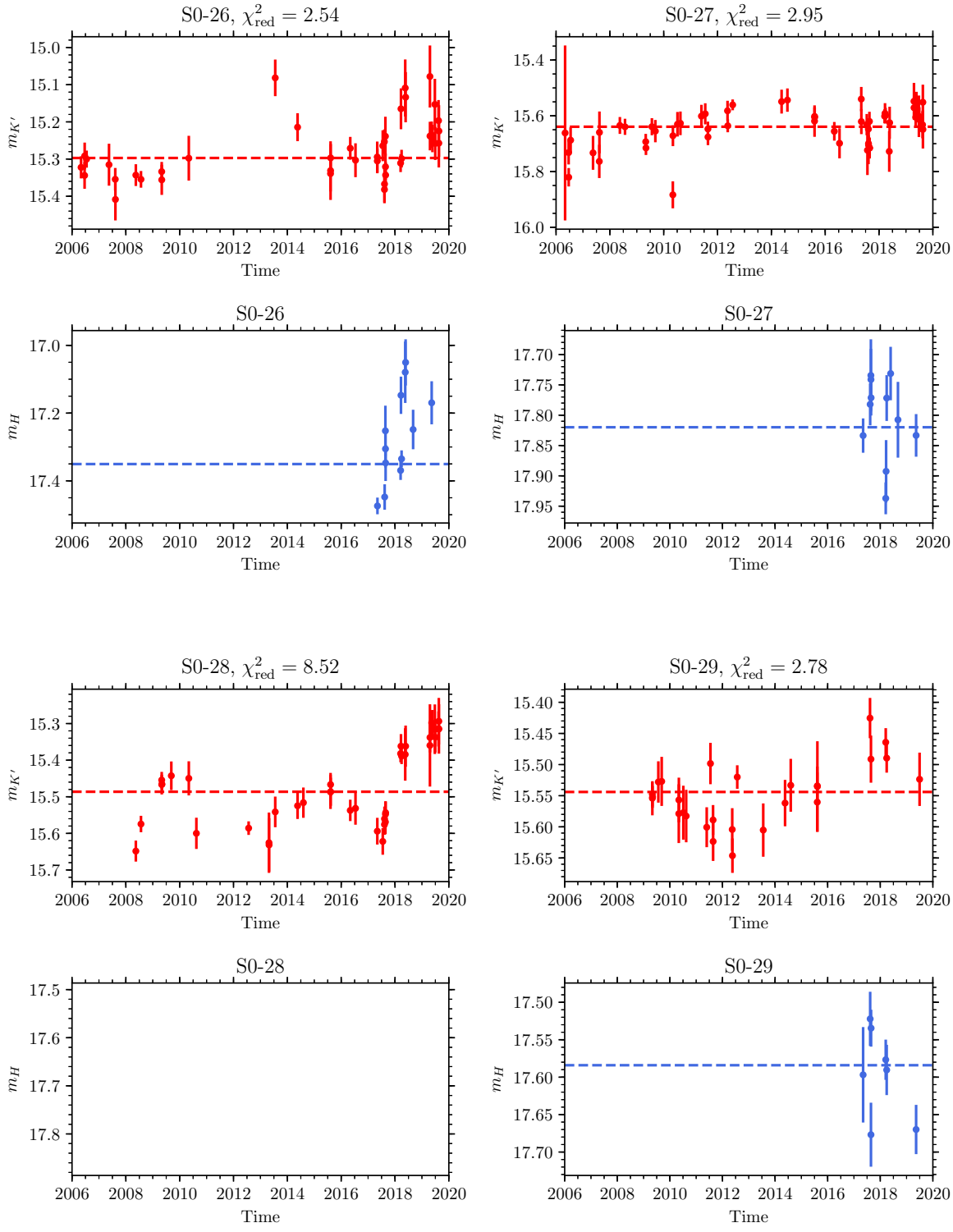
S0-26, $\chi^2_{\rm red} = 2.54$
S0-27, $\chi^2_{\rm red} = 2.95$
S0-26
S0-27
S0-28, $\chi^2_{\rm red} = 8.52$
S0-29, $\chi^2_{\rm red} = 2.78$
S0-28
S0-29
$m_{K'}$
m_H
Time

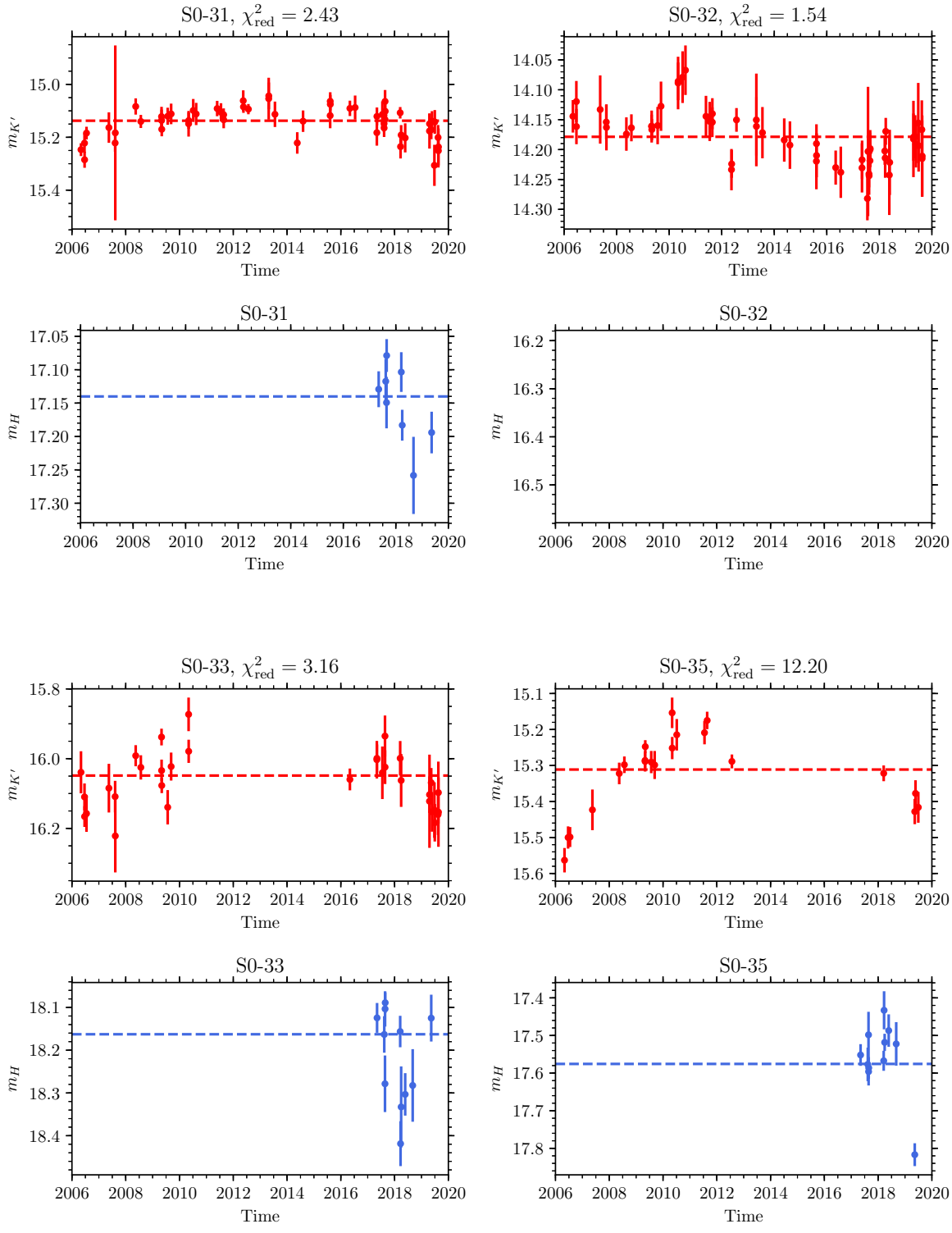
S0-31, $\chi^2_{\rm red} = 2.43$
S0-32, $\chi^2_{\rm red} = 1.54$
S0-31
S0-32
S0-33, $\chi^2_{\rm red} = 3.16$
S0-35, $\chi^2_{\rm red} = 12.20$
S0-33
S0-35
$m_{K'}$
m_H
Time

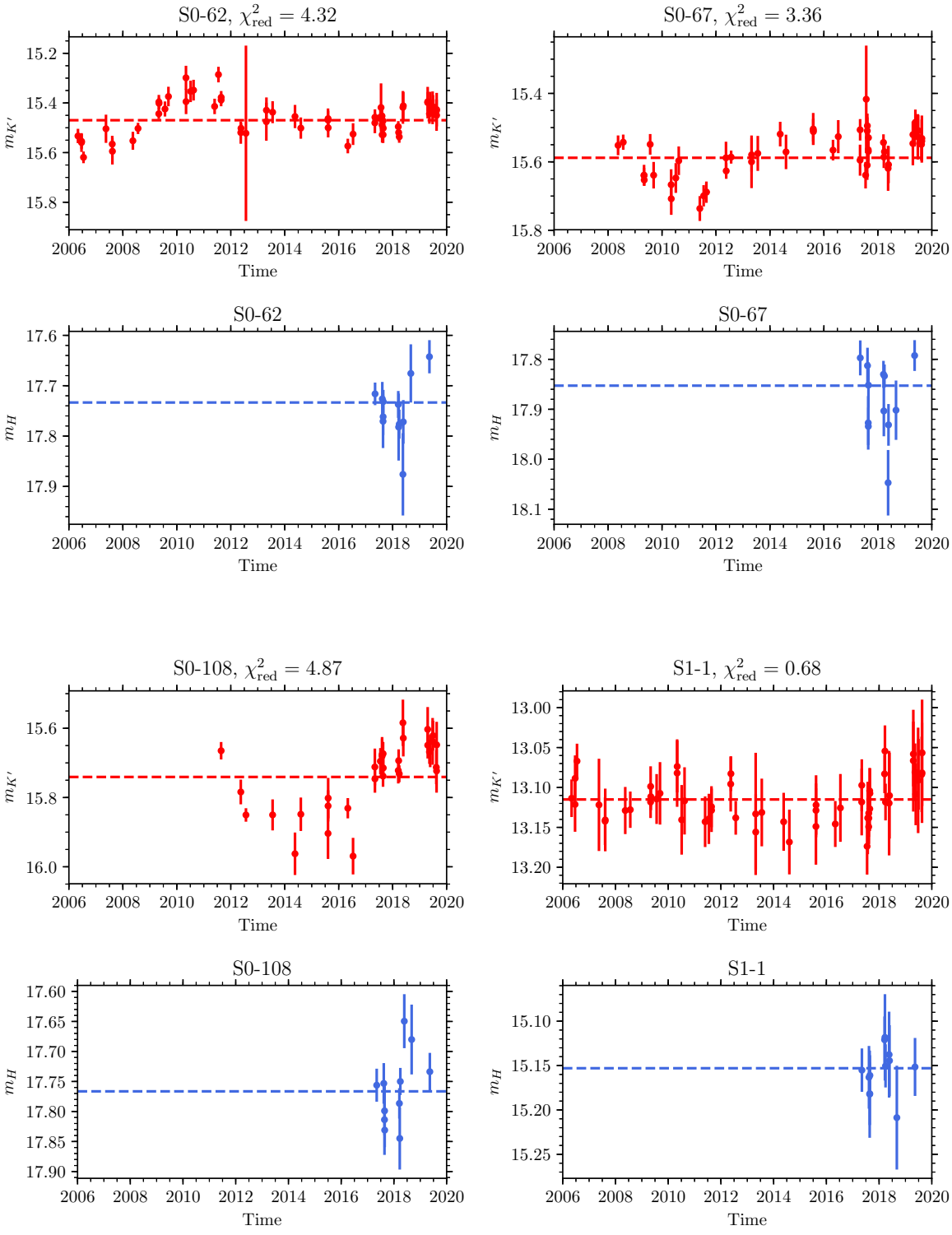
S0-62, $\chi^2_{\rm red} = 4.32$
S0-67, $\chi^2_{\rm red} = 3.36$
S0-62
S0-67
S0-108, $\chi^2_{\rm red} = 4.87$
S1-1, $\chi^2_{\rm red} = 0.68$
S0-108
S1-1
$m_{K'}$
m_H
Time

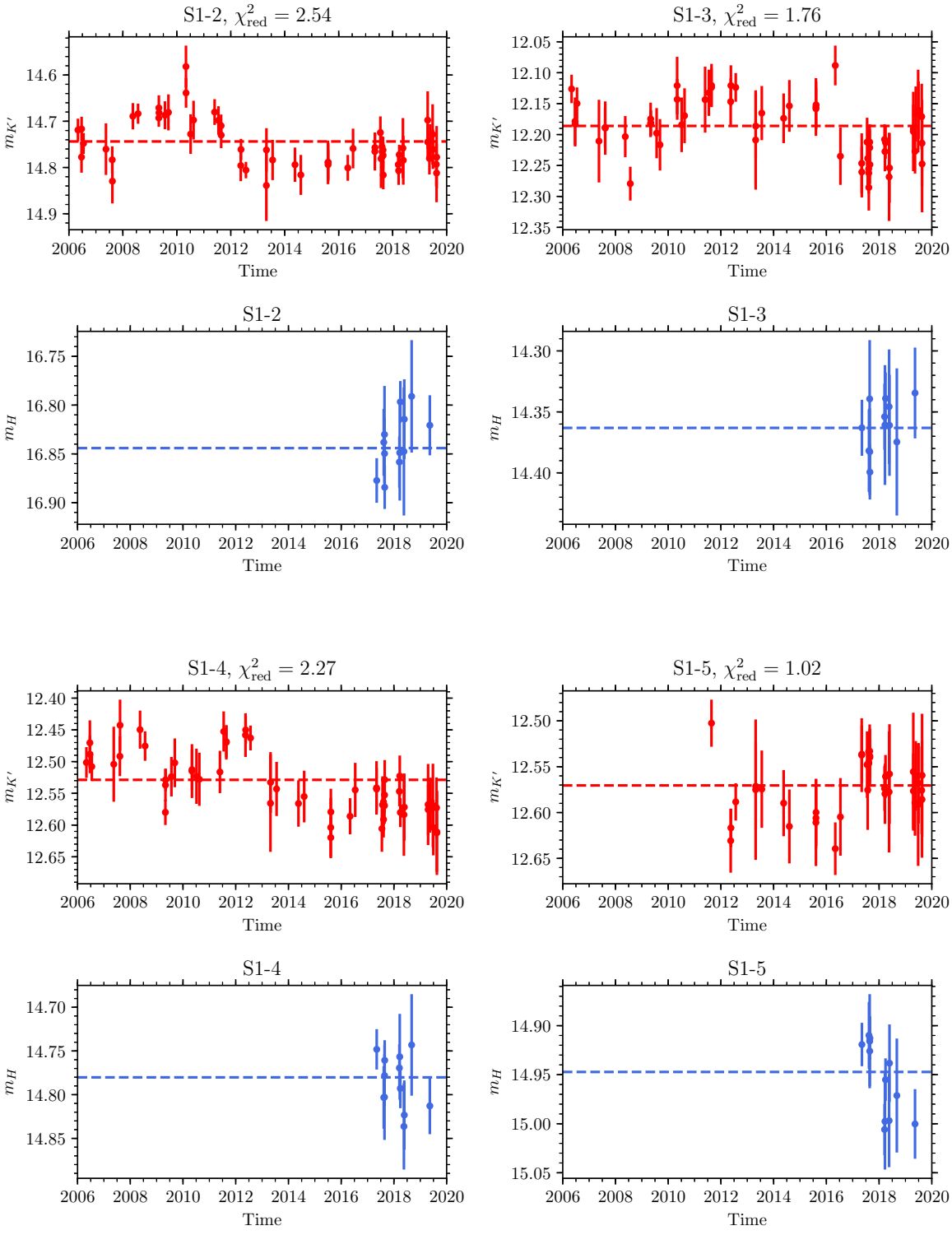
S1-2, $\chi^2_{\rm red} = 2.54$
S1-3, $\chi^2_{\rm red} = 1.76$
S1-2
S1-3
S1-4, $\chi^2_{\rm red} = 2.27$
S1-5, $\chi^2_{\rm red} = 1.02$
S1-4
S1-5
$m_{K'}$
m_H
Time

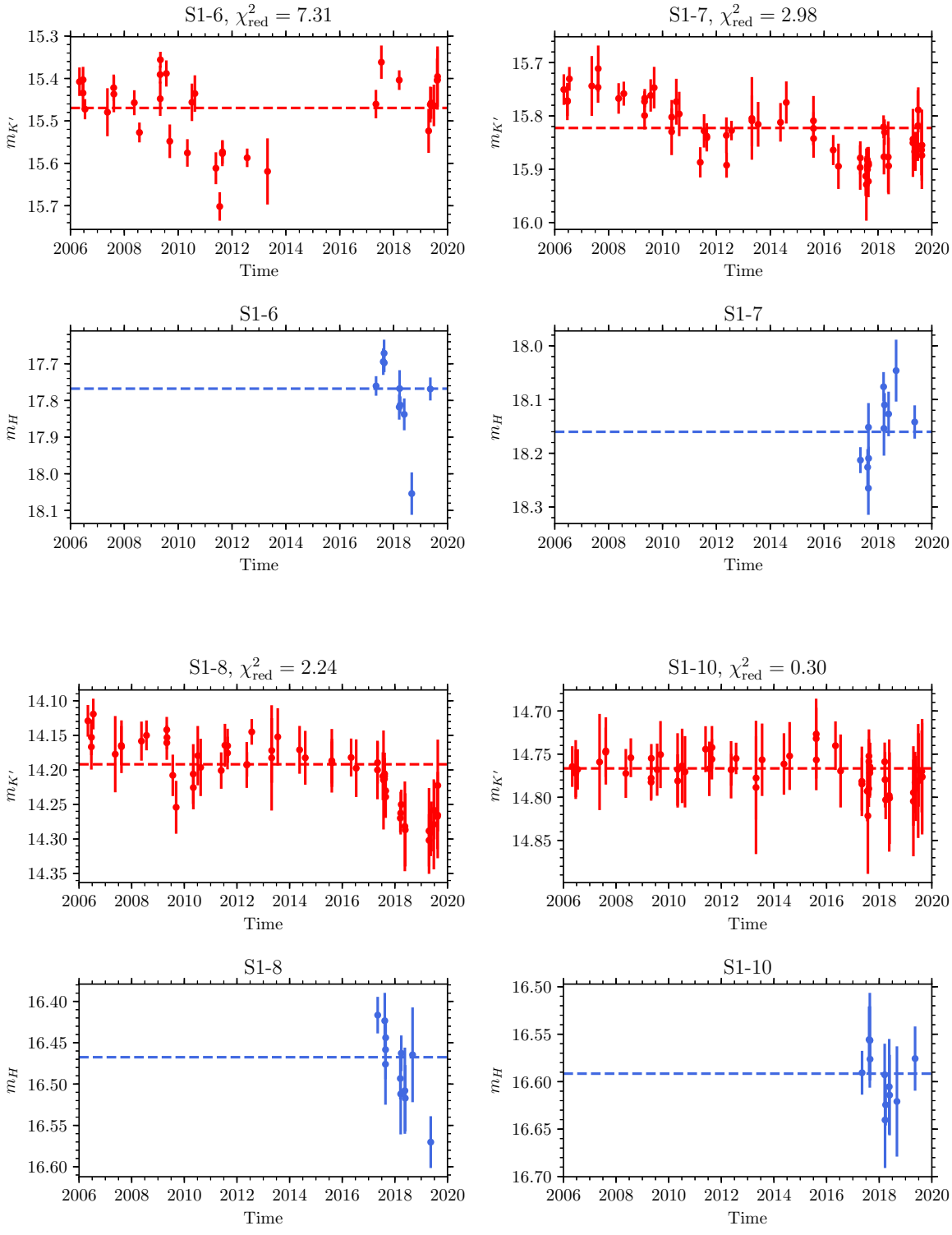
S1-6, $\chi^2_{\rm red} = 7.31$
S1-7, $\chi^2_{\rm red} = 2.98$
S1-6
S1-7
S1-8, $\chi^2_{\rm red} = 2.24$
S1-10, $\chi^2_{\rm red} = 0.30$
S1-8
S1-10
$m_{K'}$
m_H
Time

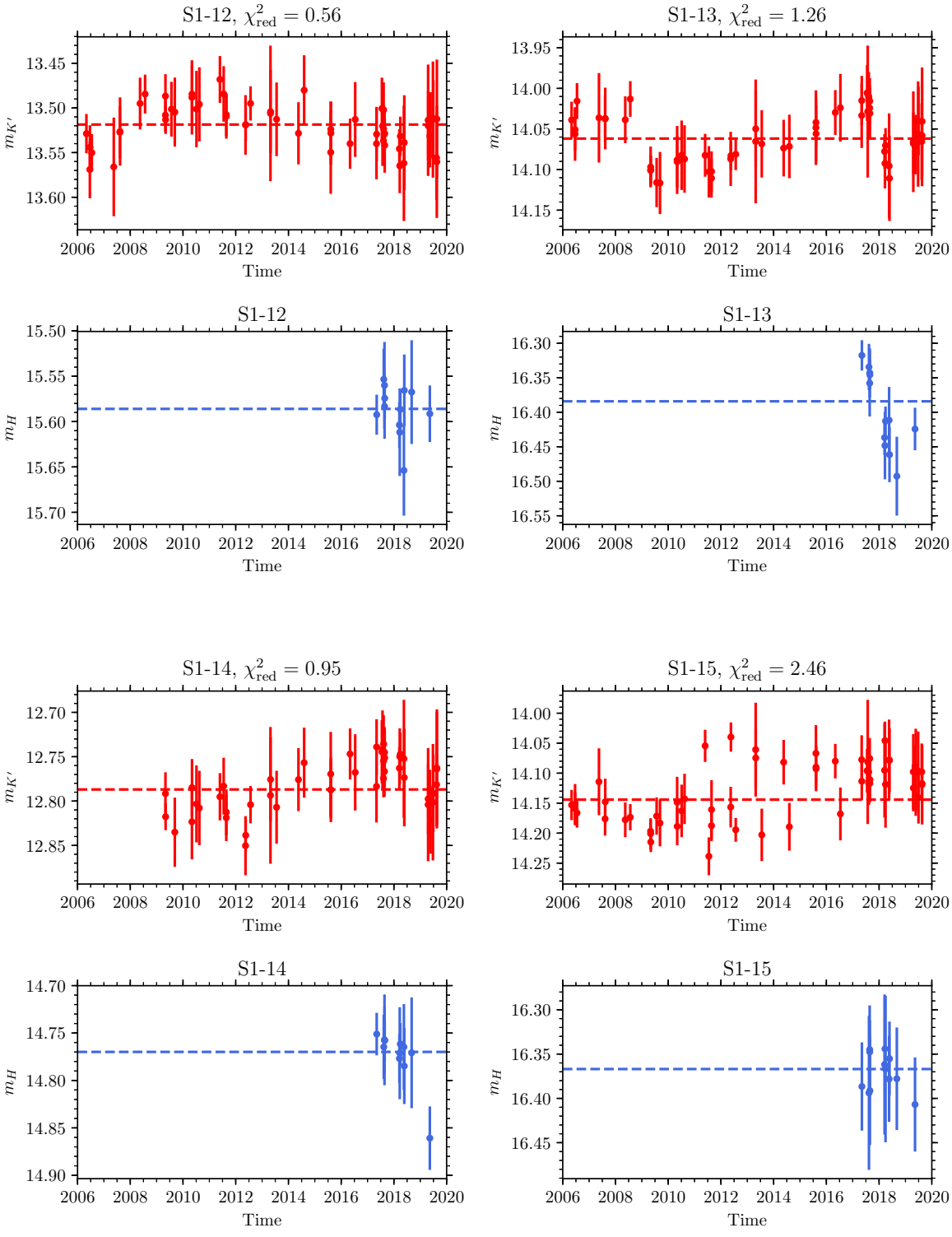
S1-12, $\chi^2_{\rm red} = 0.56$
S1-13, $\chi^2_{\rm red} = 1.26$
S1-12
S1-13
S1-14, $\chi^2_{\rm red} = 0.95$
S1-15, $\chi^2_{\rm red} = 2.46$
S1-14
S1-15
$m_{K'}$
m_H
Time

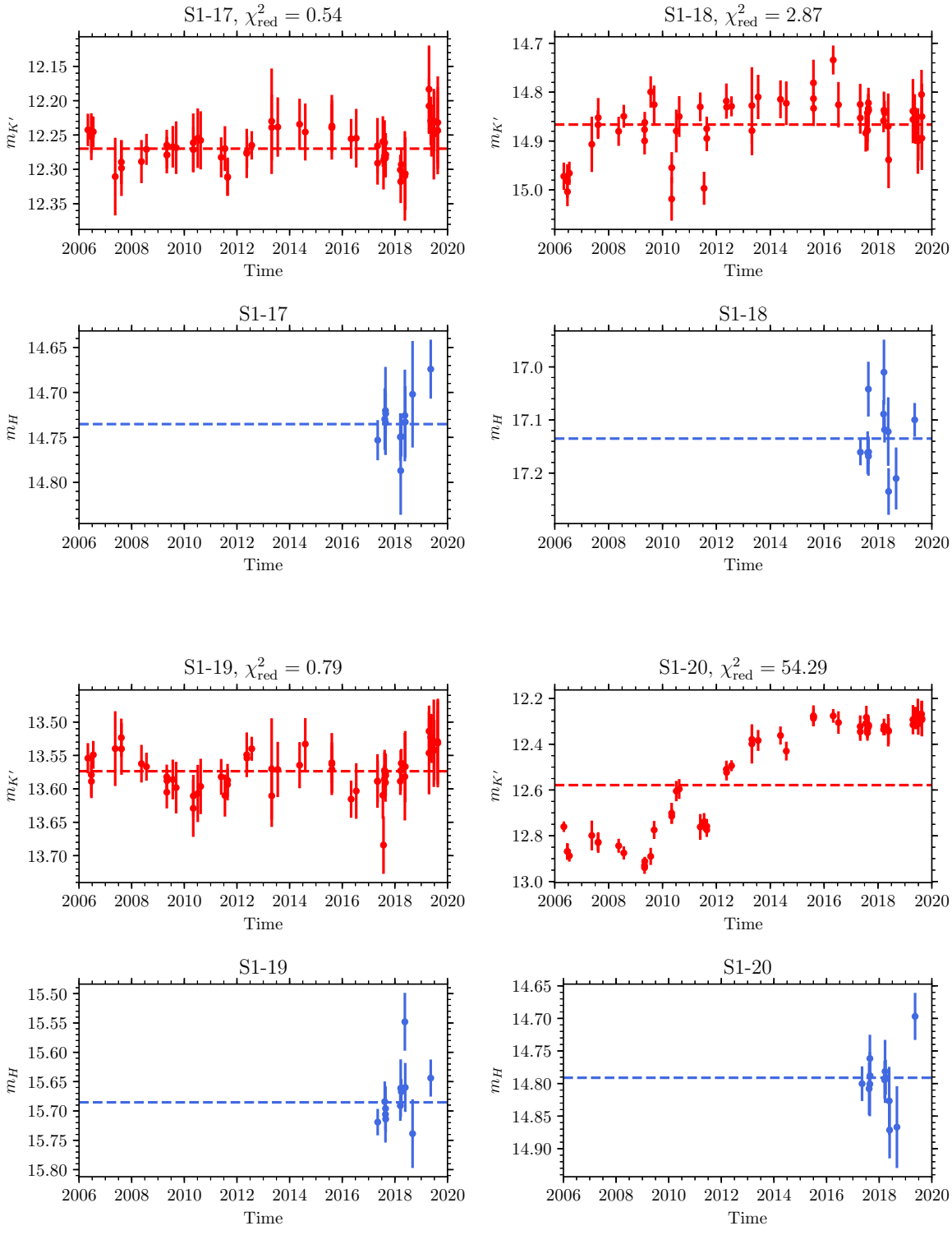
S1-17, $\chi^2_{\rm red} = 0.54$
S1-18, $\chi^2_{\rm red} = 2.87$
S1-17
S1-18
S1-19, $\chi^2_{\rm red} = 0.79$
S1-20, $\chi^2_{\rm red} = 54.29$
S1-19
S1-20
$m_{K'}$
m_H
Time

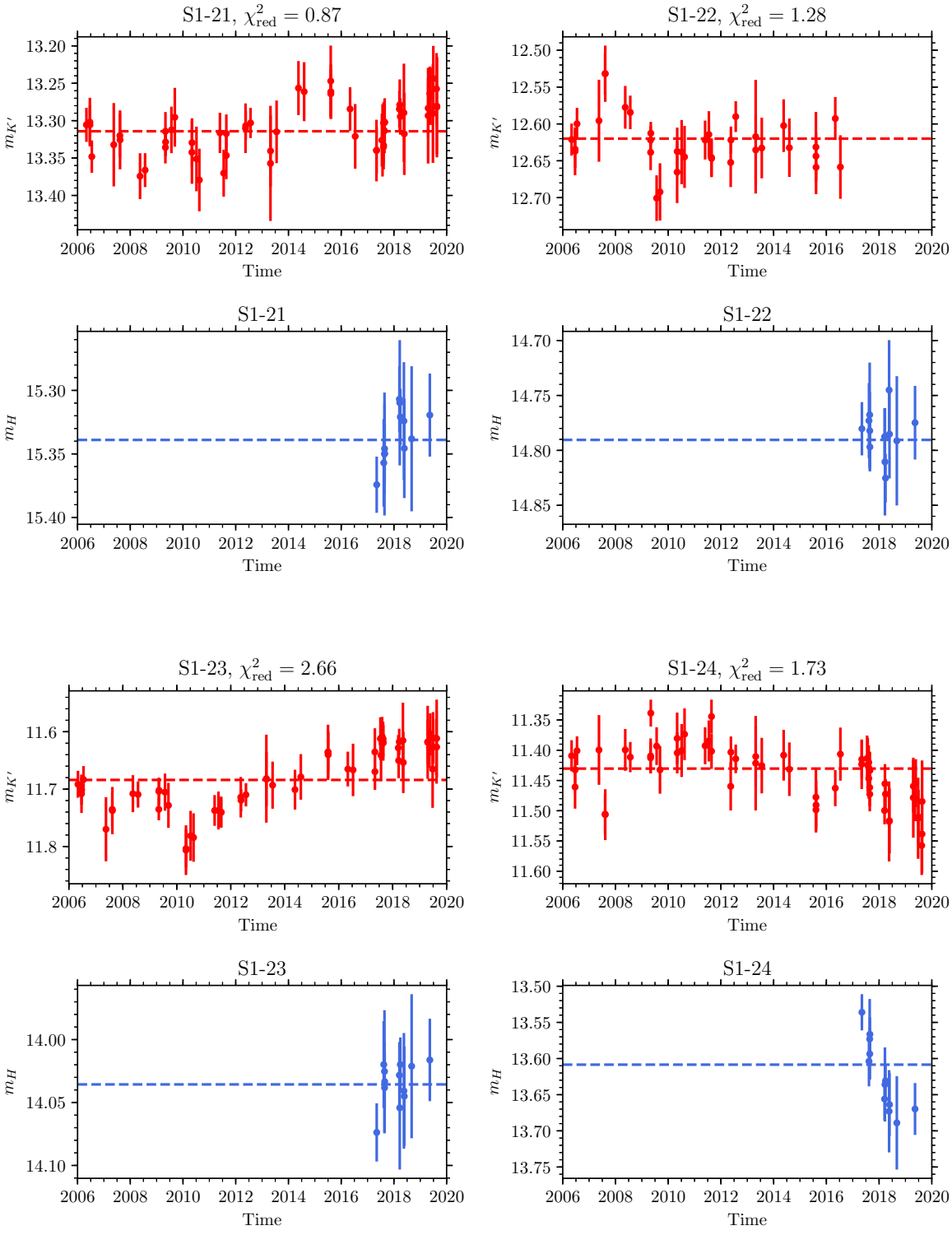
S1-21, $\chi^2_{\rm red} = 0.87$
S1-22, $\chi^2_{\rm red} = 1.28$
S1-21
S1-22
S1-23, $\chi^2_{\rm red} = 2.66$
S1-24, $\chi^2_{\rm red} = 1.73$
S1-23
S1-24
$m_{K'}$
m_H
Time

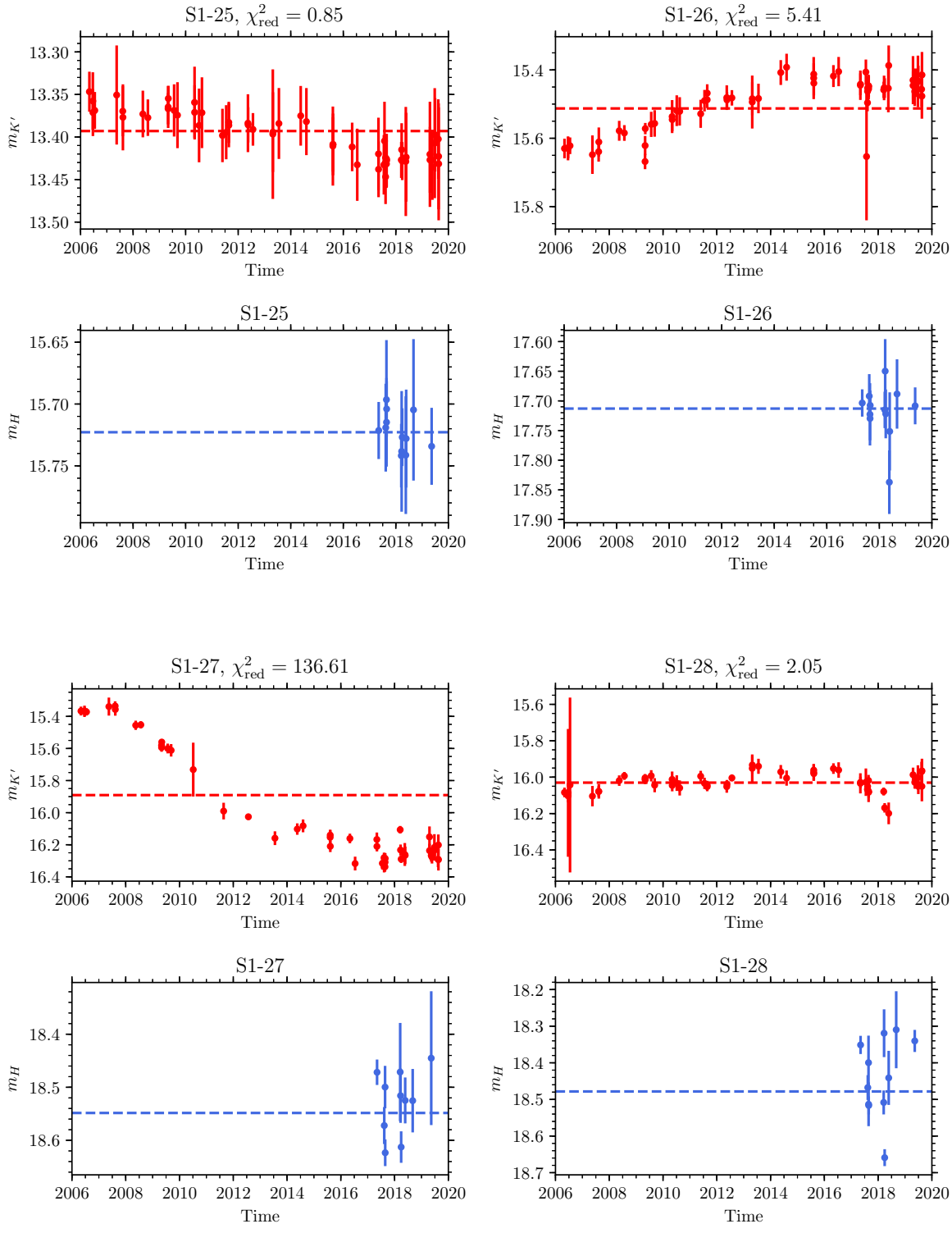
S1-25, $\chi^2_{\rm red} = 0.85$
S1-26, $\chi^2_{\rm red} = 5.41$
S1-25
S1-26
S1-27, $\chi^2_{\rm red} = 136.61$
S1-28, $\chi^2_{\rm red} = 2.05$
S1-27
S1-28
$m_{K'}$
m_H
Time

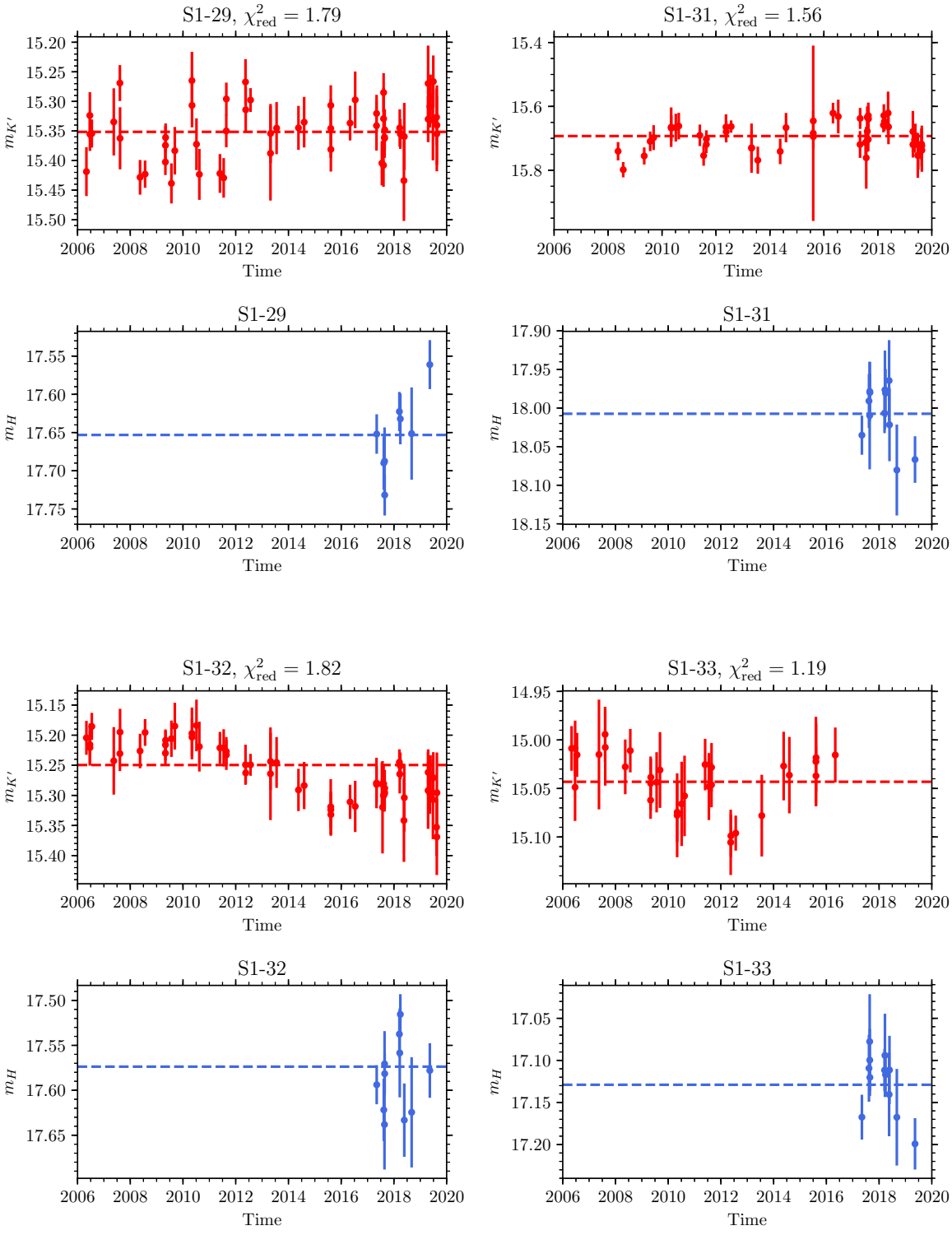
S1-29, $\chi^2_{\rm red} = 1.79$
S1-31, $\chi^2_{\rm red} = 1.56$
S1-29
S1-31
S1-32, $\chi^2_{\rm red} = 1.82$
S1-33, $\chi^2_{\rm red} = 1.19$
S1-32
S1-33
$m_{K'}$
m_H
Time

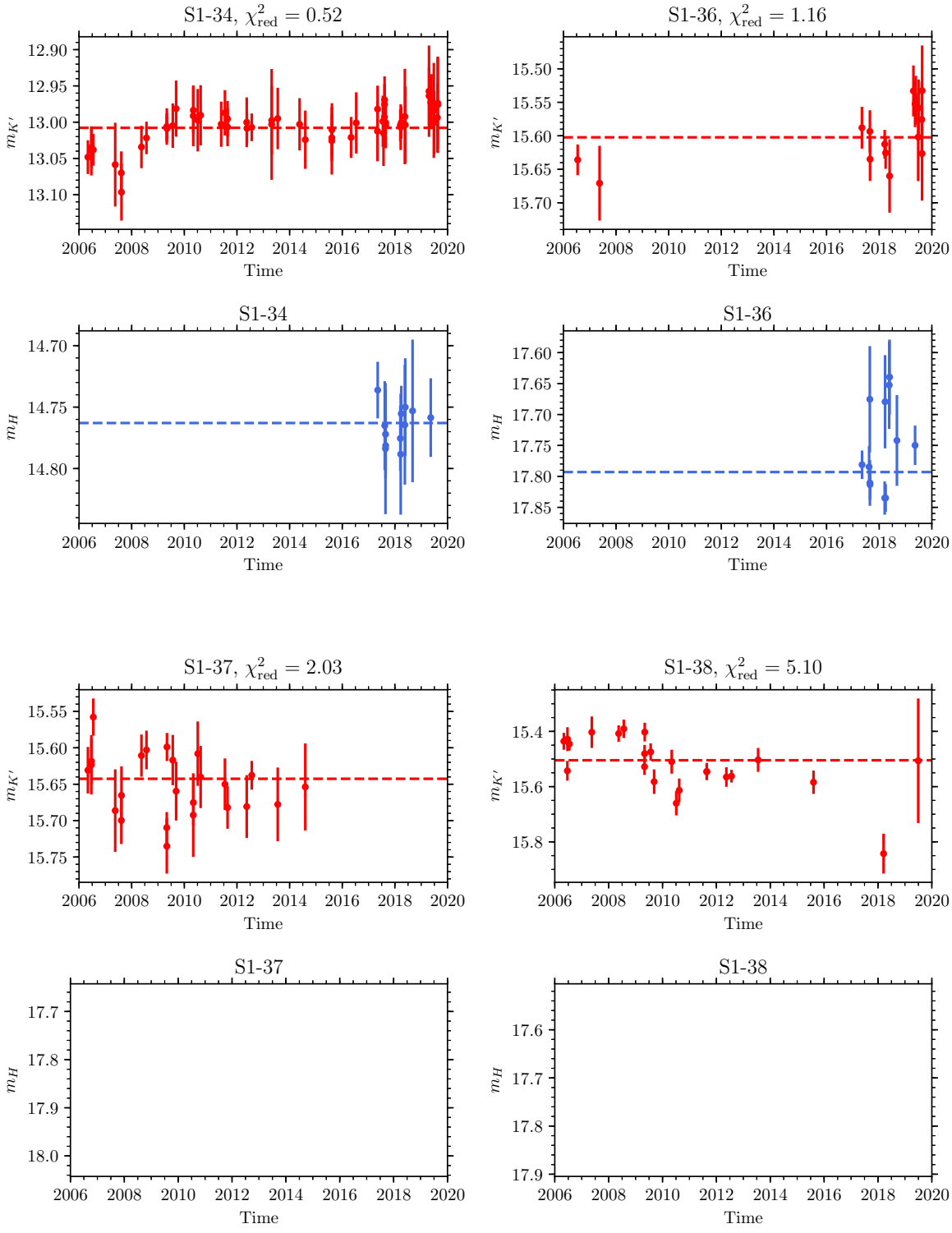
S1-34, $\chi^2_{\rm red} = 0.52$
S1-36, $\chi^2_{\rm red} = 1.16$
S1-34
S1-36
S1-37, $\chi^2_{\rm red} = 2.03$
S1-38, $\chi^2_{\rm red} = 5.10$
S1-37
S1-38
$m_{K'}$
m_H
Time

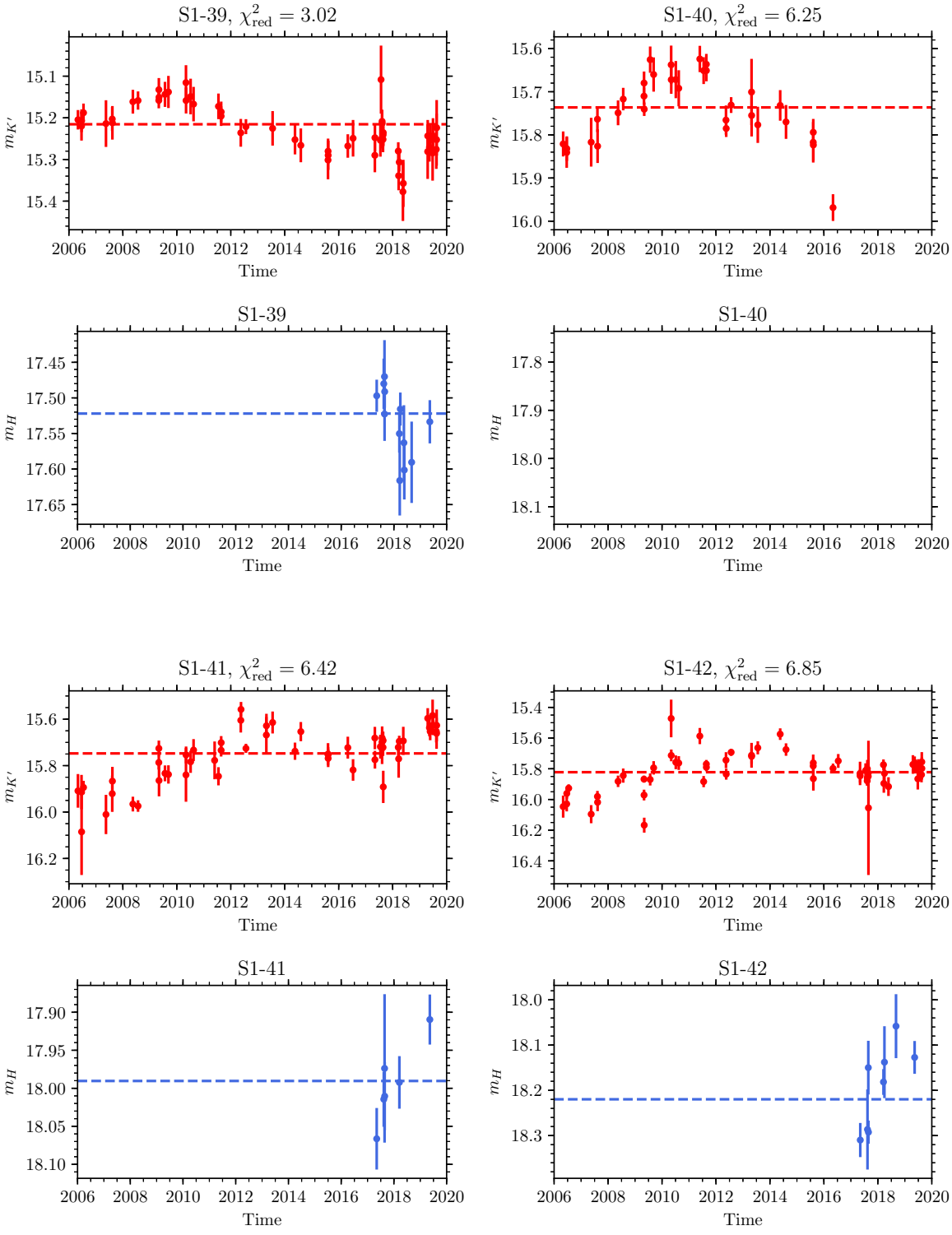
S1-39, $\chi^2_{\rm red} = 3.02$
S1-40, $\chi^2_{\rm red} = 6.25$
S1-39
S1-40
S1-41, $\chi^2_{\rm red} = 6.42$
S1-42, $\chi^2_{\rm red} = 6.85$
S1-41
S1-42
$m_{K'}$
m_H
Time

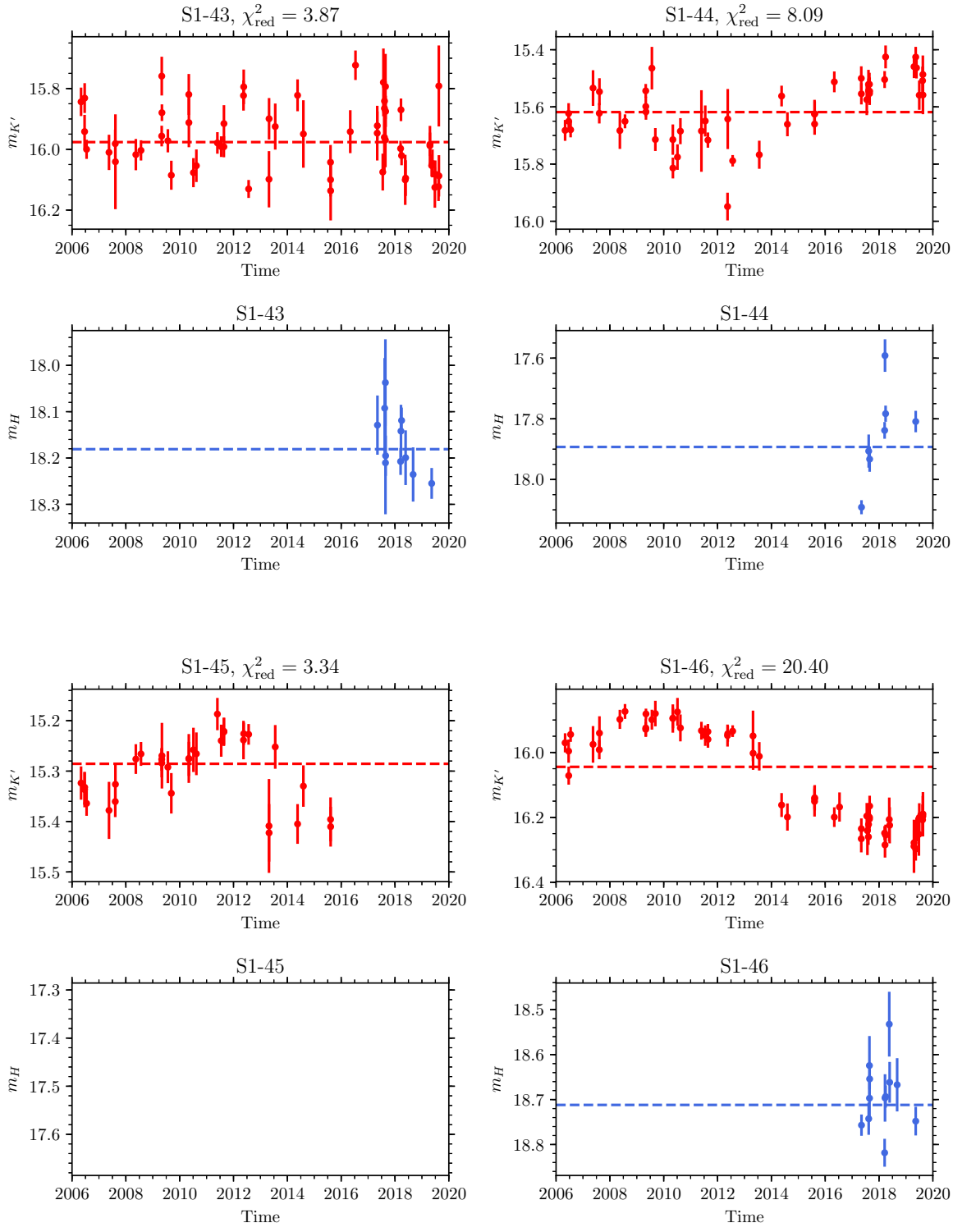
S1-43, $\chi^2_{\rm red} = 3.87$
S1-44, $\chi^2_{\rm red} = 8.09$
S1-43
S1-44
S1-45, $\chi^2_{\rm red} = 3.34$
S1-46, $\chi^2_{\rm red} = 20.40$
S1-45
S1-46
$m_{K'}$
m_H
Time

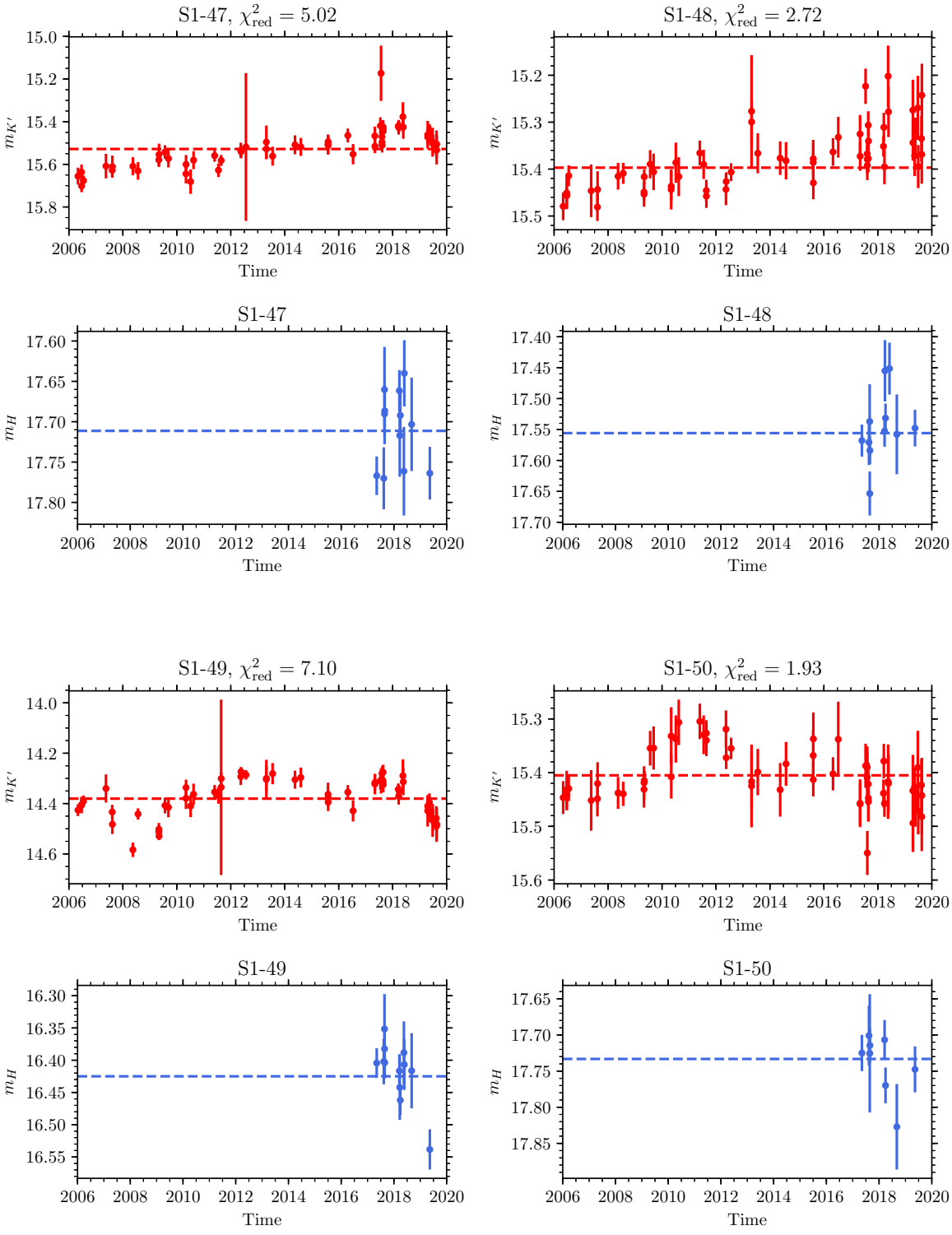
S1-47, $\chi^2_{\rm red} = 5.02$
S1-48, $\chi^2_{\rm red} = 2.72$
S1-47
S1-48
S1-49, $\chi^2_{\rm red} = 7.10$
S1-50, $\chi^2_{\rm red} = 1.93$
S1-49
S1-50
$m_{K'}$
m_H
Time

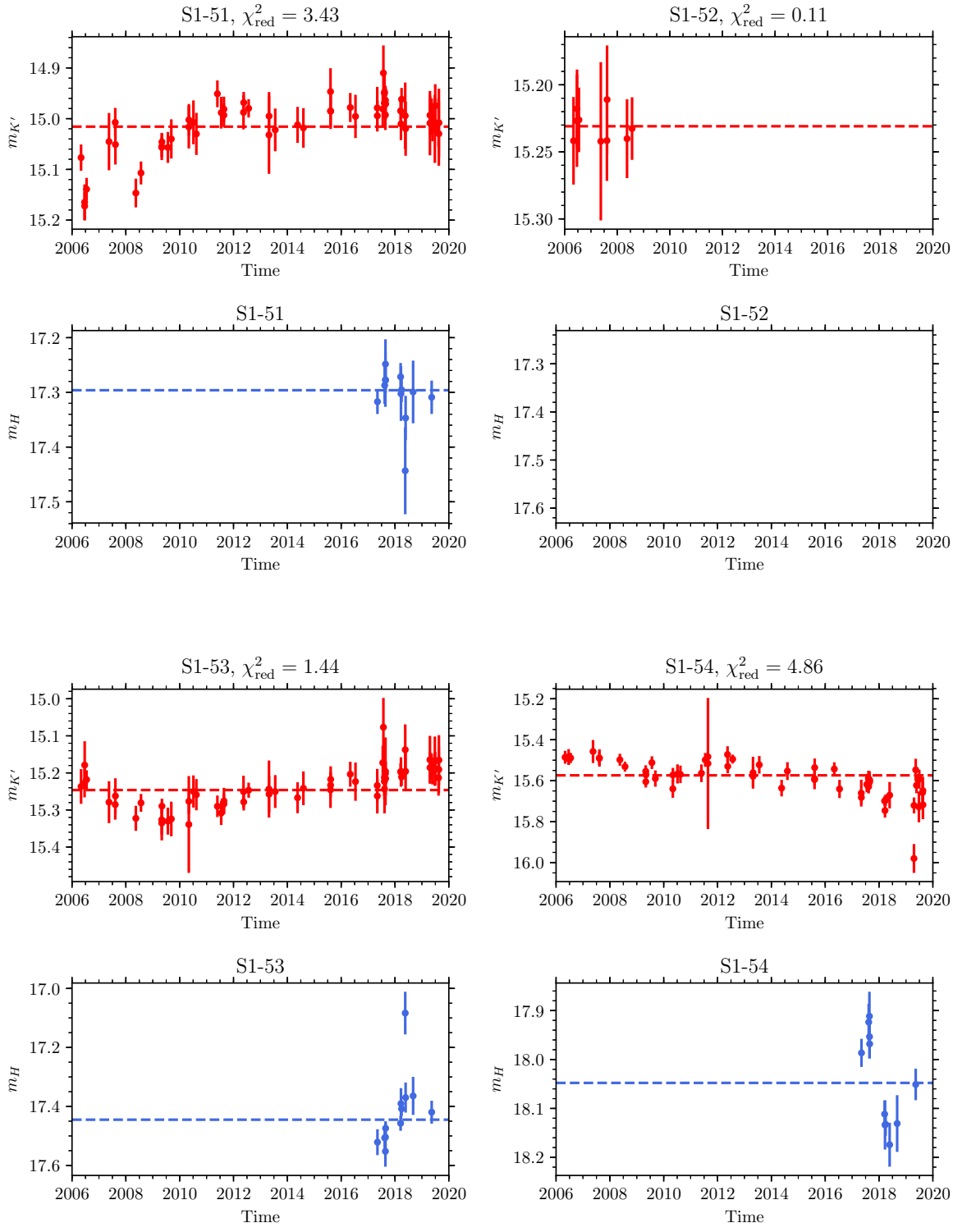
S1-51, $\chi^2_{\rm red} = 3.43$
S1-52, $\chi^2_{\rm red} = 0.11$
S1-51
S1-52
S1-53, $\chi^2_{\rm red} = 1.44$
S1-54, $\chi^2_{\rm red} = 4.86$
S1-53
S1-54
$m_{K'}$
m_H
Time

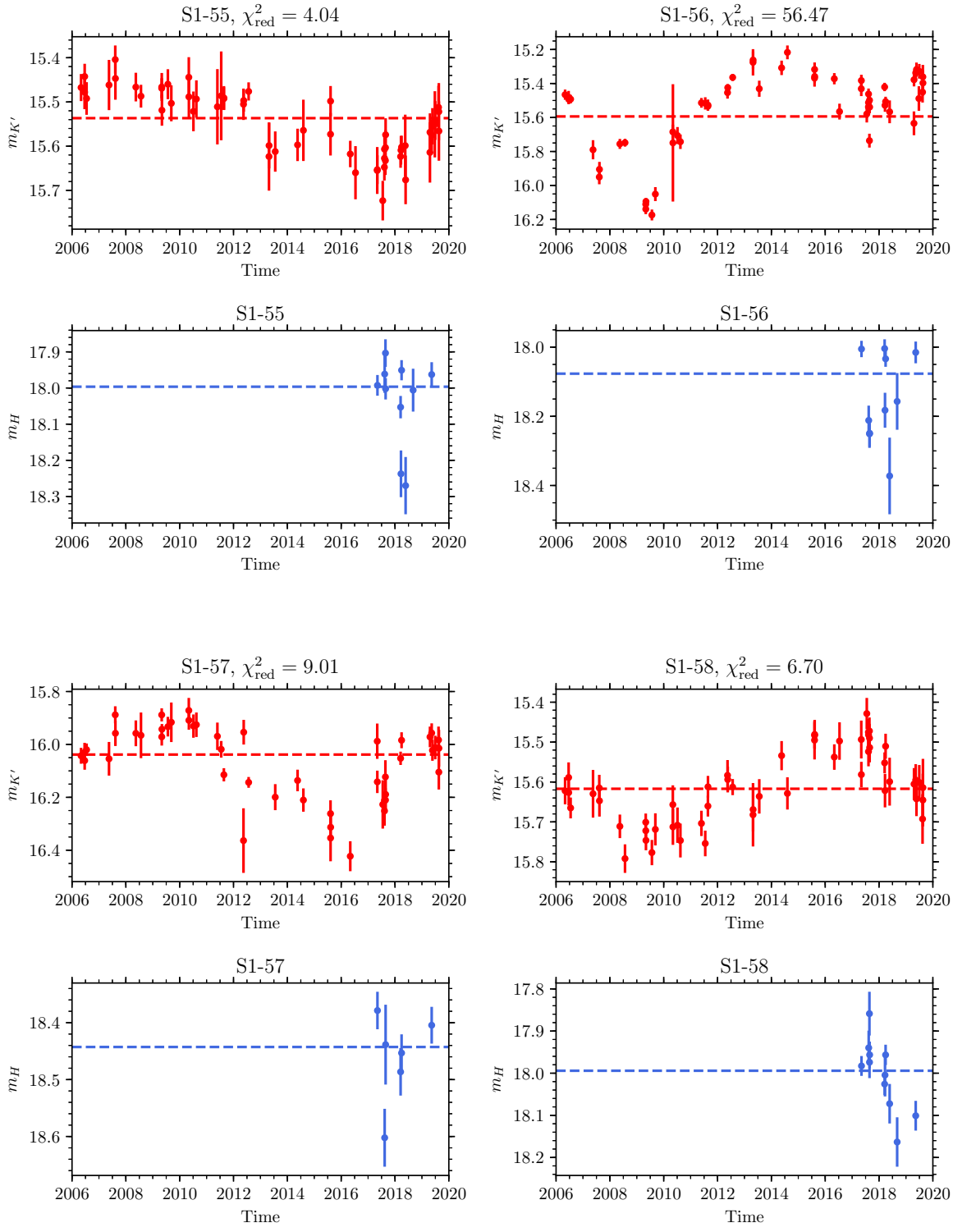
S1-55, $\chi^2_{\rm red} = 4.04$
S1-56, $\chi^2_{\rm red} = 56.47$
S1-55
S1-56
S1-57, $\chi^2_{\rm red} = 9.01$
S1-58, $\chi^2_{\rm red} = 6.70$
S1-57
S1-58
$m_{K'}$
m_H
Time

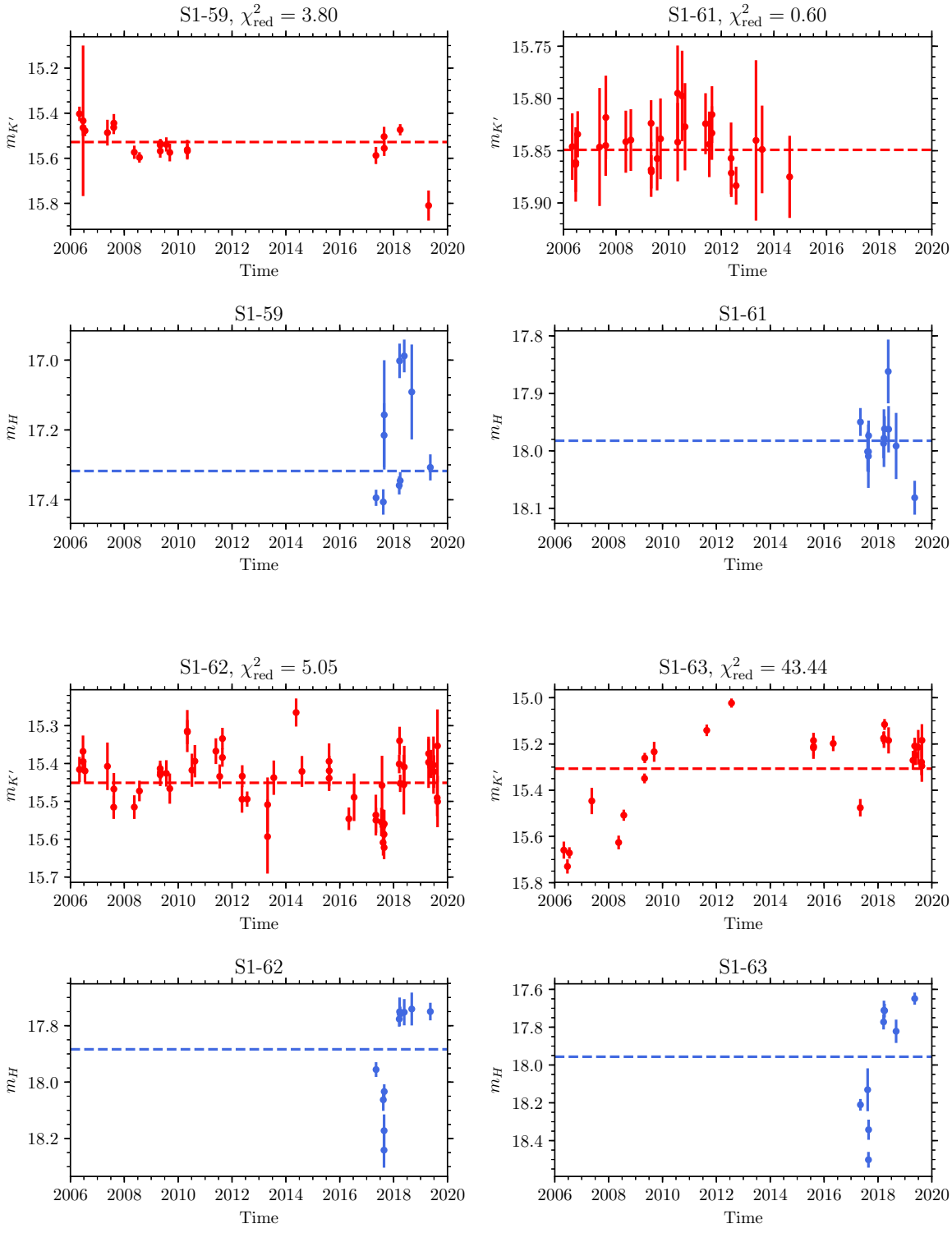
S1-59, $\chi^2_{\rm red} = 3.80$
S1-61, $\chi^2_{\rm red} = 0.60$
S1-59
S1-61
S1-62, $\chi^2_{\rm red} = 5.05$
S1-63, $\chi^2_{\rm red} = 43.44$
S1-62
S1-63
$m_{K'}$
m_H
Time

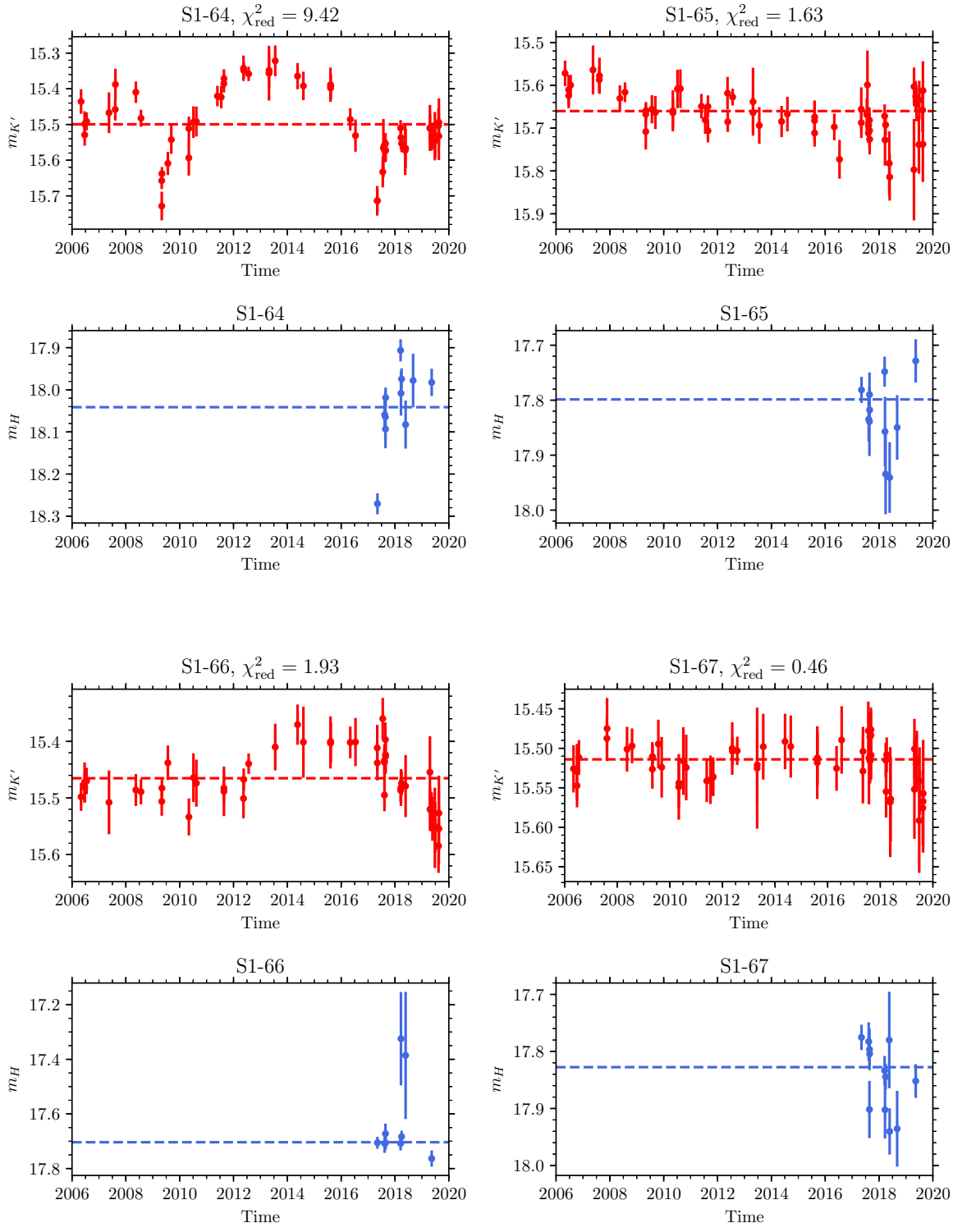
S1-64, $\chi^2_{\rm red} = 9.42$
S1-65, $\chi^2_{\rm red} = 1.63$
S1-64
S1-65
S1-66, $\chi^2_{\rm red} = 1.93$
S1-67, $\chi^2_{\rm red} = 0.46$
S1-66
S1-67
$m_{K'}$
m_H
Time

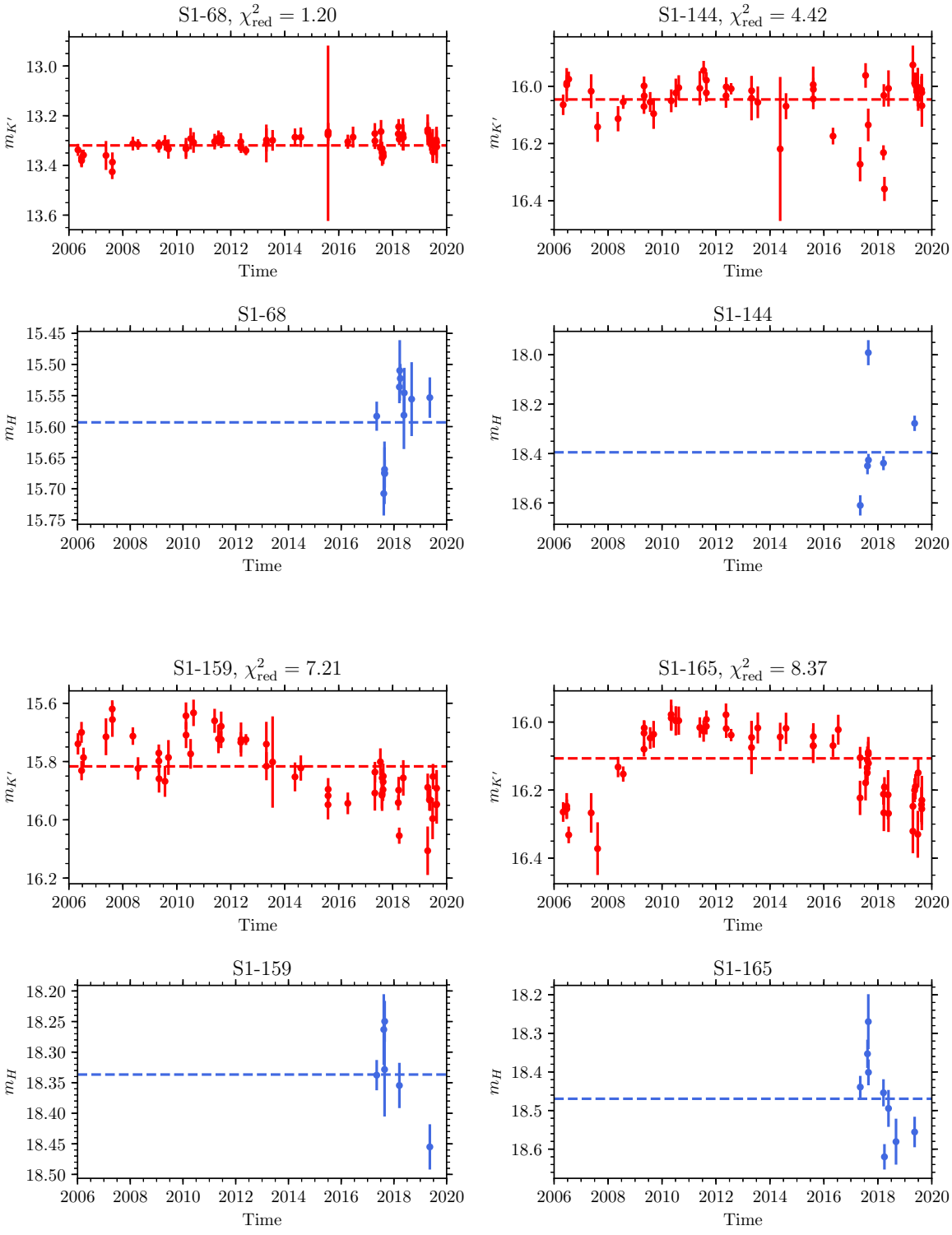
S1-68, $\chi^2_{\rm red} = 1.20$
S1-144, $\chi^2_{\rm red} = 4.42$
S1-68
S1-144
S1-159, $\chi^2_{\rm red} = 7.21$
S1-165, $\chi^2_{\rm red} = 8.37$
S1-159
S1-165
$m_{K'}$
m_H
Time

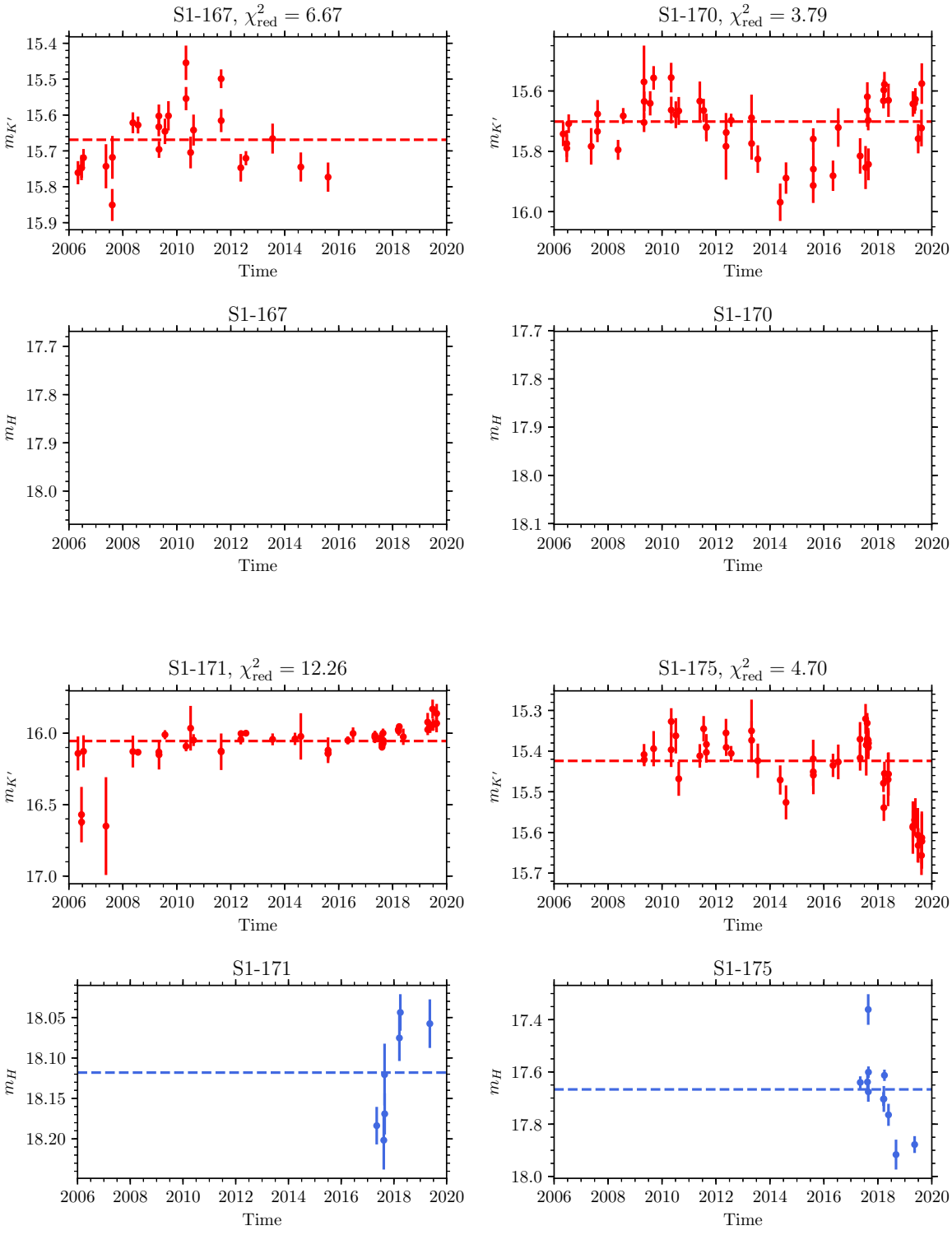
S1-167, $\chi^2_{\rm red} = 6.67$
S1-170, $\chi^2_{\rm red} = 3.79$
S1-167
S1-170
S1-171, $\chi^2_{\rm red} = 12.26$
S1-175, $\chi^2_{\rm red} = 4.70$
S1-171
S1-175
$m_{K'}$
m_H
Time

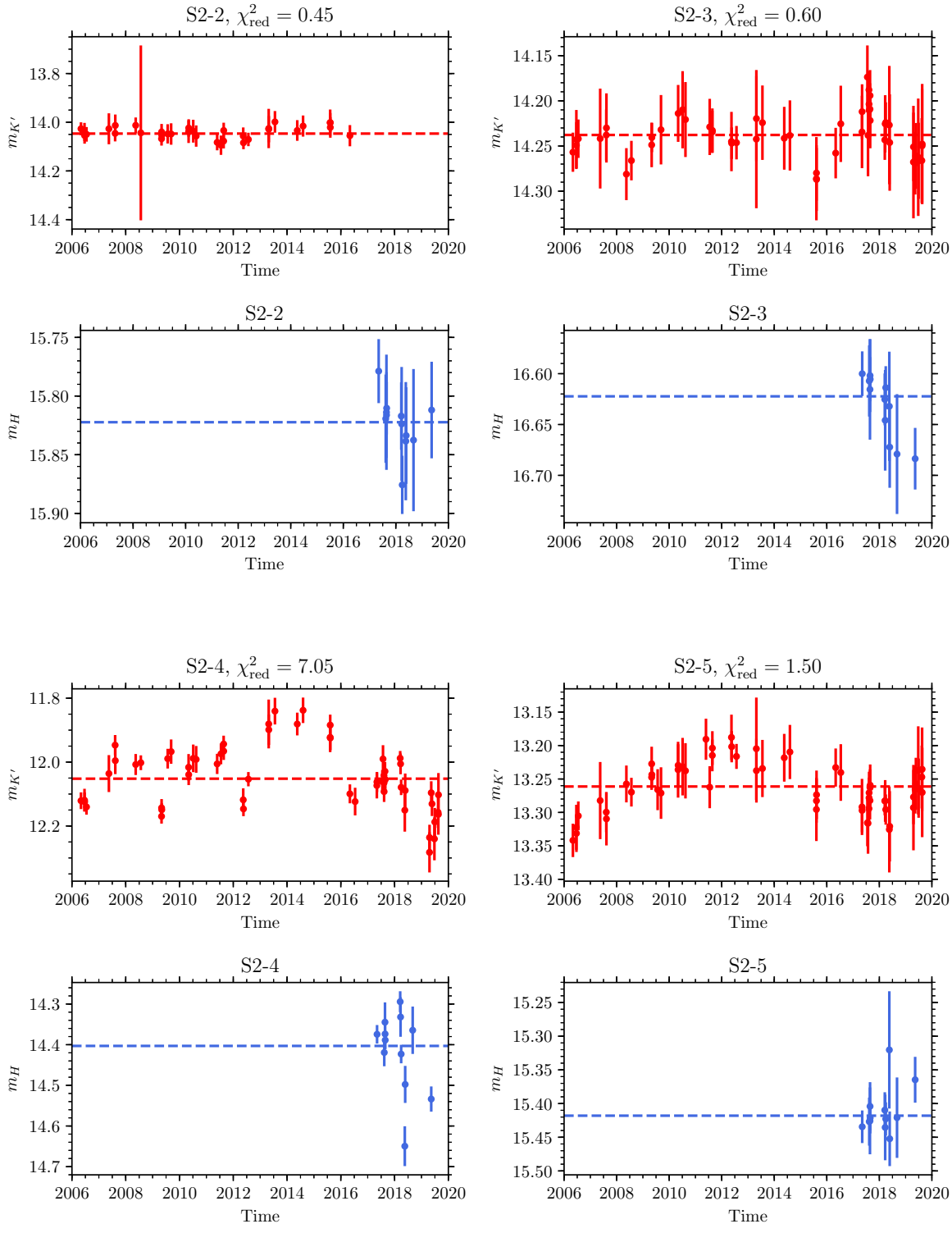
S2-2, $\chi^2_{\rm red} = 0.45$
S2-3, $\chi^2_{\rm red} = 0.60$
S2-2
S2-3
S2-4, $\chi^2_{\rm red} = 7.05$
S2-5, $\chi^2_{\rm red} = 1.50$
S2-4
S2-5
$m_{K'}$
m_H
Time

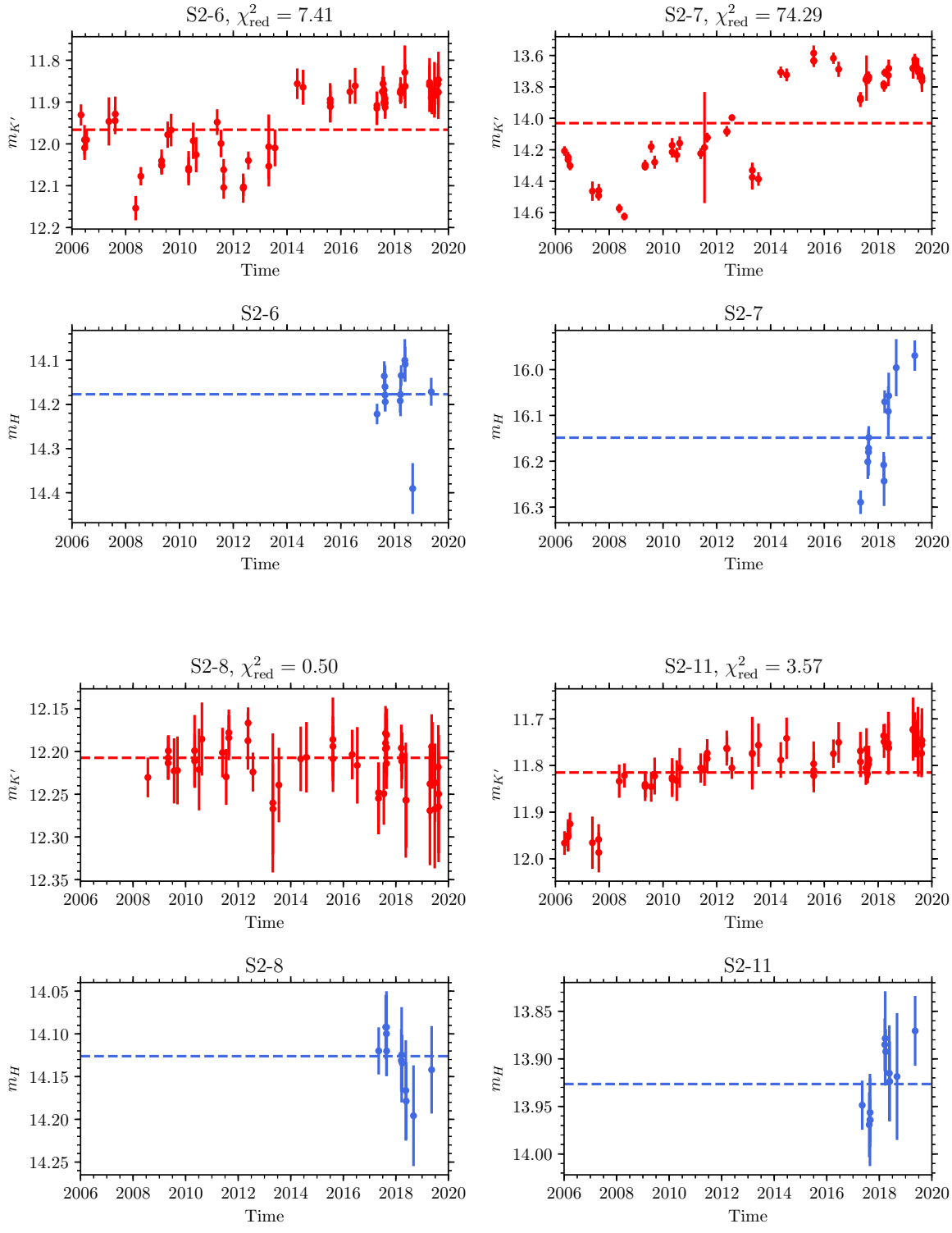
S2-6, $\chi^2_{\rm red} = 7.41$
S2-7, $\chi^2_{\rm red} = 74.29$
S2-6
S2-7
S2-8, $\chi^2_{\rm red} = 0.50$
S2-11, $\chi^2_{\rm red} = 3.57$
S2-8
S2-11
$m_{K'}$
m_H
Time

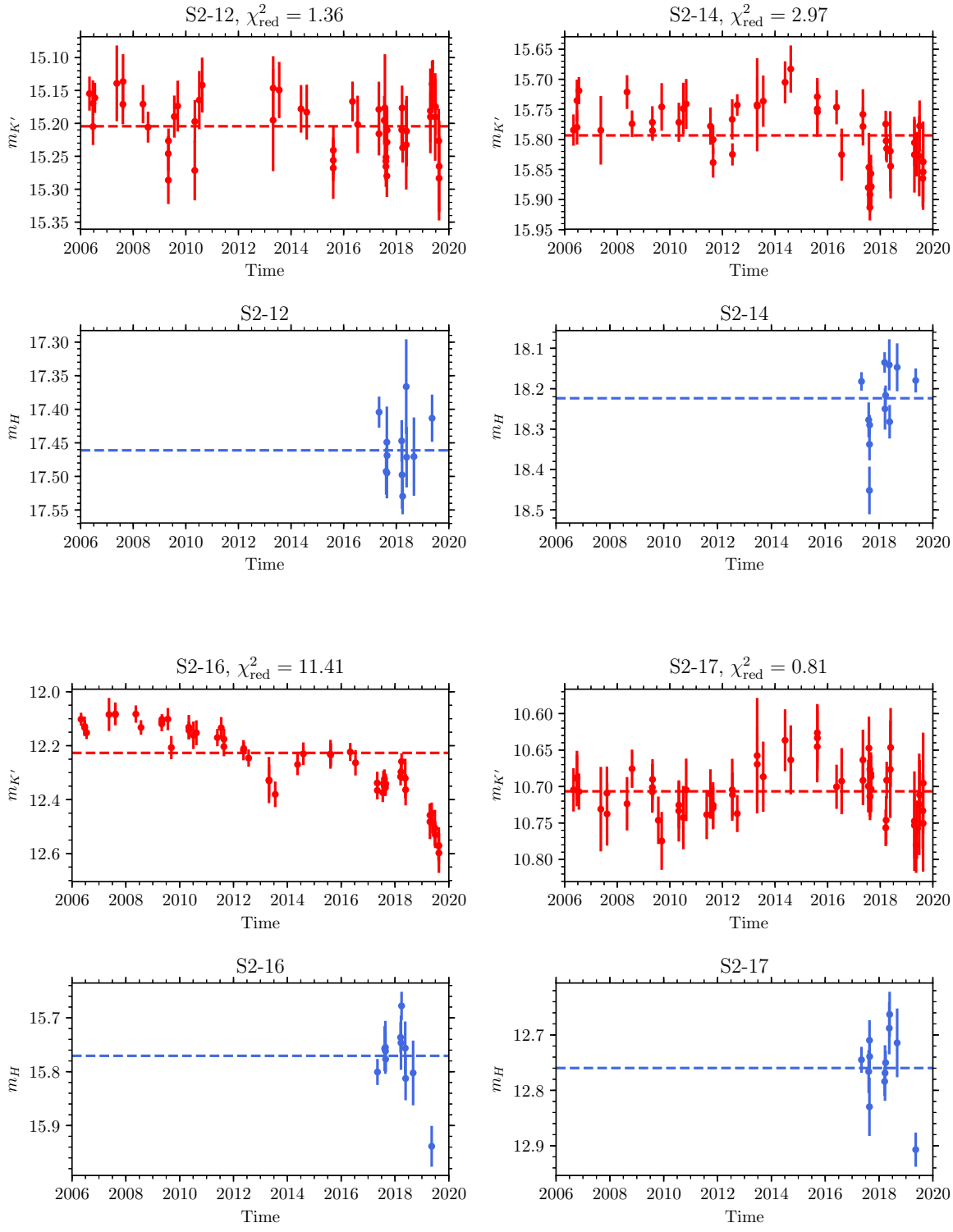
S2-12, $\chi^2_{\rm red} = 1.36$
S2-14, $\chi^2_{\rm red} = 2.97$
S2-12
S2-14
S2-16, $\chi^2_{\rm red} = 11.41$
S2-17, $\chi^2_{\rm red} = 0.81$
S2-16
S2-17
$m_{K'}$
m_H
Time

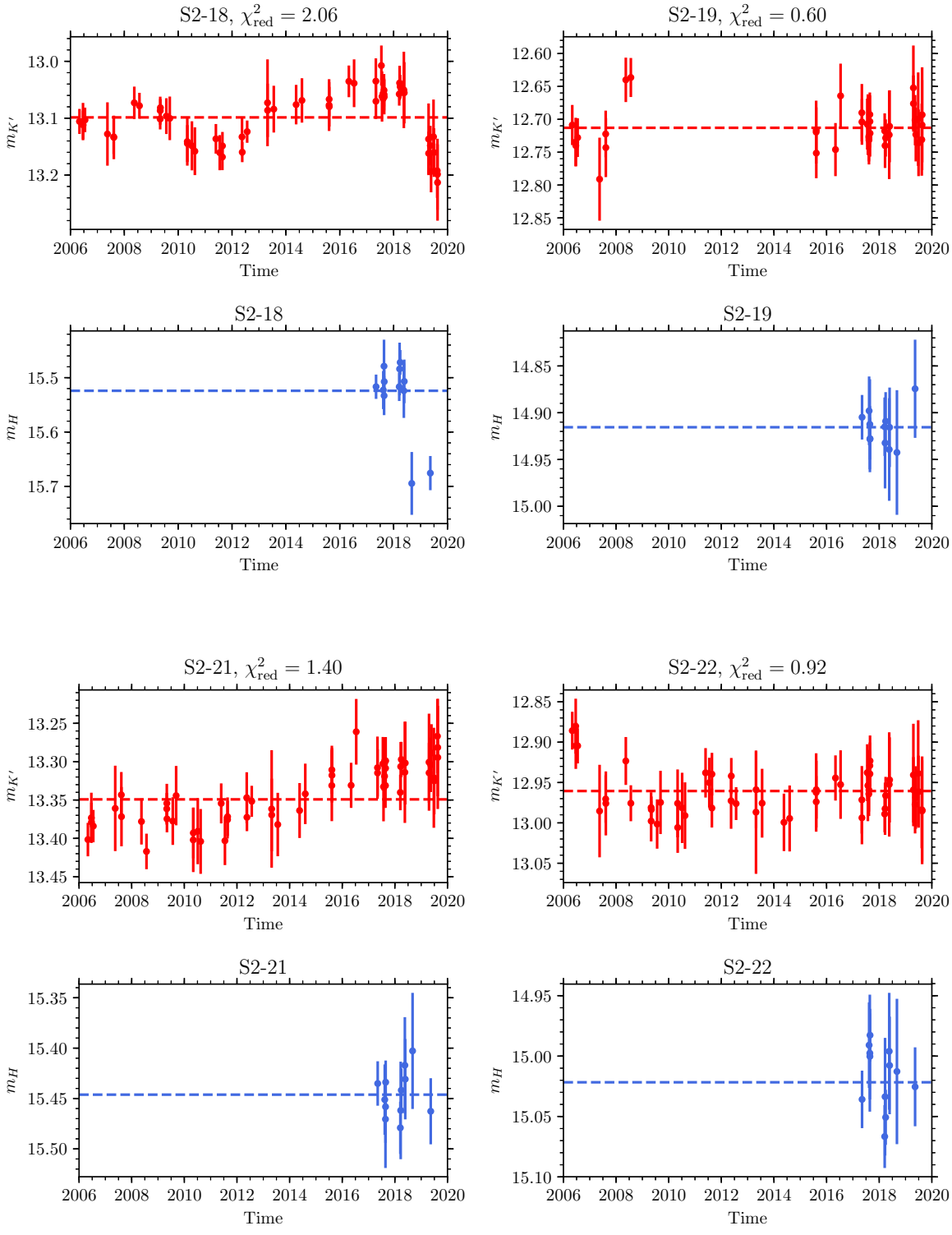
S2-18, $\chi^2_{\rm red} = 2.06$
S2-19, $\chi^2_{\rm red} = 0.60$
S2-18
S2-19
S2-21, $\chi^2_{\rm red} = 1.40$
S2-22, $\chi^2_{\rm red} = 0.92$
S2-21
S2-22
$m_{K'}$
m_H
Time

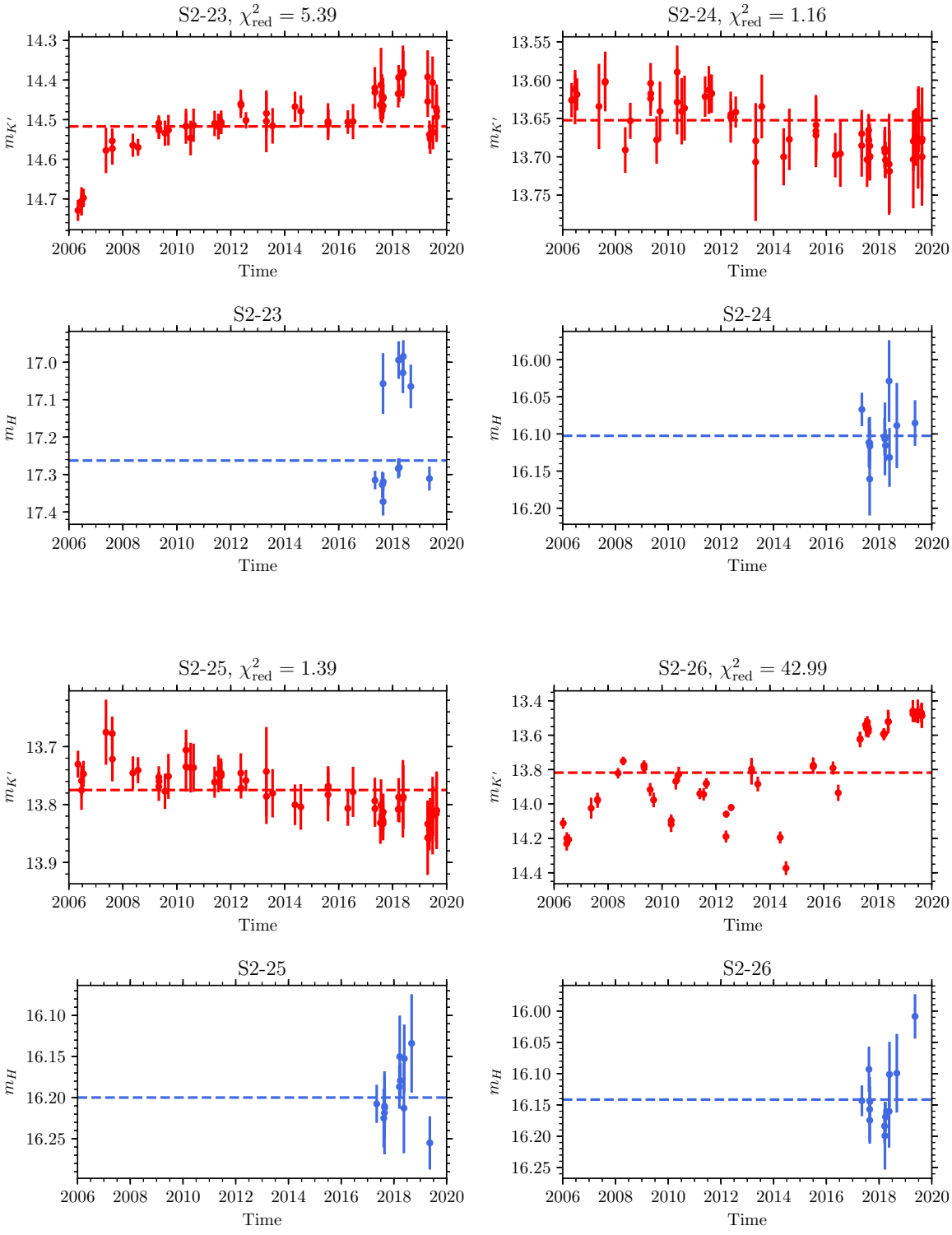
S2-23, $\chi^2_{\rm red} = 5.39$
S2-24, $\chi^2_{\rm red} = 1.16$
S2-23
S2-24
S2-25, $\chi^2_{\rm red} = 1.39$
S2-26, $\chi^2_{\rm red} = 42.99$
S2-25
S2-26
$m_{K'}$
m_H
Time

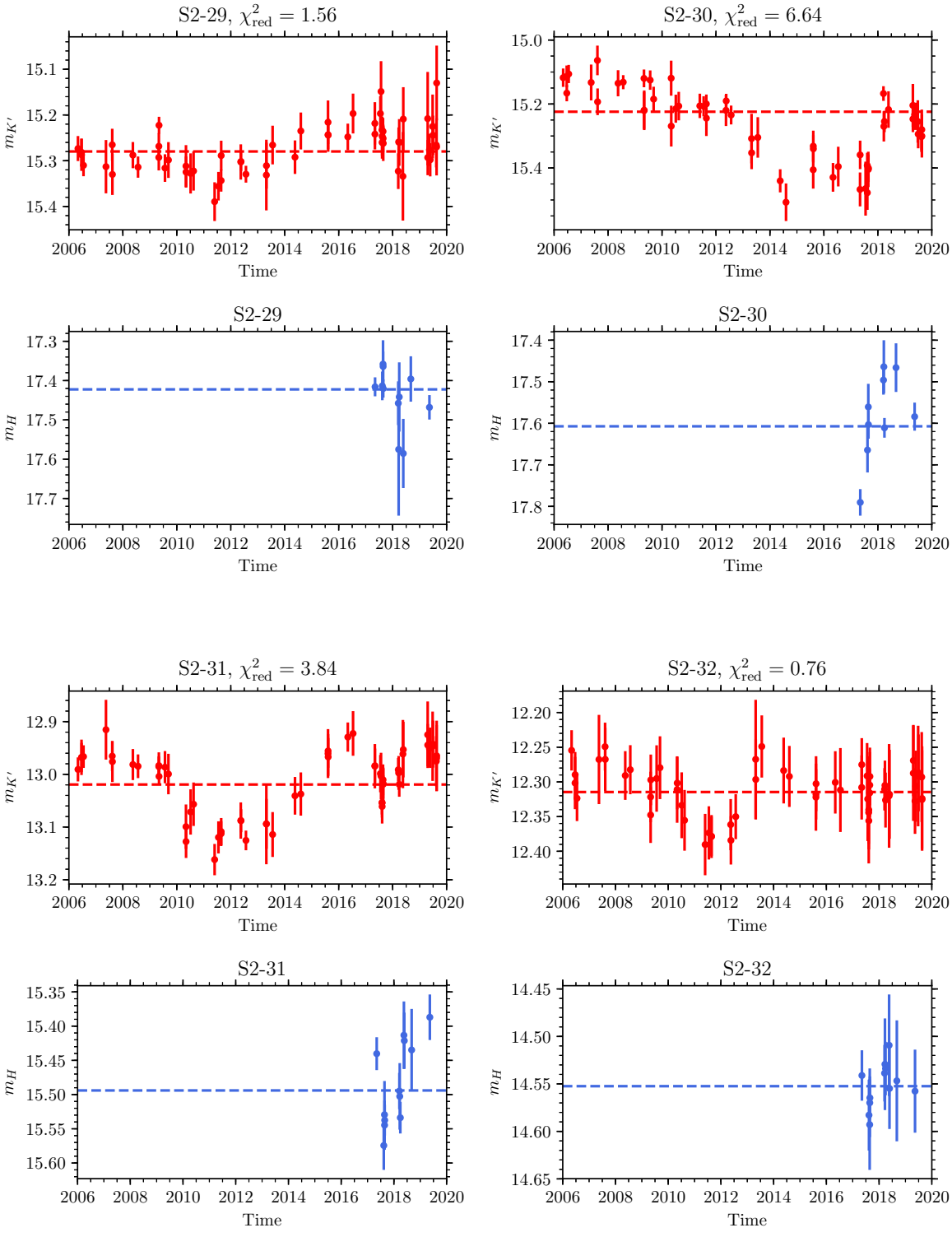
S2-29, $\chi^2_{\rm red} = 1.56$
S2-30, $\chi^2_{\rm red} = 6.64$
S2-29
S2-30
S2-31, $\chi^2_{\rm red} = 3.84$
S2-32, $\chi^2_{\rm red} = 0.76$
S2-31
S2-32
$m_{K'}$
m_H
Time

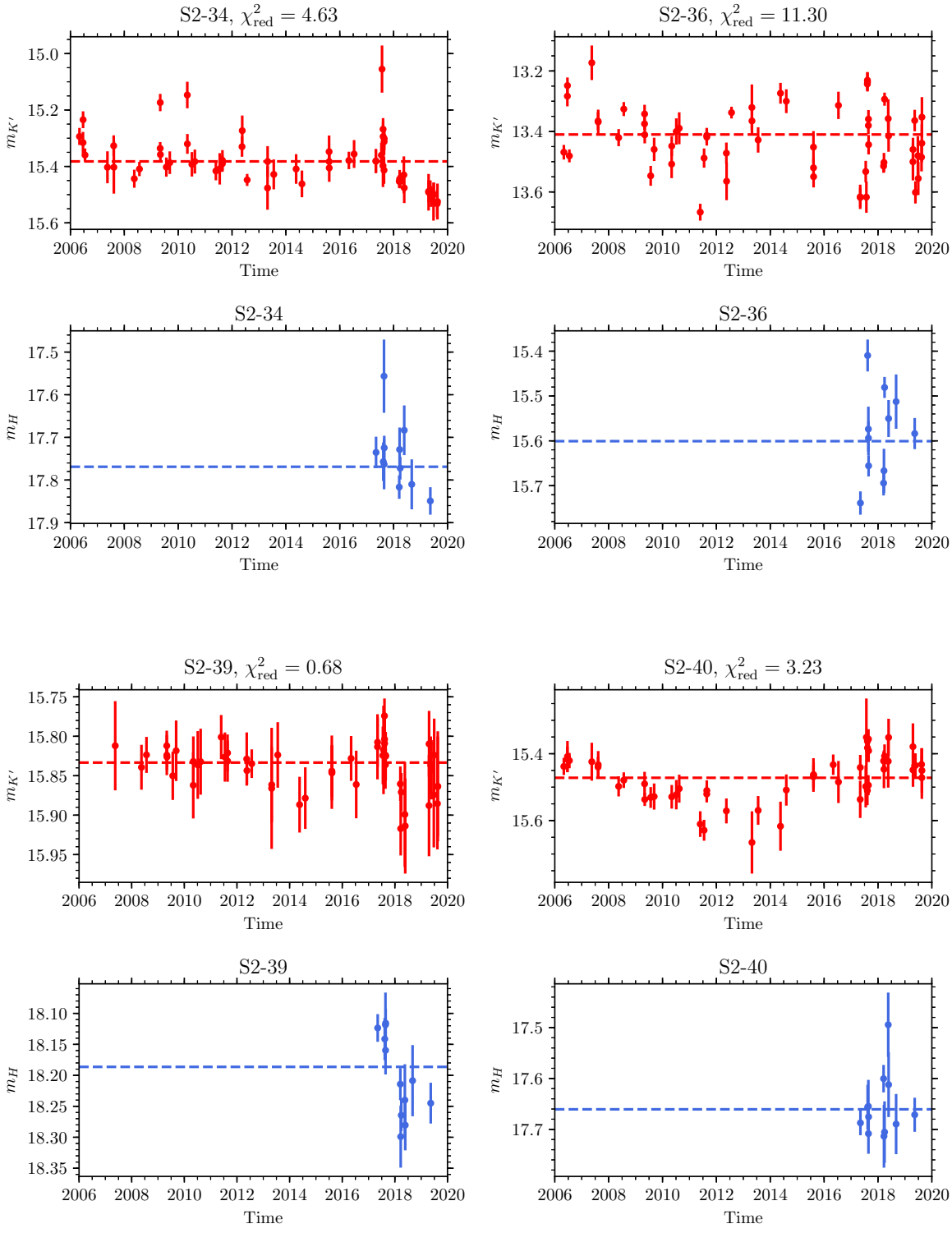
S2-34, $\chi^2_{\rm red} = 4.63$
S2-36, $\chi^2_{\rm red} = 11.30$
S2-34
S2-36
S2-39, $\chi^2_{\rm red} = 0.68$
S2-40, $\chi^2_{\rm red} = 3.23$
S2-39
S2-40
$m_{K'}$
m_H
Time

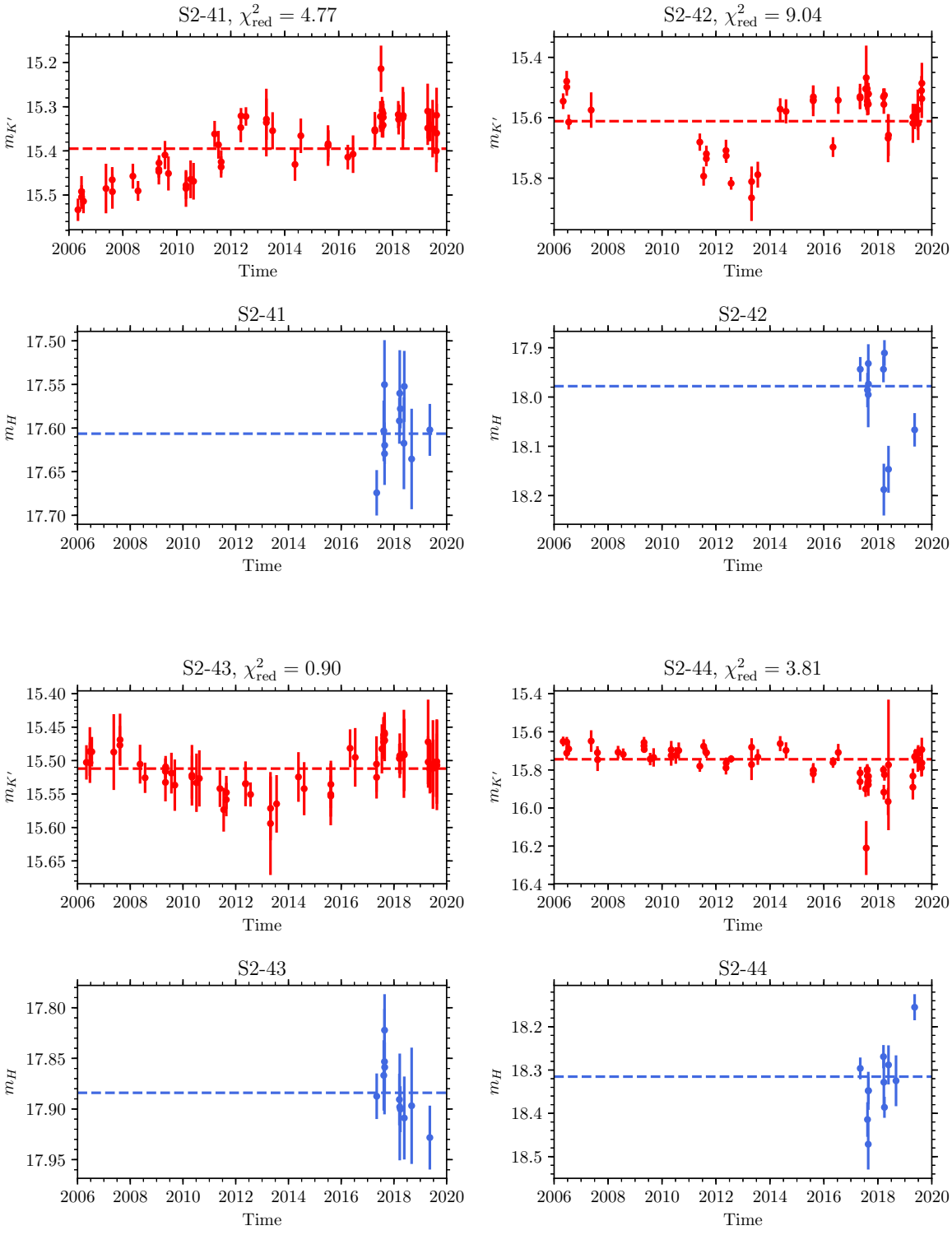
S2-41, $\chi^2_{\rm red} = 4.77$
S2-42, $\chi^2_{\rm red} = 9.04$
S2-41
S2-42
S2-43, $\chi^2_{\rm red} = 0.90$
S2-44, $\chi^2_{\rm red} = 3.81$
S2-43
S2-44
$m_{K'}$
m_H
Time

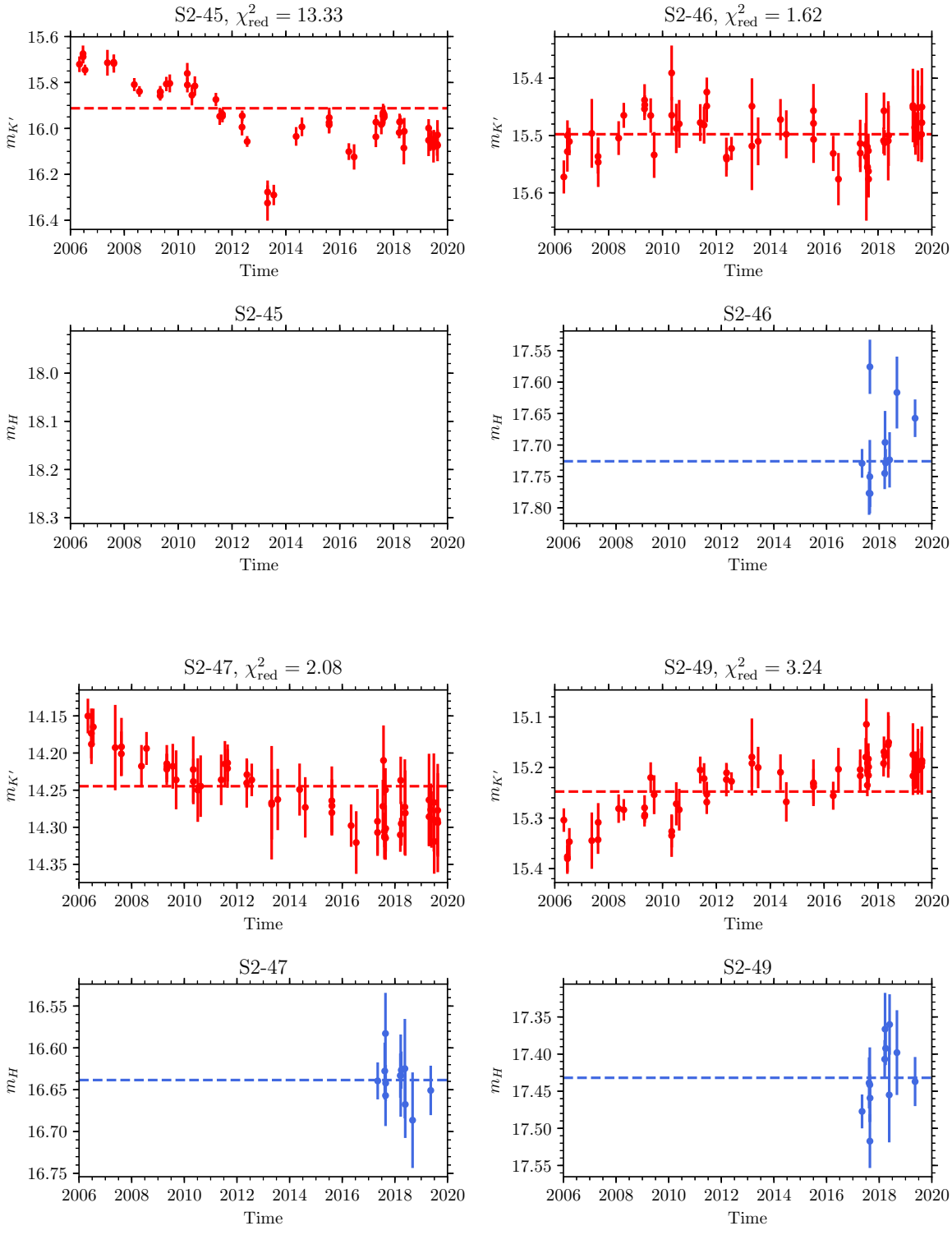
S2-45, $\chi^2_{\rm red} = 13.33$
S2-46, $\chi^2_{\rm red} = 1.62$
S2-45
S2-46
S2-47, $\chi^2_{\rm red} = 2.08$
S2-49, $\chi^2_{\rm red} = 3.24$
S2-47
S2-49
$m_{K'}$
m_H
Time

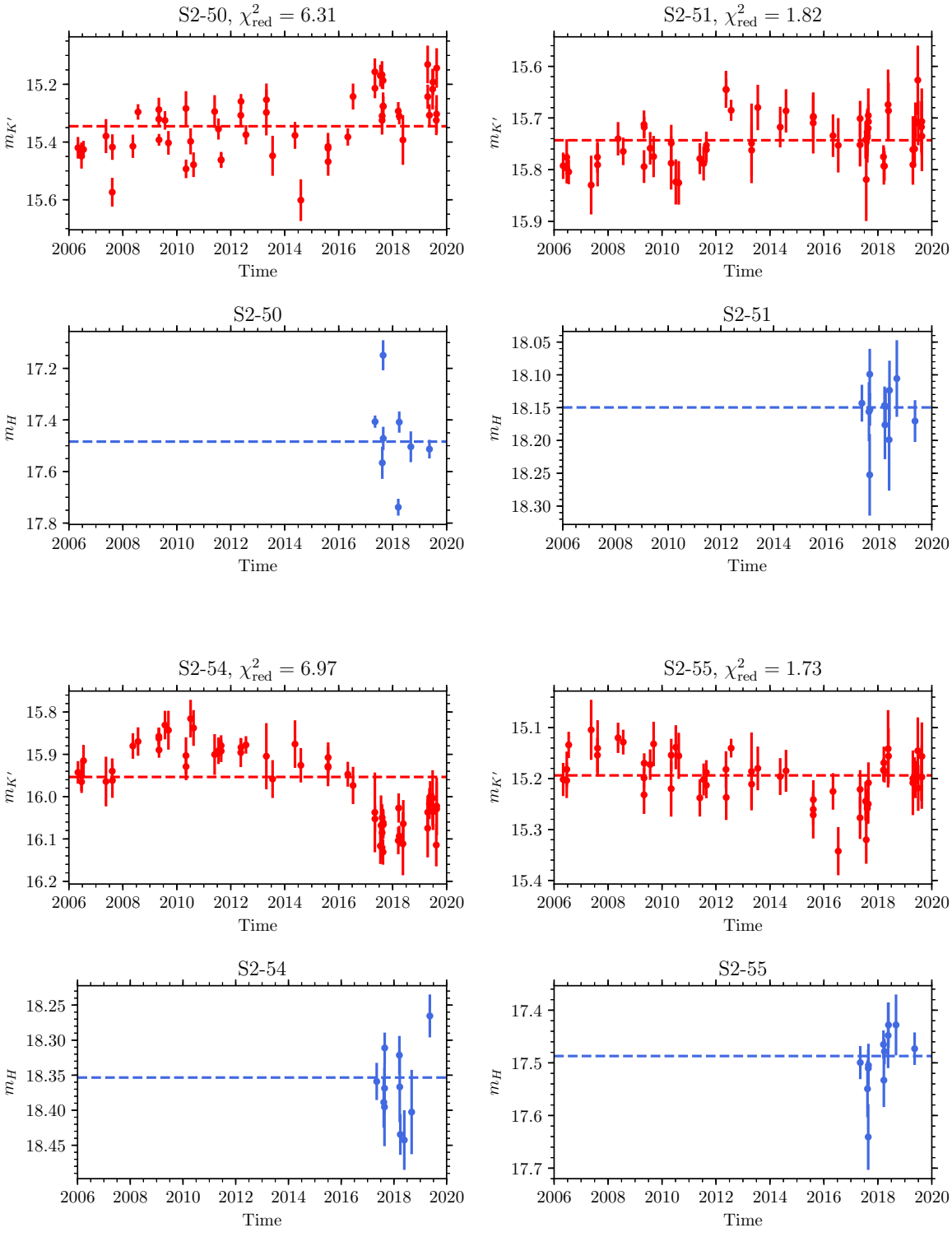
S2-50, $\chi^2_{\rm red} = 6.31$
S2-51, $\chi^2_{\rm red} = 1.82$
S2-50
S2-51
S2-54, $\chi^2_{\rm red} = 6.97$
S2-55, $\chi^2_{\rm red} = 1.73$
S2-54
S2-55
$m_{K'}$
m_H
Time

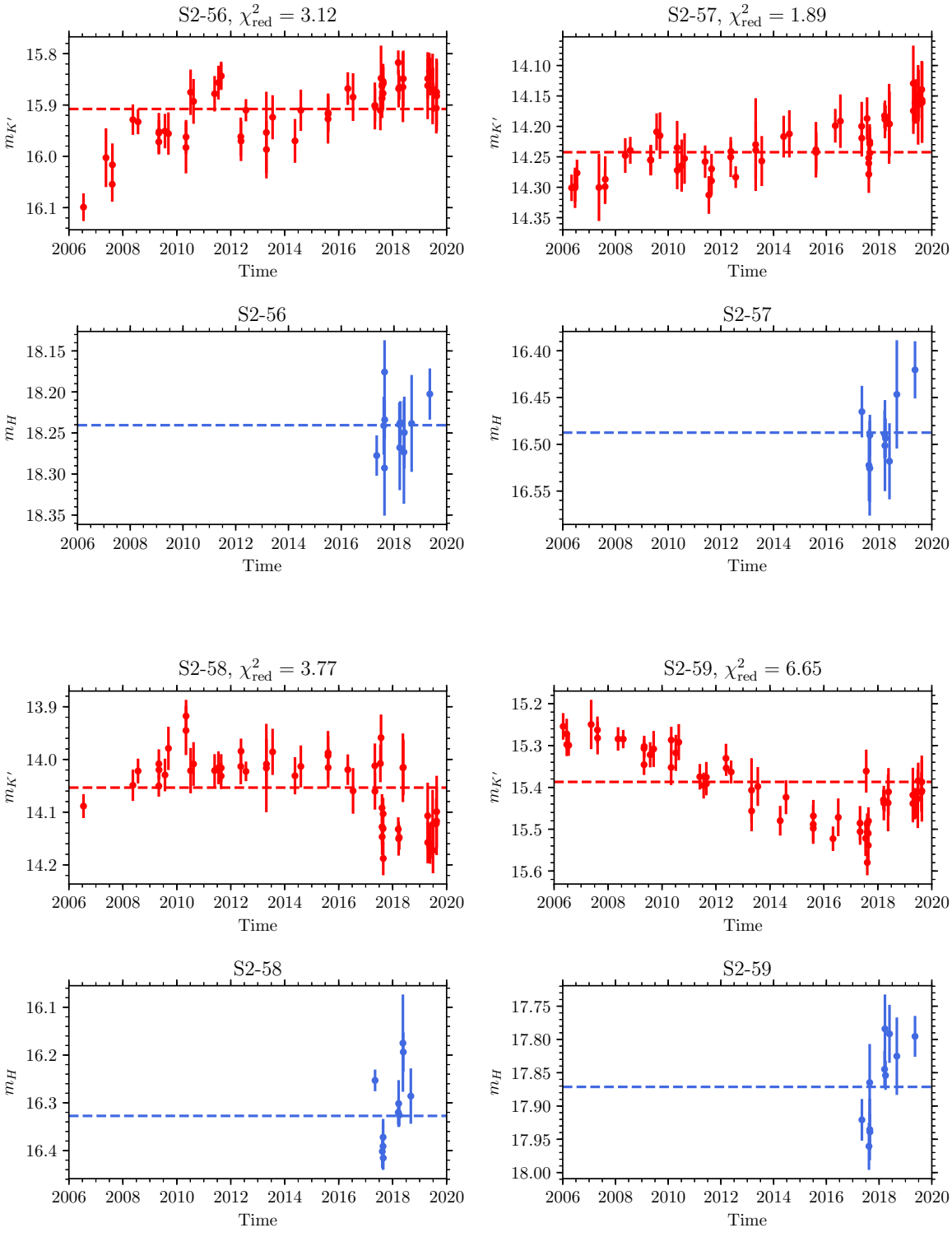
S2-56, $\chi^2_{\rm red} = 3.12$
S2-57, $\chi^2_{\rm red} = 1.89$
S2-56
S2-57
S2-58, $\chi^2_{\rm red} = 3.77$
S2-59, $\chi^2_{\rm red} = 6.65$
S2-58
S2-59
$m_{K'}$
m_H
Time

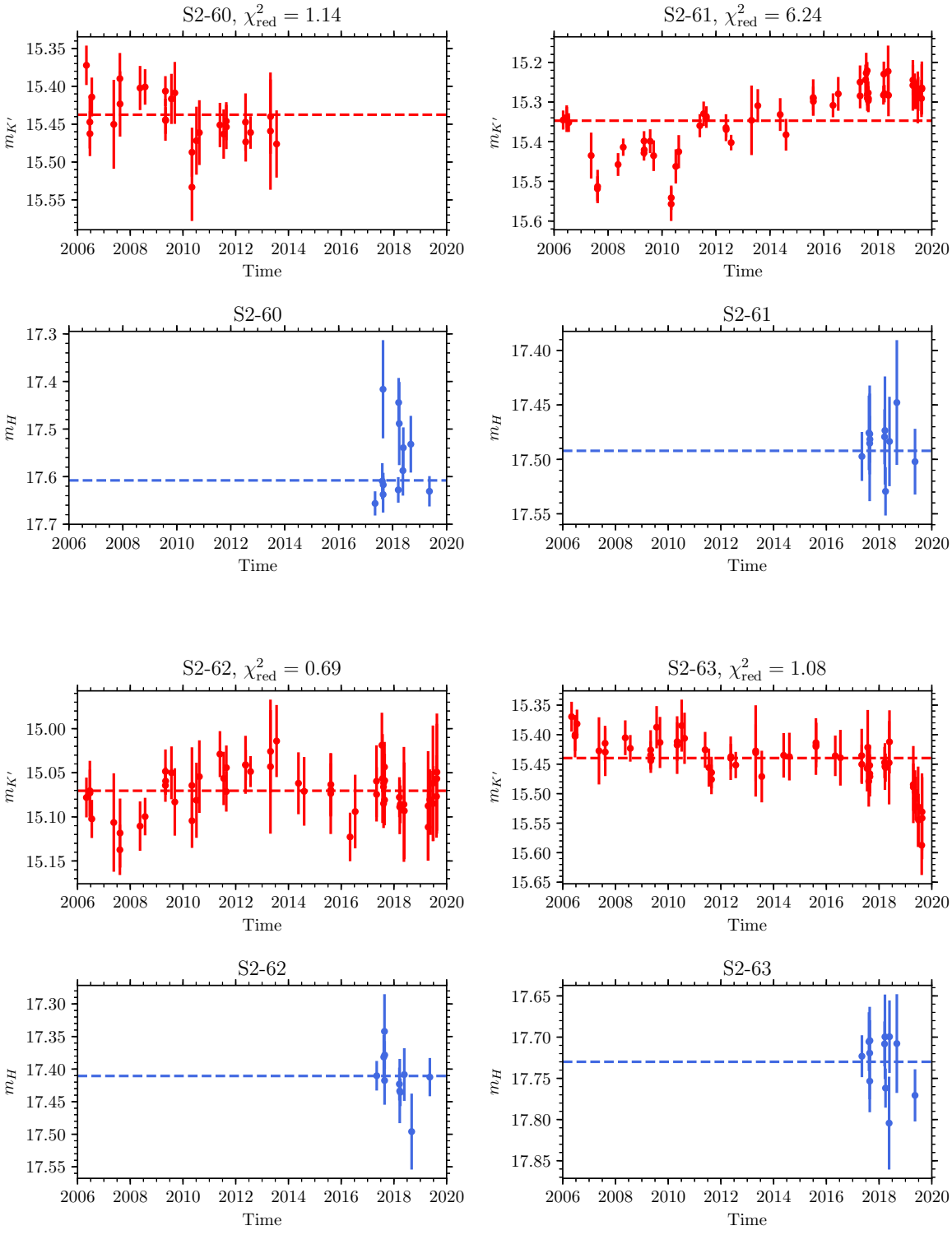
S2-60, $\chi^2_{\rm red} = 1.14$
S2-61, $\chi^2_{\rm red} = 6.24$
S2-60
S2-61
S2-62, $\chi^2_{\rm red} = 0.69$
S2-63, $\chi^2_{\rm red} = 1.08$
S2-62
S2-63
$m_{K'}$
m_H
Time

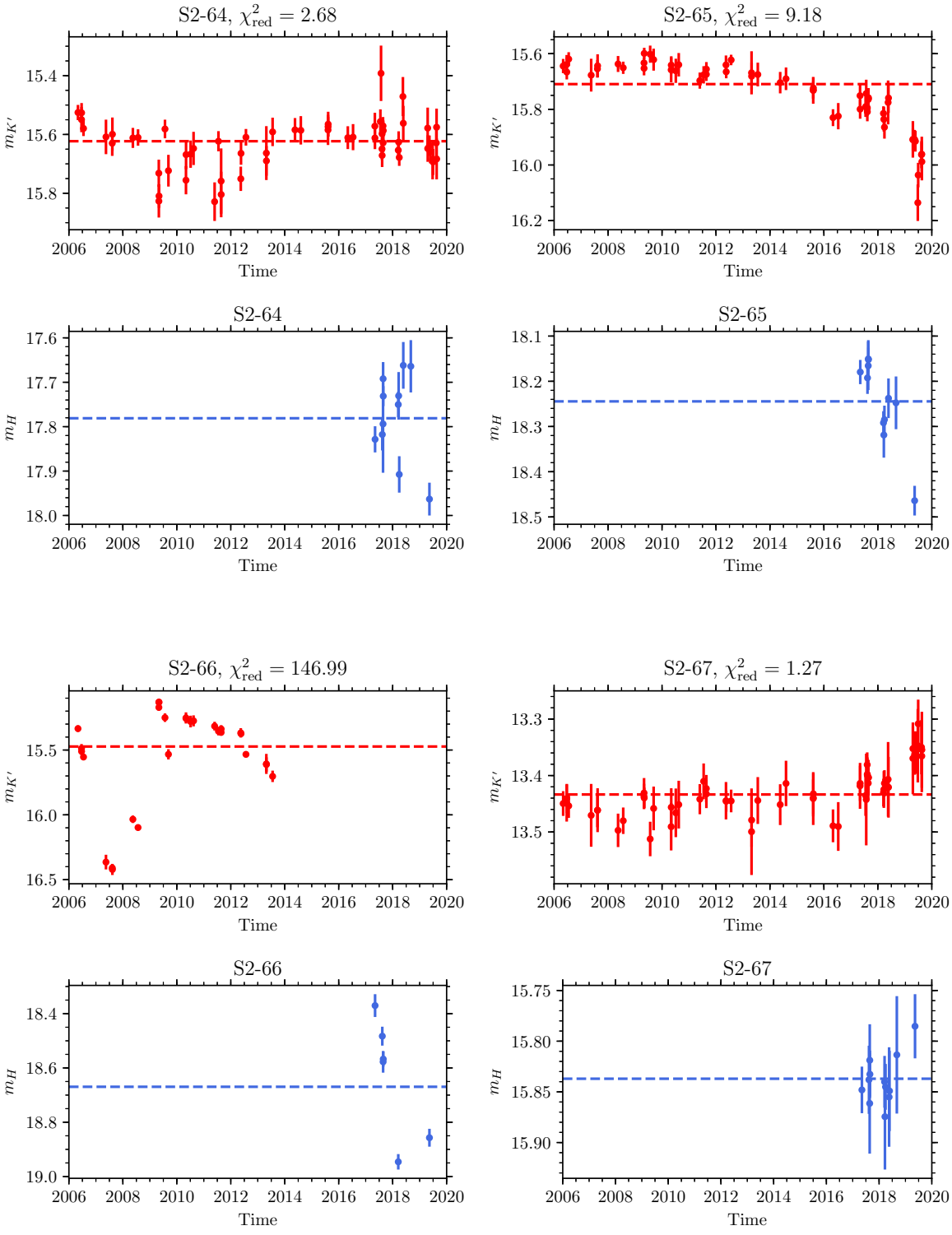
S2-64, $\chi^2_{\rm red} = 2.68$
S2-65, $\chi^2_{\rm red} = 9.18$
S2-64
S2-65
S2-66, $\chi^2_{\rm red} = 146.99$
S2-67, $\chi^2_{\rm red} = 1.27$
S2-66
S2-67
$m_{K'}$
m_H
Time

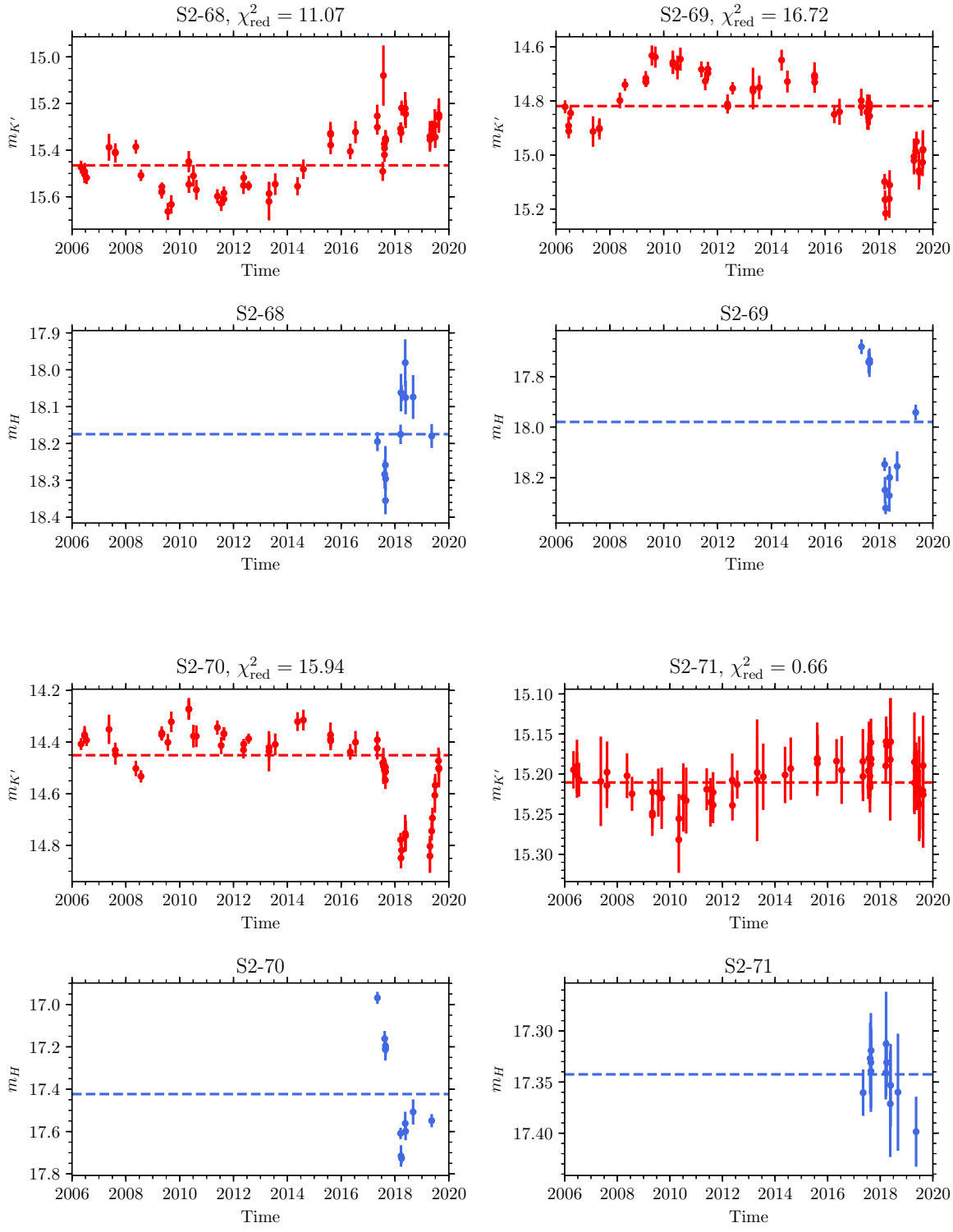
S2-68, $\chi^2_{\rm red} = 11.07$
S2-69, $\chi^2_{\rm red} = 16.72$
S2-68
S2-69
S2-70, $\chi^2_{\rm red} = 15.94$
S2-71, $\chi^2_{\rm red} = 0.66$
S2-70
S2-71
$m_{K'}$
m_H
Time

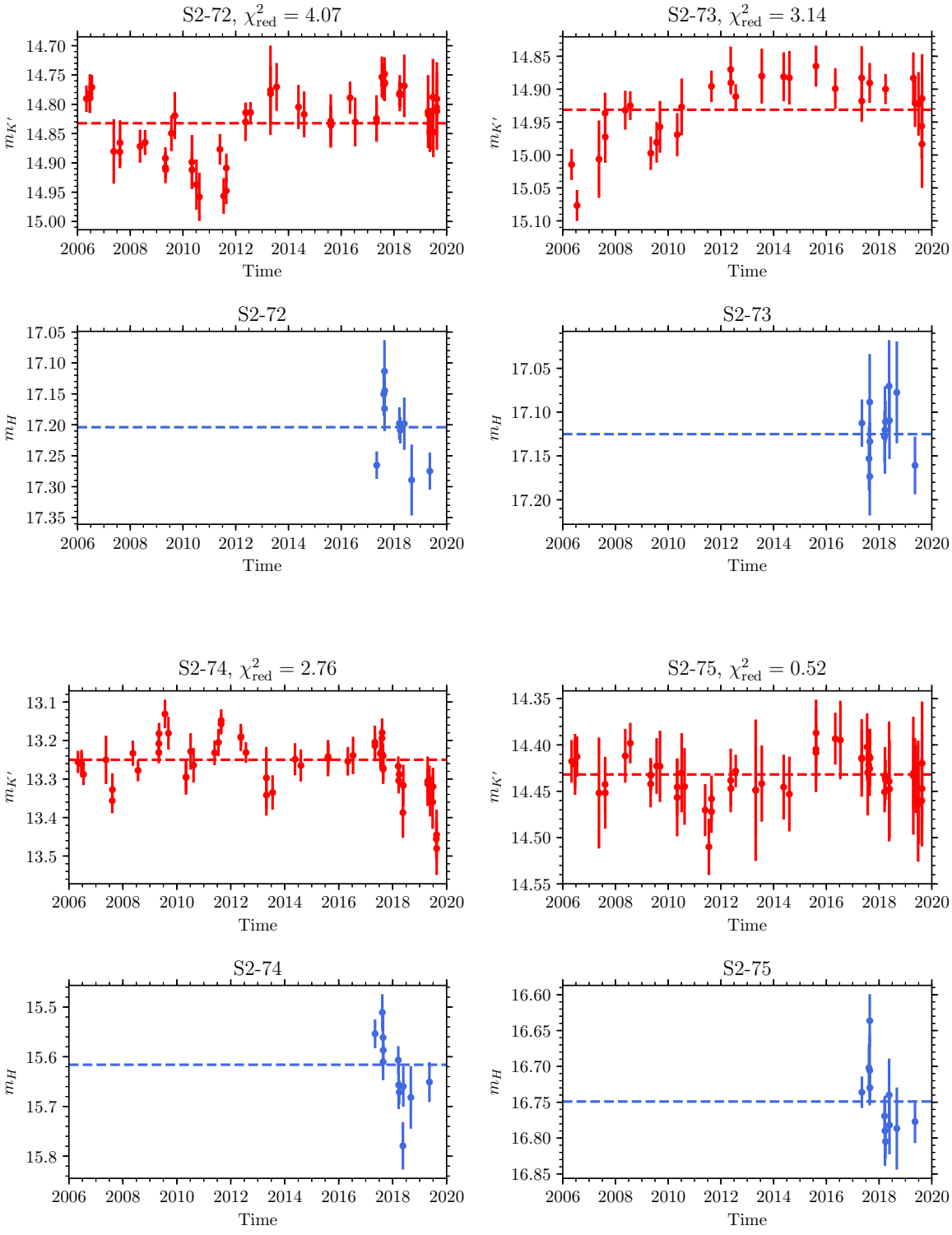
S2-72, $\chi^2_{\rm red} = 4.07$
S2-73, $\chi^2_{\rm red} = 3.14$
S2-72
S2-73
S2-74, $\chi^2_{\rm red} = 2.76$
S2-75, $\chi^2_{\rm red} = 0.52$
S2-74
S2-75
$m_{K'}$
m_H
Time

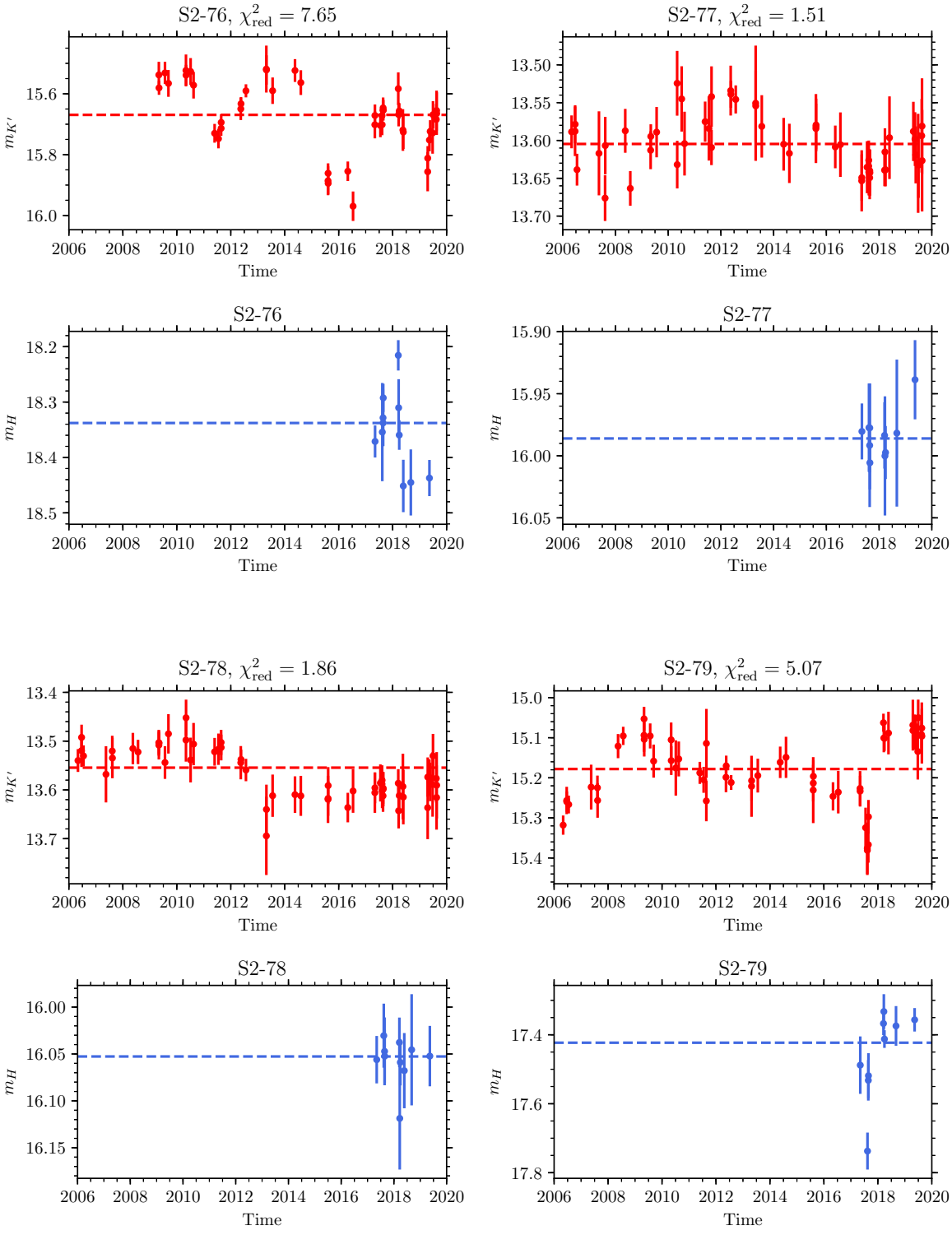
S2-76, $\chi^2_{\rm red} = 7.65$
S2-77, $\chi^2_{\rm red} = 1.51$
S2-76
S2-77
S2-78, $\chi^2_{\rm red} = 1.86$
S2-79, $\chi^2_{\rm red} = 5.07$
S2-78
S2-79
$m_{K'}$
m_H
Time

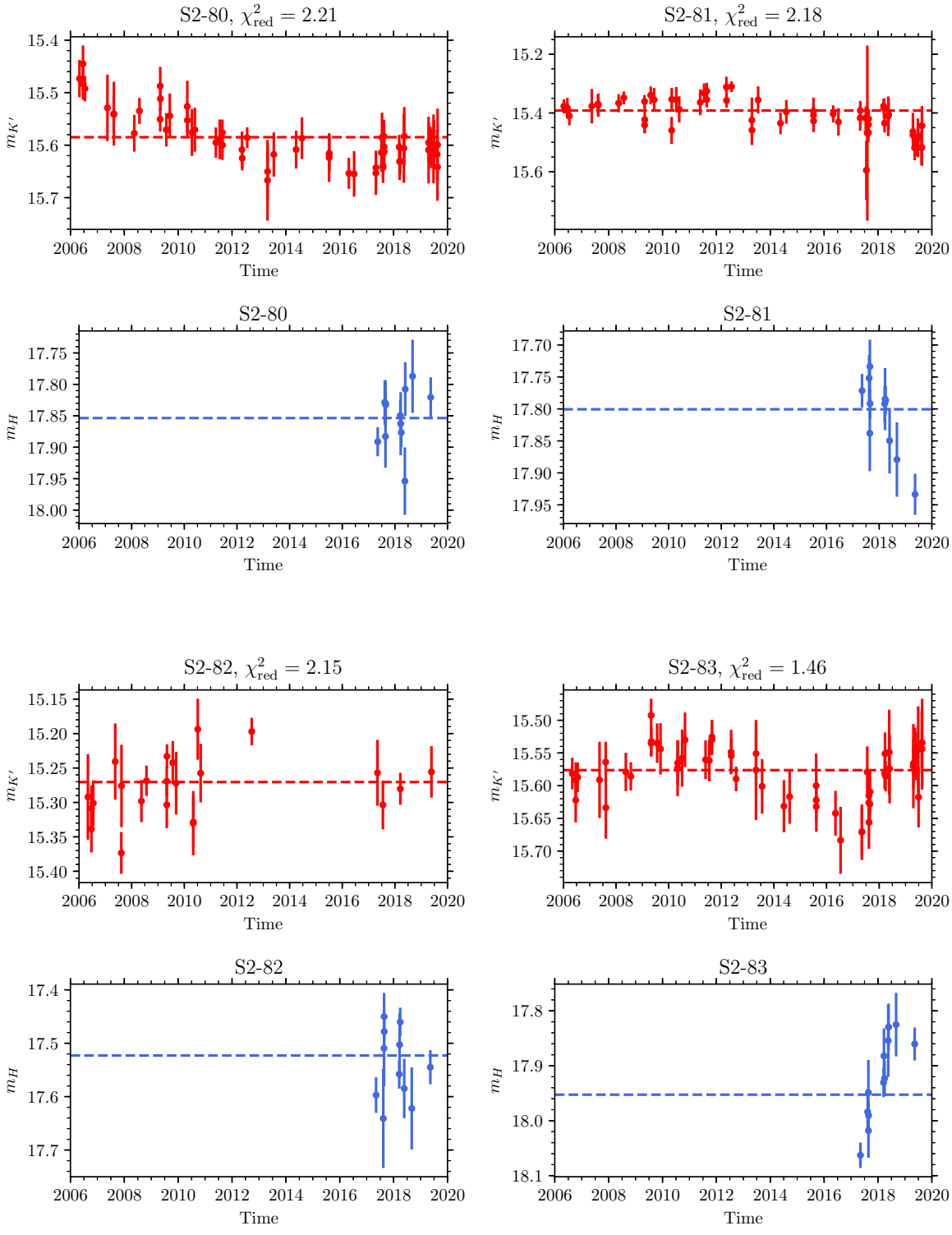
S2-80, $\chi^2_{\rm red} = 2.21$
S2-81, $\chi^2_{\rm red} = 2.18$
S2-80
S2-81
S2-82, $\chi^2_{\rm red} = 2.15$
S2-83, $\chi^2_{\rm red} = 1.46$
S2-82
S2-83
$m_{K'}$
m_H
Time

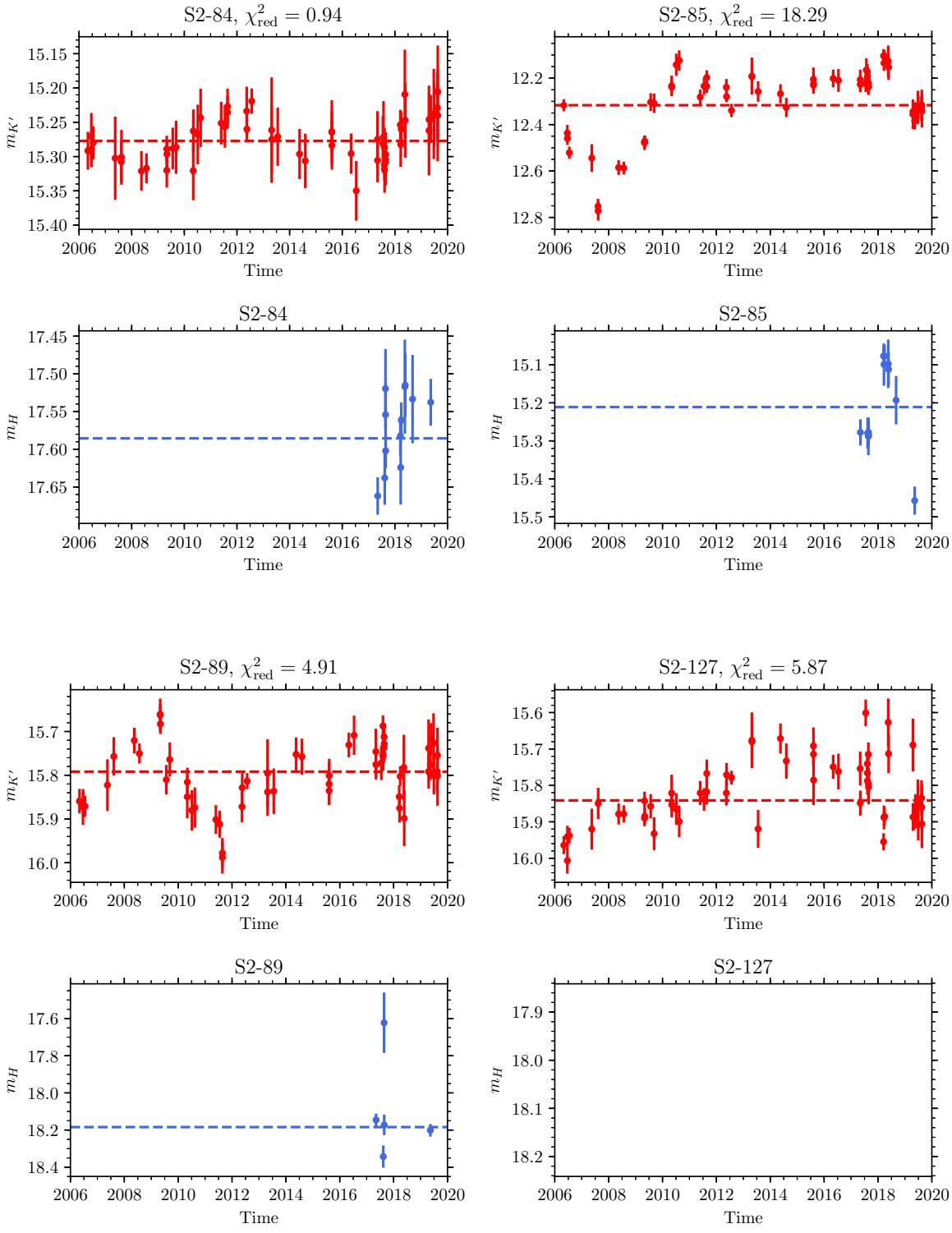
S2-84, $\chi^2_{\rm red} = 0.94$
S2-85, $\chi^2_{\rm red} = 18.29$
S2-84
S2-85
S2-89, $\chi^2_{\rm red} = 4.91$
S2-127, $\chi^2_{\rm red} = 5.87$
S2-89
S2-127
$m_{K'}$
m_H
Time

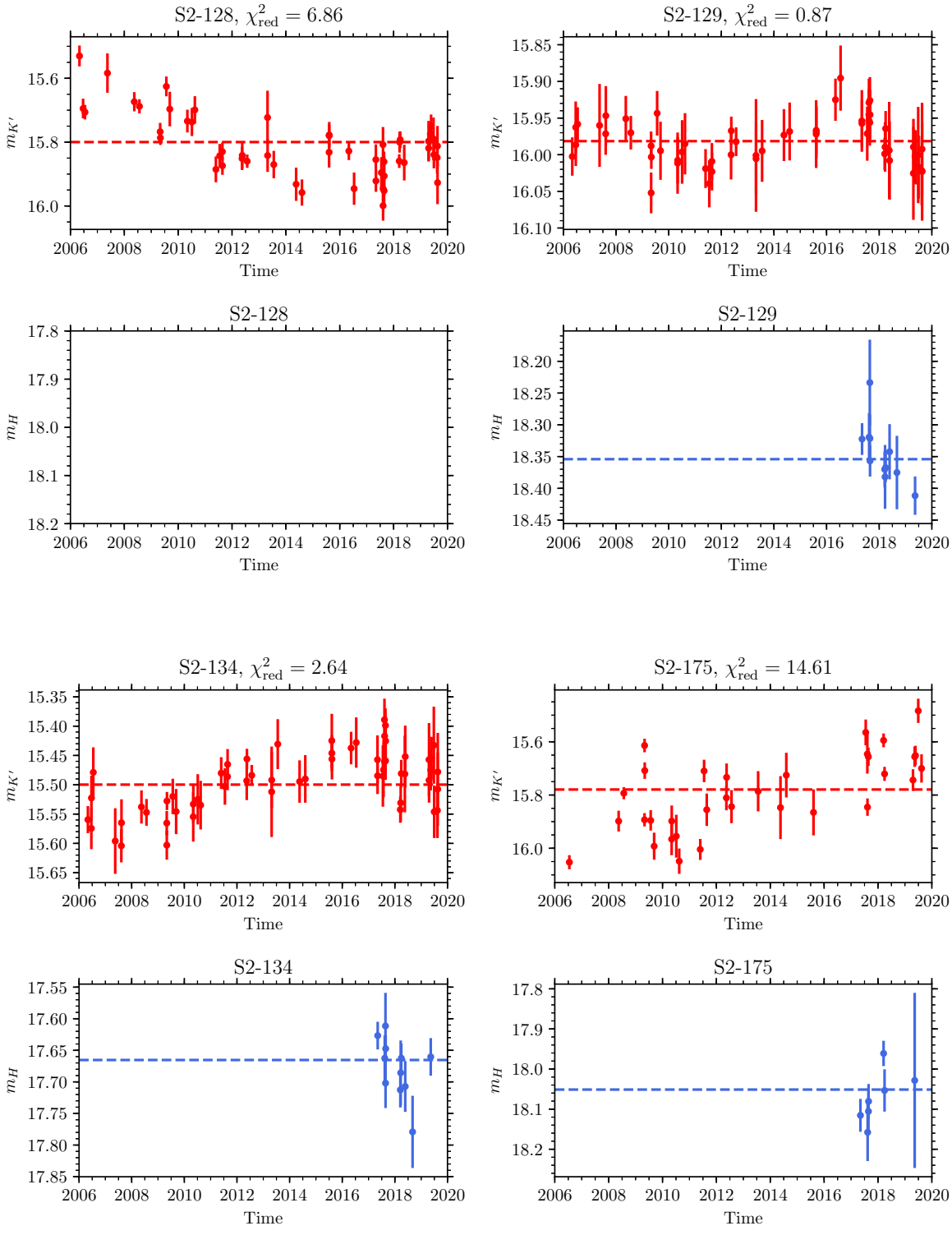
S2-128, $\chi^2_{\rm red} = 6.86$
S2-129, $\chi^2_{\rm red} = 0.87$
S2-128
S2-129
S2-134, $\chi^2_{\rm red} = 2.64$
S2-175, $\chi^2_{\rm red} = 14.61$
S2-134
S2-175
$m_{K'}$
m_H
Time

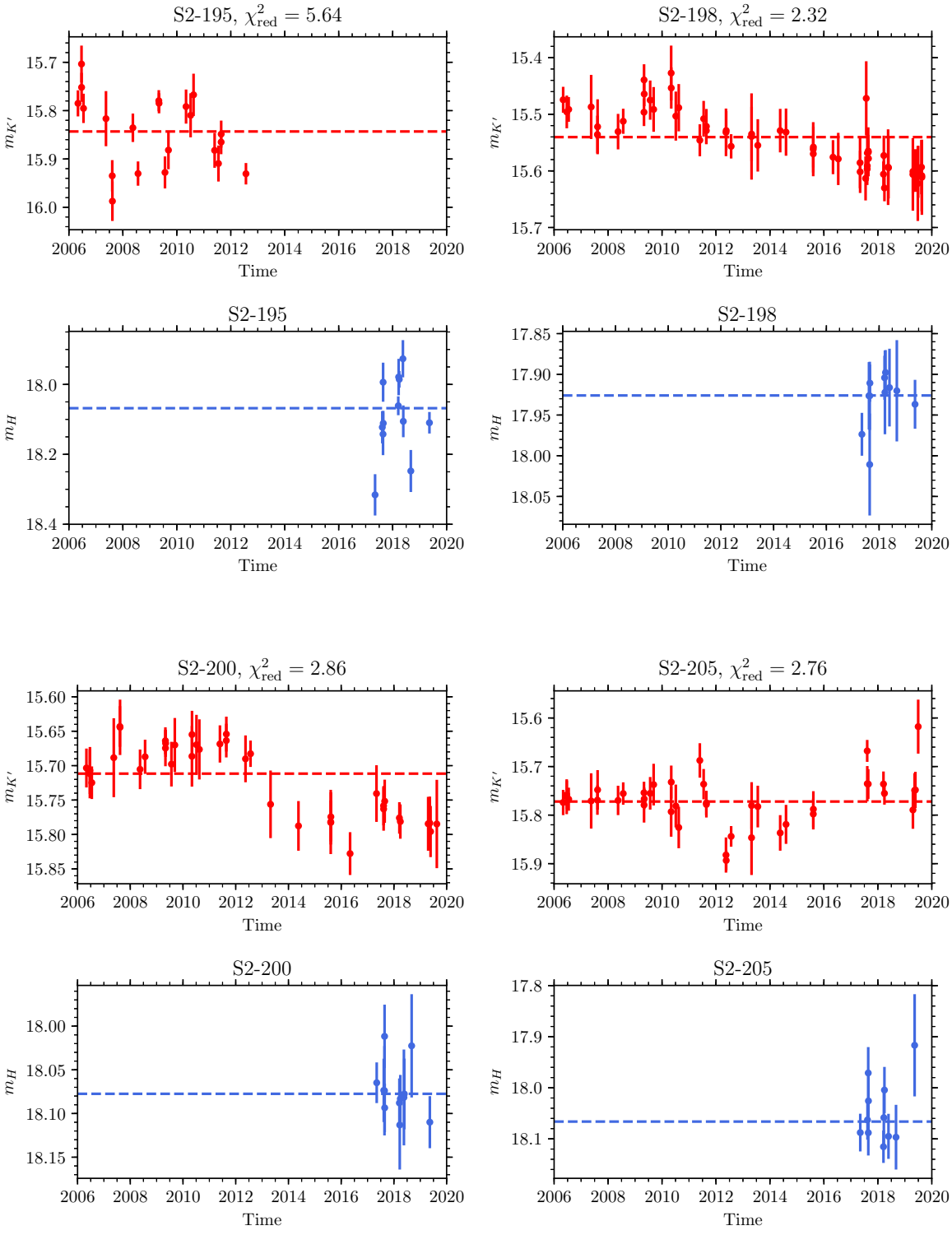
S2-195, $\chi^2_{\rm red} = 5.64$
S2-198, $\chi^2_{\rm red} = 2.32$
S2-195
S2-198
S2-200, $\chi^2_{\rm red} = 2.86$
S2-205, $\chi^2_{\rm red} = 2.76$
S2-200
S2-205
$m_{K'}$
m_H
Time

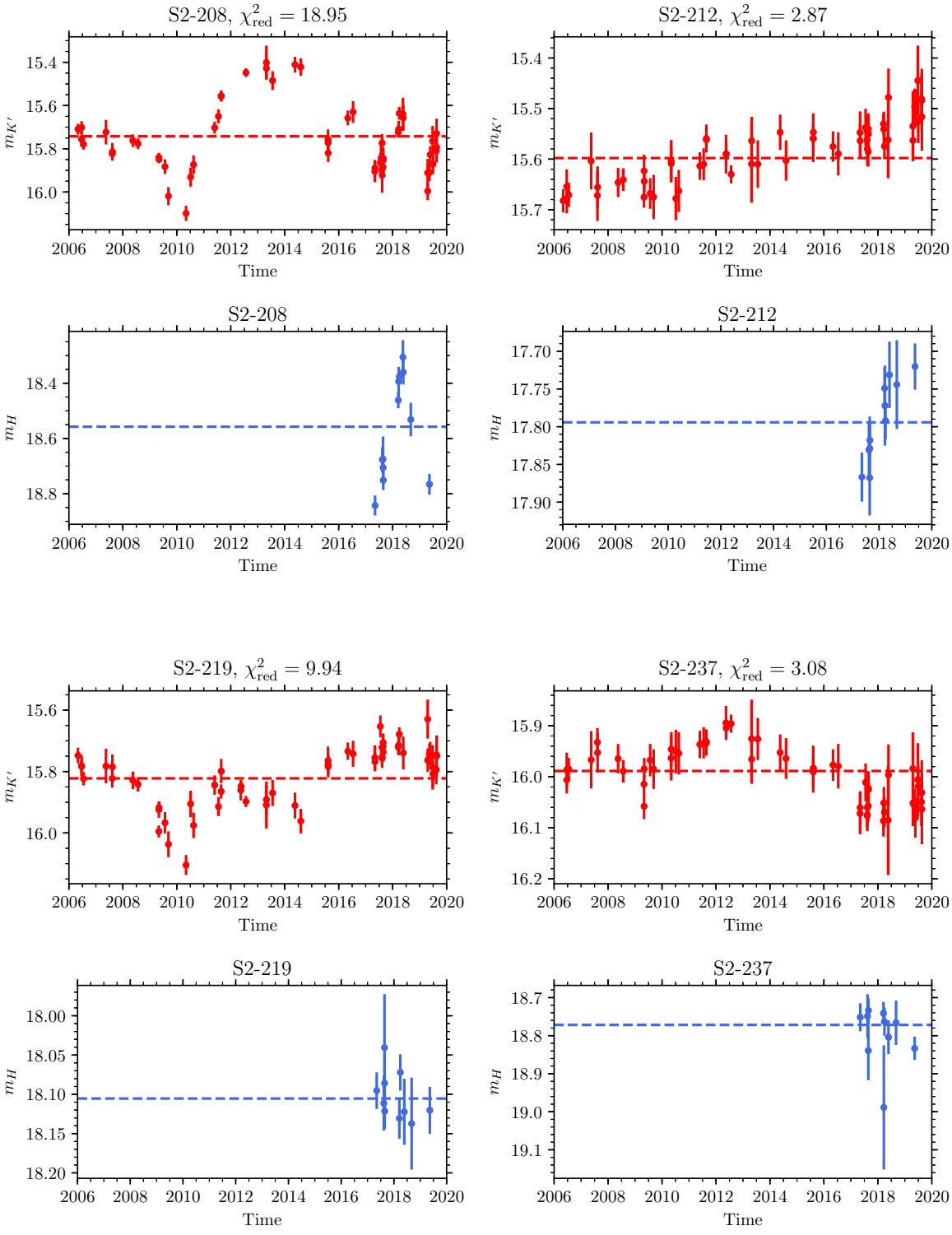
S2-208, $\chi^2_{\rm red} = 18.95$
S2-212, $\chi^2_{\rm red} = 2.87$
S2-208
S2-212
S2-219, $\chi^2_{\rm red} = 9.94$
S2-237, $\chi^2_{\rm red} = 3.08$
S2-219
S2-237
$m_{K'}$
m_H
Time

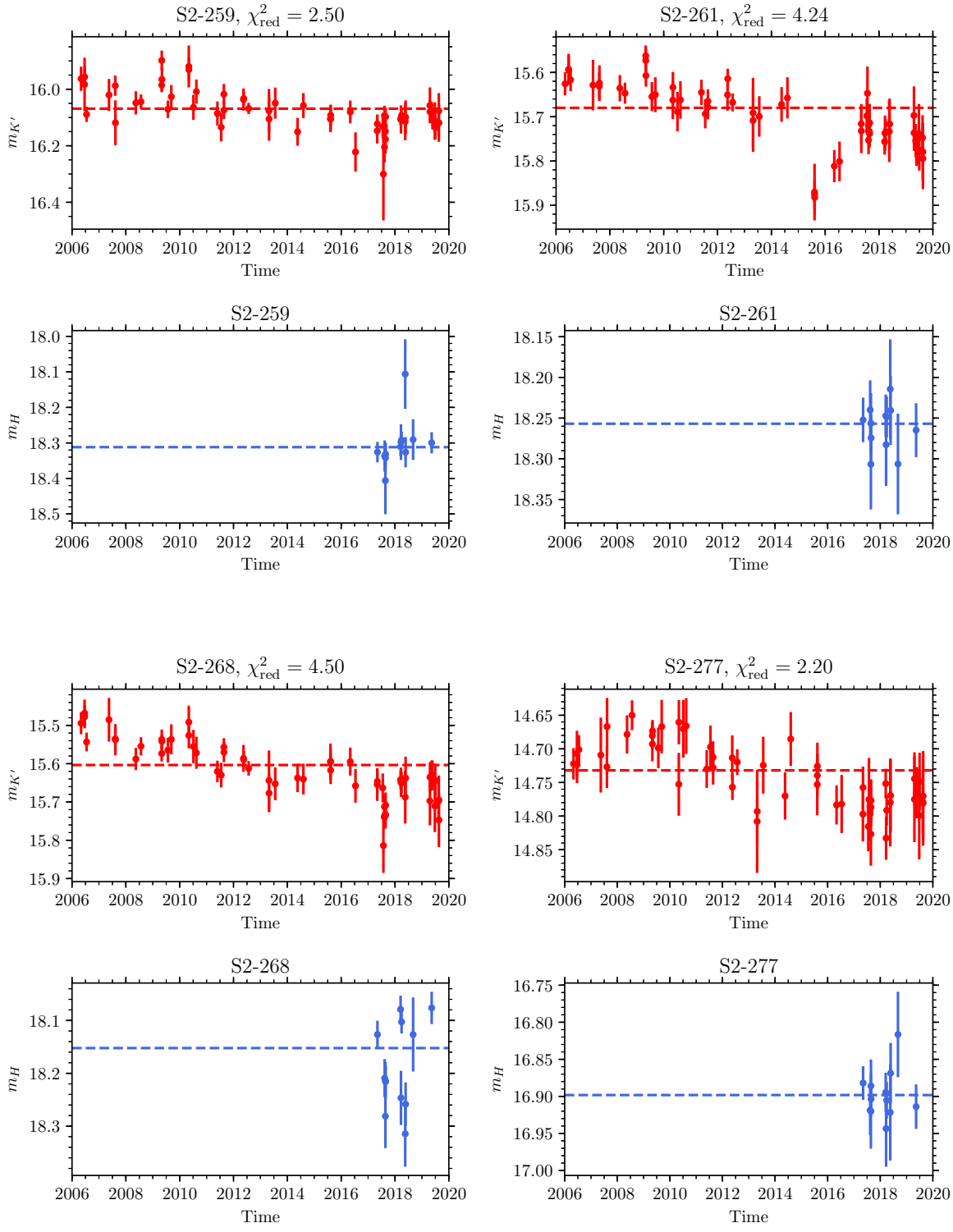
S2-259, $\chi^2_{\rm red} = 2.50$
S2-261, $\chi^2_{\rm red} = 4.24$
S2-259
S2-261
S2-268, $\chi^2_{\rm red} = 4.50$
S2-277, $\chi^2_{\rm red} = 2.20$
S2-268
S2-277
$m_{K'}$
m_H
Time

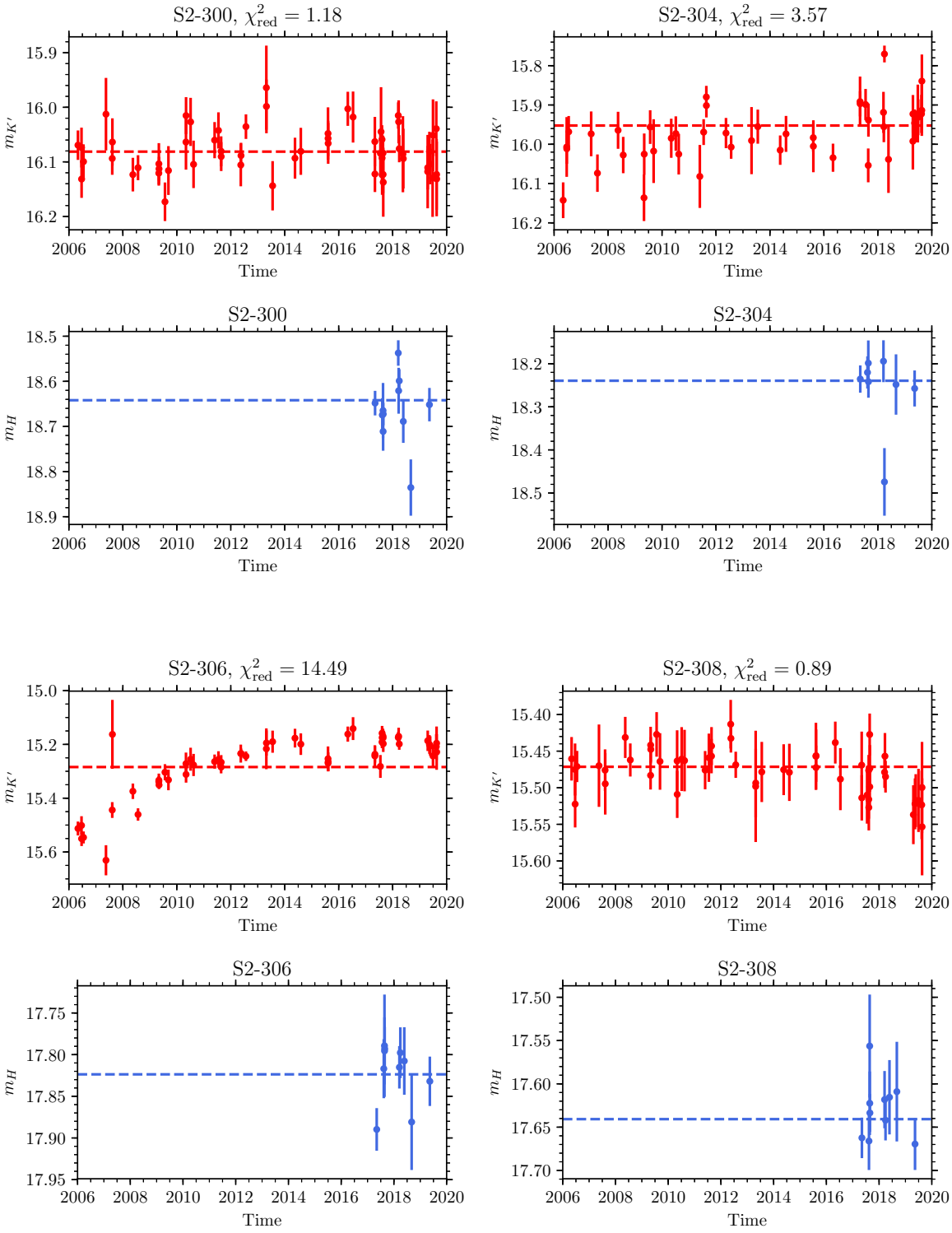
S2-300, $\chi^2_{\rm red} = 1.18$
S2-304, $\chi^2_{\rm red} = 3.57$
S2-300
S2-304
S2-306, $\chi^2_{\rm red} = 14.49$
S2-308, $\chi^2_{\rm red} = 0.89$
S2-306
S2-308
$m_{K'}$
m_H
Time

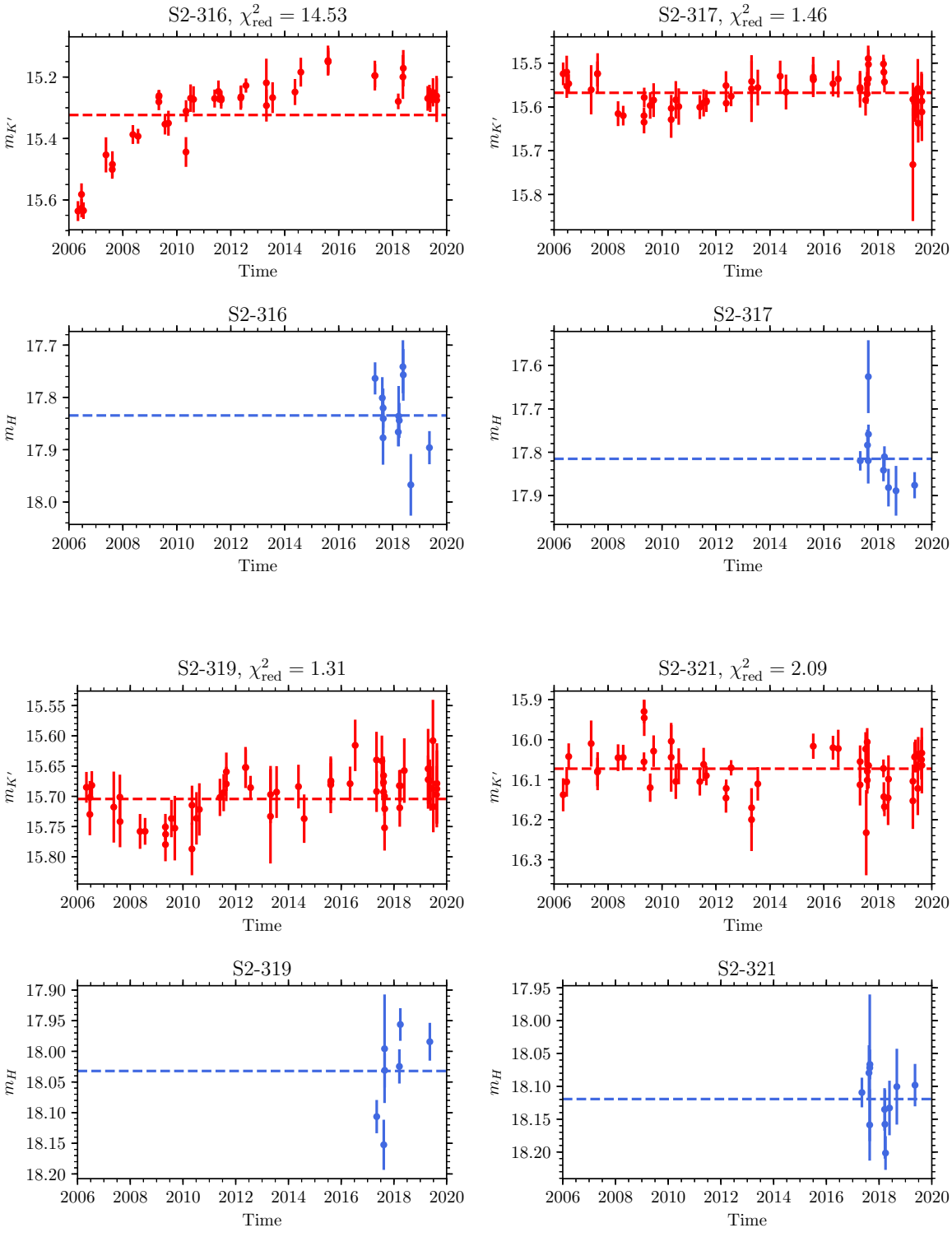
S2-316, $\chi^2_{\rm red} = 14.53$
S2-317, $\chi^2_{\rm red} = 1.46$
S2-316
S2-317
S2-319, $\chi^2_{\rm red} = 1.31$
S2-321, $\chi^2_{\rm red} = 2.09$
S2-319
S2-321
$m_{K'}$
m_H
Time

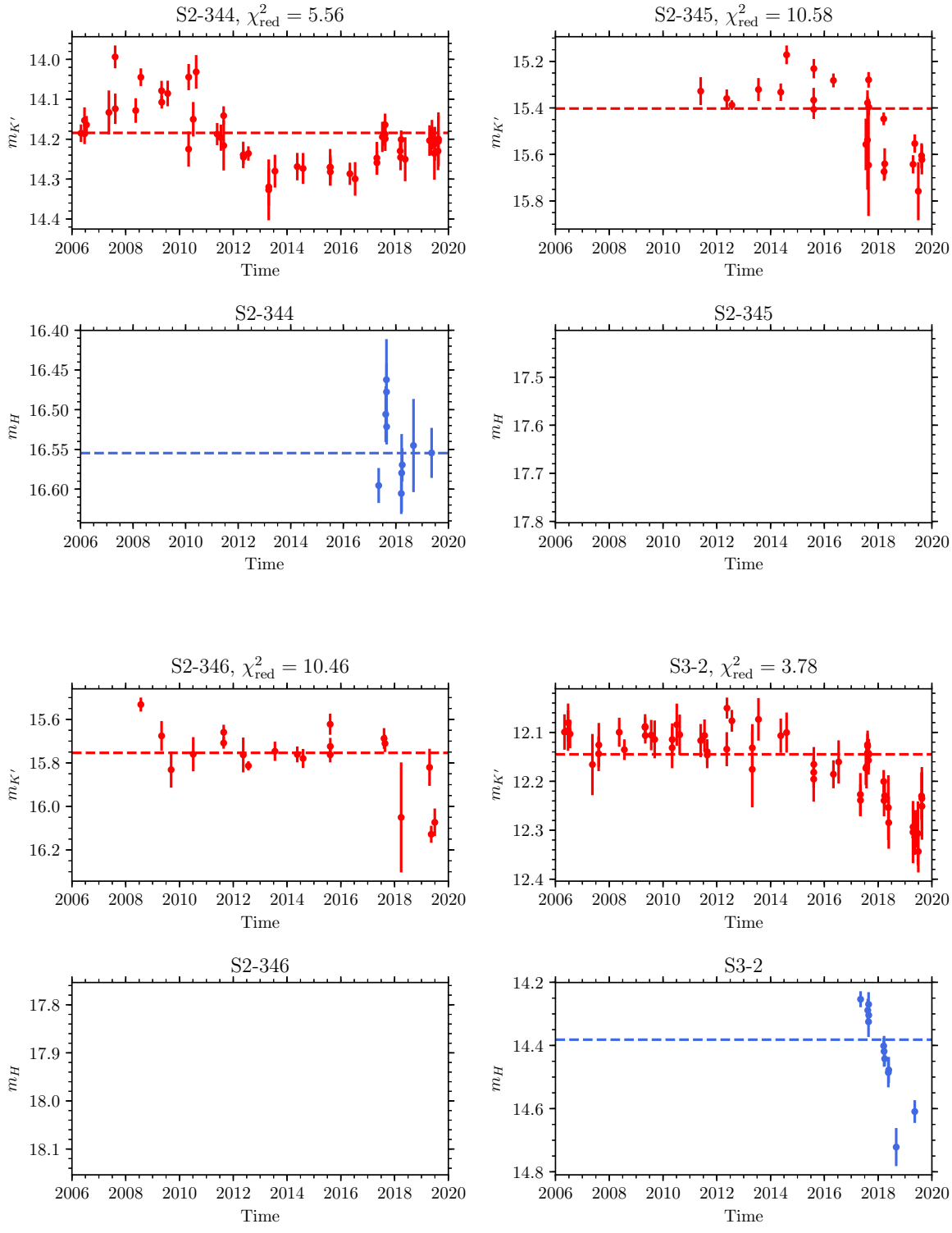
S2-344, $\chi^2_{\rm red} = 5.56$
S2-345, $\chi^2_{\rm red} = 10.58$
S2-344
S2-345
S2-346, $\chi^2_{\rm red} = 10.46$
S3-2, $\chi^2_{\rm red} = 3.78$
S2-346
S3-2
$m_{K'}$
m_H
Time

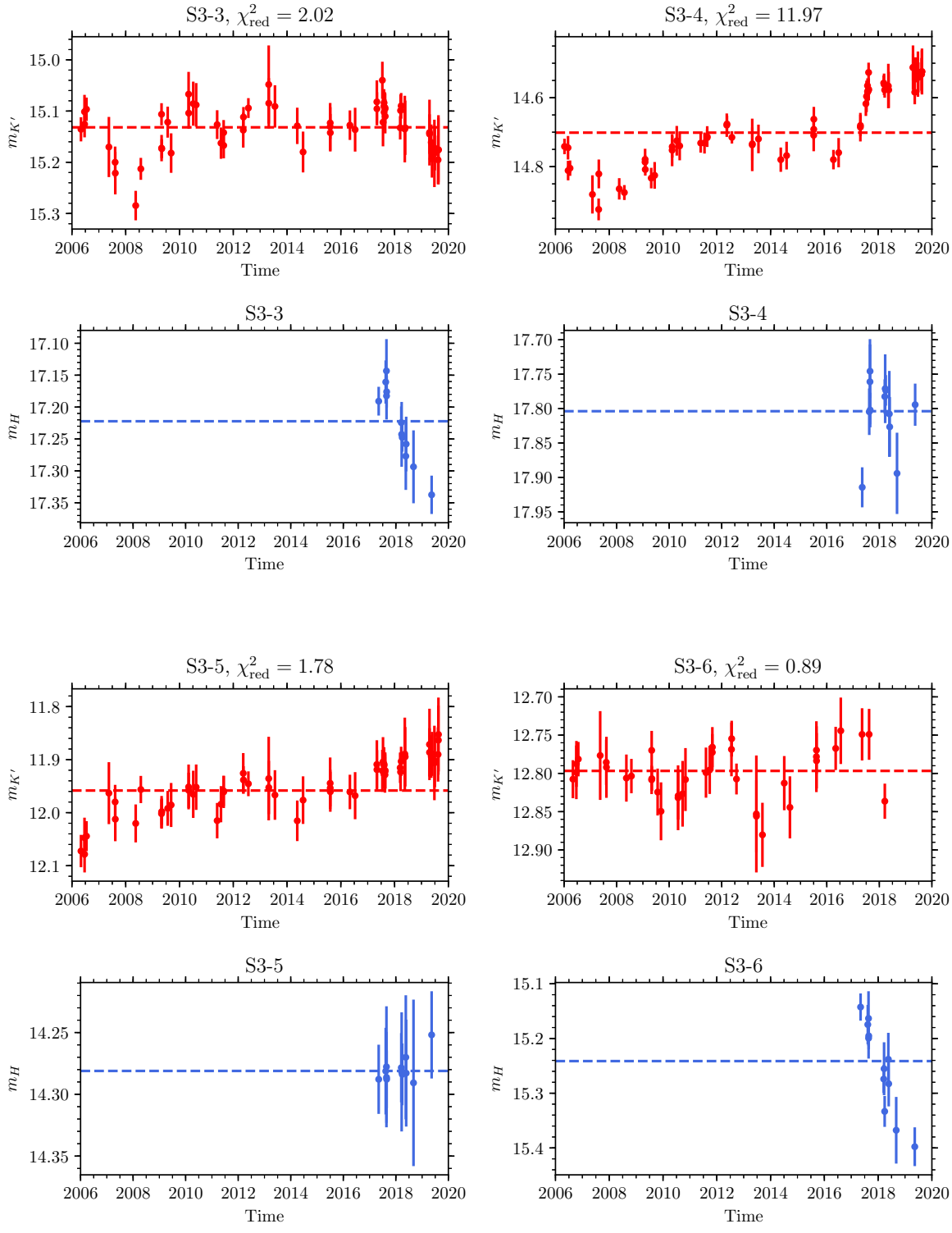
S3-3, $\chi^2_{\rm red} = 2.02$
S3-4, $\chi^2_{\rm red} = 11.97$
S3-3
S3-4
S3-5, $\chi^2_{\rm red} = 1.78$
S3-6, $\chi^2_{\rm red} = 0.89$
S3-5
S3-6
$m_{K'}$
m_H
Time

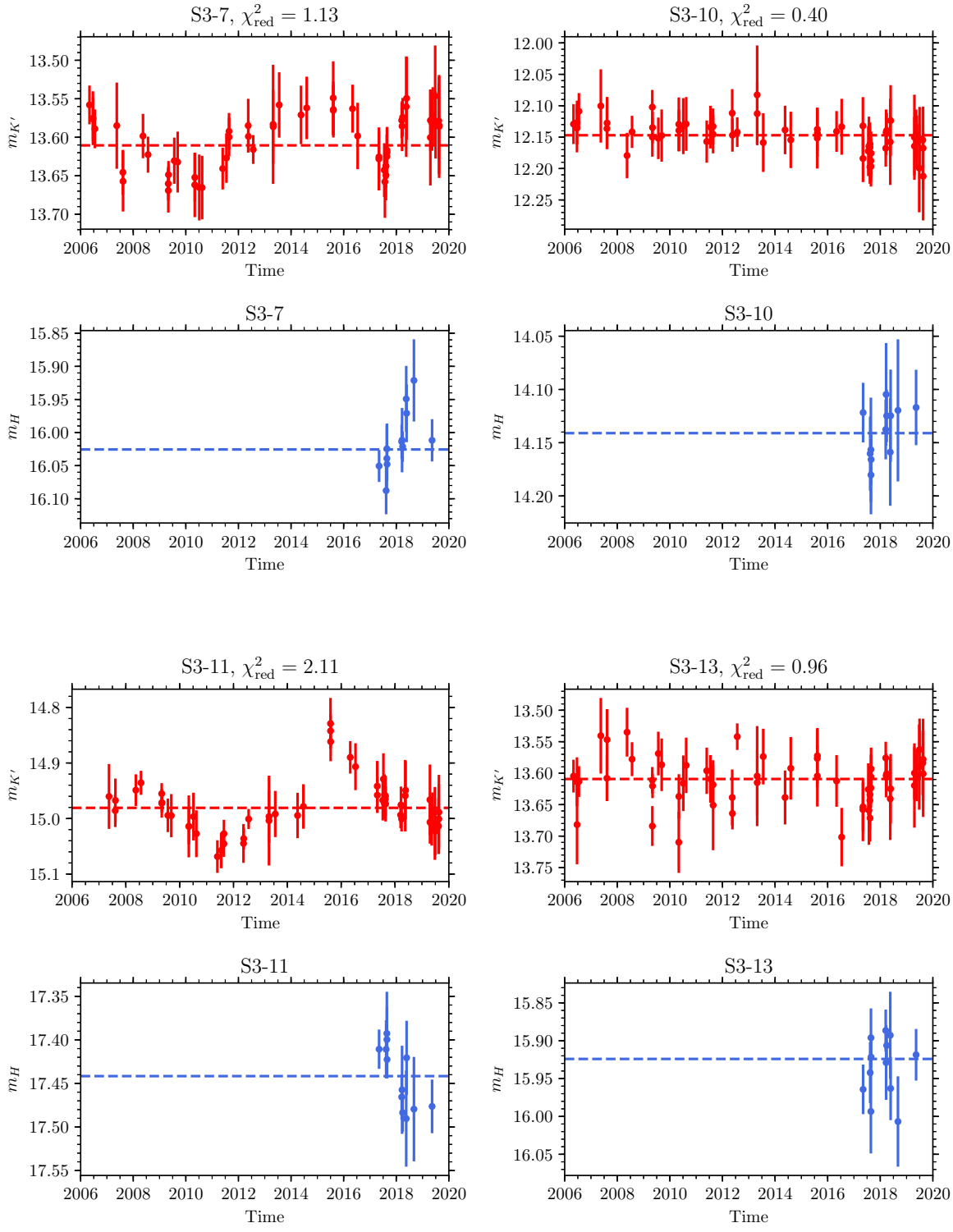
S3-7, $\chi^2_{\rm red} = 1.13$
S3-10, $\chi^2_{\rm red} = 0.40$
S3-7
S3-10
S3-11, $\chi^2_{\rm red} = 2.11$
S3-13, $\chi^2_{\rm red} = 0.96$
S3-11
S3-13
$m_{K'}$
m_H
Time

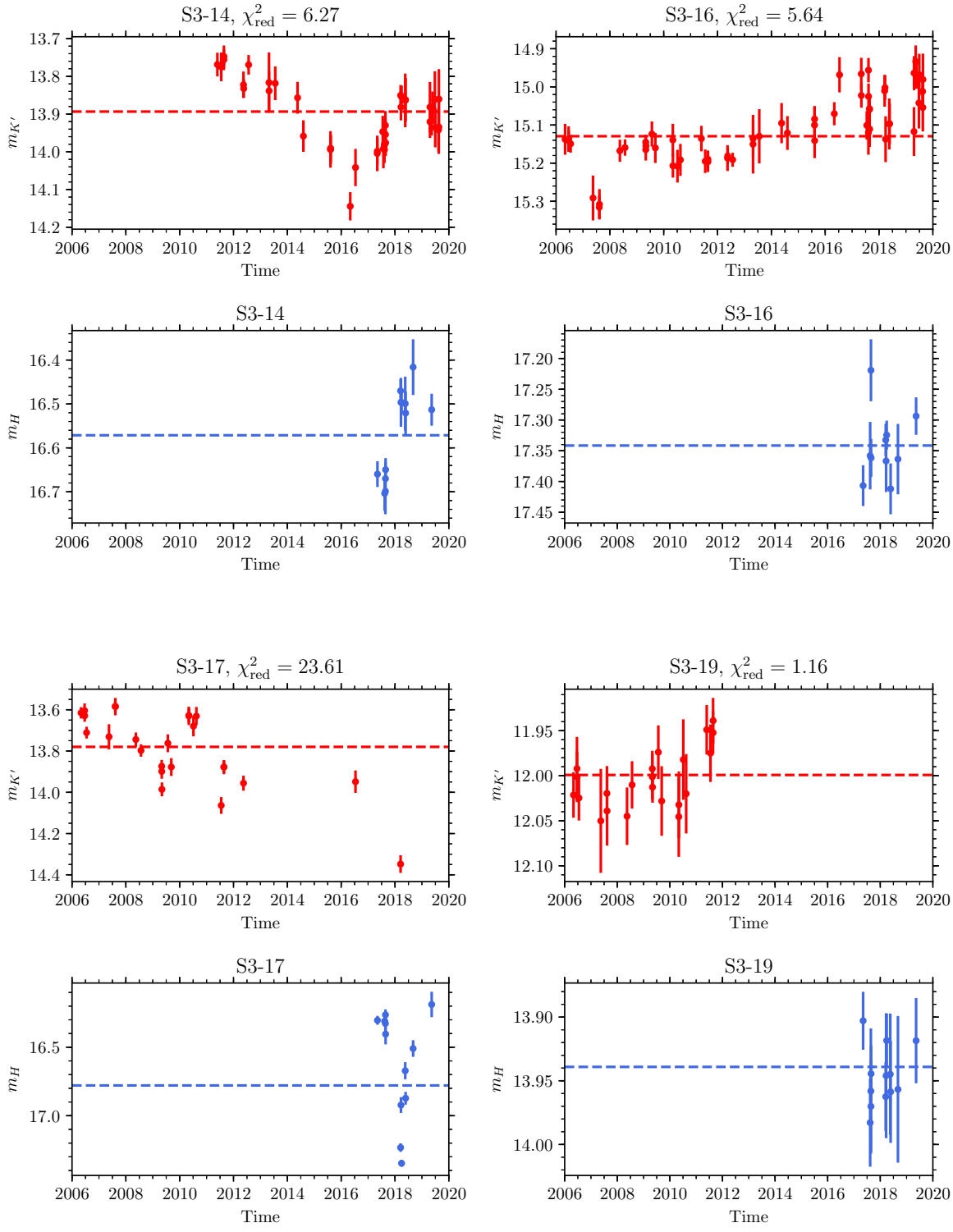
S3-14, $\chi^2_{\rm red} = 6.27$
S3-16, $\chi^2_{\rm red} = 5.64$
S3-14
S3-16
S3-17, $\chi^2_{\rm red} = 23.61$
S3-19, $\chi^2_{\rm red} = 1.16$
S3-17
S3-19
$m_{K'}$
m_H
Time

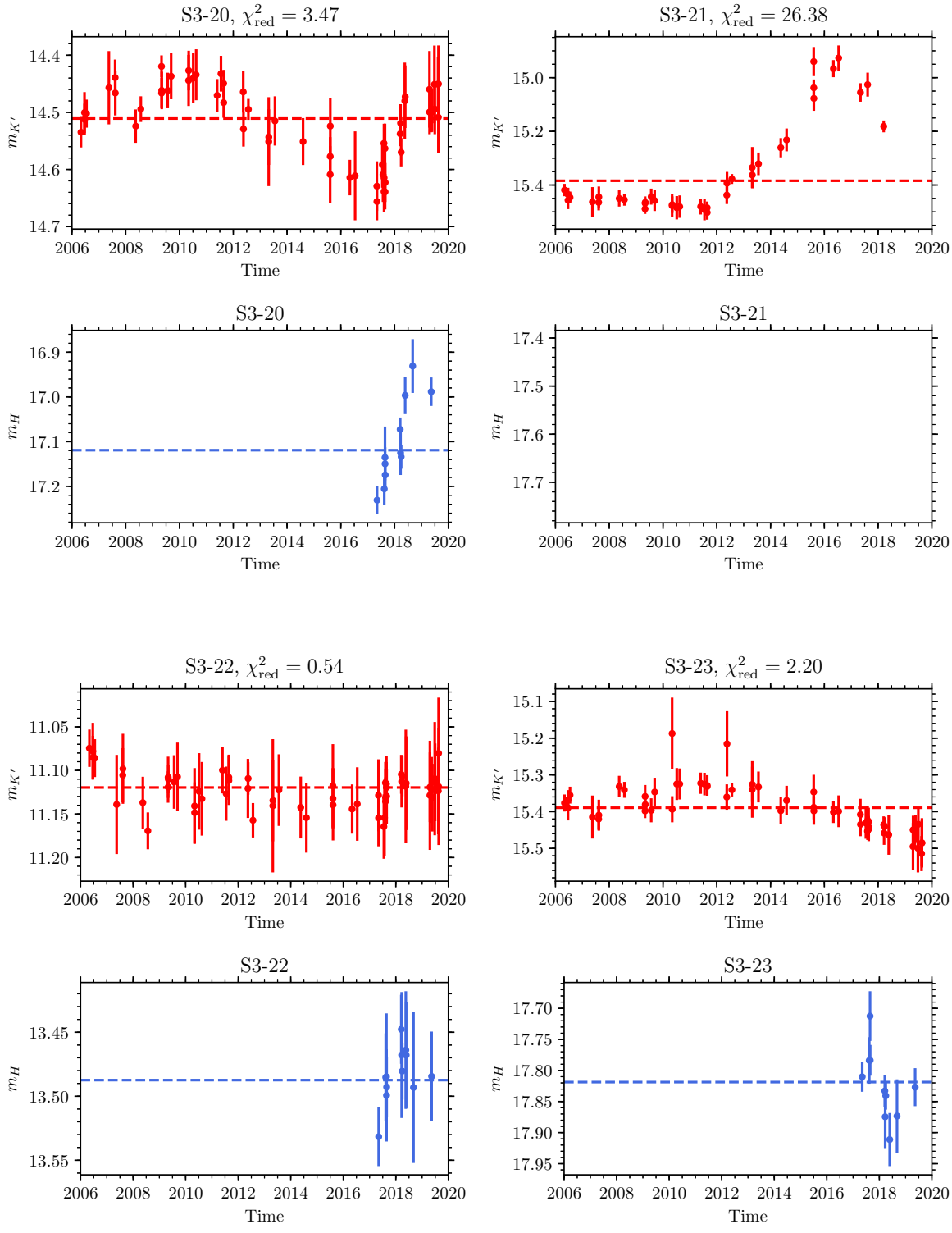
S3-20, $\chi^2_{\rm red} = 3.47$
S3-21, $\chi^2_{\rm red} = 26.38$
S3-20
S3-21
S3-22, $\chi^2_{\rm red} = 0.54$
S3-23, $\chi^2_{\rm red} = 2.20$
S3-22
S3-23
$m_{K'}$
m_H
Time

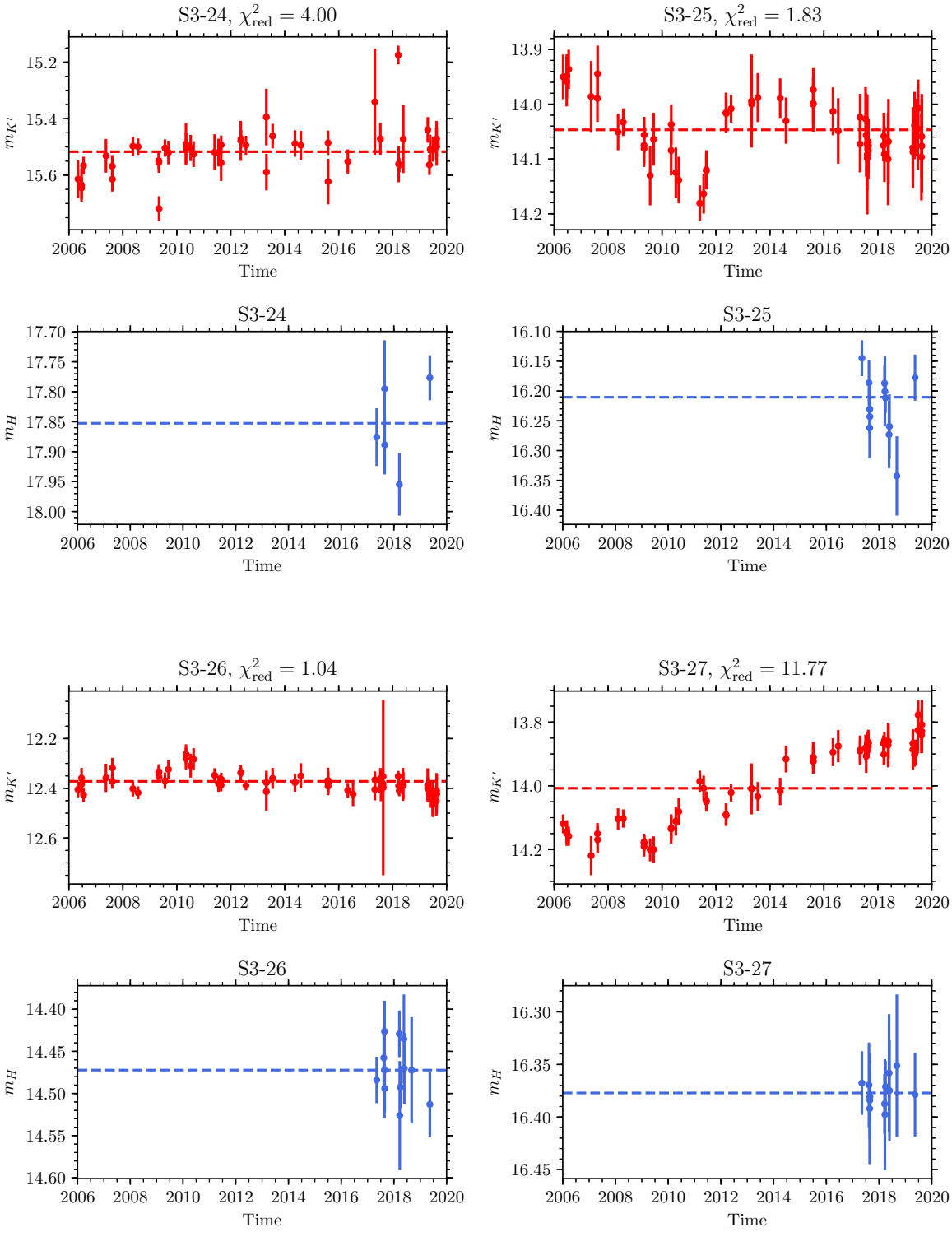
S3-24, $\chi^2_{\rm red} = 4.00$
S3-25, $\chi^2_{\rm red} = 1.83$
S3-24
S3-25
S3-26, $\chi^2_{\rm red} = 1.04$
S3-27, $\chi^2_{\rm red} = 11.77$
S3-26
S3-27
$m_{K'}$
m_H
Time

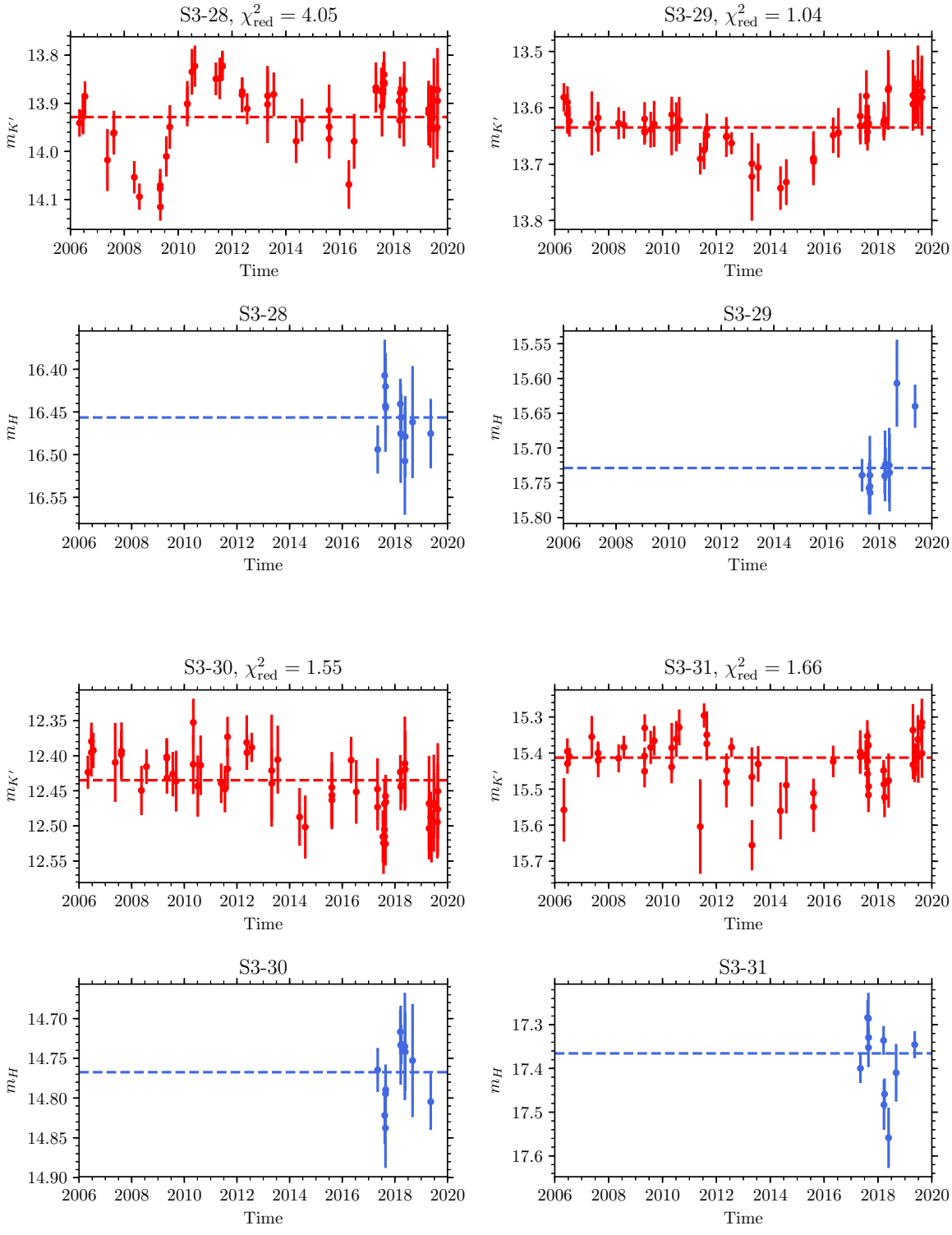
S3-28, $\chi^2_{\rm red} = 4.05$
S3-29, $\chi^2_{\rm red} = 1.04$
S3-28
S3-29
S3-30, $\chi^2_{\rm red} = 1.55$
S3-31, $\chi^2_{\rm red} = 1.66$
S3-30
S3-31
$m_{K'}$
m_H
Time

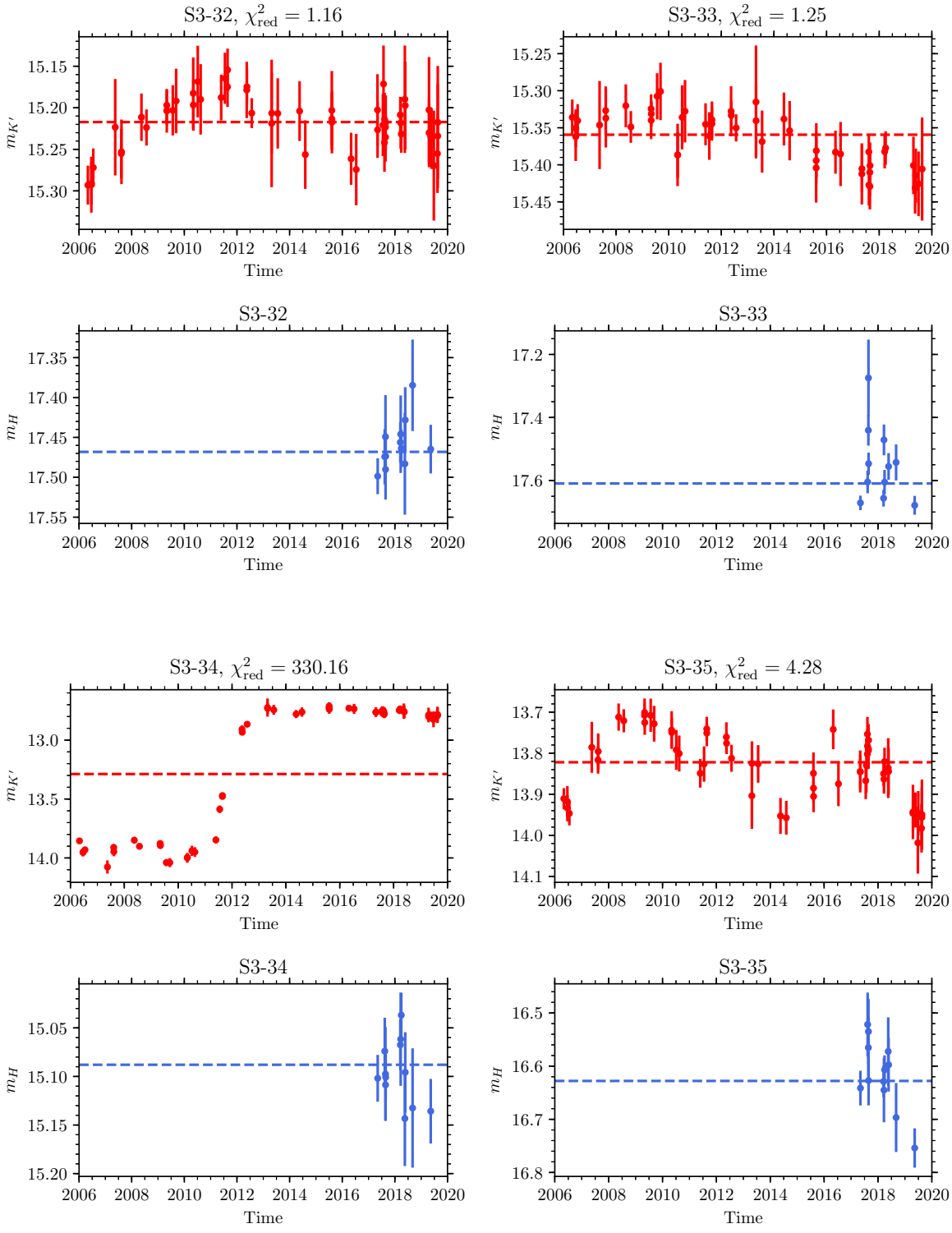
S3-32, $\chi^2_{\rm red} = 1.16$
S3-33, $\chi^2_{\rm red} = 1.25$
S3-32
S3-33
S3-34, $\chi^2_{\rm red} = 330.16$
S3-35, $\chi^2_{\rm red} = 4.28$
S3-34
S3-35
$m_{K'}$
m_H
Time

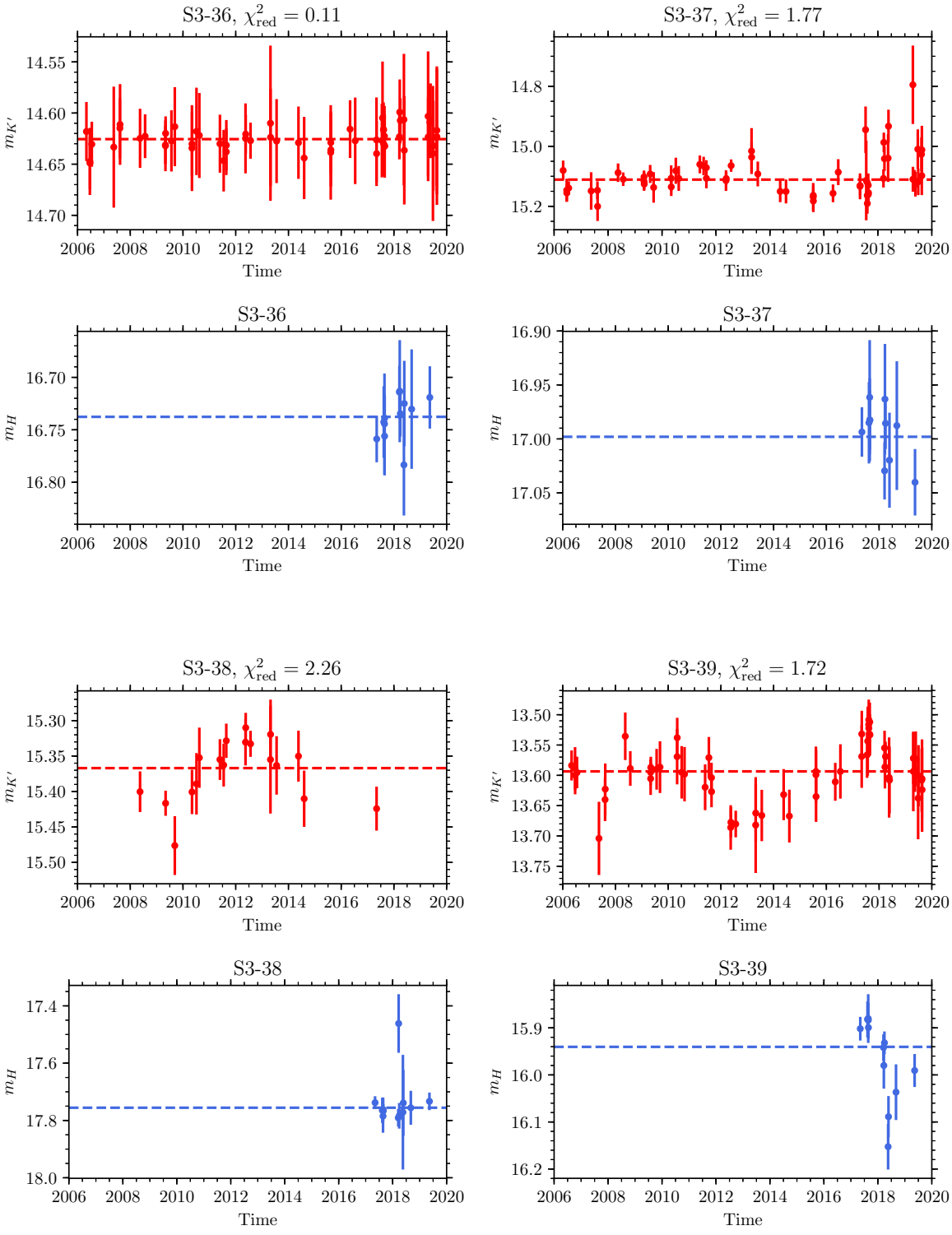
S3-36, $\chi^2_{\rm red} = 0.11$
S3-37, $\chi^2_{\rm red} = 1.77$
S3-36
S3-37
S3-38, $\chi^2_{\rm red} = 2.26$
S3-39, $\chi^2_{\rm red} = 1.72$
S3-38
S3-39
$m_{K'}$
m_H
Time

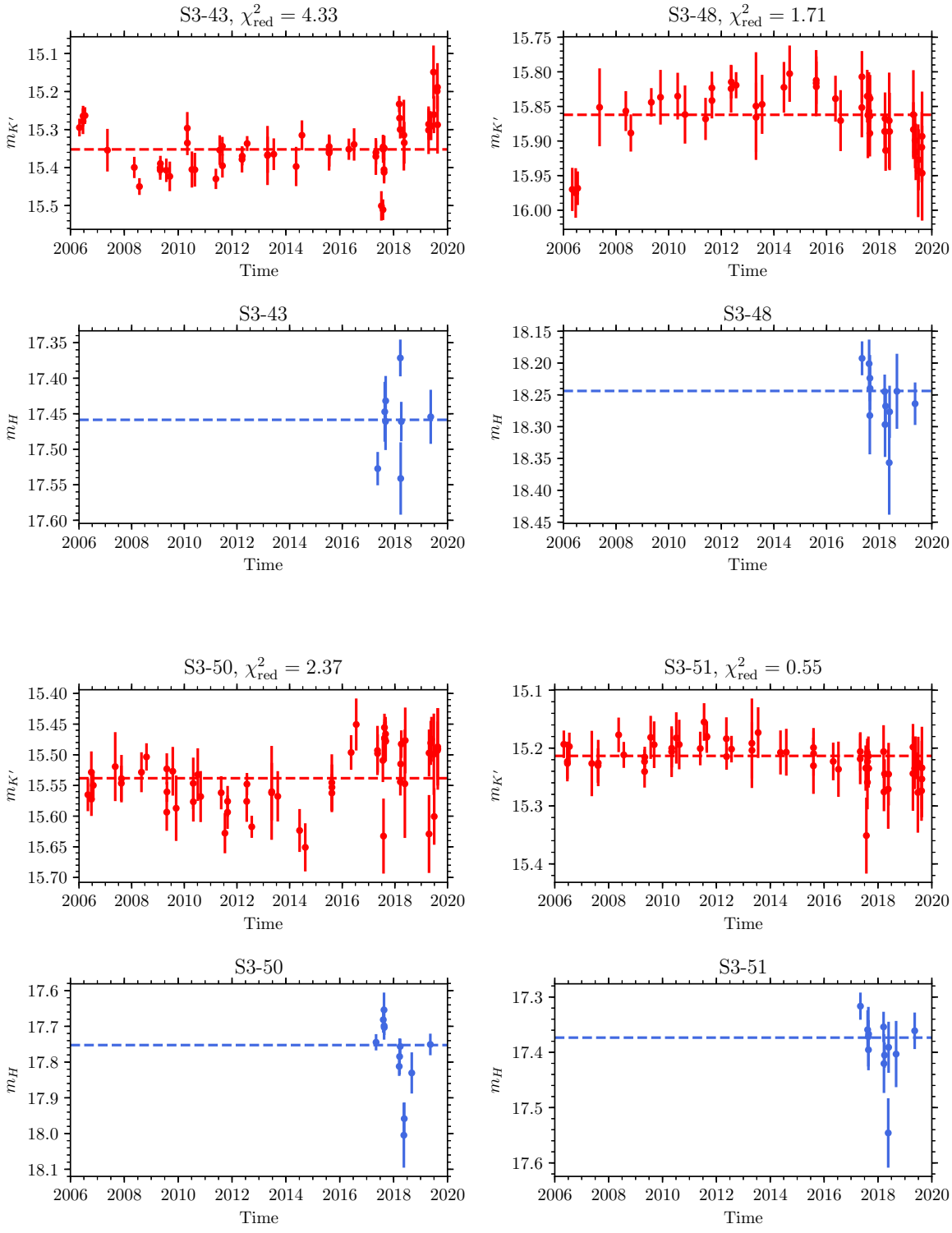
S3-43, $\chi^2_{\rm red} = 4.33$
S3-48, $\chi^2_{\rm red} = 1.71$
S3-43
S3-48
S3-50, $\chi^2_{\rm red} = 2.37$
S3-51, $\chi^2_{\rm red} = 0.55$
S3-50
S3-51
$m_{K'}$
m_H
Time

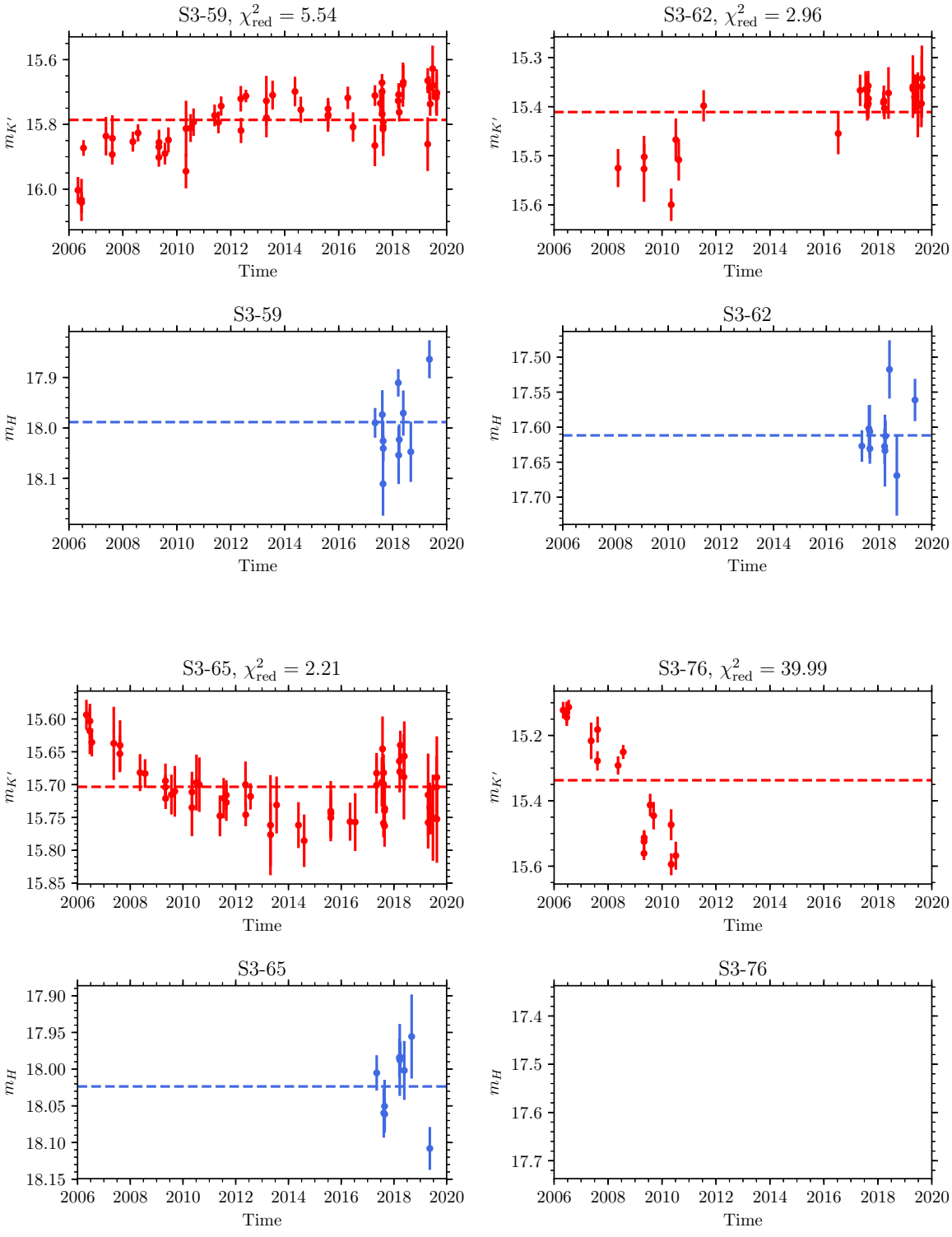
S3-59, $\chi^2_{\rm red} = 5.54$
S3-62, $\chi^2_{\rm red} = 2.96$
S3-59
S3-62
S3-65, $\chi^2_{\rm red} = 2.21$
S3-76, $\chi^2_{\rm red} = 39.99$
S3-65
S3-76
$m_{K'}$
m_H
Time

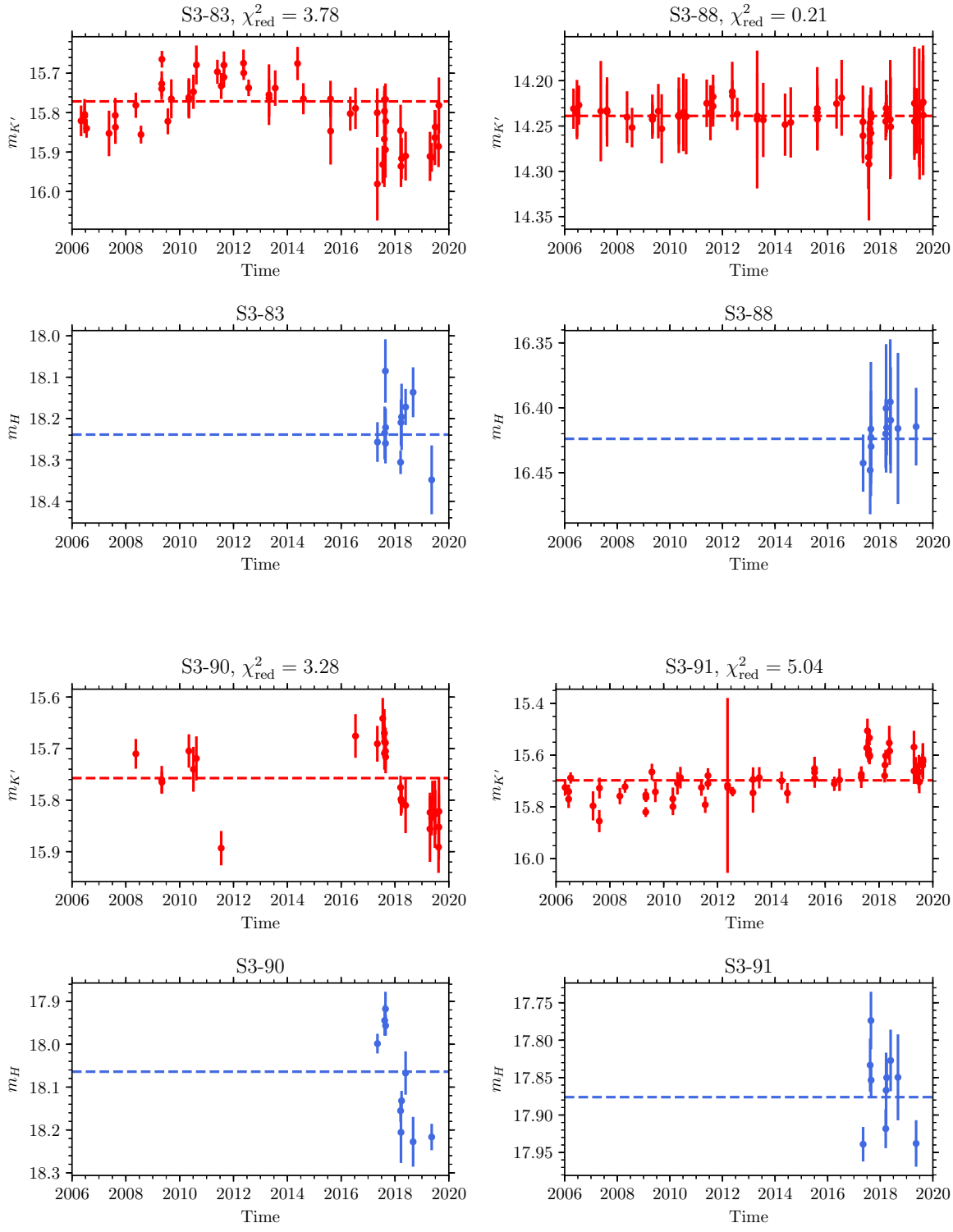
S3-83, $\chi^2_{\rm red} = 3.78$
S3-88, $\chi^2_{\rm red} = 0.21$
S3-83
S3-88
S3-90, $\chi^2_{\rm red} = 3.28$
S3-91, $\chi^2_{\rm red} = 5.04$
S3-90
S3-91
$m_{K'}$
m_H
Time

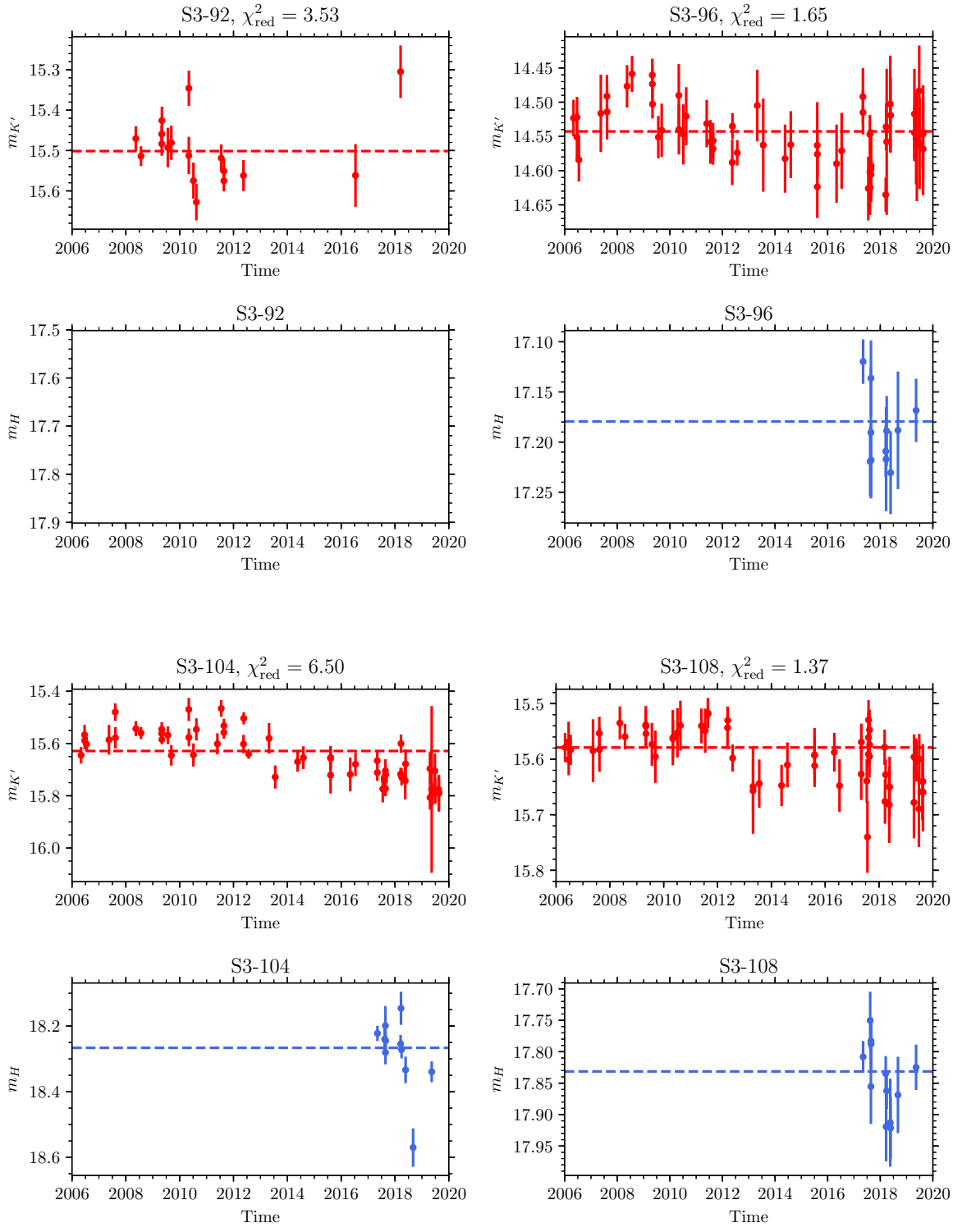
S3-92, $\chi^2_{\rm red} = 3.53$
S3-96, $\chi^2_{\rm red} = 1.65$
S3-92
S3-96
S3-104, $\chi^2_{\rm red} = 6.50$
S3-108, $\chi^2_{\rm red} = 1.37$
S3-104
S3-108
$m_{K'}$
m_H
Time

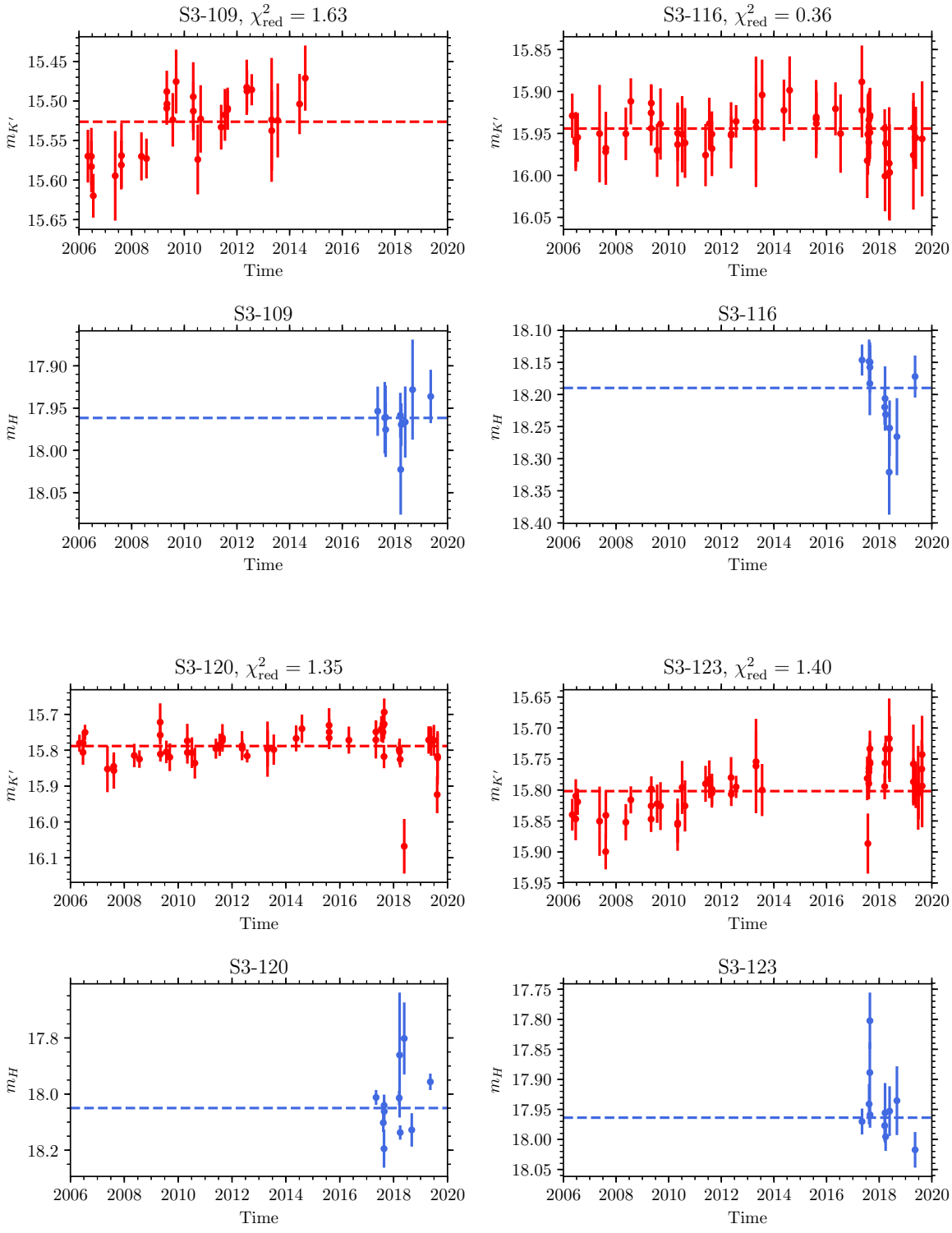
S3-109, $\chi^2_{\rm red} = 1.63$
S3-116, $\chi^2_{\rm red} = 0.36$
S3-109
S3-116
S3-120, $\chi^2_{\rm red} = 1.35$
S3-123, $\chi^2_{\rm red} = 1.40$
S3-120
S3-123
$m_{K'}$
m_H
Time

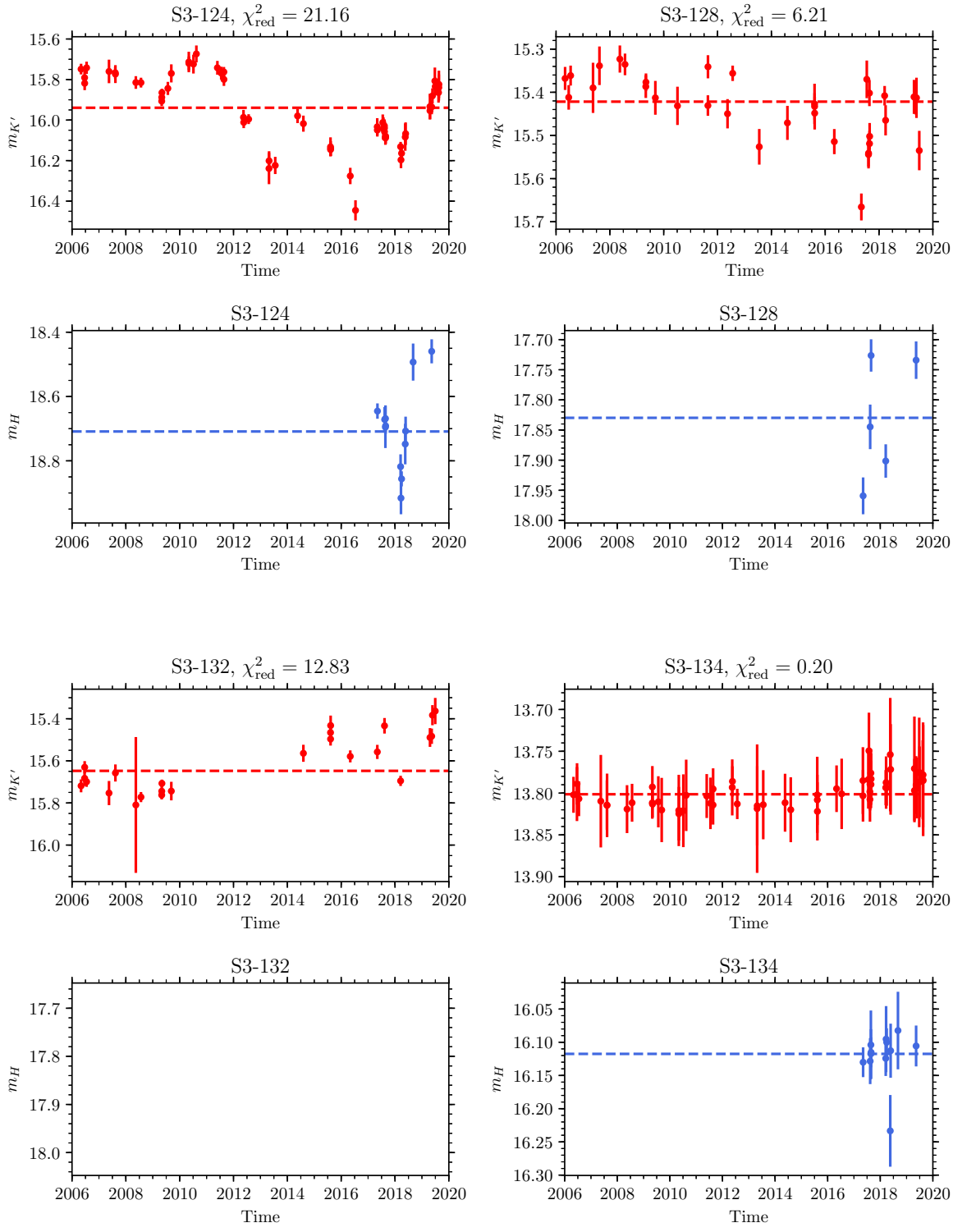
S3-124, $\chi^2_{\rm red} = 21.16$
S3-128, $\chi^2_{\rm red} = 6.21$
S3-124
S3-128
S3-132, $\chi^2_{\rm red} = 12.83$
S3-134, $\chi^2_{\rm red} = 0.20$
S3-132
S3-134
$m_{K'}$
m_H
Time

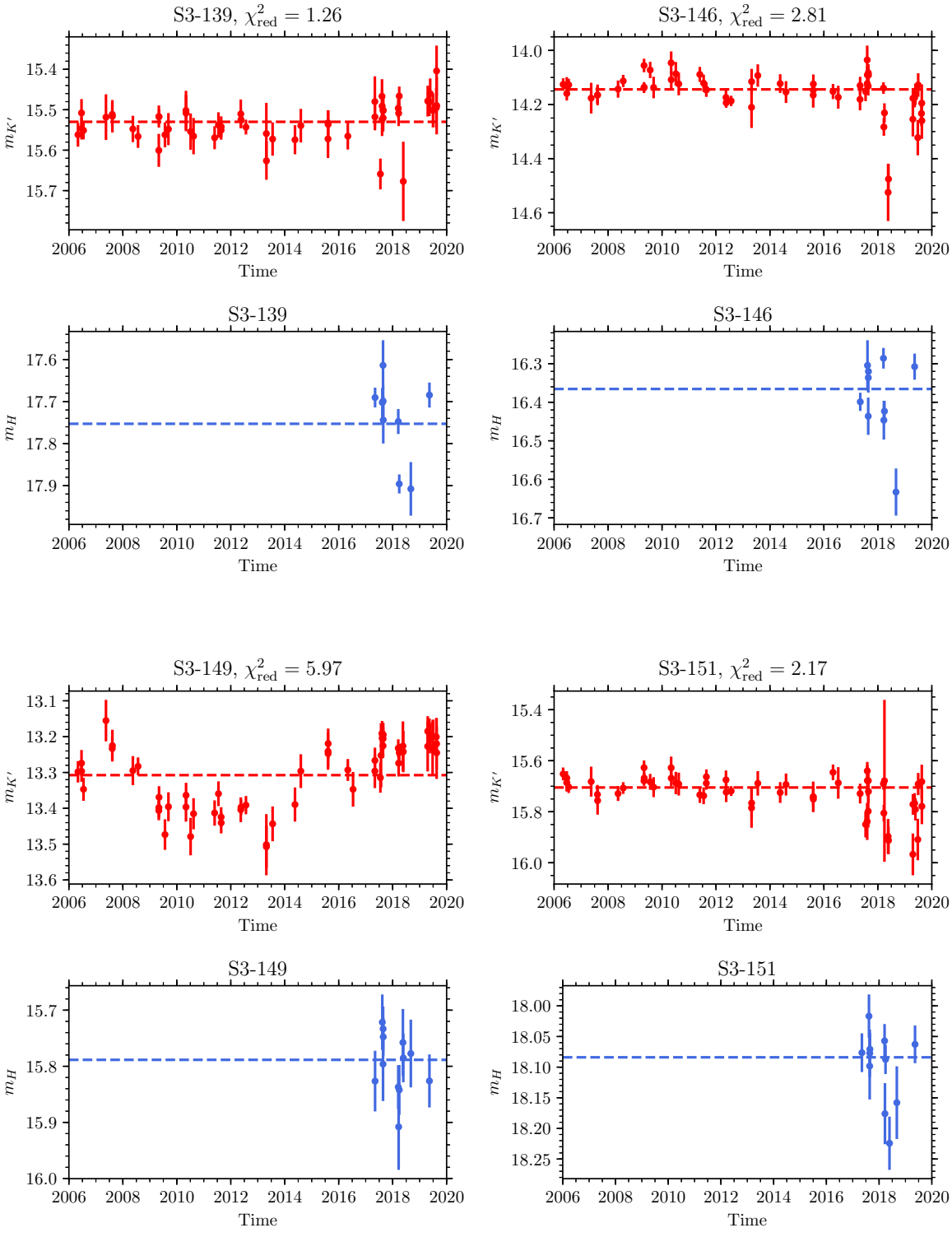
S3-139, $\chi^2_{\rm red} = 1.26$
S3-146, $\chi^2_{\rm red} = 2.81$
S3-139
S3-146
S3-149, $\chi^2_{\rm red} = 5.97$
S3-151, $\chi^2_{\rm red} = 2.17$
S3-149
S3-151
$m_{K'}$
m_H
Time

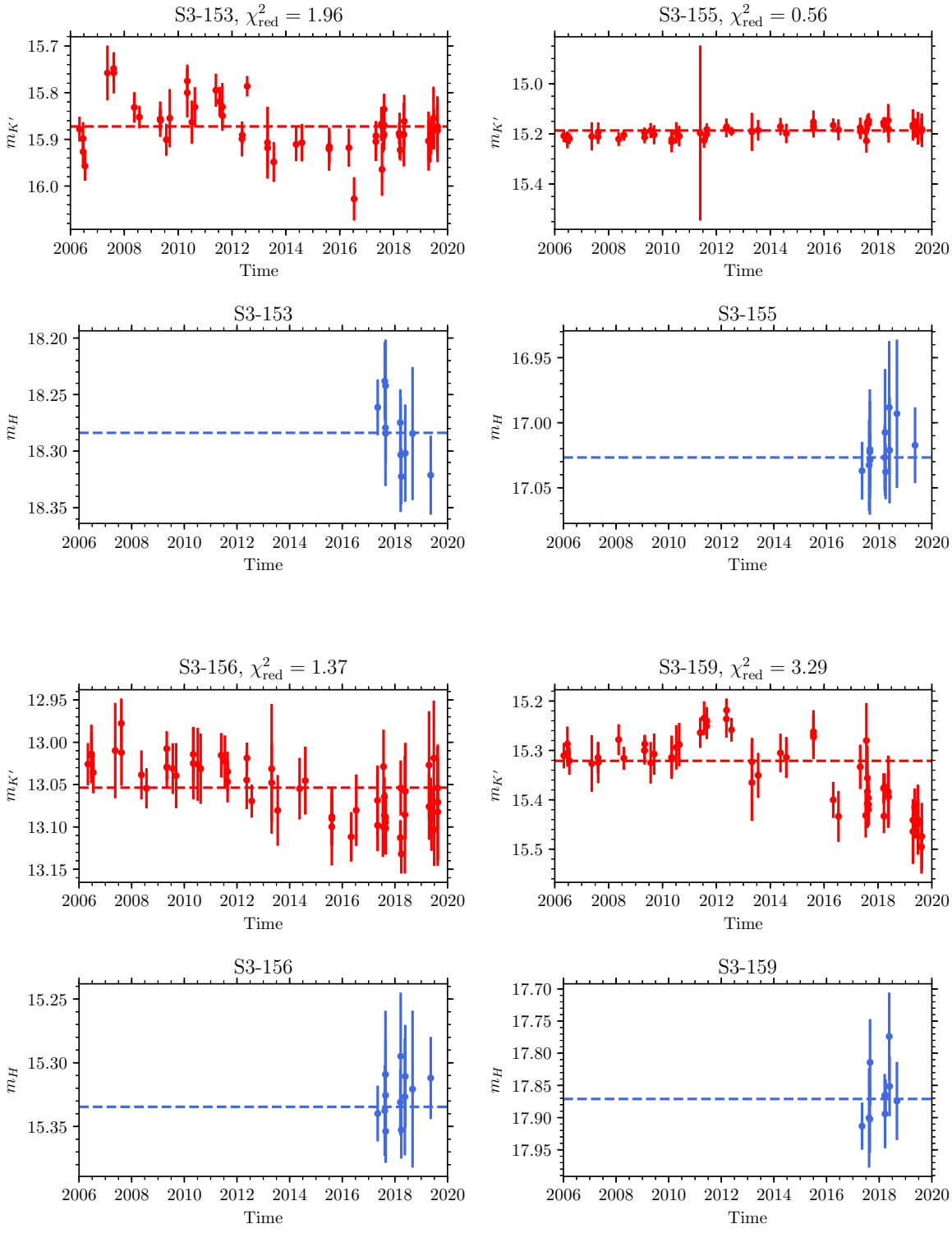
S3-153, $\chi^2_{\rm red} = 1.96$
S3-155, $\chi^2_{\rm red} = 0.56$
S3-153
S3-155
S3-156, $\chi^2_{\rm red} = 1.37$
S3-159, $\chi^2_{\rm red} = 3.29$
S3-156
S3-159
$m_{K'}$
m_H
Time

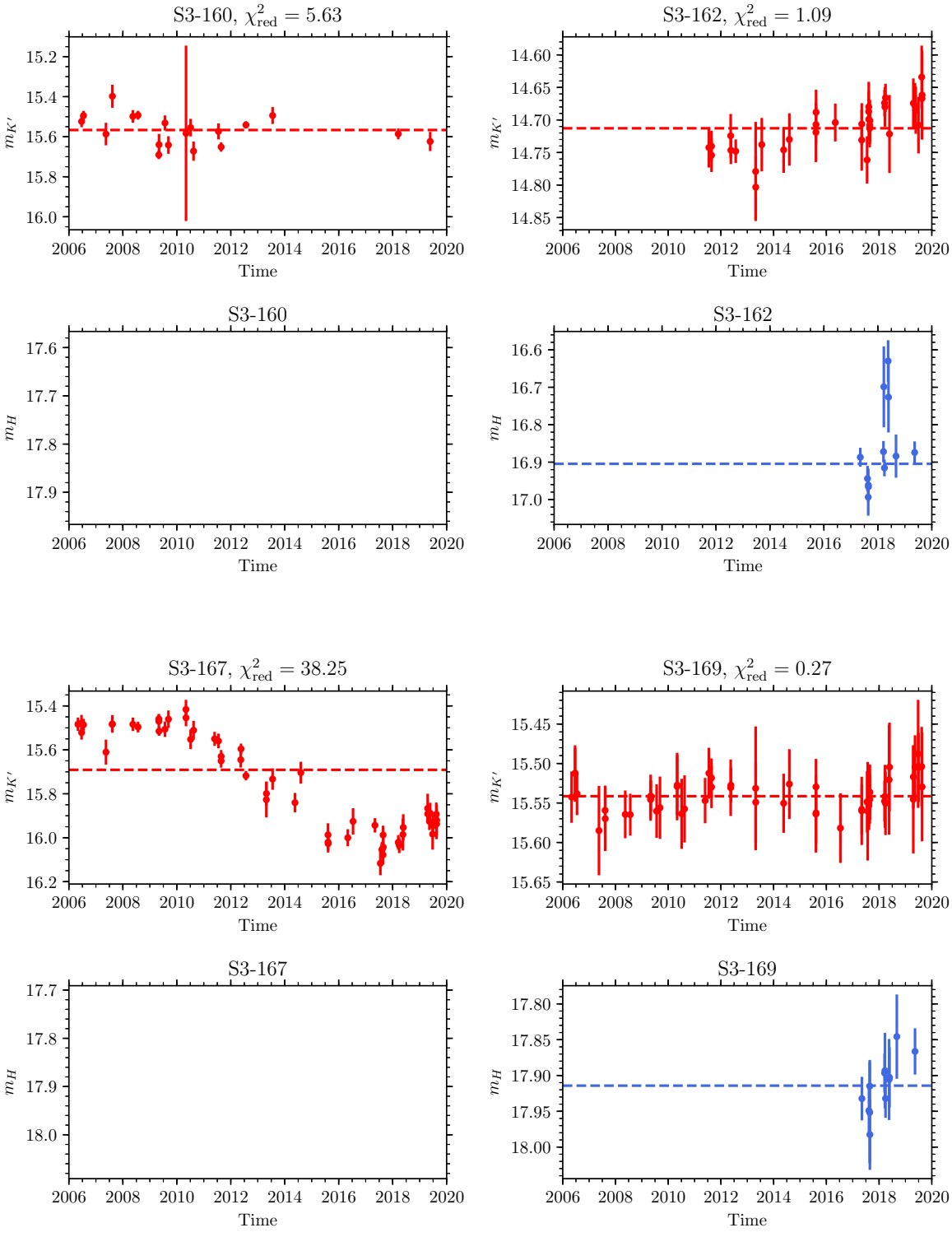
S3-160, $\chi^2_{\rm red} = 5.63$
S3-162, $\chi^2_{\rm red} = 1.09$
S3-160
S3-162
S3-167, $\chi^2_{\rm red} = 38.25$
S3-169, $\chi^2_{\rm red} = 0.27$
S3-167
S3-169
$m_{K'}$
m_H
Time

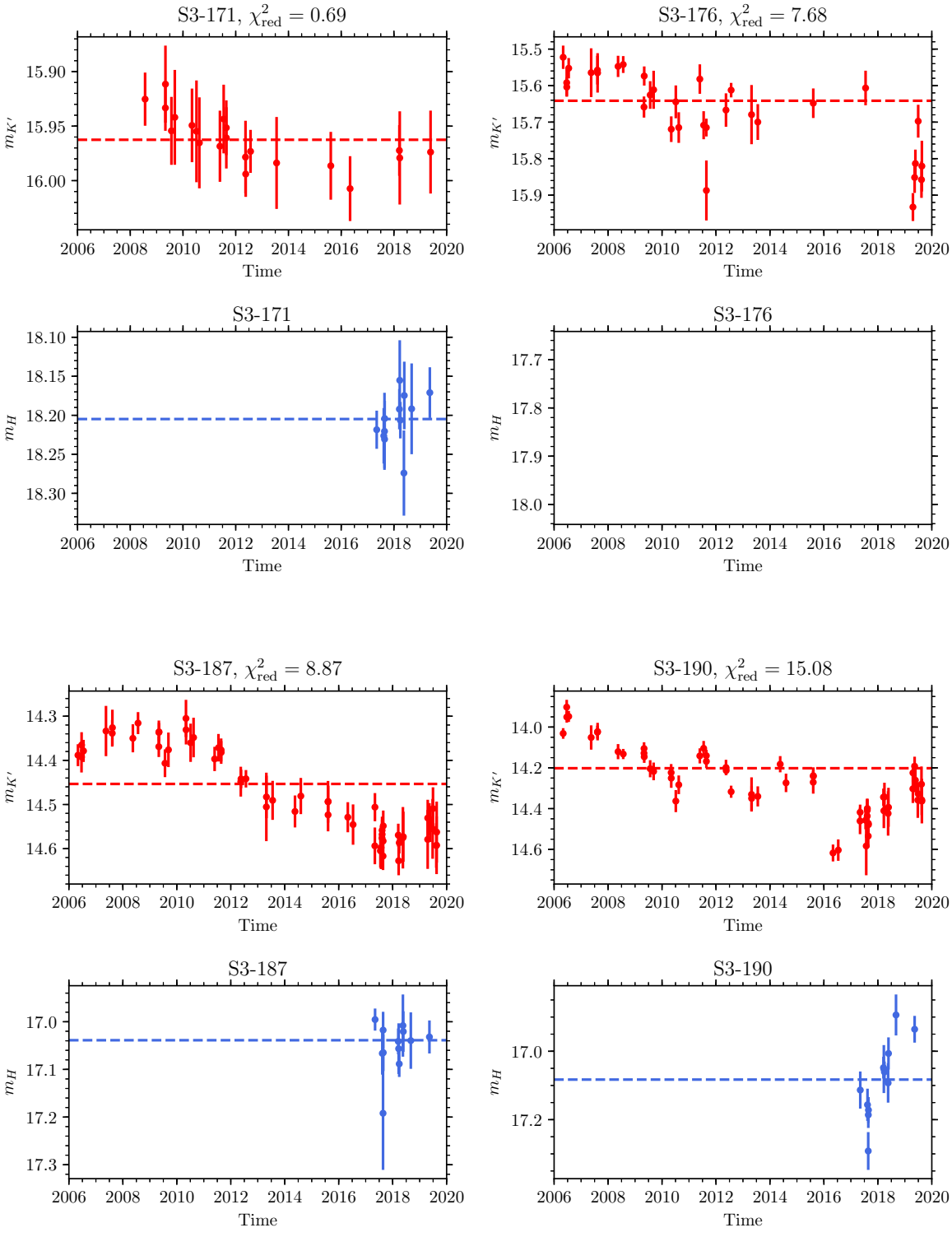
S3-171, $\chi^2_{\rm red} = 0.69$
S3-176, $\chi^2_{\rm red} = 7.68$
S3-171
S3-176
S3-187, $\chi^2_{\rm red} = 8.87$
S3-190, $\chi^2_{\rm red} = 15.08$
S3-187
S3-190
$m_{K'}$
m_H
Time

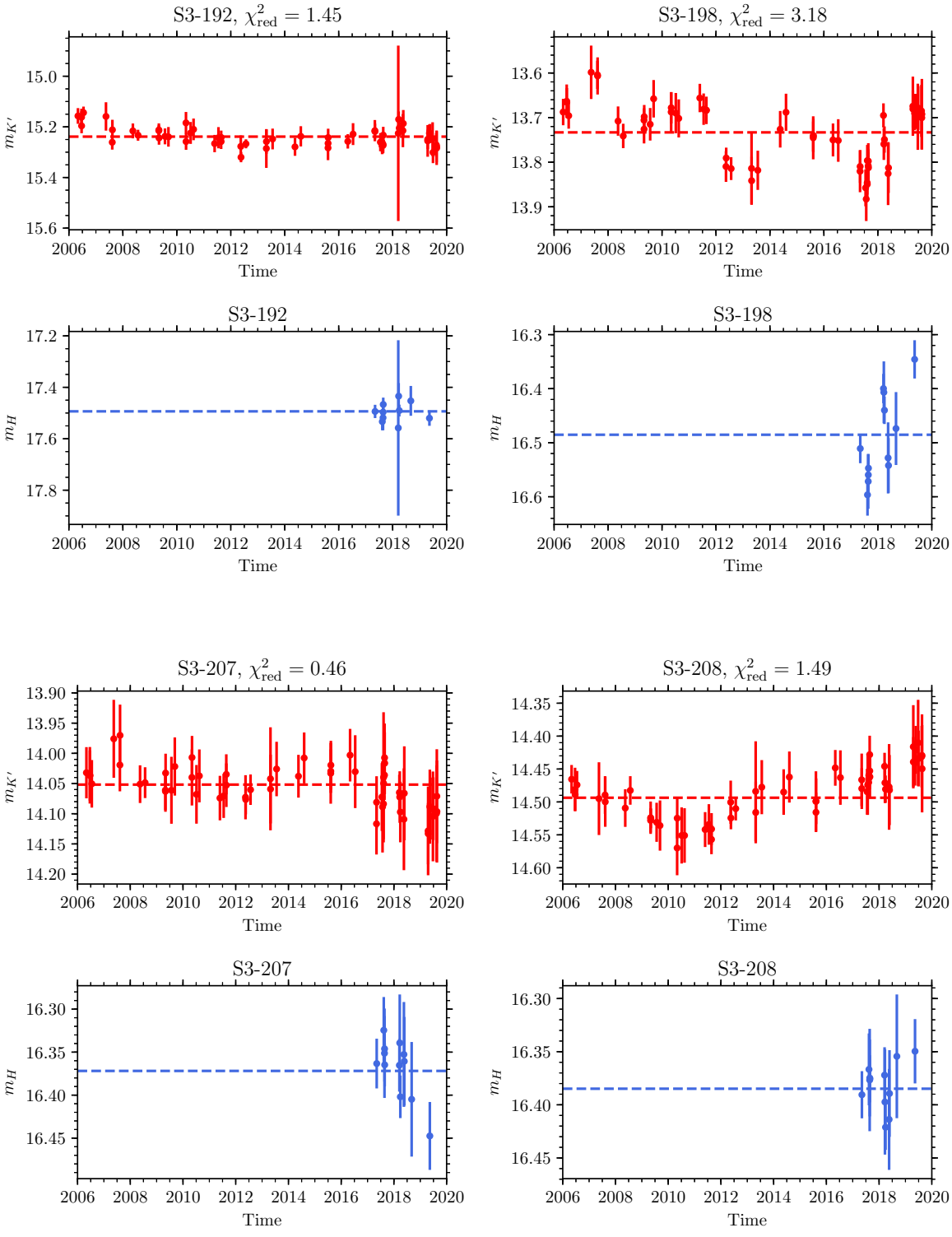
S3-192, $\chi^2_{\rm red} = 1.45$
S3-198, $\chi^2_{\rm red} = 3.18$
S3-192
S3-198
S3-207, $\chi^2_{\rm red} = 0.46$
S3-208, $\chi^2_{\rm red} = 1.49$
S3-207
S3-208
$m_{K'}$
m_H
Time

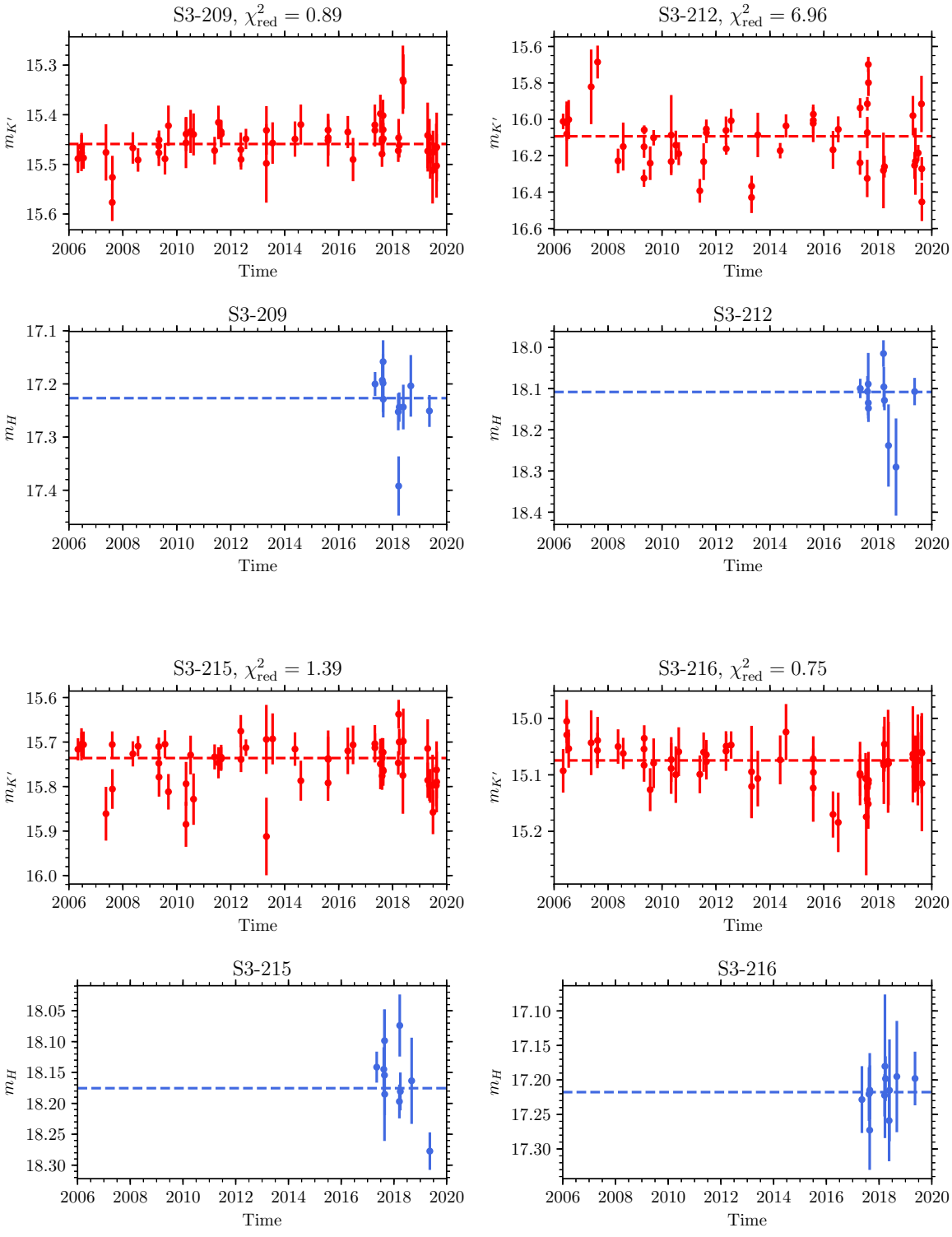
S3-209, $\chi^2_{\rm red} = 0.89$
S3-212, $\chi^2_{\rm red} = 6.96$
S3-209
S3-212
S3-215, $\chi^2_{\rm red} = 1.39$
S3-216, $\chi^2_{\rm red} = 0.75$
S3-215
S3-216
$m_{K'}$
m_H
Time

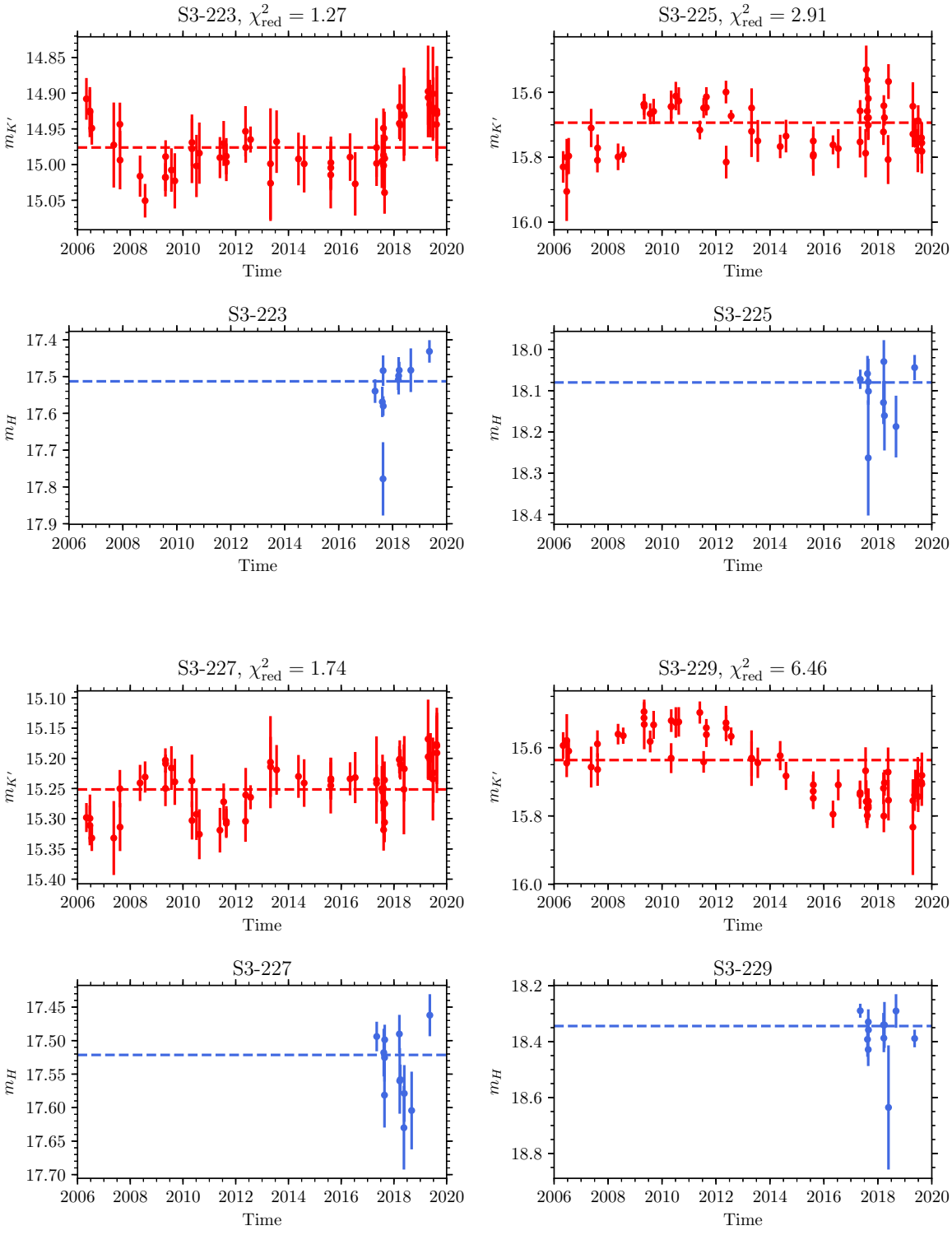
S3-223, $\chi^2_{\rm red} = 1.27$
S3-225, $\chi^2_{\rm red} = 2.91$
S3-223
S3-225
S3-227, $\chi^2_{\rm red} = 1.74$
S3-229, $\chi^2_{\rm red} = 6.46$
S3-227
S3-229
$m_{K'}$
m_H
Time

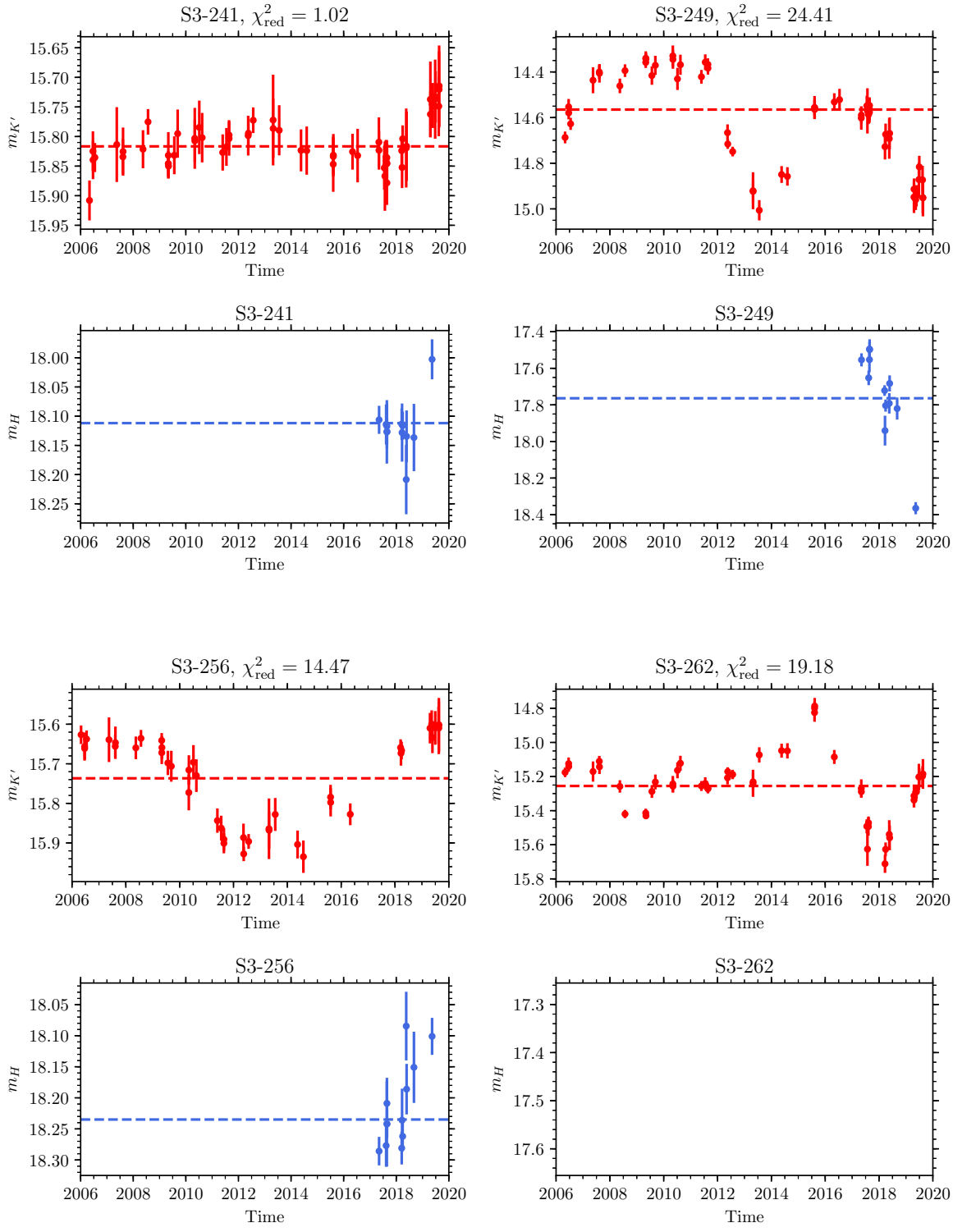
S3-241, $\chi^2_{\rm red} = 1.02$
S3-249, $\chi^2_{\rm red} = 24.41$
S3-241
S3-249
S3-256, $\chi^2_{\rm red} = 14.47$
S3-262, $\chi^2_{\rm red} = 19.18$
S3-256
S3-262
$m_{K'}$
m_H
Time

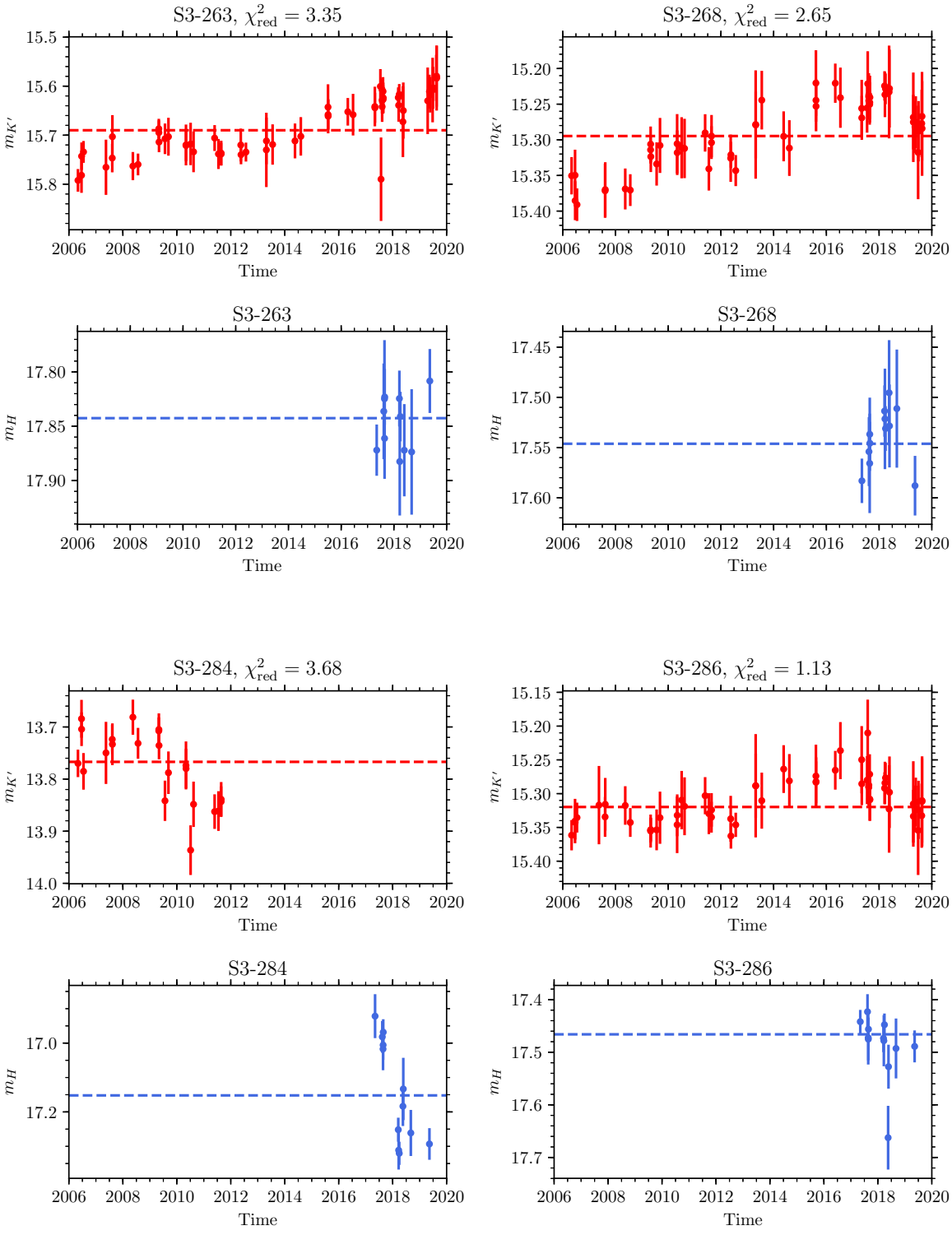
S3-263, $\chi^2_{\rm red} = 3.35$
S3-268, $\chi^2_{\rm red} = 2.65$
S3-263
S3-268
S3-284, $\chi^2_{\rm red} = 3.68$
S3-286, $\chi^2_{\rm red} = 1.13$
S3-284
S3-286
$m_{K'}$
m_H
Time

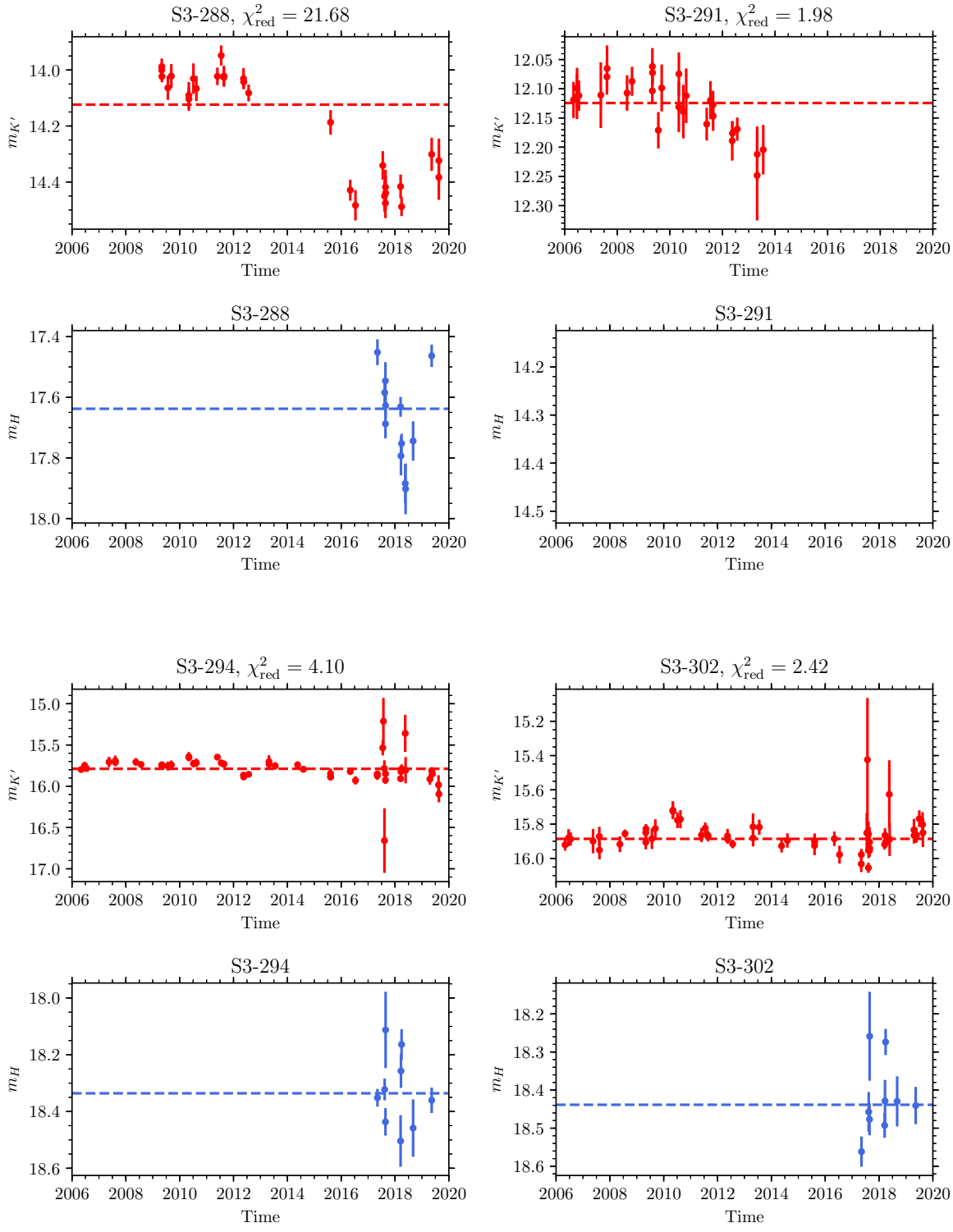
S3-288, $\chi^2_{\rm red} = 21.68$
S3-291, $\chi^2_{\rm red} = 1.98$
S3-288
S3-291
S3-294, $\chi^2_{\rm red} = 4.10$
S3-302, $\chi^2_{\rm red} = 2.42$
S3-294
S3-302
$m_{K'}$
m_H
Time

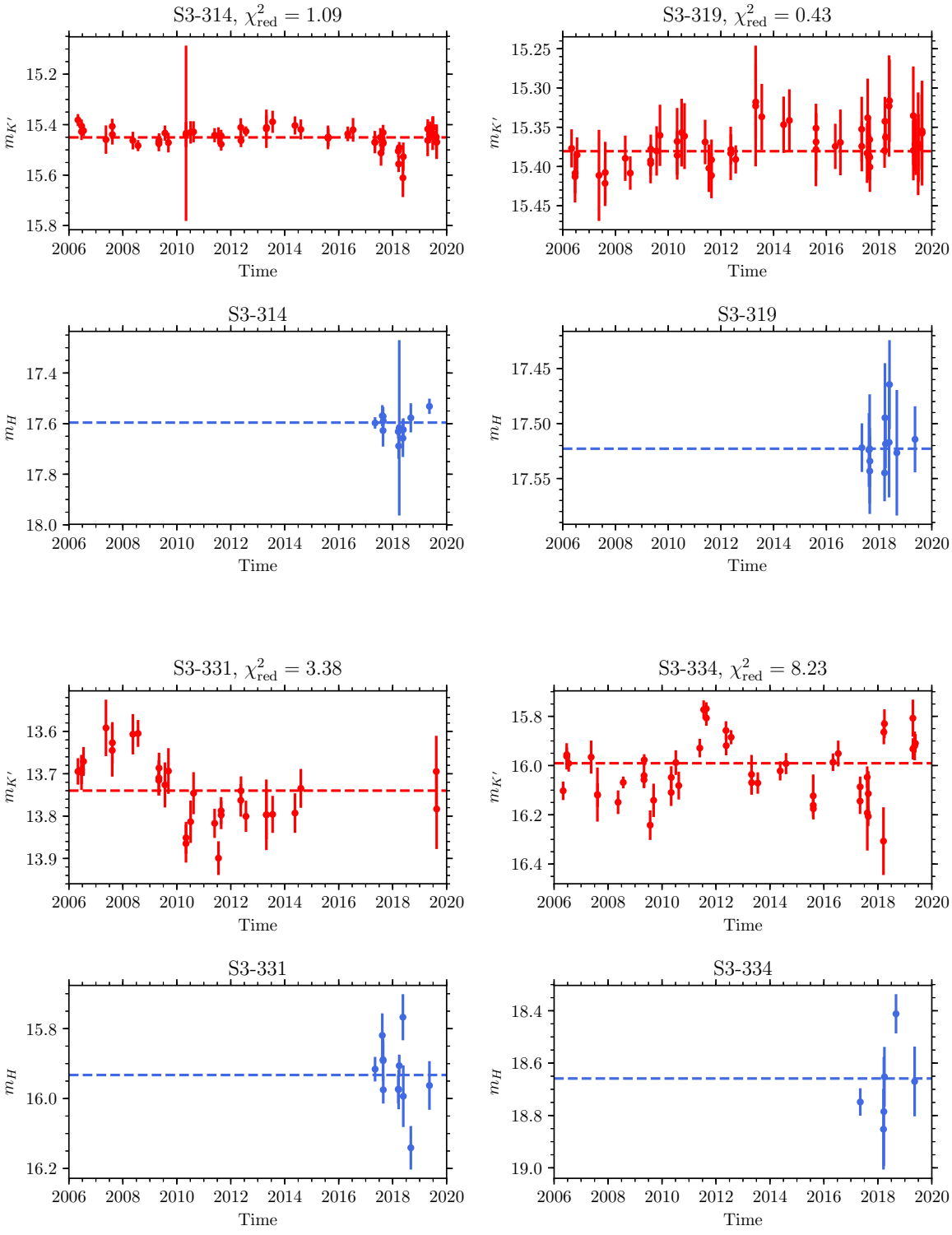
S3-314, $\chi^2_{\rm red} = 1.09$
S3-319, $\chi^2_{\rm red} = 0.43$
S3-314
S3-319
S3-331, $\chi^2_{\rm red} = 3.38$
S3-334, $\chi^2_{\rm red} = 8.23$
S3-331
S3-334
$m_{K'}$
m_H
Time

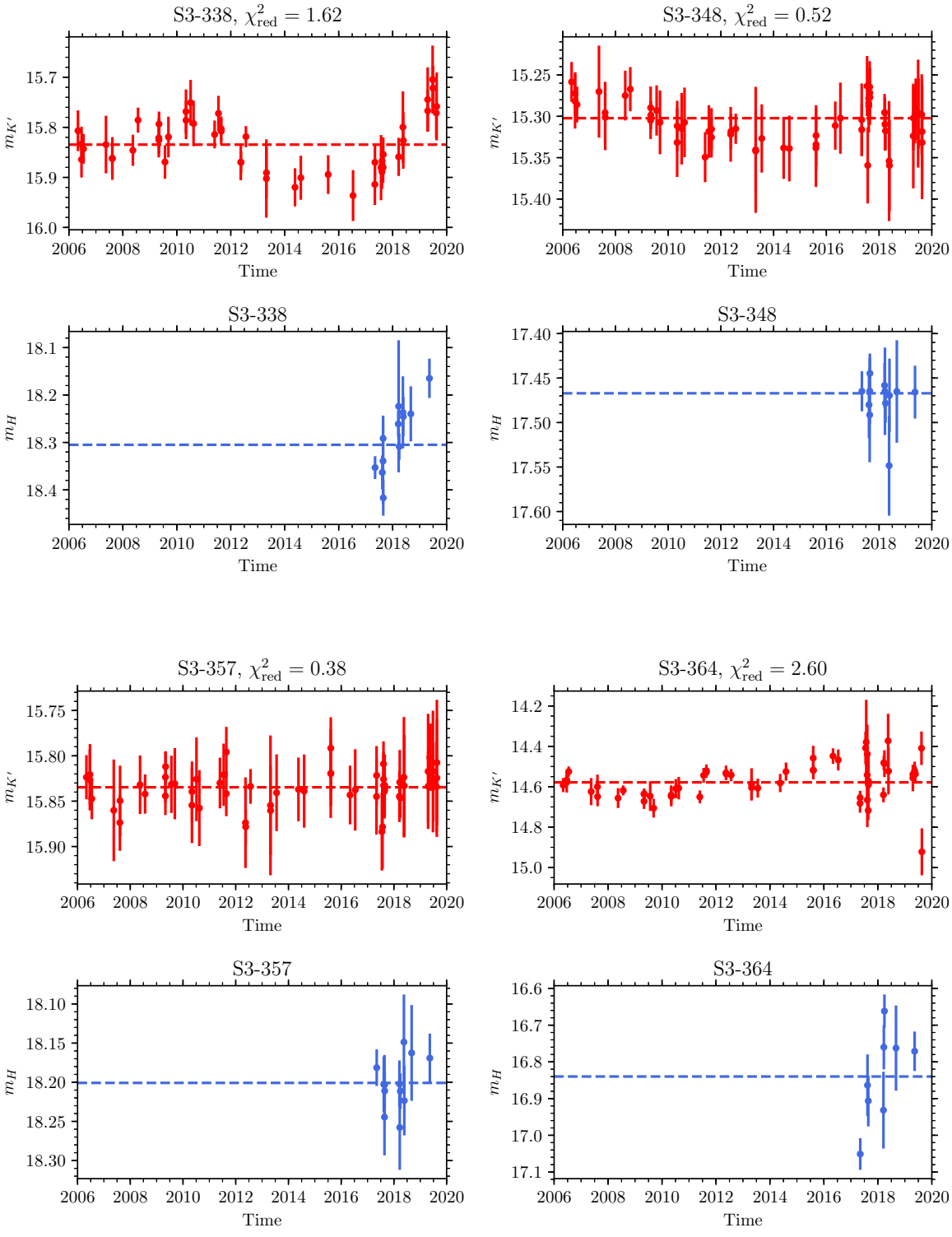
S3-338, $\chi^2_{\rm red} = 1.62$
S3-348, $\chi^2_{\rm red} = 0.52$
S3-338
S3-348
S3-357, $\chi^2_{\rm red} = 0.38$
S3-364, $\chi^2_{\rm red} = 2.60$
S3-357
S3-364
$m_{K'}$
m_H
Time

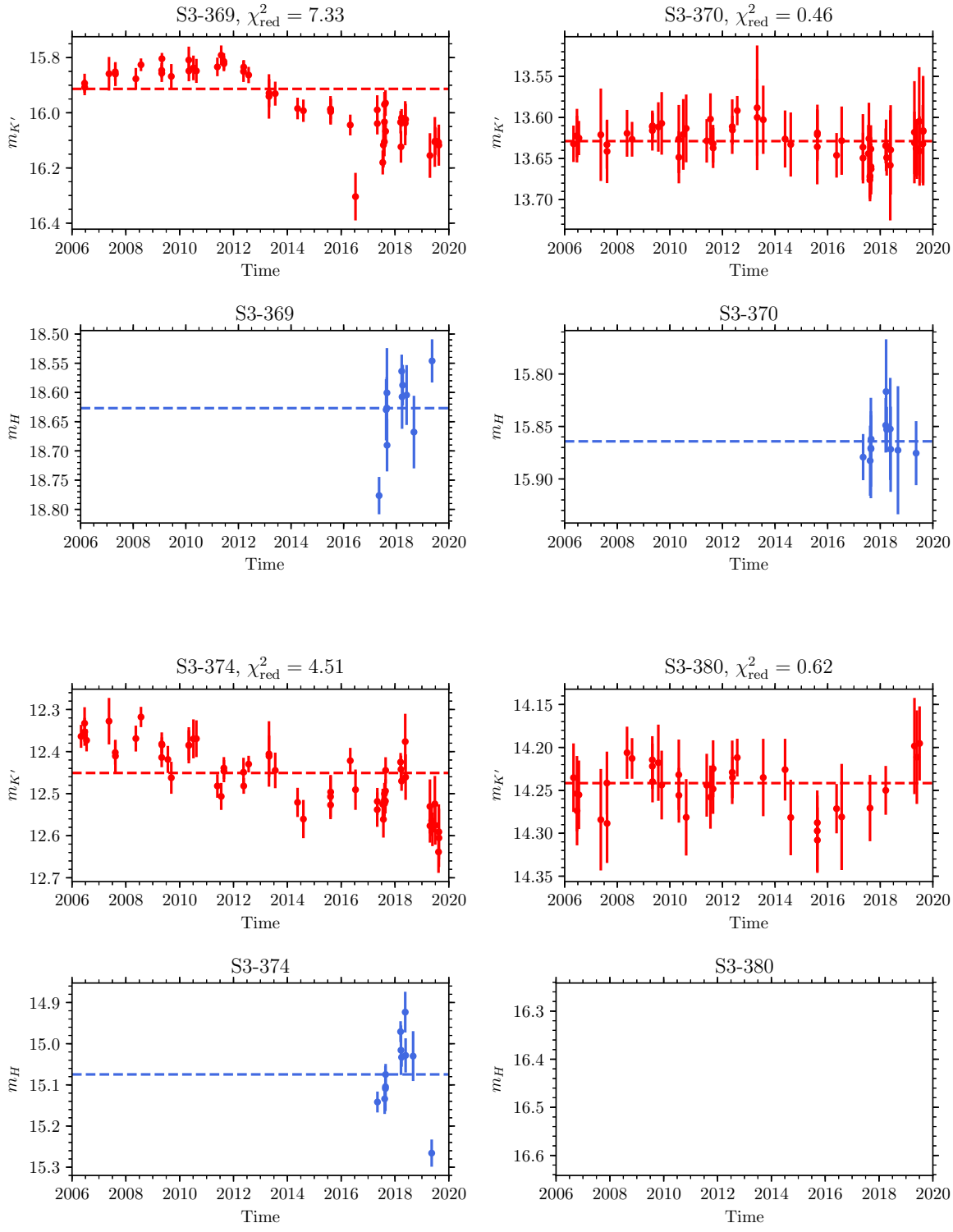
S3-369, $\chi^2_{\rm red} = 7.33$
S3-370, $\chi^2_{\rm red} = 0.46$
S3-369
S3-370
S3-374, $\chi^2_{\rm red} = 4.51$
S3-380, $\chi^2_{\rm red} = 0.62$
S3-374
S3-380
$m_{K'}$
m_H
Time

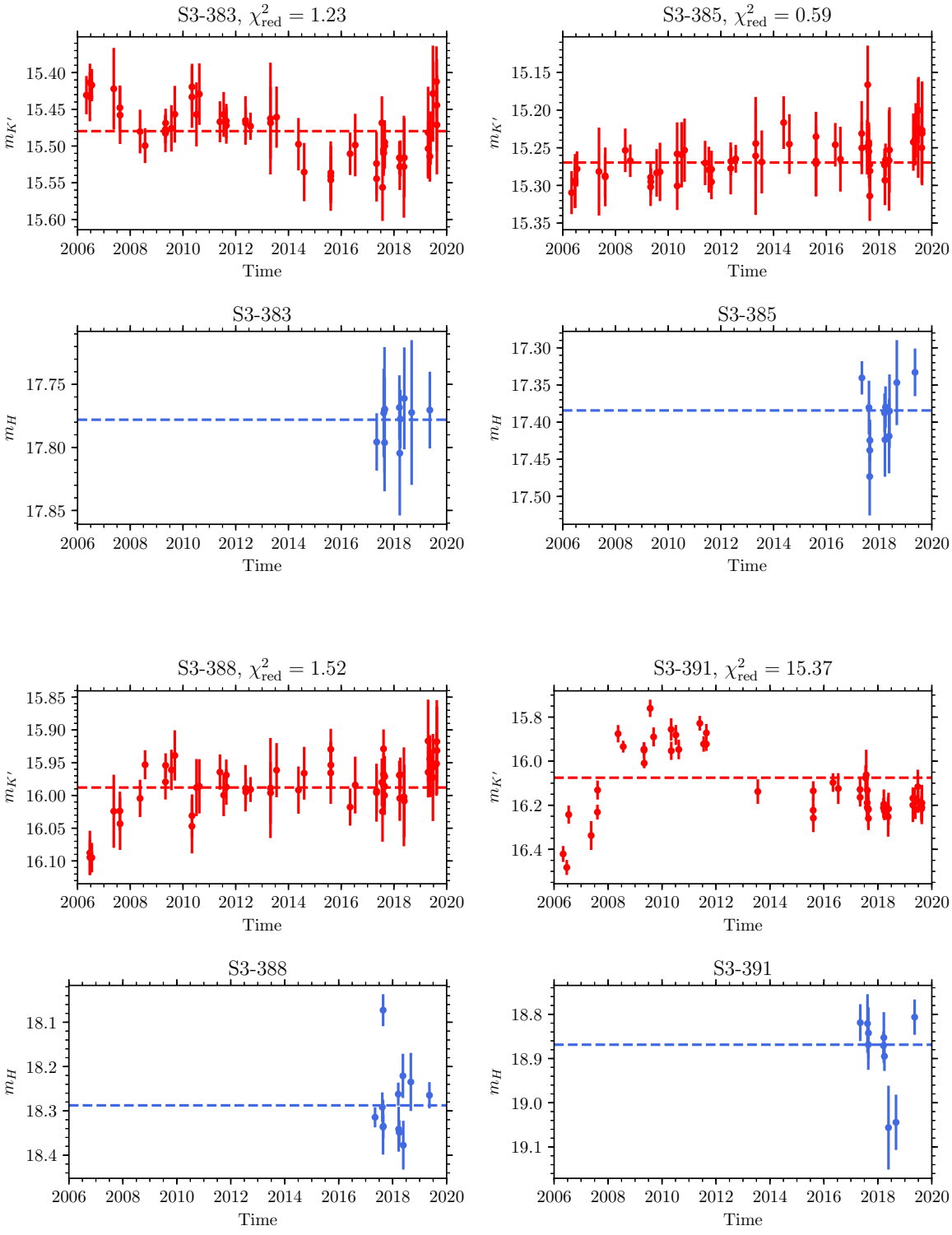
S3-383, $\chi^2_{\rm red} = 1.23$
S3-385, $\chi^2_{\rm red} = 0.59$
S3-383
S3-385
S3-388, $\chi^2_{\rm red} = 1.52$
S3-391, $\chi^2_{\rm red} = 15.37$
S3-388
S3-391
$m_{K'}$
m_H
Time

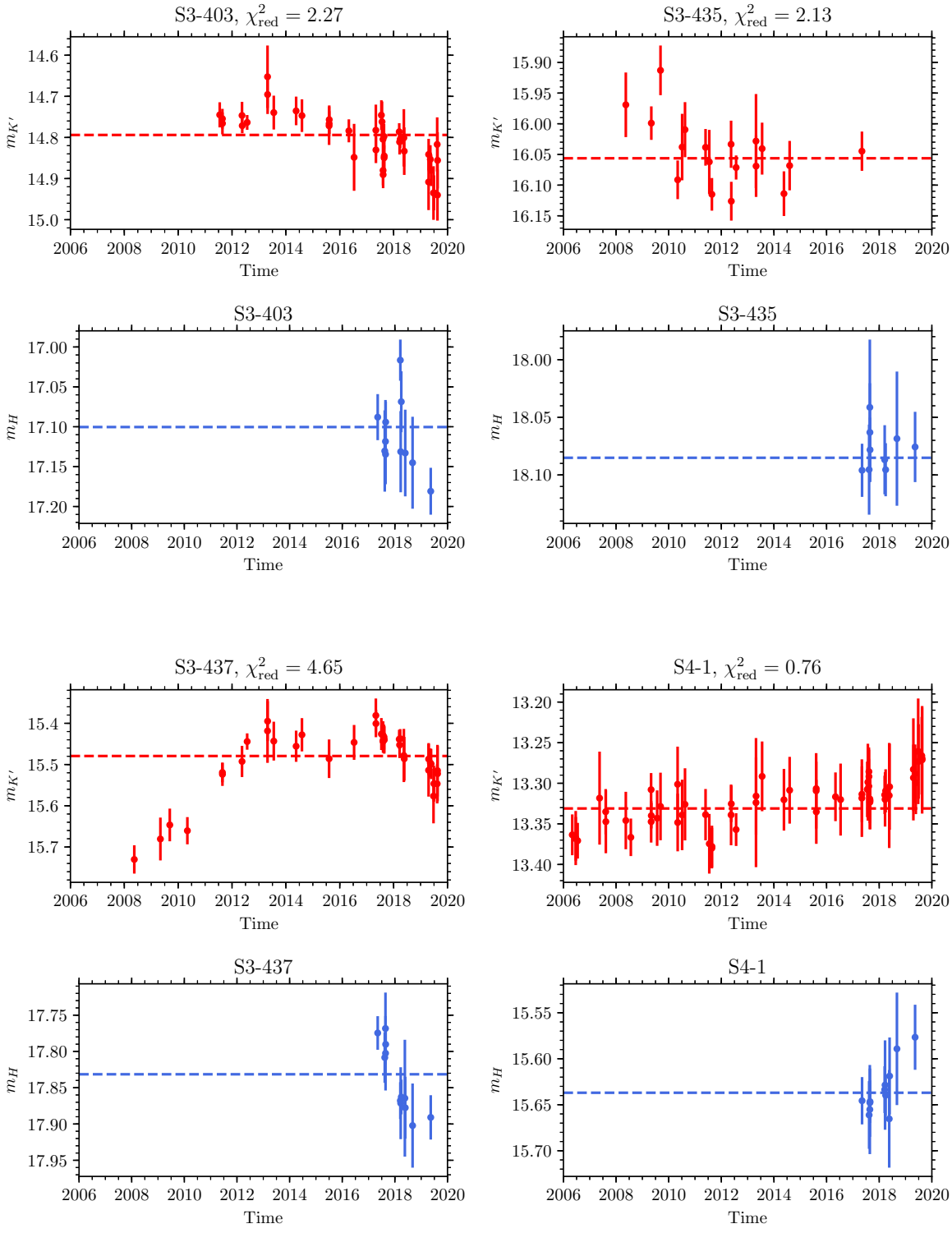
S3-403, $\chi^2_{\rm red} = 2.27$
S3-435, $\chi^2_{\rm red} = 2.13$
S3-403
S3-435
S3-437, $\chi^2_{\rm red} = 4.65$
S4-1, $\chi^2_{\rm red} = 0.76$
S3-437
S4-1
$m_{K'}$
m_H
Time

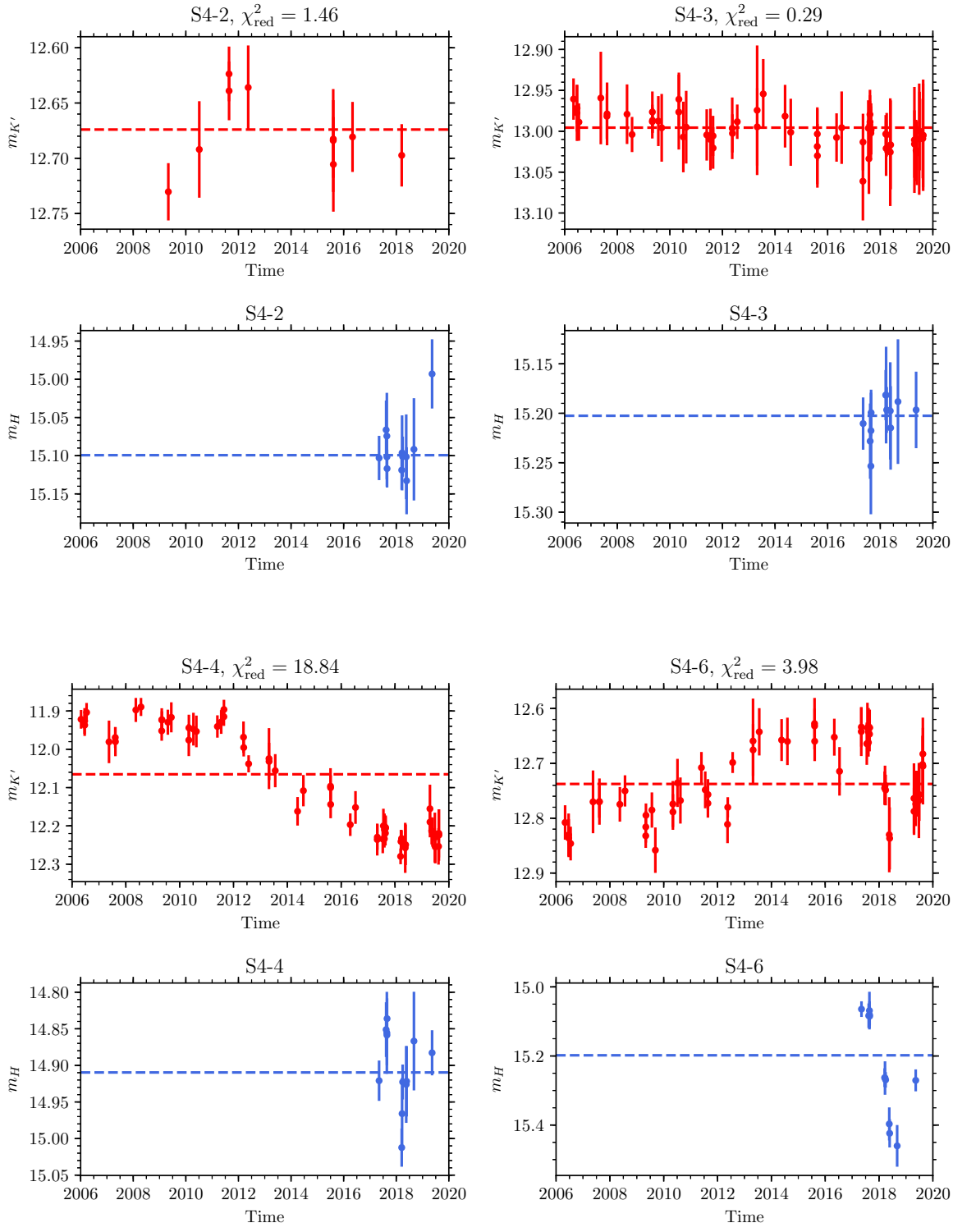
S4-2, $\chi^2_{\rm red} = 1.46$
S4-3, $\chi^2_{\rm red} = 0.29$
S4-2
S4-3
S4-4, $\chi^2_{\rm red} = 18.84$
S4-6, $\chi^2_{\rm red} = 3.98$
S4-4
S4-6
$m_{K'}$
m_H
Time

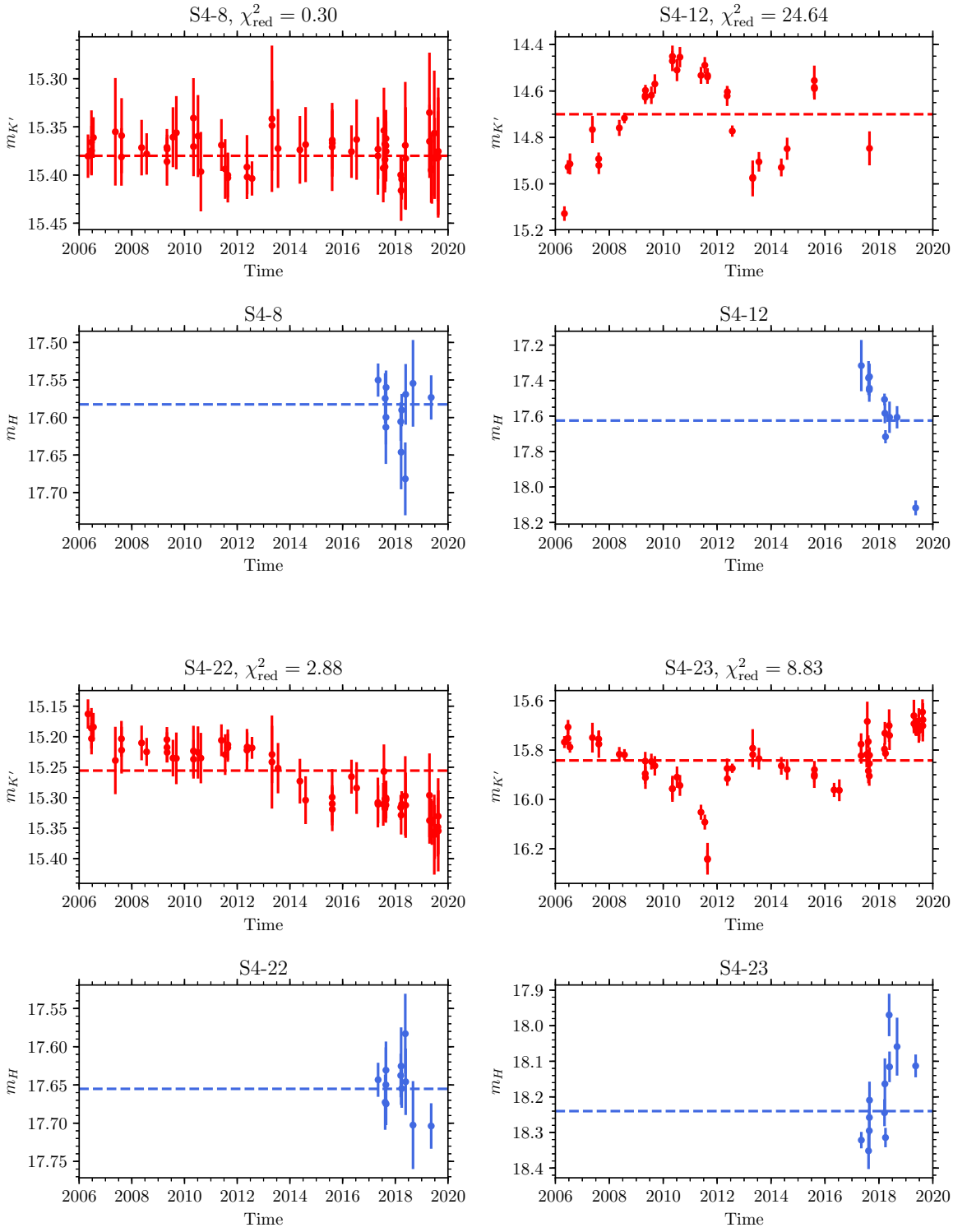
S4-8, $\chi^2_{\rm red} = 0.30$
S4-12, $\chi^2_{\rm red} = 24.64$
S4-8
S4-12
S4-22, $\chi^2_{\rm red} = 2.88$
S4-23, $\chi^2_{\rm red} = 8.83$
S4-22
S4-23
$m_{K'}$
m_H
Time

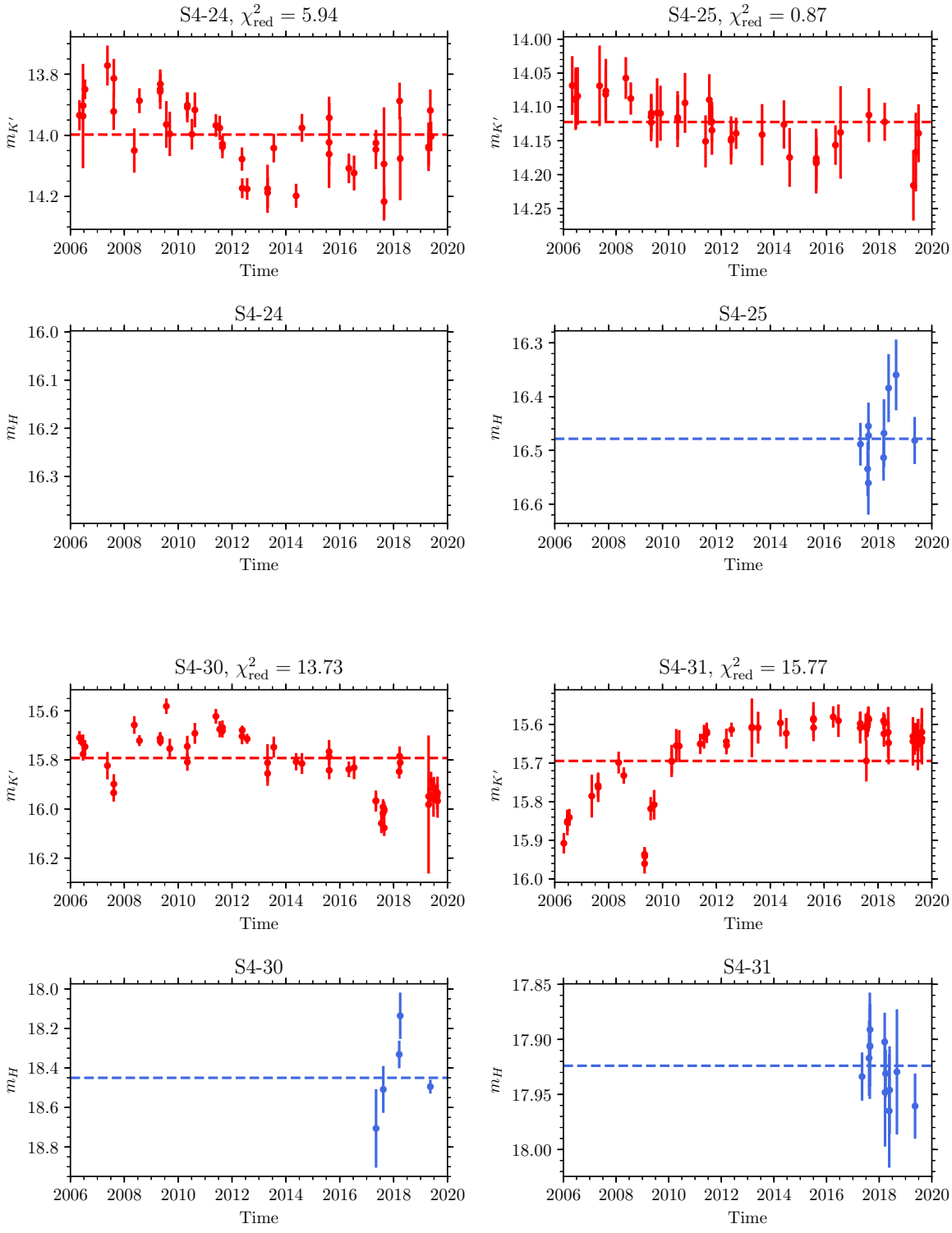
S4-24, $\chi^2_{\rm red} = 5.94$
S4-25, $\chi^2_{\rm red} = 0.87$
S4-24
S4-25
S4-30, $\chi^2_{\rm red} = 13.73$
S4-31, $\chi^2_{\rm red} = 15.77$
S4-30
S4-31
$m_{K'}$
m_H
Time

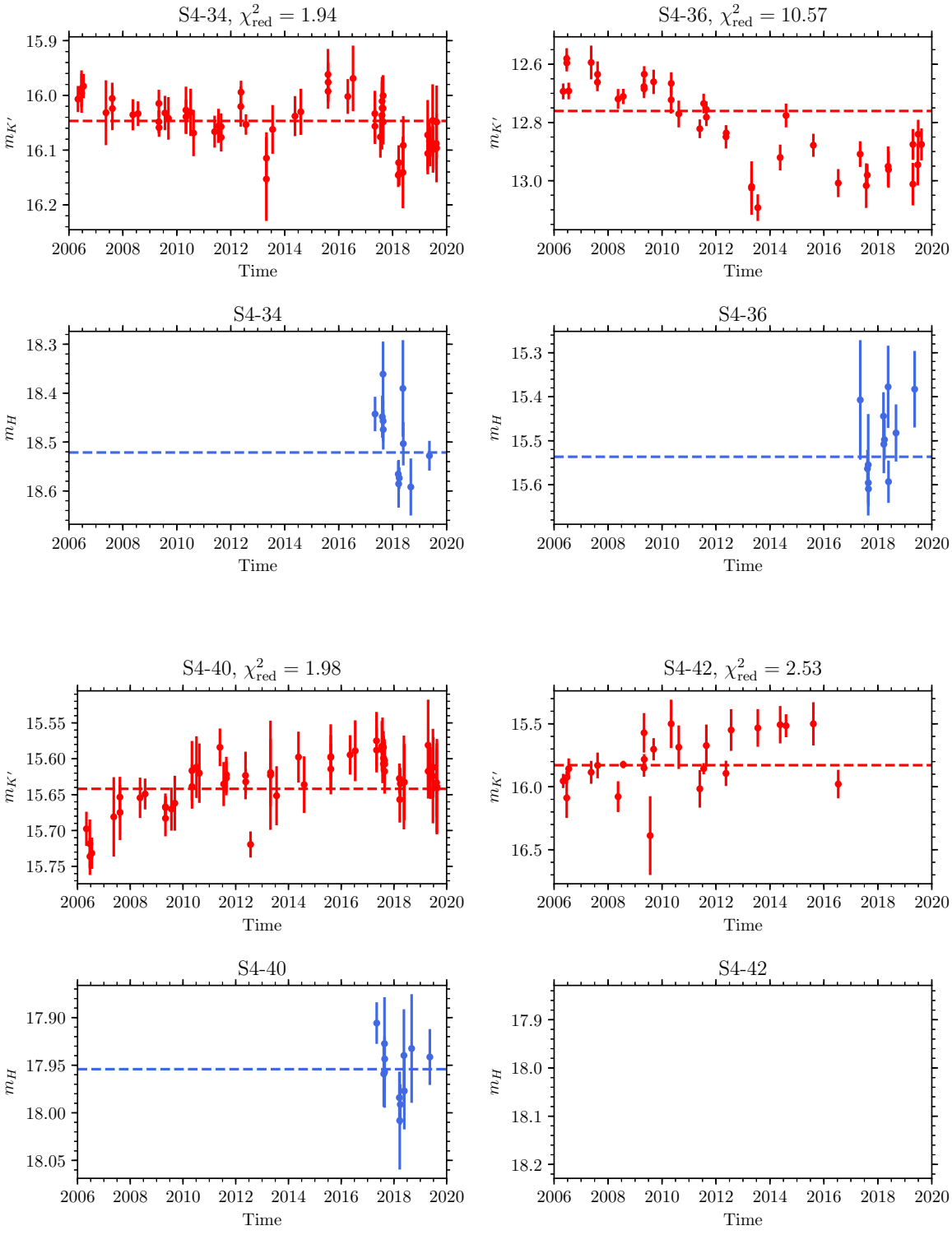
S4-34, $\chi^2_{\rm red} = 1.94$
S4-36, $\chi^2_{\rm red} = 10.57$
S4-34
S4-36
S4-40, $\chi^2_{\rm red} = 1.98$
S4-42, $\chi^2_{\rm red} = 2.53$
S4-40
S4-42
$m_{K'}$
m_H
Time

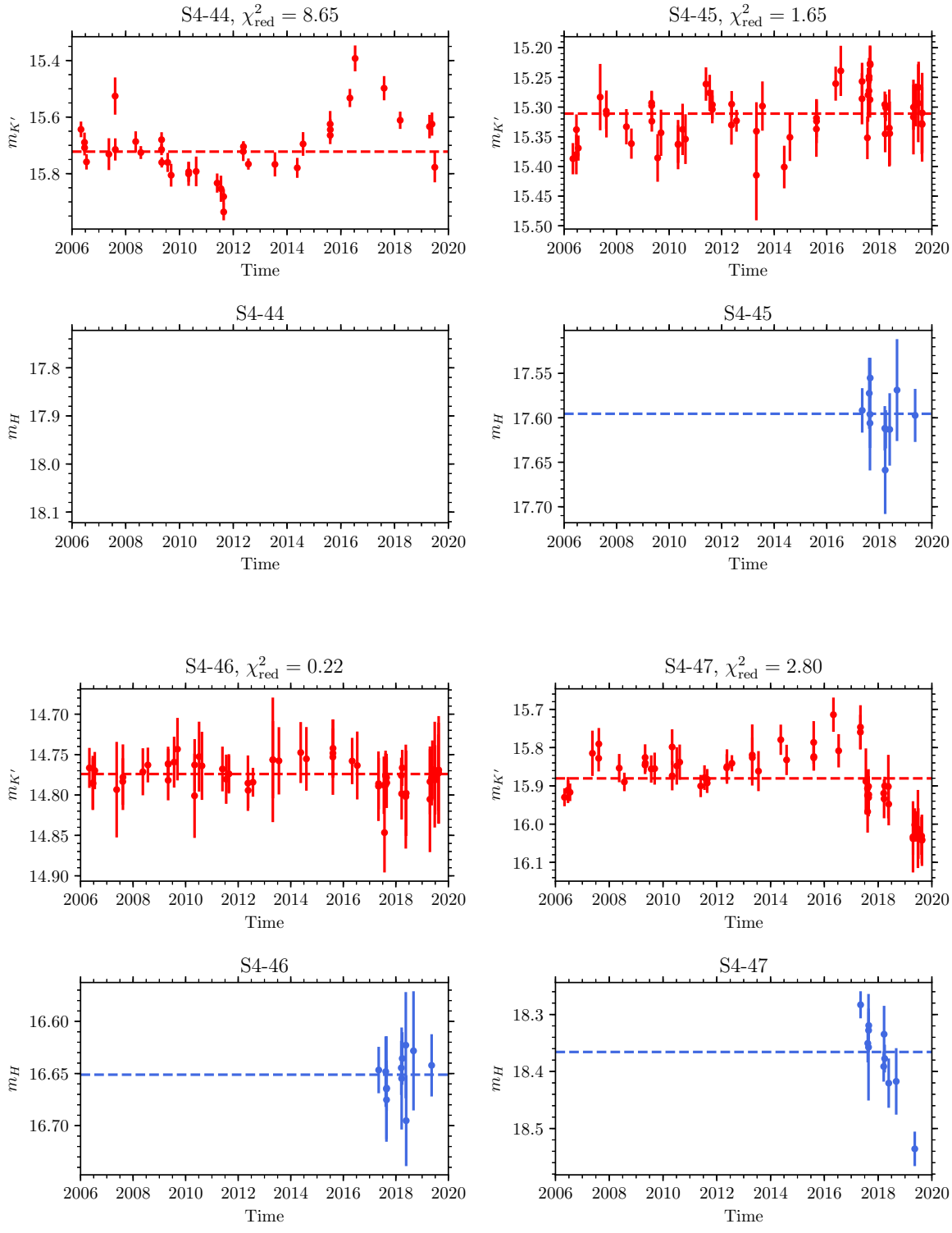
S4-44, $\chi^2_{\rm red} = 8.65$
S4-45, $\chi^2_{\rm red} = 1.65$
S4-44
S4-45
S4-46, $\chi^2_{\rm red} = 0.22$
S4-47, $\chi^2_{\rm red} = 2.80$
S4-46
S4-47
$m_{K'}$
m_H
Time

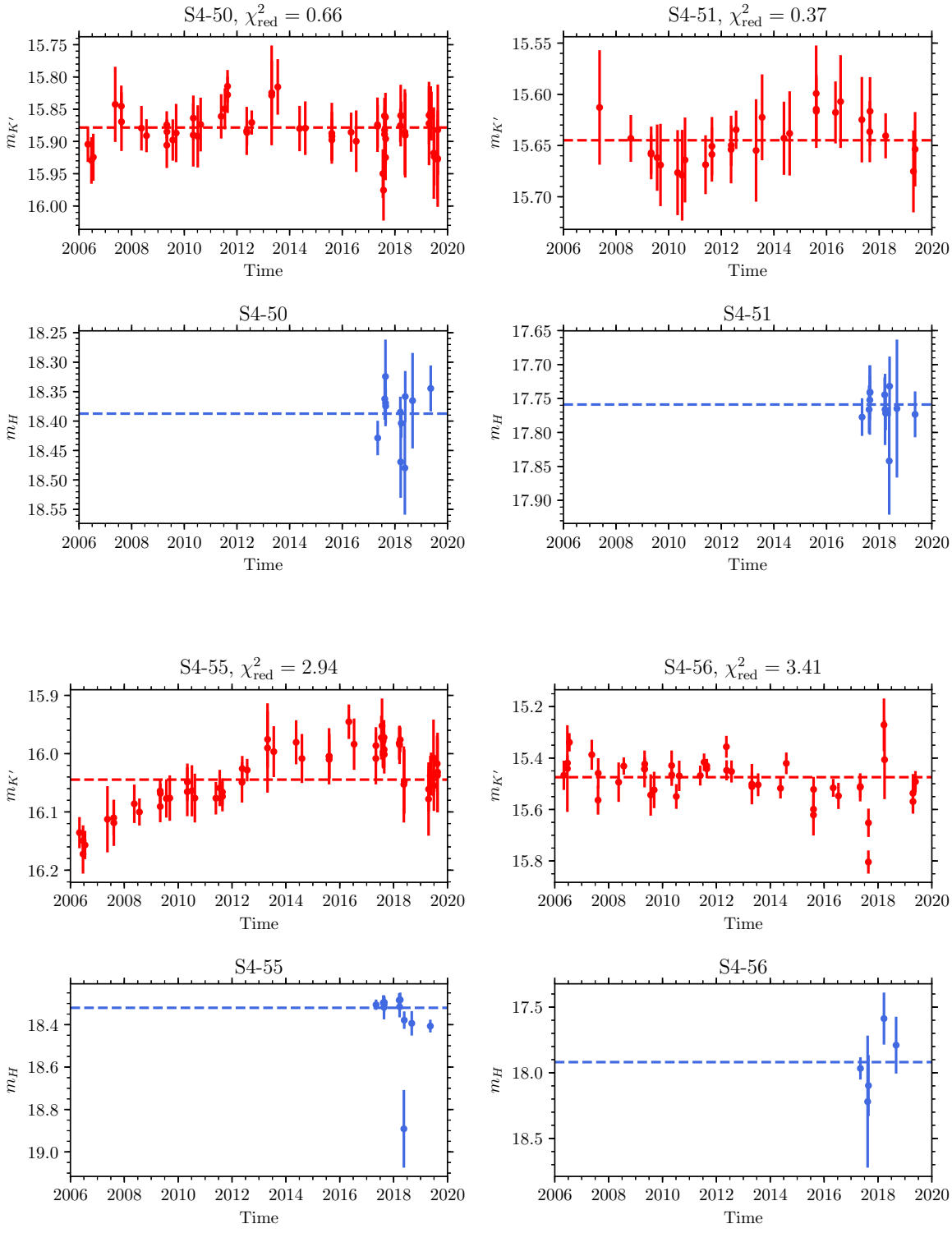
S4-50, $\chi^2_{\rm red} = 0.66$
S4-51, $\chi^2_{\rm red} = 0.37$
S4-50
S4-51
S4-55, $\chi^2_{\rm red} = 2.94$
S4-56, $\chi^2_{\rm red} = 3.41$
S4-55
S4-56
$m_{K'}$
m_H
Time

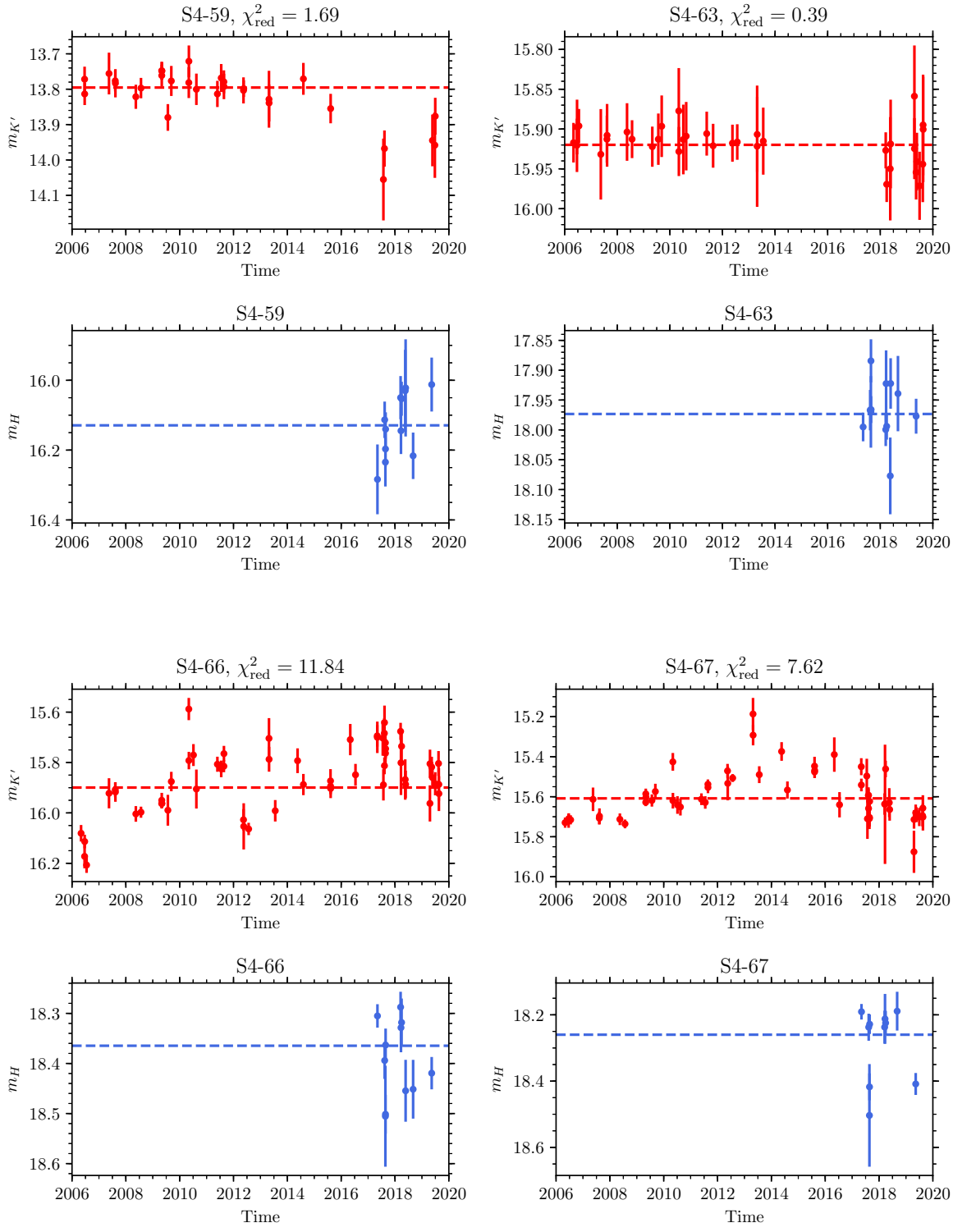
S4-59, $\chi^2_{\rm red} = 1.69$
S4-63, $\chi^2_{\rm red} = 0.39$
S4-59
S4-63
S4-66, $\chi^2_{\rm red} = 11.84$
S4-67, $\chi^2_{\rm red} = 7.62$
S4-66
S4-67
$m_{K'}$
m_H
Time

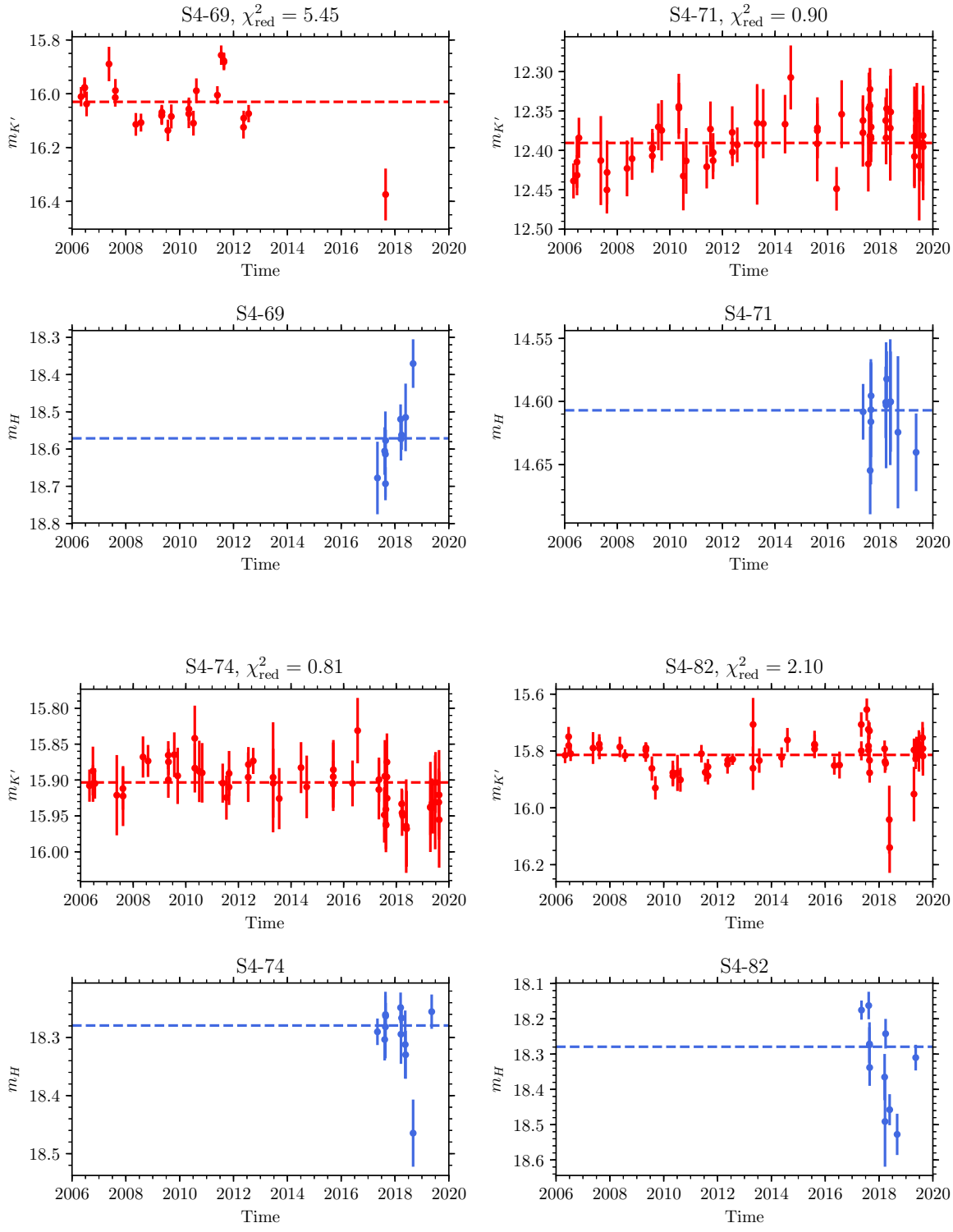
S4-69, $\chi^2_{\rm red} = 5.45$
S4-71, $\chi^2_{\rm red} = 0.90$
S4-69
S4-71
S4-74, $\chi^2_{\rm red} = 0.81$
S4-82, $\chi^2_{\rm red} = 2.10$
S4-74
S4-82
$m_{K'}$
m_H
Time

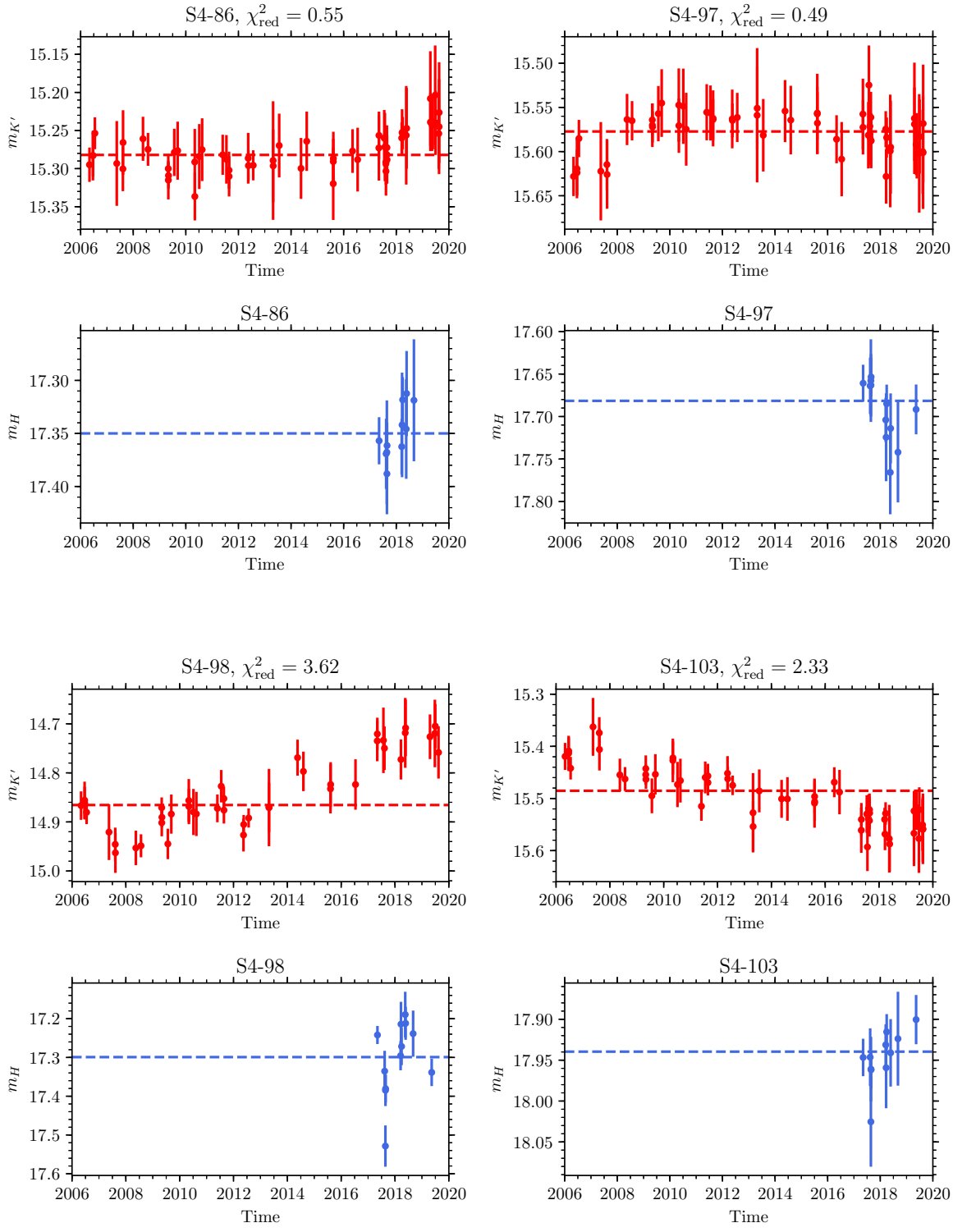
S4-86, $\chi^2_{\rm red} = 0.55$
S4-97, $\chi^2_{\rm red} = 0.49$
S4-86
S4-97
S4-98, $\chi^2_{\rm red} = 3.62$
S4-103, $\chi^2_{\rm red} = 2.33$
S4-98
S4-103
$m_{K'}$
m_H
Time

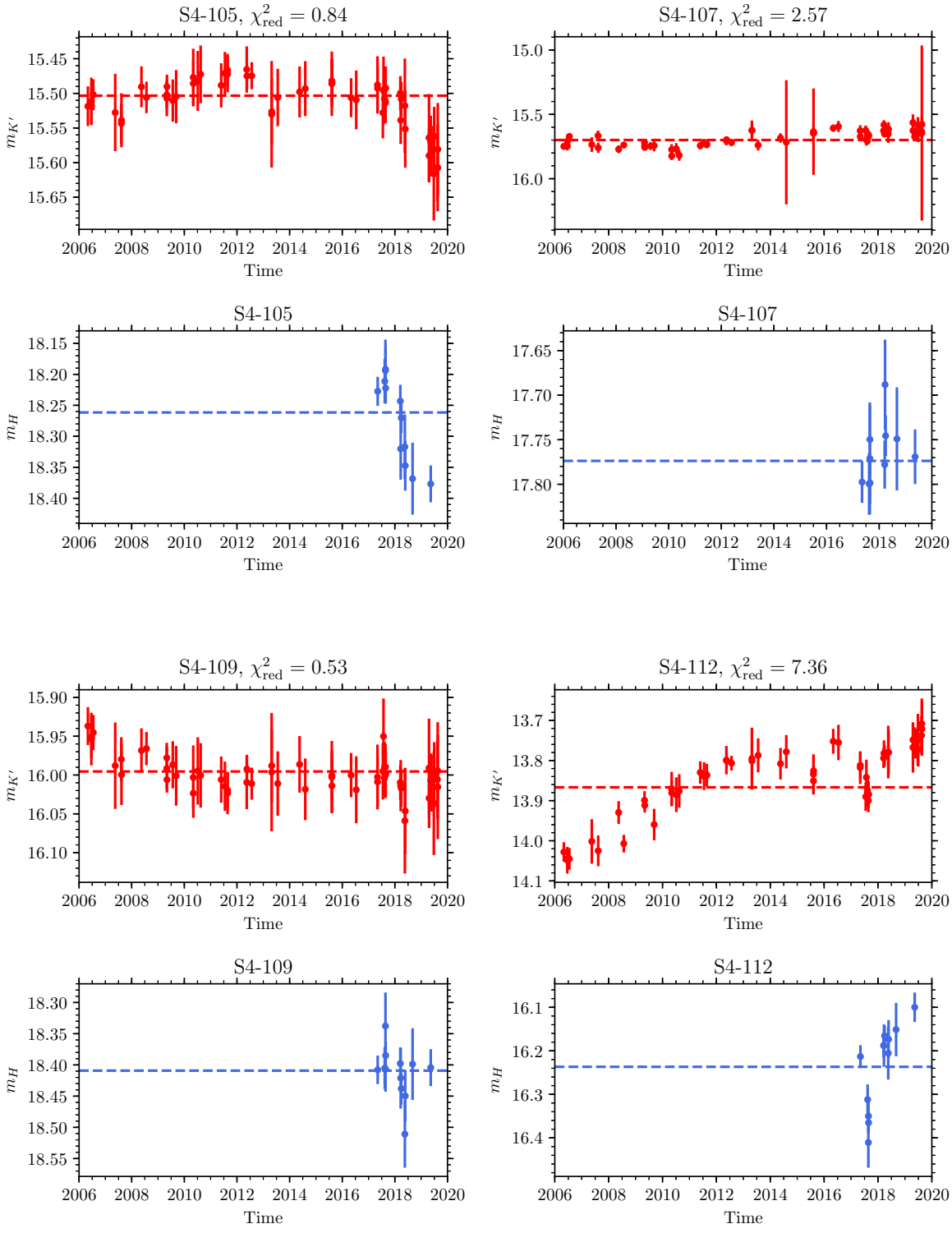
S4-105, $\chi^2_{\rm red} = 0.84$
S4-107, $\chi^2_{\rm red} = 2.57$
S4-105
S4-107
S4-109, $\chi^2_{\rm red} = 0.53$
S4-112, $\chi^2_{\rm red} = 7.36$
S4-109
S4-112
$m_{K'}$
m_H
Time

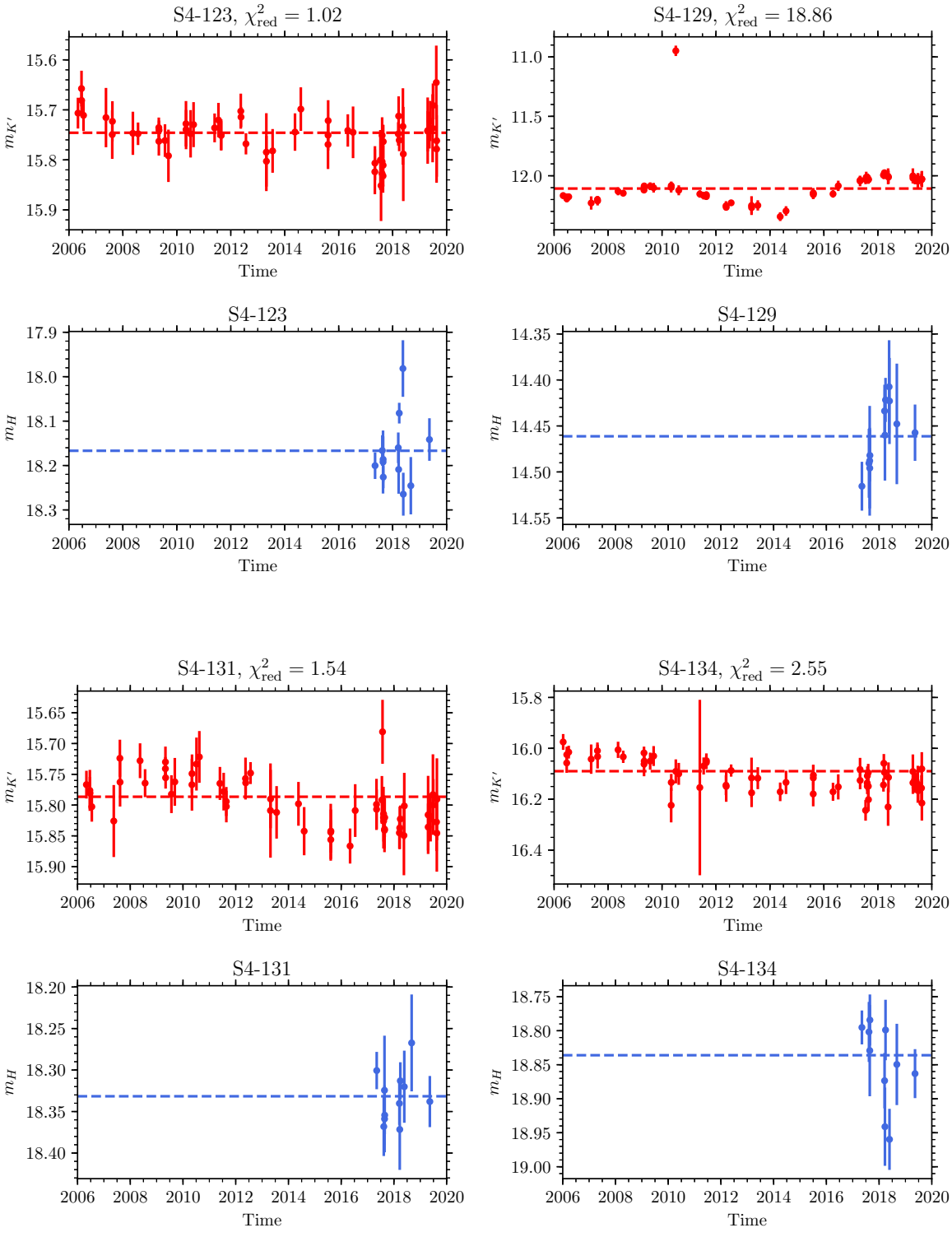
S4-123, $\chi^2_{\rm red} = 1.02$
S4-129, $\chi^2_{\rm red} = 18.86$
S4-123
S4-129
S4-131, $\chi^2_{\rm red} = 1.54$
S4-134, $\chi^2_{\rm red} = 2.55$
S4-131
S4-134
$m_{K'}$
m_H
Time

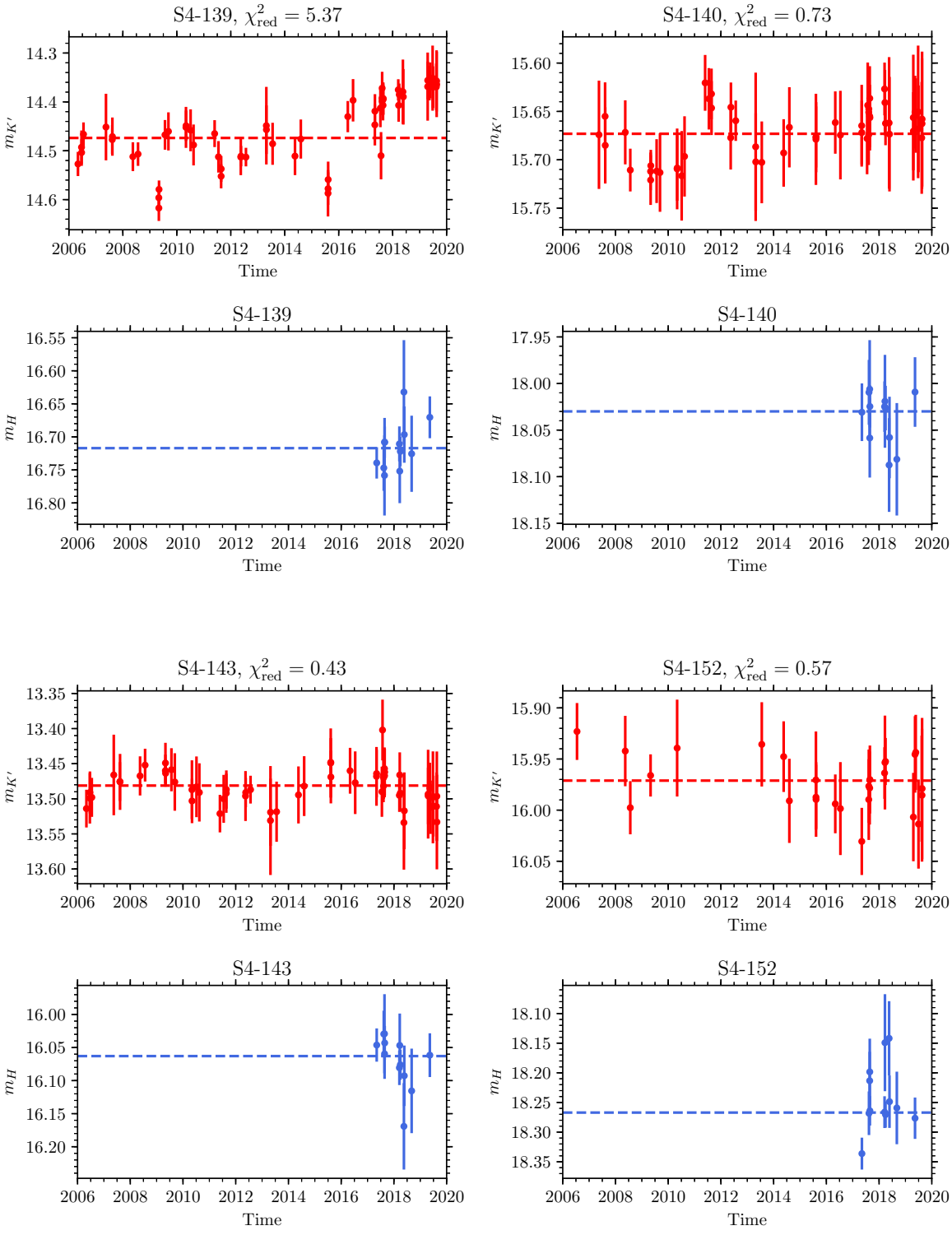
S4-139, $\chi^2_{\rm red} = 5.37$
S4-140, $\chi^2_{\rm red} = 0.73$
S4-139
S4-140
S4-143, $\chi^2_{\rm red} = 0.43$
S4-152, $\chi^2_{\rm red} = 0.57$
S4-143
S4-152
$m_{K'}$
m_H
Time

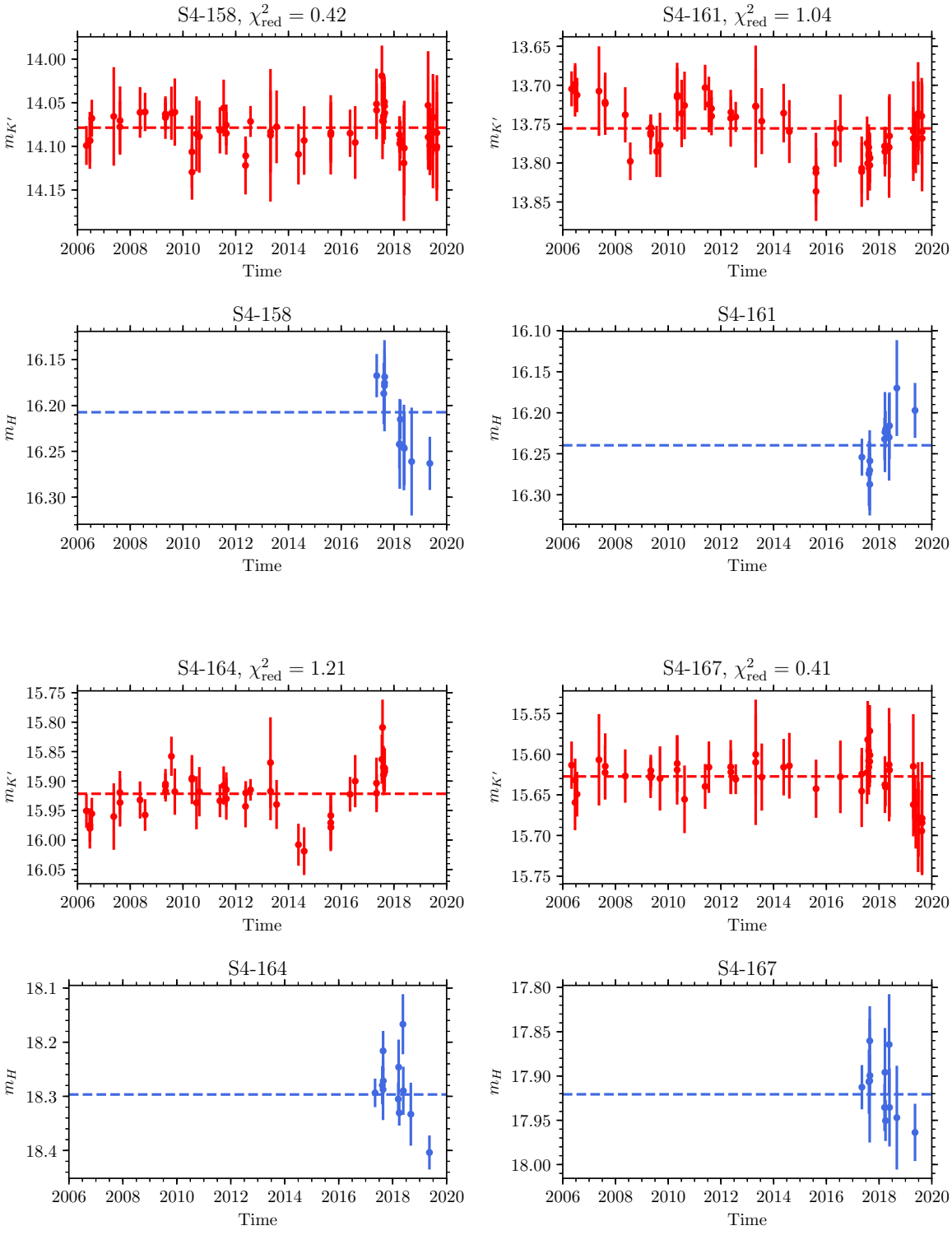
S4-158, $\chi^2_{\rm red} = 0.42$
S4-161, $\chi^2_{\rm red} = 1.04$
S4-158
S4-161
S4-164, $\chi^2_{\rm red} = 1.21$
S4-167, $\chi^2_{\rm red} = 0.41$
S4-164
S4-167
$m_{K'}$
m_H
Time

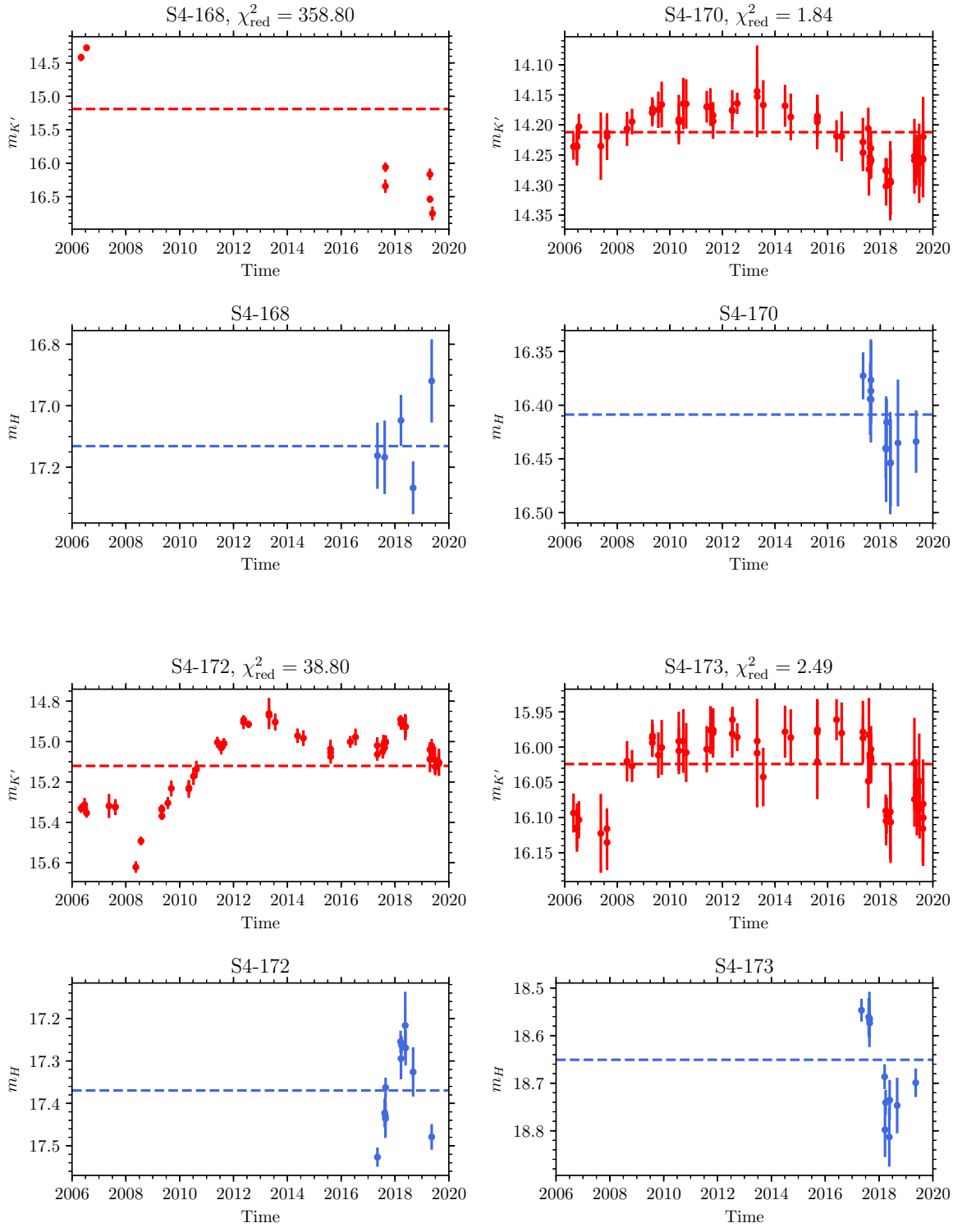
S4-168, $\chi^2_{\rm red} = 358.80$
S4-170, $\chi^2_{\rm red} = 1.84$
S4-168
S4-170
S4-172, $\chi^2_{\rm red} = 38.80$
S4-173, $\chi^2_{\rm red} = 2.49$
S4-172
S4-173
$m_{K'}$
m_H
Time

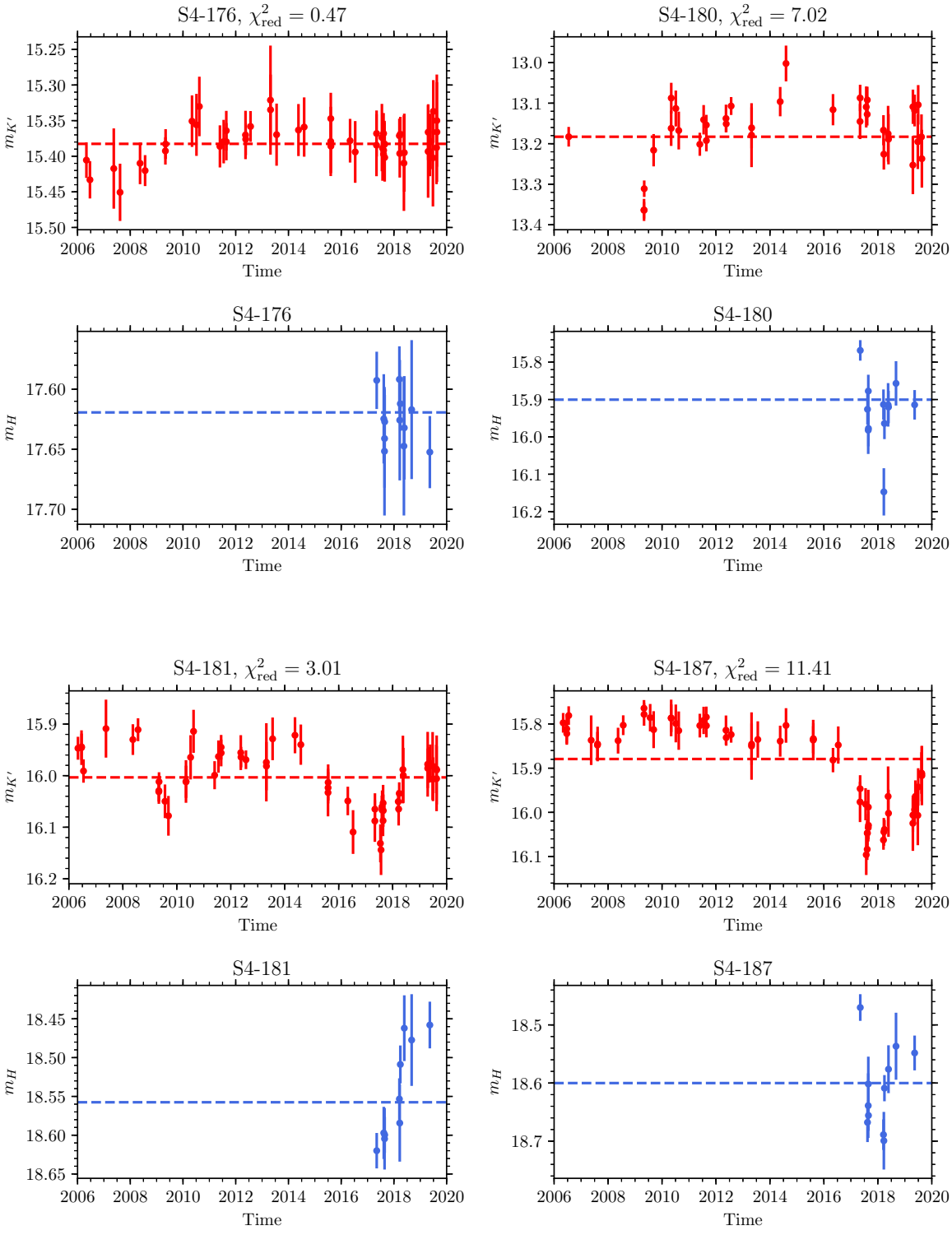
S4-176, $\chi^2_{\rm red} = 0.47$
S4-180, $\chi^2_{\rm red} = 7.02$
S4-176
S4-180
S4-181, $\chi^2_{\rm red} = 3.01$
S4-187, $\chi^2_{\rm red} = 11.41$
S4-181
S4-187
$m_{K'}$
m_H
Time

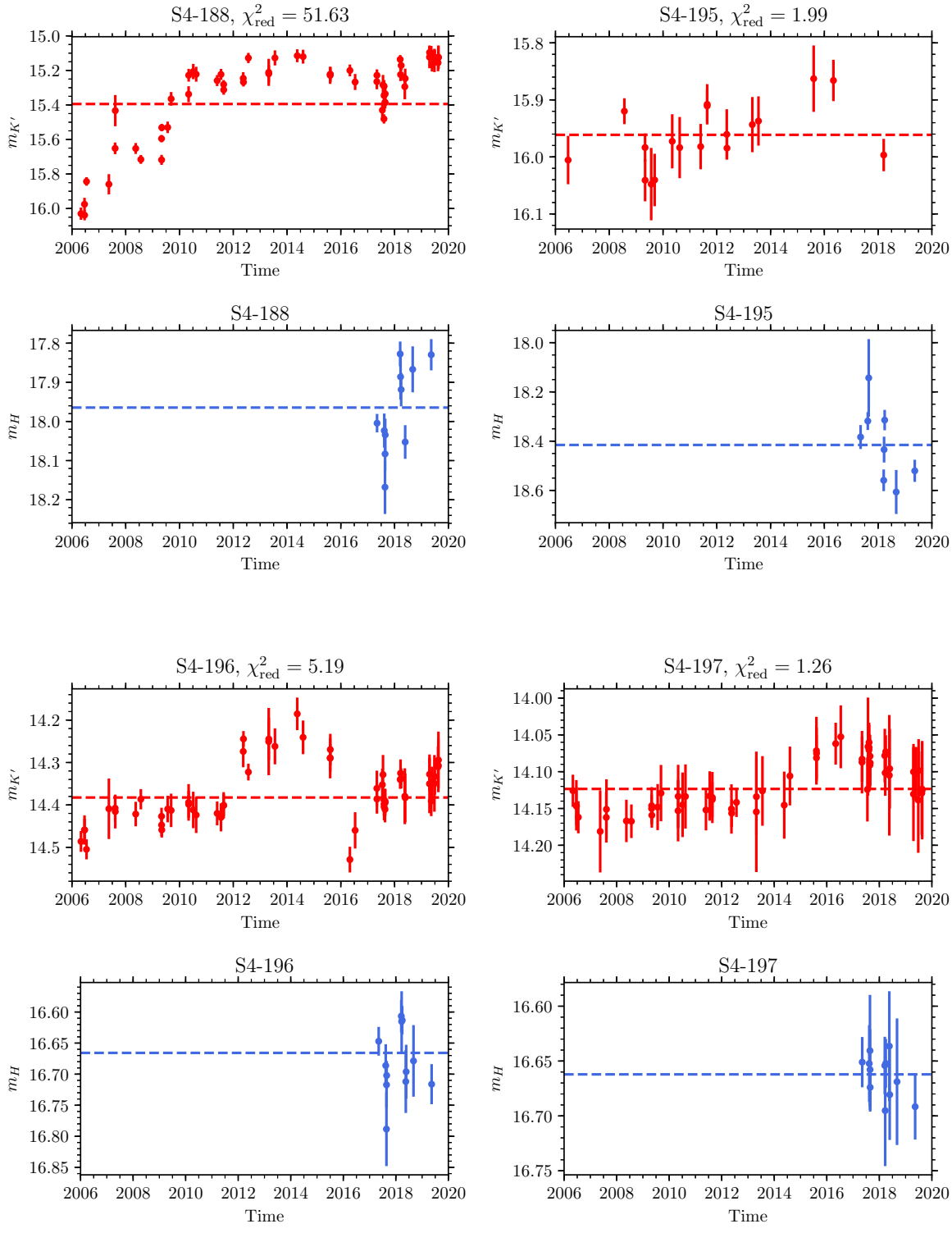
S4-188, $\chi^2_{\rm red} = 51.63$
S4-195, $\chi^2_{\rm red} = 1.99$
S4-188
S4-195
S4-196, $\chi^2_{\rm red} = 5.19$
S4-197, $\chi^2_{\rm red} = 1.26$
S4-196
S4-197
$m_{K'}$
m_H
Time

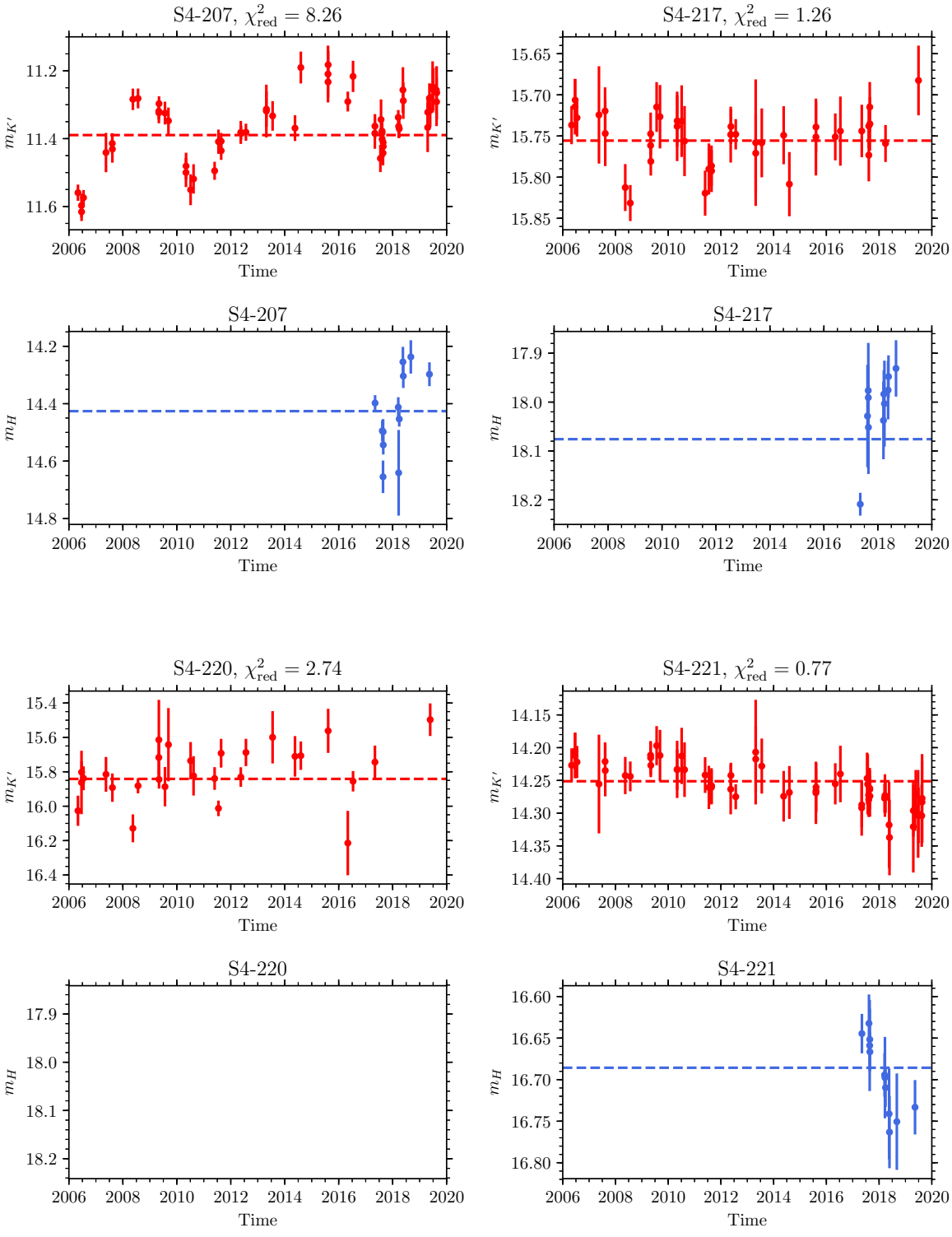
S4-207, $\chi^2_{\rm red} = 8.26$
S4-217, $\chi^2_{\rm red} = 1.26$
S4-207
S4-217
S4-220, $\chi^2_{\rm red} = 2.74$
S4-221, $\chi^2_{\rm red} = 0.77$
S4-220
S4-221
$m_{K'}$
m_H
Time

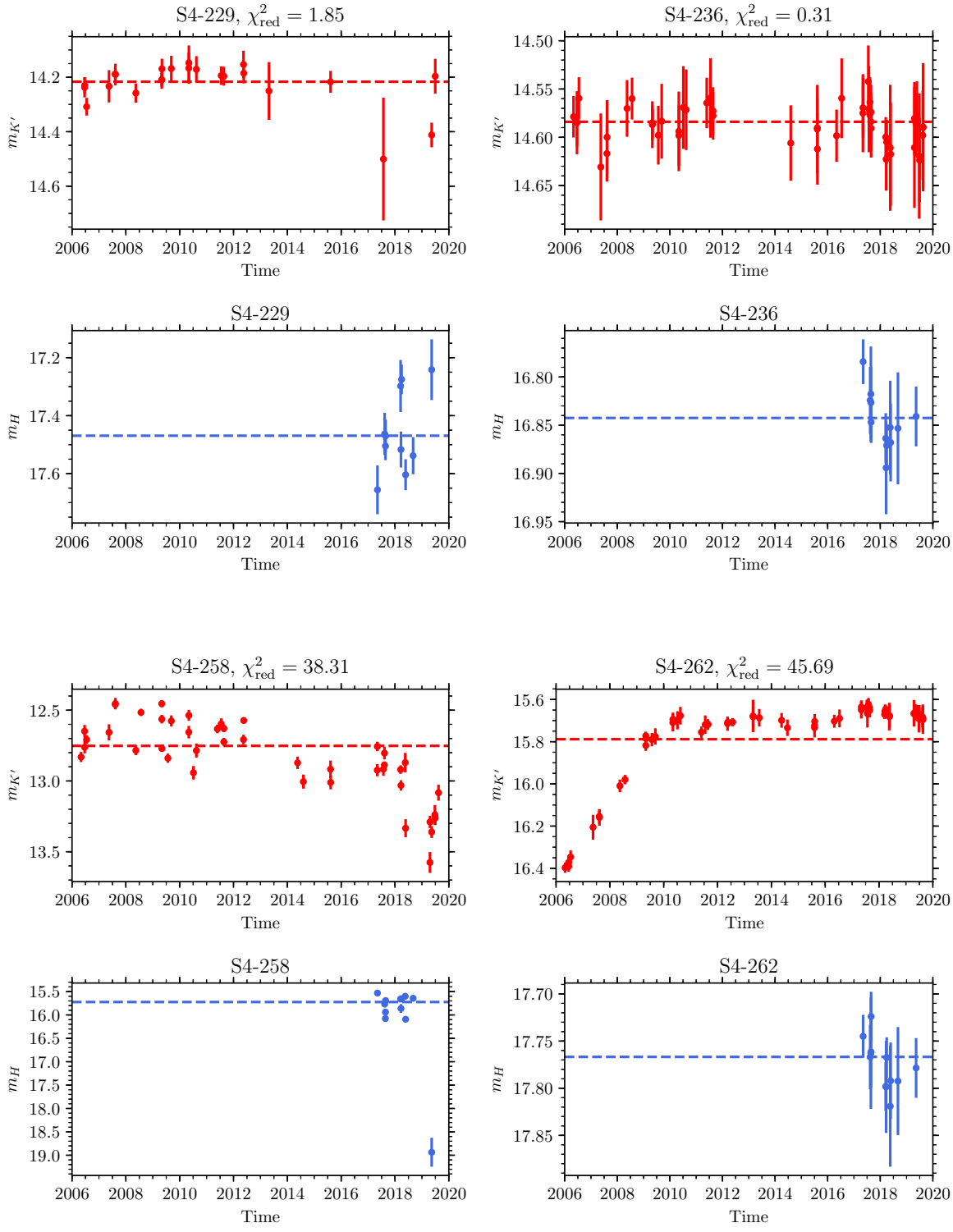
S4-229, $\chi^2_{\rm red} = 1.85$
S4-236, $\chi^2_{\rm red} = 0.31$
S4-229
S4-236
S4-258, $\chi^2_{\rm red} = 38.31$
S4-262, $\chi^2_{\rm red} = 45.69$
S4-258
S4-262
$m_{K'}$
m_H
Time

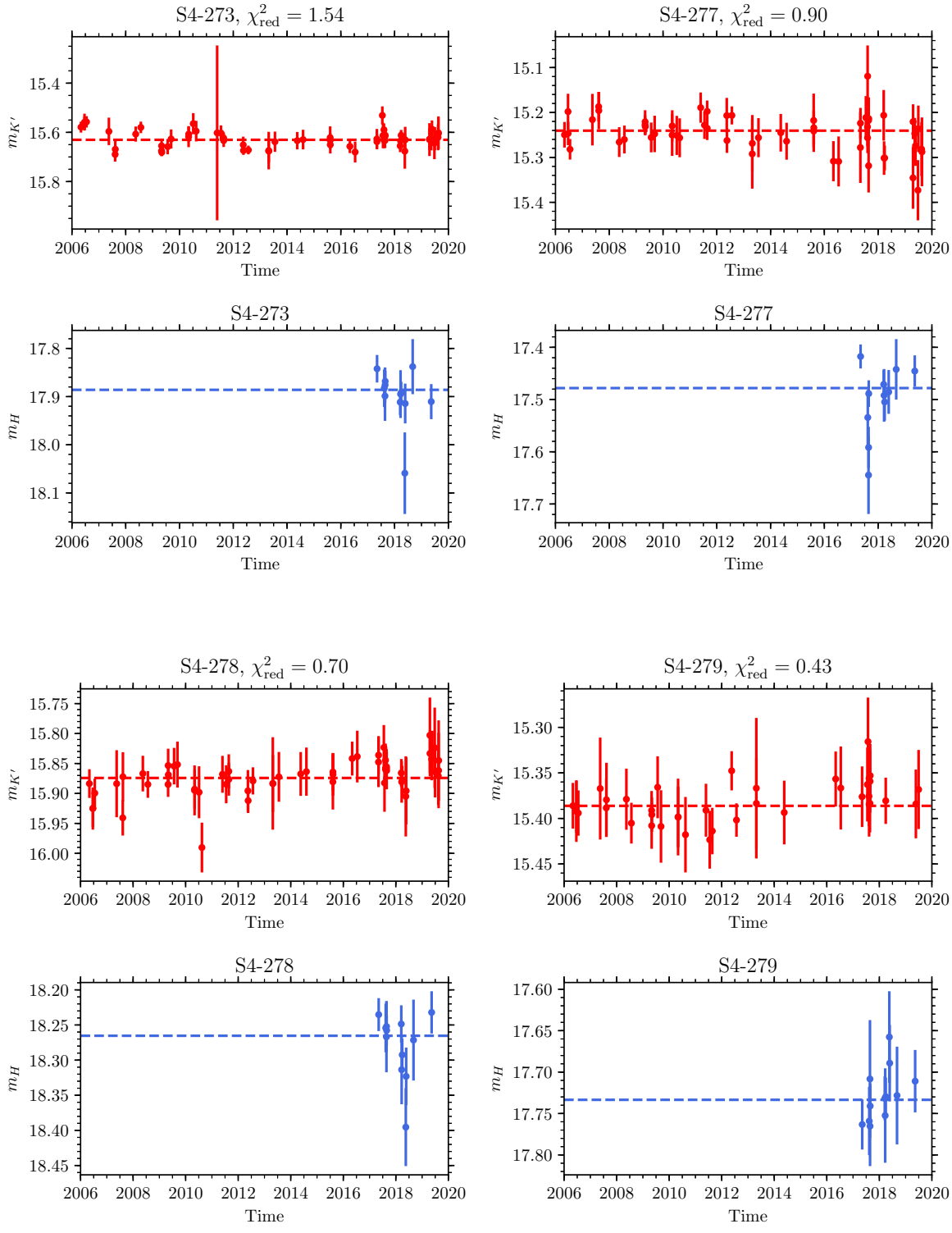
S4-273, $\chi^2_{\rm red} = 1.54$
S4-277, $\chi^2_{\rm red} = 0.90$
S4-273
S4-277
S4-278, $\chi^2_{\rm red} = 0.70$
S4-279, $\chi^2_{\rm red} = 0.43$
S4-278
S4-279
$m_{K'}$
m_H
Time

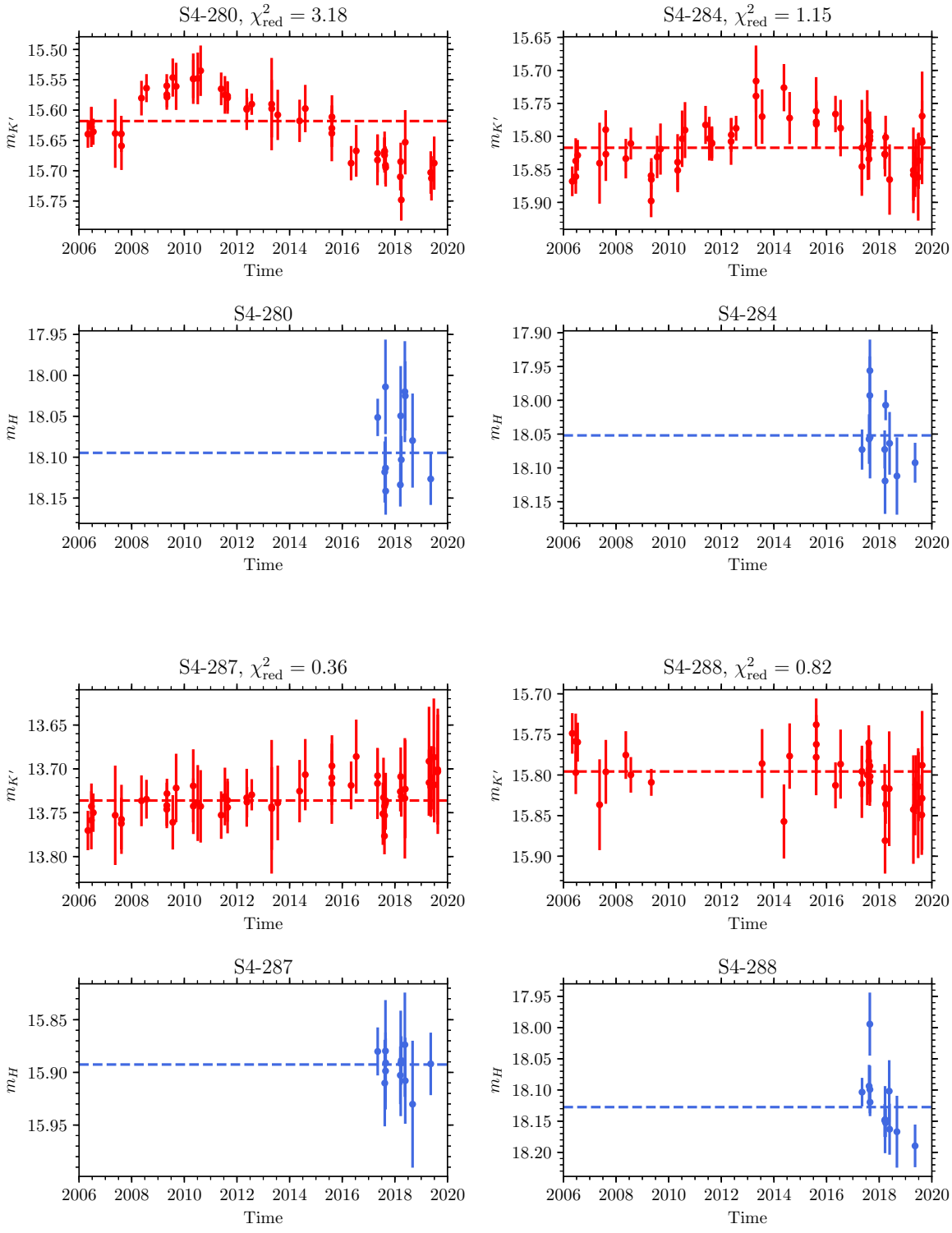
S4-280, $\chi^2_{\rm red} = 3.18$
S4-284, $\chi^2_{\rm red} = 1.15$
S4-280
S4-284
S4-287, $\chi^2_{\rm red} = 0.36$
S4-288, $\chi^2_{\rm red} = 0.82$
S4-287
S4-288
$m_{K'}$
m_H
Time

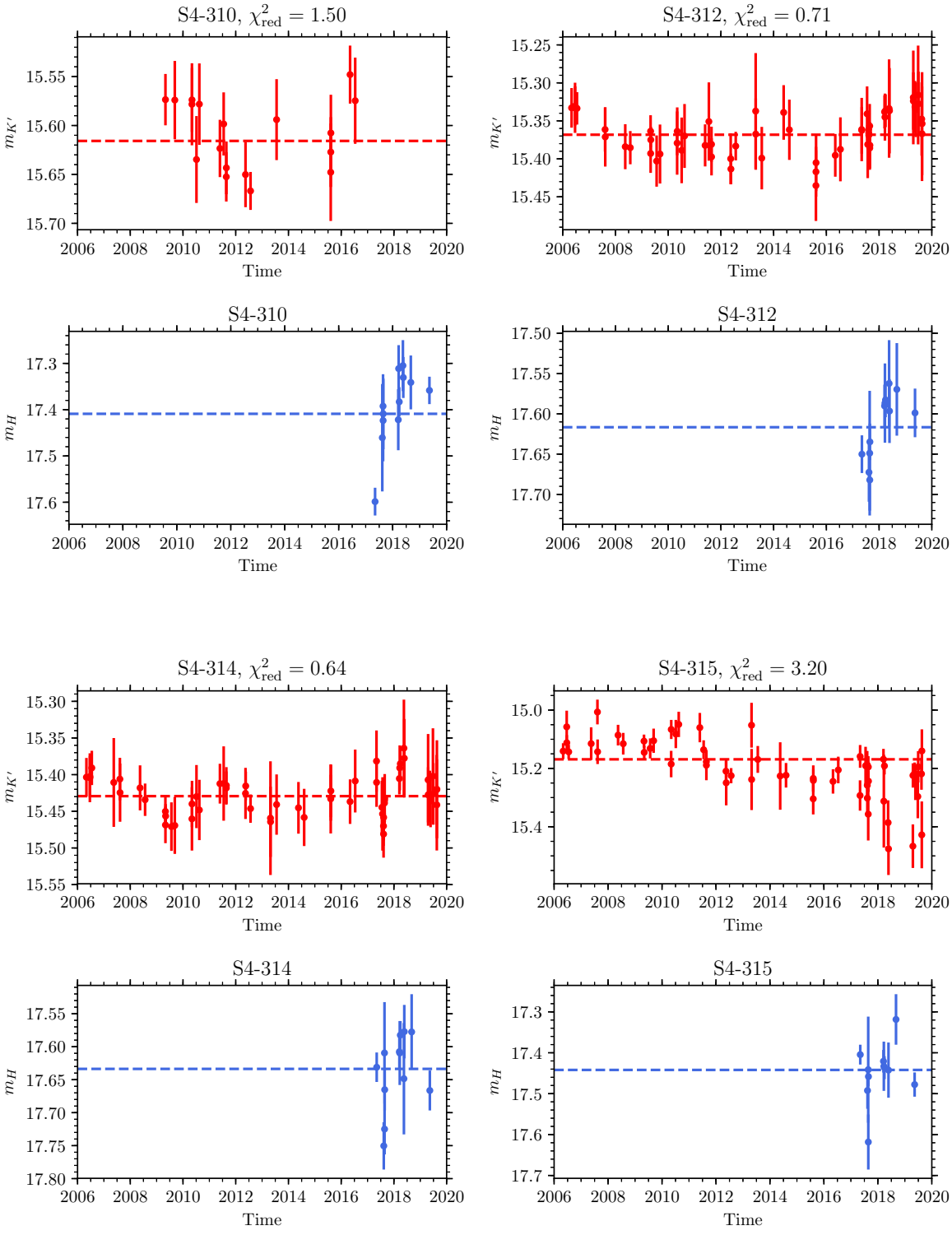
S4-310, $\chi^2_{\rm red} = 1.50$
S4-312, $\chi^2_{\rm red} = 0.71$
S4-310
S4-312
S4-314, $\chi^2_{\rm red} = 0.64$
S4-315, $\chi^2_{\rm red} = 3.20$
S4-314
S4-315
$m_{K'}$
m_H
Time

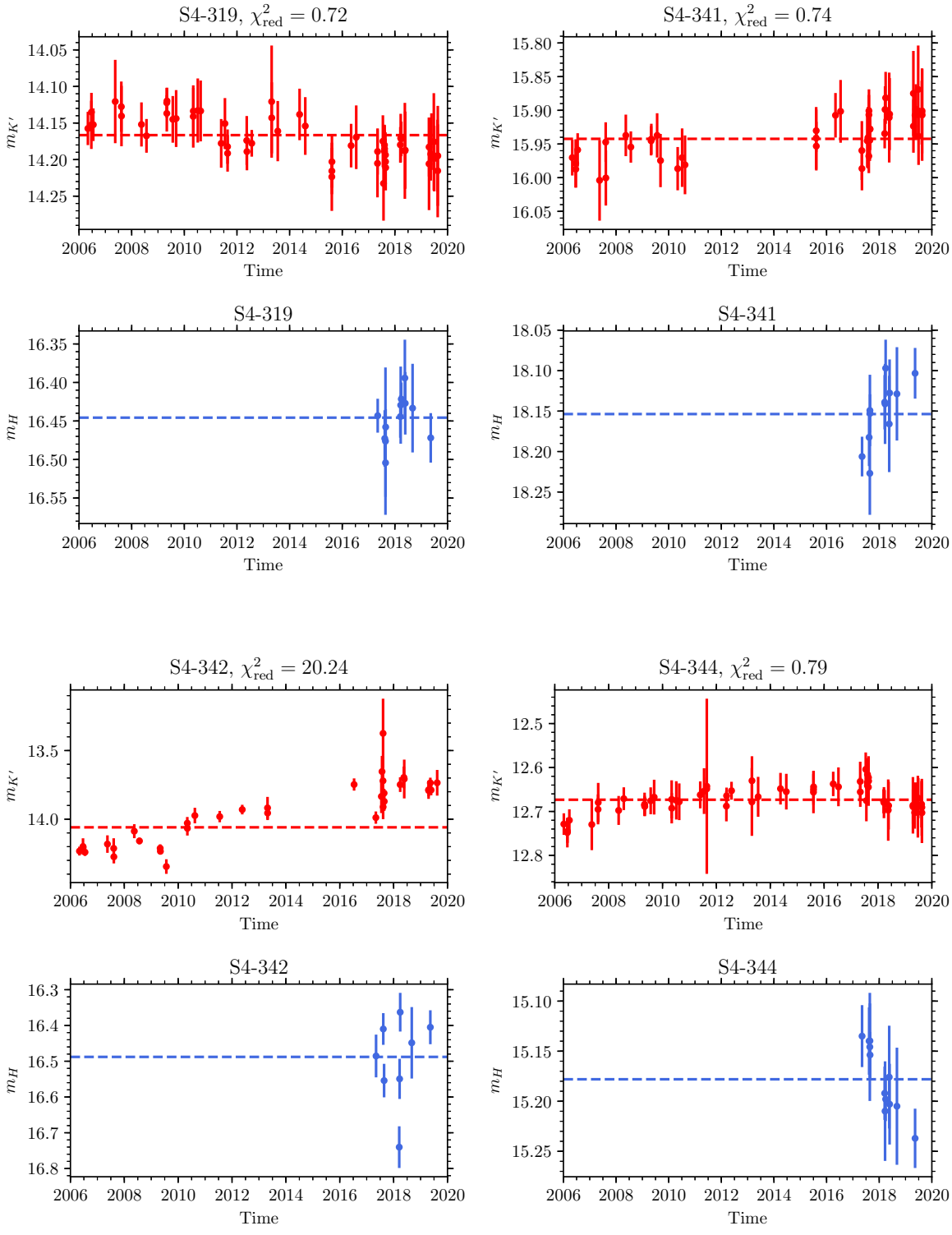
S4-319, $\chi^2_{\rm red} = 0.72$
S4-341, $\chi^2_{\rm red} = 0.74$
S4-319
S4-341
S4-342, $\chi^2_{\rm red} = 20.24$
S4-344, $\chi^2_{\rm red} = 0.79$
S4-342
S4-344
$m_{K'}$
m_H
Time

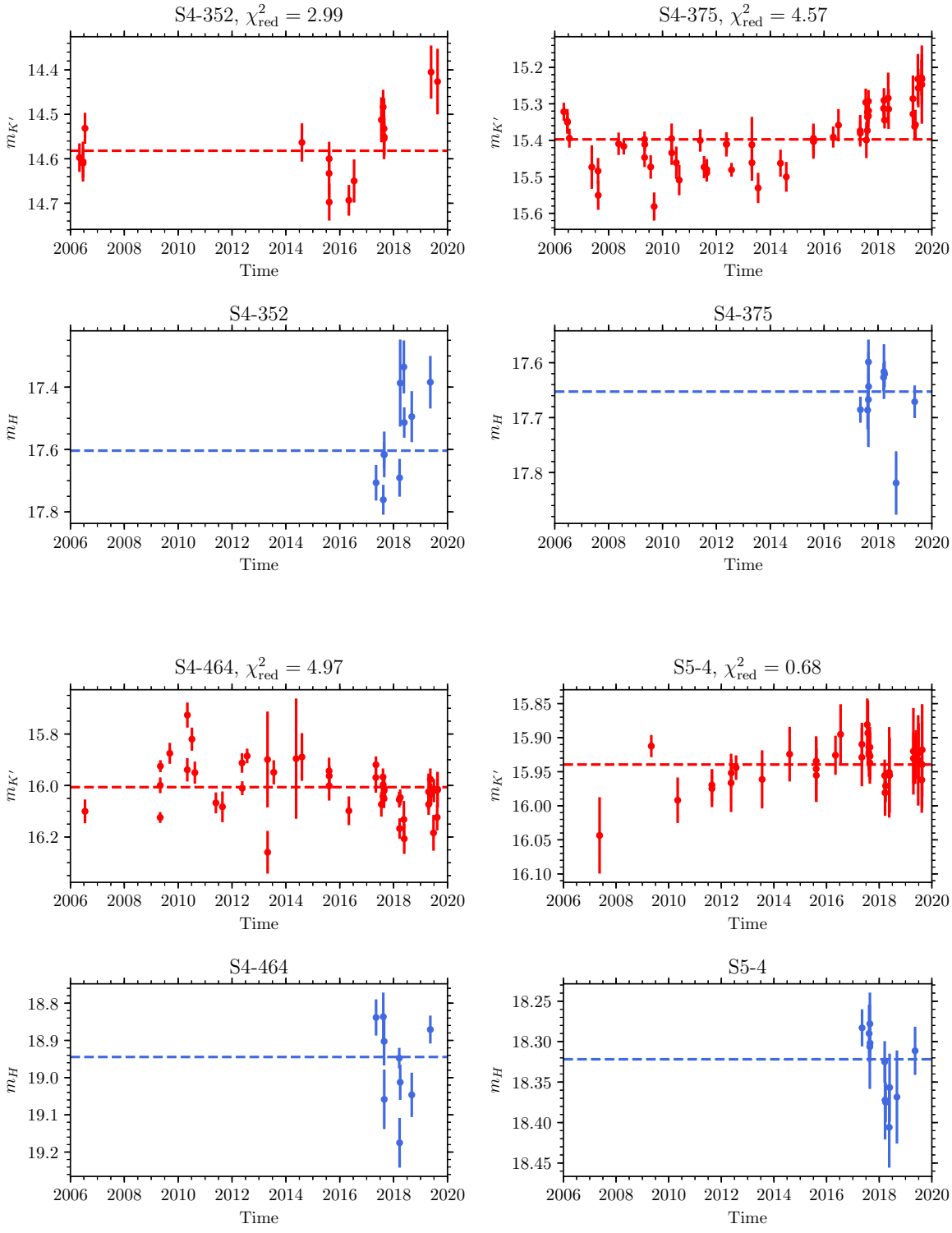
S4-352, $\chi^2_{\rm red} = 2.99$
S4-375, $\chi^2_{\rm red} = 4.57$
S4-352
S4-375
S4-464, $\chi^2_{\rm red} = 4.97$
S5-4, $\chi^2_{\rm red} = 0.68$
S4-464
S5-4
$m_{K'}$
m_H
Time

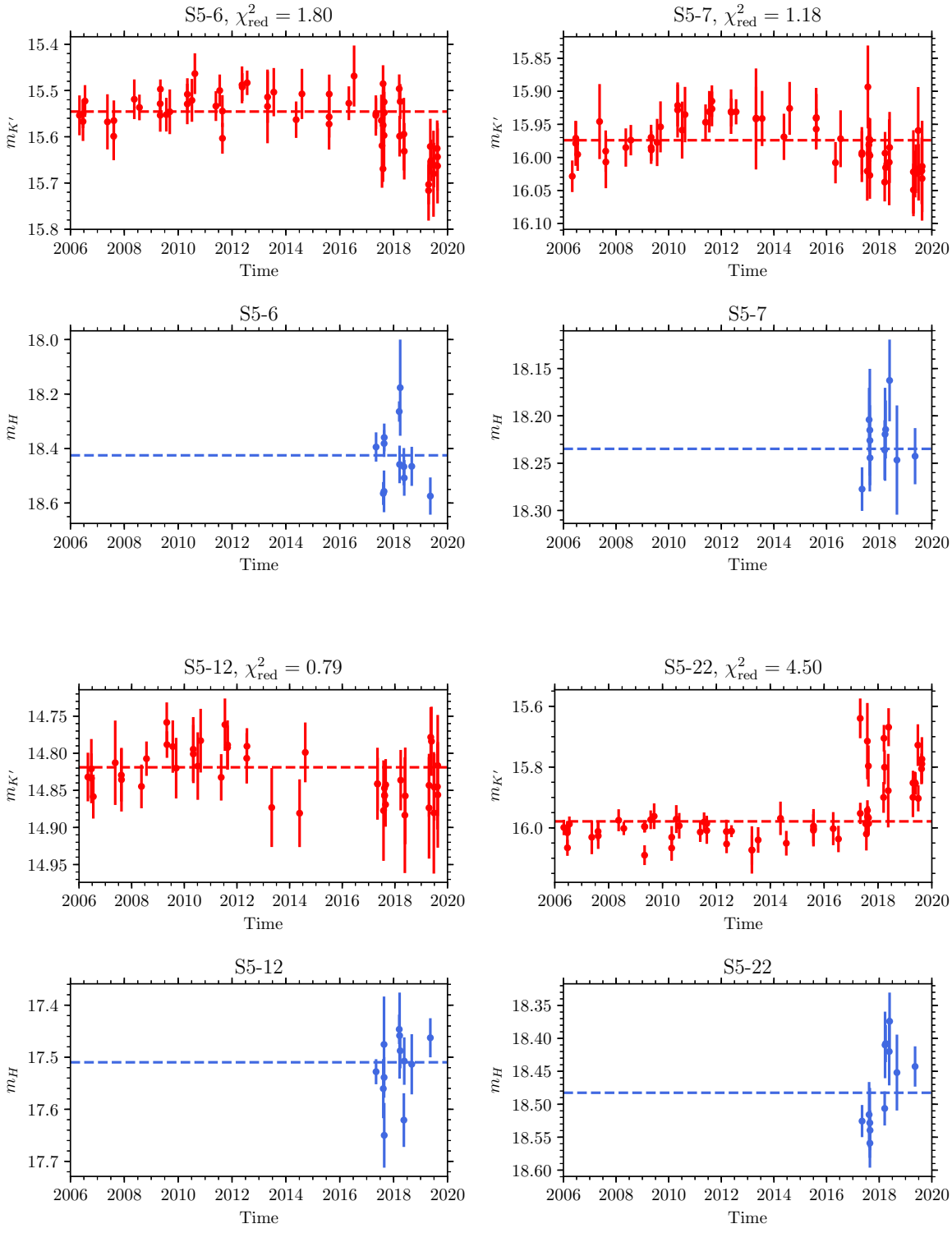
S5-6, $\chi^2_{\rm red} = 1.80$
S5-7, $\chi^2_{\rm red} = 1.18$
S5-6
S5-7
S5-12, $\chi^2_{\rm red} = 0.79$
S5-22, $\chi^2_{\rm red} = 4.50$
S5-12
S5-22
$m_{K'}$
m_H
Time

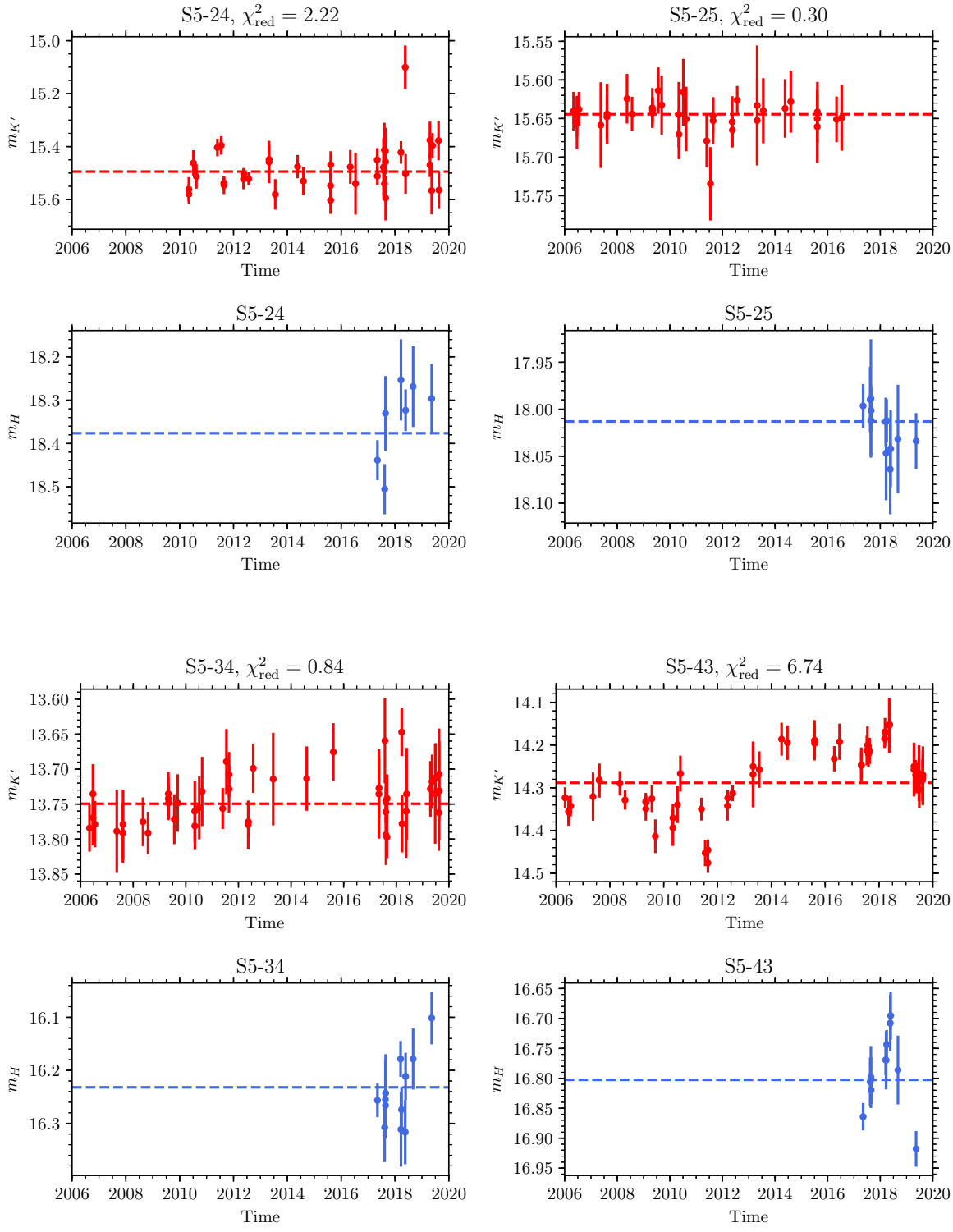
S5-24, $\chi^2_{\rm red} = 2.22$
S5-25, $\chi^2_{\rm red} = 0.30$
S5-24
S5-25
S5-34, $\chi^2_{\rm red} = 0.84$
S5-43, $\chi^2_{\rm red} = 6.74$
S5-34
S5-43
$m_{K'}$
m_H
Time

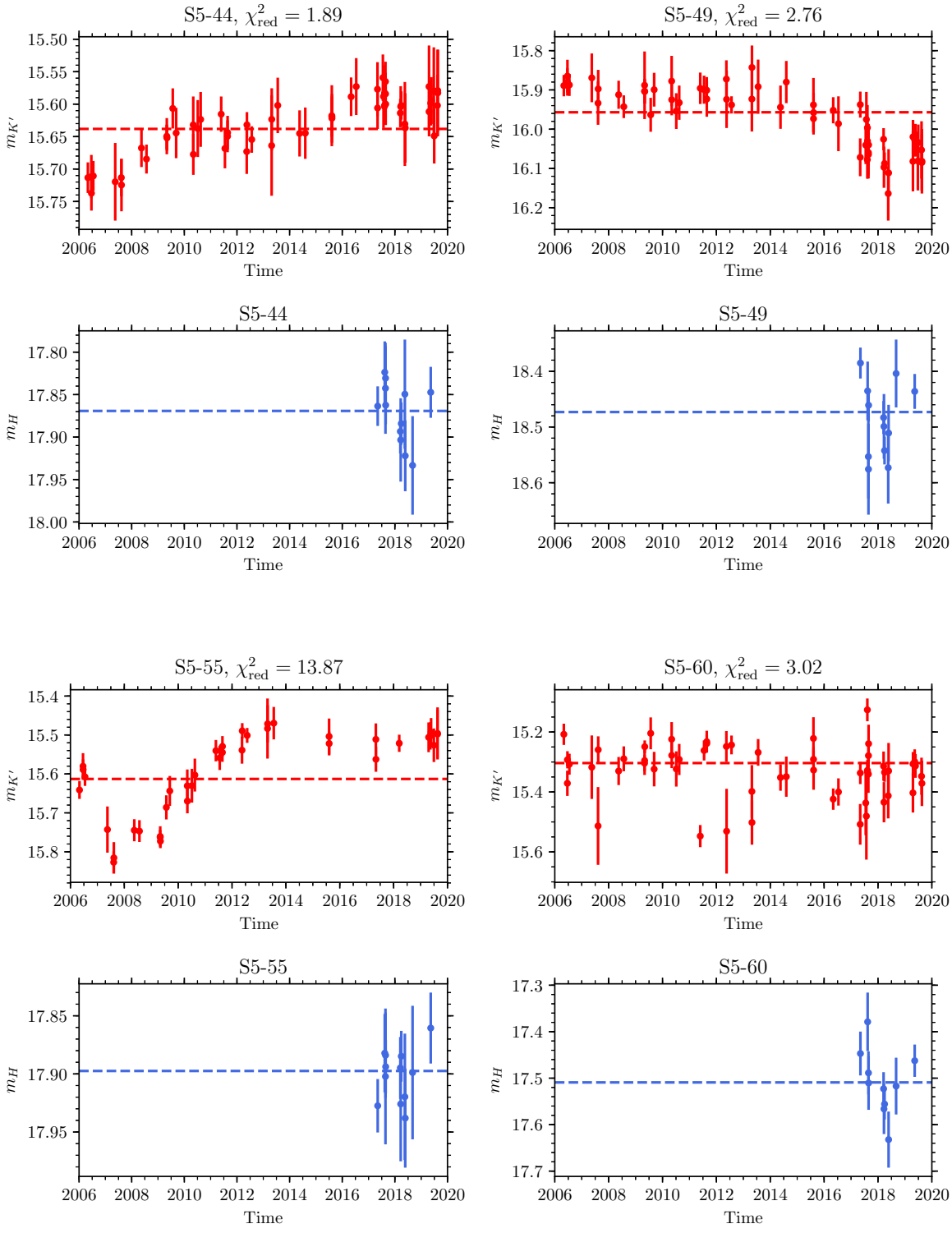
S5-44, $\chi^2_{\rm red} = 1.89$
S5-49, $\chi^2_{\rm red} = 2.76$
S5-44
S5-49
S5-55, $\chi^2_{\rm red} = 13.87$
S5-60, $\chi^2_{\rm red} = 3.02$
S5-55
S5-60
$m_{K'}$
m_H
Time

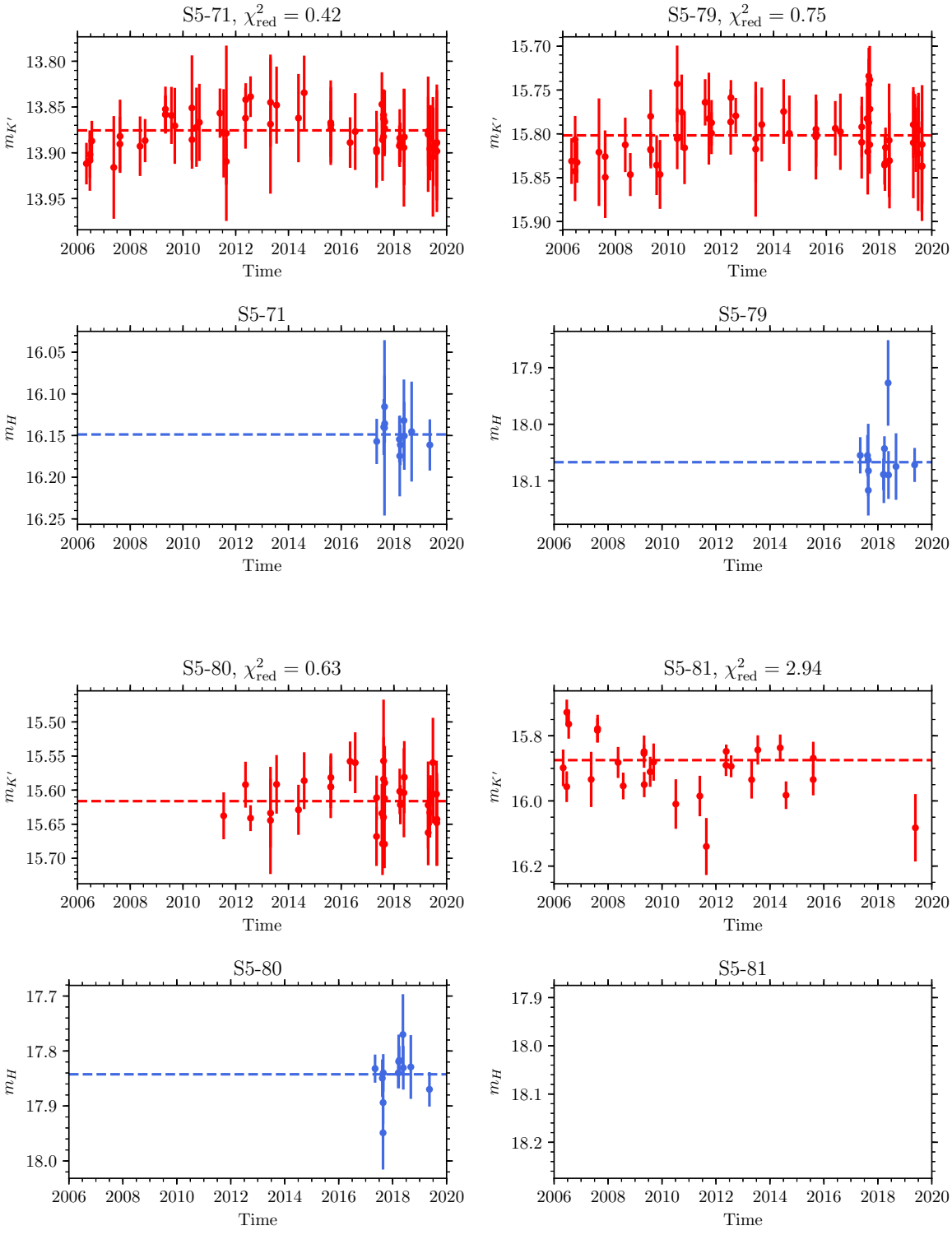
S5-71, $\chi^2_{\rm red} = 0.42$
S5-79, $\chi^2_{\rm red} = 0.75$
S5-71
S5-79
S5-80, $\chi^2_{\rm red} = 0.63$
S5-81, $\chi^2_{\rm red} = 2.94$
S5-80
S5-81
$m_{K'}$
m_H
Time

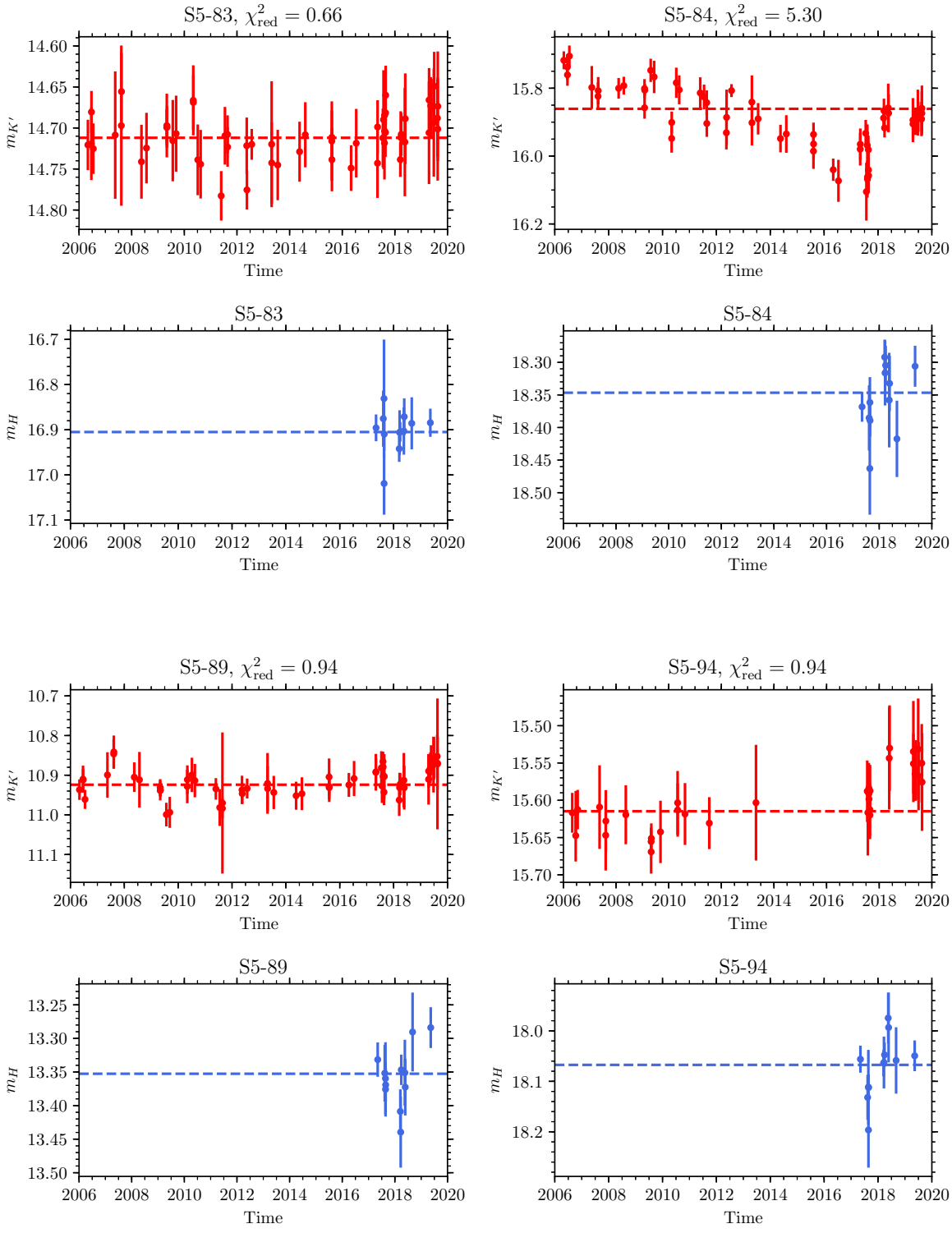
S5-83, $\chi^2_{\rm red} = 0.66$
S5-84, $\chi^2_{\rm red} = 5.30$
S5-83
S5-84
S5-89, $\chi^2_{\rm red} = 0.94$
S5-94, $\chi^2_{\rm red} = 0.94$
S5-89
S5-94
$m_{K'}$
m_H
Time

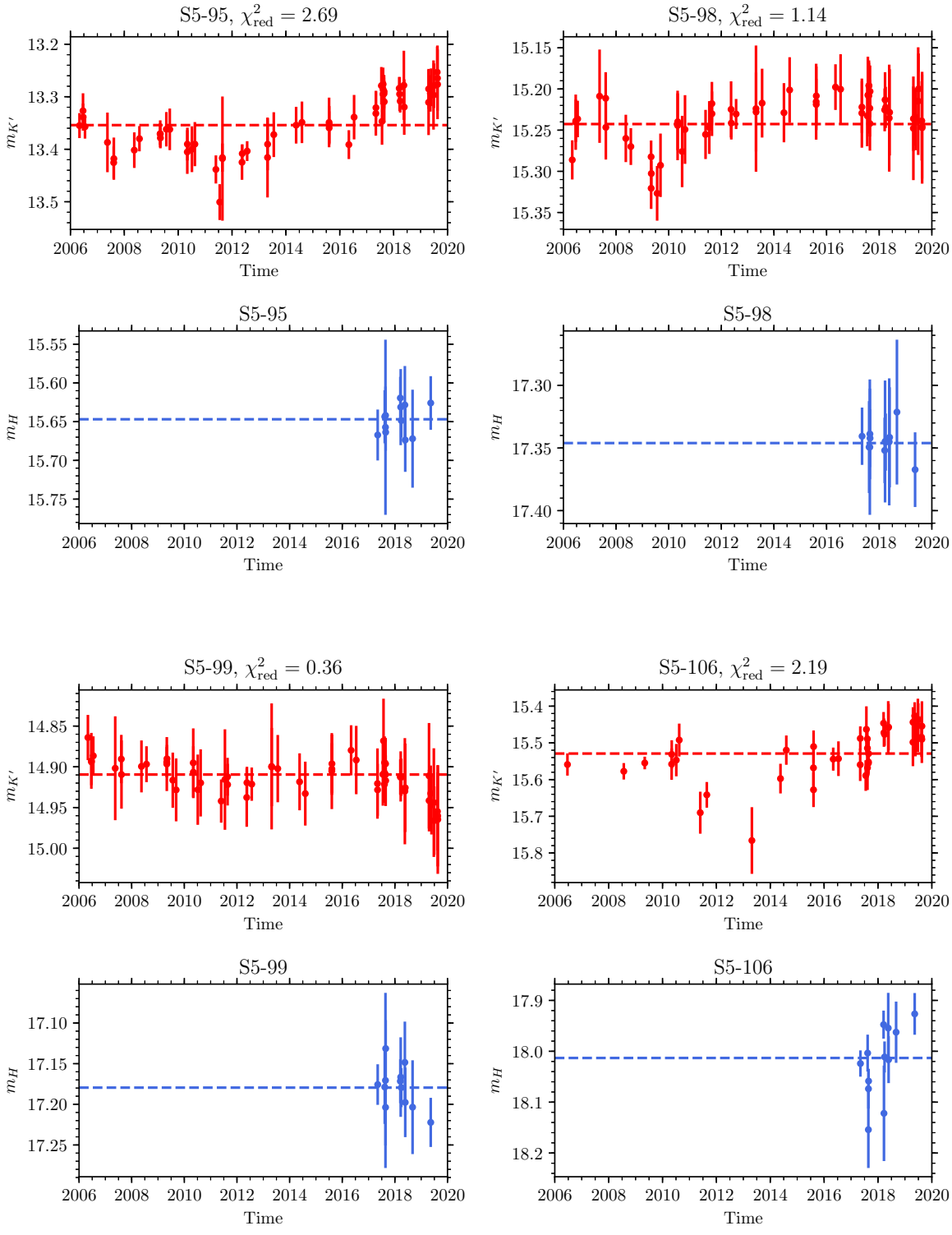
S5-95, $\chi^2_{\rm red} = 2.69$
S5-98, $\chi^2_{\rm red} = 1.14$
S5-95
S5-98
S5-99, $\chi^2_{\rm red} = 0.36$
S5-106, $\chi^2_{\rm red} = 2.19$
S5-99
S5-106
$m_{K'}$
m_H
Time

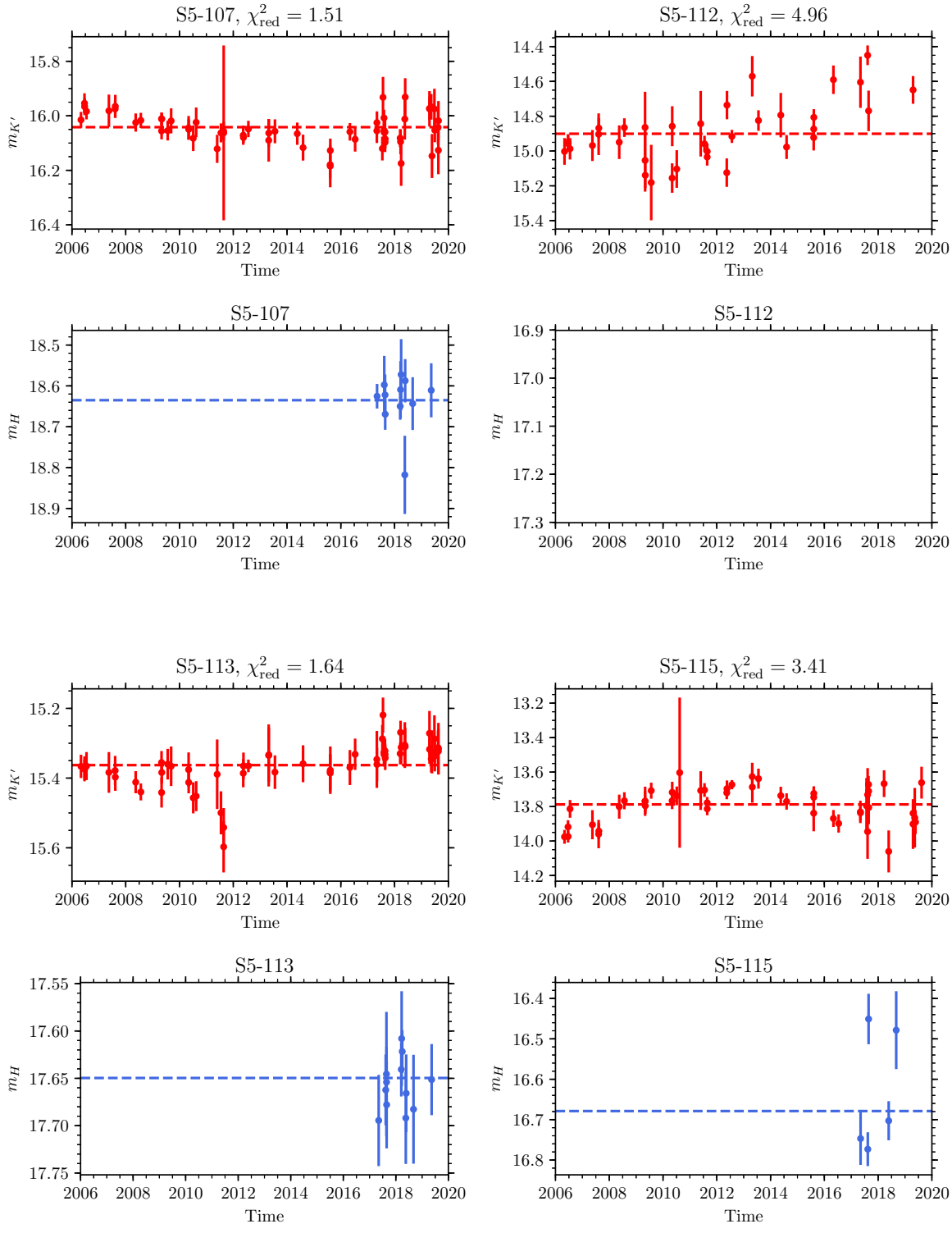
S5-107, $\chi^2_{\rm red} = 1.51$
S5-112, $\chi^2_{\rm red} = 4.96$
S5-107
S5-112
S5-113, $\chi^2_{\rm red} = 1.64$
S5-115, $\chi^2_{\rm red} = 3.41$
S5-113
S5-115
$m_{K'}$
m_H
Time

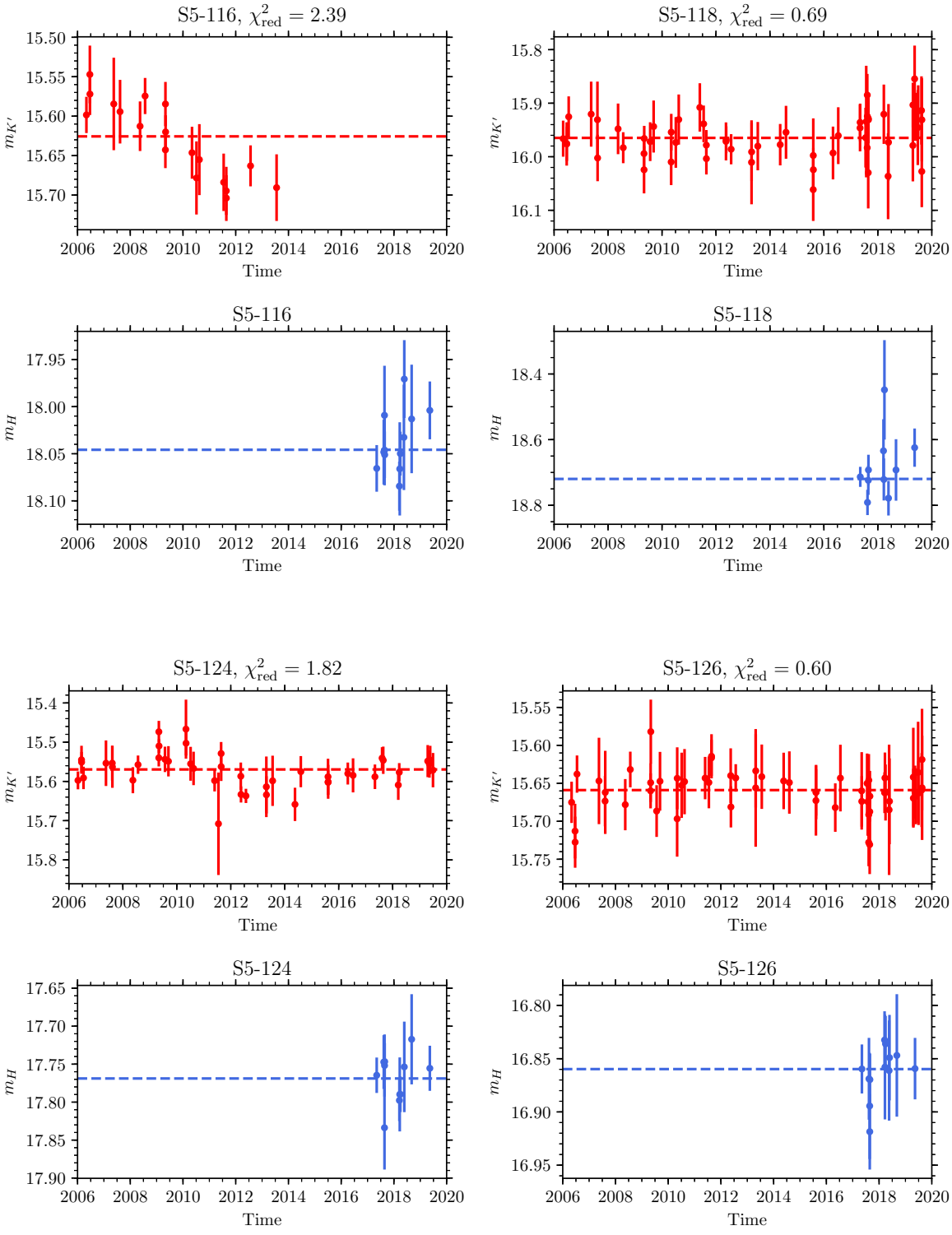
S5-116, $\chi^2_{\rm red} = 2.39$
S5-118, $\chi^2_{\rm red} = 0.69$
S5-116
S5-118
S5-124, $\chi^2_{\rm red} = 1.82$
S5-126, $\chi^2_{\rm red} = 0.60$
S5-124
S5-126
$m_{K'}$
m_H
Time

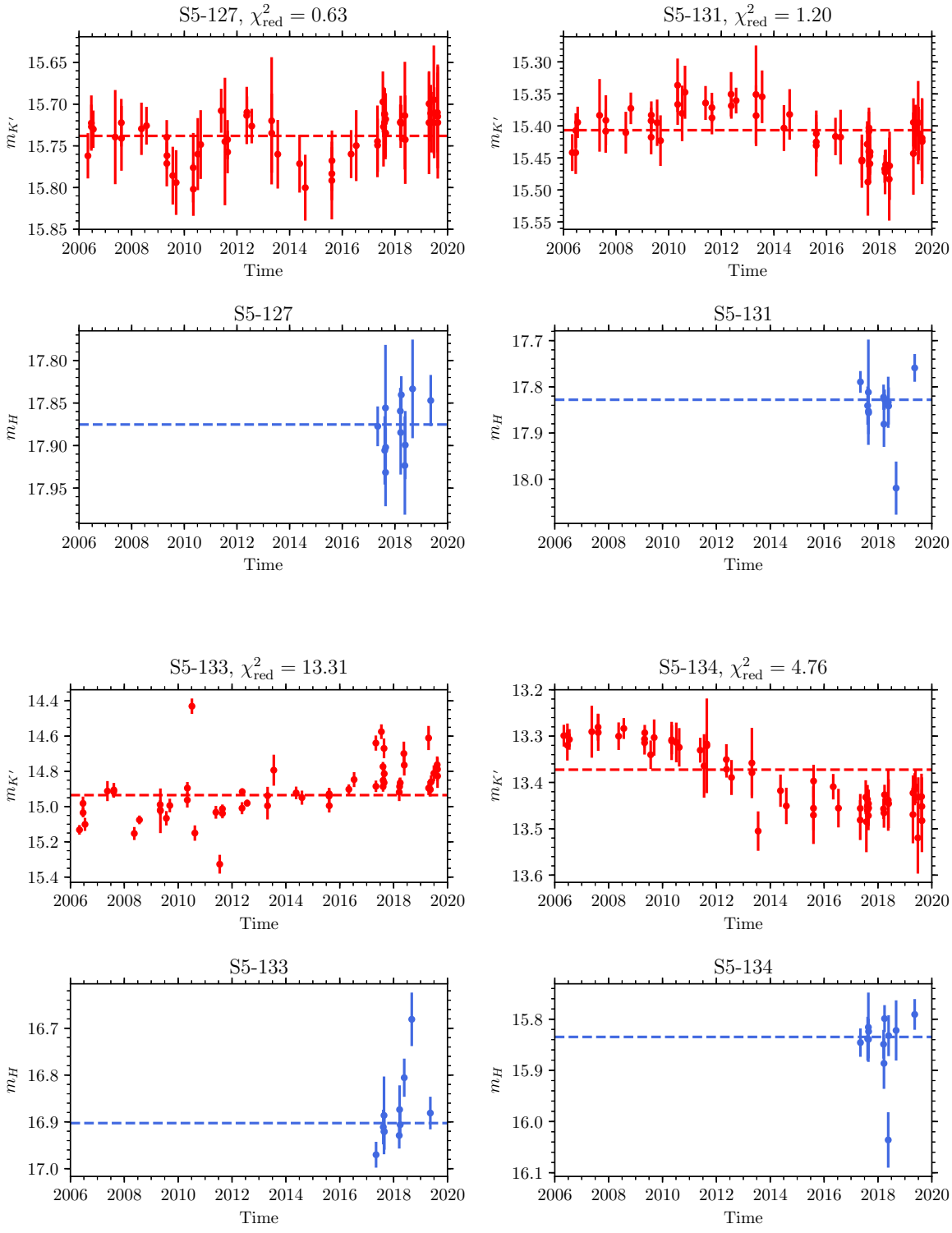
S5-127, $\chi^2_{\rm red} = 0.63$
S5-131, $\chi^2_{\rm red} = 1.20$
S5-127
S5-131
S5-133, $\chi^2_{\rm red} = 13.31$
S5-134, $\chi^2_{\rm red} = 4.76$
S5-133
S5-134
$m_{K'}$
m_H
Time

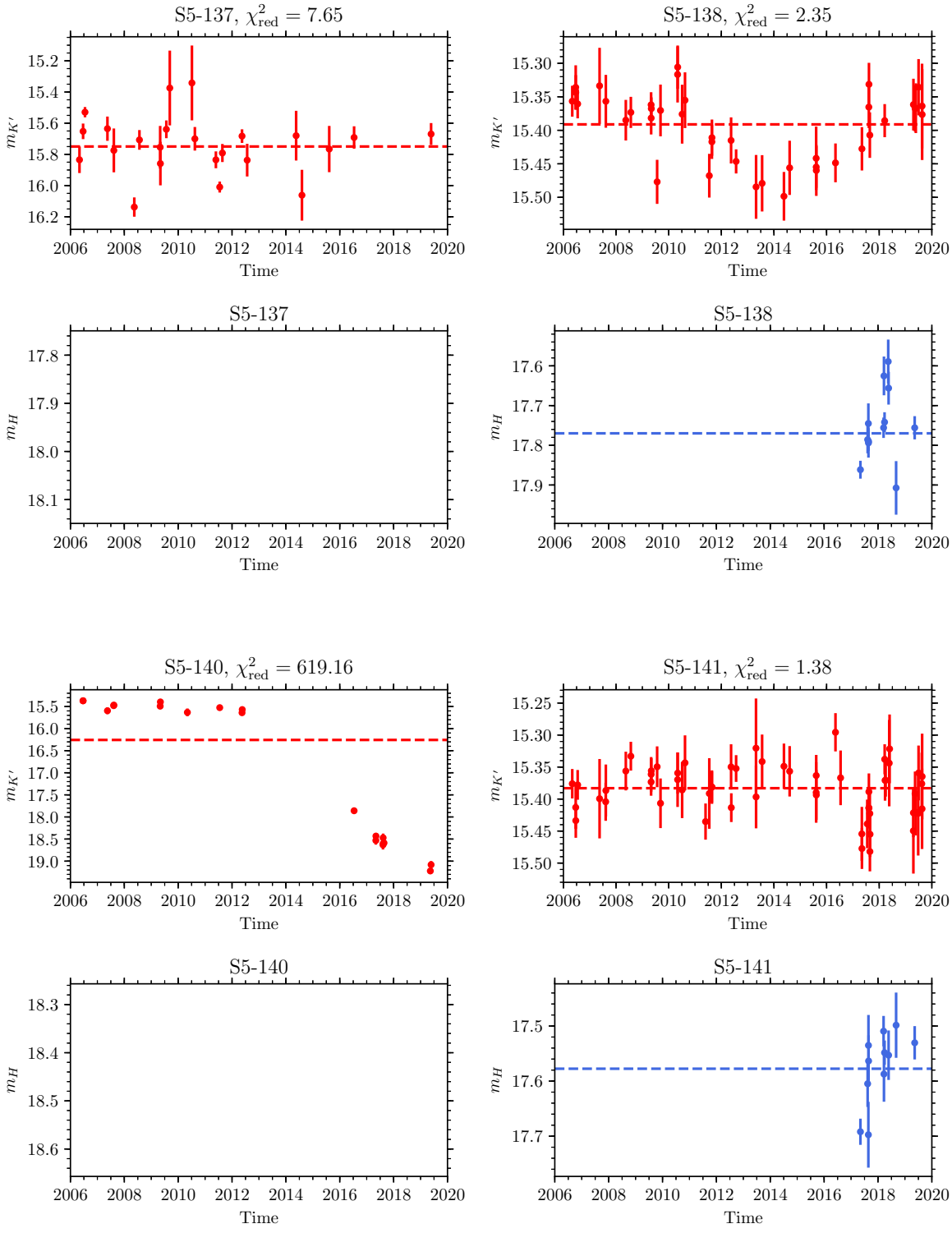
S5-137, $\chi^2_{\rm red} = 7.65$
S5-138, $\chi^2_{\rm red} = 2.35$
S5-137
S5-138
S5-140, $\chi^2_{\rm red} = 619.16$
S5-141, $\chi^2_{\rm red} = 1.38$
S5-140
S5-141
$m_{K'}$
m_H
Time

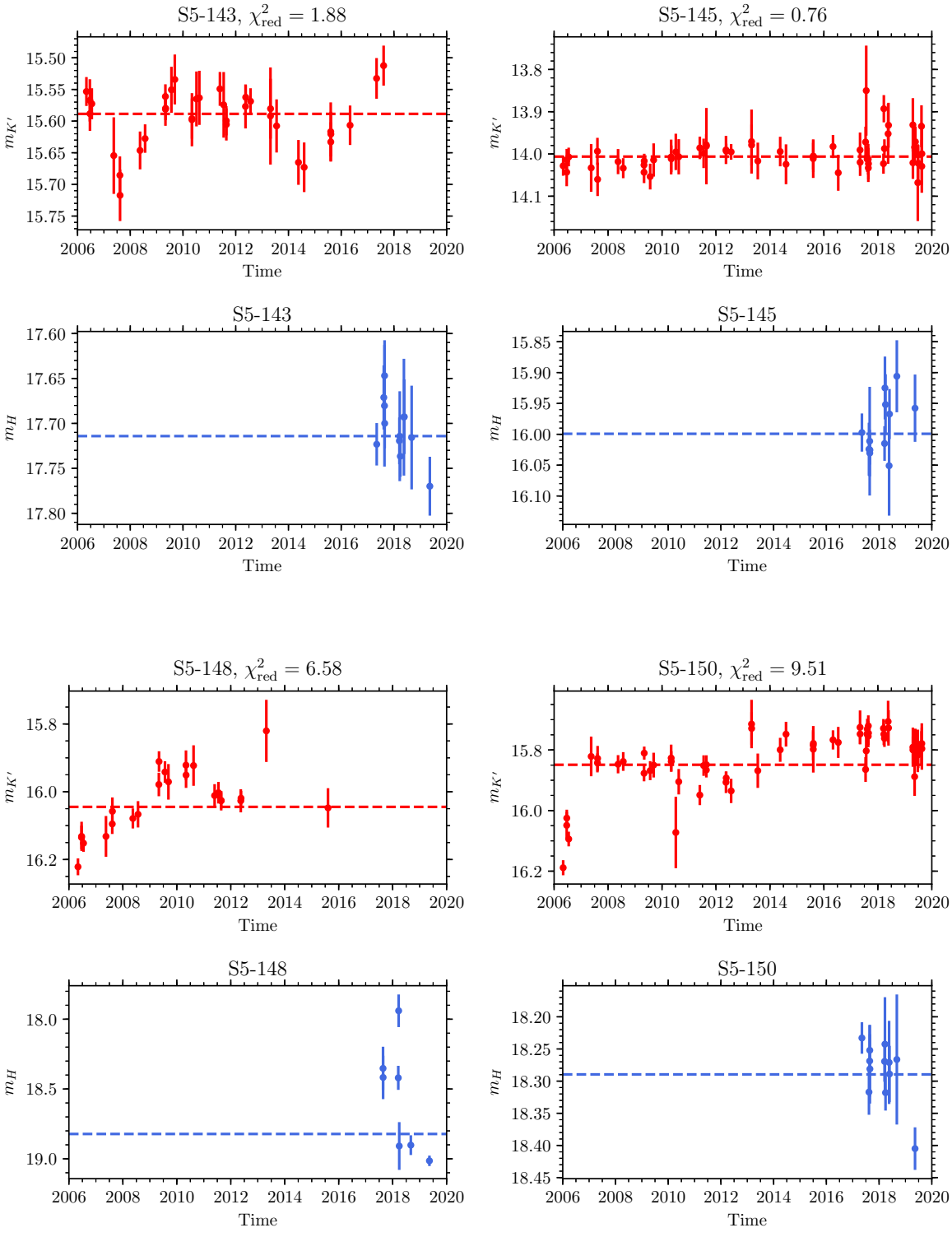
S5-143, $\chi^2_{\rm red} = 1.88$
S5-145, $\chi^2_{\rm red} = 0.76$
S5-143
S5-145
S5-148, $\chi^2_{\rm red} = 6.58$
S5-150, $\chi^2_{\rm red} = 9.51$
S5-148
S5-150
$m_{K'}$
m_H
Time

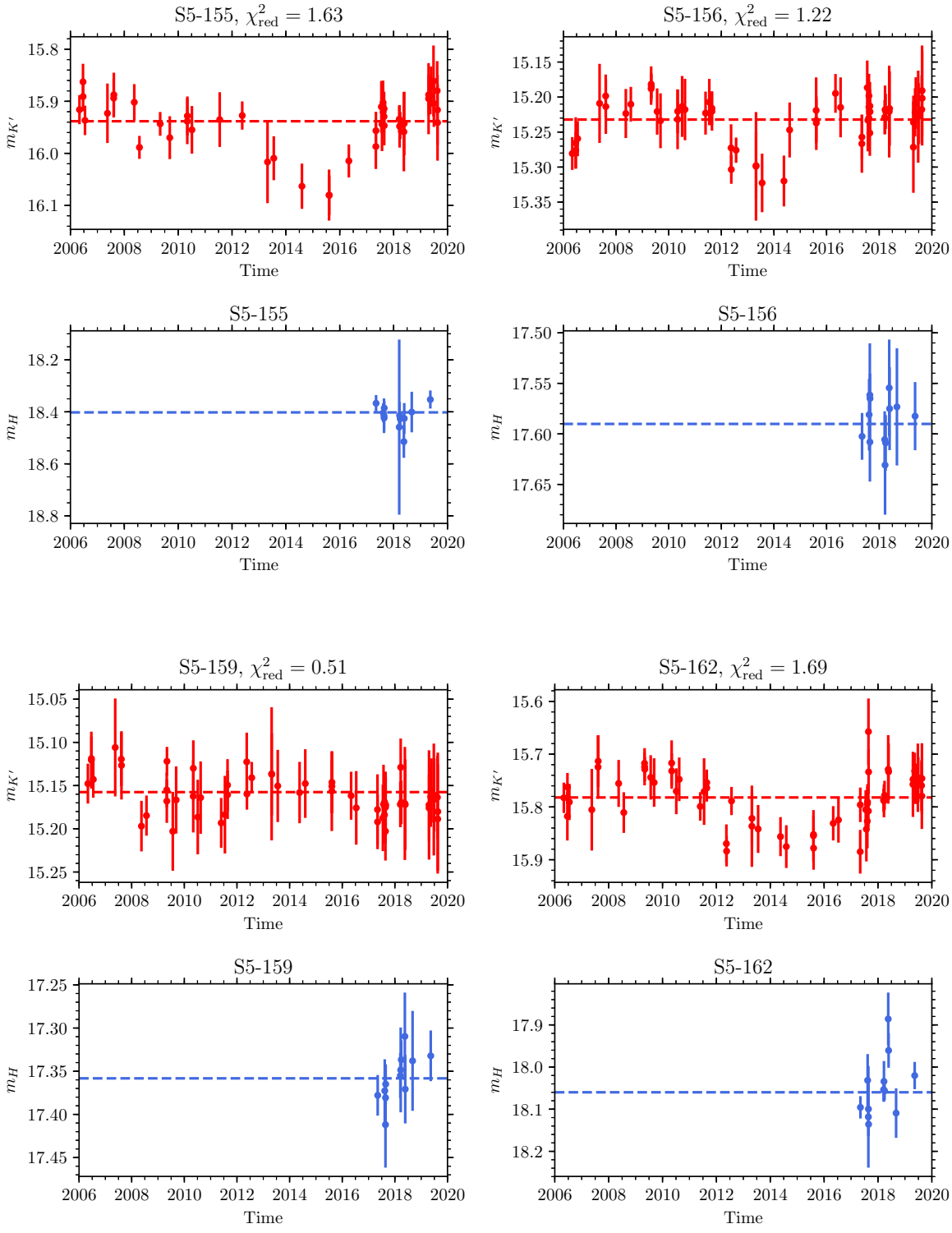
S5-155, $\chi^2_{\rm red} = 1.63$
S5-156, $\chi^2_{\rm red} = 1.22$
S5-155
S5-156
S5-159, $\chi^2_{\rm red} = 0.51$
S5-162, $\chi^2_{\rm red} = 1.69$
S5-159
S5-162
$m_{K'}$
m_H
Time

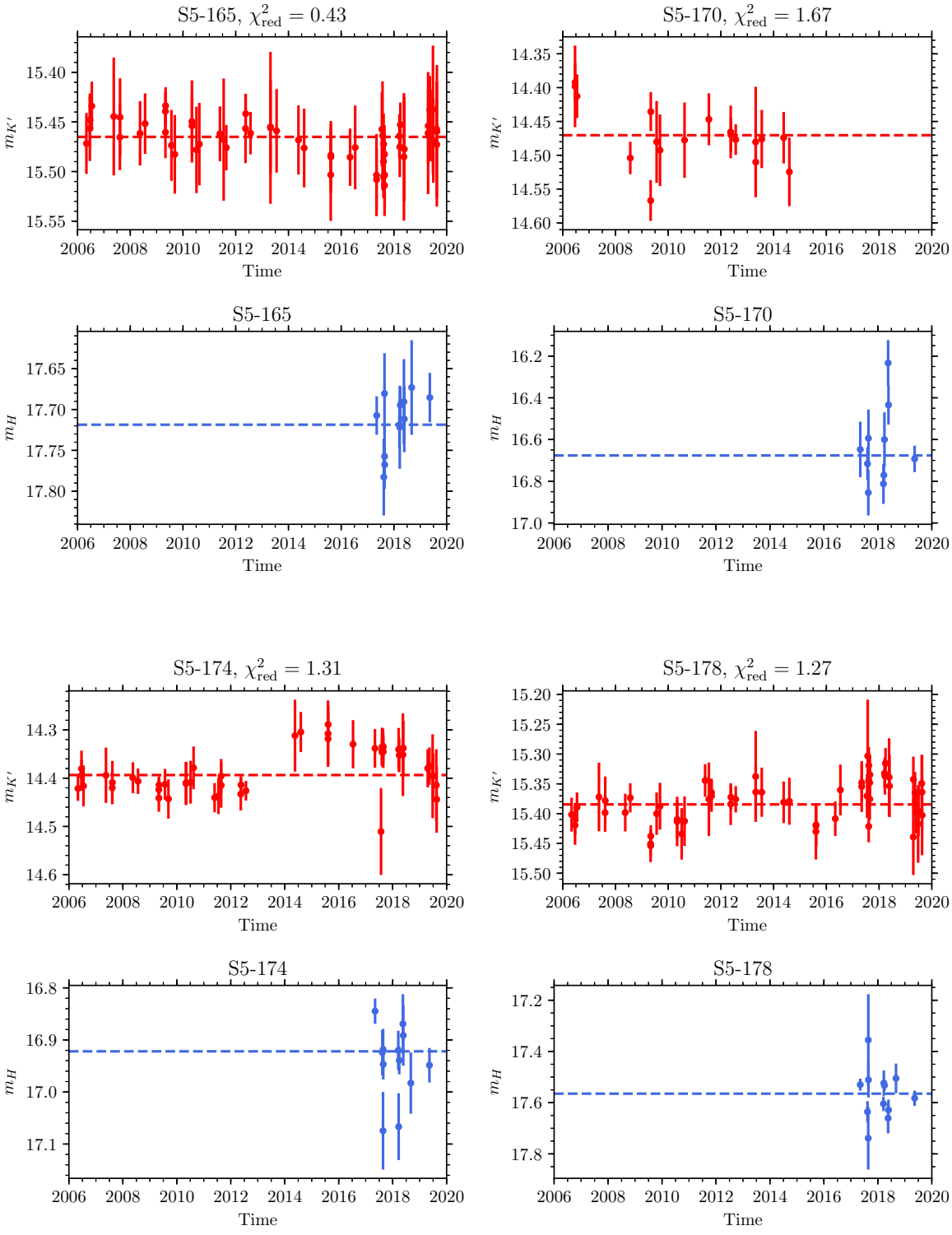
S5-165, $\chi^2_{\rm red} = 0.43$
S5-170, $\chi^2_{\rm red} = 1.67$
S5-165
S5-170
S5-174, $\chi^2_{\rm red} = 1.31$
S5-178, $\chi^2_{\rm red} = 1.27$
S5-174
S5-178
$m_{K'}$
m_H
Time

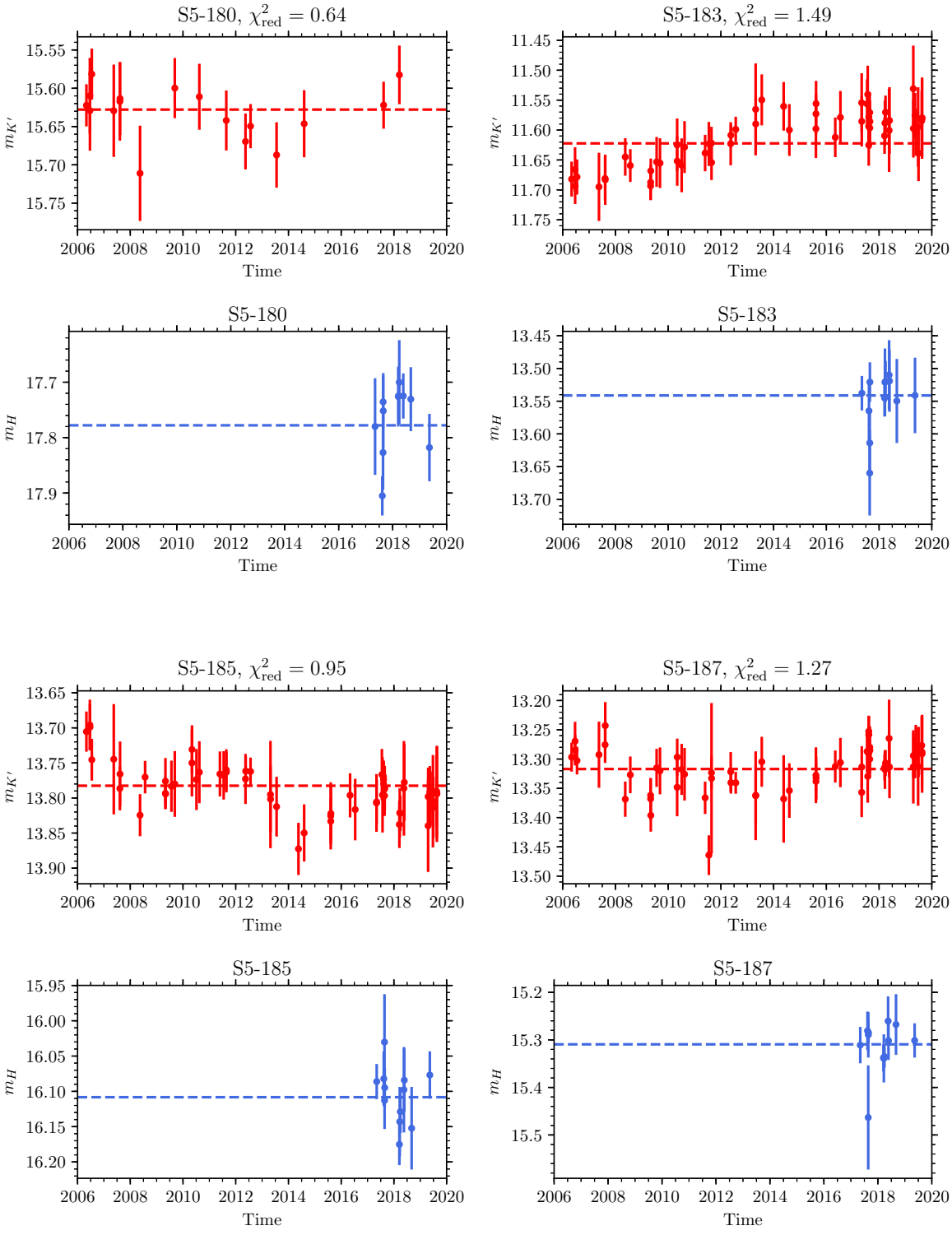
S5-180, $\chi^2_{\rm red} = 0.64$
S5-183, $\chi^2_{\rm red} = 1.49$
S5-180
S5-183
S5-185, $\chi^2_{\rm red} = 0.95$
S5-187, $\chi^2_{\rm red} = 1.27$
S5-185
S5-187
$m_{K'}$
m_H
Time

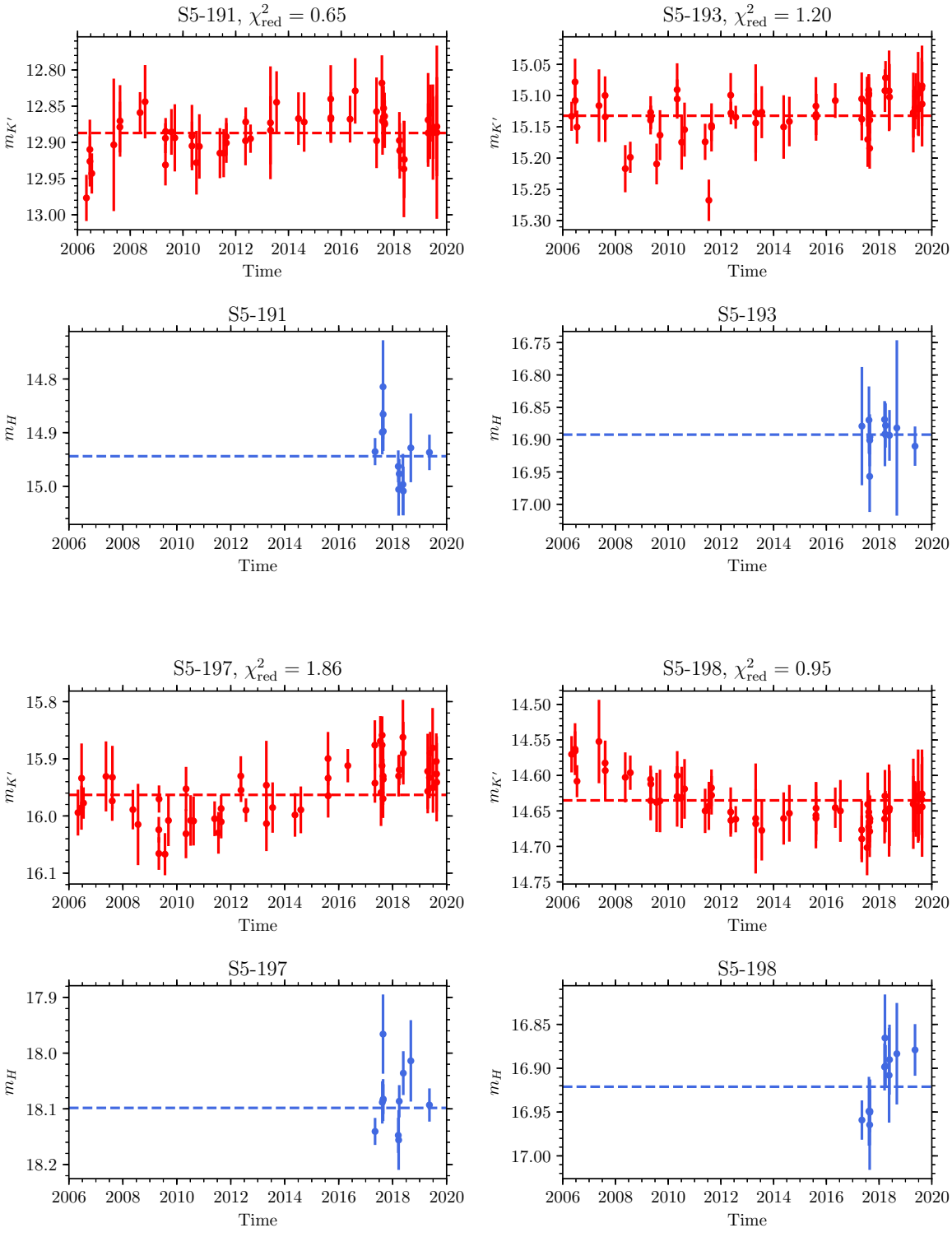
S5-191, $\chi^2_{\rm red} = 0.65$
S5-193, $\chi^2_{\rm red} = 1.20$
S5-191
S5-193
S5-197, $\chi^2_{\rm red} = 1.86$
S5-198, $\chi^2_{\rm red} = 0.95$
S5-197
S5-198
$m_{K'}$
m_H
Time

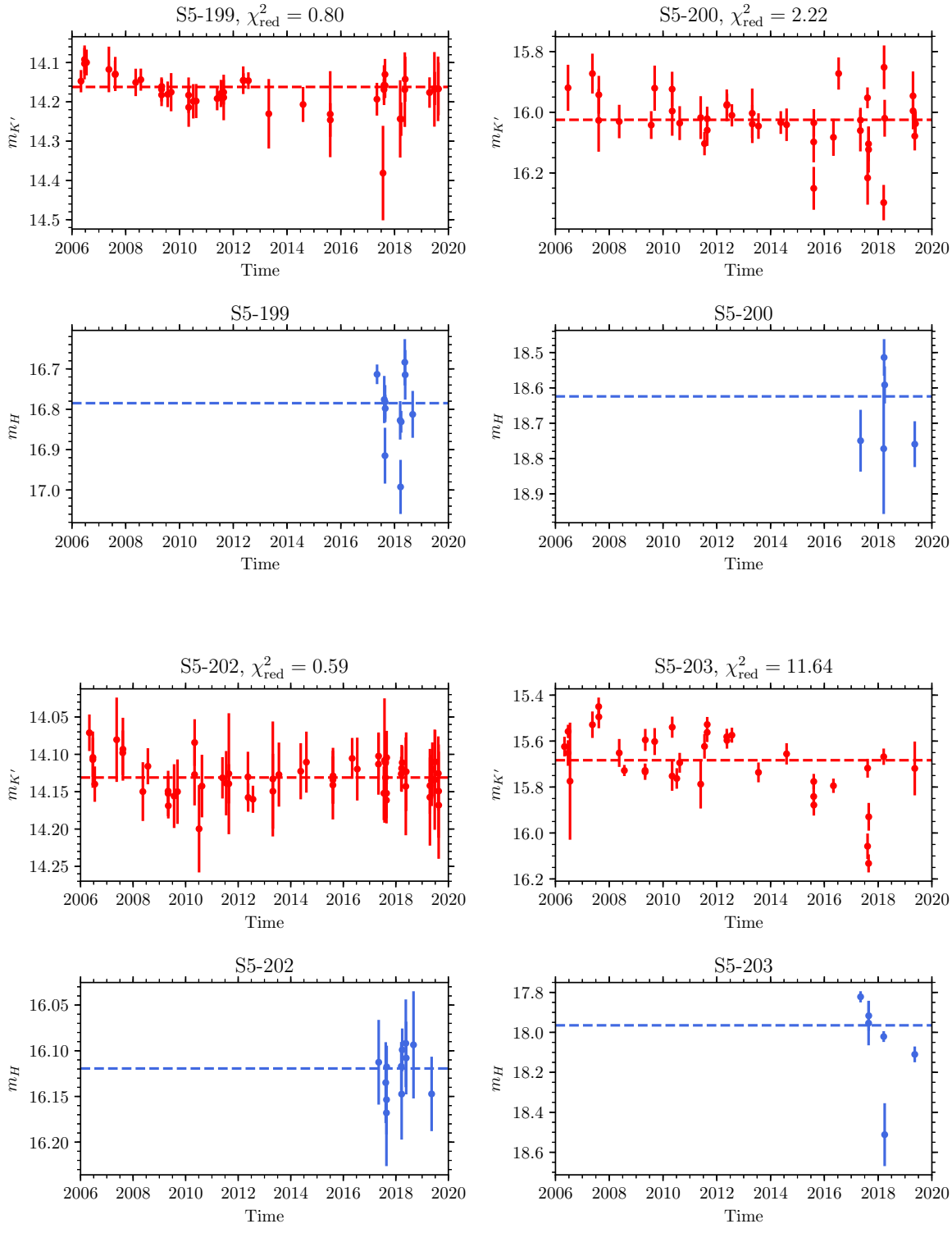
S5-199, $\chi^2_{\rm red} = 0.80$
S5-200, $\chi^2_{\rm red} = 2.22$
S5-199
S5-200
S5-202, $\chi^2_{\rm red} = 0.59$
S5-203, $\chi^2_{\rm red} = 11.64$
S5-202
S5-203
$m_{K'}$
m_H
Time

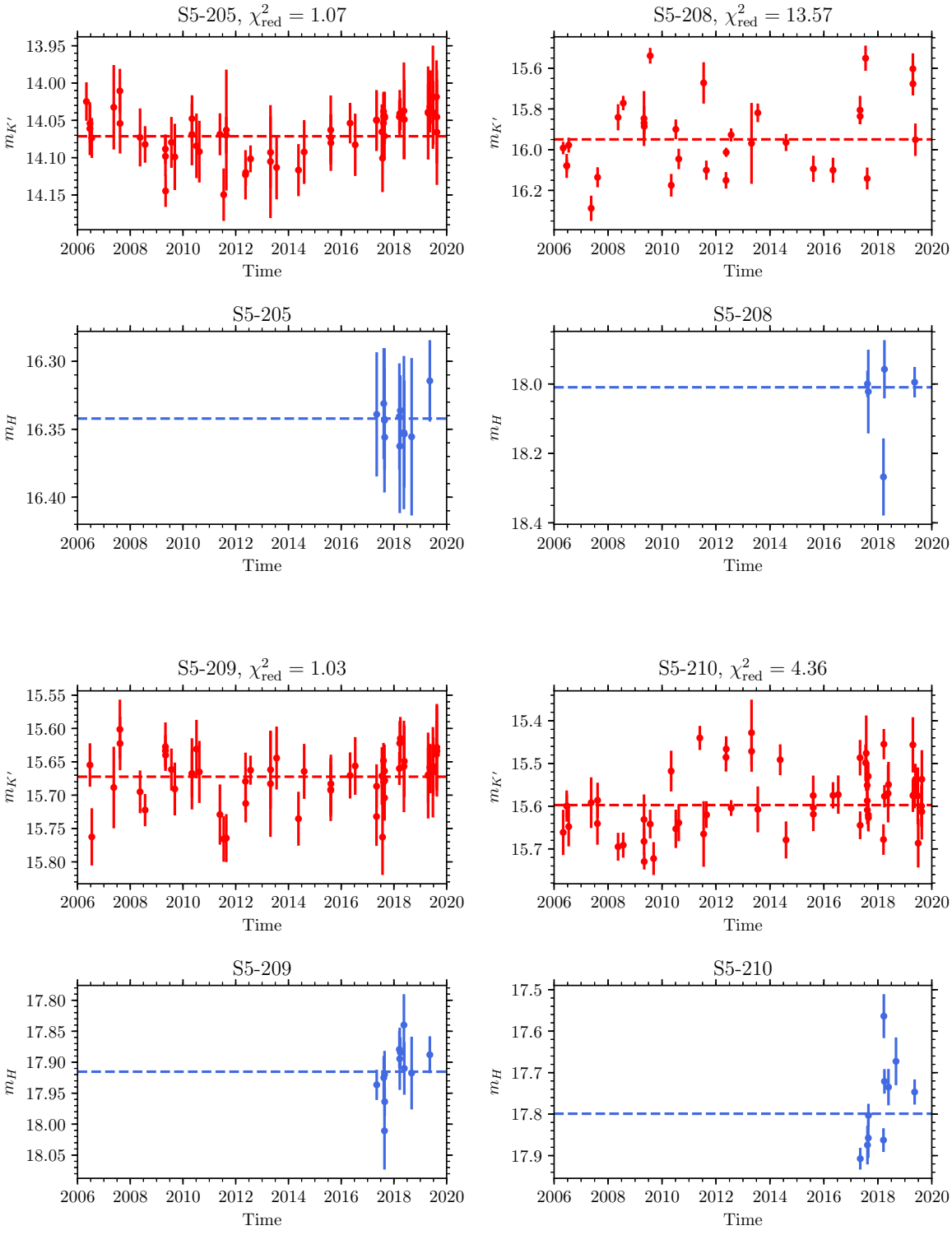
S5-205, $\chi^2_{\rm red} = 1.07$
S5-208, $\chi^2_{\rm red} = 13.57$
S5-205
S5-208
S5-209, $\chi^2_{\rm red} = 1.03$
S5-210, $\chi^2_{\rm red} = 4.36$
S5-209
S5-210
$m_{K'}$
m_H
Time

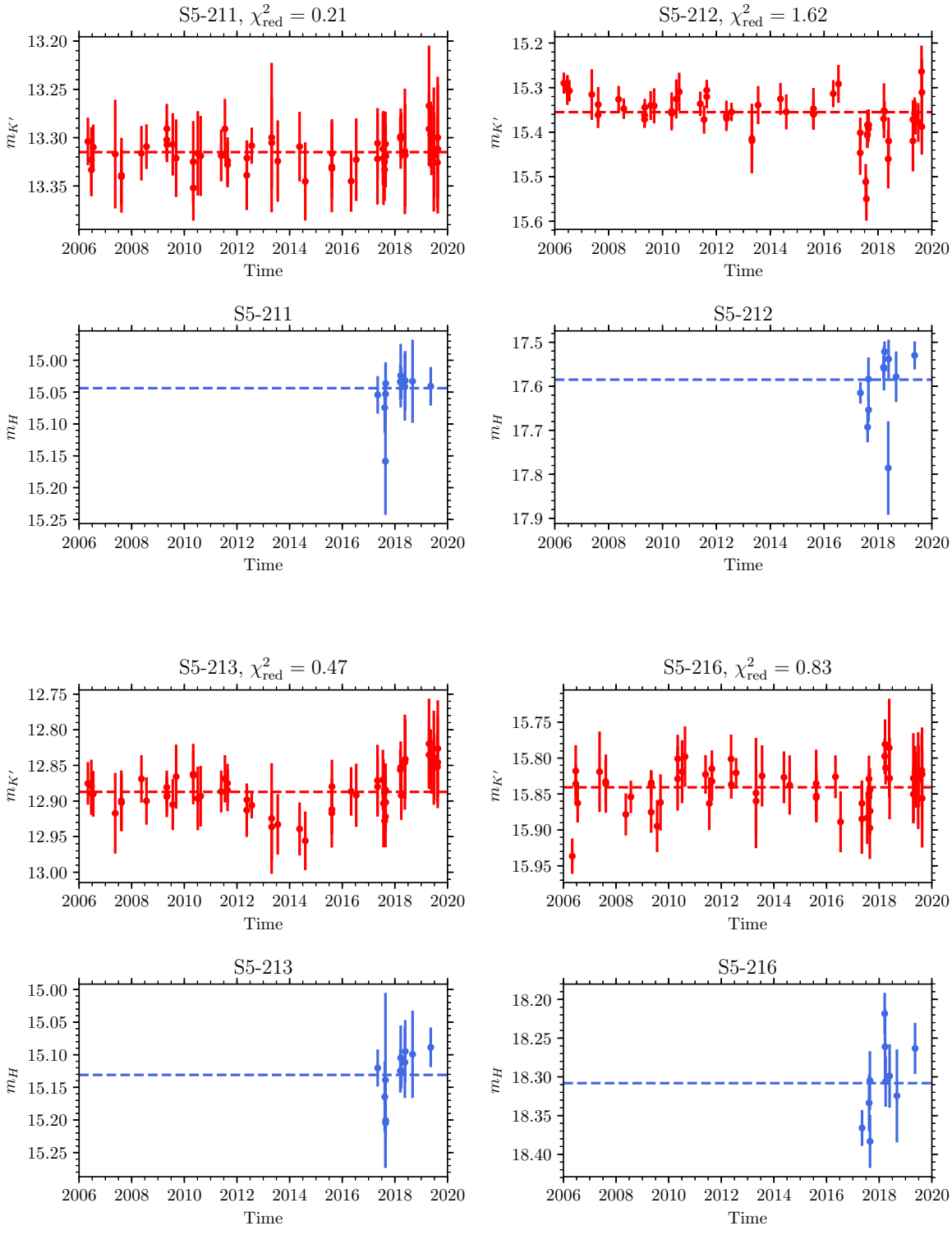
S5-211, $\chi^2_{\rm red} = 0.21$
S5-212, $\chi^2_{\rm red} = 1.62$
S5-211
S5-212
S5-213, $\chi^2_{\rm red} = 0.47$
S5-216, $\chi^2_{\rm red} = 0.83$
S5-213
S5-216
$m_{K'}$
m_H
Time

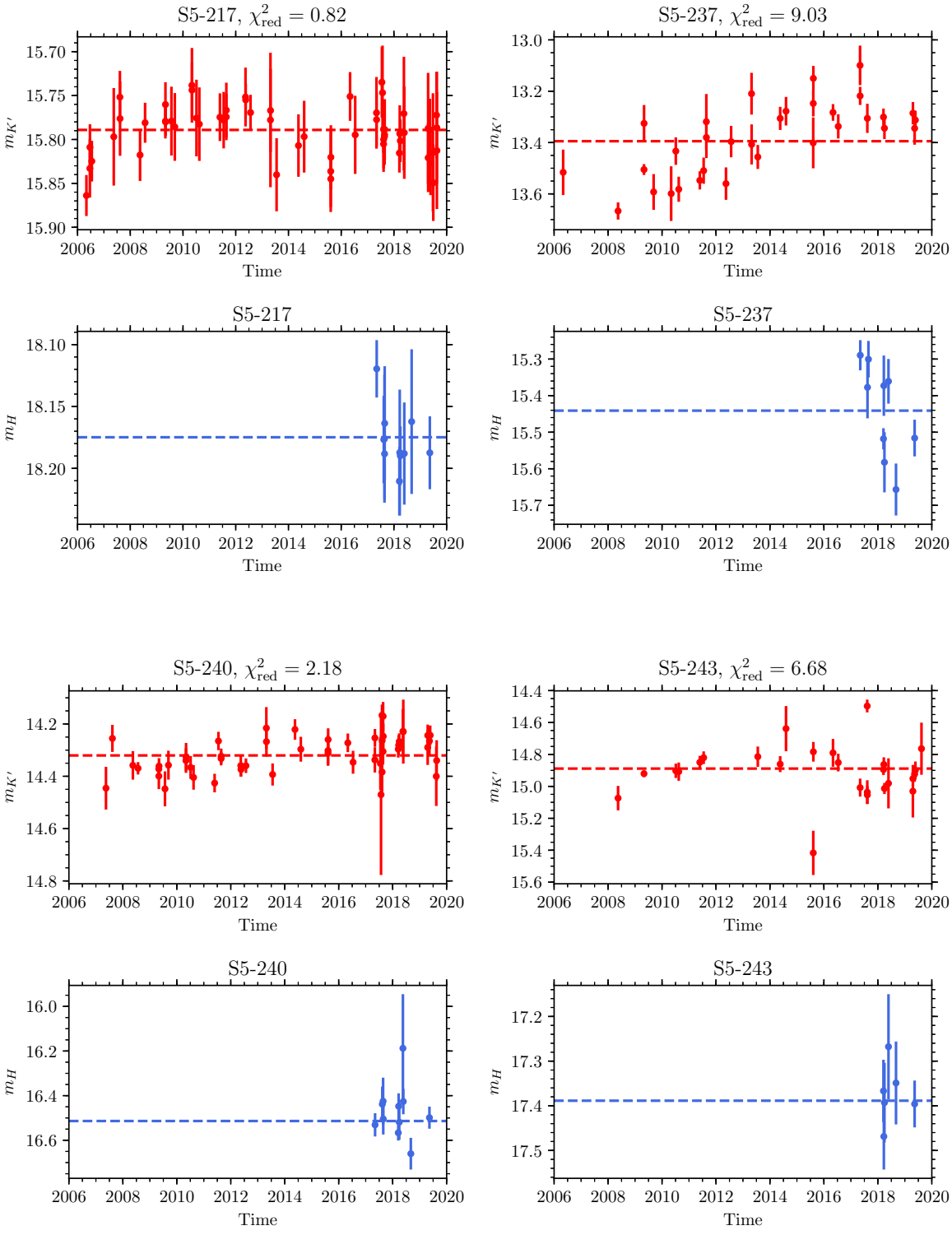
S5-217, $\chi^2_{\rm red} = 0.82$
S5-237, $\chi^2_{\rm red} = 9.03$
S5-217
S5-237
S5-240, $\chi^2_{\rm red} = 2.18$
S5-243, $\chi^2_{\rm red} = 6.68$
S5-240
S5-243
$m_{K'}$
m_H
Time

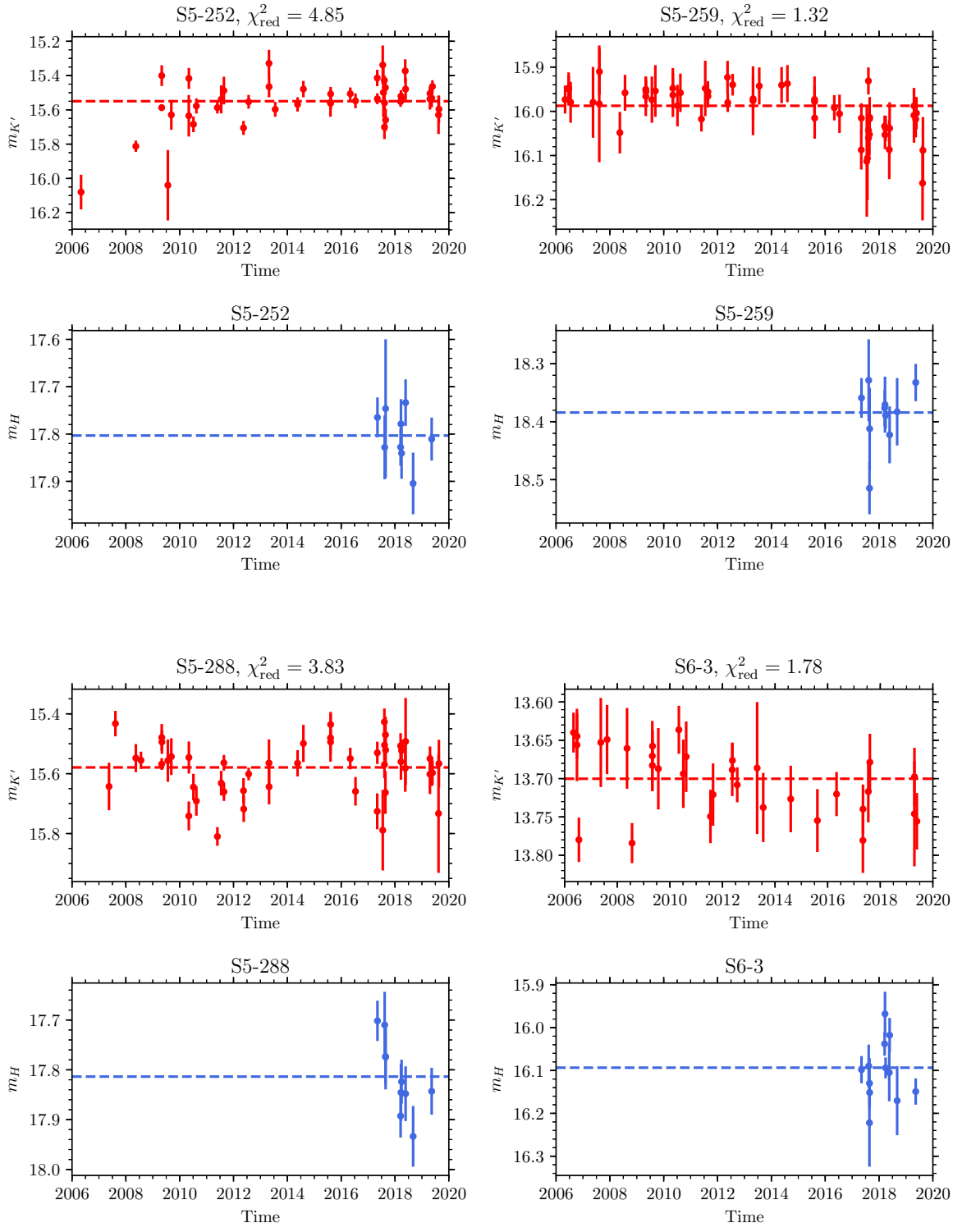
S5-252, $\chi^2_{\rm red} = 4.85$
S5-259, $\chi^2_{\rm red} = 1.32$
S5-252
S5-259
S5-288, $\chi^2_{\rm red} = 3.83$
S6-3, $\chi^2_{\rm red} = 1.78$
S5-288
S6-3
$m_{K'}$
m_H
Time

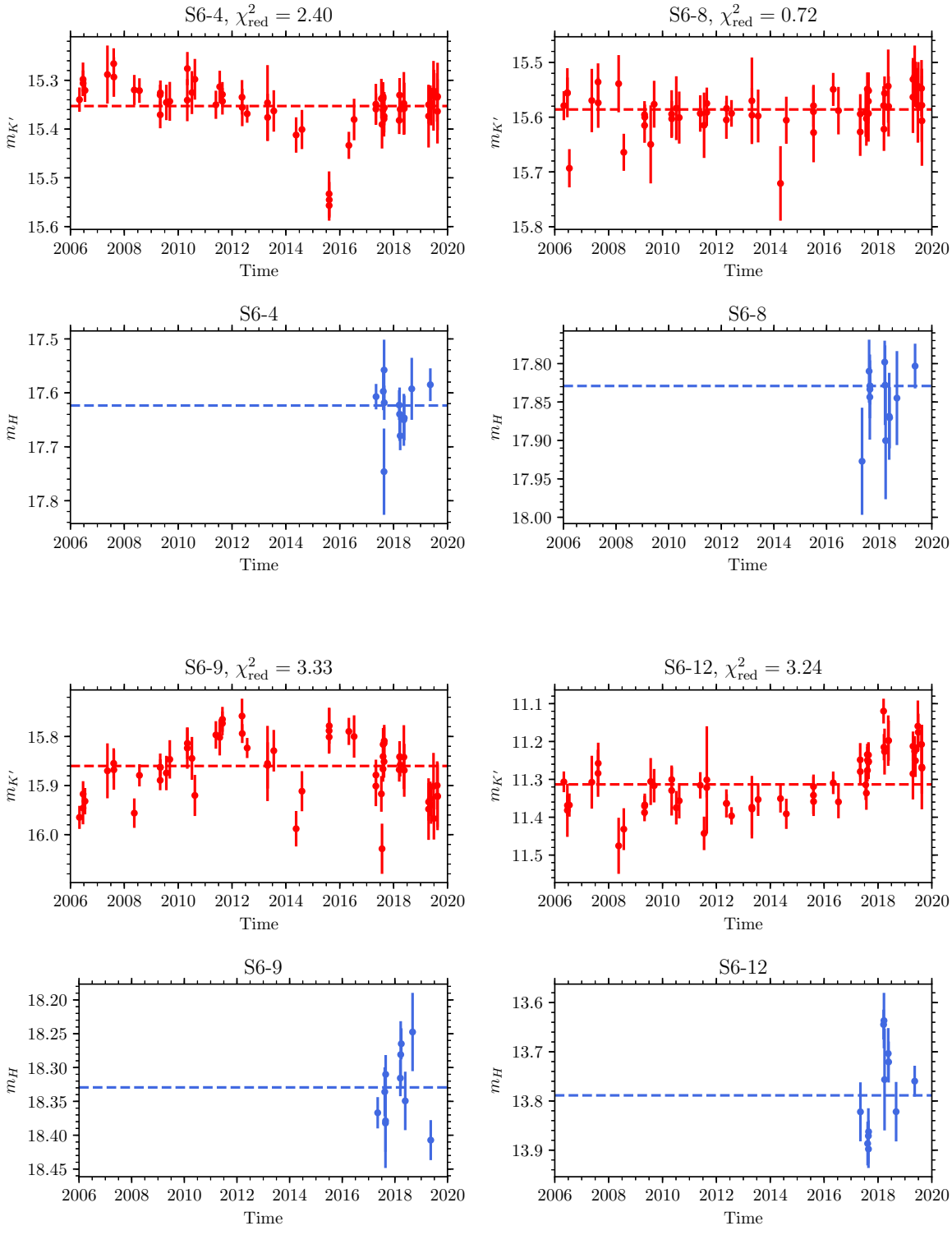
S6-4, $\chi^2_{\rm red} = 2.40$
S6-8, $\chi^2_{\rm red} = 0.72$
S6-4
S6-8
S6-9, $\chi^2_{\rm red} = 3.33$
S6-12, $\chi^2_{\rm red} = 3.24$
S6-9
S6-12
$m_{K'}$
m_H
Time

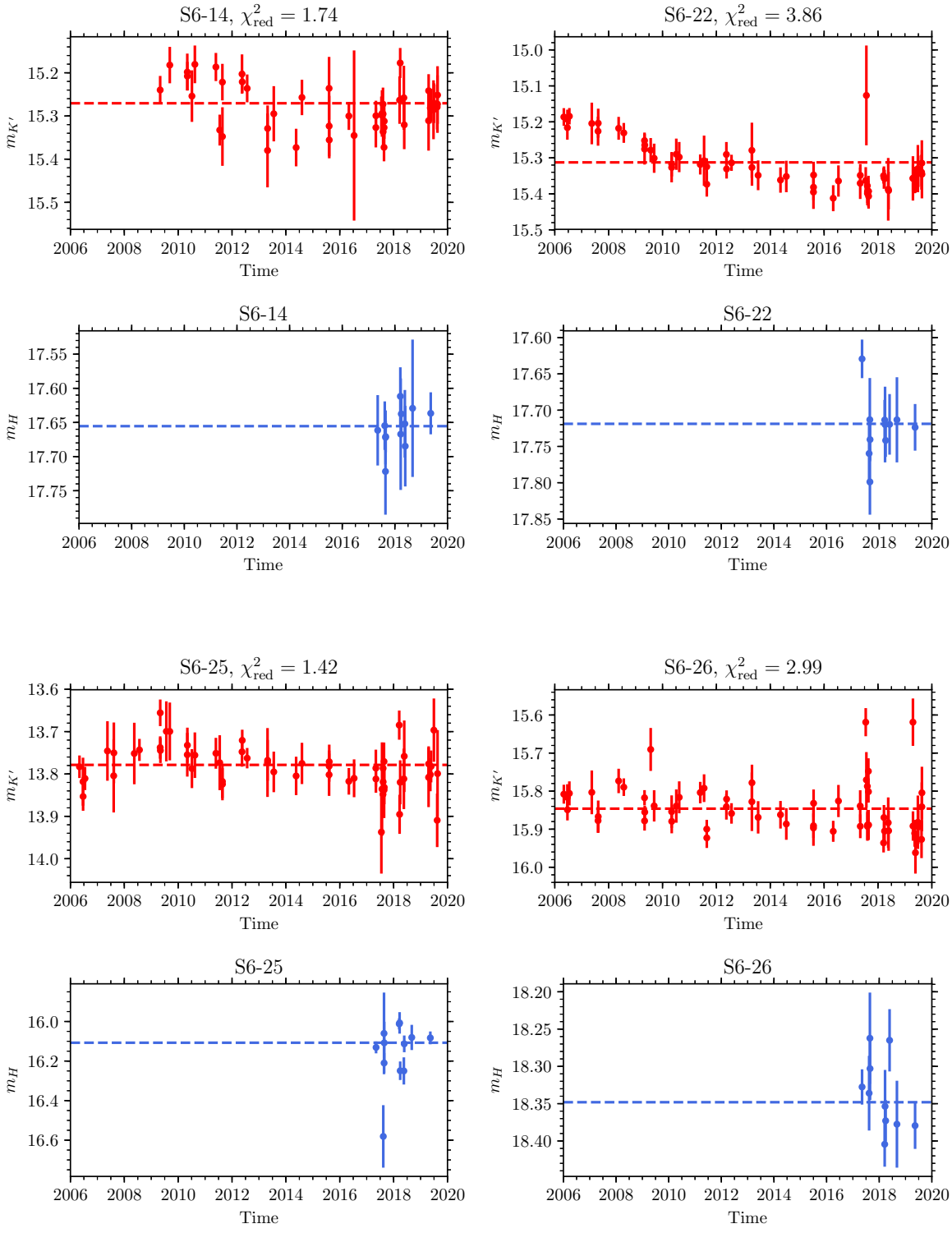
S6-14, $\chi^2_{\rm red} = 1.74$
S6-22, $\chi^2_{\rm red} = 3.86$
S6-14
S6-22
S6-25, $\chi^2_{\rm red} = 1.42$
S6-26, $\chi^2_{\rm red} = 2.99$
S6-25
S6-26
$m_{K'}$
m_H
Time

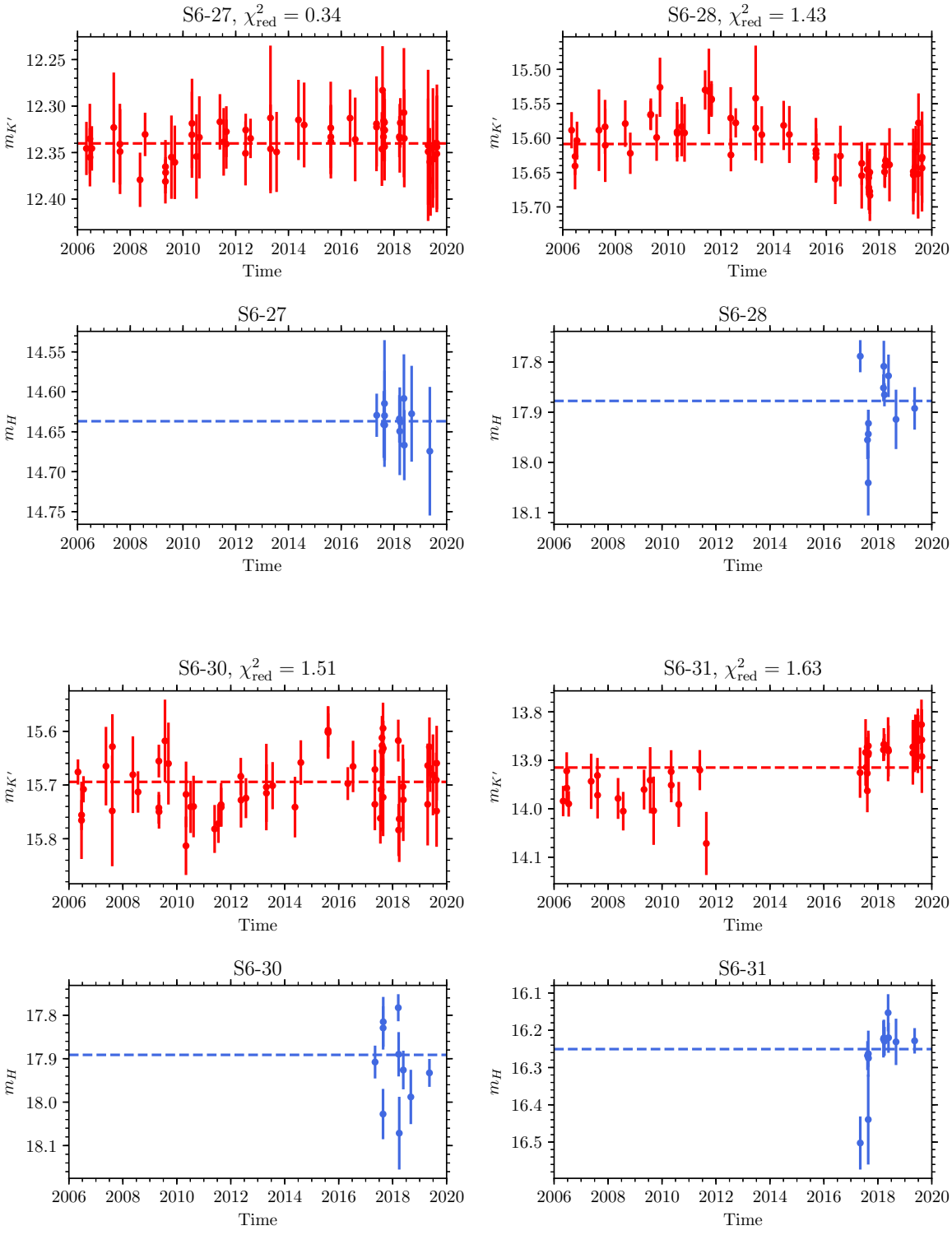
S6-27, $\chi^2_{\rm red} = 0.34$
S6-28, $\chi^2_{\rm red} = 1.43$
S6-27
S6-28
S6-30, $\chi^2_{\rm red} = 1.51$
S6-31, $\chi^2_{\rm red} = 1.63$
S6-30
S6-31
$m_{K'}$
m_H
Time

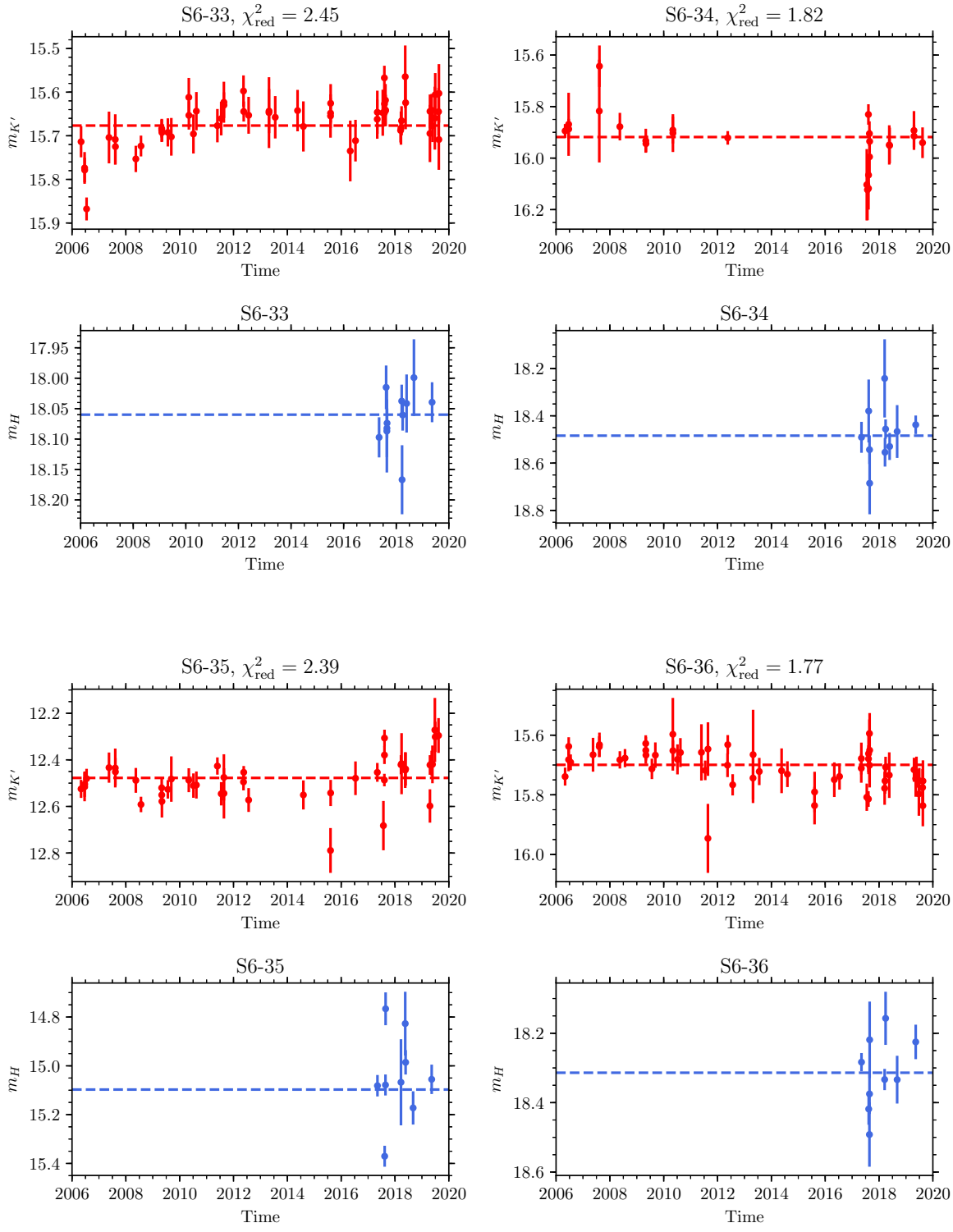
S6-33, $\chi^2_{\rm red} = 2.45$
S6-34, $\chi^2_{\rm red} = 1.82$
S6-33
S6-34
S6-35, $\chi^2_{\rm red} = 2.39$
S6-36, $\chi^2_{\rm red} = 1.77$
S6-35
S6-36
$m_{K'}$
m_H
Time

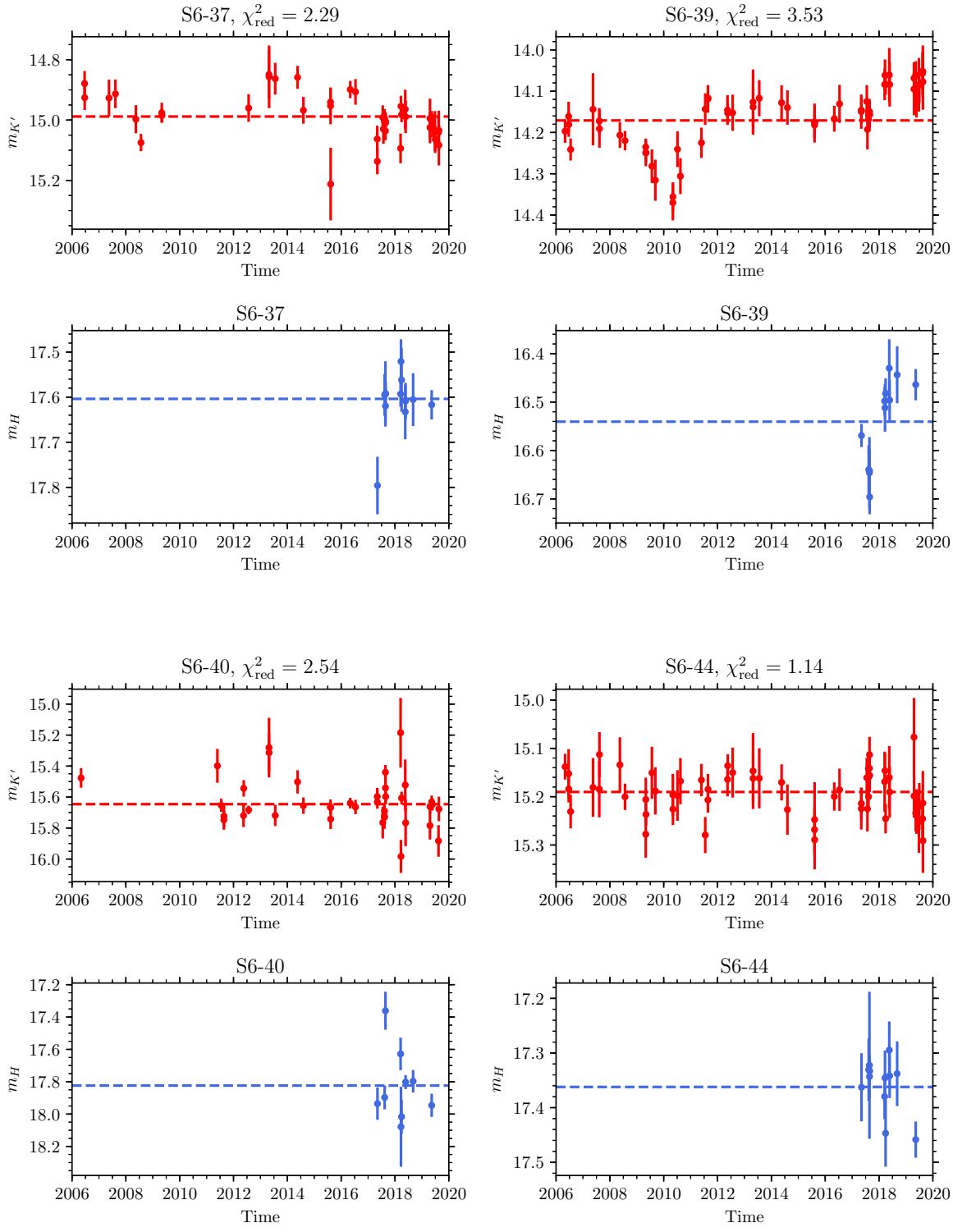
S6-37, $\chi^2_{\rm red} = 2.29$
S6-39, $\chi^2_{\rm red} = 3.53$
S6-37
S6-39
S6-40, $\chi^2_{\rm red} = 2.54$
S6-44, $\chi^2_{\rm red} = 1.14$
S6-40
S6-44
$m_{K'}$
m_H
Time

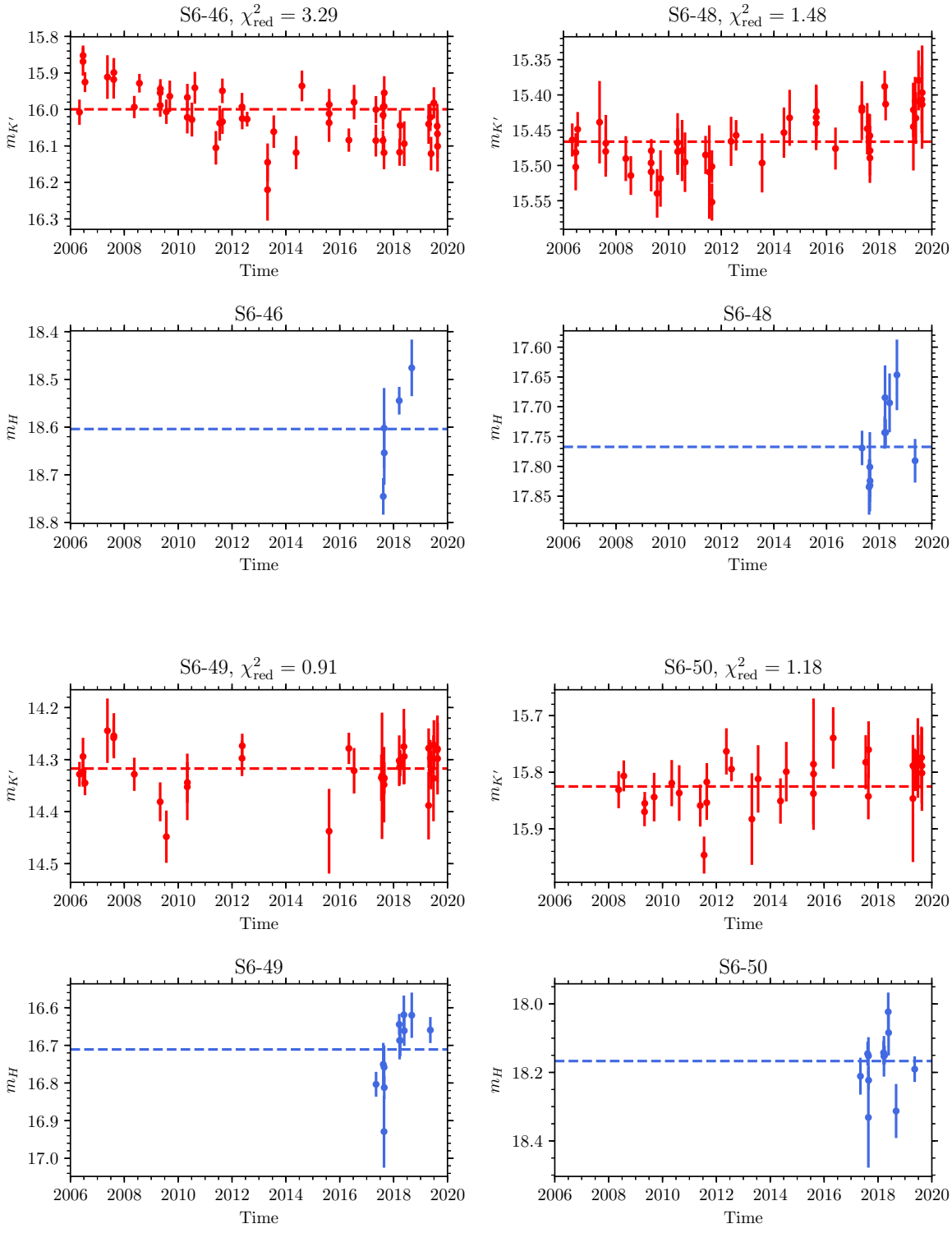
S6-46, $\chi^2_{\rm red} = 3.29$
S6-48, $\chi^2_{\rm red} = 1.48$
S6-46
S6-48
S6-49, $\chi^2_{\rm red} = 0.91$
S6-50, $\chi^2_{\rm red} = 1.18$
S6-49
S6-50
$m_{K'}$
m_H
Time

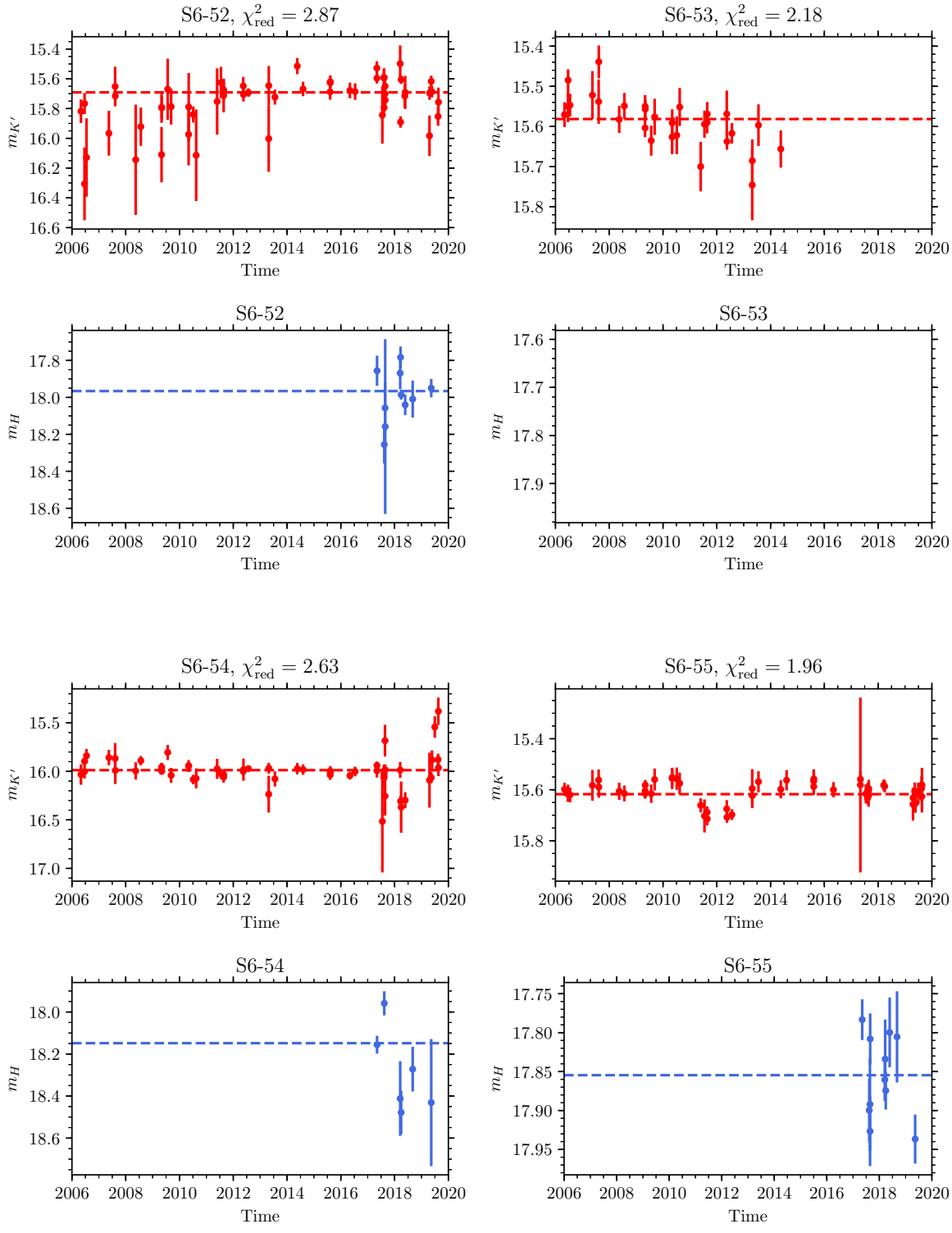
S6-52, $\chi^2_{\rm red} = 2.87$
S6-53, $\chi^2_{\rm red} = 2.18$
S6-52
S6-53
S6-54, $\chi^2_{\rm red} = 2.63$
S6-55, $\chi^2_{\rm red} = 1.96$
S6-54
S6-55
$m_{K'}$
m_H
Time

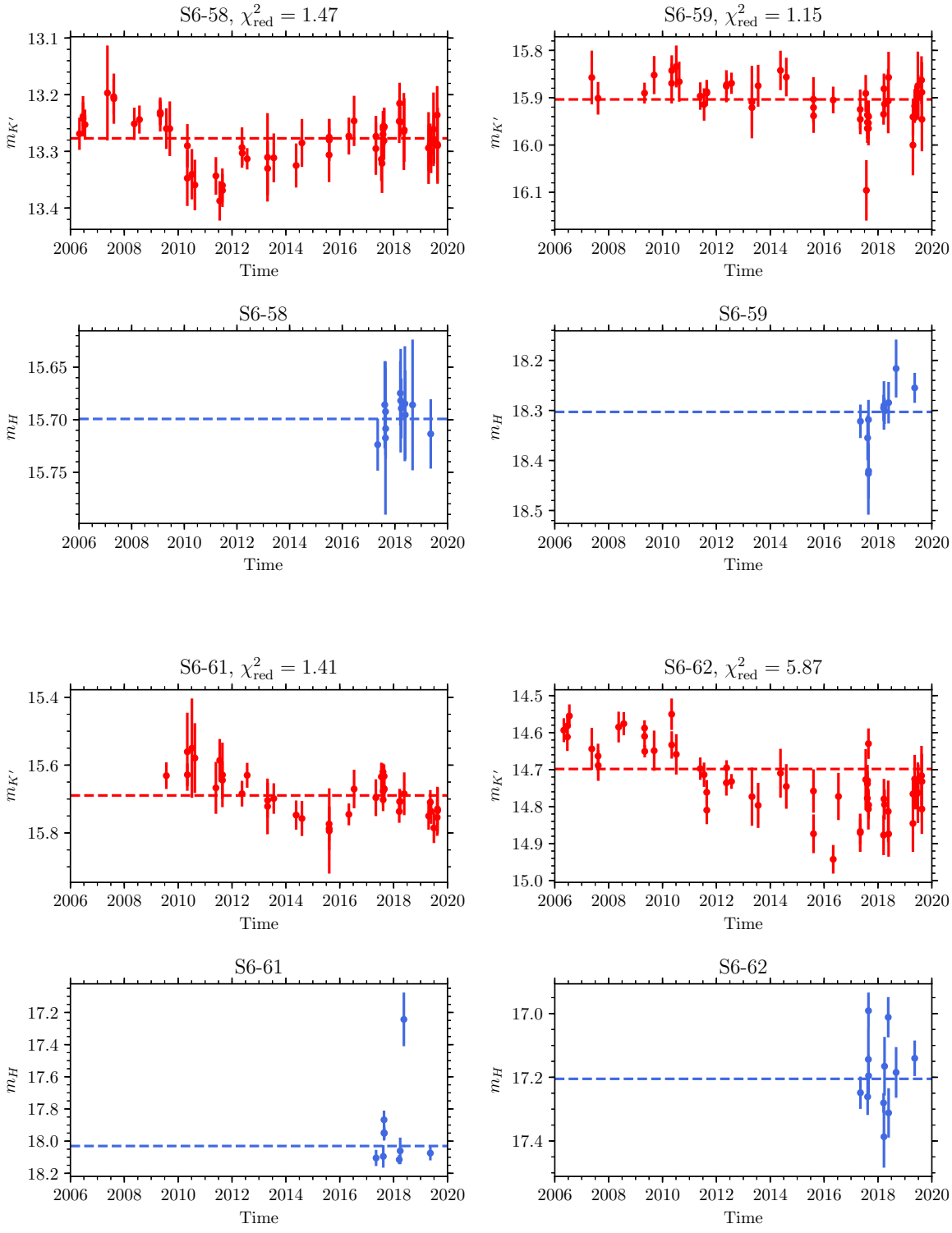
S6-58, $\chi^2_{\rm red} = 1.47$
S6-59, $\chi^2_{\rm red} = 1.15$
S6-58
S6-59
S6-61, $\chi^2_{\rm red} = 1.41$
S6-62, $\chi^2_{\rm red} = 5.87$
S6-61
S6-62
$m_{K'}$
m_H
Time

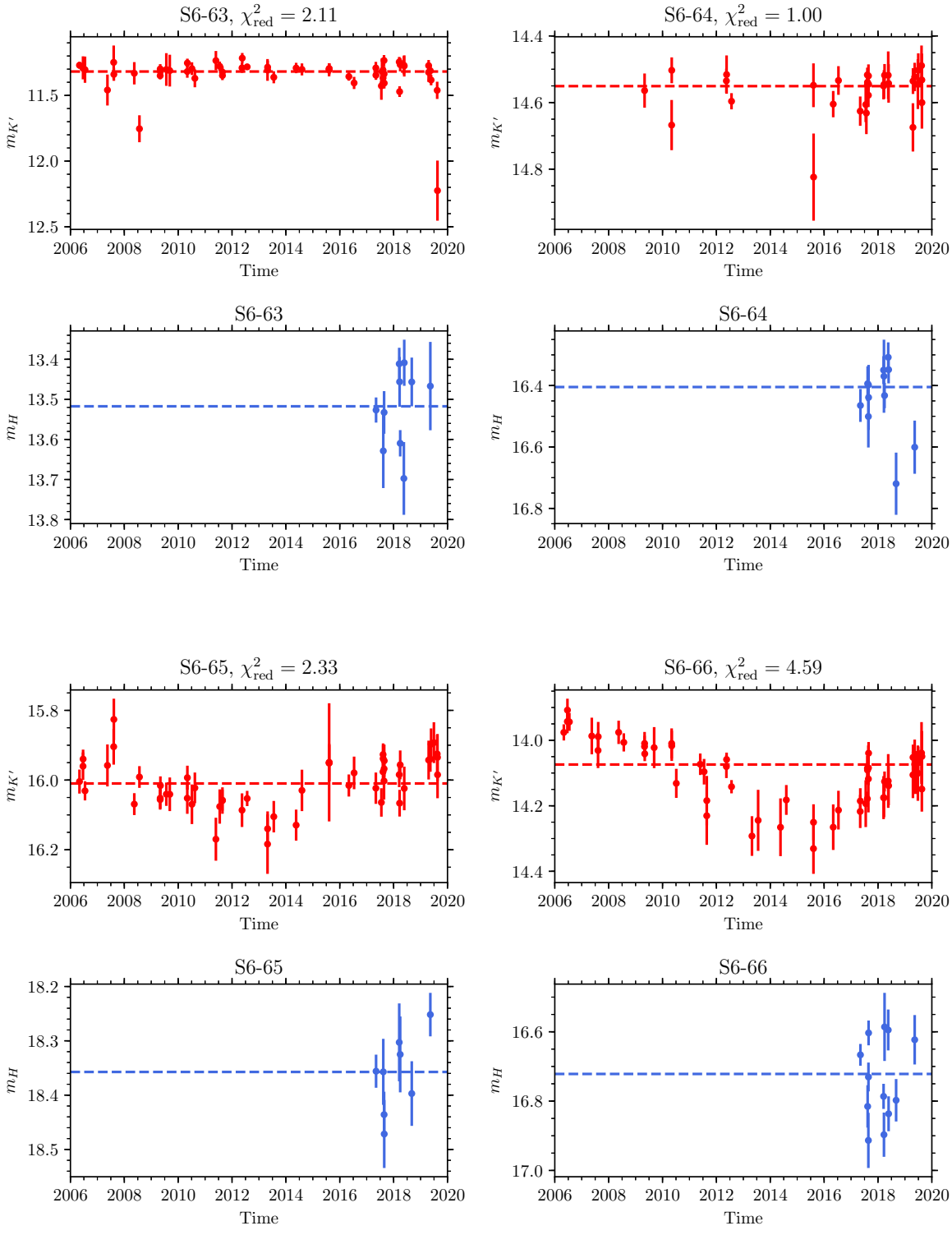
S6-63, $\chi^2_{\rm red} = 2.11$
S6-64, $\chi^2_{\rm red} = 1.00$
S6-63
S6-64
S6-65, $\chi^2_{\rm red} = 2.33$
S6-66, $\chi^2_{\rm red} = 4.59$
S6-65
S6-66
$m_{K'}$
m_H
Time

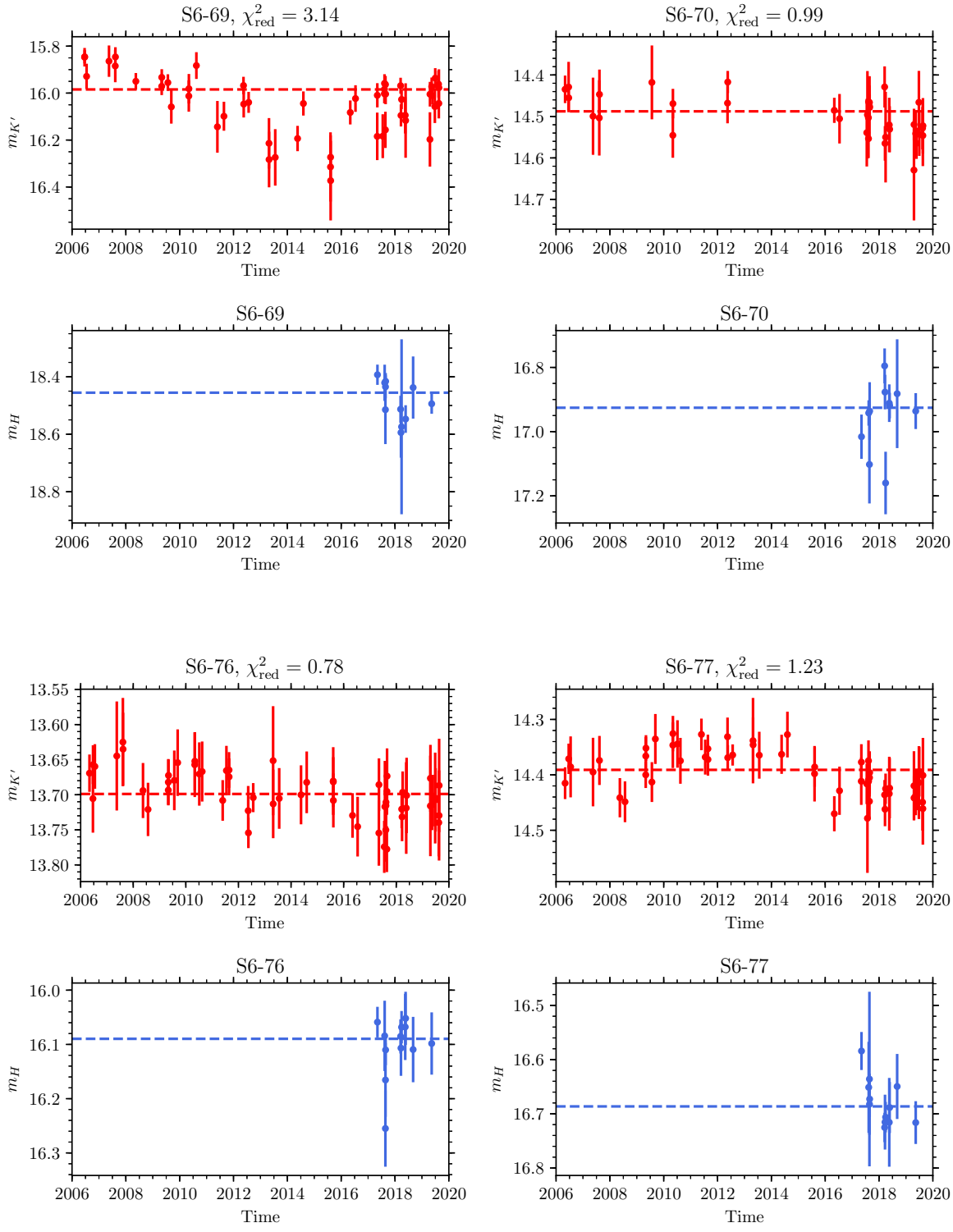
S6-69, $\chi^2_{\rm red} = 3.14$
S6-70, $\chi^2_{\rm red} = 0.99$
S6-69
S6-70
S6-76, $\chi^2_{\rm red} = 0.78$
S6-77, $\chi^2_{\rm red} = 1.23$
S6-76
S6-77
$m_{K'}$
m_H
Time

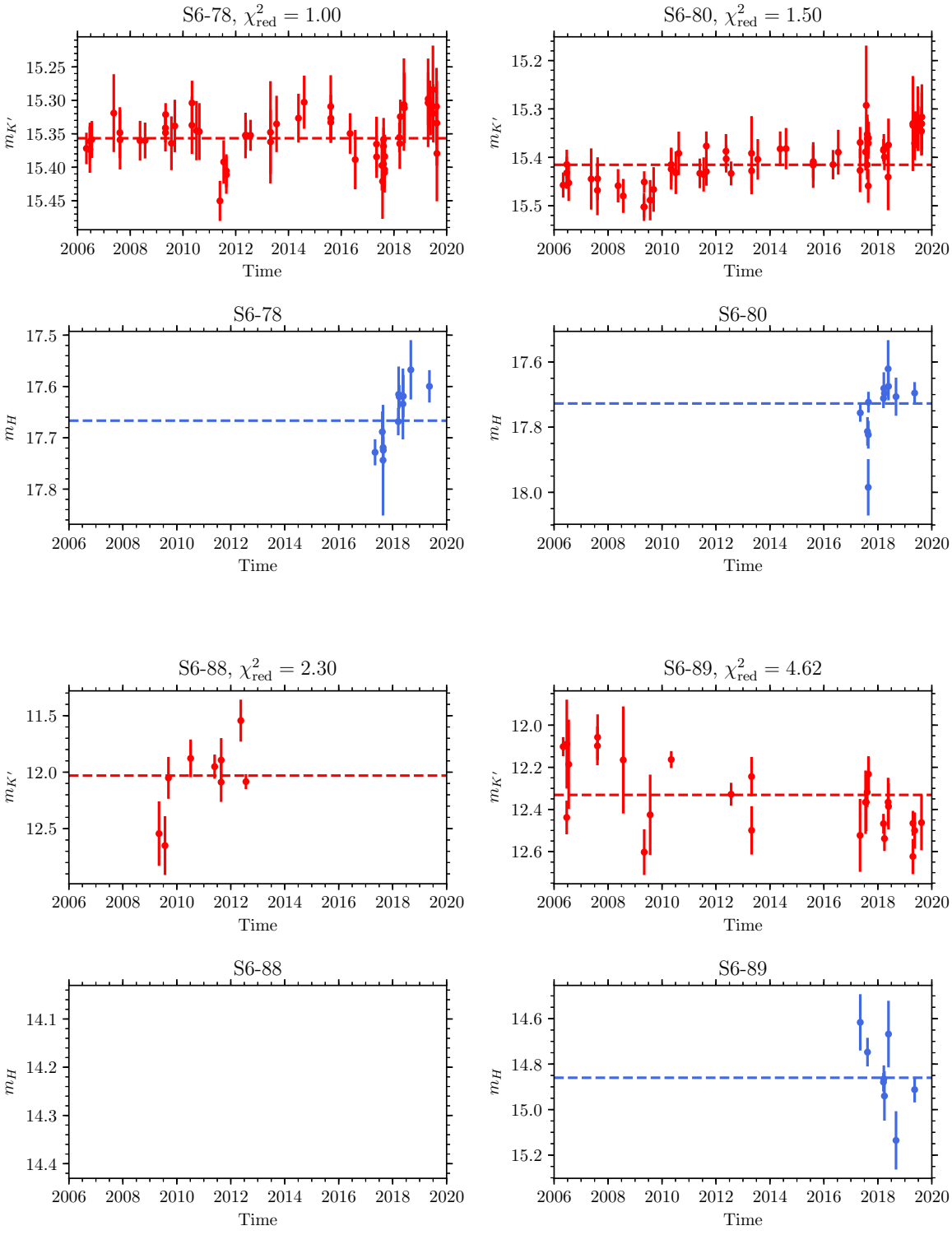
S6-78, $\chi^2_{\rm red} = 1.00$
S6-80, $\chi^2_{\rm red} = 1.50$
S6-78
S6-80
S6-88, $\chi^2_{\rm red} = 2.30$
S6-89, $\chi^2_{\rm red} = 4.62$
S6-88
S6-89
$m_{K'}$
m_H
Time

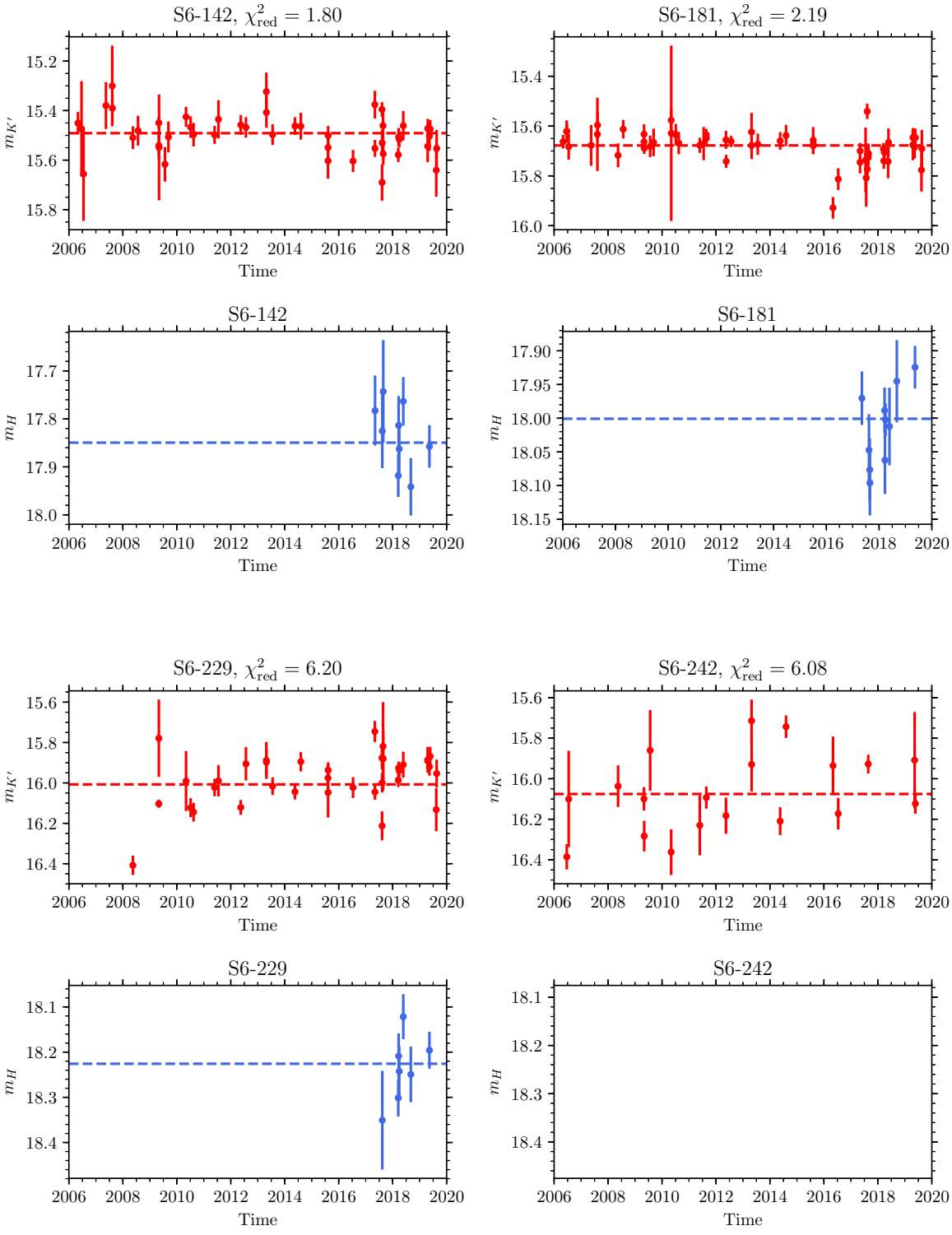
S6-142, $\chi^2_{\rm red} = 1.80$
S6-181, $\chi^2_{\rm red} = 2.19$
S6-142
S6-181
S6-229, $\chi^2_{\rm red} = 6.20$
S6-242, $\chi^2_{\rm red} = 6.08$
S6-229
S6-242
$m_{K'}$
m_H
Time

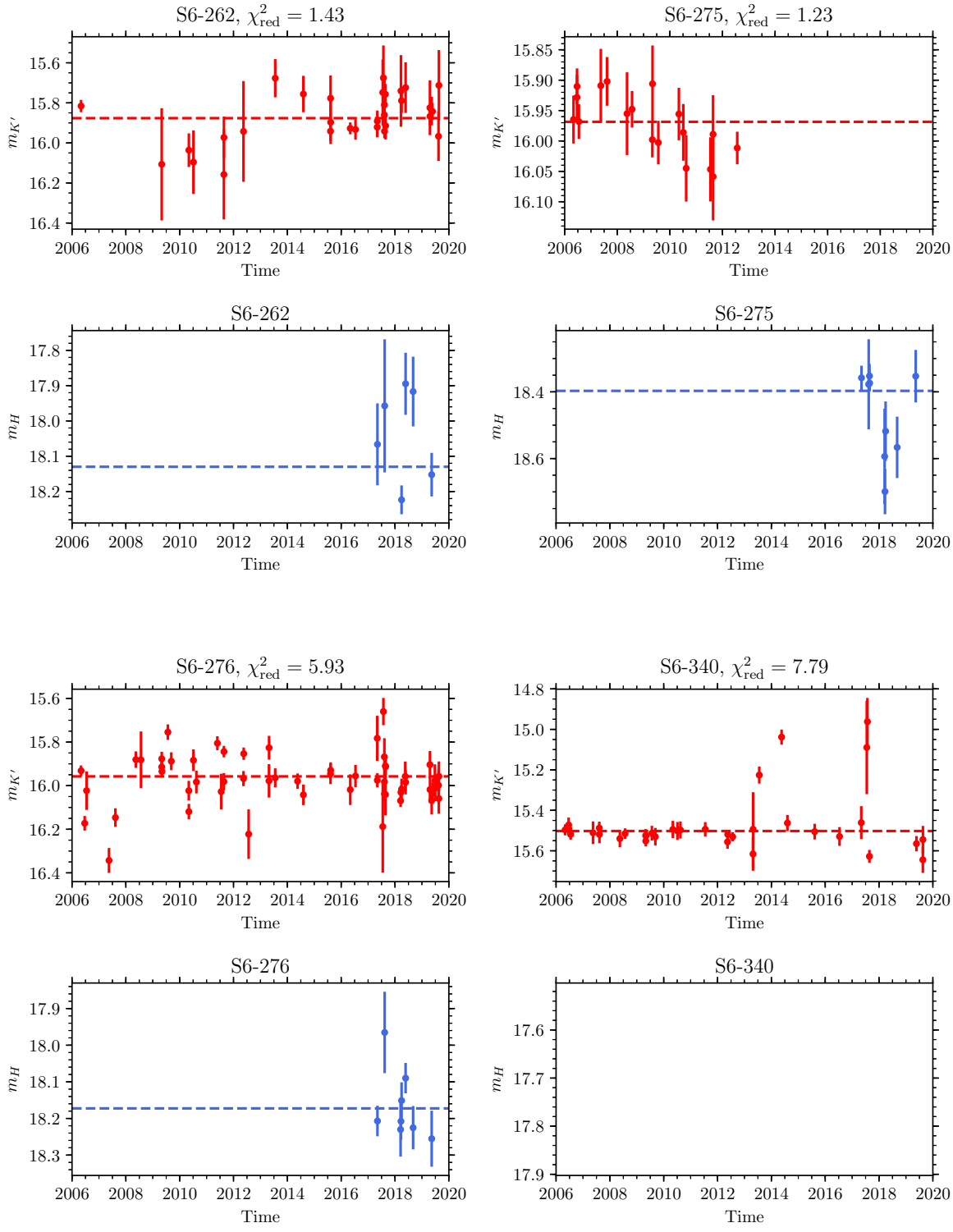
S6-262, $\chi^2_{\rm red} = 1.43$
S6-275, $\chi^2_{\rm red} = 1.23$
S6-262
S6-275
S6-276, $\chi^2_{\rm red} = 5.93$
S6-340, $\chi^2_{\rm red} = 7.79$
S6-276
S6-340
$m_{K'}$
m_H
Time

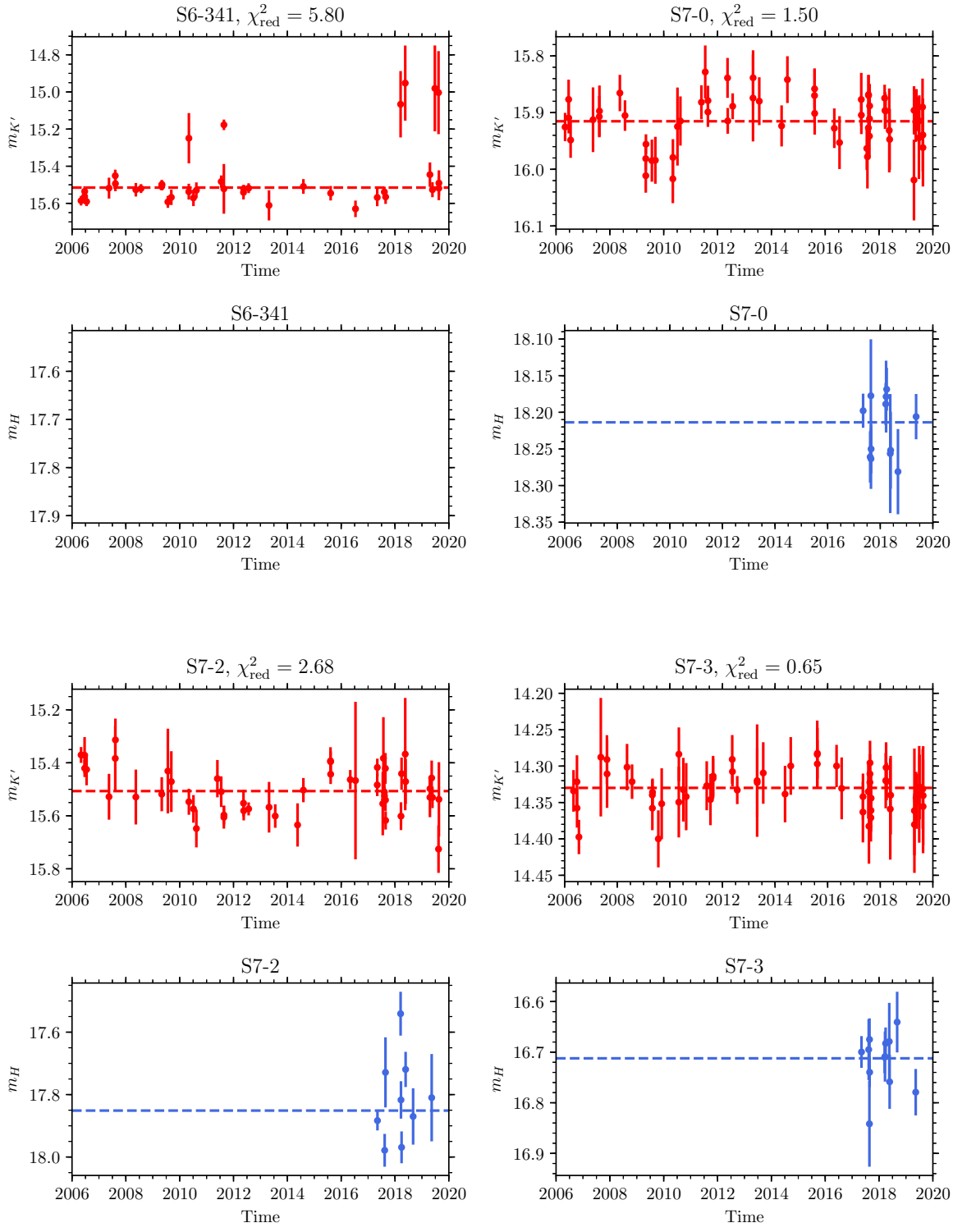
S6-341, $\chi^2_{\rm red} = 5.80$
S7-0, $\chi^2_{\rm red} = 1.50$
S6-341
S7-0
S7-2, $\chi^2_{\rm red} = 2.68$
S7-3, $\chi^2_{\rm red} = 0.65$
S7-2
S7-3
$m_{K'}$
m_H
Time

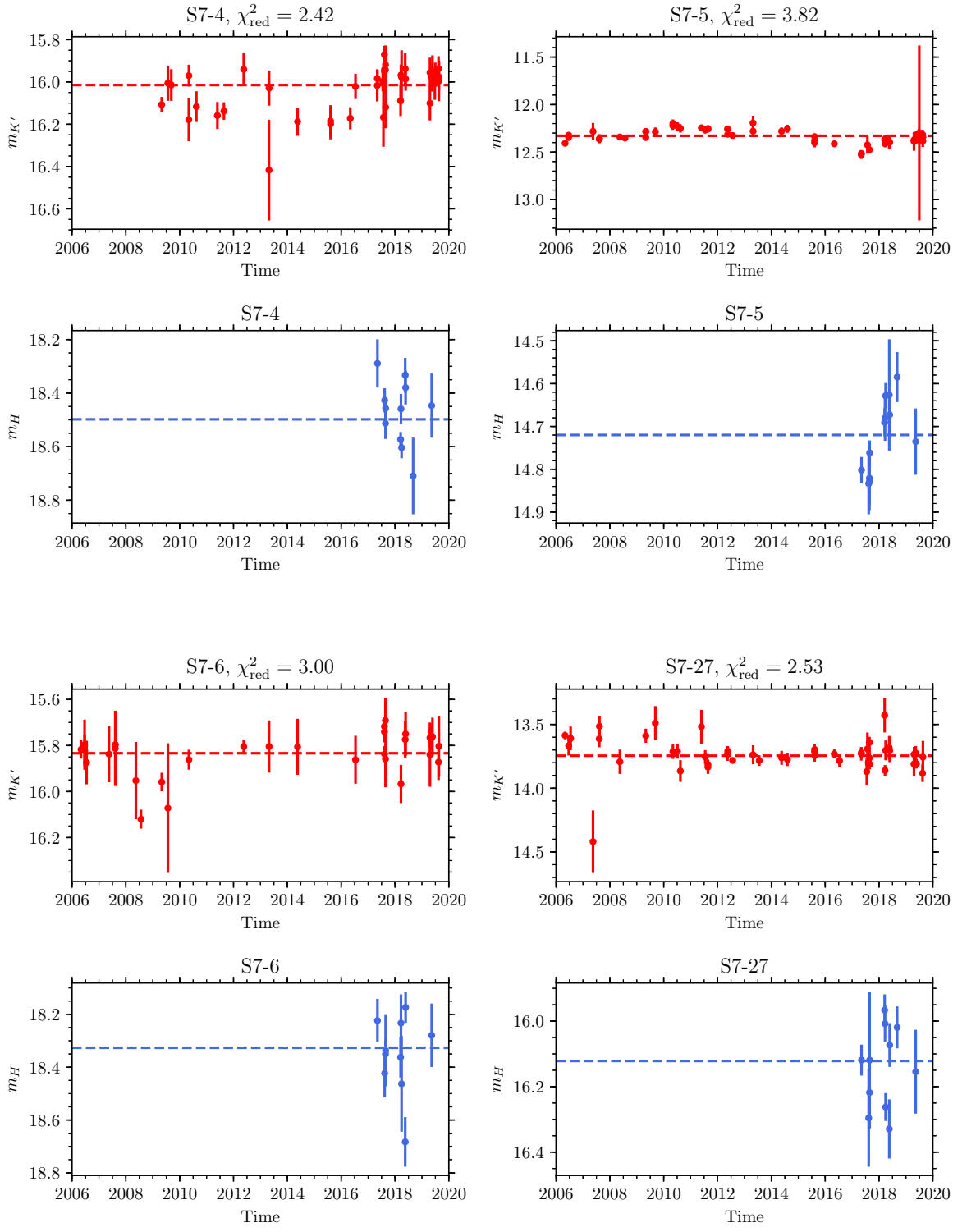
S7-4, $\chi^2_{\rm red} = 2.42$
S7-5, $\chi^2_{\rm red} = 3.82$
S7-4
S7-5
S7-6, $\chi^2_{\rm red} = 3.00$
S7-27, $\chi^2_{\rm red} = 2.53$
S7-6
S7-27
$m_{K'}$
m_H
Time

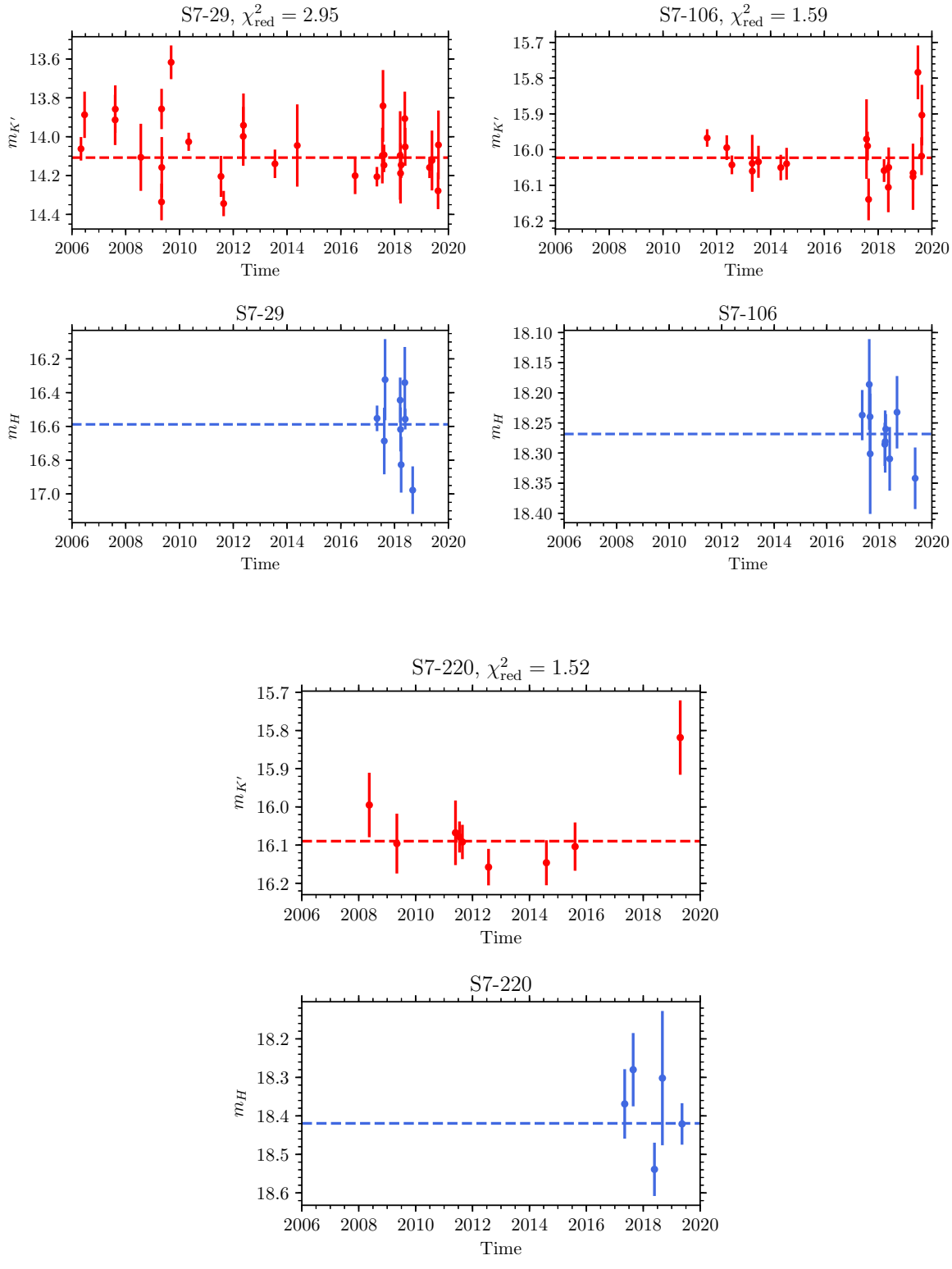
S7-29, $\chi^2_{\rm red} = 2.95$
S7-106, $\chi^2_{\rm red} = 1.59$
S7-29
S7-106
S7-220, $\chi^2_{\rm red} = 1.52$
S7-220
$m_{K'}$
m_H
Time

A.2 Periodic Variable Detections

This section has been updated from Appendix E in Gautam et al. (2019) with the following change: likely periodic and possible periodic variables shown here were identified with the updated periodicity search methodology outlined in Section 4.2 rather than our previous results detailed in Section 2.5.2.

A.2.1 Likely Periodic Variables

Likely periodic variables identified with updated periodicity search methodology in Section 4.2 include IRS 16SW (Figure 4.2), S4-258 (Figure 4.3), S2-36 (Figure 4.4). These three stars were also previously identified as likely periodic in Gautam et al. (2019). We additionally identify likely periodic variability in the stars S4-308 (Figure 4.5) and S3-438 (Figure 4.6).

A.2.2 Possible Periodic Signals

Possible periodic variables plotted here were identified with the updated periodicity search methodology described in Section 4.2. In each plot, Keck NIRC2 photometric measurements are shown in the K'- (top row panels) and H-band (bottom row panels). The left panels show the light curve over our entire experiment time baseline. The solid colored lines show the long-term linear trend components of the best-fit trended sinusoid model in each band, with 3σ uncertainty in the linear fit indicated by the shaded regions. The right panels show the same photometric data phased to $2\times$ the best-fit period from our trended Lomb-Scargle analysis and with the best-fit long-term linear trend removed. The solid, colored lines in each panel indicate the best-fit sinusoid model to the observed data, with 3σ uncertainty in the sinusoid fit indicated by the shaded regions.

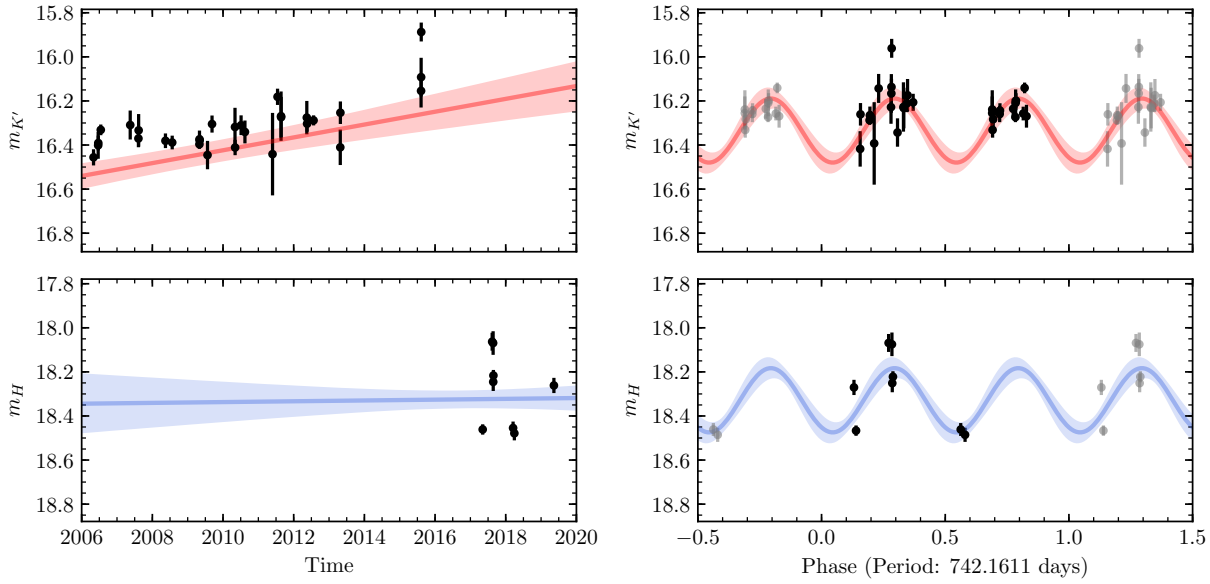

Figure A.1: Possible periodic variable candidate S4-133.

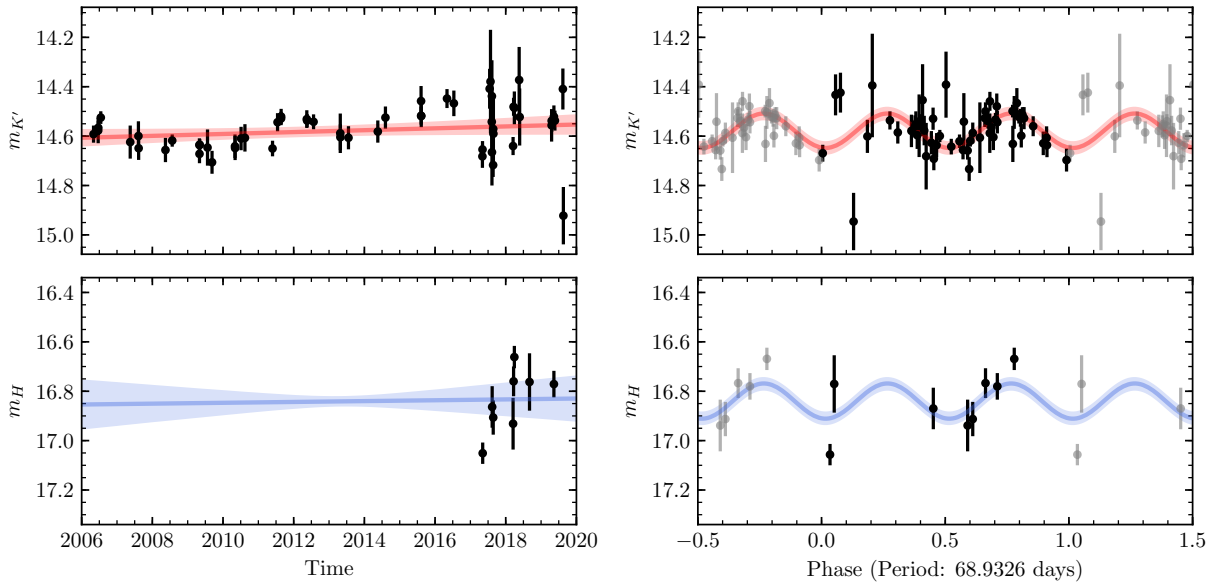

Figure A.2: Possible periodic variable candidate S3-364.

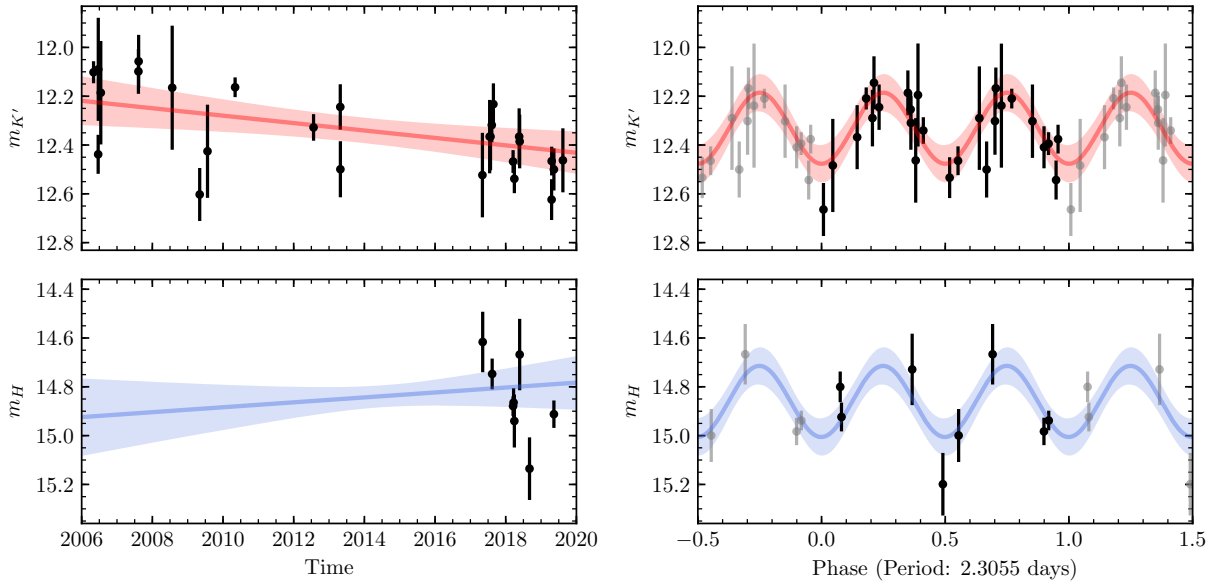

Figure A.3: Possible periodic variable candidate S6-89.

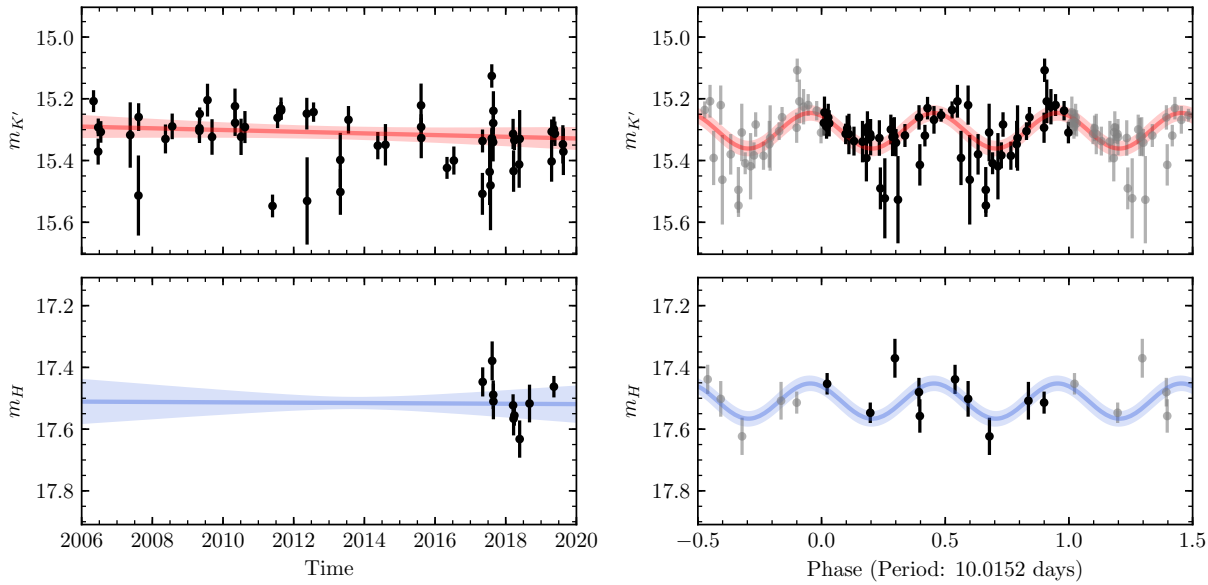

Figure A.4: Possible periodic variable candidate S5-60.

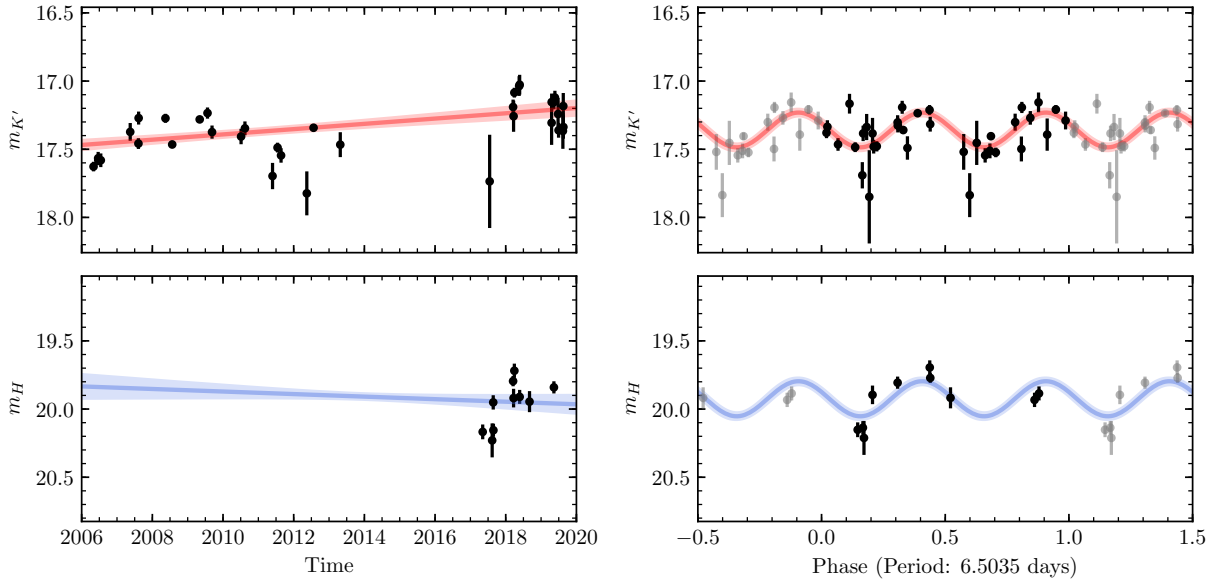

Figure A.5: Possible periodic variable candidate S2-301.

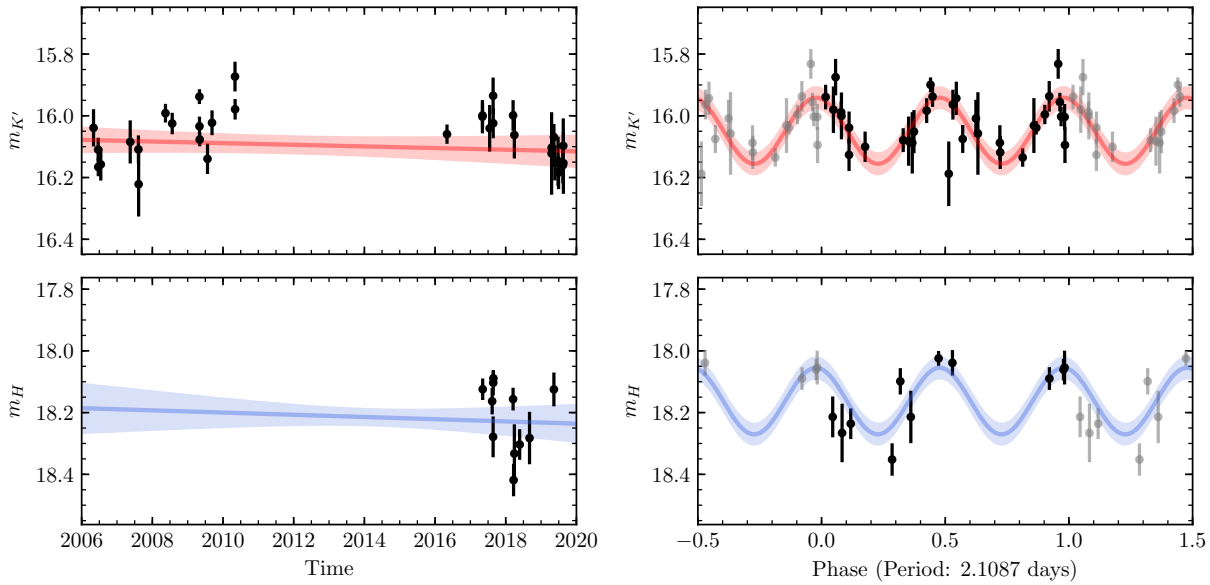

Figure A.6: Possible periodic variable candidate S0-33.

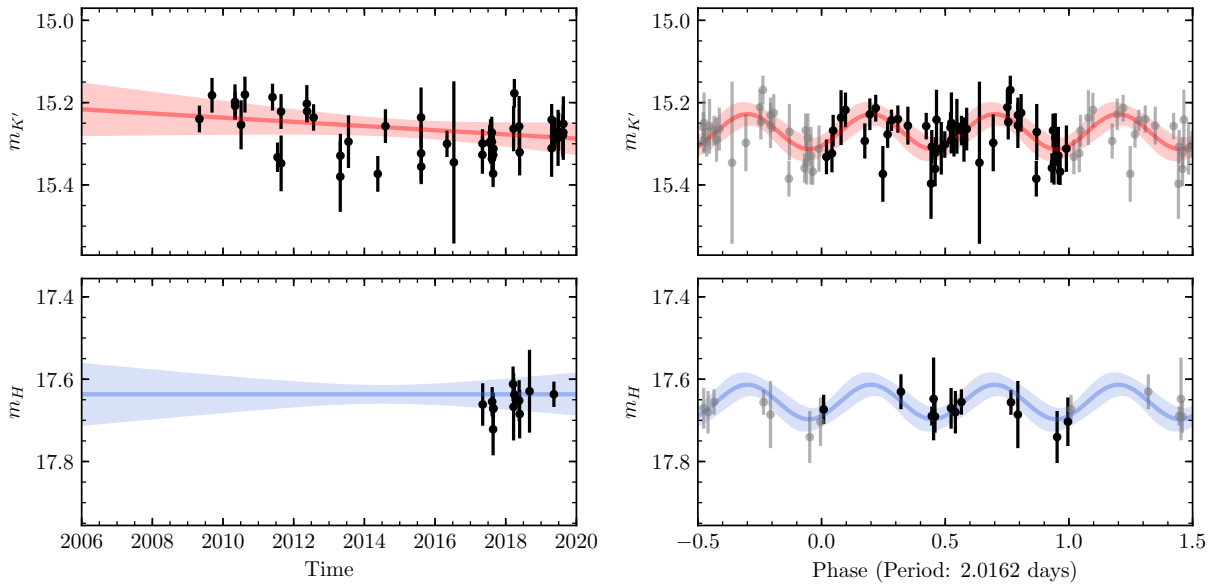

Figure A.7: Possible periodic variable candidate S6-14.

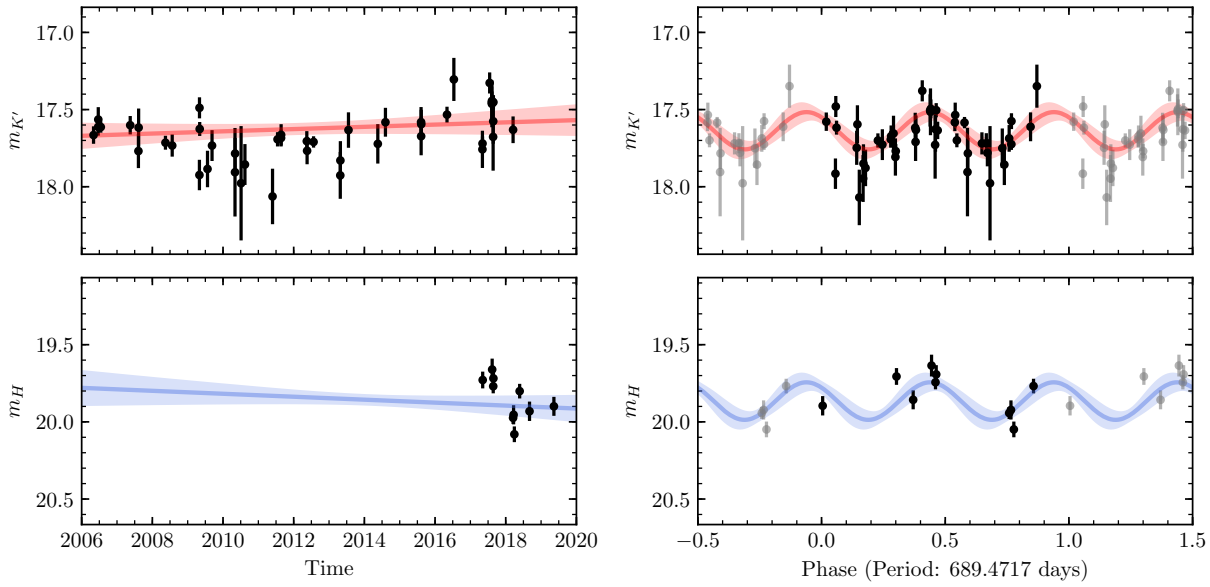

Figure A.8: Possible periodic variable candidate S2-284.

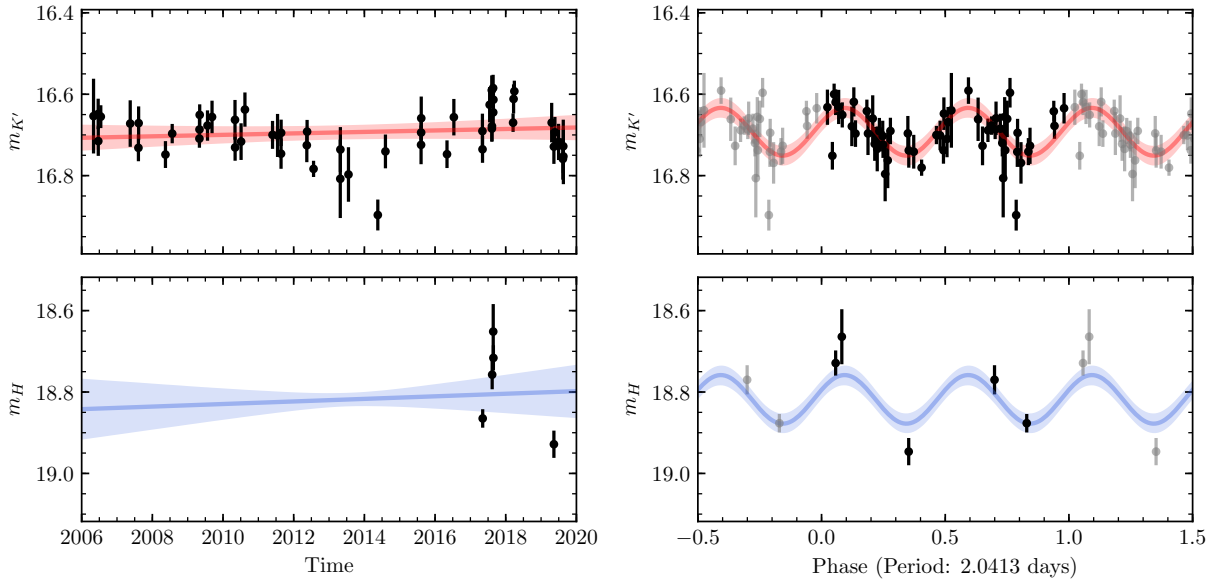

Figure A.9: Possible periodic variable candidate S3-235.

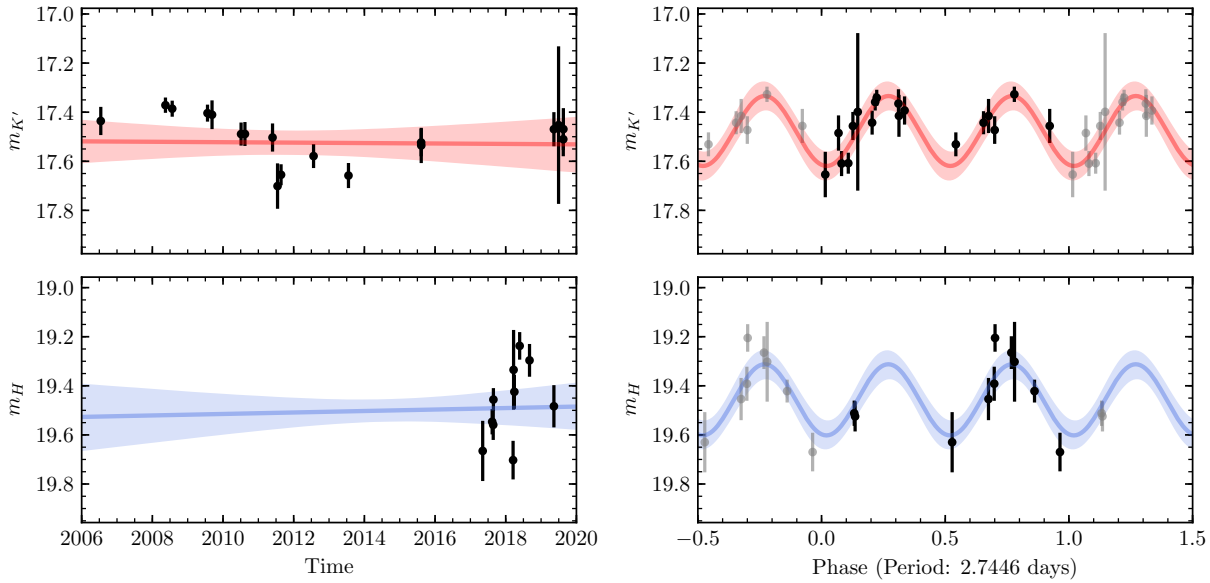

Figure A.10: Possible periodic variable candidate S1-148.

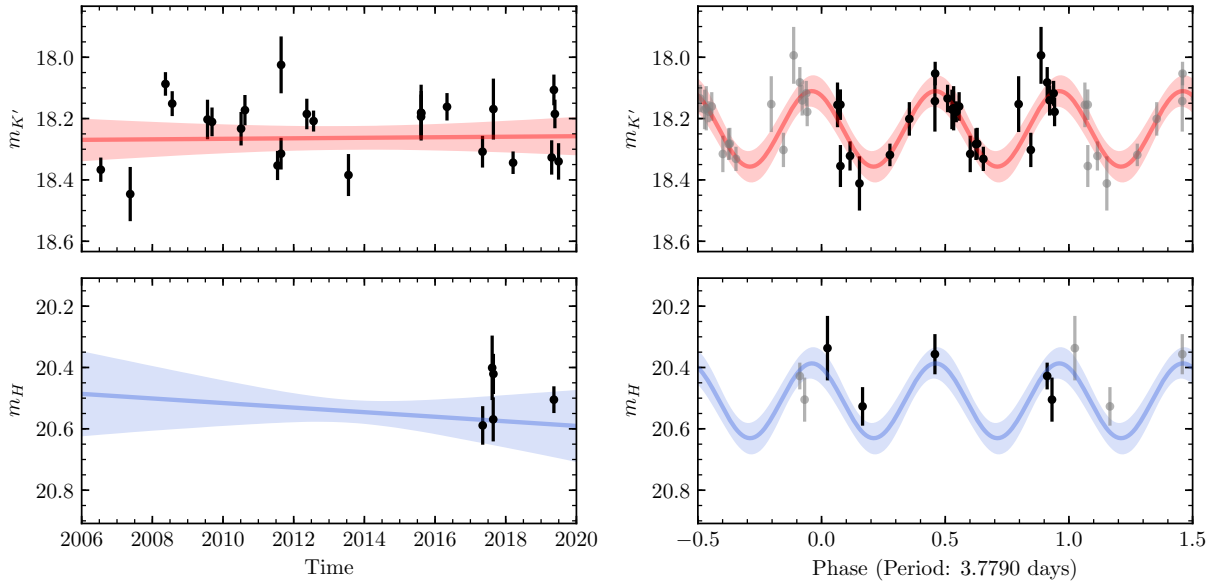

Figure A.11: Possible periodic variable candidate S3-280.

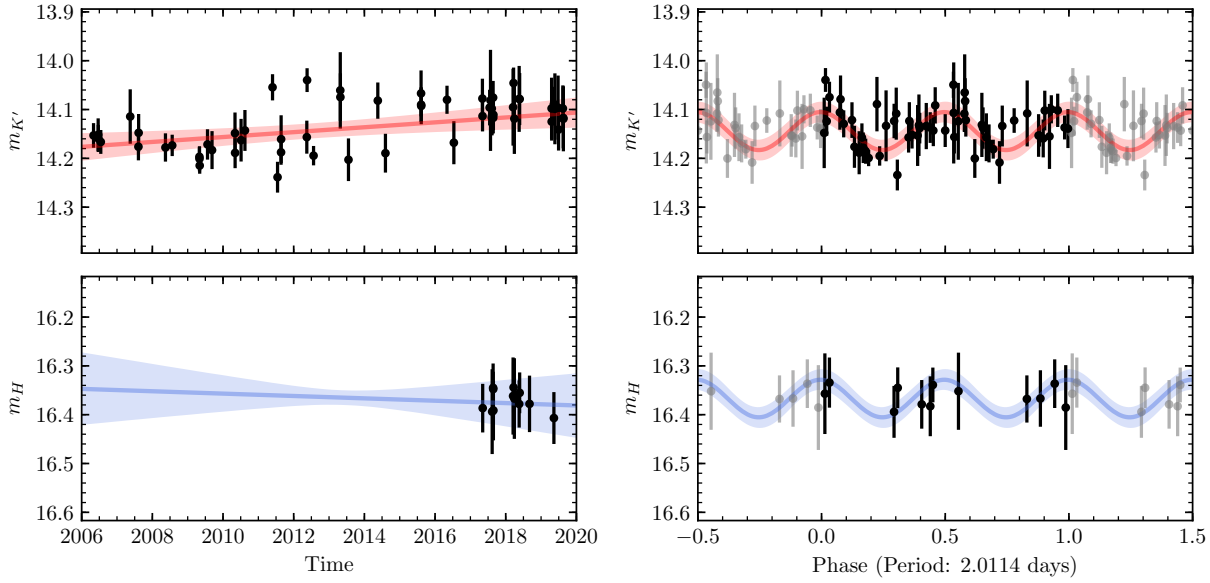

Figure A.12: Possible periodic variable candidate S1-15.

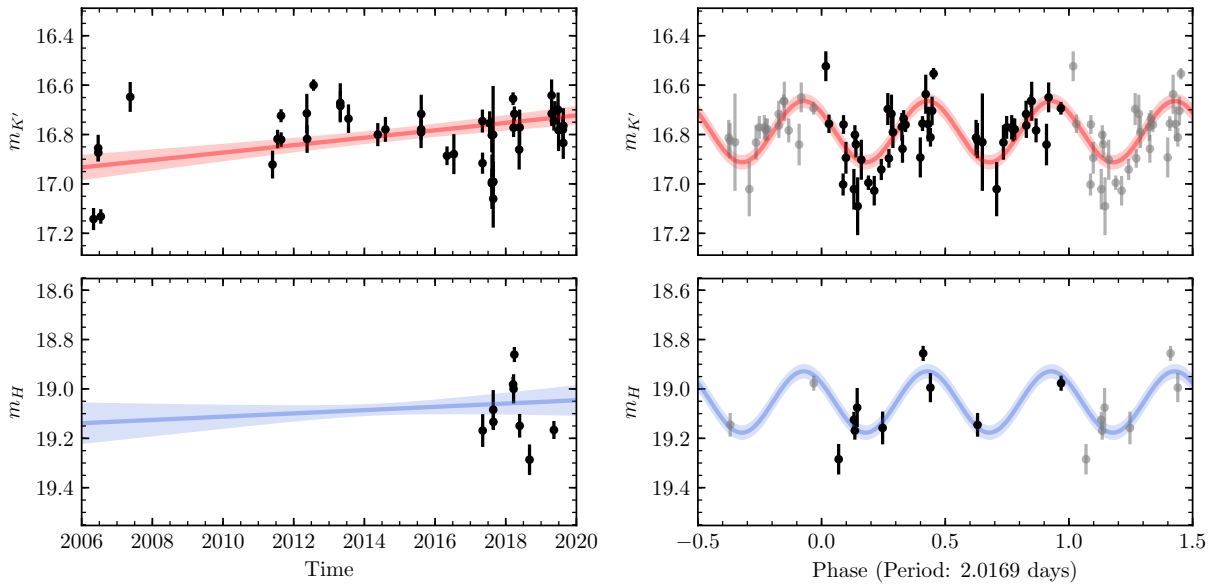

Figure A.13: Possible periodic variable candidate S2-133.

Bibliography

Abbott, B. P., Abbott, R., Abbott, T. D., et al. 2017, Phys. Rev. Lett., 118, 221101

Alexander, R. D., Armitage, P. J., & Cuadra, J. 2008, MNRAS, 389, 1655

Alexander, T., & Hopman, C. 2009, ApJ, 697, 1861

Alexander, T., & Loeb, A. 2001, ApJ, 551, 223

Alexander, T., & Pfuhl, O. 2014, ApJ, 780, 148

Amaro-Seoane, P., & Chen, X. 2014, ApJL, 781, L18

Antonini, F. 2014, ApJ, 794, 106

Antonini, F., Capuzzo-Dolcetta, R., Mastrobuono-Battisti, A., & Merritt, D. 2012, ApJ, 750, 111

Astropy Collaboration, Robitaille, T. P., Tollerud, E. J., et al. 2013, A&A, 558, A33

Bahcall, J. N., & Wolf, R. A. 1976, ApJ, 209, 214

—. 1977, ApJ, 216, 883

Bar-Or, B., Kupi, G., & Alexander, T. 2013, ApJ, 764, 52

Bartko, H., Martins, F., Fritz, T. K., et al. 2009, ApJ, 697, 1741

Bartko, H., Martins, F., Trippe, S., et al. 2010, ApJ, 708, 834

Binney, J., & Tremaine, S. 2008, Galactic Dynamics: Second Edition (Princeton University Press)

Blum, R. D., Ramírez, S. V., Sellgren, K., & Olsen, K. 2003, ApJ, 597, 323

Blum, R. D., Sellgren, K., & Depoy, D. L. 1996, ApJ, 470, 864

Boehle, A., Ghez, A. M., Schödel, R., et al. 2016, ApJ, 830, 17

Bozza, V., & Mancini, L. 2005, ApJ, 627, 790

Buchholz, R. M., Schödel, R., & Eckart, A. 2009, A&A, 499, 483

Capuzzo-Dolcetta, R., & Miocchi, P. 2008, ApJ, 681, 1136

Castelli, F., & Kurucz, R. L. 2004, arXiv, arXiv:astro

Catelan, M., & Smith, H. A. 2015, Pulsating Stars (mcatelan@astro.puc.cl: Pulsating Stars (Wiley-VCH))

Chanamé, J., Gould, A., & Miralda-Escudé, J. 2001, ApJ, 563, 793

Chatzopoulos, S., Fritz, T. K., Gerhard, O., et al. 2015, MNRAS, 447, 948

Chen, X., de Grijs, R., & Deng, L. 2017, MNRAS, 464, 1119

Choi, J., Dotter, A., Conroy, C., et al. 2016, ApJ, 823, 102

Chu, D. S., Do, T., Hees, A., et al. 2018, ApJ, 854, 12

Ciurlo, A., Campbell, R. D., Morris, M. R., et al. 2020, Nature, 577, 337

Clénet, Y., Rouan, D., Gendron, E., et al. 2004, A&A, 417, L15

Collaboration, G., Abuter, R., Amorim, A., et al. 2018, A&A, 615, L15

Dale, J. E., Davies, M. B., Church, R. P., & Freitag, M. 2009, MNRAS, 393, 1016

Desvignes, G., Eatough, R. P., Pen, U. L., et al. 2018, ApJL, 852, L12

Diolaiti, E., Bendinelli, O., Bonaccini, D., et al. 2000, Astronomy and Astrophysics Supplement, 147, 335

Do, T., Ghez, A. M., Morris, M. R., et al. 2009, ApJ, 703, 1323

Do, T., Kerzendorf, W., Winsor, N., et al. 2015, 809, 143

Do, T., Lu, J. R., Ghez, A. M., et al. 2013a, ApJ, 764, 154

Do, T., Ghez, A., Lu, J. R., et al. 2012, J. Phys.: Conf. Ser., 372, 012016

Do, T., Martinez, G. D., Yelda, S., et al. 2013b, ApJL, 779, L6

Do, T., Hees, A., Ghez, A., et al. 2019, Sci, 365, 664

Dong, H., Schödel, R., Williams, B. F., et al. 2017, MNRAS, 470, 3427

Dotter, A. 2016, ApJS, 222, 8

Duchêne, G., & Kraus, A. 2013, Annual Review of Astronomy and Astrophysics, 51, 269

Eisenhauer, F., Genzel, R., Alexander, T., et al. 2005, 628, 246

Ekström, S., Georgy, C., Eggenberger, P., et al. 2012, A&A, 537, A146

Figuera Jaimes, R., Bramich, D. M., Skottfelt, J., et al. 2016a, A&A, 588, A128

Figuera Jaimes, R., Bramich, D. M., Kains, N., et al. 2016b, A&A, 592, A120

Foreman-Mackey, D., Hogg, D. W., Lang, D., & Goodman, J. 2013, PASP, 125, 306

Fraser, O. J., Hawley, S. L., Cook, K. H., & Keller, S. C. 2005, AJ, 129, 768

Gallego-Cano, E., Schödel, R., Dong, H., et al. 2018, A&A, 609, A26

Gautam, A. K., Do, T., Ghez, A. M., et al. 2019, ApJ, 871, 103

Generozov, A., Stone, N. C., Metzger, B. D., & Ostriker, J. P. 2018, MNRAS, 478, 4030

Gezari, D., & Yusef-Zadeh, F. 1991, ASP Conference Series, 14, 214

Ghez, A. M., Klein, B. L., Morris, M. R., & Becklin, E. E. 1998, ApJ, 509, 678

Ghez, A. M., Lu, J. R., Le Mignant, D., et al. 2005, ApJ, 635, 1087

Ghez, A. M., Salim, S., Weinberg, N. N., et al. 2008, ApJ, 689, 1044

Gillessen, S., Eisenhauer, F., Trippe, S., et al. 2009, ApJ, 692, 1075

Gillessen, S., Plewa, P. M., Eisenhauer, F., et al. 2017, ApJ, 837, 30

Glass, I. S., Matsumoto, S., Carter, B. S., & Sekiguchi, K. 1999, MNRAS, 304, L10

Goodman, J., & Tan, J. C. 2004, 608, 108

Green, G. M., Schlafly, E., Zucker, C., Speagle, J. S., & Finkbeiner, D. 2019, ApJ, 887, 93

Gültekin, K., Richstone, D. O., Gebhardt, K., et al. 2009, ApJ, 698, 198

Hailey, C. J., Mori, K., Bauer, F. E., et al. 2018, Nature, 556, 70

Heggie, D. C. 1975, MNRAS, 173, 729

Hills, J. G. 1975, AJ, 80, 809

—. 1988, Nature, 331, 687

Hoang, B.-M., Naoz, S., Kocsis, B., Rasio, F. A., & Dosopoulou, F. 2018, ApJ, 856, 140

Hopman, C., & Alexander, T. 2006, ApJ, 645, 1152

Horvat, M., Conroy, K. E., Pablo, H., et al. 2018, ApJS, 237, 26

Hosek, M. W. J., Lu, J. R., Lam, C. Y., et al. 2020, arXiv, arXiv:2006.06691

Husser, T. O., Wende-von Berg, S., Dreizler, S., et al. 2013, A&A, 553, A6

Ivezić, Ž., Connelly, A. J., VanderPlas, J. T., & Gray, A. 2014, Statistics, Data Mining, and Machine Learning in Astronomy, A Practical Python Guide for the Analysis of Survey Data (Princeton University Press)

—. 2019, Statistics, Data Mining, and Machine Learning in Astronomy, A Practical Python Guide for the Analysis of Survey Data (Princeton University Press)

Jia, S., Lu, J. R., Sakai, S., et al. 2019, ApJ, 873, 9

Kieffer, T. F., & Bogdanovic, T. 2016, ApJ, 823, 155

Kim, S. S., Figer, D. F., & Morris, M. R. 2004, ApJ, 607, L123

Kim, S. S., & Morris, M. R. 2003, ApJ, 597, 312

Koren, S. C., Blake, C. H., Dahn, C. C., & Harris, H. C. 2016, AJ, 151, 57

Kourniotis, M., Bonanos, A. Z., Soszynski, I., et al. 2014, A&A, 562, A125

Lata, S., Pandey, A. K., Panwar, N., et al. 2016, MNRAS, 456, 2505

Lefèvre, L., Marchenko, S. V., Moffat, A. F. J., & Acker, A. 2009, A&A, 507, 1141

Levin, Y., & Beloborodov, A. M. 2003, 590, L33

Li, G., Ginsburg, I., Naoz, S., & Loeb, A. 2017, ApJ, 851, 131

Lomb, N. R. 1976, Astrophysics and Space Science, 39, 447

Lu, J. R., Do, T., Ghez, A. M., Yelda, S., & Matthews, K. 2013, ApJ, 764, 155

Maness, H., Martins, F., Trippe, S., et al. 2007, 669, 1024

Mapelli, M., & Gualandris, A. 2016, Astrophysical Black Holes, 905, 205

Martinez, G. D., Minor, Q. E., Bullock, J., et al. 2011, ApJ, 738, 55

Matsunaga, N., Kawadu, T., Nishiyama, S., et al. 2009, MNRAS, 399, 1709

Matsunaga, N., Fukushi, H., Nakada, Y., et al. 2006, MNRAS, 370, 1979

Mattei, J. A. 1997, The Journal of the American Association of Variable Star Observers, 25, 57

Matthews, K., Ghez, A. M., Weinberger, A. J., & Neugebauer, G. 1996, PASP, 108, 615

McCormac, J., Skillen, I., Pollacco, D., et al. 2014, MNRAS, 438, 3383

Miralda-Escudé, J., & Gould, A. 2000, ApJ, 545, 847

Moe, M., & Di Stefano, R. 2013, ApJ, 778, 95

—. 2015, ApJ, 810, 61

Morris, M. R. 1993, ApJ, 408, 496

Morris, M. R., & Maillard, J. P. 2000, in Imaging the Universe in Three Dimensions. Proceedings from ASP Conference Vol. 195. Edited by W. van Breugel and J. Bland-Hawthorn. ISBN: 1-58381-022-6 (2000), 196–

Morris, M. R., Zhao, J.-H., & Goss, W. M. 2017, ApJL, 850, L23

Muzic, K., Eckart, A., Schödel, R., Meyer, L., & Zensus, A. 2007, A&A, 469, 993

Naoz, S., Ghez, A. M., Hees, A., et al. 2018, ApJL, 853, L24

Nascimbeni, V., Bedin, L. R., Heggie, D. C., et al. 2014, MNRAS, 442, 2381

Nayakshin, S., & Cuadra, J. 2005, A&A, 437, 437

Nicholls, C. P., Wood, P. R., & Cioni, M. R. L. 2010, MNRAS, 405, 1770

Nogueras-Lara, F., Gallego-Calvente, A. T., Dong, H., et al. 2018, A&A, 610, A83

Nogueras-Lara, F., Schödel, R., Gallego-Calvente, A. T., et al. 2020, NatAs, 4, 377

Ott, T., Eckart, A., & Genzel, R. 1999, 523, 248

Paumard, T., Maillard, J. P., & Morris, M. R. 2004, A&A, 426, 81

Paumard, T., Maillard, J. P., Morris, M. R., & Rigaut, F. 2001, A&A, 366, 466

Paumard, T., Genzel, R., Martins, F., et al. 2006, ApJ, 643, 1011

Peeples, M. S., Stanek, K. Z., & Depoy, D. L. 2007, AcAau, 57, 173

Perets, H. B., & Mastrobuono-Battisti, A. 2014, ApJL, 784, L44

Pfuhl, O., Alexander, T., Gillessen, S., et al. 2014, 782, 101

Pfuhl, O., Fritz, T. K., Zilka, M., et al. 2011, 741, 108

Pietrzyński, G., Graczyk, D., Gieren, W., et al. 2013, Nature, 495, 76

Press, W. H., & Rybicki, G. B. 1989, ApJ, 338, 277

Prša, A., Conroy, K. E., Horvat, M., et al. 2016, ApJS, 227, 29

Rafelski, M., Ghez, A. M., Hornstein, S. D., Lu, J. R., & Morris, M. R. 2007, ApJ, 659, 1241

Raghavan, D., McAlister, H. A., Henry, T. J., et al. 2010, The Astrophysical Journal Supplement, 190, 1

Rice, T. S., Reipurth, B., Wolk, S. J., Vaz, L. P., & Cross, N. J. G. 2015, AJ, 150, 132

Rice, T. S., Wolk, S. J., & Aspin, C. 2012, 755, 65

Riebel, D., Meixner, M., Fraser, O., et al. 2010, ApJ, 723, 1195

Rose, S. C., Naoz, S., Gautam, A. K., et al. 2020, arXiv, arXiv:2008.06512

Sakai, S., Lu, J. R., Ghez, A., et al. 2019, ApJ, 873, 65

Sana, H., de Mink, S. E., de Koter, A., et al. 2012, Sci, 337, 444

Scargle, J. D. 1982, ApJ, 263, 835

Schödel, R., Merritt, D., & Eckart, A. 2009, A&A, 502, 91

Schödel, R., Najarro, F., Muzic, K., & Eckart, A. 2010, A&A, 511, A18

Scoville, N. Z., Stolovy, S. R., Rieke, M., Christopher, M., & Yusef-Zadeh, F. 2003, ApJ, 594, 294

Service, M., Lu, J. R., Campbell, R., et al. 2016, PASP, 128, 095004

Sokolovsky, K. V., Gavras, P., Karampelas, A., et al. 2017, MNRAS, 464, 274

Stephan, A. P., Naoz, S., Ghez, A. M., et al. 2016, MNRAS, 460, 3494

—. 2019, ApJ, 878, 58

Stolte, A., Ghez, A. M., Morris, M. R., et al. 2008, ApJ, 675, 1278

Støstad, M., Do, T., Murray, N., et al. 2015, ApJ, 808, 106

Tamura, M., Werner, M. W., Becklin, E. E., & Phinney, E. S. 1996, Astrophysical Journal v.467, 467, 645

Tanner, A., Ghez, A. M., Morris, M. R., et al. 2002, ApJ, 575, 860

Tremaine, S. D., Ostriker, J. P., & Spitzer, L. J. 1975, ApJ, 196, 407

VanderPlas, J., Naul, B., Willmer, A., Williams, P., & Morris, B. M. 2016, gatspy: Version 0.3 Feature Release, vv0.3, Zenodo, doi:10.5281/zenodo.593200. https://doi.org/10.5281/zenodo.593200

VanderPlas, J. T. 2018, ApJS, 236, 16

VanderPlas, J. T., & Ivezić, Ž. 2015, ApJ, 812, 18

Viehmann, T., Eckart, A., Schödel, R., et al. 2005, A&A, 433, 117

Wizinowich, P., Acton, D. S., Shelton, C., et al. 2000, The Publications of the Astronomical Society of the Pacific, 112, 315

Wolk, S. J., Rice, T. S., & Aspin, C. 2013, 773, 145

Wood, P. R., Alcock, C., Allsman, R. A., et al. 1999, Asymptotic Giant Branch Stars, 191, 151

Yelda, S., Ghez, A. M., Lu, J. R., et al. 2014, 783, 131

Yelda, S., Lu, J. R., Ghez, A. M., et al. 2010, ApJ, 725, 331

Yu, Q., Lu, Y., & Lin, D. N. C. 2007, ApJ, 666, 919

Yu, Q., & Tremaine, S. 2003, ApJ, 599, 1129

Yusef-Zadeh, F., Roberts, D. A., & Biretta, J. 1998, ApJ, 499, L159

Yusef-Zadeh, F., Wardle, M., Cotton, W., et al. 2017, ApJ, 837, 93

Zhao, J.-H., & Goss, W. M. 1998, ApJ, 499, L163